

Proceedings

2nd Conference on Engine Processes
July 02 - 03, 2015, Berlin

In association with



Marc Sens | Roland Baar (eds.)

**2nd Conference on Engine Processes
Proceedings**

July 2–3, 2015
Berlin

Universitätsverlag der TU Berlin

Bibliographic information published by the Deutsche Nationalbibliothek

The Deutsche Nationalbibliothek lists this publication in the Deutsche Nationalbibliografie; detailed bibliographic data are available in the Internet at <http://dnb.dnb.de>.

Universitätsverlag der TU Berlin, 2015

<http://verlag.tu-berlin.de>

Fasanenstr. 88, 10623 Berlin

Tel.: +49 (0)30 314 76131 / Fax: -76133

E-Mail: publikationen@ub.tu-berlin.de

License: This work – except for quotes, figures and where otherwise noted – is licensed under the Creative Commons License CC BY 3.0 DE

<http://creativecommons.org/licenses/by-sa/3.0/de/>

Layout and cover picture: IAV GmbH Ingenieurgesellschaft Auto und Verkehr

ISBN 978-3-7983-2768-9 (online)

Published online on the Digital Repository of the Technische Universität Berlin:

URN [urn:nbn:de:kobv:83-opus4-66261](https://nbn-resolving.org/urn:nbn:de:kobv:83-opus4-66261)

<http://nbn-resolving.de/urn:nbn:de:kobv:83-opus4-66261>

Content

SuperGen – A Novel Low Cost Electro-Mechanical Mild Hybrid and Boosting System for Engine Efficiency Enhancements

Jason King, Luke Barker, John Martin, James Turner..... 6

Experimental Modelling of Adiabatic Turbocharger Conditions to Investigate the isentropic Turbine Efficiency

Roland Baar, Clemens Biet, Rainer Zimmermann..... 18

Transient Simulation of Nitrogen Oxide Emissions of CI Engines

Benjamin Kaal, Massimiliano Sosio, Michael Grill, Michael Bargende 30

Physical modeling of combustion for diesel engines and assessment of a NO_x-kinetic for gasoline, gas and diesel engines

Reza Rezaei, Friedrich Dinkelacker, Benjamin Tilch, Thaddäus Delebinski, Maximilian Brauer..... 59

Drive-E Petrol Combustion System Design

Roy Ogink..... 76

The analysis of flame propagation and temperature distribution in combustion process in dual injector SIDI engine

Krzysztof Wiśłocki, Ireneusz Pielecha, Przemysław Borowski, Wojciech Bueschke, Wojciech Cieślík, Maciej Skowron 88

Efficiency Benefits of Optimising Downsized Boosted Engines for High Octane Fuel

Ben Leach, Richard Pearson, John Williams, Rana Ali 101

Fuel Requirements in a Downsized, Highly Boosted DISI Engine

Roger Cracknell, Sam Akehurst, Sarah Remmert, Andrew Lewis, Karl Giles, Rishin Patel, Andrew Popplewell, James Turner..... 116

**Optical analysis of combustion chamber and fuel spray interaction
in terms of chamber geometry modification and
injection parameters change**

Krzysztof Wiślocki, Ireneusz Pielecha, Przemysław Borowski,
Wojciech Bueschke, Wojciech Cieślík, Maciej Skowron 127

**Nozzle geometry impact on spray, ignition and combustion of
large fuel injection jets**

Fabian Pinkert, Ibrahim Najar, Martin Drescher,
Christian Fink, Horst Harndorf 140

**Influence of the spray hole geometries on cavitation formation
inside diesel injector nozzles**

Hauke Hansen, Sven Jollet, Dirk Niemeyer, Lennart Thimm,
Friedrich Dinkelacker 158

**Simulation of auto-ignition behaviour for varying gasoline engine
operating conditions**

Karl Georg Stapf, Benjamin Reis 169

**Investigations of Diesel Spray structure using
Spray Momentum Measurements and link to injector performance**

Gavin Dober, Christophe Garsi, Noureddine Guerrassi, Thomas Leonard 182

**Development of an optical sensor for determination of
swirl level in diesel engines**

Robin Vanhaelst, Jakub Czajka 196

Diesel Engine Performance Mapping Using the Stochastic Reactor Model

Michał Pasternak, Andrea Matrisciano, Fabian Mauß 217

Modeling of Spray Combustion under Diesel Engine Conditions

Harry Lehtiniemi, Anders Borg, Fabian Mauß 233

**Experimental investigations of a dual-fuel combustion system
for passenger car Diesel engines with gasoline and Diesel fuel**

Benedikt Heuser, Florian Kremer, Stefan Pischinger, Hans Rohs,
Bastian Holderbaum, Thomas Körfer, Christof Schernus 250

**Investigation of the Combustion Process of a Small Direct Injection Spark
Ignition Engine**

Arne Siedentop, Jörn Schech, Andreas Bradenstahl, Peter Eilts 274

**Zero-Dimensional Analysis of Spark Ignition Engines with High Variability
under Transient Conditions**

Thorben Walder, André Casal Kulzer, Michael Bargende 299

**Real-time Capable 1-D Engine Simulation Model with the Fast Fourier
Transformation (FFT) Concept**

Aras Mirfendreski, Andreas Schmid, Michael Grill,
Immanuel Kutschera, Michael Bargende 326

Simulation of heat transfer with variation of the operating conditions

Volker Zeitz, Patrick Varga, Hermann Rottengruber, Helmut Tschöke,
Jürgen Schmidt..... 339

**The Benefits of an Exhaust-gas Heat-recovery Unit – The Inverted Brayton
Cycle**

Colin Copland, Zhihang Chen..... 357

**Using 1D simulations to optimize a supercharger for a
twin charged DI gasoline engine**

Ragnar Burenus..... 372

SuperGen – A Novel Low Cost Electro-Mechanical Mild Hybrid and Boosting System for Engine Efficiency Enhancements

Jason King
Luke Barker
John Martin
James Turner

Abstract

SuperGen is a Belt Integrated Starter Generator (B-ISG) combined with a novel electro-mechanical power split transmission system providing variable speed centrifugal supercharger capability, all in one compact package. This paper initially discusses the analysis of SuperGen's application to a gasoline SUV in order to examine the B-ISG power and voltage mild hybrid functionality trade-off versus fuel consumption reduction on drive cycle. A significant engine down speeding was also applied based on the low speed torque enhancement afforded by SuperGen's boosting capability, both transiently, and sustainably at steady state engine operation. This has been demonstrated and reported on the well-published Jaguar Land Rover (JLR) Ultraboost project. Finally, the part load "boost-on-demand" was used to evaluate advanced combustion modes not easily achievable with conventional turbocharger technology, namely; aggressive Miller cycle with early inlet valve closing; EGR diluted stoichiometric homogenous operation and un-throttled lean stratified combustion.

1. Introduction

Engine downsizing has been clearly demonstrated as a way to improve vehicle fuel consumption. While the level of fuel economy improvement from a downsizing strategy can be readily estimated [2], the actual ability to successfully downsize any spark ignited engine is subject to several limiting factors, the most important of which are the ability to resist abnormal combustion, and the capability of the charging system to supply the required air at the necessary response rate. During the 'Ultraboost' project [1] it was reported that a downsizing factor of 60% could be realized over an advanced large-capacity naturally-aspirated engine, but the key challenge was the engines air delivery system; SuperGen variable-speed centrifugal supercharger was tested on this engine and proved capable of meeting many of the very challenging boosting system requirements [3]. Also highlighted from the Ultraboost testing, but not evaluated during this work, was the potential mild hybrid capability of Supergen.

The mass-market advancement of hybrid vehicles still requires significant reduction in product cost. Recent analysis by many credible sources, including OEM's, indicates that current hybrid cars offer only marginal Total Cost of Ownership savings unless these cost reductions are realized. The analysis also continues to indicate that deploying lower cost technologies across a large number of vehicles remains more cost-effective than deploying costly technology to a few. State-of-the-art stop/start micro hybrid B-ISG systems and boosting, both of which will become ubiquitous in advanced passenger cars, offer the best value route to lower fleet CO₂. SuperGen provides micro hybrid functionality (as well as replacement of the alternator charging function to support base vehicle electrical loads), however, by linking both electric Motor-Generator Units (MGU) within the device together, significant mild hybrid braking energy recuperation and torque assist is enabled. SuperGen is fundamentally voltage agnostic, with mild hybridization being applied at either 12V or 48V, but due to energy storage medium technology and limitations such as peak charge and discharge currents applied power levels are naturally higher with higher system voltages, as are costs.

Finally, considerable research is being undertaken within the industry to re-visit advanced gasoline combustion technologies in the drive for better fuel consumption. Miller cycle, as defined as with boosting and late or early inlet valve closing, is being looked at as an enabler to raise the geometric compression ratio (CR) of gasoline engines for part load cycle efficiency gains. The next logical step is to add diluent, through excess air and / or EGR, whilst maintaining a homogenous mixture, for reduced throttling and heat losses, with a final step to fully un-throttled lean stratified combustion. The combination of the above have the requirements for increased peak pressure ratio, excellent boost response, and the most challenging requirement to provide boost at a part load condition with low exhaust enthalpy – SuperGen can meet these requirements.

2. The SuperGen System

SuperGen uses an electro-mechanical power-split transmission system to provide an 'on-demand' boosting system in addition to the potential hybrid capabilities. From the boosting side it is primarily intended to be used in series with a turbocharger for both gasoline and diesel engines, giving similar map width to series turbocharger systems whilst improving transient response. It can also be used as the sole boosting device on less aggressively boosted engines. The electrical transmission path provides response, controllability and refinement, and the parallel mechanical path greatly reduces the size and cost of the electrical components necessary to produce the boosting range while increasing efficiency and enabling steady-state, charge-neutral operation. It also functions as an alternator replacement, as can be seen in figure 1, thus facilitating packaging in a wide range of applications, and when equipped with appropriate internal clutches, a Belt Integrated Starter (B-ISG) providing stop-start and mild hybrid functionality too, all whilst only requiring a 12V electrical architecture in the vehicle.

2.1 System Overview

Figure 2 shows the major internal component layout of SuperGen. Power is inputted to a pulley (1) via a drive from the crankshaft. The input shaft carries the rotor (2) of electrical machine E1 and drives the annulus of an epicyclic traction-drive gearset (4). The rotor (5) of a second electrical machine (E2) is connected to the planet carrier of the gearset (4) and is supported on bearings (6). The sun shaft of the gearset passes through the centre of the rotor (5) and is connected to a radial flow impeller (7). The device is plumbed into the engine water charge air cooling system (9) for cooling. The motors are permanent magnet (PM) devices.



Figure 1: Typical SuperGen installation on engine

SuperGen varies the drive ratio between the FEAD pulley and the compressor by using the power split enabled by the traction drive and two electric machines. Power can be transmitted via two paths (mechanical and electrical), and recombined in order to decouple the speed of the compressor from that of the crankshaft, as described in more detail below.

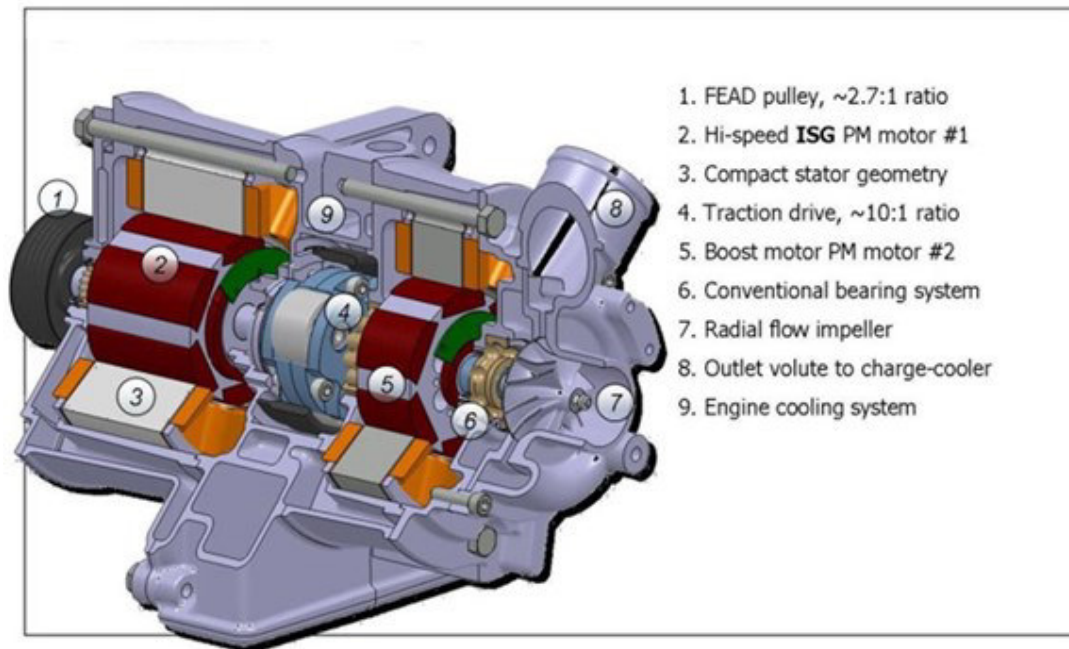


Figure 2: SuperGen system cutaway (illustration purposes only)

The PM motors are controlled by integrated 14V inverters which are connected directly to the vehicle board-net eliminating any requirement for a DC-DC converter or higher voltage energy storage. In higher voltage SuperGen applications a DC-DC converter would be included to allow energy to be sent from the SuperGen device to the vehicle low-voltage electrical systems.

The combined power of the two machines can be greater than 8 kW at 14V, and considerably higher at increased voltage, and thus as mentioned above, by combining the output of both PM machines micro and mild hybrid functions including B-ISG stop-start, electrical recuperation and boost for next generation mild hybridization applications.

2.1.1 Principle of power-split system functionality

The power delivery to the compressor sun shaft can be achieved simultaneously by both pure mechanical means and by transferring power between E1 and E2 (in either direction). This enables full control over the compressor speed whilst requiring only 20% of the electrical power of an equivalent e-booster system.

The power-split system enables the compressor speed to be continuously and accurately matched to boosting requirements of an engine without the need for clutches, recirculation or throttle valves (Figure 3). When no boost is required, parasitic losses are low as the complete traction drive and compressor rotate at pulley speed.

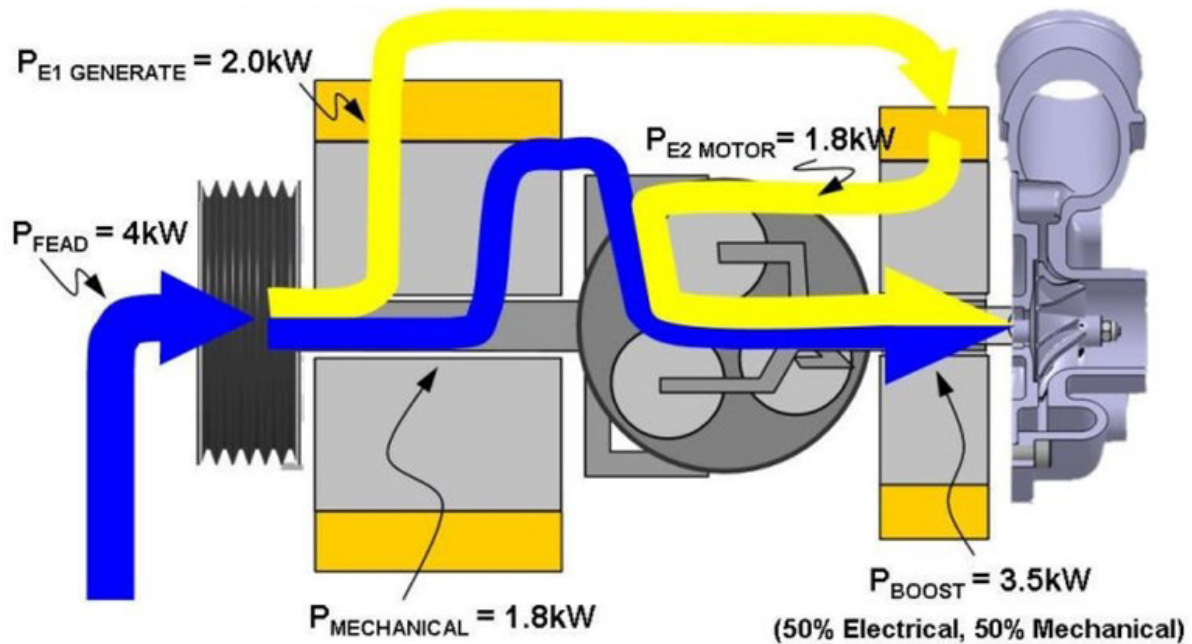


Figure 3: Power-split electro-mechanical transmission system

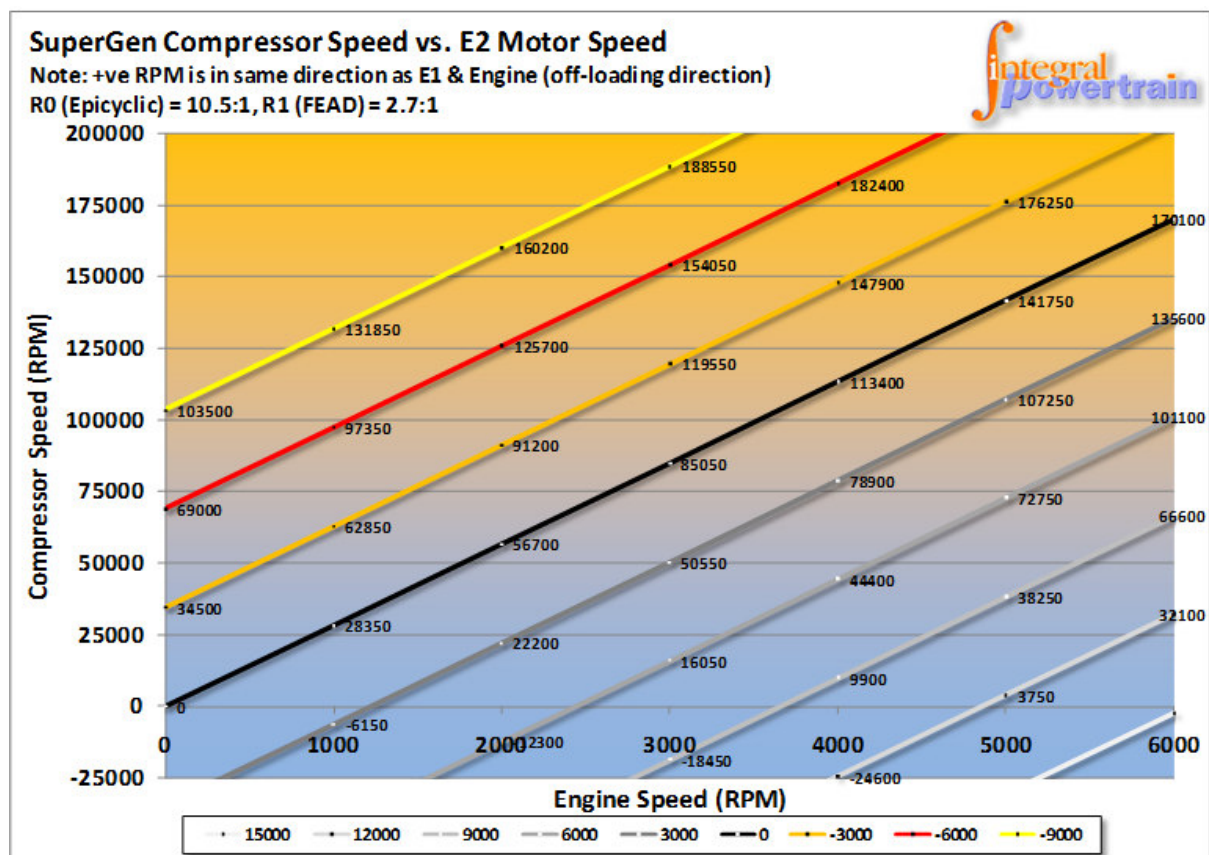


Figure 4: Typical compressor speed map for SuperGen

2.2 Boost control philosophy

During the transient work undertaken on the 'Ultraboost' project [1], some of which is presented here, boost was controlled from SuperGen by demanding a plenum pressure and using the device to make up the difference between the target boost pressure and what the turbocharger could supply. A simple "open or closed" bypass system was also fitted in parallel to SuperGen, and was closed during this time. When SuperGen was not required to operate, the bypass was opened to minimise pumping losses and the device was idled. The variable-ratio characteristic means that this control system can be used across the engine speed and load range and so provide seamless blending of the two pressure-charging stages.

3. Simulation Overview

In order to examine the potential benefits of SuperGen boosting and hybridization capability, a baseline vehicle with correlated fuel consumption data, as measured over the NEDC, was selected, and the specification of this is shown below:

- SUV, 2017MY Baseline Vehicle
- ~1750kg Kerb Weight
- 0.36CD, 2.6m²
- Baseline 2.0L DI VVT W/G T/C ~100kW/L
- 8/9-speed Transmission
- Stop-start as standard
- NEDC Cycle
- Baseline simulation result = 163g/km
 - Correlates <1% of OEM in-house simulation
 - Compared to ~220g/km for previous generation with ~3.5L V6 ('past-baseline')

The SuperGen system was added to 2.0L baseline in a 2-stage Turbo-SuperGen with the device in the high-pressure (HP) position after low-pressure (LP) turbocharger, as shown in figure 5.

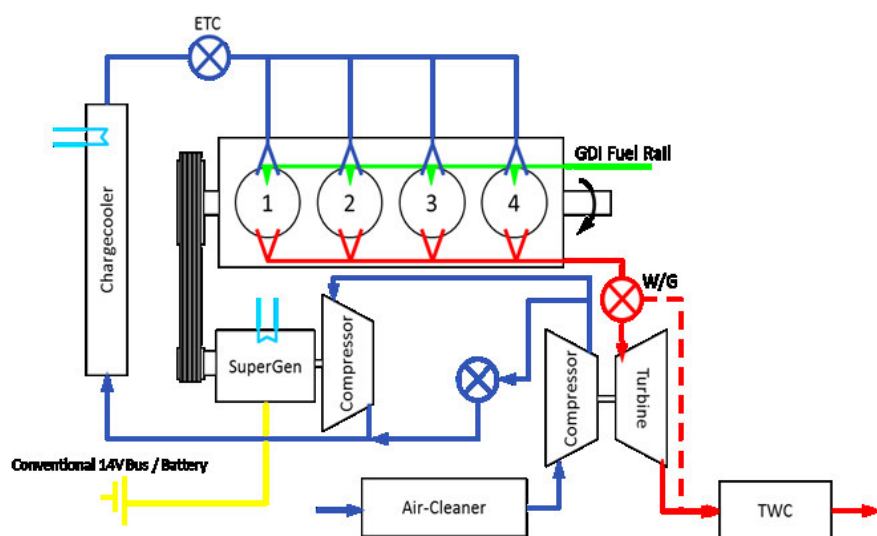


Figure 5: Schematic of air flow path for SuperGen charging system

The analysis conducted to investigate SuperGen benefits were undertaken in the following order:

- Stop-start as per baseline system; no change to CO₂ but more refined starting (often a 1 – 2% benefit can be derived from faster start and revised starting strategies). Anti-stall functionality also from device (not simulated)
- Boosting system is independent of the vehicle battery (self-sustaining) and unaffected by a depleted battery - capable of continuous operation of up to 15 kW boost at 12 V, allowing increased down-speeding of 20% as per demo-car experience & simulation
- Mild hybridization with maximum brake energy recuperation between 4 and 17 kW depending on version (potential advanced modes such as sailing not included)
- New combustion strategies (i.e. Miller, Lean-Homogenous, Stratified-Lean Burn)
- Increased down-sizing as per the Ultraboost engine, demo-car experience & simulation

4. Test Results

A summary of the analysis results covering the down-speeding and mild hybrid effects can be seen in figure 6 below.

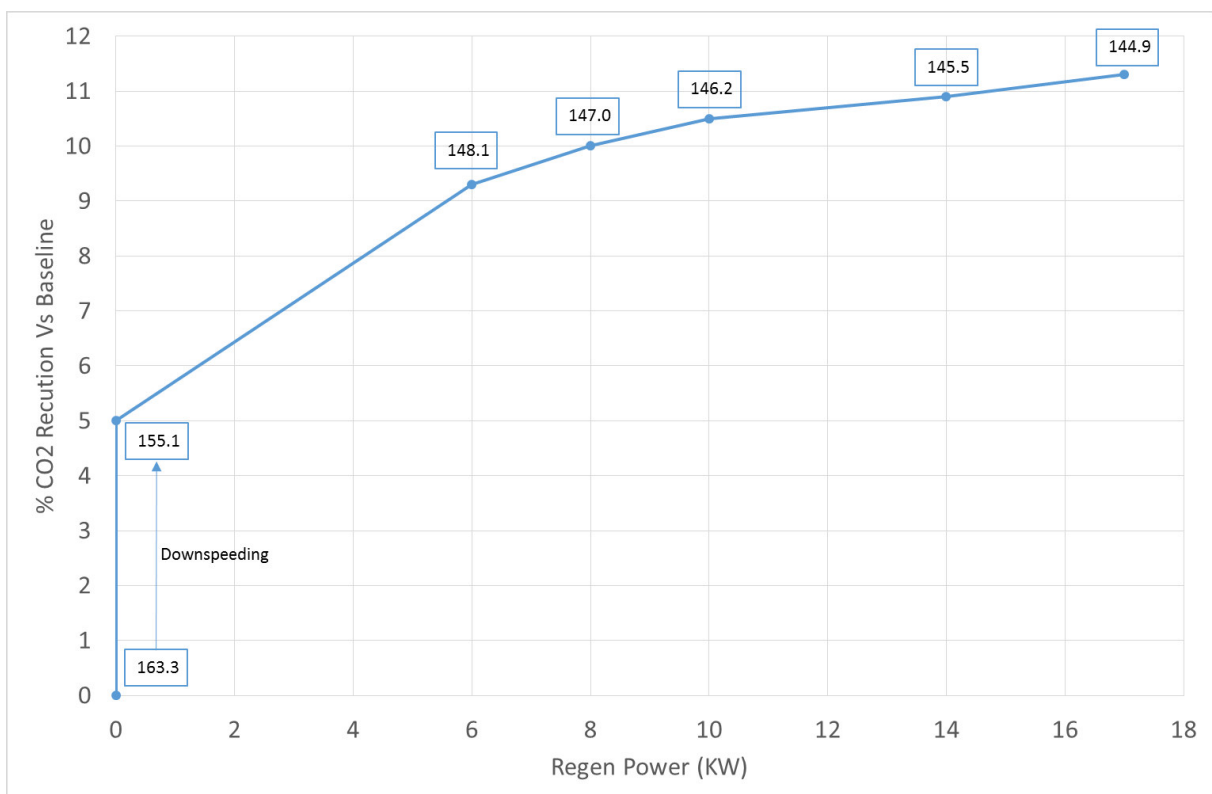


Figure 6: Simulated engine down-speeding and mild hybridization benefits

4.1 Base Engine Results

The mild hybrid energy recuperation and torque assist of 6 kW at 12 - 14V showed a CO₂ benefit of 7g/km (4.3%) in addition to the 20% down speeding improvement of 8.2g/km (5%) on cycle; this benefit was taken forward for all other investigations. From figure 6 it can additionally be seen that further reductions with increased power capability are limited by available energy after road-load, aerodynamic drag, engine friction and other driveline drag losses. The re-gen versus CO₂ benefit gave the following as shown in figure 6; 8kW and 8.1g/km (5.0%), 10kW and 8.9g/km (5.5%), 14kW and 9.6g/km (5.9%), 17kW and 10.2g/km (6.2%). In summary, a 14V SuperGen on 'standard' 2.0L engine showed potential benefits up to -10.5% CO₂ or +12% mpg on cycle.

4.2 Advanced Combustion System Simulation Results

Utilisation of Miller-cycle and/or advanced charge motion and full load Wide Open Throttle (WOT) EGR to extend knock limit enables a potential significant increase in CR. Likewise, adding part load diluent in the form of excess air or EGR to reduce pumping and heat-rejection losses will further increase engine efficiency provided combustion efficiency can be maintained. Most strategies are not suited to pure turbocharged systems due to the conflict between available exhaust enthalpy, compressor and turbine match and combustion requirements. Using a simplified model of the benefits based on in-house and public domain data, Miller cycle with increased compression ratio and three-way catalyst was approximated at ~5% reduction in CO₂, dilute-homogenous mode with EGR dilution and Lambda of 1 at ~8%, and lean-stratified mode with EGR and air dilution operation (LNT required for highest gains) at ~12%. Table 1 shows that when combining the down-speeding and regen benefits it could be possible to attain between a 15-22% overall reduction in CO₂.

2017MY SUV NEDC Cycle CO ₂ - SuperGen Simulation Results			Cycle g/km				% Reduction g/km			
Simulation Run-Case *Note: All except baselines are for Turbo (LP) + SuperGen (HP)	Specification Notes	Regen Power	Baseline Vehicle	Miller-Cycle / $\lambda=1$ (TWC), 5% Benefit	Miller-Cycle / Stratified-Homogenous $\lambda=1$ (TWC), 8% Benefit	Miller-Cycle / Stratified-Lean (TWC+LNT), 12-15% Benefit	Baseline Vehicle	Miller-Cycle / $\lambda=1$ (TWC), 5% Benefit	Miller-Cycle / Stratified-Homogenous $\lambda=1$ (TWC), 8% Benefit	Miller-Cycle / Stratified-Lean (TWC+LNT), 12-15% Benefit
Past Baseline Vehicle	3.5L V-6 Naturally Aspirated	kW	222.0	212.0	204.0	195.8	-35.9%	-29.8%	-24.9%	-19.9%
Baseline Vehicle	Baseline 2.0L T/C FGT	0	163.3	155.7	149.7	144.0	0.0%	4.7%	8.3%	11.8%
Down-speeding 20%	Down-speeding 20%	0	155.1	147.8	142.1	136.7	5.0%	9.5%	13.0%	16.3%
VV-Type	6kW Regen	6	148.1	141.2	135.7	130.6	9.3%	13.5%	16.9%	20.0%
V-Type	8kW Regen	8	147.0	140.2	134.7	129.7	10.0%	14.1%	17.5%	20.6%
P-Type	10kW Regen	10	146.2	139.4	133.9	128.9	10.5%	14.6%	18.0%	21.1%
V-Type 48V	14kW Regen (48V)	14	145.5	138.7	133.3	128.3	10.9%	15.1%	18.4%	21.4%
P-Type 48V	17kW Regen (48V)	17	144.9	138.2	132.8	127.8	11.3%	15.4%	18.7%	21.7%
Composite with 20% D/Size	Downsizing to 1.6L T/C with 20% DSpd & 10kW regen	10	137.1	130.7	125.6	120.9	16.0%	20.0%	23.1%	26.0%

Table 1: Summary of simulation results

4.3 Future Stretch Opportunity to Down Sizing to >130kW/L

Results from the Ultraboost and other projects have indicated potential to down-size to over 130kW/L whilst still maintaining excellent transient response and high levels of Brake Mean Effective Pressure, even from low engine speed. From table 1 it can be seen that down-sizing to 1.6L versus the baseline 2.0L reduces CO₂ by further 9g/km (5%).

Figure 7 shows an example of the low-speed full-load performance based on the gasoline 2.0L 4 cylinder Ultraboost research engine with SuperGen and the original Ultraboost UB200 [1] Eaton R410 supercharger and turbocharger version of the engine (same turbocharger carried over) versus the target production JLR AJ133 5 litre V8 torque curve [3]. When operating with SuperGen the target torque curve was matched from 1250 rpm and it also enabled a significant increase in performance at 1000 rpm over the UB200: at this speed, the torque for the UB200 build [1] was 283 Nm (17.8 bar BMEP), whereas the SuperGen maximum performance was 358 Nm (22.5 bar BMEP). Thus while the full-load target has still not been fully met, the improvement is very significant at 26.5%. This represents a shortfall of only 10.5% versus the AJ133 target of 400 Nm (the UB200 specification having missed the target by 29.3% at this speed). While operating the engine, it was found to be quite straightforward to exceed the Ultraboost target curve at 1500 rpm and above.

Figure 8 shows the Ultraboost engine transient torque curve response at 2500 rpm with and without SuperGen being operated. Clearly the turbocharger sizing is overly large for various reasons, but the effect of SuperGen is highlighted even more and brings the 10 to 90% time-to-torque (TTT) target to less than 1.2 seconds. With some optimisation and more appropriate sizing of the turbocharger it would be expected that the 10-90 TTT would be reduced to well under 0.7 seconds, as demonstrated on other SuperGen projects. Note that in these early tests the full-load torque target of 478 Nm was readily overshoot: the maximum point is 506 Nm.

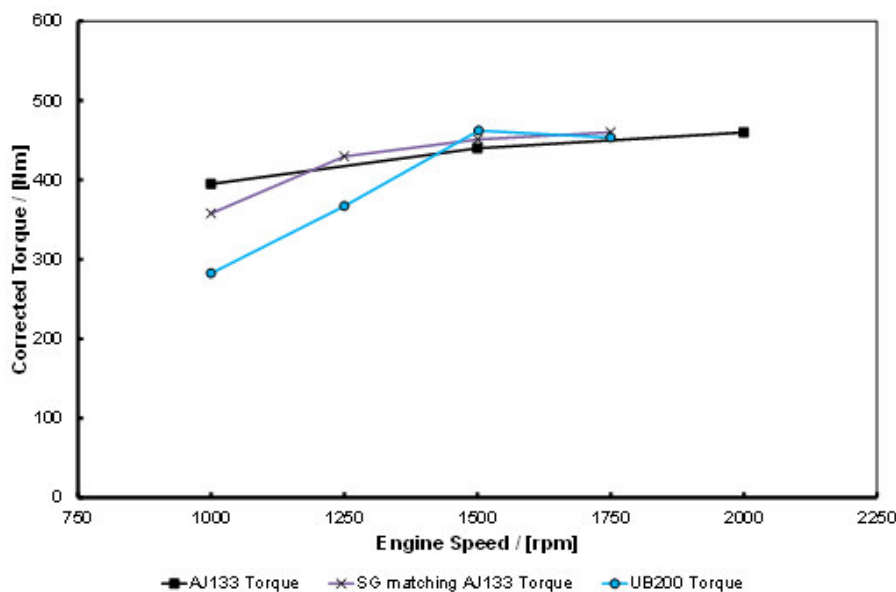


Figure 7: Full load SuperGen performance on the Ultraboost engine Vs the equivalent part of the AJ133 target torque curve and original Eaton Supercharged Specification

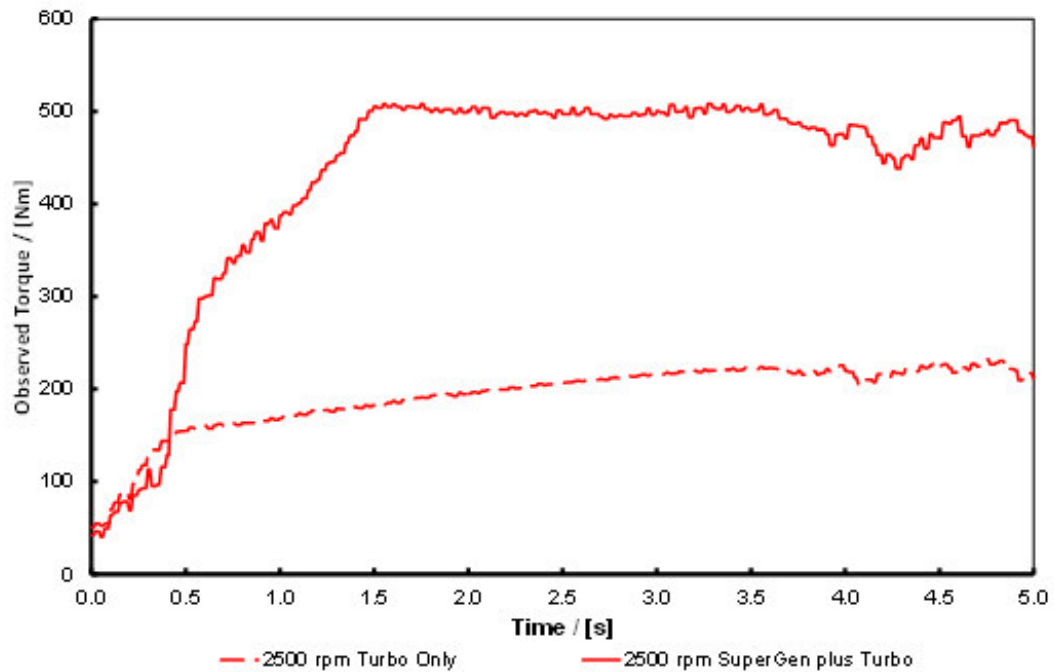


Figure 8: Ultraboost transient performance of turbo only vs SuperGen plus turbo

5. Discussion

The transient response and low speed torque augmentation from Supergen, enabled through its sustained boosting capability, enables aggressive down-speeding and downsizing. The results showed that the majority of the total fuel consumption improvements came from this, especially when combined with the engine efficiency enhancements from advanced combustion strategies. The mild hybrid energy recuperation and torque assist results showed that the majority of this benefit could be achieved at only 12V. Cost implications of 48V included an additional battery on the vehicle plus the requirement for a DC-DC converter also, so the 12V option gives the best CO₂ to cost trade-off by some margin, and the functionality comes “for free” in the device itself, but will require an enhanced 12V energy storage medium to maximise benefit.

Miller cycle with early IVC, enabled through the high boosting capability of SuperGen in series with a LP turbocharger, plus advanced charge motion and WOT EGR to extend knocking limits, meant that the compression ratio was increased resulting in an simulated 5% cycle efficiency benefit at part load. Whilst geometrical design constraints would struggle to allow such a high compression ratio, part load dilute homogenous operation, using low pressure EGR as the diluent to maintain lambda 1 air fuel ratio, with an advanced ignition system (such as corona discharge) plus high charge motion chamber in order to tolerate the high percentages of diluent without significant detriment to burn duration has been demonstrated. When combined with some of the cycle efficiency gains feasible with Miller cycle, a predicted 8% improvement in CO₂ was considered reasonable. The three benefits of cycle efficiency, reduced pumping, and reduced heat losses are at a maximum with lean stratified engine operation, assuming combustion efficiency degradation can be minimised, and

this was estimated at 12% when allowing for the FC penalty associated with LNT re-generation.

In the last two cases, diluent mass flow and pressure ratio control, partly independent of engine speed and load, and more importantly, turbocharger performance with the reduced exhaust enthalpy, were considered to require a boosting device such as SuperGen in order to properly enable these strategies with consideration for also maximising full load engine performance. Finally, the capability of SuperGen to achieve high full load requirements and excellent transient response has been demonstrated and published on the Ultraboost project. In summary, a 14V SuperGen with conventional engine can deliver up to -16% CO₂, +19% on mpg, but by applying an advanced combustion system this extends to -26% CO₂ or +35% on mpg.

6. Conclusions

- SuperGen can provide class leading mild hybrid capability with peak recuperation power potentially approaching 20 kW
- However, due to the cost versus capability / life of the energy storage mediums required for optimum mild hybrid performance, the best £/CO₂ trade-off is achieved at 12V
- SuperGen as a boosting system with class leading response and sustainable, continuous operation compressor powers beyond any pure eBooster system
- The boosting capability enables extreme downsizing and downspeeding of both gasoline and Diesel engines
- The Ultraboost project has shown that SuperGens ability to improve low-speed torque and transient response may enable downsizing to be taken beyond 60%, with further significant fuel economy potential
- The ability to generate sustained mass flow and pressure ratio largely independent of engine speed and load also enables advanced combustion strategies in gasoline engines for significant thermal efficiency improvements and thus further reductions in fuel consumption

References

- [1] Turner, J.W.G., Popplewell, A., Patel, R., Johnson, T., Darnton, N.J., Richardson, S., Bredda, S.W., Jackson, R., Bithell, C., Tudor, R., Fernandes, J., Remmert, S., Cracknell, R., Lewis, A.G.J., Akehurst, S., Brace, C.J., Copeland, C., Martinez-Botas, R., Romagnoli, A. and Burluka, A.A.; "Ultra Boost for Economy: Extending the Limits of Extreme Engine Downsizing", SAE paper number 2014-01-1185, SAE 2014 World Congress, Detroit, Michigan, USA, 8th-10th April, 2014 and SAE Int. J. Engines 7(1):2014, doi:10.4271/2014-01-1185.
- [2] McAllister, M.J. and Buckley D.J.; "Future gasoline engine downsizing technologies - CO2 improvements and engine design considerations", paper number C684/018, pp. 19-26, Institution of Mechanical Engineers Internal Combustion Engines Conference, London, UK, 8th-9th December, 2009.
- [3] Turner, J. W. G., Popplewell, A., Marshall, D. J., Johnson, T. R., Barker, L., King, J., Martin, J., Lewis, A. G. J., Akehurst, S., Brace, C. J. and Copeland, C. D.; "SuperGen on Ultraboost: Variable-Speed Centrifugal Supercharging as an Enabling Technology for Extreme Engine Downsizing," SAE Int. J. Engines 8(4):2015, doi:10.4271/2015-01-1282.

The Authors:

BEng (Hons), Jason King, Integral Powertrain, Milton Keynes, UK

BEng (Hons), Luke Barker, Integral Powertrain, Milton Keynes, UK

BEng (Hons), John Martin, Integral Powertrain Technology, Milton Keynes, UK

MEng, PhD, CEng, FIMechE, Professor James Turner, University of Bath, UK

Licence:

This document is licensed under the Creative Commons Attribution 3.0 DE License (CC-BY 3.0 DE): <http://creativecommons.org/licenses/by/3.0/de/>

Experimental Modelling of Adiabatic Turbocharger Conditions to Investigate the Isentropic Turbine Efficiency

Roland Baar
Clemens Biet
Rainer Zimmermann

Abstract

Characteristic maps for turbochargers are recorded as a steady state data set from hot gas test benches, which are the common state of the art fundament for engine turbocharger matching and engine process simulation. One problem is the heat transfer within the turbocharger, which is inevitable on standard maps. In this paper an approach to minimize heat transfer within the turbocharger is presented. Additionally, this approach enables the direct determination of the isentropic turbine efficiency. Experimental results for this approach are shown for four turbochargers. Subsequently a criterion to describe the quality of adiabatic measurements is introduced. Finally, this criterion is applied to four different turbochargers under different exhaust gas temperatures.

1. Introduction

The recent development of automotive engines is strongly driven by the concept of downsizing. In this approach, the continuous reduction of fuel consumption requirement is satisfied by reducing the engine displacement as well as increasing the boost pressure in order to accomplish the same power outputs. The turbocharger evolved into an essential component within modern engines. As a result, there is an increasing demand on detailed knowledge of characteristic turbocharger values, one of them being the isentropic turbine efficiency. Complex CFD simulations can supply quite accurate solutions for the aerodynamic and thermodynamic states within a turbocharger, only if detailed design information in form of CAD data is available. Nevertheless, the validation at a test bench is still considered to be an indispensable measure to obtain the required information. The isentropic compressor efficiency can easily be determined by static measurements of the respective pressures, temperatures, and mass flow. However, the measurement of the isentropic turbine efficiency at standard conditions is much more challenging due to the complex flow conditions at the turbine outlet. Consequently, new methods for measuring turbochargers have been developed in order to determine a reliable value for the isentropic turbine efficiency.

2. Problem formulation

The recommendations in SAE J922 and J1826 are widely accepted as reference conditions for measurements in turbocharger test benches. The agreement on these standards, including the recommended turbine inlet temperature of a constant 600 °C, resemble the real world application to a proper degree, which allows the comparison between different turbocharger test benches. As a drawback, it is accepted that the isentropic turbine efficiency cannot be obtained using this measurement setup by applying the following equation, which assumes adiabatic conditions.

$$\eta_{Tis} = \frac{T_3 - T_4}{T_3 - T_{4is}} \quad \text{Eq. 1}$$

There are two major issues causing this problem: Firstly, a reliable measurement of the turbine outlet temperature T_4 with conventional equipment is difficult due to high temperature gradients and complex flow situations. This is described in detail in [11]. Secondly, the significant heat loss, between the measurement planes of turbine inlet and turbine outlet, to the environment as well as the heat transfer within the turbocharger decreases the measured T_4 and thus seemingly increases the isentropic turbine efficiency – at low turbocharger speeds often times even over the value of 1. It is possible to influence the impact of these problems by changing the position of the T_4 sensor. Unfortunately, there is a general trade-off between both problems:

If the sensor is positioned close to the turbine, the heat losses across the measuring pipes can be expected to be small, but the high temperature gradients within the flow cross section prohibit simple temperature measurements. On the other hand, if the sensor is positioned relatively far away from the turbine, the temperature gradients will decrease, but the recorded temperature will not resemble the actual turbine outlet temperature anymore due to significant heat losses prior to the measurement.

In order to avoid this problem, SAE J922 and J1826 suggest obtaining the effective turbine efficiency instead, since this can be calculated without the turbine outlet temperature T_4 by using the turbocharger main equation.

$$P_C = P_T \quad \text{Eq. 2}$$

where

$$P_C = \frac{\dot{m}_C \cdot \Delta h_{Cis}}{\eta_{Cis}} \quad \text{Eq. 3}$$

and

$$P_T = \dot{m}_T \cdot \Delta h_{Tis} \cdot \eta_{Tis} \cdot \eta_{Tm} \quad \text{Eq. 4}$$

This can be transformed to the following equation by assuming that all mechanical losses of the turbocharger are included in the turbine efficiency.

$$\eta_T = \eta_{Tis} \cdot \eta_{Tm} = \frac{1}{\eta_{Cis}} \cdot \frac{\dot{m}_C}{\dot{m}_T} \cdot \frac{\Delta h_{Cis}}{\Delta h_{Tis}} \quad \text{Eq. 5}$$

Therefore, the effective turbine efficiency is the product of the isentropic turbine efficiency and the mechanical efficiency of the turbocharger. As a result, the effective turbine efficiency does not allow distinguishing whether the obtained turbine efficiency values are affected by the friction in the turbocharger bearing or the aerodynamic quality of the turbine.

3. Approach

Since there is a high interest in determining the correct isentropic turbine efficiency, new measuring equipment has been developed and new measuring conditions have been suggested. The first problem can be solved by the use of a mixer between the physical turbine outlet and the actual measurement plane of the turbine outlet temperature as described in [11]. The mixer significantly reduces the temperature gradients within the cross section of the exhaust pipe. This allows conventional sensors to provide a reliable measurement of the gas temperature at that point. At the same time, the heat loss across the measuring pipes will increase while using a mixer. This is caused by an increased surface area for thermal convection which is a result of the long distance between the physical turbine outlet and the actual measurement plane as well as the big surface area from the geometry of the mixer itself. Thus, the application of a mixer can eliminate the first problem while amplifying the second one. A common approach to deal with the second problem is to use “adiabatic measurement conditions”. The probably more correct term should be “minimal diabatic measurement conditions” since the goal is to reduce any heat flows to the lowest possible value. This includes heat flows within the turbocharger, from the turbocharger to the environment or towards other media like the oil supply. However, a complete elimination of all heat transfer is not possible since the two thermodynamic processes of compression and expansion are naturally accompanied by temperature changes. This implies the need for a criterion to underline the validity of equation eq. 5. This paper aims to introduce a new criterion to evaluate the degree of absence of heat flows for these measurements. The used adiabatic measurement condition is:

$$T_2 = T_3 = T_{Oil,mean}$$

Eq. 6

The reason why this condition is often chosen for adiabatic measurements is that it significantly reduces the heat flows within the turbocharger [14]. Figure 1 illustrates that T_2 , T_3 and the oil temperature are primarily responsible for heat flows within the turbocharger housing. This assumption is based on the relatively large areas for heat transfer between the corresponding sections of the turbocharger.

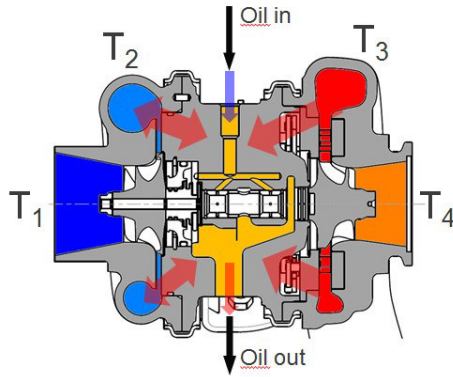


Figure 1: Dominant temperatures within a turbocharger

4. Methods

In this paper, the measurements of four different turbochargers were examined, including both, Waste-Gate and VTG turbine housings. The turbochargers were taken from different suppliers and range from small to medium sizes. All measurements have been performed at the turbocharger test bench at TU Berlin. For each turbocharger, standard measurements according to SAE J922 as well as adiabatic measurements under the earlier stated condition of $T_2 = T_3 = T_{oil}$ have been taken. The turbine outlet temperature was recorded using a mixer and three thermocouples. A photograph of the adiabatic measurement setup is shown in Figure 2.

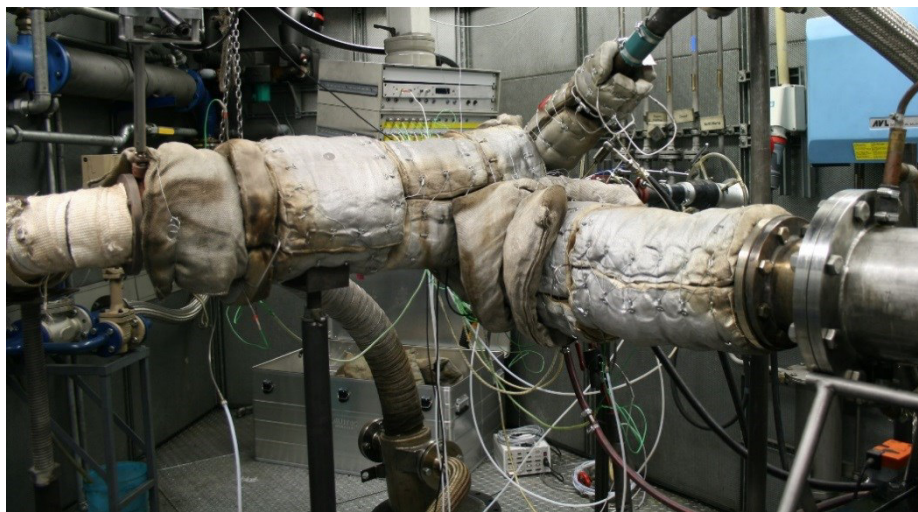


Figure 2: Turbocharger setup in hot gas test bench at the Technical University of Berlin

5. Results

Equations 5 and 1 were used to calculate the effective and the isentropic turbine efficiency for all adiabatic measurements. The results are shown in Figure 3 as a function of the blade speed ratio (u/c_0). This abscissa was chosen to provide a mean to compare the different turbocharger to one another. The plot includes all speed lines of the adiabatic measurements of each turbocharger. For all throughout this paper the turbochargers will be named after the convention given in Figure 3. As expected, η_{Tis} is slightly higher than η_T for all cases. Comparing the isentropic efficiencies with experiences from CFD calculations the values for the isentropic turbine efficiency appear to be in the correct range.

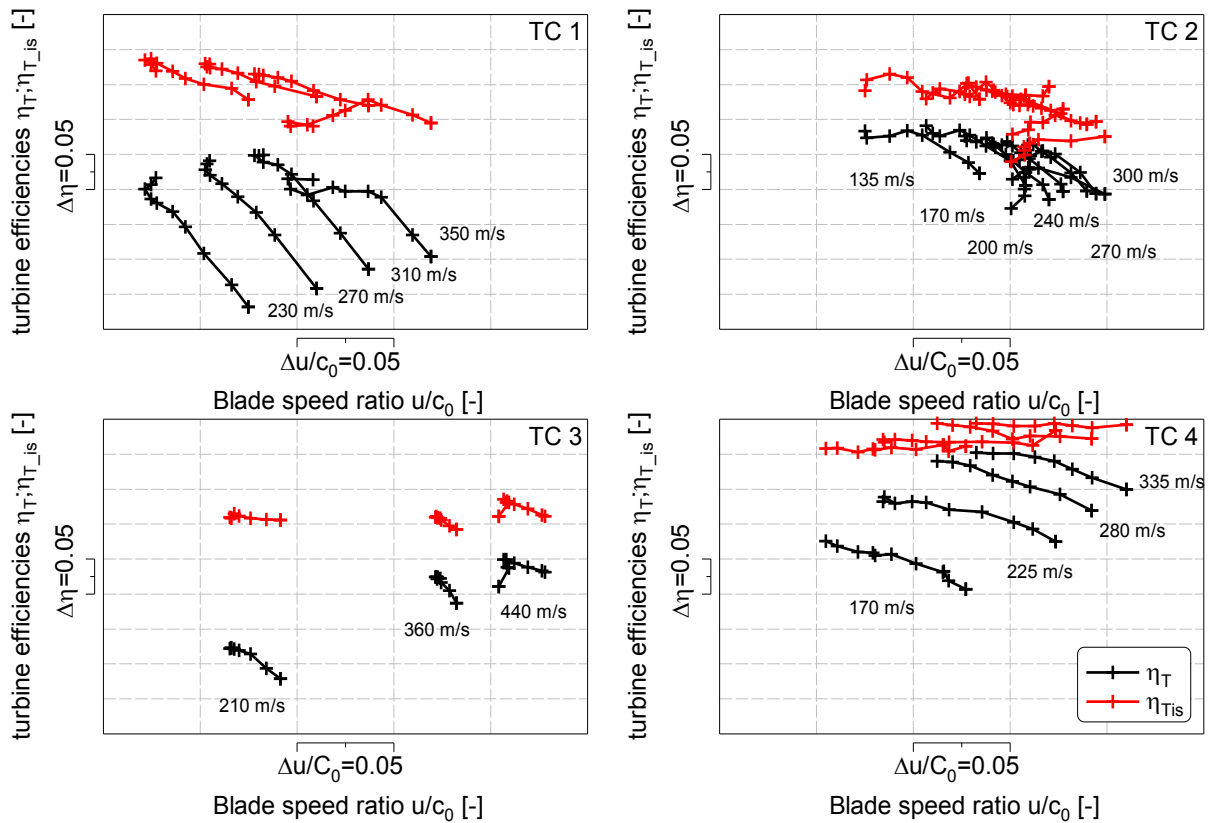


Figure 3: effective and isentropic efficiencies of all investigated turbochargers

It can also be observed that the effective turbine efficiency slightly increases with higher turbine speeds whereas the isentropic turbine efficiency stays at a relatively constant level. As a result, their difference becomes smaller for higher turbocharger speeds. This behaviour can be explained by the assumption that the absolute power of the turbine increases much more rapidly than the losses due to friction within the bearings. Consequently, the relative proportion of the mechanical efficiency decreases which increases the effective turbine efficiency.

6. The new criterion for adiabatic conditions

The measurement campaign under adiabatic conditions led to reasonable isentropic turbine efficiencies, but what is still missing is a possibility to quantify whether the measurement itself was sufficiently adiabatic or not. Already obtaining a possibility to gather adiabatic characteristic turbine maps there is still missing a criterion to determine, if the given measurement fulfills adiabatic conditions to a sufficient level or not. There exist already some approaches to define an adiabatic criterion e.g. the X-criterion developed by IAV Berlin [13].

6.1 Definition

To develop an easy criterion, without detailed knowledge of the turbocharger construction, to determine whether a measurement is adiabatic or not, it is important to decide for a quantity to use for comparing different measurement conditions with each other. In order to achieve this, it is at first necessary to look into the measurement signals, which are given by the turbocharger test bench. The objective is to find a base solely based upon quantities that are reliable. Reliable means in this case, that those quantities must not be affected by the heat transfer that inertly happens in every turbocharger. This leads to the quantities on the system inlet boundaries. Because on both system entries there is no heat transfer that influences the measurement values. Any prior heat transfer may happen, but is not affecting any equation regarding the observed system. To compare properties of the turbocharger turbine under different conditions, usually the reduced turbocharger speed and other reduced quantities are employed. This decision is based upon the equivalent theorem of Mach. But observing the compressor side on different turbine temperatures and taking reduced turbocharger speeds into account is difficult, because the power consumption of the compressor is strictly related to the real, the physical turbocharger speed. Therefore a power based observation seems more effective than the observation of reduced quantities.

In order to pursue the idea of a power based approach a reliable x-coordinate is needed first. The quantity to plot a proper criterion over is the isentropic compressor power. This does not seem fit on first regard but on looking deeper into it, it perhaps is the only possible choice. The big advantage is the independency from all occurring heat flows. Isentropic compressor power, as shown in eq. 7, only uses the compressor inlet temperature as only temperature and this is the most reliable temperature available at the system boundaries of a turbocharger. Since it is only depended from ambient temperature.

$$P_{Cis} = \dot{m}_c \cdot c_{pC} \cdot T_1 \cdot \left(\Pi_{C_{tt}}^{\frac{\kappa-1}{\kappa}} - 1 \right) \quad \text{Eq. 7}$$

The next reason is based on the fundamental character of the compressor. Neither its isentropic compressor power nor its isentropic compressor efficiency is affected by the state of the fluid. Both features are also independent from any heat flow. The measured isentropic compressor efficiency is affected by the occurring heat flows from the turbine and the housing into the compressor and heat transfer from the compressor into the environment. But this is only the measurement mistake.

The Temperatures needed to obtain the isentropic efficiency are affected by the heat transfer. But the actual isentropic compressor efficiency remains unaffected. At one

certain compressor operation point with one dedicated mass flow rate, a defined speed, and pressure ratio, the compressor will always need the same amount of power, regardless of the turbine side. Due to this, always the same turbine shaft power is needed. This provides a basis to compare turbocharger measurements under different thermal conditions with each other.

To determine whether the measurement is sufficiently adiabatic on the turbine side the total enthalpy flow over the turbine can be observed. As mentioned before to on the identical compressor operation point it is always exactly the same amount of turbine shaft power needed. In other publications it is already mentioned that the measured turbine power can be divided into two parts. One part is the aerodynamic power, which goes into the turbine shaft and the rest is energy with is transferred in form of heat flow into the environment or adjacent turbocharger components. Concluding this, the total turbine power is used as axis of ordinates for this criterion.

The idea behind this is quite simple. If all the turbine power is used to be converted into compressor power, then when the required compressor power reaches zero, the turbine power has to be down to zero as well. In Figure 4 the plots of total turbine enthalpy drop above the isentropic compressor power are shown for a small automotive turbo charger. Additionally in the figure also show the connection between the measurement points at maximum isentropic compressor power at each speed line as interpolated straight line (solid). This approach follows the idea, that the point of maximum compressor power is part of all compressor characteristic maps and contrarily to the resistance line or the choke line not affected by the test bench setup. As said before, the chosen comparison point itself is not important, it is only important, to use the same point for all speed lines. Investigations on using different compressor operation points will be discussed later. The interpolated line cuts the x-coordinate almost at zero, missing zero by 0,165 kW.

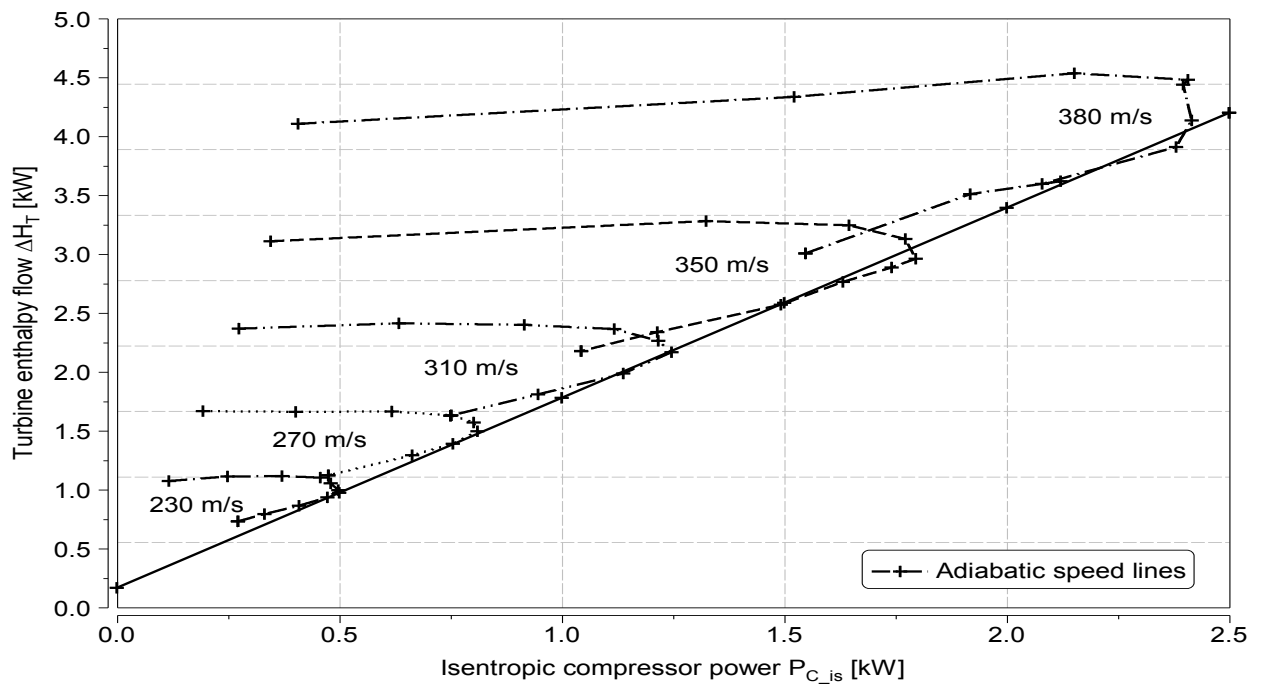


Figure 4: isentropic compressor power and turbine enthalpy flow under adiabatic conditions

This assumes an almost adiabatic measurement. It is also remarkable, how well all the points of maximum compressor power fit onto the straight line. To illustrate to impact of heat transfer in this criterion the adiabatic measurements are compared to standard measurements under SAE conditions. The results are listed and described in the following section.

6.2 Experimental results

During recent experiments multiple turbochargers have been tested under the adiabatic conditions defined in eq. 6. All the turbochargers have been tested at the same test bench with equal adjacent geometry, equal instrumentation and equal insulation. These facts ensure good comparison between the single measurement campaigns. The results for those investigations are shown in Figure 5. The red lines represent the hot gas measurements at a turbine entry temperature of 600°C according to the SAE J922. The black lines represent the adiabatic measurement recorded under the adiabatic definition introduced above. The solid lines show the connection between the points of maximum isentropic compressor power and the extrapolation towards zero isentropic compressor power. The remaining offset from the x-axis of the charts can be regarded as heat loss at zero compressor power. The adiabatic measurements show almost no remaining heat loss at zero compressor power. This can be observed for all four investigated turbochargers.

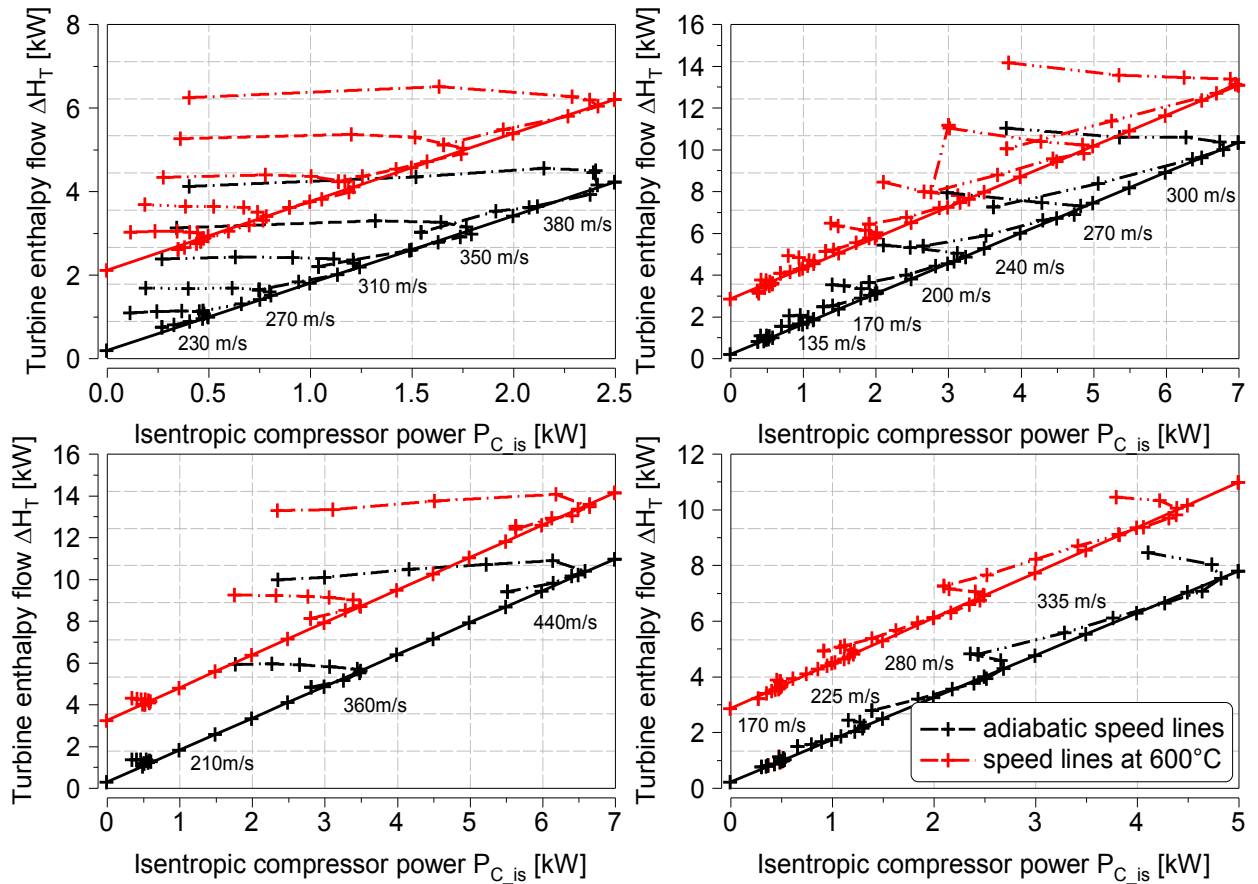


Figure 5: Adiabatic criterion for adiabatic conditions and for hot conditions

In the same manner as for all adiabatic measurements the turbine power at zero isentropic compressor decreases to zero, it can be observed, that for the SAE conditioned measurement a certain amount of turbine power remains at zero isentropic compressor power. This can be interpreted as minimal heat transfer into the environment during the measurement and is a clear sign that the measurement does not fulfill adiabatic conditions.

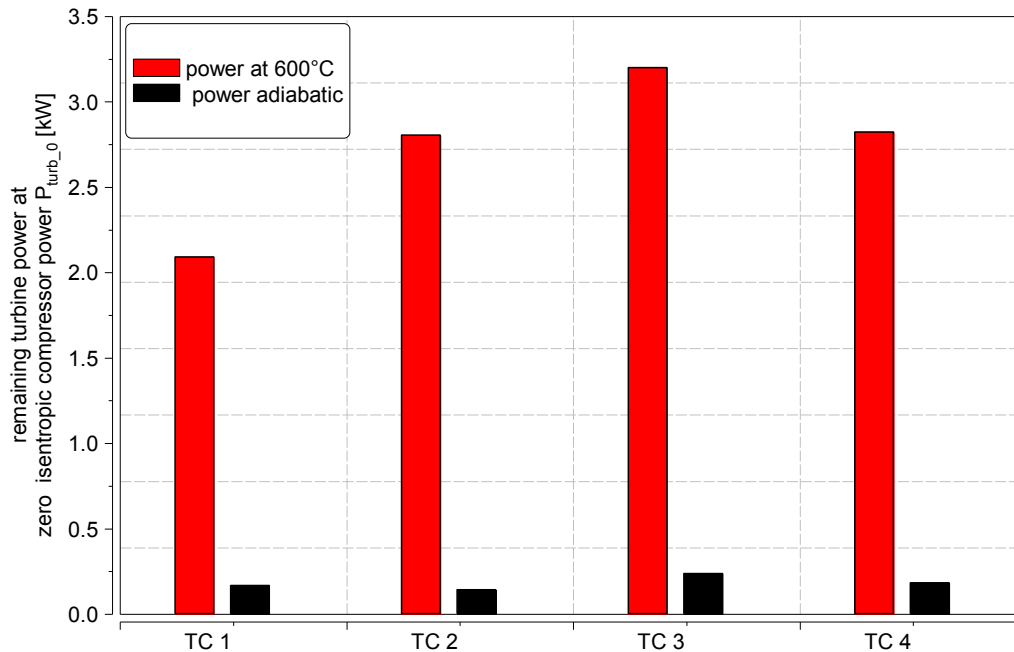


Figure 6: Heat flow at zero isentropic compressor power for all investigated turbochargers

The remaining heat flow rates differ depending on the turbochargers from 2 to 3 kW. The exact values and their comparison to the adiabatic measurements are shown in in Figure 6. This figure underlines the huge difference in heat transfer and resulting needed turbine power for the same amount of power on the turbine shaft.

6.3 Deeper analysis of the criterion

To solidify the approach, deeper investigations have been performed on those turbochargers, where additional measurement data has been available. The first variation discussed is a variation of turbine entry temperature. For two of the four turbochargers (TC1 and TC3) additional characteristic maps at different turbine entry temperatures had been taken. For TC1 the additional turbine temperature was 200°C and for TC3 the additional temperature was 900°C. The charts of those additional maps have been added to the prior shown charts. Both variations are presented in Figure 7.

For the smaller turbocharger TC1 the temperature being lower than 600°C but still higher than temperature needed for adiabatic conditions the reference line can be found in between both lines and closer to the adiabatic line. For TC3 the highest turbine entry temperature also induces the highest heat flow and therefore the highest straight line. But for both temperature variations the criterion fits well too. This variation proves that the established criterion works on a wide range of turbine entry temperatures and that it can occupy a wide range of heat transfer.

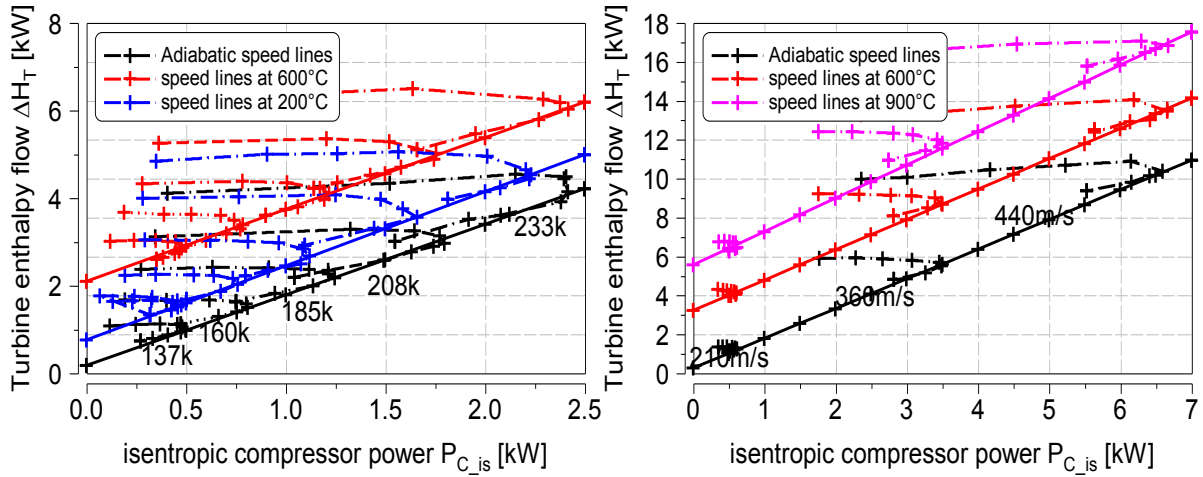


Figure 7: Turbine inlet temperature variation for two turbochargers (TC1 left with additional 200°C and TC3 right with additional 900°C)

7. Conclusion and outlook

With the fitting adiabatic conditions and a slightly improved test bench setup, it was possible to take aim for the isentropic turbine efficiency directly. The newly found criterion adds up to this by creating a possibility to validate the adiabatic conditions and therefore the measurement itself. The criterion was applied to several turbochargers and it worked well at all of them. In the process of defining an advanced turbocharger model, which is based on standard test bench measurements with minimal additional effort, the first steps have been taken.

For future work the adiabatic approach needs to be compared to other analytical and experimental approaches. Furthermore, a sensitivity analysis of the approach is planned. The newly found criterion also looks very promising therefore further investigation in this matter will be preceded.

References

- [1] Berndt, R.; Grigoriadis, P.; Nickel, J.; Abdelhamid, S.; Hagelstein, D., 2003, TC-Gesamtkennfeldbestimmung - Vorhaben Nr. 754, Erweiterte Darstellung und Extrapolation von Turbolader-Kennfeldern als Randbedingung der Motorprozesssimulation, Abschlussbericht, Forschungsvereinigung Verbrennungskraftmaschinen (FVV), Frankfurt am Main
- [2] Boxberger, V.; Mai, H.; Baar, R.; Kadunic, S., 2013, Herausforderungen an die Validierung von CFD-Simulationen mit Heissgasversuchen an Turboladern, 1st International Conference on Engine Processes, Berlin
- [3] Griffith, R. C.; Mavrosakis, P. E.; Slaughter, S.E., 2007, Applying Ball Bearings to the Series Turbocharger for the Caterpillar Heavy-Duty On-Highway Truck Engines, SAE Paper 2007-01-4235
- [4] Grigoriadis, P.; Nickel, J.; Pucher, H., 2004, Experimentelle Untersuchungen instationärer Phänomene in Fahrzeug-Turboladern, 9. Aufladetechnische Konferenz Dresden
- [5] Kraume, M., 2012, Transportvorgänge in der Verfahrenstechnik: Grundlagen und apparative Anwendung, 2. Auflage, Springer-Verlag, Berlin Heidelberg
- [6] Reuter, S., 2010, Erweiterung des Turbinenkennfeldes von Pkw-Abgasturboladern durch Impulsbeaufschlagung, Dissertation, TU Dresden
- [7] Society of Automotive Engineers, 1995, "SAE-Standard J922: "Turbocharger Nomenclature and Terminology"
- [8] Society of Automotive Engineers, 1995, "SAE-Standard J1826: Turbocharger Gas Stand Test Code"
- [9] Scharf, J., 2010, Extended Turbocharger Mapping and Engine Simulation, Dissertation RWTH Aachen
- [10] GVC-Fachausschuss Mischvorgänge, 1998, Mischen und Rühren, Grundlagen und moderne Verfahren für die Praxis, VDI-Gesellschaft Verfahrenstechnik und Chemieingenieurwesen
- [11] R. Baar C. Biet, V. Boxberger, H. Mai, R. Zimmermann, 2013 Möglichkeiten der direkten Bestimmung des isentropen Turbinenwirkungsgrads, Aufladetechnische Konferenz Dresden 2013
- [12] Biet C., Boxberger V., Mai H., Zimmermann R., Baar R., New Evaluation of Turbocharger Components based on Turbine Outlet Temperature Measurements in Adiabatic Conditions, 15th International Symposium on Transport Phenomena and Dynamics of Rotating Machinery, ISROMAC-15, Honolulu, 2014
- [13] Binder M., Böttcher L., Grigoriadis P., Advanced Turbocharger Model for 1D ICE, I-mech E London 2012
- [14] Baines N., Developments in turbocharger measurement and simulation, IQPC 4th International Congress, 2012

The Authors:

Professor Dr.-Ing. Roland Baar, Technical University Berlin, Berlin

M.Sc. Clemens Biet, Technical University Berlin, Berlin

Dipl.-Ing. Rainer Zimmermann, Technical University Berlin, Berlin

Licence:

This document is licensed under the Creative Commons Attribution 3.0 DE License (CC-BY 3.0 DE): <http://creativecommons.org/licenses/by/3.0/de/>

Transient Simulation of Nitrogen Oxide Emissions of CI Engines

Benjamin Kaal
Massimiliano Sosio
Michael Grill
Michael Bargende

Abstract

This report presents a quasi-dimensional emissions model for calculating the transient nitric oxide emissions of a diesel engine. Initially, using conventional and high-speed measurement technology, the stationary and transient emissions of a V6 diesel engine are examined.

A direct influence of the combustion chamber wall temperatures on the nitric oxide emissions can be shown based on the measured load steps, as well as additional stationary measurements. Load steps to and from, as well as stationary measurements at low global combustion air ratios were used to examine the behavior of nitric oxide formation under these operating conditions.

Following a comparison of various models for calculating the nitric oxide emissions of diesel engines, the emission model according to Kožuch, from the FVV project "Optische Thermodynamik", was selected as the foundation best suited for the new model, due to its strong phenomenological structure and its good predictability. This emissions model was then expanded in order to represent the direct influence of the combustion chamber wall temperature on the nitric oxide emissions. In addition, the emissions model was supplemented in order to enable the forecasting of nitric oxide emissions of operating points with low global combustion air ratios. These two points are particularly important for the simulation of transient emissions. They also contribute to improving forecasting at stationary operating points, however, and to enabling forecasting to occur at all in the case of low global combustion air ratios.

The new emissions model was validated for both stationary as well as transient cases using the performed measurements. In the area of the measured engine characteristics, an improved forecasting quality of the new model was already demonstrated in the case of the stationary operating points. The simulated transient load steps delivered significantly improved forecasts with the new model.

Overall, the new model thus enables not only the prediction of nitric oxide emissions in a wider operating range, but rather also delivers more precise forecasts within the complete performance map, as well as in the case of transient operation.

1. Introduction

Thanks to forced induction and the development of modern and efficient injection systems, the diesel engine has achieved a high status, with sales numbers even leading the gasoline engine in Europe [1]. This widespread distribution of diesel engines in cars, together with a growing awareness among the public of the effects of various pollutants on health and quality of life, has resulted in an increasing relevance of diesel emissions. The stationary and transient measurement of emissions and their modeling has consequently garnered the interest of the academic and scientific world in recent decades.

Representing stationary exhaust emissions by means of mathematical and physical models was the first prerequisite, and a logical consequence of the combustion models which were developed in parallel. Transient emissions differ from the stationary in the difficulty of general understanding, as well as in the technical measurement of exhaust concentrations, which often vary too quickly. The measurement of such pollutant gradients is still partly reaching technical limits. However, some manufacturers have been able to drastically reduce the response time of their exhaust measurement technology, so that nitrogen oxide and hydrocarbons, for example, can be measured at an exceptional operating cycle resolution: the T90 constant for these measurement devices is at a few milliseconds.

Using high-speed exhaust measurement technology, this paper attempts to examine the background of inaccuracy in today's mathematical models and to improve understanding of pollutant origination in transient operation, in order to be able to develop an improved 0D/1D model. For nitrogen monoxide emissions, a fundamental dependency of the formation of this combustion product on the operating temperature is known from the literature. The combustion chamber wall temperature is of particular importance, because it has a direct influence on the mass mean temperature of the cylinder charge and, consequently, on the formation of the emissions. The thermal inertia of the engine mass and the resulting substantially slower heating or cooling of the engine are aspects which are not yet precisely represented in the current emissions models, however.

Using multiple temperature and pressure measurement points, high and low pressure indexing and high-speed exhaust measurement devices, this paper attempts to research the most important physical mechanisms on a turbo-charged automobile diesel engine and to provide them as the basis for a successful exhaust emissions modeling method, so that it can be used both for stationary and transient operating conditions.

2. State of the Art

In [2], Kožuch developed a phenomenological model which calculates nitric oxide emissions by means of an admixture from the unburned zone into the burned zone. The model according to Kožuch relies on a 2-zone process calculation. The combustion occurs stoichiometrically and the additional admixture from the unburned zone occurs past the flame directly into the burned zone, whereby the temperature and composition can be adjusted in the burned zone.

The admixture is phenomenologically modeled according to *Eq. 2.1*. The first term is calculated using a turbulent velocity $u_{\text{turb,g}}$ on the basis of a $k-\varepsilon$ model, from the density of the unburned zone ρ_{ub} , the volume of the burned zone V_b and the number of nozzle

holes N_N . The unitless constant c_g serves to tune this first, turbulence-proportional term.

Another term is added to this first term which models the dependency of the admixture on the combustion. The combustion process has direct effect on this combustion process-proportional term. This term is tuned with the unitless constant c_{ga} , following a corresponding conversion of the time scale.

$$g = \frac{dm_{ub,ad}}{dt} = c_g \cdot \rho_{ub} \cdot u_{turb,g} \cdot V_b^{\frac{2}{3}} \cdot N_N + c_{ga} \cdot \frac{dm_B}{d\phi} \cdot 6 \cdot n \quad Eq. 2.1$$

Eq. 2.1 thus supplies a phenomenologically determined admixture mass flow which introduces unburned mixture into the burned zone. On the one hand, this mass flow lowers the temperature in the burned zone, and on the other, it increases the oxygen concentration there. Because the temperature dependency prevails, the admixture provides for a reduction of simulated NO.

In addition to the simulation of NO emissions, the emissions model according to Kožuch can also forecast soot emissions. The approach is fundamentally based on the approach by Hiroyasu presented in [3]. Figure 2.1 shows a schematic view of the complete emissions model according to Kožuch, with nitric oxide formation and soot oxidation in the burned zone as well as soot formation in the fuel rich flame.

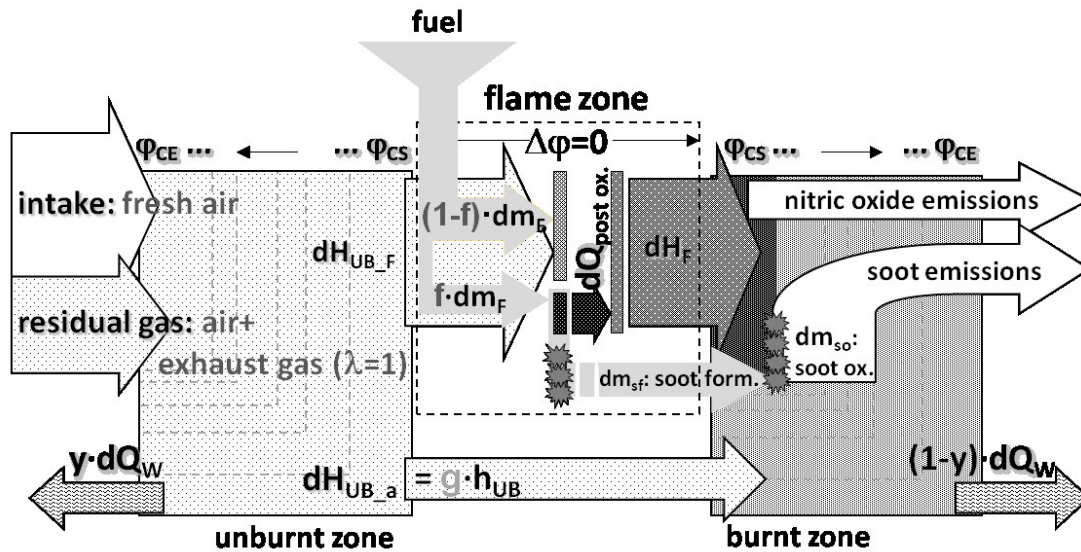


Figure 2.1: Diagram of emissions model according to Kožuch [2]

The advantage of the combination of nitric oxide and soot modeling in the model according to Kožuch lies in the simplified tuning of both partial models; see Figure 2.2. First the nitric oxide model is tuned. The turbulence can be adjusted via various parameters to the present engine as needed. The constant c_g of the admixture function g is then tuned so that the deviation of the simulated from the measured NO emissions is minimal. Following this tuning, the admixture from the unburned zone into the burned zone and thus the temperature and oxygen concentration within it are specified. Since the temperature in the burned zone is also incorporated in the soot oxidation, it thus is also specified.

The simulated soot formation can then be adjusted, via a tuning of the fuel richness function f , in order to minimize errors in comparison to the measured soot emissions.

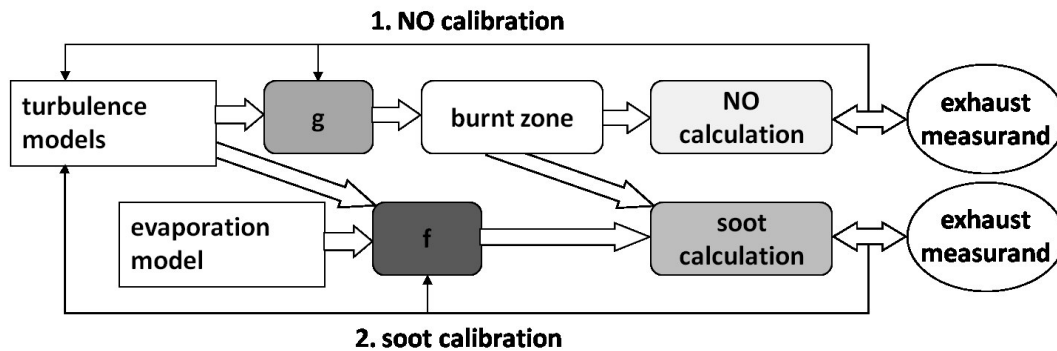


Figure 2.2: Joint tuning of emissions model according to Kožuch [2]

The emissions model according to Kožuch is not only purely phenomenologically structured, but also circumvents the disadvantages of some other emissions models. In contrast to the model according to Hiroyasu [3], it is not based on a flame temperature and does not have to be tuned via the reaction-kinetic constants. The model according to Kožuch can still admix after the combustion is completed, in contrast to the model according to Hohlbaum [4], and is not dependent on abrupt admixture upon outlet opening. The similar restriction of the homogeneous temperature distribution upon outlet opening in the model according to Heider [5] is also not required. Consequently, the emissions model according to Kožuch is built upon in this undertaking for calculation of transient NO emissions.

3. Test Setup

The test bench trials were carried out on a highly dynamic engine test bench of the Institute for Internal Combustion Engines and Automotive Engineering at the University of Stuttgart. The test specimen was a 3l-TDI OM 642 diesel engine, which was actuated by means of a production series ECU. Multiple temperature and pressure sensors were used together with extensive measurement devices for emissions measurement.

3.1 Test Specimen

The test specimen is the Euro 5 variant of the V6-TDI engine OM 642, with single-stage charging and common rail injection system. The engine differs from the production series primarily – in addition to the 1600 bar injection nozzles used – both in the complete omission of any exhaust treatment system as well as in the special pistons which reduce the compression ratio. The main characteristics of the engine are summarized in *Table 3.1*.

The interface for engine control was implemented via an original Bosch EDC17 ECU, with software adapted to have expanded adjustment options available. The data of the ECU could only be output at a frequency of 2 Hz, however, so they had little value for the transient trials.

Engine designation	Daimler OM 642
Type	6 cylinder – V72°
Valve train	4v, DOHC
Displacement	2987 cm ³
Bore x stroke	83 mm x 92 mm
Therm. compression ratio	14.3:1
Injector system	Bosch CR Piezo nozzle ($P_{Inj,max} = 1600$ bar)
Charging system	Single-stage turbocharger (with VTG) – Garrett GT2056v
Max. torque & nominal power	510 Nm – 165 kW (with series $\epsilon_{geom} = 15.5$)

Table 3.1: Characteristics of the test engine

3.2 Sensor Equipment

The engine was equipped with 19 temperature and 12 pressure recording points which, together with the measured ECU values, enabled complete measurement of the air pathway at every important location. The most important measurement points are shown in Figure 3.1.

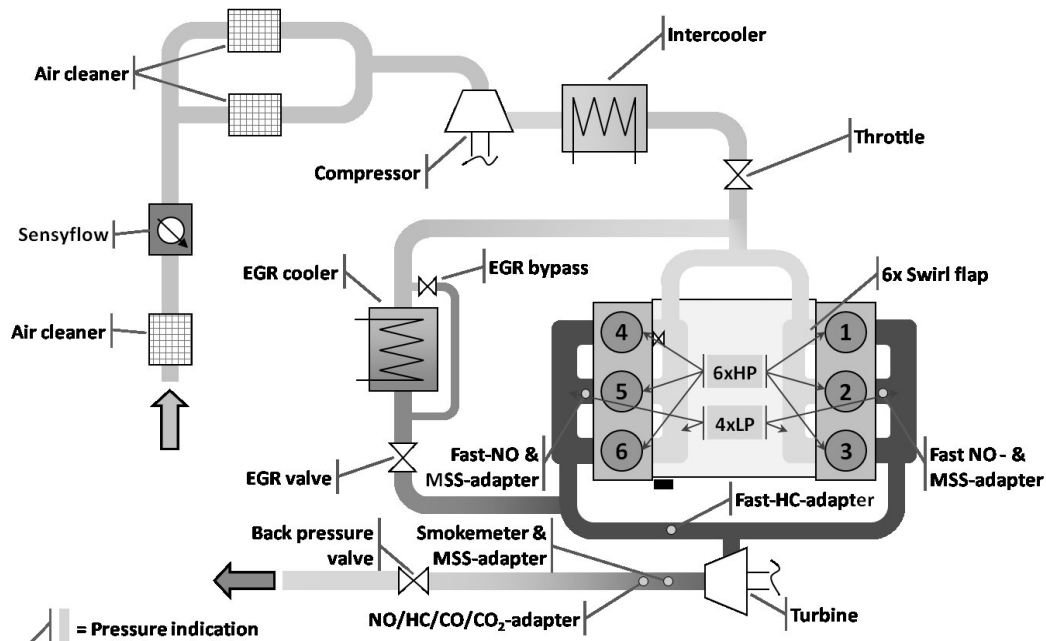


Figure 3.1: Measurement point plan of the OM642

In dependence on the application and the requirements of the measurement campaign, two types of measurement devices were generally used: the conventional exhaust measurement technology, as well as the high-speed exhaust measurement technology developed specifically for transient measurements.

In this second group, some of the measurement devices use the same measurement principle, but are designed for the special requirements of transient measurement: the chemiluminescence detector (CLD) and the flame ionization detector (FID) used are an example of this.

4. Stationary Emissions Measurement

Before the transient examinations are presented, this chapter will describe the stationary measurements which were relevant for the development of the new emissions model. An interesting parameter variation in consideration of the formation of nitrogen monoxide emissions in transient processes is the variation of engine operating temperature, which has effects on multiple aspects. First of all, the friction mean effective pressure increases at lower engine temperatures, since the viscosity of the engine oil rises disproportionately to the lowering oil temperature. There is a second large influence on the combustion, because there is a strong temperature dependency of the combustion process in the diesel engine: the combustion of the pre-injections – particularly the second and possibly third – is heavily affected, with combustion of these small fuel volumes tending to be incomplete.

In this series of measurements, the injection strategy (control times and rail pressure) as well as the VTG-, inlet port shutoff, ECB- and throttle valve position were held constant. The trials were carried out without exhaust gas recirculation in order to enable simpler regulation of the charge air temperature to approx. 25 °C. The charge temperature thus determined and the fixed position of the aforementioned valves together enabled a deviation in the charge of less than 1 %. Four different coolant temperatures with three different oil temperatures each were examined. The load was at 3 bar IMEP.

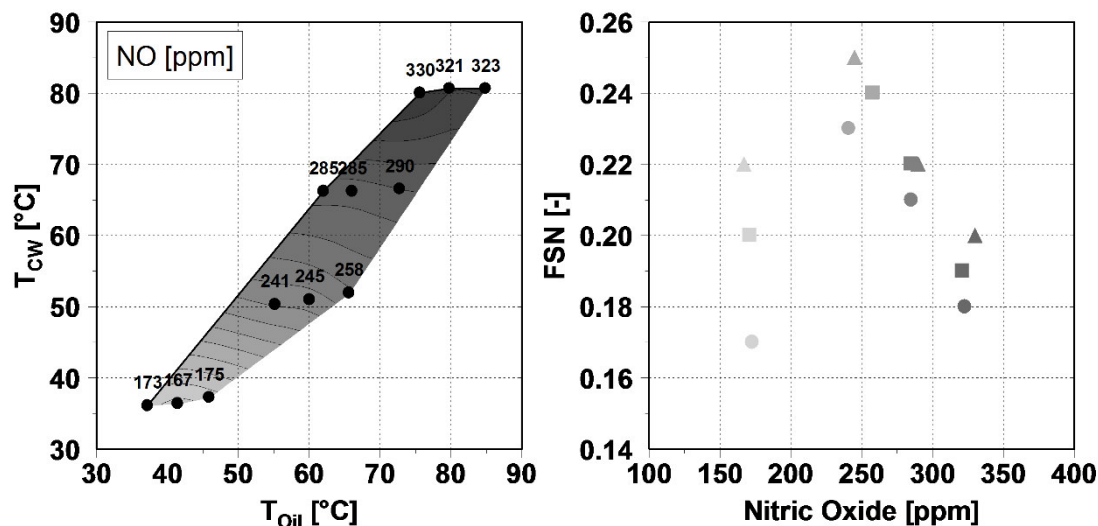


Figure 4.1: NO emissions over T_{cw} and T_{oil} and soot(FSN)/NO-gap

With increasing wall and charge temperature, the first pre-injection fires sooner. This phenomenon, together with the gas temperature which is already higher at the start and with the stronger heat release before TDC of the firing stroke, results in an up to 55 K hotter maximum mass mean temperature; see Figure 4.2.

The falling temperature of the burned mass with lowering of the charge air temperature causes a concurrent fall-off of NO emissions and an increase of soot emissions; see Figure 4.1.

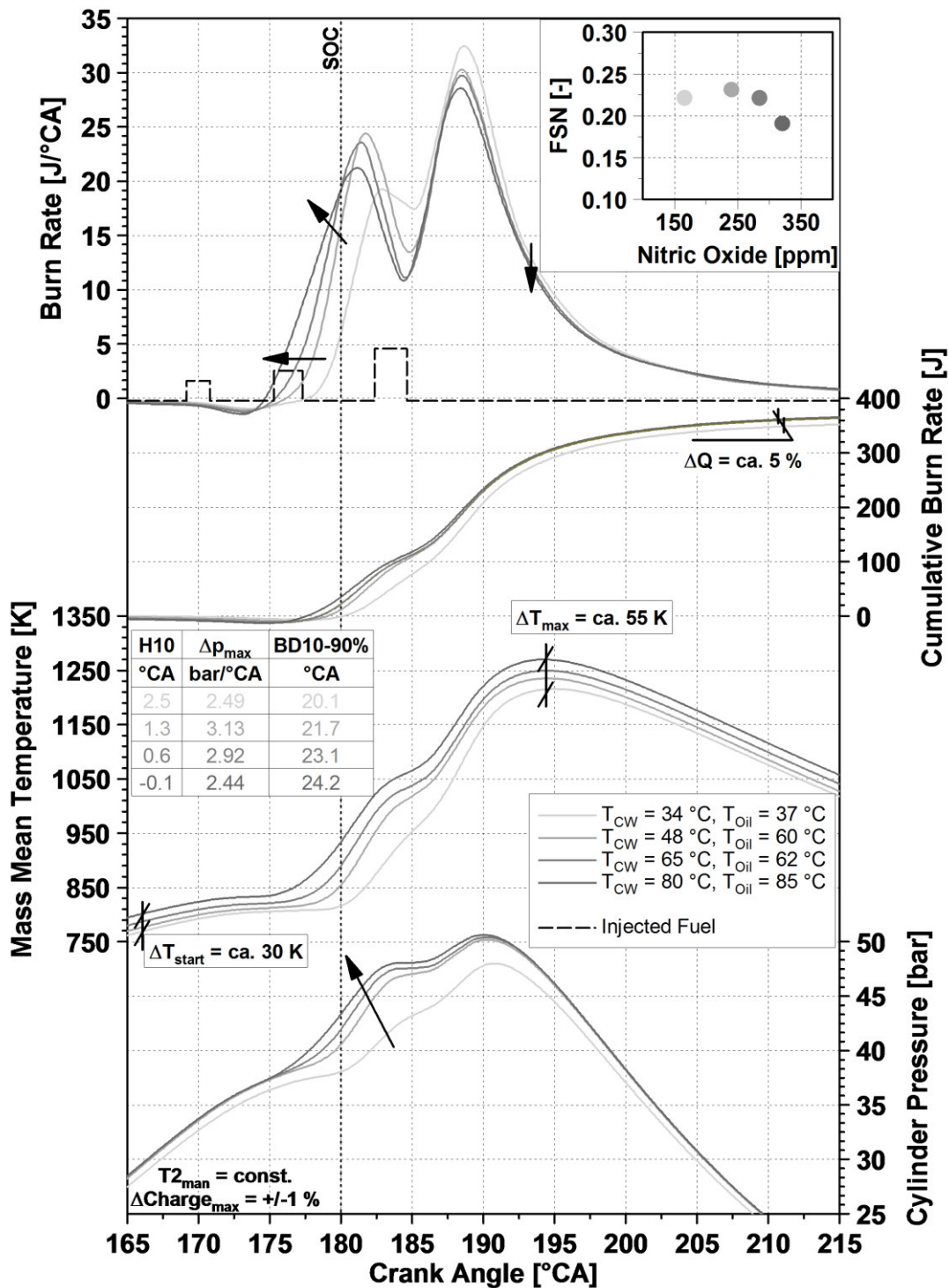


Figure 4.2: T_{CW}/T_{Oil} -Variation. 850 min⁻¹, 3 bar IMEP, without EGR

5. Transient Emissions Measurement

The measurement of exhaust emissions in transient states represents a great challenge which demands constant maintenance of the measurement devices in order to achieve good reproducibility of measurements. Regular maintenance of the measurement devices is important because the high-speed measurement technology used forgoes any type of filter and therefore responds with extreme sensitivity to high particle concentrations.

5.1 Potential of the Measurement Devices

An engine start from coasting at constant engine speed is first examined which is intended to representatively demonstrate the potential of the measurement devices. In *Figure 5.1*, cylinder pressure profiles are shown together with NO emissions. The exhaust gas was extracted with an extraction line directly in the outlet duct of the second cylinder. It is noticeable that the fast-CLD detects an increase in nitric oxides within the shortest period of time, already 8 ms after the opening of the outlet valve of the first cylinder. It can also be seen how, as a result of the V6 engine arrangement, of the position of the probe and of the pulsing mass flow, as well as of the reflow of the exhaust into the outlet ducts, the emissions of the other cylinders are also measured, in attenuated form.

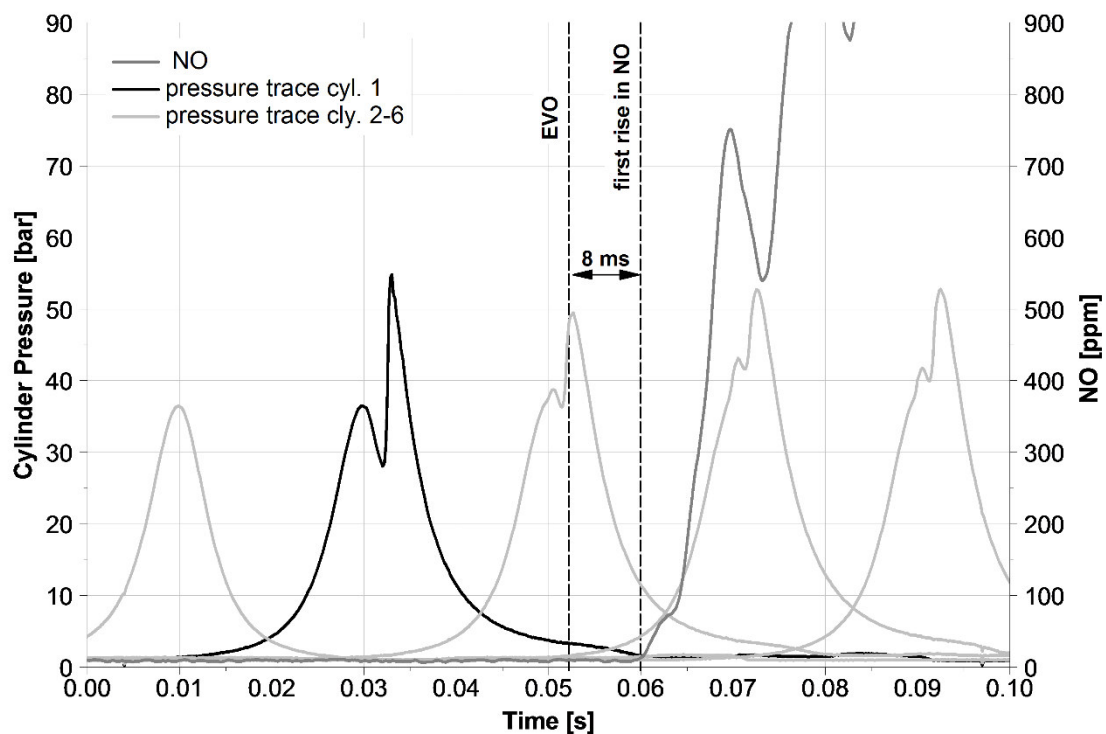


Figure 5.1: Engine start after coasting, 1000 min⁻¹, 0...7 bar IMEP

5.2 Analysis of the Thermal Effect on NO Emissions

A cold start measurement with a load increase at 850 min^{-1} is shown in the following. Although the influence of the charge pressure on the measured nitric oxide was identified as nearly negligible in previous trials, it is further minimized for this load step in that the charging capability of the engine was weakened by the 50 % opening of the VTG. The charge pressure increase could thus be limited to a few millibars.

The load increase was carried out by modifying the fuel volume of the primary injection (from $2.8 \text{ mm}^3/\text{stroke}$ to $18.7 \text{ mm}^3/\text{stroke}$) with an otherwise constant injection strategy. The EGR flap was completely closed and the other actuators were held constant. The low operating temperature ($\text{TCW}=35^\circ\text{C}$) promotes the strong NO increase after the load change so that, in the first 30 seconds after the load change, at a negligible charge pressure build-up of 5 mbar, the NO emissions increase by 40 % (see Figure 5.2).

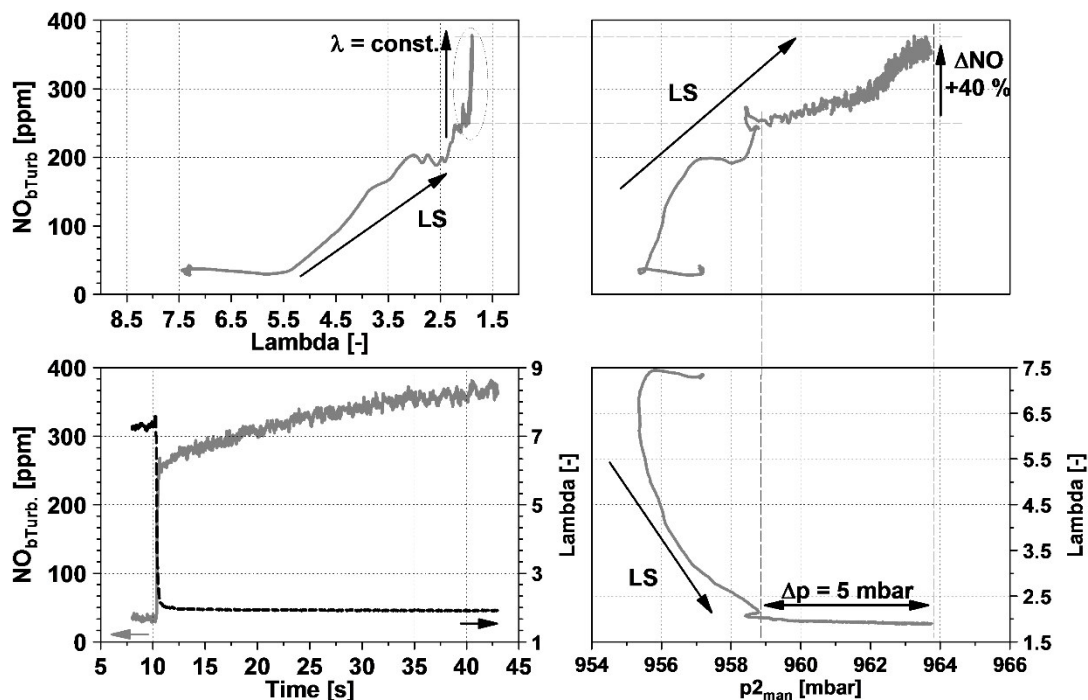


Figure 5.2: NO emission progression over load step (850 min^{-1} , 1...7 bar IMEP)

A similar trend arises in the case of a load reduction mirroring this load increase (approx. 7 to 1 bar IMEP). In Figure 5.3, the NO emissions on cylinder 2 are shown. The transiently measured nitrogen monoxides remain for many seconds at a level that is significantly higher than the NO values measured stationary.

In addition to the examined cold start, an engine operating temperature variation was also carried out. The load increase was run with two different coolant and corresponding engine oil temperatures (approx. 50°C and approx. 90°C). The temperatures were regulated via two external conditioning systems so that a nearly stationary basic state was maintained. The direct comparison of the two measurements shows that, at higher temperatures, the increase of the nitrogen monoxide emissions is higher over the load change. The results are shown analogously to the depiction of the cold start in Figure 5.4.

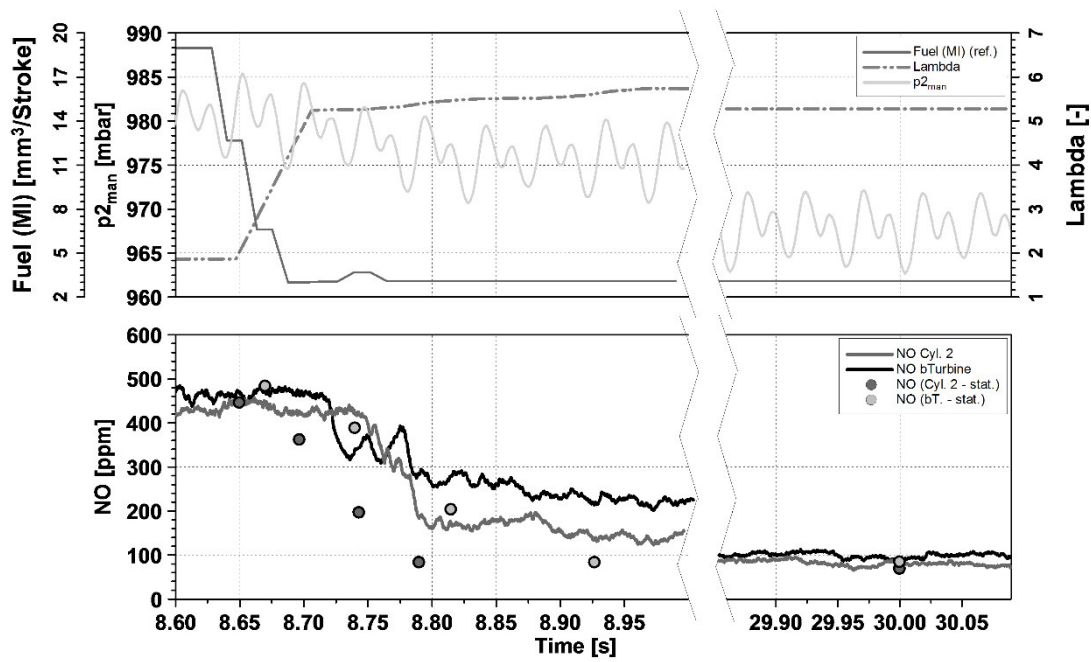


Figure 5.3: NO emission progression over load reduction (850 min⁻¹, 7...1 bar IMEP)

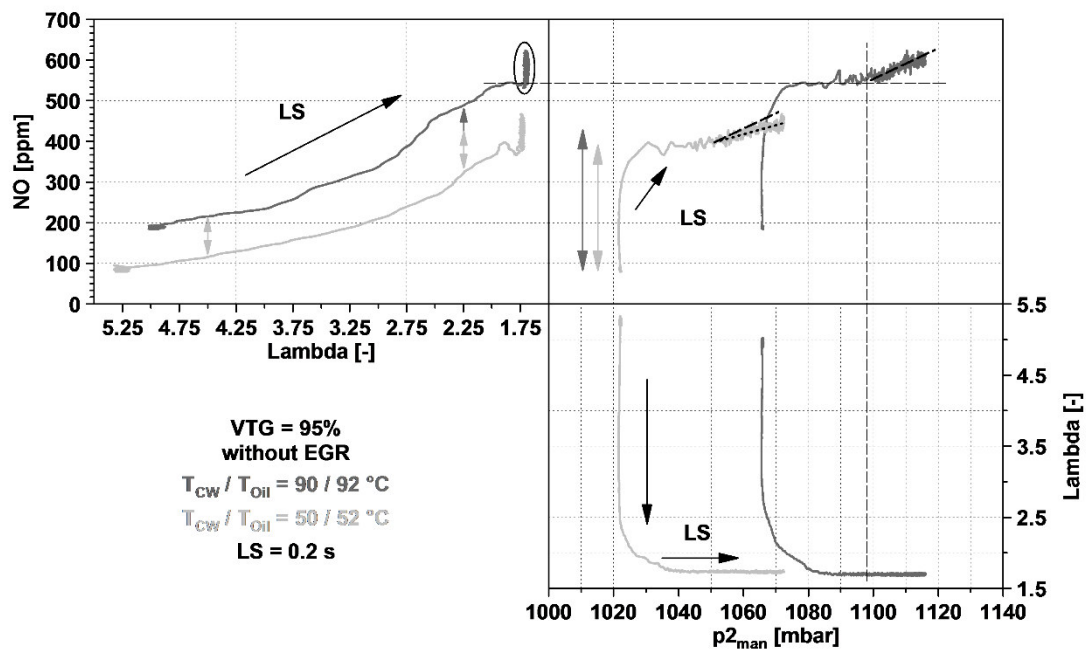


Figure 5.4: NO emission progression over load step (850 min⁻¹, 1...7 bar IMEP)

6. Model Expansion

The intention was to develop an emissions model which enables the simulation of nitric oxide emissions of a diesel engine during transient processes: the foundation was the emissions model according to Kožuch, which demonstrates the greatest potential of the currently available emissions models.

6.1 Wall Temperature Influence

In the evaluation of the measurement data, it has already been shown that there is a significant influence by the combustion chamber wall temperatures on the nitric oxide emissions. Load steps, which were specially selected in order to keep as large a number of engine operating parameters as possible as constant as was feasible, demonstrated a significant change to the nitric oxide emissions with heating and cooling of the engine. This effect of the combustion chamber wall temperature could not be explained solely by cross-influences, so that a direct influence of the combustion chamber wall temperature on the nitric oxide emissions is postulated.

The emissions model according to Kožuch integrates no direct consideration of the influence of the combustion chamber wall temperature on the NO emissions whatsoever. It reacts indirectly, however, exactly like all other simulation models used, to the ancillary conditions changing with the temperature. In order to be able to separate the various influences of the combustion chamber wall temperature on the emissions simulation from each other and to thereby also be able to clearly differentiate between a direct influence and an influence via ancillary conditions, a theoretical analysis is applied.

The combustion chamber wall temperature has influence on the results of a simulation calculation via a plurality of effect pathways. Most of these influences have effect on the simulated emissions. In this study the effect pathways of the combustion chamber wall temperature on the nitric oxide emissions shown in *Figure 6.1* were examined through simulation.

The nitric oxide emissions primarily depend on the temperature profile in the cylinder. Only through the weaker influence of the oxygen concentration can the cylinder charge and the combustion also have direct influence on the nitric oxide emissions. The cylinder charge has direct effect only in the case of globally almost stoichiometric or even rich conditions. In the case of such ancillary conditions, a reduction of the cylinder charge can lead to an oxygen deficiency, so that the nitric oxide formation is directly influenced in (locally) rich areas. The combustion can likewise have a direct effect on the nitric oxide formation, via the formation of locally rich areas in which the temperature and oxygen concentration are lower.

Some of the effect pathways of the influence on nitric oxide emissions by the combustion chamber wall temperature can be specifically examined through simulation. The advantage of simulated examination lies in the possibility of being able to easily deactivate individual sub-models or influences of the combustion chamber wall temperature and to thereby separate the individual effect pathways. Through corresponding simulations, it was shown that the various models in the simulation demonstrate the correct tendencies in case of modification of the combustion chamber wall temperatures in relation to nitric oxide emissions [13]. If the coolant and oil temperature variations from Chapter 4.1 are re-simulated, it will be shown whether this is already sufficient to represent the measured behavior or whether a direct influence not previously considered must be integrated in the NO model.

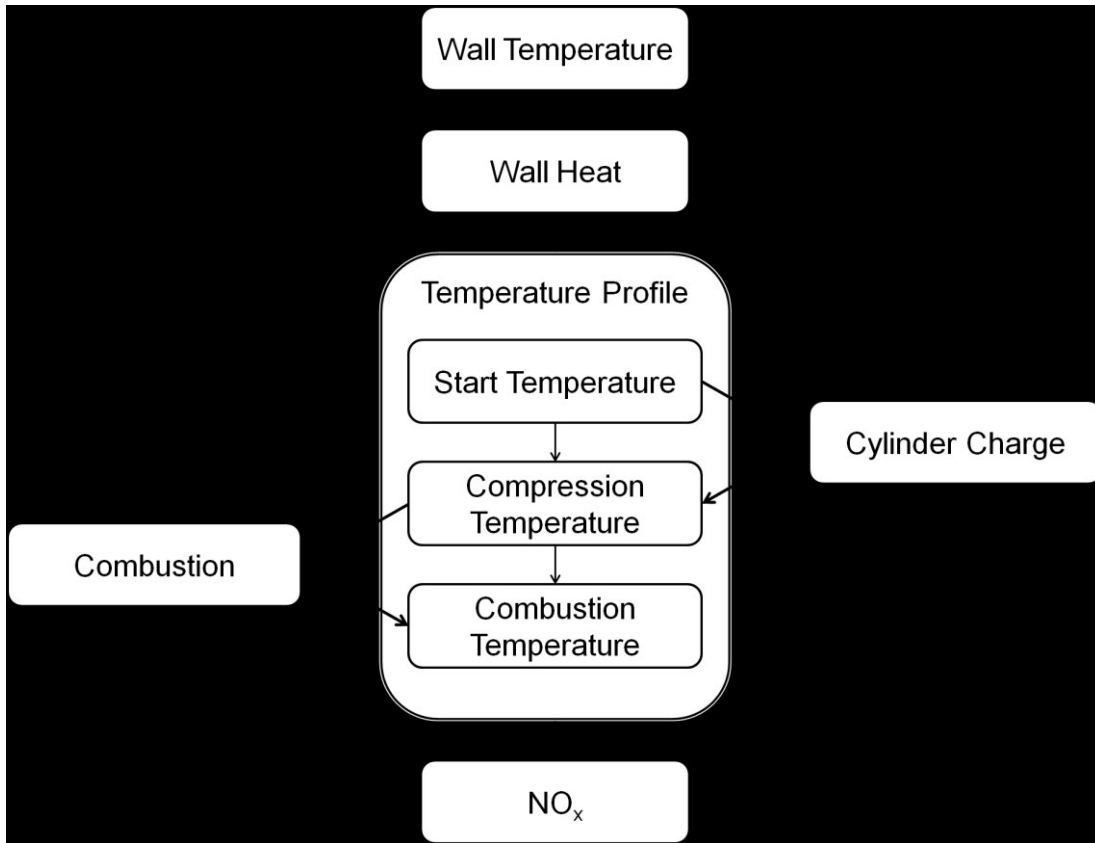


Figure 6.1: Effect pathways of the wall temperature influence

Figure 6.2 shows the comparison of the measurement with the simulation for the coolant and oil temperature variation, including the average combustion chamber wall temperature. The results show that the emissions model according to Kožuch cannot or can only much too weakly reproduce the superimposed trend of clearly rising NO values for rising combustion chamber wall temperatures.

The hypothesis is thus confirmed that, in addition to the already described effect pathways of the combustion chamber wall temperature on the NO emissions, a direct influence must also be integrated into the emissions model. As already shown in Figure 6.1, the combustion chamber wall temperature only has effect on the nitric oxide emissions via the wall heat. The new model representation for describing the direct wall temperature influence correspondingly builds on the theory of wall heat losses.

Figure 6.3 shows a schematic diagram of the temperature and flow boundary layer on the combustion chamber wall, as it is used for fundamental description of the wall heat losses. The temperature boundary layer occurs due to the heat flow and provides for a temperature gradient between the combustion chamber wall and the gas mixture in the cylinder. The wall heat in the combustion chamber is primarily transferred by means of forced convection, which is why an additional flow boundary layer is relevant which fulfills the no-slip condition on the wall side [6]. Both boundary layers interact with each other.

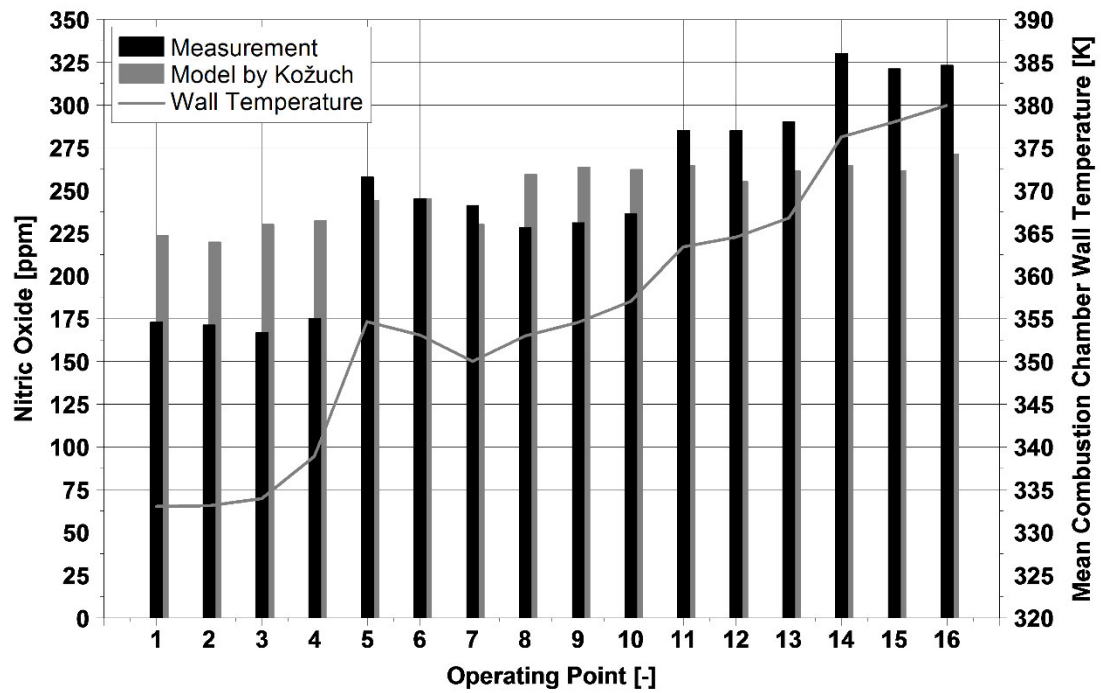


Figure 6.2: Coolant and oil temperature variation – 850 min⁻¹, 3 bar IMEP

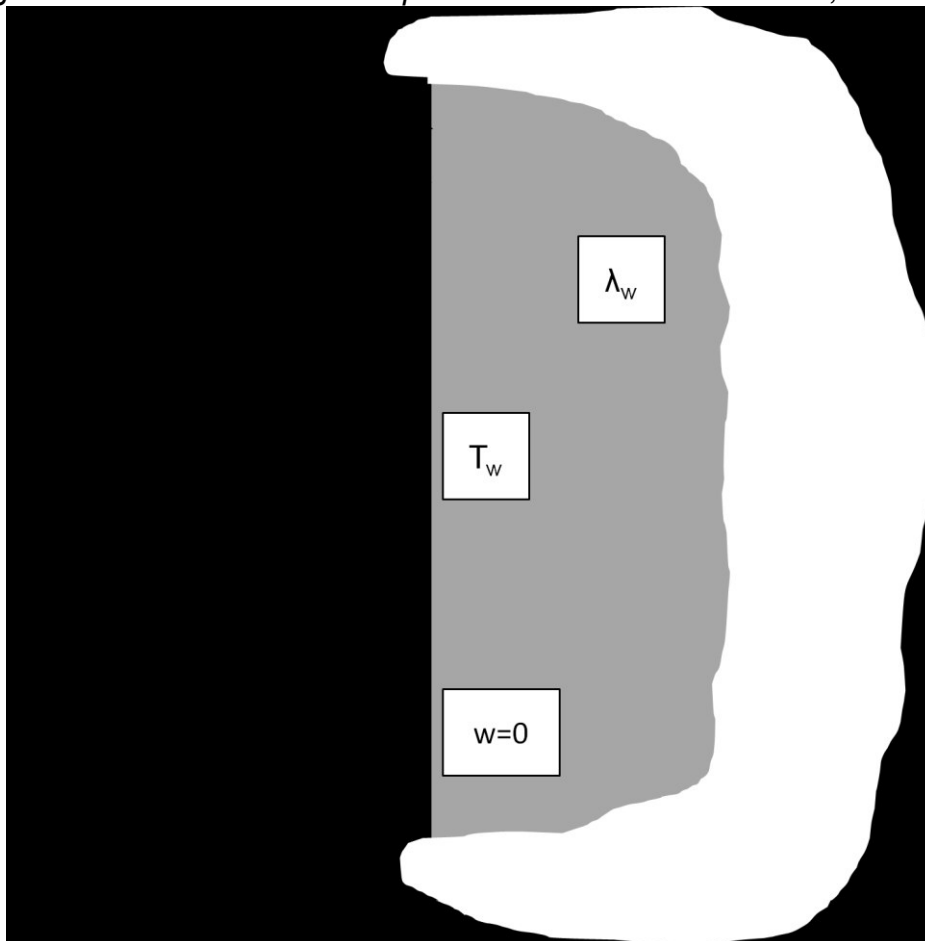


Figure 6.3: Temperature and flow boundary layer on the combustion chamber wall

Because emissions in the diesel engine are always also a consequence of inhomogeneities and the theory of wall heat losses already postulates a temperature boundary layer, it appears sensible to upgrade the boundary layer to a peripheral zone for modeling the influence of the combustion chamber wall temperatures on the nitric oxides. This peripheral zone is directly adjacent to the combustion chamber wall and thus encloses a core zone of the combustion chamber which has no direct contact with the combustion chamber walls. The temperature progression within the temperature boundary layer is interpreted such that a lower mean temperature prevails within the peripheral zone than in the core zone, which is isolated from the cool combustion chamber walls by the peripheral zone. *Figure 6.4* shows a schematic view of this model representation, with a cold peripheral zone and a hot core zone.



Figure 6.4: Model representation of combustion chamber wall temperature influence

Two different variants are possible for modeling the influence of the combustion chamber wall temperature on nitric oxide formation with this representation. The combustion chamber wall temperature could influence the temperature in the peripheral zone or determine the size of the peripheral zone. In reality, the thickness of such a peripheral zone and its average temperature are necessarily interrelated: An infinitely thin peripheral zone will assume the temperature of the combustion chamber wall. A peripheral zone with a thickness of half the bore diameter will assume a temperature of the average combustion chamber temperature. A clear definition of a peripheral zone is generally difficult in reality, because the strongly inhomogeneous flow field in the cylinder does not allow for the occurrence of a clear boundary layer with a thickness of δ_t , as is shown for the temperature progression in *Figure 6.3*. Consequently, any definition of a peripheral zone thickness is partially arbitrary. In the following, therefore, the peripheral zone is defined as the area near the wall in which no nitric oxide formation is possible due to temperatures being too low. This has the advantage that a Zeldovich mechanism no longer has to be applied in the peripheral zone. Due to the strong temperature gradients from the burned temperature to the combustion chamber wall temperature and the exponential temperature dependency

of the reaction kinetics upon application to an average temperature of the peripheral zone, this would return incorrect results anyhow.

The temperature of the burned zone calculated in the simulation is retained for the hot core zone. Nitric oxide thus continues to form in this zone. Through the definition of a peripheral zone, the total quantity of nitrogen monoxide formed is accordingly reduced. In tuning the new model, this circumstance must later be accounted for as applicable by a reduced admixture and consequently increased nitric oxide formation in the core zone.

The first principle of thermodynamics is obviously violated by this temperature selection. The lower temperature required for nitric oxide simulation in the peripheral zone otherwise cannot be achieved, since a corresponding increase of temperature in the core zone in order to comply with the first principle leads to nonsensical behavior. This would namely result in the wholly unrealistic behavior that a colder combustion chamber wall temperature with a larger peripheral zone would require a hotter core zone. The temperature of the peripheral zone should therefore only be considered to be a virtual temperature for calculation of the NO formation, which has no significance for the rest of the simulation of the diesel engine combustion. Alternatively, the definition of a pseudo-zone from [7], opposed to a thermodynamic zone, can be called on.

Once the temperatures are specified by the model representation, the size of the peripheral zone must be specified in dependence on the combustion chamber wall temperature in order to be able to represent the influence on nitric oxide emissions. As shown in *Figure 6.4*, the three boundaries of the combustion chamber, created by the demarcation of cylinder head, piston and bushing each span the peripheral zone perpendicularly in the direction of the combustion chamber. The size of the peripheral zone (and consequently the core zone) is thus completely described by the (momentary) combustion chamber size and one thickness for each of the three boundaries.

The respective thickness of the peripheral zone on the three boundaries of the combustion chamber must be in relation to the combustion chamber wall temperature in order to be able to reproduce its influence on NO formation. The depiction in *Figure 6.5* with peripheral thicknesses optimized to the measured emissions suggests a linear connection between the temperature of the combustion chamber walls and the thickness of the peripheral zone. However, such a linear connection already requires a peripheral thickness of 0 mm at the relatively low wall temperature of approx. 410 K. Influencing the nitric oxide formation at higher combustion chamber wall temperatures would thus no longer be possible.

In this case, returning to the wall heat losses as the starting point of the model representation is sensible. In the case of thermal transfer between gas and combustion chamber wall, a phenomenon has long been known which is described by the French name "Convection Vive." "Convection Vive" translates as strong convection and explains why the heat flow from the gas into the combustion chamber wall rises again in the case of very high wall temperatures instead of falling further due to the dropping driving temperature difference (see also [8], [9] and [10]).

If this stabilization of the thermal transfer at high combustion chamber wall temperatures due to an increased thermal transfer coefficient is considered, a linear connection of the peripheral thickness to the temperature of the combustion chamber walls is eliminated. Instead, an exponential connection seems appropriate. Such an exponential approximation can reproduce the optimized peripheral thicknesses of the coolant and oil temperature variation almost as well and can additionally represent a slow fading at higher combustion chamber wall temperatures. Overall, a progression

of the peripheral thickness over the average combustion chamber wall temperature results, which appears to be sensible in the complete temperature range, which can realistically be anticipated.

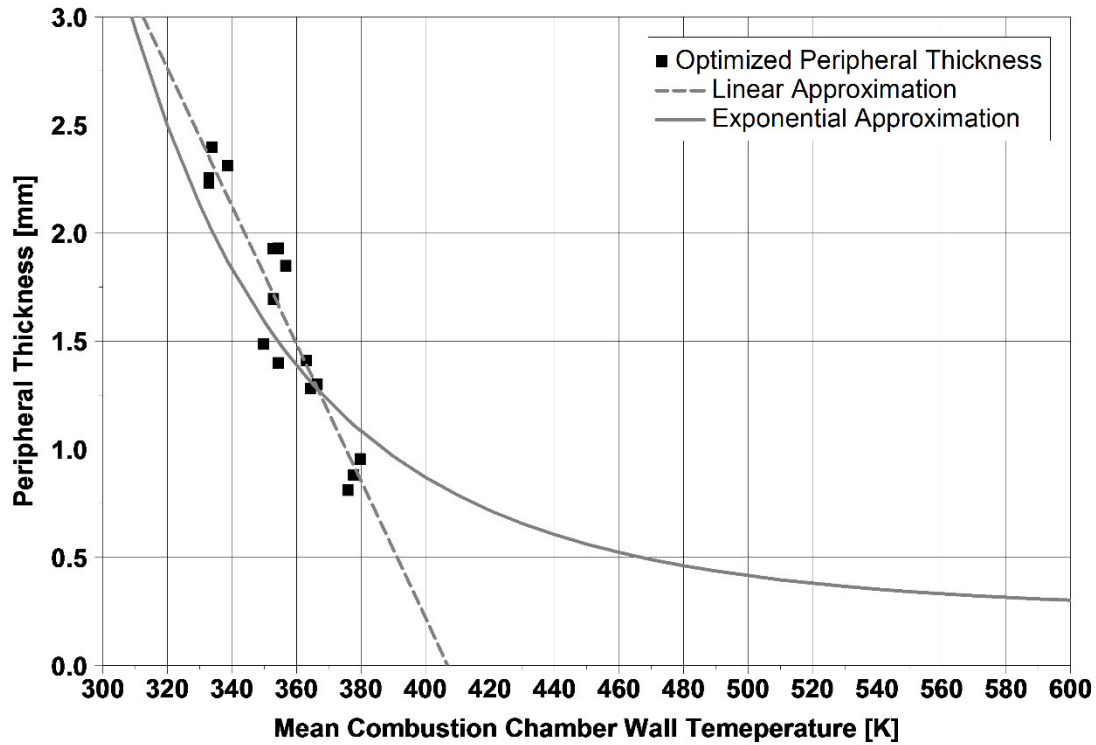


Figure 6.5: Linear and exponential approximation of peripheral thickness

For the exponential approximation, a general exponential function was selected, as is described in Eq. 6.1. If this approximation is adjusted by means of its constants to the optimized wall thicknesses, peripheral thicknesses between 0.26 and 3.5 mm are calculated in the temperature range relevant for combustion chamber walls, between 300 and 700 K. Solely for extremely cold combustion chamber walls, such as during the first operating cycles of a cold start, the peripheral thickness can become significantly larger, so that, under certain circumstances, the entire burned zone is incorporated by the peripheral zone and, accordingly, no nitric oxides are formed. Specifications of $\delta_T \approx 1$ mm [11] and $\delta_{th} \approx 0.2$ -8 mm [12] are found in the literature for the thickness of the thermal boundary layer. The calculated peripheral thicknesses are thus on the same scale as the thickness of the thermal boundary layer, which was used as a derivation of the model representation.

$$b = F \cdot \left(\frac{T_{Wall}}{400} \right)^E + C \quad \text{Eq. 6.1}$$

Figure 6.6 shows the comparison between the measured NO values as well as the simulated NO values from the model according to Kožuch and the new model. The poor reproduction of the NO emissions in the model according to Kožuch was already shown in Figure 6.2. By contrast, the new model is able to represent the combustion chamber wall temperature influence, follows the trend of the measurement data and exhibits a substantially better correspondence with the measured values.

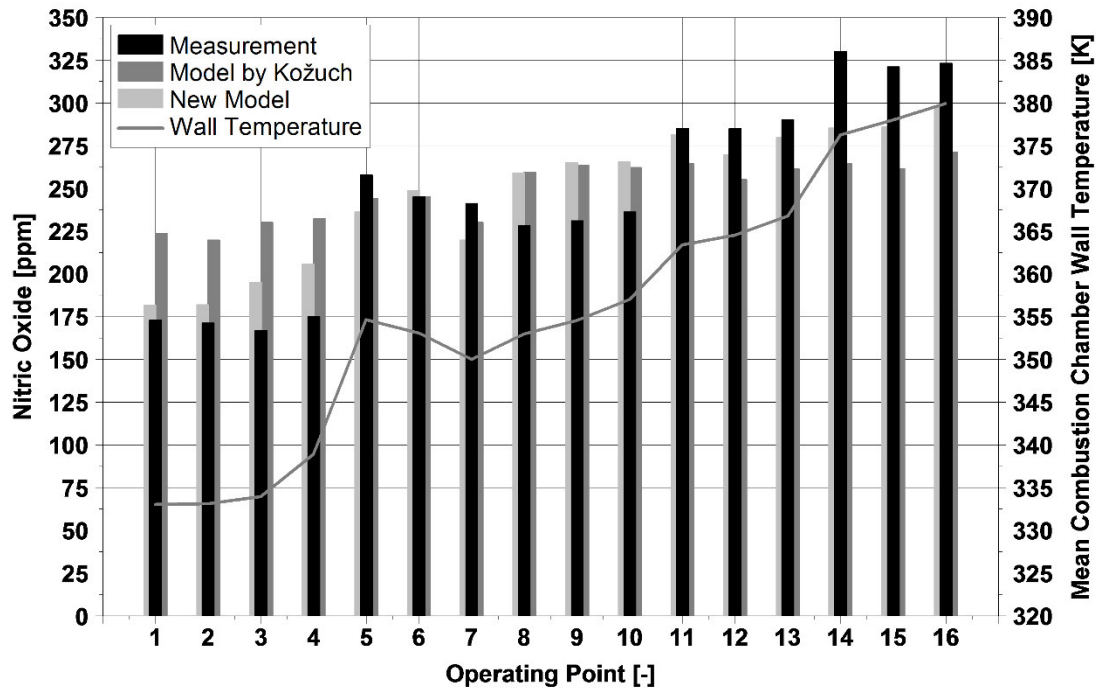


Figure 6.6: Coolant and oil temperature variation – 850 min^{-1} , 3 bar IMEP

6.2 Air Deficiency Influence

An additional weak point in the model representation of the emissions model according to Kožuch can be identified through theoretical considerations. The determination of the temperature in the burned zone is substantially influenced by the admixture from the unburned zone. This approach becomes problematic as soon as the mixture in the combustion chamber nears the stoichiometric composition. The majority of the unburned mass is already required for the stoichiometric combustion of the fuel in this case, and only a very small mass remains available for the admixture. If this remaining unburned mass is then completely consumed at an operating point with strong admixture, the admixture from the unburned zone into the burned zone suddenly stops, whereby the temperature in the burned zone is no longer correctly modeled. If the admixture break occurs early enough, during NO formation, correspondingly higher nitric oxide emissions occur due to the higher temperatures, an effect which increases with falling combustion air ratios. This does not correspond to the behavior in reality, where nitric oxide emissions are reduced in the case of nearly stoichiometric air ratios; see Figure 6.7.

When the emissions model according to Kožuch was developed, this did not represent much of a limitation because diesel engines were only operated with a significantly leaner mixture. However, modern diesel engines are operated significantly closer to a stoichiometric gas composition. This particularly applies to the full-load area at low speeds. However, in the partial-load range at low speeds, due to now higher EGR rates, λ values are run closer to a stoichiometric composition as well. Future applications to comply with new emission limits will presumably require even higher EGR rates and intensify this problem in the model according to Kožuch. The same trend will presumably be exhibited when changing to new, more dynamic test cycles, such as the Worldwide Harmonized Light Vehicles Test Procedures (WLTP) or

introducing Real Driving Emissions (RDE). Because then EGR will probably be applied to a greater degree, even in the full-load area.

The application in the case of acceleration processes is no longer limited by the air ratio, since particle filters prevent the formerly problematic black smoke puffs during acceleration. This exacerbates the existing problem that for transient processes, due to the inertia of the turbocharger, already richer conditions than those that were applied stationary can occur in the cylinder. Together with the new and more dynamic test cycles already mentioned, corresponding acceleration processes will also become relevant for certification, so that these two effects will mutually intensify each other. Accordingly, the model weakness at low λ values is also of decisive importance for the simulation of transient emissions.

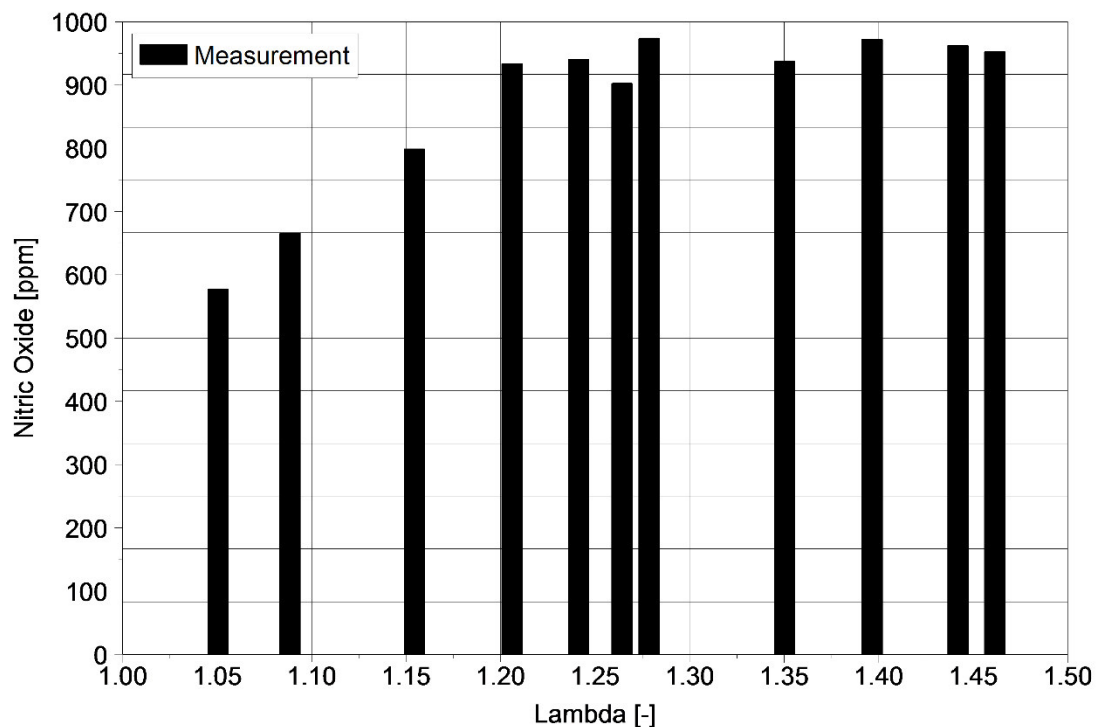


Figure 6.7: Nitric oxide over combustion air ratio – 1000 min⁻¹, ~11 bar IMEP

Figure 6.8 shows the progressions of temperature and the concentrations of atomic and molecular oxygen in the burned zone, the mass of the unburned zone as well as the admixture and the nitric oxide concentration for the emissions model according to Kožuch for an operating cycle at a global air ratio of $\lambda = 1.3$. The breaking admixture at 13°CA a. TDC as well as the subsequent complete run-out of the burned zone by the combustion are clearly recognizable. The breaking off of the admixture causes the previously described faulty modeling of the temperature in the burned zone, which is exhibited in the diagram by a kink, and which significantly delays the declining slope. The delayed temperature drop after break-off of the admixture causes a strong rise of the simulated NO concentration, since it takes place in the critical phase of the NO formation. The progressions of values in Figure 6.8 thus confirm the theoretically derived model weakness at low global λ values.

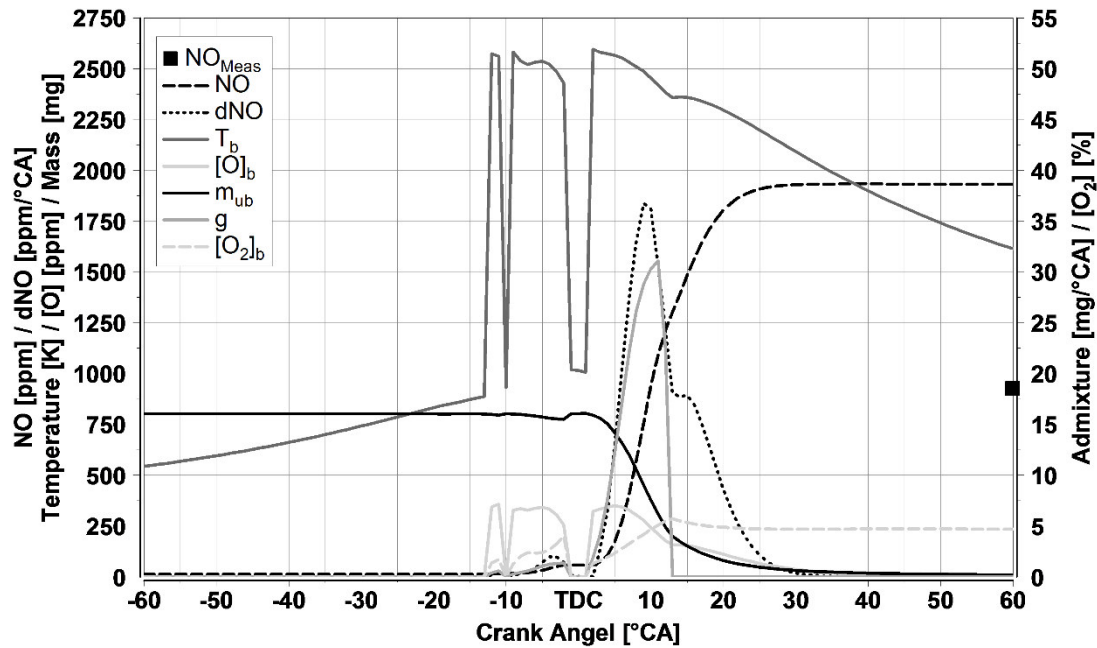


Figure 6.8: Operating cycle with breaking admixture¹ - 1200 min⁻¹, 14 bar IMEP

Because the model representation according to Kožuch is sensibly and also phenomenologically structured, it appears desirable to retain it and to adapt the modeling for areas with low global λ values. In this way, the good predictability of the model would be retained outside of low global λ values. The emissions model according to Kožuch influences the nitric oxide formation solely via the admixture, however, so that the retaining of the model representation is equivalent to an optimization of the admixture in one way or another. However, investigations have shown that an optimization of the admixture is not productive, because it runs completely contrary to a physical model representation and leaves too little reserve for even richer operating points [13]. Even a rich combustion following the model representation according to Hohlbaum [4] did not prove to be productive, because the simulated nitric oxide emissions reacted far too sensitively to the tuning values and the model thus could not be tuned [13].

A physically correct, zero-dimensional modeling of the nitric oxide emissions of a diesel engine thus does not appear to be practicable. For this reason, an approach based on pseudo-zones was selected, as previously in the case of the wall temperature influence in Chapter 6.1, in order to model the nitric oxide formation. As already similarly occurred for the modeling of the wall temperature influence, the burned zone is subdivided into additional pseudo-zones. The hot core zone, in which the entire nitric oxide formation occurs, is further sub-divided into two individual pseudo-zones.

¹ Two discontinuities are exhibited in the progression of values until shortly after TDC of the firing stroke. These occur because a complete mixing of the created burned and unburned zone occurs in the model after combustion of a pre-injection. This provides for homogeneous conditions before each new combustion.

One of these pseudo-zones receives a rich composition, while the other "stoichiometric" pseudo-zone² receives the composition of the thermodynamically burned zone, including the admixture from the unburned zone (see *Figure 6.9*). Both zones again pseudo-zones which thus have no influence on the simulation of the thermodynamic zones.

As previously discussed for the wall temperature influence, with this representation it is possible to implement the air deficiency influence in two different variants: A fixed division with variable composition of the pseudo-zones or a variable division with fixed composition. The maximum reduction of nitric oxide formation in this model representation, in comparison to the modeling according to Kožuch, is limited by the size of the rich pseudo-zone: Namely for the case that this pseudo-zone contains a sufficiently rich mixture in order to not allow any nitric oxides to form there at all. Accordingly, it does not appear sensible to choose an implementation with fixed size division but variable compositions, because the rich pseudo-zone would have to be differently sized depending on the application case. For this reason, an implementation with variable division was chosen, as previously in the case of the wall temperature influence.

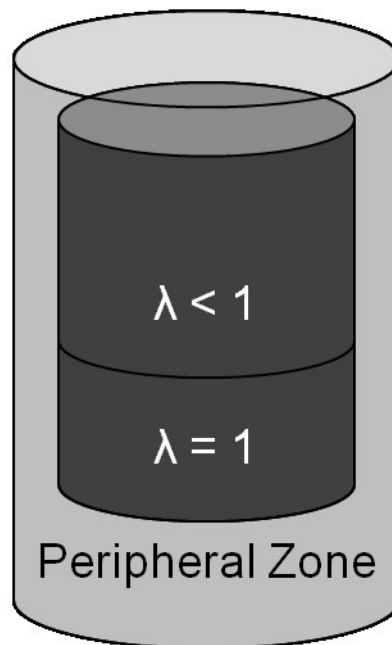


Figure 6.9: Model representation, air deficiency influence

For modeling of the nitric oxide emissions with sufficiently lean conditions, the emissions model according to Kožuch shall continue to be applied. The transition into the new model representation must therefore occur continually in every case, so that no kink occurs in the simulated nitric oxide concentration upon crossing into the new model representation.

² This pseudo-zone is designated in the following, not wholly correctly, as a stoichiometric (pseudo)-zone, although its composition is normally lean. The name comes from its composition occurring via a stoichiometric combustion and only becoming lean via the admixture.

For this reason, the stoichiometric zone takes on both the composition as well as the temperature of the thermodynamic burned zone; that is, according to a combustion at $\lambda = 1$ and the admixture modeled in the model according to Kožuch.

Additionally, for a global composition with a $\lambda < 1$, the rich composition of the thermodynamic burned zone is elevated to a stoichiometric composition for the stoichiometric pseudo-zone.

The rich zone is modeled with a composition as it occurs at a combustion of $\lambda = 0.6$. The temperature in the rich zone is calculated according to *Eq. 6.2* from the temperature of the thermodynamic burned zone reduced by the difference of the adiabatic isobaric flame temperatures for a stoichiometric flame and a flame at $\lambda = 0.6$. This approach is used to estimate the modified temperature of a burned zone in the case of rich combustion.

$$T_r = T_b - (T_{AIFT,st} - T_{AIFT,r}) \quad \text{Eq. 6.2}$$

After the definition of the conditions in the two pseudo-zones, the division of the core zones must still be specified. To this end, 11 operating points of a λ variation were simulated with the new modeling and the proportion of the rich pseudo-zone was optimized to the measured nitric oxide concentration. The result of the optimized proportion of the rich zone is shown in *Figure 6.10*. A linear approximation delivers only moderate correspondence, since the available curvature in the progression of the simulation results cannot be represented. A trigonometric approximation with a cosine function (*Eq. 6.3*) exhibits a particularly good correspondence with the results.

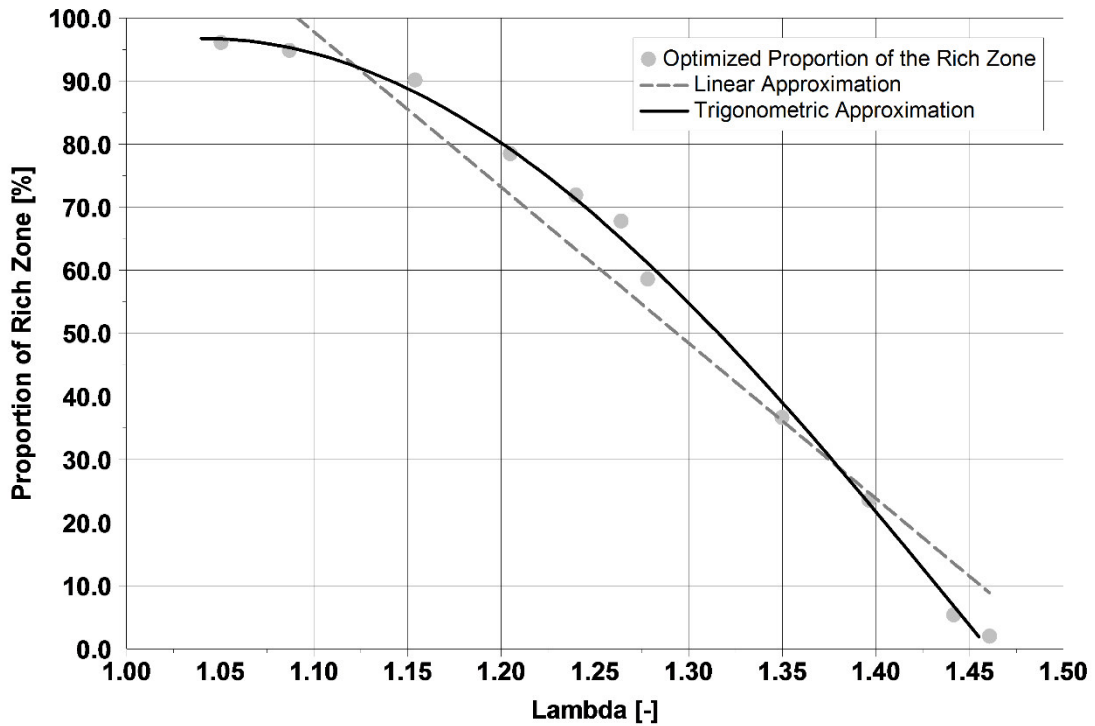


Figure 6.10: Linear and trigonometric approximation of rich proportion

$$a = \cos(A \cdot \lambda \cdot \pi + P \cdot \pi) + O$$

Eq. 0.1

Figure 6.11 shows a comparison between the measured values as well as the values simulated with the model according to Kožuch and the new model. It is clearly shown that the model according to Kožuch, as expected according to the remarks in this chapter, delivers nitric oxide concentrations which are completely false, due to being too high, for operating points with low global λ values. For these operating points, the modeled admixture breaks off at some point during the nitric oxide formation, the temperature in the burned zone rises and the nitric oxide concentration rapidly increases. This effect noticeably increases at lower λ values. The actual progression of nitric oxide concentration exhibits a reversed behavior, with a clear decrease for the operating points closest to the stoichiometric composition. The new model, by contrast, exhibits a very good correspondence with the measured nitric oxide values. Both the tendencies toward lower nitric oxide concentrations for very low λ values as well as the absolute values are represented very well by the model. The new model is thus able to correctly predict the nitric oxide concentrations even down to the lowest λ values.

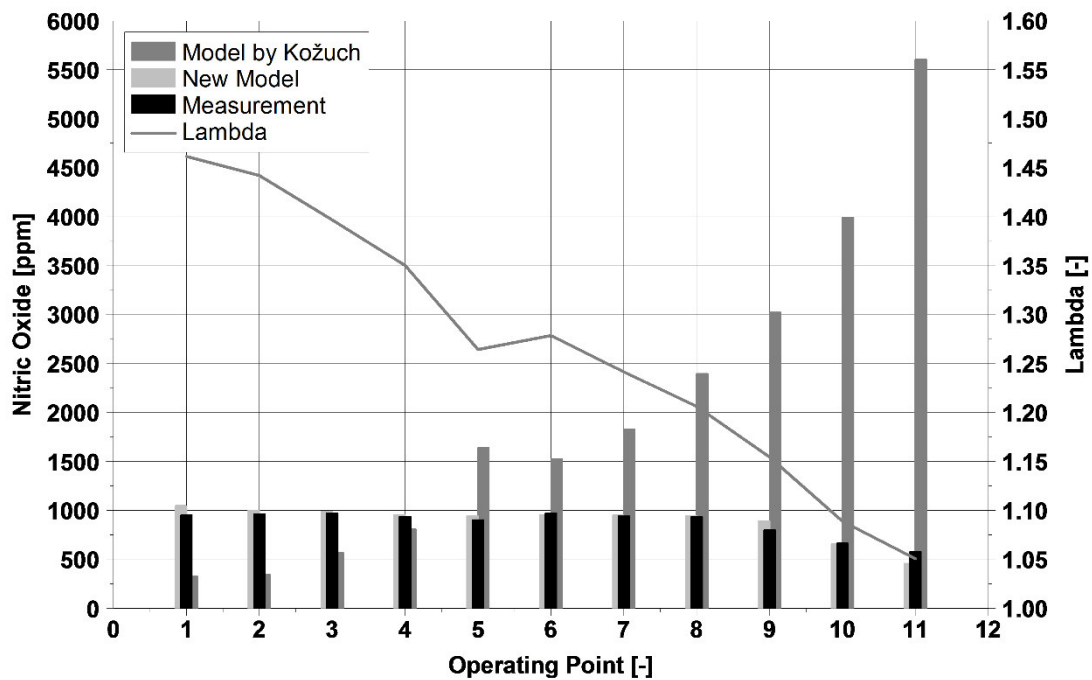


Figure 6.11: λ -Variation – Comparison of nitric oxide – 1000 min⁻¹, 11...14 bar IMEP

7. Model Tuning and Model Validation

7.1 Model Tuning

The new model can, in addition to the model according to Kožuch, model the wall temperature influence as well as simulate operating points with low global air ratios, while the base model according to Kožuch is retained for the simulation of nitric oxide concentrations. Therefore, for a tuning of the new model the base model according to Kožuch must first be tuned as usual. The potential tuning of the wall temperature as well as the air deficiency influence are independent of this and of each other. In comparison to the emissions model according to Kožuch, however, a significant improvement to predictability results via the new model even without explicit tuning, because the wall temperature influence was not considered and the predicting of emissions at operating points with low global λ values was not even possible with the base model. The new model can thus be used advantageously even without additional tuning effort or in the case of missing corresponding measurement data. For the best possible forecasting quality, an explicit tuning of the wall temperature and air deficiency influence is nevertheless required, whereby the two sub-models can be tuned separately from each other, as already mentioned. Both a simplified as well as a detailed tuning is possible for both sub-models. In the following, however, only the simplified tunings are presented. For the detailed tunings, see [13].

A simplified tuning of the wall temperature influence can be carried out with a single tuning parameter at only one measurement point. Parameter F can be tuned to an operating point with very low coolant temperatures once the admixture parameter c_g has been tuned on the hot engine. With this, the progression of the approximation over the temperature can be scaled without too severely changing the basic form. The parameter C should not be adjusted here. It describes the minimum wall thickness at high wall temperatures and would always have to be balanced by an adjustment of the parameter c_g to the admixture in the base model according to Kožuch. Parameter E should only be carefully changed or not changed at all in the case of only little applicable measurement data, since it can heavily influence the form of the approximation over temperature.

A simplified tuning of the air deficiency influence can also be carried out with only one tuning parameter. In this case the tuning occurs via the parameter P, which adjusts, in a certain range, the lambda value from which the model has effect. In this case, a single operating point with a sufficiently low air ratio, so that the model already takes effect, suffices for tuning of the air deficiency influence. The parameter O describes the stoichiometric remainder at maximum effectiveness of the model and should not be adjusted, because there is normally no data for such low air ratios without special measurements. Parameter A causes a deformation of the tuning curve and should not be adjusted, because this deformation must be balanced via the other parameters and more measurement data is required for this.

7.2 Model Validation

For model validation, the new model will first be compared to the measurement data from the performance map measurement. It will thus be shown whether the model expansions correctly reproduce the combustion chamber wall temperature and air deficiency influence in general. A validation will then be performed on transient measurements performed on load steps.

7.2.1 Stationary

In this chapter, a comparison is made between the emissions model according to Kožuch, the new model and the measurement data. The new model retains the parameters specified in Chapter 6.1 for consideration of the wall temperature influence, as well as the parameters tuned in Chapter 6.2 for consideration of the air deficiency influence. *Figure 7.1* shows the simulation results of the two models together with the measurement data.

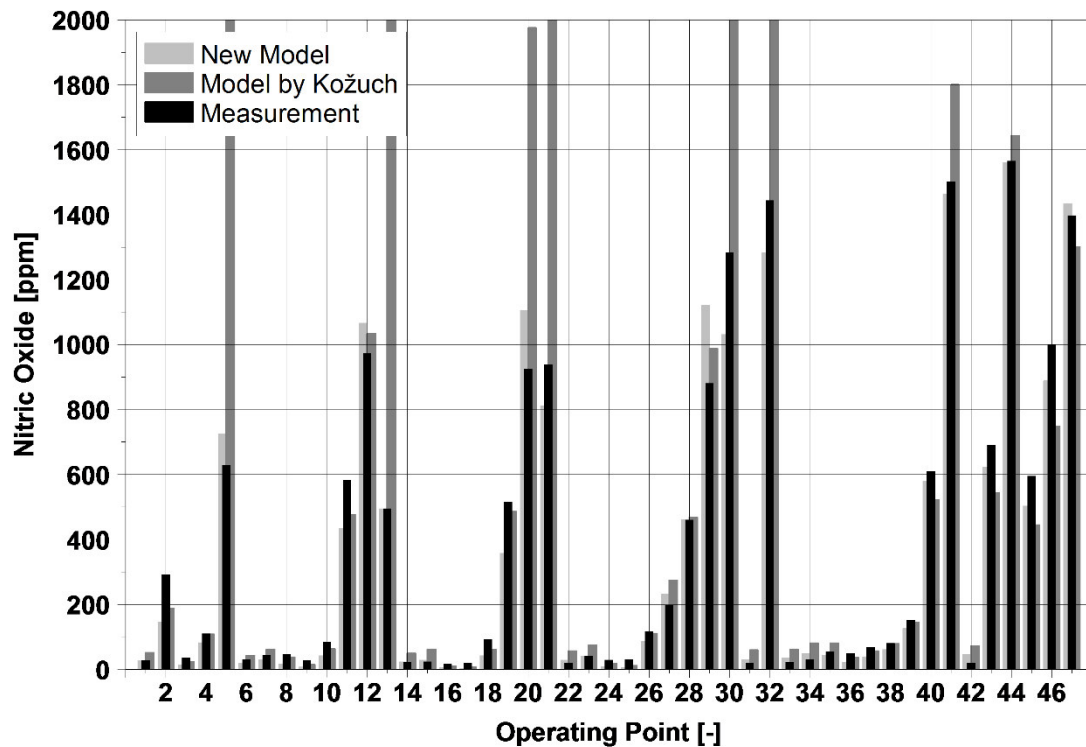


Figure 7.1: Model validation on the performance map

For the model according to Kožuch, at first, operating points 5, 13, 20, 21, 30 and 32 stand out, since, due to their low air ratios, they show a breaking admixture with the effects described in Chapter 6.2. The simulation results of the new model show, however, that it is able to predict emissions even for the operating points with the lowest global λ values. Agreement with the measured values has also mostly improved for the remaining operating points. This can be best determined based on the results from operating point 33 and higher. The highest speeds of 2000, 2400 and 3000 min^{-1} are found here, at which the temperature influence is strongest due to the increase in load between 1 and > 20 bar IMEP and the λ values are still sufficiently large so that the combustion chamber wall temperature influence is not overlapped by the air deficiency influence. At these operating points, the new model shows a significantly better correspondence with the measurement values than the model according to Kožuch, thanks to the consideration of the combustion chamber wall temperatures. In summary, it can be said that the new model exhibits overall better forecasting quality. This particularly applies when the operating points with low global air ratios are included in the consideration, since a prediction of the nitric oxide concentrations for such operating points only becomes possible with the new model in the first place.

7.2.2 Transient

The new emissions model was developed with the goal of simulating transient emissions and shall be accordingly validated based on transient measurements in this chapter.

Temperature Load Steps

The new emissions model is first validated based on two identical load steps at different engine temperatures. The load steps each occur from approx. 1 bar to 6 bar IMEP at 850 min⁻¹. One load step occurs with the engine cold, at a coolant and oil temperature of 35 °C each; the second with the engine hot at 85 °C each. The two load steps thus have differing combustion chamber wall temperatures at the beginning and likewise exhibit differing steps for those temperatures. The models were each tuned to the best possible correspondence with the measured values after both load steps. The results of the simulation, together with the measured nitric oxide concentrations, are shown in *Figure 7.2*.

Particularly in the case of the "cold" load steps, saw-tooth-shaped spikes are recognizable in the simulated NO curves. These originate from the combustion model, whose ignition delay reacts too sensitively to the modified temperature level. The corresponding jumps in the simulated nitric oxide emissions in *Figure 7.2* are thus not due to the emissions models, but rather the combustion model, and cannot be avoided in connection with this study.

In comparison with the measured data, the emissions model according to Kožuch shows a spread of results for the hot and the cold load step which is far too small. For the concrete load steps, even a false tendency is returned: the model according to Kožuch simulates higher nitric oxide concentrations for the cold load step than for the hot, in the case of a common tuning for both load steps to the measured nitric oxide concentrations after the load steps. The differences in the ancillary conditions of the two load steps caused by the different temperature levels thus result in a trend which is contrary to the measured nitric oxide concentrations in the case of the model according to Kožuch.

In the case of the new model, the trend corresponds to the measured behavior: the hot load step returns higher simulated nitric oxide concentrations than the cold. While the emissions after the cold load step are well on target, they are just slightly under the measured values for the hot load step. Likewise, the strongly pronounced emissions peaks directly after the load steps simulated by the model according to Kožuch are extensively eliminated with the new model.

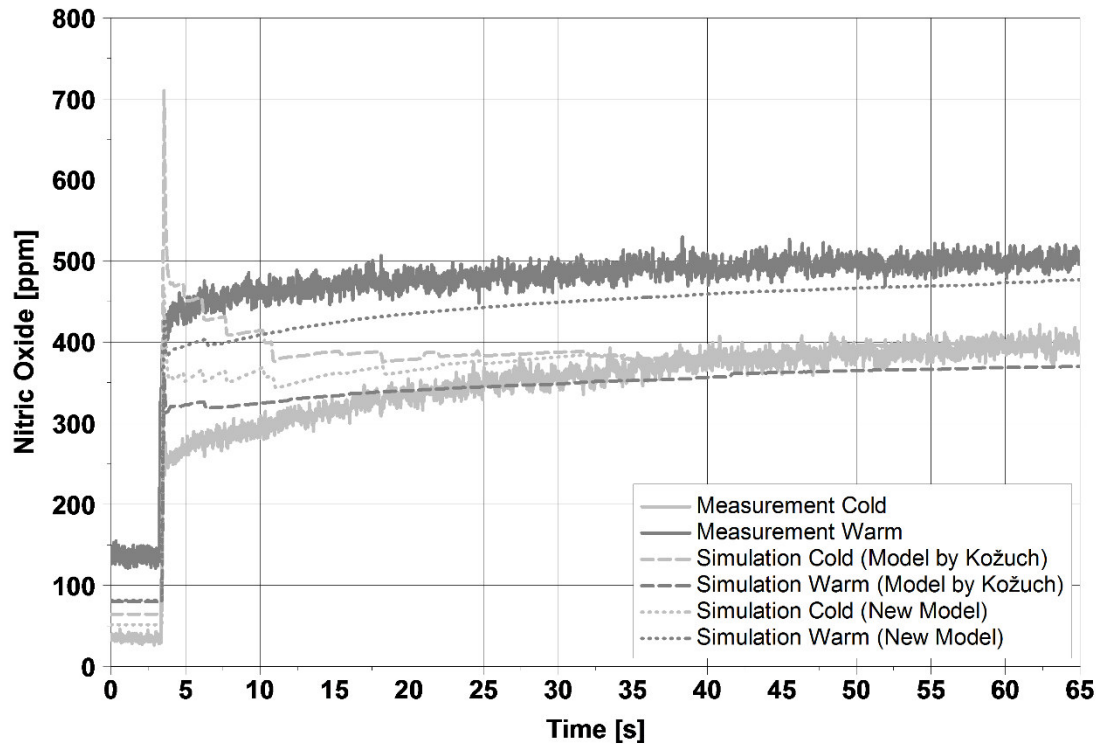


Figure 7.2: Model validation based on temperature load steps – cold and hot

Lambda Load Step

For validation of the representation of the air deficiency influence while transient, a load step from zero load to full load is considered (1...12 bar IMEP, 850 min⁻¹) with a correspondingly large spread of the combustion air ratio: ideal prerequisites for validation of the new sub-model.

Figure 7.3 shows the nitric oxide concentrations over time simulated with the two models compared with those measured. Whereas the new model can follow the measured values during the load step very well, except for a minor temporal delay, and also reproduces the progression and the absolute values after the load step well, the model according to Kožuch reacts too slowly to the load step and especially does not exhibit the drop in nitric oxide concentrations after reaching a maximum value, which is visible in the measurement.

An alternative depiction with the simulated and measured nitric oxide concentrations over the air ratio is shown in Figure 7.4. In this depiction, the missing prediction of the nitric oxide emissions for low air ratios by the model according to Kožuch becomes particularly clear. For falling λ values, the emissions first rise for both models, just as for the measurement. At $\lambda = 1.58$ for the measurement or $\lambda = 1.46$ for the new model, the nitric oxide emissions decrease again. The model according to Kožuch does not exhibit this behavior, but rather continually and even increasingly steeply rising nitric oxide concentrations.

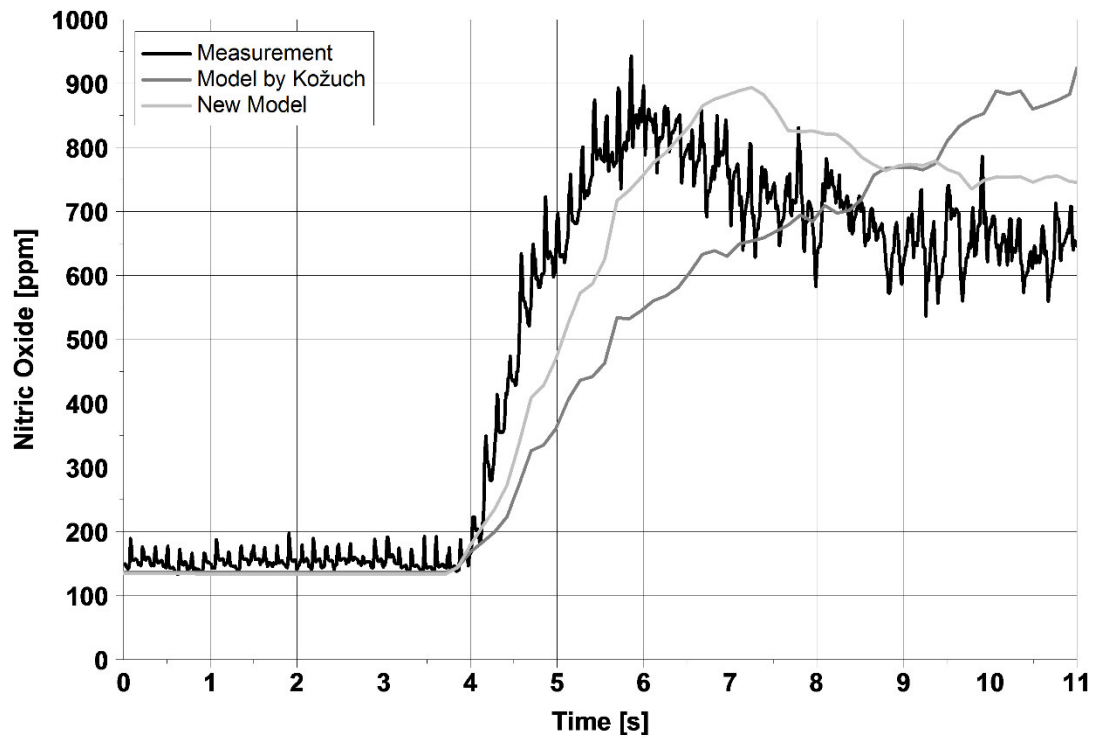


Figure 7.3: Lambda load step – NO over time

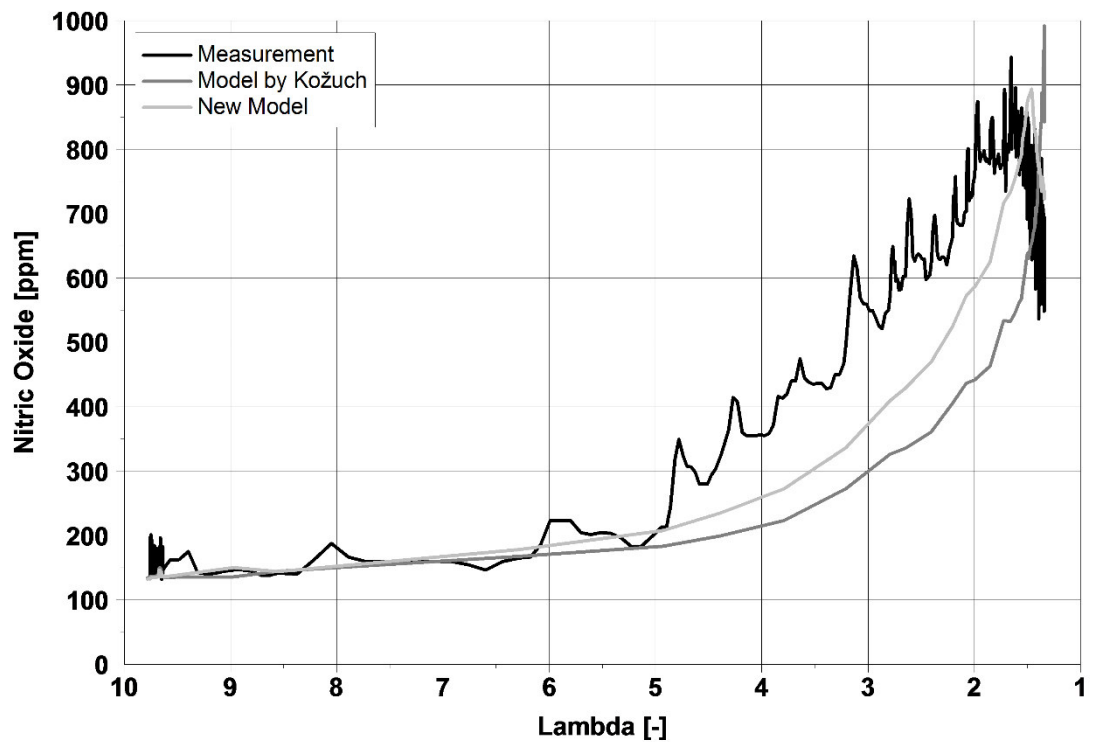


Figure 7.4: Lambda load step – NO over combustion air ratio

References

- [1] „Das Statistik-Portal,“ 2014. [Online]. Available: <http://de.statista.com/statistik/daten/studie/30846/umfrage/dieselanteil-an-den-pkw-neuzulassungen-in-westeuropa/>
- [2] P. Kožuch, Ein phänomenologisches Modell zur kombinierten Stickoxid- und Rußberechnung bei direkteinspritzenden Dieselmotoren, Dissertation: Universität Stuttgart, 2004
- [3] H. Hiroyasu, T. Kadota and M. Arai, "Development and Use of a Spray Combustion Modeling to Predict Diesel Engine Efficiency and Pollutant Emissions," Bulletin of the JSME, vol. 26, no. 214, pp. 569–575, April 1983
- [4] B. Hohlbaum, „Beitrag zur rechnerischen Untersuchung der Stickstoffoxid-Bildung schnelllaufender Hochleistungsdieselmotoren,“ Dissertation, Universität Fridericiana Karlsruhe, 1992
- [5] G. Heider, Rechenmodell zur Vorausrechnung der NO-Emission von Dieselmotoren, Dissertation: Technische Universität München, 1996
- [6] M. Heinle, Ein verbesserter Berechnungsansatz der instationären Wandwärmeverluste in Verbrennungsmotoren, Dissertation: Universität Stuttgart, 2013
- [7] M. Grill, Objektorientierte Prozessrechnung von Verbrennungsmotoren, Promotion: Universität Stuttgart, 2006
- [8] G. Woschni, K. Kolesa and W. Spindler, "Untersuchung des Verhaltens eines Dieselmotors mit wärmedichtem Brennraum," in Forschungsberichte Verbrennungskraftmaschinen, vol. 311, Frankfurt am Main, Forschungsvereinigung Verbrennungskraftmaschinen eV, 1986
- [9] W. Spindler and K. Kolesa, "Ermittlung des Wärmeübergangskoeffizienten bei hohen Wandtemperaturen," in Forschungsberichte Verbrennungskraftmaschinen, vol. 399, Frankfurt am Main, Forschungsvereinigung Verbrennungskraftmaschinen eV, 1987
- [10] N.-N. Nguyen, Über den Einfluss der Wandtemperatur auf die Reaktionsbedingungen in der Grenzschicht und insbesondere auf den konvektiven Wärmeübergang einer Propan-Luftflamme, Dissertation: Universität Kaiserslautern, 1983
- [11] G. P. Merker, C. Schwarz, G. Stiesch and F. Otto, Verbrennungsmotoren: Simulation der Verbrennung und Schadstoffbildung, Wiesbaden: B. G. Teubner, 2007
- [12] C. Eiglmeier, Phänomenologische Modellbildung des gaseitigen Wandwärmeeüberganges in Dieselmotoren, Dissertation: Universität Hannover, 2000
- [13] B. Kaal and M. Sosio, Instationäre Emissionsmodellierung am Dieselmotor, Vols. 1062 - 2015, Frankfurt am Main: Forschungsvereinigung Verbrennungskraftmaschinen e.V., 2015

The Authors:

Dipl.-Ing. Benjamin Kaal, Forschungsinstitut für Kraftfahrwesen und Fahrzeugmotoren Stuttgart, Stuttgart

Dipl.-Ing. Massimiliano Sosio, Forschungsinstitut für Kraftfahrwesen und Fahrzeugmotoren Stuttgart, Stuttgart

Dr.-Ing. Michael Grill, Forschungsinstitut für Kraftfahrwesen und Fahrzeugmotoren Stuttgart, Stuttgart

Prof. Dr.-Ing. Michael Bargende, Forschungsinstitut für Kraftfahrwesen und Fahrzeugmotoren Stuttgart, Stuttgart

Licence:

This document is licensed under the Creative Commons Attribution 3.0 DE License (CC-BY 3.0 DE): <http://creativecommons.org/licenses/by/3.0/de/>

Physical modeling of combustion for diesel engines and assessment of a NO_x-kinetic for gasoline, gas and diesel engines

Reza Rezaei
Friedrich Dinkelacker
Benjamin Tilch
Thaddäus Delebinski
Maximilian Brauer

Abstract

Enhancing the predictive quality of engine models, while maintaining an affordable computational cost is of great importance. In this study, a phenomenological combustion model for diesel combustion and a tabulated NO_x kinetics model for methane, iso-octane and diesel fuel are presented. The combustion model uses physical and chemical sub-models for local processes like injection, spray formation, ignition and combustion. Modeling of NO_x formation is based on detailed tabulated chemistry methods. The applied combustion model accounts for the turbulence-controlled as well as the chemistry-controlled combustion in compression ignition engines. The phenomenological combustion model is first assessed for passenger car application, especially with multiple pilot injections and high EGR ratios for low load operating points. The validation results are presented for representative operating conditions from a single-cylinder light-duty diesel engine and also a heavy-duty diesel engine.

In the second part of this study a novel approach for accurate and very fast modeling of NO formation in combustion engines is proposed. This approach is based on tabulation of detailed chemical kinetic and is validated against the detailed chemical reaction mechanism at all engine-relevant conditions with variation of pressure, temperature, and air/fuel ratio under stationary and ramp-type transient conditions in a perfectly-stirred reactor considering different fuels for gasoline, gas and diesel engines. Using this approach, a very good match to the results from calculations with the detailed chemical mechanism is observed. Finally, the tabulated NO_x kinetic model is implemented in the combustion model for in-cylinder NO_x prediction and compared with experimental engine measurement for instance a diesel engine.

1. Introduction

Numerical simulation methods are utilized as a standard tool for the description of internal combustion engine processes, and for the optimization to fulfill future emission standards, fuel consumption reduction and improved safety and drivability, see e.g. Heywood [1]. A predictive model that accounts for several engine processes such as combustion and emission formation plays a decisive role in powertrain development, including optimization of engine components as well as development, testing, and model-based calibration of combustion and aftertreatment control strategies [2].

Fast empirical combustion models, e.g. Vibe function [3], often suffer from a lack of predictability. Phenomenological models have the advantage of being both easy to handle and computationally efficient. In addition, they are capable of predicting several effects of important parameters on the combustion process and emission formation.

In recent years, multiple modeling approaches have been studied by various investigators. For instance, the approach proposed by Chmela et al. [4, 5] is a global model based on a single-zone description of the combustion chamber. It does not require subdividing of the combustion chamber into zones of different compositions and temperatures. Therefore, it offers a fast and computationally efficient modeling. This is categorized as a phenomenological combustion model, since it relates the burning rate to the engine characteristic parameters (e.g. the injection rate as a time-dependent input parameter) [6, 7]. The main issue of this model is the hypothesis that the rate of fuel combustion is determined by the rate of air-fuel mixing. The rate of air-fuel mixing depends on the injection rate as well as turbulent kinetic energy.

More detailed models are generally less computational efficient. For example the so-called packet model from Hiroyasu et al. [8, 9] can be mentioned, in which the compression stroke is modeled with one zone, while the injection spray is discretized into small packets in axial and radial directions. Other authors follow this concept, e.g. [10, 11, 12]. Stiesch and Merker [12] modified this model so that the maximum burning rate of each packet depends not only on the vaporized fuel and the available air but also on the maximum chemical reaction rate. Barba [7] proposed an empirical and a phenomenological combustion model. The phenomenological combustion model accounts for premixed and also the diffusion combustion in combination with an ignition delay model.

2. Combustion model formulation

As the focus of the current study is set on highly efficient modeling of combustion, the approach of Chmela et al. [5] for single-zone modeling of spray and combustion is used as basis of the development while the spray is not modeled with the packet approach. The time evolution of spray characteristics are governed by mass and momentum conservation equation of the spray control volume. The model is integrated as a user subroutine in the simulation software GT-Power [13] accounting for two-zone description of the cylinder thermodynamics. The working fluid consists of an unburned zone and a burned zone with energy and mass interactions between themselves. For each zone, the thermodynamic properties such as temperature, gas composition, etc. are calculated separately.

For brevity, only the highlights of the combustion model for modeling the multiple pilot injections for passenger car application under low load and high exhaust gas recirculation ratio are described here. More detail about the physical sub-models such as injection, spray formation, and combustion can be found in [14].

2.1 Ignition model

The applied ignition model employs semi-empirical models for both physical and chemical sub-processes accounting for ignition delay. Modeling of the chemical ignition delay is performed by a least-square fitted ignition model of Weisser [15] that enables the capture of the low temperature and high temperature ignition behavior, including the negative temperature (NTC) region in between, Figure 1. In order to consider the effect of physical sub-processes on ignition delay, a simple formulation used by Barba [7] is used to describe the physical ignition delay.

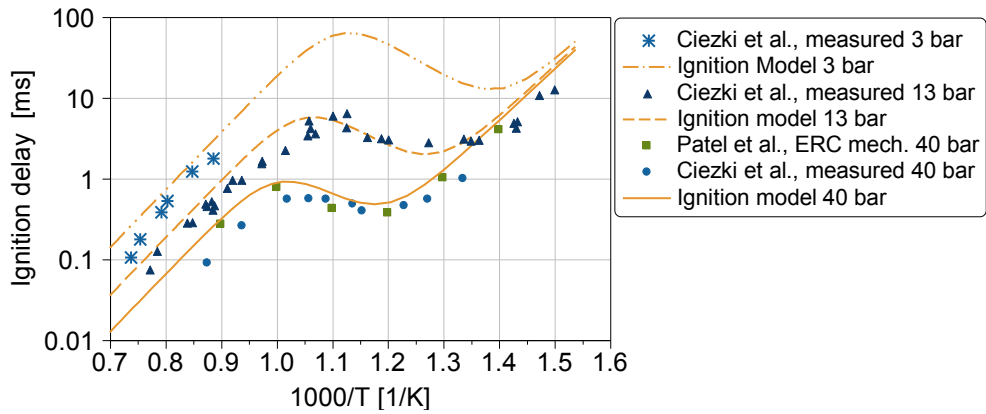


Figure 1: Comparison of the ignition delay sub-model with experimental measurements of Ciezki et al [16] and the reduced reaction kinetic mechanism of Patel et al. [17]

2.2 Premixed and diffusion combustion modeling

The combustion model is principally a laminar-and-turbulent characteristic-time combustion model which is frequently used in CFD models for diesel engine combustion [18] with improvements accounting for the premixed, diffusion, and burn-out combustion [14]. This handles the two extremes of combustion, reactions limited by kinetics and those limited by mixing.

For the reaction kinetics limit, the laminar time scale, τ_l is calculated according to Kong et al. [18],

$$\tau_l = A[fuel]^{0.75}[O_2]^{-1.5} \exp(E / RT) \quad (1)$$

The effects of exhaust gas recirculation and oxygen concentration as well as fuel concentration in the mixture are taken into account.

Combustion limited by mixing is the other extreme, if the chemical time scales are negligibly small compared to the turbulent mixing time scales. For instance, the Eddy Break-Up (EBU) model assumes the resulting effective reaction rate to be proportional to the reciprocal of the turbulent time scale [19]. In fact, the entire spectrum of combustion regimes can be found in diesel engine combustion. This means that at any

time, there may be a partial burning in either a kinetically-limited or mixing-limited way, while the overall combustion often lies somewhere in between these extremes. The developed combustion model accounts for both laminar and turbulent time scales.

For passenger car applications, there are considerable amount of low-load points in the engine map which are operated in the New European Driving Cycle (NEDC). These points may have moderate or high EGR rates with multiple pilot injections and therefore a major portion of the combustion is premixed and chemically controlled. The combustion model is improved here in order to calculate the ignition delay considering the low temperature, NTC ignition, and the high temperature ignition which may happen by an early pilot injection, late main, or a post injection. The ignition delay is calculated for each injection event. The spray model calculates the mixture preparation for each event individually. The effect of air-entrainment and dilution of mixture before and after combustion have an important effect on ignition and premixed combustion afterwards. This is considered in the spray model, providing the mass fraction of the mixed fuel above a certain relative air-fuel ratio as a function of mixing time, and this crucial input is used by the combustion model for each injection event separately.

3. Test engines

The combustion model is validated using measurement data of different diesel engines, from passenger car up to heavy-duty applications, utilizing EGR and various injection strategies. For brevity, only two validation engines are presented here.

3.1 Light-duty passenger car diesel engine

The presented combustion model is modified for passenger car light-duty application with relatively high EGR ratios and multiple pilot injections with focus on part and low-load cases which are relevant for the European exhaust-emission legislation in the NEDC cycle. The thermodynamic measurements are conducted on a passenger car single-cylinder engine with a displacement of approximately 536 cm³. The engine has an eight-hole nozzle with a common-rail injection system. All relevant pressures and temperatures (intake air, EGR, exhaust gas, lubricant, coolant) are controlled externally by the test bench. The main engine parameters are listed in Table 1:

Bore	83 mm
Stroke	99 mm
Compression ratio	16.2
Max. peak firing pressure	220 bar
Number of nozzle holes	8
Nozzle hydraulic flow rate	710 cm³ / min @ 100bar

Table 1: Specifications of the passenger car single-cylinder test engine

3.2 Heavy duty diesel engines

The second validation engine is a heavy-duty diesel engine, certified for the non-road Tier 4i emission standard. It has a displacement of approximately 2000 cm³ for each cylinder and an eight-hole nozzle equipped with a common-rail injection system. No EGR is applied at this engine. All points on the engine map are considered, Figure 2.

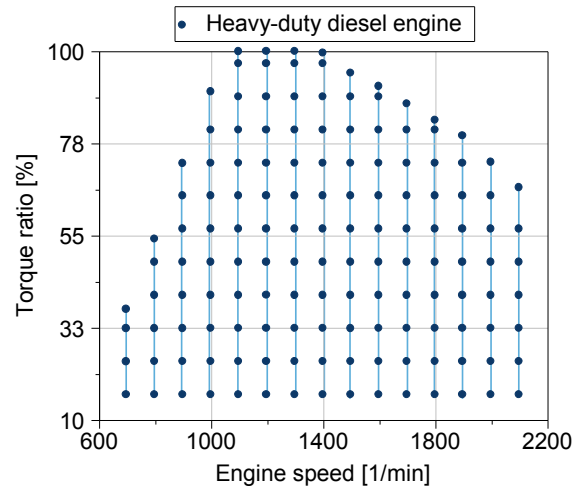


Figure 2: The investigated engine operating points of the heavy-duty diesel engine

4. Validation of the phenomenological combustion model

4.1 Light-duty passenger car diesel engine

For the light-duty passenger car engine, at first, a full load operating point is selected for validation of the combustion model with variation of the rail-pressure. For the two part load operating points, a start of injection (SOI) variation and an EGR variation are carried out. As given in Table 2, the engine speed differs for the part and full load cases. GT-Power is used as simulation platform and the integrated combustion model is used for modeling of heat release rate with the same parameters for all operating points.

Operating point	Engine speed [1/min]	Mean effective pressure [bar]	Rail-pressure [bar]	EGR rate [%]
A	3700	14.9-17.4	1600-2200	0
B	1200	6.2-6.5	800	34-38
C	1200	6.2-6.3	800	0-41

Table 2: Investigated operating points using the passenger car single-cylinder engine

Figure 3 compares the simulated in-cylinder pressure with the measurement. Shifting the start of injection to an earlier time, increases the maximum cylinder pressure and the pressure gradient, which are both reproduced properly by simulation. A good match is observed between simulation and measurement in Figure 3.

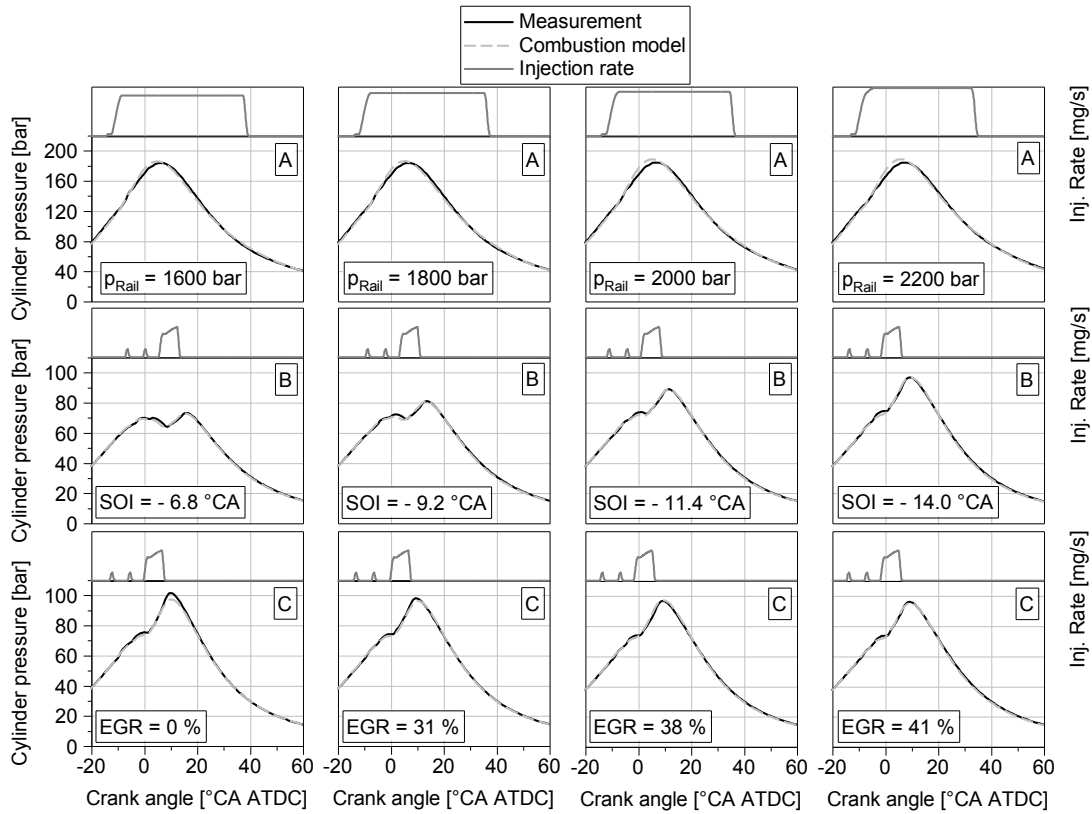


Figure 3: Comparison of the simulated in-cylinder pressure with measurement. Operating points A, B, and C correspond to $n=3700$, 1200 , and 1200 1/min

4.2 Heavy-duty diesel engine

Additionally, the phenomenological combustion model is investigated on a heavy-duty diesel engine. Calibration of the combustion model parameters is carried out for nine representative operating points and then used with the same parameters for the entire engine map.

Three important engine speeds of 1200 , 1500 , and 1900 1/min with engine load of 25% , 50% , 75% , and 100% are selected for plotting in Figure 4. The simulated heat release rate is compared with results obtained from the thermodynamic analysis of the measured cylinder pressure. A good concordance between simulation and measurement is obtained for all the full and part load cases.

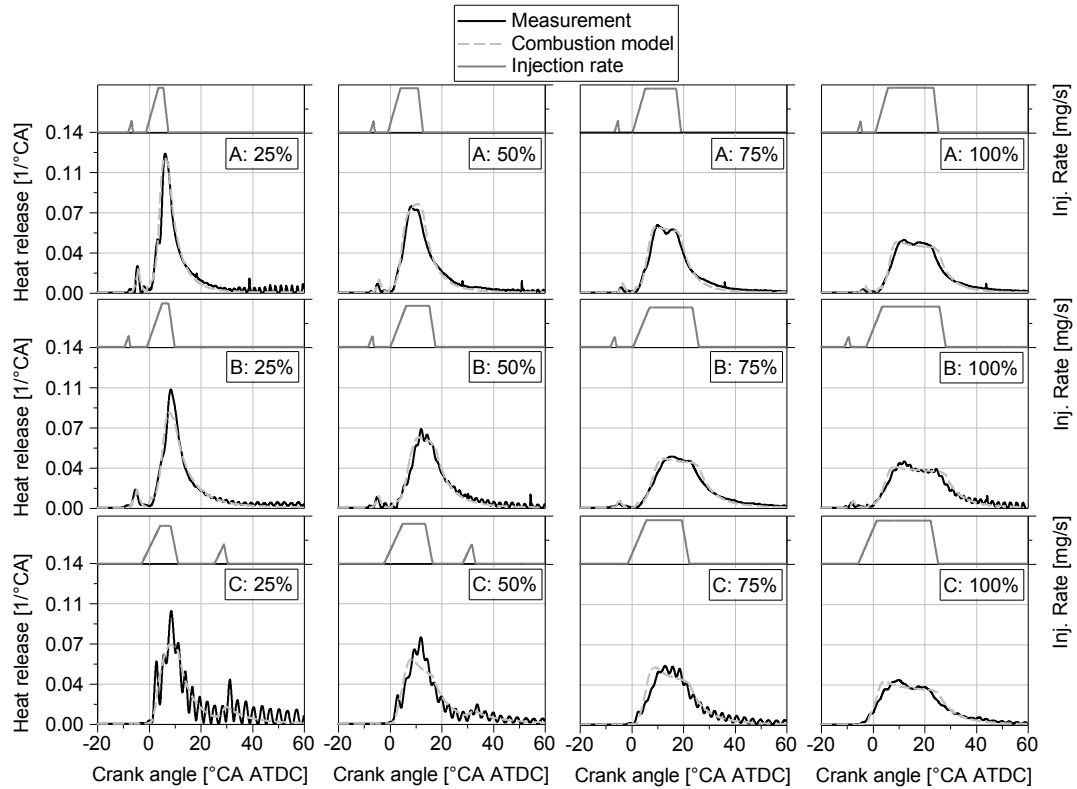


Figure 4: Heat release rate obtained from the combustion model and thermodynamic analysis of experimental investigation. Operating points A, B, and C correspond to $n=1200$, 1500 , and 1900 1/min with 25%, 50%, 75%, and 100% load respectively

5. Tabulated NO_x Kinetic Model

The emission of nitrogen oxides (NO_x) is limited for internal combustion engines. The formation of NO or NO₂ is determined by complex chemical processes, being strongly dependent on temperature. A fast and efficient prediction of the NO_x emissions depending on the engine parameters is therefore a rather difficult task. Thermal equilibrium calculations are the first approximation, but are commonly known to be insufficient. In the following work this will be compared with three other approaches: the extended Zeldovich mechanism, a fully detailed reaction mechanism which, however, is much too slow for in-situ calculations, and a newly developed combined method of a tabulation and a relaxation procedure, being very fast.

The extended Zeldovich mechanism [20] is a common reaction kinetic to model the thermal NO formation and is often used in 1-D as well 3-D simulation tools, employing three kinetic reactions and assuming further equilibrium reactions. These equilibrium reactions are required to calculate the H, O, and OH radicals for the three slower kinetic reactions, determining the NO concentration.

In this study, an analytical investigation of NO_x formation kinetics in all engine-relevant conditions is carried out, using the detailed chemical reaction mechanism GRI-Mech 3.0 [21] with 325 reactions and 53 species for different fuels. Figure 5 shows the investigated operating conditions from 2000 to 3000 K as well as various relative air-fuel ratios from 0.4 to 3.0. Each of these operating conditions is simulated in a perfectly-stirred and adiabatic reactor. The reactor pressure and temperature are defined as constant values at start of the simulation. The mole fraction of each species, O, H, OH,

etc. is initialized equal to its mole fraction in the equilibrium condition by the given pressure, temperature, and air-fuel ratio, assuming that combustion is very fast compared to the NO kinetic and the combustion products are in equilibrium state at the start of the reactor simulation. The composition of each investigated fuel is considered in the combustion products initialized in the equilibrium condition at the start of reactor simulations.

NO is initialized as zero and is formed in this perfectly-stirred reactor until reaching its value at the equilibrium condition. The rate constants of the Zeldovich mechanism are used as given by Bowman [22]. The same initial conditions such as temperature, pressure and species concentration are implied for both the detailed kinetic and Zeldovich mechanism at the start of reactor simulation.

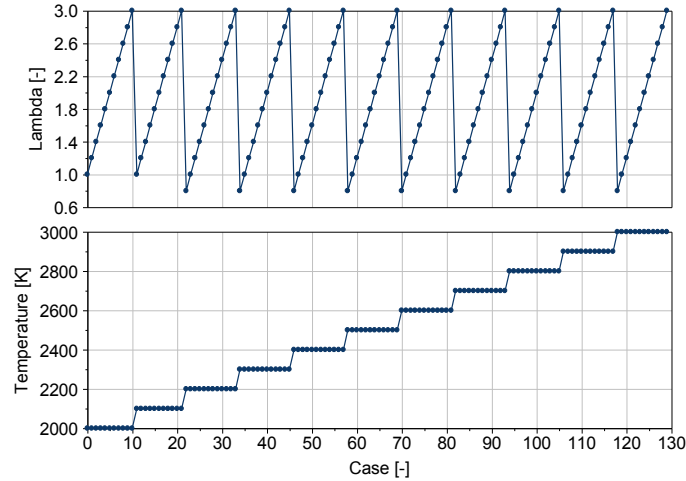


Figure 5: Temperature and pressure variation for each reactor simulation case

In order to evaluate the Zeldovich mechanism, NO concentrations at the different representative times after start of NO formation are compared with values from the detailed kinetic as well as their values in the equilibrium condition for tetradecane, Figure 6.

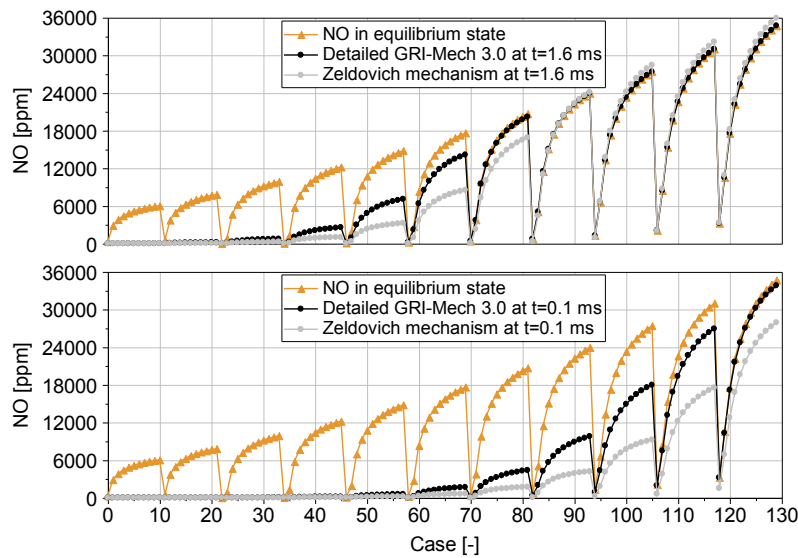


Figure 6: Comparison of the NO concentration in a perfectly-stirred reactor at 0.1 ms and 1.6 ms after start of NO formation for various operating conditions for tetradecane

The selected post-processing time of 1.6 ms in Figure 6, corresponds to e.g. 12 °CA at 1250 1/min, which is an important time scale for combustion and emission formation. As Figure 6 illustrates, large deviation between the calculated NO by the Zeldovich mechanism and the detailed GRI-Mech 3.0 mechanism is observed during the formation phase. Depending on operating conditions and completeness of NO formation, an inaccuracy factor of about approximately 2 is observed in the formation phase. This correlates with an uncertainty factor of 2 for NO formation reactions [1]. It can be concluded here that the Zeldovich mechanism with a big deviation in prediction of the NO formation phase, could be a source of inaccuracy in simulation of NO_x emissions in combustion engines. However a direct implementation of a detailed reaction mechanism like GRI-Mech 3.0 or even a reduced mechanism with fewer reactions as proposed e.g. by Yoshikawa and Reitz [23], is computationally not affordable for a fast-running phenomenological combustion model. For improving the accuracy and computational time, a tabulated chemistry method for modeling the NO formation, based on the characteristic chemical relaxation time scale is proposed. This is similar to the proposed model of Kong et al. [18] for modeling the premixed combustion,

$$\frac{\partial \tilde{Y}_i}{\partial t} = -\frac{\tilde{Y}_i - \tilde{Y}_i^*}{\tau_{chem}} \quad (2)$$

Here, for NO formation, τ_{chem} is taken as the characteristic formation time scale and \tilde{Y}_i^* as the NO concentration in the equilibrium state. Solving the above differential equation with initial conditions of $NO(t=0)=0.0$ leads to:

$$NO(t) = NO^* - NO^* e^{-\frac{t}{\tau_{chem}}} \quad (3)$$

In order to calculate the NO concentration using (3), the characteristic chemical time, τ_{chem} and the NO concentration in equilibrium condition, NO^* are required. These values can be calculated from the GRI-Mech 3.0 detailed chemical reaction mechanism in a perfectly-stirred reactor for various temperatures and air-fuel ratios and are provided as look-up tables. A temperature range from 2000 to 3000 K and different gas compositions according to relative air-fuel ratios from 0.4 to 3.0 at a constant pressure of 80 bar, are selected for tabulation of the required parameters. Calibration of the proposed reaction mechanism and calculation of both parameters for each simulation case is performed by minimization of error using the particle swarm optimization solver [24]. Figure 7 compares the NO formation at 80 bar and temperature of 2700 K for different relative air-fuel ratios.

A very good match between the proposed NO_x kinetic model and results obtained from the detailed GRI-Mech 3.0 mechanism with 325 reactions and 35 species is obtained. In order to assess the accuracy of the proposed kinetic, the deviation from the simulated NO by the detailed mechanism during the formation phase is calculated and the relative error (in percent) is given by (4).

$$Relative\ error = \frac{\int_0^{t_{equil}} |NO_{Tab.Model}(t) - NO_{Detailed\ mech.}(t)| dt}{\int_0^{t_{equil}} NO_{Detailed\ mech.}(t) dt} \cdot 100\% \quad (4)$$

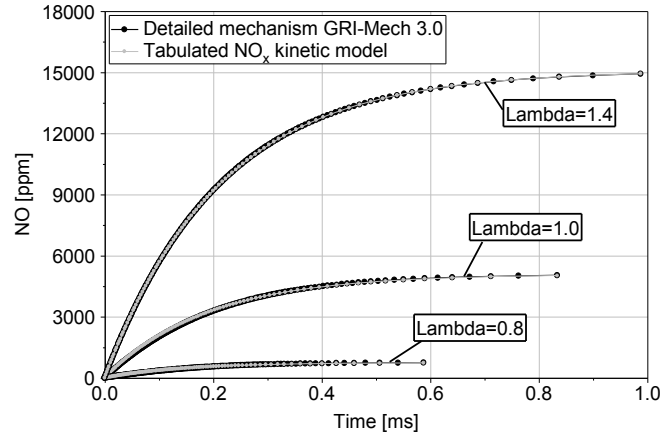


Figure 7: Validation of the tabulated NO_x kinetic model for NO formation in a perfectly-stirred reactor at 2700 K and 80 bar for different relative air/fuel ratios for tetradecane

Figure 8, right side, shows that the relative error for the majority of simulated cases is lower than one percent. For some points with low temperature and rich mixture, a higher relative error is observed; however, as shown at the left side of Figure 8, the NO concentration for this region is lower than 5 ppm, so overall a very good match is reached for the tetradecane as a reprehensive diesel fuel. With this very fast modeling approach neither kinetics nor equilibrium reactions need to be solved. Consequently the computational speed is significantly improved without loss in accuracy which enables this approach even for engine control unit (ECU) applications.

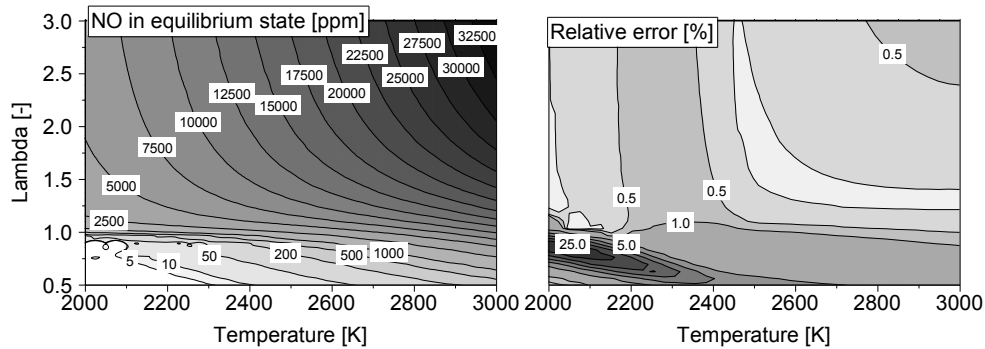


Figure 8: Evaluation of the tabulated NO_x kinetic model for NO formation in a perfectly-stirred reactor at various temperatures and air-fuel ratios for the tetradecane fuel

An important parameter which is investigated in this study is the effect of NO concentration at the start of the reactor simulation on the chemical time constant. In engine simulation, in the early phase of combustion with relatively high temperature, NO is formed in the burned zone and in the later phase of combustion, because of fast mixing with the unburned mixture, the temperature is reduced. Therefore, it may happen that the local concentration of NO is higher than the NO concentration in the equilibrium condition of the corresponding temperature and thus a backward reaction occurs.

In order to evaluate the ability of the proposed kinetic in such conditions, all mentioned operating conditions, temperature, and air-fuel ratio variations are simulated with a

start value of NO concentration equal to the NO concentration of the corresponding equilibrium conditions plus 2000 ppm.

It is observed that a modification of the chemical reaction time scale is necessary. In order to reach the best match, the chemical time can be given as an additional look-up table or be correlated as:

$$\tau_{2000ppm}(T, \lambda) = (C_T \cdot T + C_\lambda \cdot \lambda + C) \cdot \tau_{0ppm} \quad (5)$$

$$C_T = 5.568E-4, C_\lambda = 7.599E-2, \text{ and } C = -5.337E-1$$

Where τ_{0ppm} is the chemical time scale for calculation of NO concentration when the instantaneous value of NO concentration is lower than the equilibrium value of NO by the corresponding temperature and air-fuel ratio, otherwise the correlated time scale, $\tau_{2000ppm}$, can be used.

In order to reduce the amount of tabulated data and increase the computational speed, only one constant pressure of 80 bar is considered and the effect of the reactor pressure is treated as the next step. A variation of reactor pressure from 80 to 200 bar is carried out for all of the above mentioned temperatures and air-fuel ratios. It is observed from the pressure variation, that the value of the NO in equilibrium condition does not change significantly with pressure. But for the characteristic chemical time scale, a simple correlation for considering of the effect of pressure is proposed in (6).

$$\tau(p) = \begin{cases} 15.4196 \cdot p^{-0.5538} \cdot \tau_{140bar}; & T \geq 2400 K, \lambda > 1 \\ 22.3089 \cdot p^{-0.6285} \cdot \tau_{140bar}; & T < 2400 K, \lambda > 1 \end{cases} \quad (6)$$

The best correlation for the pressure variation from 80 bar to 200 bar is obtained if 140 bar is taken as the basis pressure. For brevity, the deviation analysis is not plotted for all investigated pressures. When using (6), the average error is lower than one percent for each pressure, considering all temperatures and air-fuel ratios.

All of the above mentioned investigations are carried out with stationary reactor simulation. Evaluation of the developed kinetic in transient conditions is performed, first in a perfectly-stirred reactor with a ramp-type temperature increase. Figure 9 illustrates the temperature ramp in the reactor and compares the NO concentration from the proposed kinetic to the simulated value using the detailed mechanism. The calculated NO in the reactor by the tabulated kinetic model correlates well with results of the detailed mechanism.

As the final step for evaluation of the developed reaction kinetic, the calculated NO_x emissions are compared with the results from the detailed GRI-Mech 3.0 mechanism under different engine operating points of a diesel engine. Both GRI-Mech 3.0 and the developed NO_x kinetic are coupled with the same combustion model and two-zone temperature model for calculating the burned and unburned temperatures. Figure 10 compares the NO_x calculated by the detailed mechanism with the results obtained from the tabulated kinetic model using tetradecane for different engine speeds of the heavy-duty diesel engine with 55% load.

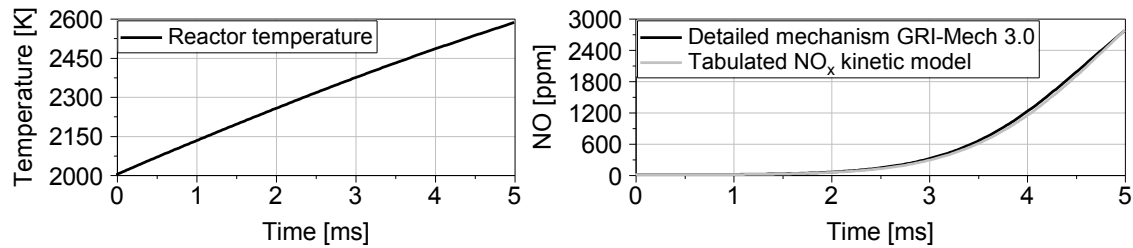


Figure 9: Evaluation of the tabulated NO_x kinetic model for NO formation in a perfectly-stirred reactor and a transient temperature ramp using tetradecane fuel

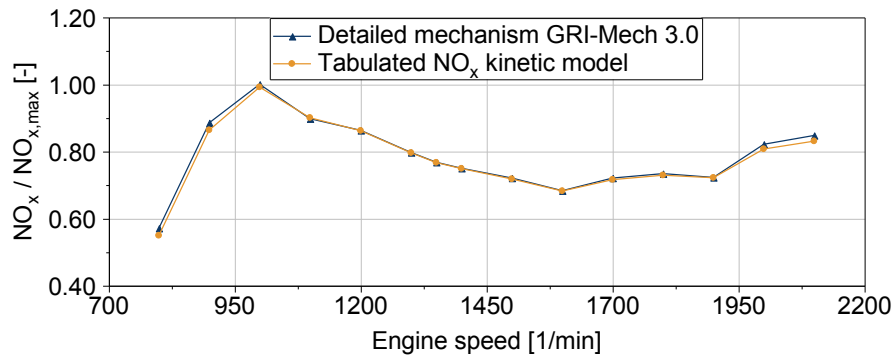


Figure 10: Comparison of the simulated NO_x emissions by the detailed GRI-Mech 3.0 mechanism and the tabulated kinetic model for the heavy-duty diesel engine with 55% load and tetradecane fuel

As is depicted in Figure 10, a very good match between the NO_x calculated by the detailed mechanism and the proposed kinetic model with a transient variation of temperature, pressure, and air-fuel ratio in the burned zone under real diesel engine operating conditions for various engine speeds is obtained.

Finally, the tabulated NO_x kinetic model is implemented in the phenomenological combustion model. Both NO_x and combustion models are coupled to the GT-Power software for simulation of combustion and in-cylinder NO_x emissions. The combustion model calculates the burning rate, and the NO_x model, with the new kinetic mechanism, calculates the NO_x in the burned zone. Calculation of the burned zone temperature is simply based on the two-zone modeling approach commonly used in computationally efficient phenomenological models. Figure 11 illustrates the calculated and measured NO_x emissions obtained from the new NO_x kinetic coupled with the above mentioned phenomenological combustion model for the heavy-duty diesel engine. Both the simulated and measured NO_x emissions are normalized by the same reference value. A relatively good match between the measured and simulated NO_x is obtained.

It should be noted that an accurate calculation of in-cylinder NO_x emissions strongly depends on the calculation of the burned zone temperature and the mixing rate between the burned and unburned zone. The crucial information about spray formation, turbulent kinetic energy, ignition delay, and distribution of the air-fuel mixture in the combustion chamber can be provided by a phenomenological combustion model, which enhances the accuracy of temperature calculation and consequently the predictability of the NO_x model. However, the focus of this study is the development of an improved NO_x kinetic mechanism. Further improvement of the two-zone mixing model of the diesel engine combustion with help of the combustion model is a focus of future works.

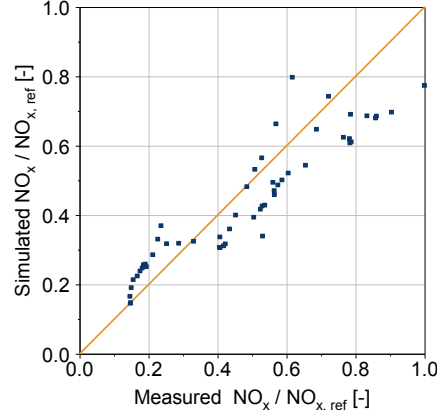


Figure 11: Comparison of NO_x emissions using the developed kinetic for tetradecane with measurement results for the heavy-duty diesel engine in overall operating points

The proposed method for tabulation of NO_x kinetic for diesel engine is generalized for simulation of gasoline as well as natural gas engines. Iso-octane (C₈H₁₈) is considered as the representative fuel for gasoline and methane (CH₄) is investigated for natural gas engines.

Similar to the above described approach, for each fuel, the reactor pressure and temperature are varied and the values in eq. 3 are calculated for each reactor condition. The relative error and NO in the equilibrium condition are plotted for the iso-octane and methane fuels, Figure 12.

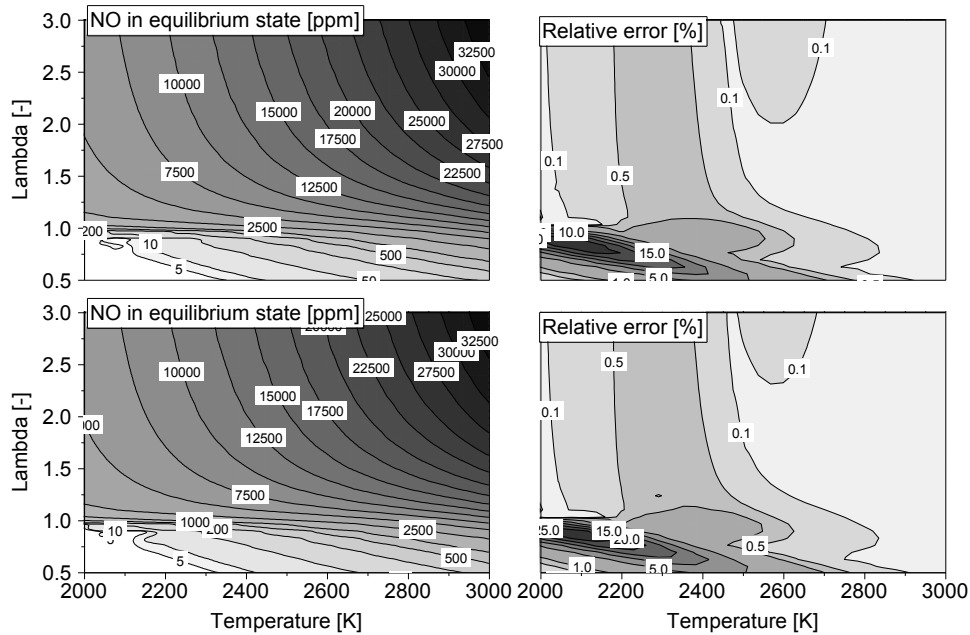


Figure 12: Evaluation of the tabulated NO_x kinetic model in a perfectly-stirred reactor at various temperatures and air-fuel ratios for the iso-octane (top) and methane (bottom)

As shown in Figures 12 for both fuels the relative error in the NO formation phase for the majority of simulated cases is lower than one percent. For some points with low temperature and rich mixture, a higher relative error is observed; however, as shown at the left side of Figure 12, the NO concentration for this region is low.

Overall a very good match is reached for the tetradecane as a representative diesel fuel as well for methane and iso-octane as representative fuels for natural gas and gasoline engines.

6. Conclusion

A phenomenological combustion model with a novel NO_x reaction kinetic model has been developed. The combustion model exhibits a good predictability for different combustion systems and engine sizes from passenger car to heavy-duty diesel engines, under different operating conditions. The combustion model has a high computational speed and can provide a good platform for evaluation of control strategies as well as engine transient cycles when integrated in the simulation software GT-Power. The present study is especially focused on model simplification and thereby reduction of the computational effort. This enables an implementation of such physical-based models as a platform for combustion control and emission calculation in the next generation of the engine control units.

The tabulated kinetic model enables fast execution as it relies on a single equation and does not require any equilibrium reaction for NO calculation. This enables the model to be used in a detailed 3-D CFD simulation or even for NO_x calculation in engine control units with low computational capacity. The proposed NO_x kinetic shows very good accuracy in comparison with the detailed GRI-Mech 3.0 mechanism in stationary as well as in transient conditions in a perfectly-stirred reactor and also in combination with the phenomenological combustion model under real-engine operating conditions.

7. Acknowledgement

The authors would like to thank colleagues at IAV GmbH, Mrs. H. Puschmann, Mr. E. Neumann, and Mr. J. Seebode as well as Mr. K. Kuppa from the Institute for Technical Combustion at the University of Hanover, for their valuable help and technical support.

References

- [1] Heywood, J.B.: Internal Combustion Engine Fundamentals, McGraw-Hill, 1988
- [2] Bertram, C.; Rezaei, R.; Tilch, B.; van Horrick, P.: Development of an Euro VI Engine Using Model-Based Calibration, MTZ worldwide, 75(10), 4-9, 2014
- [3] Vibe I.: Brennverlauf und Kreisprozess von Verbrennungsmotoren, VEB Verlag Technik, Berlin, 1970
- [4] Chmela, F.; Pirker, G.; Wimmer A.: Zero-dimensional ROHR simulation for DI diesel engines – A generic approach, Journal of energy conversion and Management, Vol. 48 pages: 2942-2950, 2007
- [5] Chmela, F.; Pirker, G.; Losonczi, B.; Wimmer, A.; Desantes, J.; García-Oliver, J.: A New Burn Rate Simulation Model for Improved Prediction of Multiple Injection Effects on Large Diesel Engines, Thiesel Conference, 2010
- [6] Stiesch, G.: Modeling Engine Spray and Combustion Processes, Springer-Verlag, 2003

- [7] Barba, C.: Erarbeitung von Verbrennungskennwerten aus Indizierdaten zur verbesserten Prognose und rechnerischen Simulation des Verbrennungsablaufes bei Pkw-DE-Dieselmotoren mit Common-Rail-Einspritzung, Diss. ETH Zürich, 2001
- [8] Hiroyasu, H.; Kadota, T.; Arai, M.: Development and Use of a Spray Combustion Modeling to Predict Diesel Engine Efficiency and Pollutant Emission, Part 1: Combustion Modeling, Bulletin of the JSME, Vol. 26, 1983
- [9] Hiroyasu, H.; Kadota, T.; Arai, M.: Development and Use of a Spray Combustion Modeling to Predict Diesel Engine Efficiency and Pollutant Emission, Part 2: Computational Procedure and Parametrical Study, Bulletin of the JSME, Vol. 26, 1983
- [10] Gao, Z.; Schreiber, W.: The Effects of EGR and Split Fuel Injections on Diesel Engine Emissions, Int. J. Automotive Technol., Vol. 2, No. 4, 2001
- [11] Morel, T.; Wahiduzzaman, S.: Modeling of Diesel Combustion and Emissions, FISITA, 1996
- [12] Stiesch, G.; Merker, G.P.: A Phenomenological Model for Accurate and Time Efficient Prediction of Heat Release and Exhaust Emissions in Direct-Injection Diesel Engines, SAE Paper 1999-01-1535, 1999
- [13] GT-Power Software, Version 7.3, Gamma Technologies Inc, Westmont, Illinois, <http://www.gtisoft.com/>
- [14] Rezaei, R.; Eckert, P.; Seebode, J.; Behnk, K.: Zero-Dimensional Modeling of Combustion and Heat Release Rate in DI Diesel Engines, SAE Int. J. Engines 5(3):874-885, 2012, doi: 10.4271 and SAE 2012-01-1065
- [15] Weisser, G.A.: Modelling of Combustion and Nitric Oxide Formation for Medium-Speed DI Diesel Engines: A Comparative Evaluation of Zero- and Three-Dimensional Approaches, Diss. ETH Zürich, 2001
- [16] Ciezki, H.K.; Adomeit, G.: Shock-tube investigation of self-ignition of n-heptane-air mixtures under engine relevant conditions, Combustion and Flame, 93(4), 421-433, 1993
- [17] Patel, A.; Kong, S.C.; Reitz, R.D.: Development and validation of a reduced reaction mechanism for HCCI engine simulations, SAE Technical Paper Series No. 2004-01-0558, 2004
- [18] Kong, S.C.; Han, Z.; Reitz, R.D.: The Development and Application of a Diesel Ignition and Combustion Model for Multidimensional Engine Simulation, SAE Technical Paper Series No. 950278, 1995
- [19] Spalding, D.B.: Mathematical models of turbulent flames; a review, Combustion Science and Technology, Vol. 13, pages: 3-25, 1976
- [20] Zeldovich, Y.B.: The oxidation of nitrogen in combustion and explosions, Acta Physicochimica, USSR 21, 577–628, 1946
- [21] Smith, G.P.; Golden, D.M.; Frenklach, M.; Moriarty, N.W.; Mikhail Goldenberg, B.E.; Bowman, C.T.; Hanson, R.K.; Song, S.; Gardiner Jr., W.C.; Lissianski, V.V.; Qin, Z.: GRI-Mech 3.0, http://www.me.berkeley.edu/gri_mech/
- [22] Bowman, C.T.: Kinetics of pollutant formation and destruction in combustion, Progress in energy and combustion science 1.1: 33-45, 1975

- [23] Yoshikawa, T.; Reitz, R.D.: Development of an improved NO_x reaction mechanism for low temperature diesel combustion modeling, SAE Technical Paper Series No. 2008-01-2413, 2008
- [24] Vaz, A.I.F.; Vicente, L.N.: A particle swarm pattern search method for bound constrained global optimization, Journal of Global Optimization, 39(2), 197-219, 2007

The Authors:

Dr.-Ing. Reza Rezaei, IAV GmbH

Prof. Dr.-Ing. Friedrich Dinkelacker,
Institut für Technische Verbrennung, Leibniz Universität Hannover

Dipl.-Ing. Benjamin Tilch, IAV GmbH

Dr.-Ing. Thaddäus Delebinski, IAV GmbH

Dr.-Ing. Maximilian Brauer, IAV GmbH

Licence:

This document is licensed under the Creative Commons Attribution 3.0 DE License (CC-BY 3.0 DE): <http://creativecommons.org/licenses/by/3.0/de/>

Drive-E Petrol Combustion System Design

Roy Ogink

Abstract

Volvo Car Corporation has recently launched a completely new engine family called Drive-E. From model year 2016, Drive-E will be powering all models in the Volvo Cars line-up. These new petrol and diesel engines are characterized by high specific performance, low friction and low fuel consumption. The number of cylinders is limited to four, which implies that these down-sized, boosted engines will replace present five and six cylinder engines. This paper focuses on the development of the Drive-E petrol combustion system, characterized by a centrally-mounted direct-injection fuel injector in combination with high-tumbling intake ports. The careful tuning process of the spray lay-out for the multi-hole injector is discussed, together with the resulting combustion system properties, such as excellent air/fuel mixing, limited wall wetting and stable combustion. The latter is due to the break-down of large-scale tumble motion into a high level of turbulence, leading to accelerated combustion.

The petrol engines span a wide range of power levels. This means that the engine at the entry power level needs to breathe less air than the 2.0L engine at the highest power level (235 kW, 320 HP). Consequently, intake port design was an important part of the combustion system development. Different intake port geometries are applied at the different power levels, and this paper describes the trade-off between a design that sets up a strong tumble motion (leading to fast combustion and thus reduced fuel consumption), and a design that optimizes engine breathing (enabling class-leading specific power, while keeping fuel-efficiency at a good level).

1. Introduction

A few years ago, Volvo Car Corporation started the development of a completely new engine family called Drive-E. At that moment a wide range of four, five and six cylinder engines had to be fitted into Volvo's car models, giving rise to a large number of engine installations. The aim of the new engine program was to significantly reduce that complexity and it was decided to focus on four-cylinder engines only. By means of down-sizing to a displacement of 2.0 litres and applying different boosting systems, the Drive-E engines will replace all five and six cylinder engines in Volvo Cars' present line-up.

This paper describes the development process of the petrol combustion system for the Drive-E family. The system relies heavily on a high-tumble concept (See *Figure 1*) [1]. Since filling is less of an issue for turbo-charged engines than it traditionally has been for naturally-aspirated engines, it becomes possible to design intake ports that set-up a strong tumbling motion inside the combustion chamber during the period the intake valves are open. The large-scale tumble motion will survive during most of the compression stroke, after which it has to be broken down into small-scale turbulence. A properly designed combustion system will then be characterized by a high level of turbulent kinetic energy inside the combustion chamber prior to, and during, combustion. Consequently, the combustion process will be stable and fast. The following typical advantages can be mentioned for a high-tumble system:

- Shortened duration from spark until combustion start, as well as fast and stable combustion.
- Increased knock resistance, implying that a spark timing closer to optimal ignition timing can be used.
- Better fuel consumption at part-load conditions due to improved capability to handle internal EGR.
- More stable combustion at low engine speeds resulting in higher BMEP, since the engine can cope with higher boost pressures.
- Higher power levels can be reached at high engine speeds until reaching the maximum exhaust temperature and/or fuel enrichment level of the engine.
- The large-scale tumble motion, followed by the high level of turbulence, will enhance air/fuel mixing.

Faster combustion at boosted conditions might lead to an increased cylinder pressure rise rate, which indicates one disadvantage of high-tumble combustion systems: Too fast combustion might lead to NVH problems.

The petrol engines in the Drive-E engine family are available at different power levels. The main properties of three variants (T4, T5 and T6) are summarized in Table 1. The two variants with the best performance (T5 and T6) are already available to customers, while other engines will be released in the near future that have slightly reduced performance but further improved fuel consumption (e.g. T4). The engines have many properties in common, such as bore, stroke and displaced volume. On the other hand, the engine with the highest performance, the T6, utilizes an advanced boosting system that consists of both a turbocharger and a supercharger, whereas the other engines are equipped with more conventional charging systems. The compression ratio is reduced in steps as the specific performance increases from T4 to T5 to T6.

As far as the combustion system is concerned, the T5 and T6 engines share similar intake ports, while the lower performance variants have intake ports that focus even more on setting up a strong tumble motion than on filling the combustion chamber with fresh charge.

Table 1: Main properties for the 2.0L, 4-cylinder T4, T5 and T6 Drive-E engines [2].

Engine	T6	T5	T4
Rated Power (kW/ hp)	235 / 320	180 / 245	140 / 190
Torque / overboost (Nm)	400	350 / 380	300 / 330
Compression ratio (-)	10.3 : 1	10.8 : 1	11.3 : 1
Bore / Stroke (mm)	82 / 93.2	82 / 93.2	82 / 93.2
Charging system	One roots + one turbo with waste gate	One turbo with waste gate	One turbo with waste gate

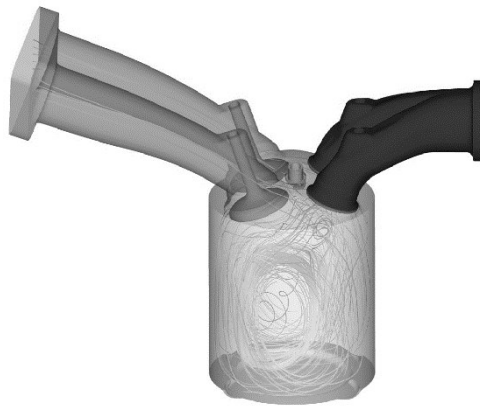


Figure 1: CFD streamlines indicating the tumble motion set up by the intake ports. The intake ports are located at the left part of the figure.

2. Petrol combustion system development process

Intake port design is the most critical step of the Drive-E petrol combustion system development, since it defines the trade-off between tumble level and filling. As soon as the intake port geometry has been decided, the so-called spray targeting can be investigated, which defines the directions for the 6 spray plumes of the centrally-mounted injector in the Drive-E cylinder head. Since the strong air jet set up by the intake ports can significantly affect the fuel spray, the design of the intake ports and the choice of spray targeting are connected to each other to a very high degree. Together, the intake ports and the spray targeting are dominating the main characteristics that the combustion systems will have. Intake port design for Drive-E is discussed first, after which spray targeting is dealt with. Design of other parts of the combustion system (such as exhaust ports, piston and flame propagation) are not discussed here.

3. Intake port design

3.1 Steady-state and transient CFD for intake port evaluation

The design process for new intake ports can be divided into several phases. During the first phase, a set of intake port designs is evaluated by means of steady-state CFD. It is a very powerful tool to quickly compare the mass flow and tumble levels for a large number of intake port geometries. The results can be added to a scatter plot (See *Figure 2*) to compare the mass flows and tumble levels for new intake port designs to each other, and to have a reference with engines developed in the past. For a certain valve lift, the scatter plot shows a very linear trade-off between filling and tumble level. Consequently, the aim is to find an intake port design that provides enough mass flow to reach the requested power level for the particular engine, and that has a tumble ratio that is as high as possible.

Besides results for mass flow and tumble, the velocity vectors of the gas flow in the CFD geometry are evaluated to understand how the present port design can be improved. Based on the flow (separation) in the ports and around the valves, input is provided for the next CFD-iteration to improve mass flow and/or tumble.

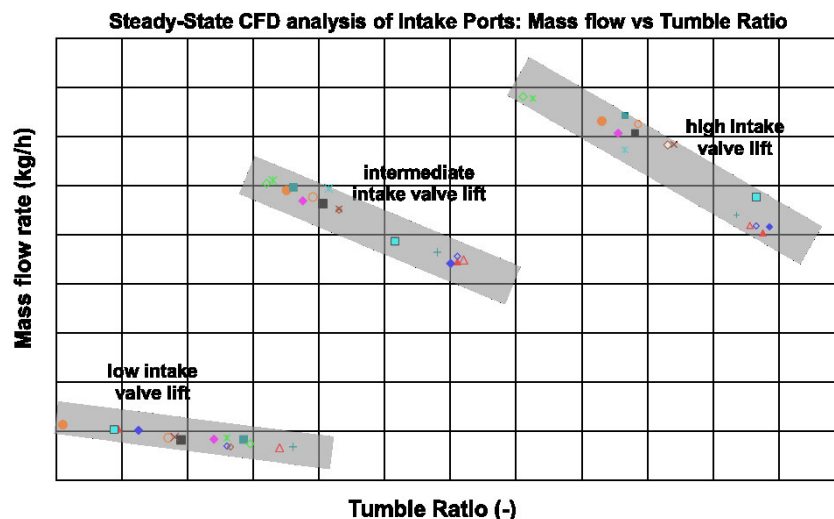


Figure 2: Example of scatter plot obtained from steady-state intake port CFD.

The outcome of the steady-state CFD analyses might e.g. be three promising designs, which are then further evaluated in the second phase: transient in-cylinder CFD. In these transient CFD analyses, different intake port design are ranked for several operating conditions based on the following criteria: 1) filling (trapped mass prior to combustion), 2) air/fuel mixing, 3) the tumble level, 4) the level of turbulent kinetic energy (TKE) in the chamber prior to combustion, and 5) wall wetting (droplet impact and liquid film on liner, piston, head and valves).

Below, CFD results for two intake port designs are discussed. For simplicity, these will be called Fill port (corresponding to the intake port for T5 and T6) and Tumble port (for the T4 power level) in the discussion below. The Fill port has a general shape that is more bend (See *Figure 3*), which is generally better for achieving a higher mass flow.

The flow will enter the combustion chamber in a more vertical way (compared with the Tumble port) and consequently the circumferential flow area around the valves can be better utilized by the flow. The Tumble port, on the other hand, has a much more straight design. Consequently, most of the incoming air is forced to enter the combustion chamber at the upper side of the intake valves.

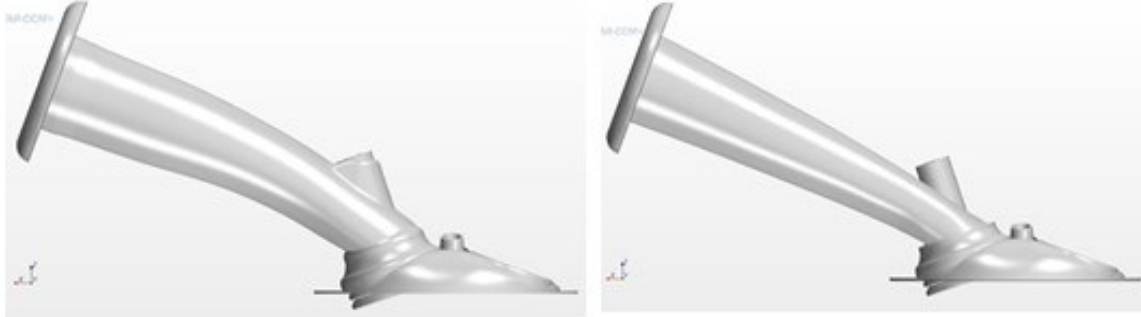


Figure 3: Intake port design for the Fill port (left) and the Tumble port (right).

The transient CFD runs have been performed for maximum power conditions (for the T5-position). As can be seen in *Figure 4*, the tumble level of the Fill port is much lower during the intake and compression strokes than the level for the Tumble port. Since the large-scale tumble motion is broken down into turbulence, the average level of TKE at the end of the compression stroke is much higher for the Tumble port than for the Fill port. It should however be noted that the average TKE level quickly decays after 690 CAD. Furthermore, the transient CFD results showed: 1) a higher trapped mass after IVC for the Fill port than for the Tumble port design, and 2) further improved air/fuel mixing for the Tumble port compared with the Fill port.

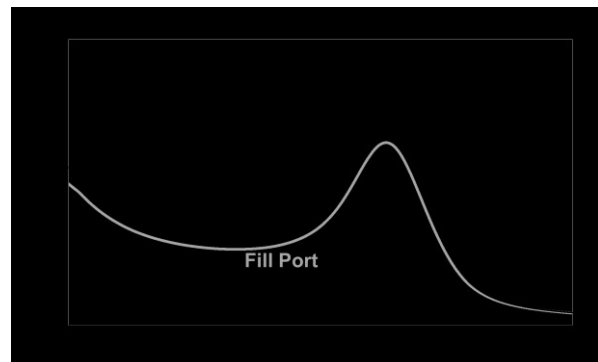
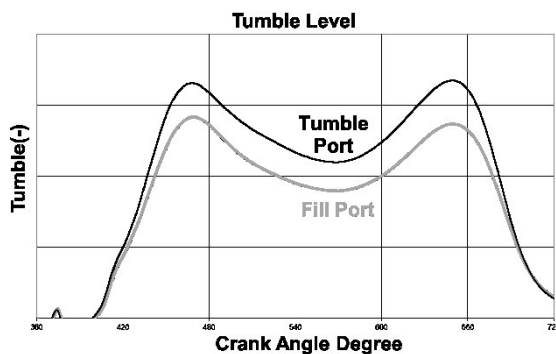


Figure 4: Transient CFD results for Tumble and Fill ports: Turbulent Kinetic Energy (right) and Tumble level (left).

The first (steady-state CFD) and second (transient in-cylinder CFD) phase of the intake port design process have been described above. After selecting the most promising intake port designs from these CFD studies, several hardware prototypes are then ordered for experimental investigations in the third phase. In early phases of an engine project, the new hardware will typically consist of new cylinder heads for the Volvo Cars single-cylinder test rig. The next section will therefore describe a typical experimental investigation of new intake ports designs performed in the single-cylinder rig.

3.2 Single-cylinder testing for intake port evaluation

To analyse the behaviour of new intake port designs, a cylinder head with the new port geometry is mounted on a single-cylinder engine. Two types of investigations are then performed to discriminate between port designs: 1) a so-called mini-map investigation consisting of 14 part-load operating points representative for the most common driving cycles and/or real customer driving. 2) a so-called Wide-Open-Throttle (WOT) investigation to study the engine's behaviour at high load. The boundary conditions for the single-cylinder experiments were adopted from multi-cylinder experiments at the T5-power position. These boundary conditions are: boost pressure, exhaust back pressure, lambda, charge air temperature and fuel pressure. This section will discuss mini-map and WOT results for the Fill and the Tumble intake port designs.

The results from the mini-map investigation, which provides a tool to investigate part-load fuel consumption, can be summarized as follows (results are averaged values for the 14 mini-map points):

- The Tumble port has 1.5% lower specific fuel consumption than the Fill port. Partially, this is due to the slightly higher compression ratio of the 1-cylinder with the Tumble-port (10.82 : 1) than the one of the Fill-port (10.75 : 1). (See *Figure 5*)
- The average burn duration (10 – 90% of the fuel burnt) of the Tumble-port is 4 crank angle degrees (CAD) shorter (See *Figure 5*).
- The Tumble-port has 0.9% (absolute) higher combustion efficiency.
- The emissions of CO₂ are 0.16% (absolute) higher for the Tumble-port, indicating better air/fuel mixing for this port: As expected, a higher level of large-scale motion and the consequent increased level of in-cylinder turbulence, contribute to mixing.
- Both the Fill- and Tumble-ports show low smoke emissions, indicating good mixing, but the Tumble-port has levels that are lower or very much lower than the results for the Fill-port.
- The Tumble-port has 21% lower emissions of unburnt hydrocarbons (HC).

These mini-map investigations clearly show the benefits obtained with the Tumble-port design during part-load operation.

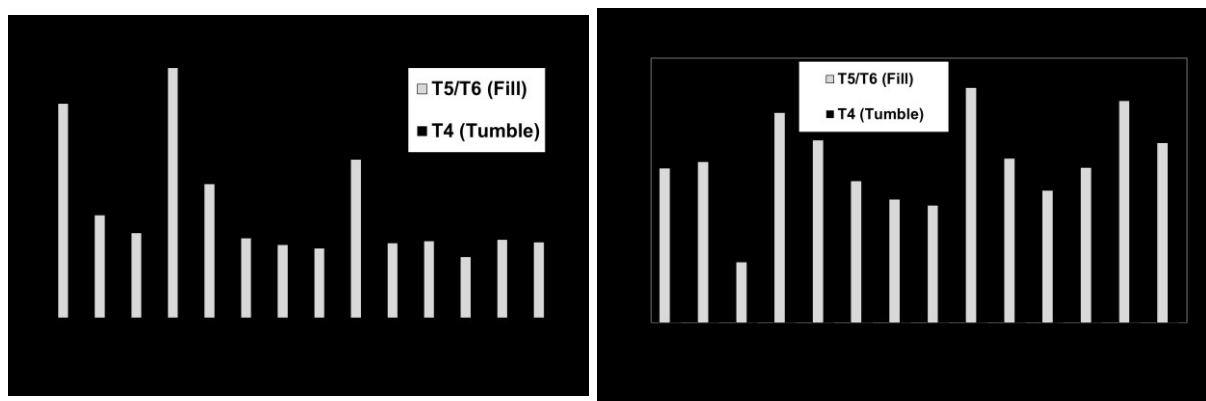


Figure 5: Mini-map results from 1-cylinder testing: Burn duration (right) and NSFC (left).

As described above, WOT-testing is the second way to experimentally compare intake port designs. Such tests have been performed from 1500 to 5700 RPM to compare the WOT-characteristics of the Tumble- and Fill-ports. For each operating point, the load

is increased until knock reaches a pre-defined level. In this way, the maximum achievable torque is obtained for the whole engine speed range. Different intake port designs will have different properties affecting the knock resistance of the engine design, such as in-cylinder turbulence levels (affecting combustion duration) and air/fuel mixing.

As far as the results are concerned, it can be observed that the Tumble-port gives rise to: 1) a 2-5 CAD faster combustion duration (See *Figure 6*), 2) a slightly more advanced spark timing and 3) an increased cylinder pressure rise rate. The disadvantage of this tumble-optimized port is that filling is sacrificed above 3900 RPM (for these experiments with T5-power-level boundary conditions): for high engine speeds, the maximum achievable torque is significantly lower for the Tumble-port than for the Fill-port (See *Figure 6*) due to the limited flow area of the Tumble-port.

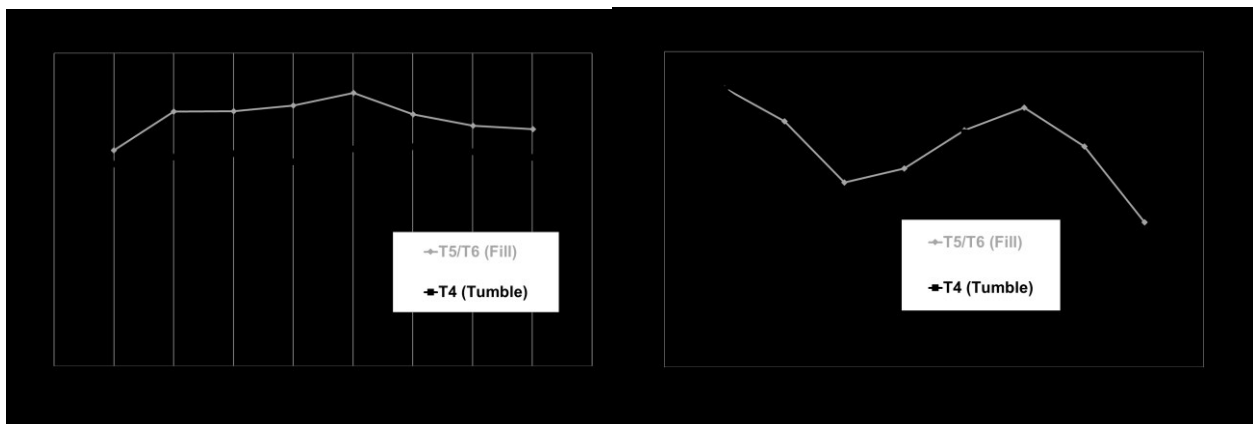


Figure 6: WOT results from 1-cylinder testing: Brake Torque (right) and 10 – 90% Burn Duration (left).

4. Spray Targeting

This section describes the process of determining the optimal spray targeting for the Drive-E petrol combustion system. To define the spray targeting for the centrally-mounted 6-hole injector one has to specify the coordinate systems for each individual spray plume. *Figure 7* shows the individual spray plumes for a lay-out typical for Drive-E. The view is from above. The following observations can be made: 1) the injector location is slightly offset from the cylinder centre, 2) the spark plug is mounted in between sprays 1 and 6, 3) the intake valves are positioned at the right 4) the spray plumes have different lengths (in the 2-D projection) and directions. Consequently, a spray plume that is short in *Figure 7* corresponds to a spray plume that is pointing more towards the piston: sprays 1, 5 and 6 are more horizontal (directed more towards the liner) than e.g. spray 4, which points most towards the piston.

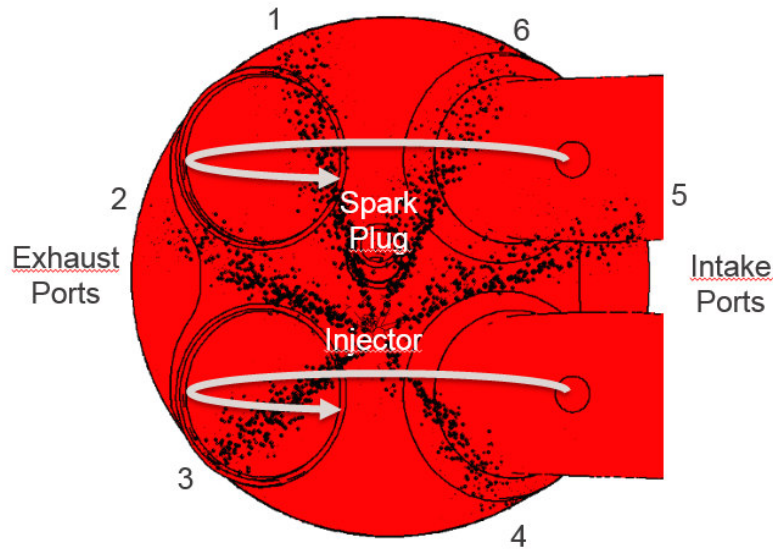


Figure 7: Typical spray lay-out for the Drive-E combustion system, where the grey arrows illustrate the tumble direction.

Both experiments and CFD are applied at Volvo Cars to determine the optimal spray shape. The spray targeting process starts with CFD analyses of different spray targeting candidates. But prior to that the spray model is calibrated based on fuel spray data obtained from the injector supplier or from measurements performed in the Volvo Cars' spray chamber. The most important data for calibration is the liquid fuel penetration, which basically is the distance the fuel droplets have travelled after a certain time. Besides comparing the liquid penetration curve obtained from experiments and CFD, spray images are typically extracted from the CFD results and compared with the images captured in the spray chamber experiments as a second means of judging the calibration status of the CFD spray model.

Once the CFD model is able to accurately predict the fuel spray event in the spray chamber, a spray targeting study is performed by means of in-cylinder CFD. Such a study is used to compare different spray targeting candidates for a set of operating points, e.g. full-power, the torque-knee point, a part-load point and a point representing cold start/cranking. The CFD results are then used to rank the spray targeting candidates based on the following criteria: 1) Air/fuel mixing (e.g. the standard deviation of λ at 30 CAD before combustion-TDC), 2) Wall wetting (i.e. spray impact on piston, liner, head, valves, as well as liquid film formation), and 3) Start-ability (i.e. the formation of an ignitable mixture cloud in the spark plug vicinity for cold-start conditions). Based on this, one can understand that the optimal spray targeting is a compromise: the fuel injection event should result in good mixing and minimal wall wetting for high, as well as low engine speeds, and should have good properties for injections of small, as well as large, quantities of fuel. Furthermore, the spray targeting is a compromise between homogeneous operation with fuel injection during the intake stroke on one hand, and engine start / catalyst heat-up on the other hand, when the fuel injection event is of a more stratified type with (part of the) fuel injection around combustion-TDC.

Oil dilution and particulate formation strongly influence the spray targeting process. When fuel droplets impact the liner, fuel will mix with the lubricant on the wall, and the oil will be diluted. Since oil dilution should be as low as possible, the aim of spray

targeting is to reduce liner wetting. On the other hand, piston wetting is undesired as well. A reason for this is that one of the main contributors to the formation of particulate emissions (PN) is the impact of fuel on the piston surface, leading to pool fires and/or diffusion flames. Multi-hole injectors are under constant development with the aim to improve atomization (i.e. produce smaller droplets) and to shorten the liquid penetration, but the spray plumes of state-of-the-art injectors still have such long penetration that either liner or piston wetting will occur. Furthermore, wetting of the valves and spark plug should be avoided too.

Figures 8 and 9 show CFD results typically used to evaluate spray targeting candidates. In Figure 8, part-load results for air/fuel mixing can be seen for the spray targeting applied to Drive-E. The results, represented by three section plots and a diagram, illustrate very good mixing: almost all of the mixture can be found in the lambda range of 1.0 – 1.1, while very lean and very rich mixtures are absent. CFD results for wall wetting can be observed in Figure 9, where the liquid film thickness is plotted for three different views. Red colour in these figures means that no liquid film is present at the walls, while blue colour indicates the regions where the spray plumes have wetted combustion chamber surfaces. It can be concluded that the 6 spray plumes first hit the piston surface and that fuel droplets impact onto the liner later on during the intake stroke when the piston has travelled further downwards.

A typical CFD spray targeting study will include the evaluation of 5 – 10 spray lay-outs. The best 3 – 4 candidates are then ordered as hardware prototypes. Once the new injectors have been received, these will be subjected to experimental investigations in Volvo Cars' spray chamber, optical engine and single-cylinder engine. Single-cylinder tests are typically performed for the following operating conditions: 1) part-load testing in a number of mini-map points, 2) WOT-testing, and 3) "cold-fluid" testing at a representative part-load point with coolant and oil temperatures below room temperature. The different spray targeting candidates under investigation are compared based on the following decision criteria: 1) fuel consumption, 2) emissions (especially soot and PN, but also other emissions), 3) air/fuel mixing and 4) combustion properties (combustion efficiency, burn duration, stability, highest achievable torque). Results from such experimental investigations are not discussed in this paper.

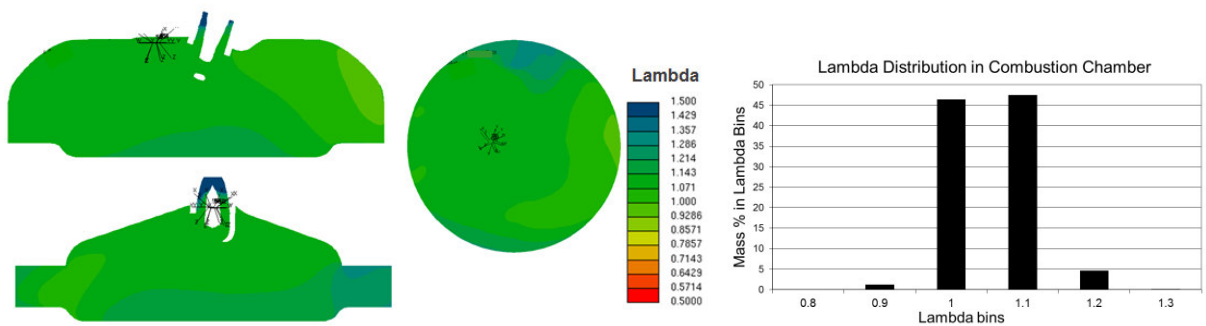


Figure 8: Example of CFD results at 1500 rpm, 5 bar BMEP: lambda distribution prior to combustion in three different sections (left) and lambda distribution diagram (right).

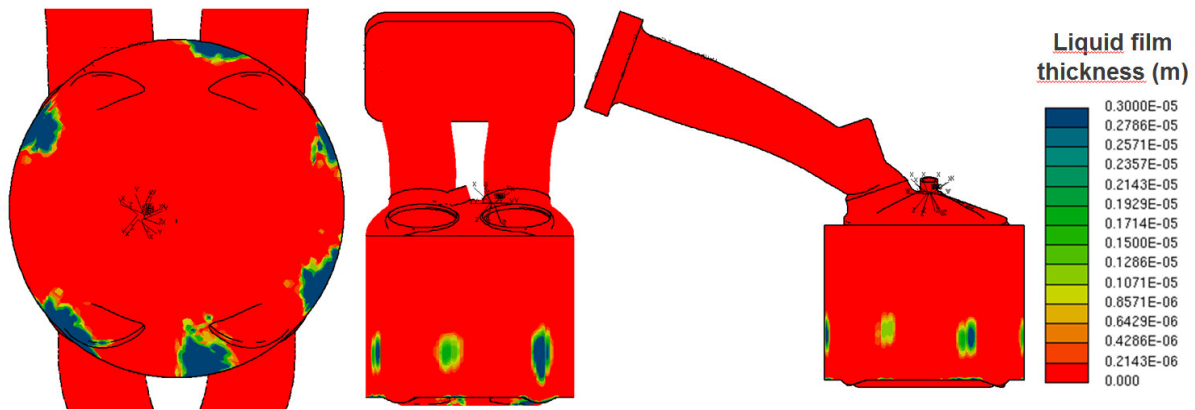


Figure 9: Example of CFD results at 1500 rpm, 5 bar BMEP: wall wetting represented by liquid film thickness.

After completing the experimental evaluation, a second iteration of spray targeting may be initiated by performing a second CFD study. Observations from loop 1 will be input to new spray targeting candidates to be evaluated in loop 2. When the engine project has progressed to the stage where multi-cylinder engines are available, the best spray lay-outs will be studied in multi-cylinder test rigs and by vehicle testing to study drive cycle emissions and fuel consumption.

A typical spray targeting for the Drive-E petrol combustion system was presented in Figure 7. It can be observed that the spray lay-out is not axisymmetric, i.e. the angle between the individual spray plumes in the X-Y plane is not 60 degrees, and the spray vectors have different lengths. An axisymmetric spray lay-out might in theory be a good way to evenly distribute liquid fuel into the combustion chamber, but a number of reasons can be given to explain why such a spray lay-out is not a good solution in practice. The first reason is that the fresh air jets flowing into the chamber during the intake stroke are affecting the spray: the higher the engine speed, the more severe the deviation of the spray plumes from their original spray direction will be (See Figure 10). Furthermore, once the fuel has been evaporated, the fuel vapour will be moved around in the combustion chamber by the large-scale tumbling motion set up by the intake ports (indicated by the grey arrows in Figure 7). The second reason is that plumes 1 and 6 play an important role during engine-start and catalyst heating, when one or more injections take place around combustion-TDC. To successfully operate the engine during the Volvo Cars' start strategy, it is important to obtain an ignitable cloud of air and fuel near the spark plug electrode. With this in mind, the distance between the injector tip and spark plug, together with the directions of sprays 1 and 6, has been carefully optimized. This basically means that sprays 1 and 6 are locked, and cannot be altered to investigate new spray lay-outs. This is true until injector properties change: modified spray penetration and/or updated individual spray cone angles (i.e. spray plume brushiness) might necessitate some tweaking of the spray vectors for sprays 1 and 6.

The spray vectors for the other sprays, 2 – 5, are the result of the spray targeting process discussed above, where numerical and experimental investigations have been performed to evaluate the most important combustion system properties, such as mixing, wall wetting, fuel consumption and emissions formation. In general, the sprays on the intake side (sprays 4 and 5) can have longer vectors in the X-Y plane (i.e. can be more horizontal) than the sprays at the exhaust side (2 and 3). In other words, sprays 4 and 5 can be pointed more towards the liner. The reason for this is the aforementioned momentum of the incoming air: liner wetting is less likely at the intake

side of the liner, which means that piston wetting can be reduced by applying a more horizontal direction for spray plumes 4 and 5. Nevertheless, *Figure 7* shows that spray 4 is the one pointing most towards the piston. This is because a more horizontal orientation of spray 4 will lead to wetting of one of the intake valves.

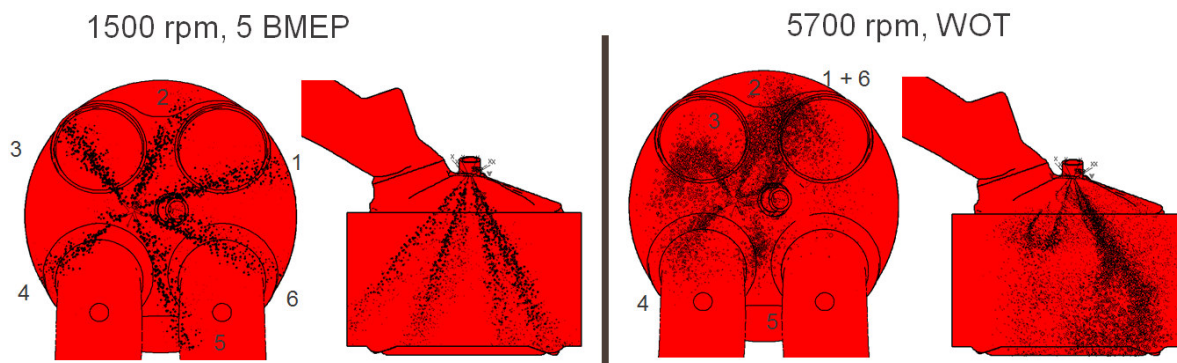


Figure 10: CFD results: impact of fresh air jets onto the fuel sprays for a low-rpm, low-load case and for high-RPM, WOT operation.

5. Conclusions

The development process of the petrol combustion system for Volvo Car's new Drive-E engine family has been discussed. Intake port design and spray targeting have been described for Drive-E, which consists of four-cylinder engines that are characterized by high specific performance and low fuel consumption. By comparing a high-tumble intake port to a port more oriented towards filling, clear advantages were observed for the tumble port. Experimental investigations showed improved fuel consumption, better mixing, lower emissions (HC, CO and soot) and superior combustion properties for the tumble port design.

Spray targeting for the multi-hole injector mounted in the Drive-E engines was discussed in the second part of the paper. It was described how the directions of individual spray plumes are carefully chosen to find the best compromise for operating at different engine conditions and for different injection strategies to obtain reduced wall wetting and optimized air/fuel mixing with the aim to reduce fuel consumption, PN-emissions and oil dilution.

6. Acknowledgments

The author would like to thank Roy Ekdahl, who performed the 1-cylinder experiments.

References

- [1] Berntsson, A.; Josefsson, G.; Ekdahl, R.; Ogink, R.; Grandin, B.: The Effect of Tumble Flow on Efficiency for a Direct Injected Turbocharged Downsized Gasoline Engine. In: SAE Paper 2011-24-0054, 2011
- [2] Crabb, D.; Fleiss, M.; Larsson, J-E.; Somhorst, J.: New Modular Engine Platform from Volvo. In: MTZ worldwide 74 (2013) No 9, 2013

The Authors:

Ph.D., Roy Ogink, Volvo Car Corporation, Gothenburg, Sweden.

M.Sc., Göran Josefsson, Volvo Car Corporation, Gothenburg, Sweden.

Ph.D., Aristotelis Babajimopoulos, Volvo Car Corporation, Gothenburg, Sweden

Licence:

This document is licensed under the Creative Commons Attribution 3.0 DE License (CC-BY 3.0 DE): <http://creativecommons.org/licenses/by/3.0/de/>

The analysis of flame propagation and temperature distribution in combustion process in dual injector SIDI engine

Krzysztof Wisłocki
Ireneusz Pielecha
Przemysław Borowski
Wojciech Bueschke
Wojciech Cieślik
Maciej Skowron

Abstract

The currently produced Internal Combustion Engines are being equipped with precise injection systems controlling fuel supplying and combustion processes. The effect of usage gasoline supply system with two direct injection injectors is unknown. The research on different injection strategies using two injectors is presented in the paper. The research was conducted on Rapid Compression Machine. The injectors were positioned with 90 degrees angle between them, with spark plug amid them. The usage of high speed camera High Speed Camera 5 equipped with dual optic enabled conducting research by two-color method. The effects of flame propagation and temperature distribution were analyzed using LaVision DaVis software. The lower and more averaged temperature in whole combustion chamber for simultaneous injection and the higher temperature in single dose strategy are presented. The thermodynamic indicators of combustion are discussed.

1. Introduction

Modern S.I. engines have been significantly developed over last 18-20 years. Much better fuel economy and lower emissions of toxic compounds together with higher power concentration from engine displacement unit have been achieved. Such a progress was possible mainly due to the implementation of new combustion systems based on the cylinder direct injection technology which made it possible to operate with higher compression ratios (resulting with higher thermal efficiency of engine thermodynamic cycle) and to control combustion process course according to mixture stratification, lean mixture combustion and multi-injection strategy.

The history of direct gasoline injection is not a very new one. Irrespective of prior solutions let us remember about Mercedes 300 SL engine concept in the years 1956-58 and many other ideas developed in the late 70s of the 20th century, such as Texaco Compound Combustion System, Programmed Combustion Process and Ford Combustion Process, Southwest Research Institute, Mitsubishi Combustion Process, Institut Francais du Petrole, and some others with prechamber, as the answers for the expected reduction of toxic compound from cars and engines resulting from the recently introduced emission regulations in California and Texas in USA. These developments lost their rules against engine external methods of reducing of emissions based on catalytic converter technologies, in those times more effective and easier for implementation in many engines, not only in engines of the newest production.

In the years 1996-98 direct gasoline injection has won the next chance for further development when the Mitsubishi GDI-engine was introduced to the market. At the beginning of the 21st century many other concepts of gasoline direct injection have been designed, extensively investigated and successfully applied. The first generation of injection systems, s.c. *Wall guided combustion* (e.g. Mitsubishi GDI, PSA HPI) was later replaced by *Air guided combustion* (e.g. FSI by Volkswagen and Audi) and followed by *Spray guided combustion* (e.g. CGI by Mercedes or BMW system), Figure 1. All these systems are based on the solutions with single injector located in the combustion chamber and apply multi-injection strategies according to the engine load and speed. In these cases the main task of the injection system is to compound the cylinder charge for the expected rate of mixture stratification in the proper time before the ignition event and to ensure controlled mixture burning rate at the expected time – it means at actual piston position or camshaft angle. It does not raise any doubts that the burning rate course should be optimized in such a way, that the maximum of the power concentration and the energy conversion efficiency together with possibly the lowest emission of toxic components should be achieved.

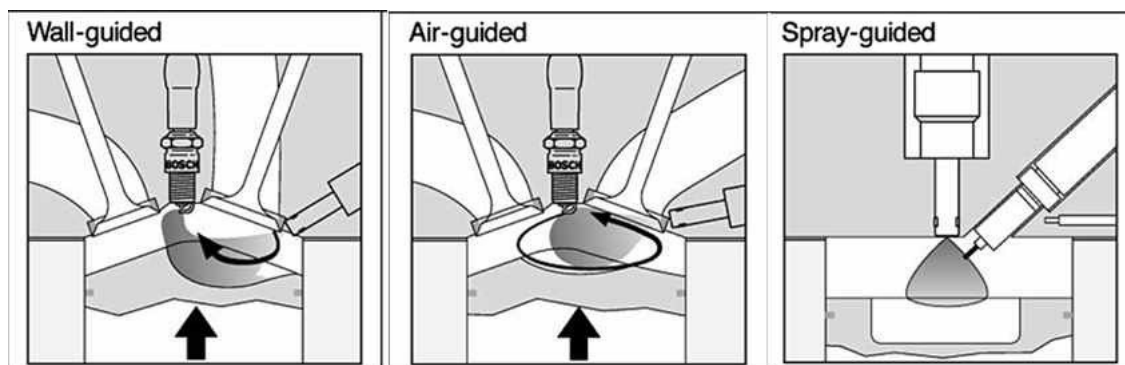


Figure 1: Systems of combustion with direct gasoline injection

In the last years there several works and investigations concerning the use of specific combustion systems and multi-injection strategies on engine operational and emission

indexes were performed. All of them were conducted for systems with one injector [6]. Therefore, the potentials and restrictions of such systems are already adequately recognized. In this paper another system is proposed for examination. As shown in Figure 2, this system consists of two gasoline injectors angularly arranged in the spherical combustion chamber. In the investigated case two outward opening injectors were applied and located in such a way, that both injected sprays of conical shape can meet in the vicinity of the spark plug electrodes.



Figure 2: View of the fuel atomization with the use of two angularly arranged injectors

The idea of using two opposite arranged injectors has already been known since over 30 years. It was proposed by prof. A. Oppenheim from University of Berkeley in the early 80th of 20th century. The idea of s.c. *impinging jets* for C.I. engines was taken from Ch. Jelitto [3] and is now being continued for S.I. engines and investigated in different aspects by the authors of papers [1, 7, 8].

2. Research problem and main objectives of the work

According to the statements made above the research problem which could be formulated as follows occurs:

For the combustion system designed for S.I. engines, equipped with two angularly arranged injectors, the main problems concerning mixture formation and its stratification in combustion area, ignition ability, flame front formation and its propagation should be experimentally recognized and described in a phenomenological manner.

Furthermore, for the proposed system the thermodynamic analysis of the cycle should be performed and the main indexes of energy conversion efficiency and ecological parameters should be determined. For the activities undertaken by the authors the following hypothesis has been accepted:

The application of two angularly arranged injectors and various injection strategies makes it possible to influence the mixture formation parameters and mixture burning rate.

To reach the goals resulting from the above formulated hypothesis, some specific tasks should be performed:

1. The evaluation and analysis of the mixture formation during the injection process and creation of mixture stratification using optical observations of the real injection process, as well as computer modeling and simulations.
2. Recording and analysis of flame propagation and burning rate evaluation using both optical observations and computer simulations.

To get the answers and solutions for the above questions and tasks the proper research methodology has to be defined and technically prepared.

3. Methodology

3.1 Test stand

For the measurements the rapid compression machine (RCM) was used to determine in-cylinder parameters, which executes one engine cycle. The construction of RCM is presented in the Figure 3.

The cylinder head contains two injectors and a spark plug. Intake and exhaust valves are connected to the ports placed in the cylinder close to the cylinder head. Optical access to the combustion chamber is realized by means of quartz window in the piston head. LaVision high speed camera is used to the registration of pictures. The view is directed at the camera with the use of a mirror mounted to the research stand foundation. The main parameters of RCM are included in Table 1.

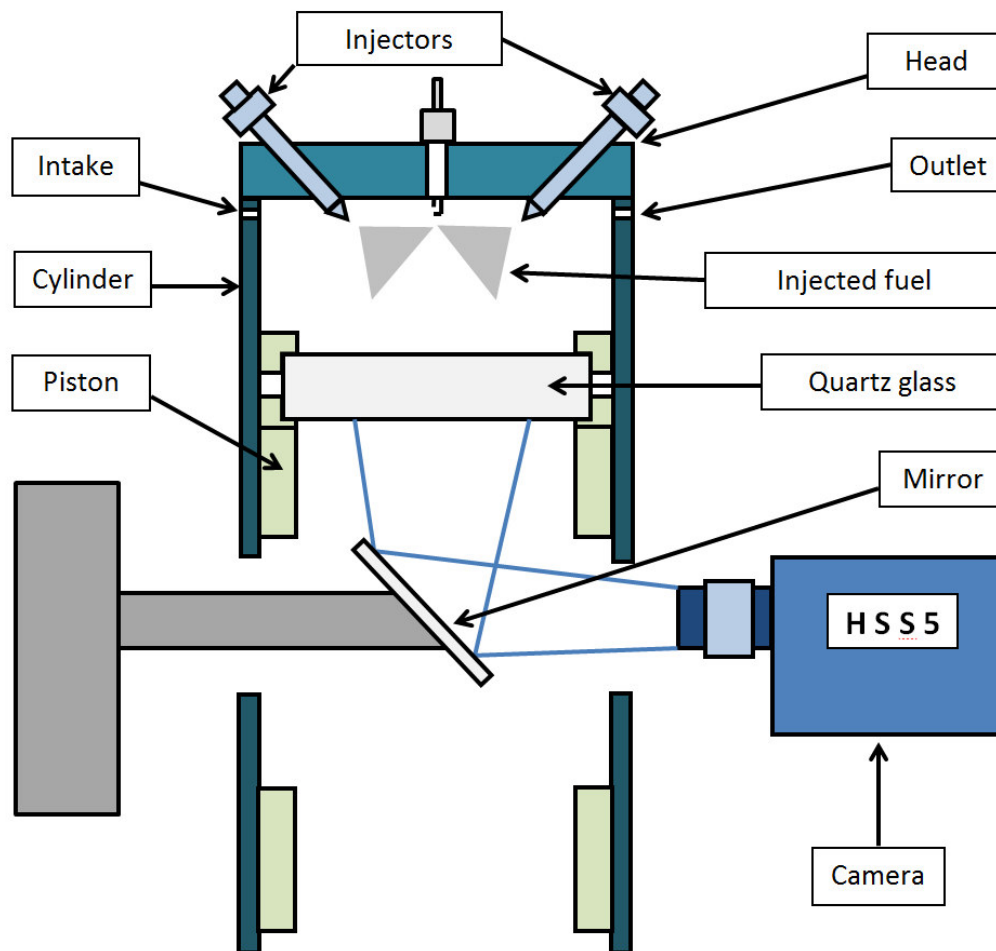


Figure 3: The optical research stand - Rapid Compression Machine

Parameter	Value
Stroke	89 mm
Cylinder diameter	80 mm
Cylinder volume	444 cm ³
Type of combustion chamber	hemispherical combustion chamber + chamber in piston
The volume of combustion chamber	16.5 cm ³
Total volume of combustion chamber	55.9 cm ³
Compression ratio	9.0
Piston sealing	Teflon piston rings
Air inlet	electromagnetic valves
Exhaust outlet	electromagnetic valves
Spark plug	NGK ZKBR7AP-HTU
Optical access	quartz glass $\phi 48$ in piston head
Supply system	direct multi-injection
Injection pressure	regulated, 5÷20 MPa
Combustion	stratified and homogeneous mixture combustion

Table 1: The parameters of RCM and main measurement equipment

The piston position sensor and chamber indicating system were used for the analysis of the combustion process parameters. Injectors were supplied with high-pressure gasoline fuel system, prepared for the direct injected combustion systems.

3.2 Assumptions and its justification

The research was conducted using RCM and a high speed camera. The injection strategy of three gasoline doses employing two injectors was used. The research results are presented for two strategies. The first strategy consists of the injection of three identical doses injected alternately with the injection time $t_{inj} = 0.3$ ms. In the second strategy the injection time for the second dose was extended to $t_{inj} = 0.7$ ms. Irrespective of the employed strategy, the first dose reaches around the spark plug in the time $t_d \approx 0.7$ s. In the first strategy the total fuel dose was 30 mg, and the resultant mixture was characterized by the air fuel ratio $\lambda = 1.4$. With the second strategy of injection the air fuel ratio $\lambda = 1.0$ was achieved with the total fuel dose equaled 44 mg. The research on the combustion of similar injection strategies has already been published by the authors [1, 7, 8] and indicates the validity of the adopted conception. The analysis of the research presented in the paper focuses on the juxtaposition of the results concerning the comparison of combustion for different strategies. The research results presented in the paper discuss the measuring possibilities of the usage of different optical filters in two-colour method. The registration parameters of the view were fixed on 20 thousand images per second with the 512 x 384 pixels resolution. A dual optic system enabling the adoption of colour filters was installed on the objective of the camera. The method relies on laying on each other identical images recorded with the use of two different wave length of optical filters. The temperature is possible to determine by the calculation of the luminescence intensity using LaVision DaVis software.

In the research the following filters were applied: the combination of red with the wave length $\lambda = 650 \pm 10$ nm and green with the wave length $\lambda = 550 \pm 10$ nm (sign – RG) and the combination of previously mentioned green filter and a blue one with the wave length $\lambda = 450 \pm 10$ nm (GB). The range of the filter colour with reference to the wave length is presented in Figure 4. The precise characteristic of the filters is presented in Figure 5.

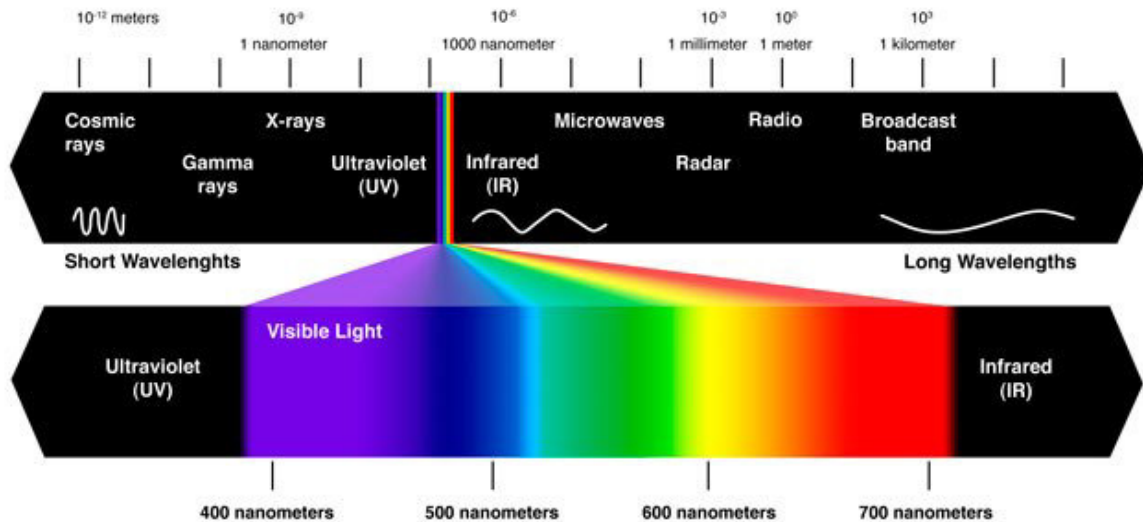


Figure 4: The optical radiation spectrum [4]

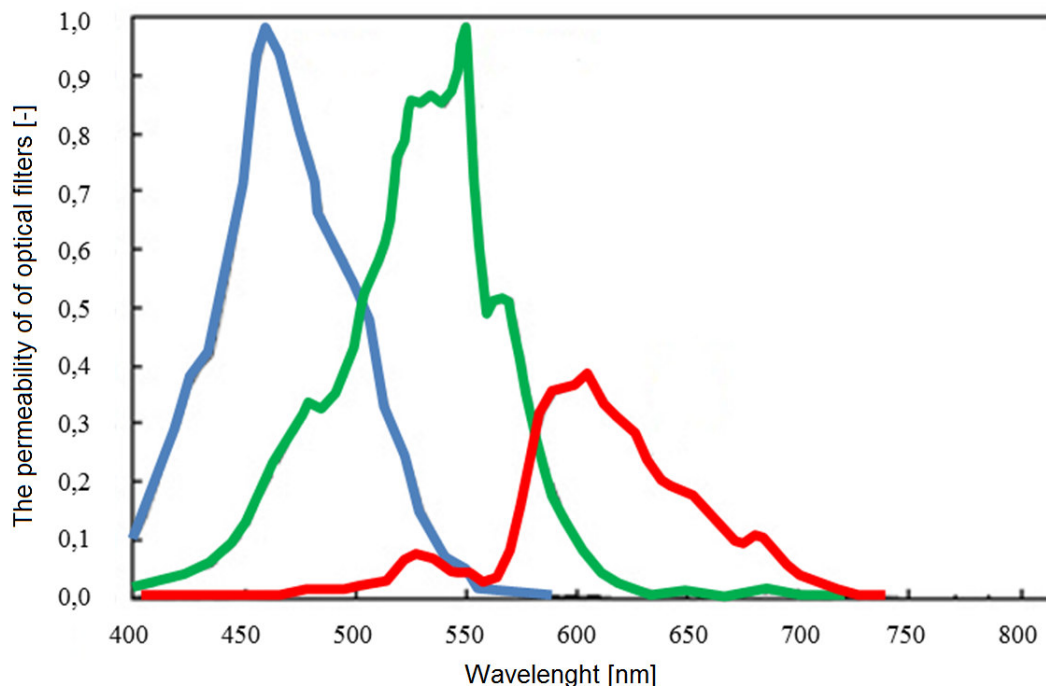


Figure 5: Optical filters permeability in dependence of wave length: blue, green and red [5]

The usage of the two-colour method makes it possible to determine the temperature in a combustion chamber basing on the radiation of two light waves length and on the comparison of them. The Planck law was applied in order to describe radiation:

$$M(\Lambda, T) = \varepsilon_{\Lambda} \cdot \frac{C_1}{\Lambda^5} \cdot \left(\exp\left(\frac{C_2}{\Lambda T}\right) - 1 \right)^{-1} \quad (1)$$

The $C_2/(\Lambda \cdot T) > 1$ condition is fulfilled when the temperature is lower than 3000 K in infrared spectrum ($\Lambda = 380\div 800$ nm). Then, the Wien law can be used:

$$M(\Lambda, T) = \varepsilon_{\Lambda} \frac{C_1}{\Lambda^5} \exp\left(-\frac{C_2}{\Lambda T}\right) \quad (2)$$

After transformation and consideration of two wave lengths, both dependences make it possible to calculate the temperature. The dependency determining temperature with consideration of the CMOS converter answer ($S_{\Lambda 2}/S_{\Lambda 1}$) is presented by the formula (3):

$$T = \frac{C_2 \left(\frac{1}{\lambda_2} - \frac{1}{\lambda_1} \right)}{\left[\ln \frac{L(\lambda_1, T)}{L(\lambda_2, T)} + \ln \frac{S_{\lambda_2}}{S_{\lambda_1}} + \left(\frac{\lambda_1}{\lambda_2} \right)^6 \right]} \quad (3)$$

4. Interpretation of results

4.1 The gasoline injection strategies

The usage of two injectors in the combustion chamber allows the usage of fuel injection strategy consisting of a sequential alternating delivery of three gasoline doses. Two injection strategies with two different injection doses were used in these studies. The optical research was conducted using constant volume chamber [2]. The division of fuel doses is presented in Figure 6. The first strategy involves the alternating injection of three equal doses injected with the injection time $t_{inj} = 0.3$ ms. In the second strategy, the injection timing for the second dose was extended to $t_{inj} = 0.7$ ms. Irrespective of injection strategy, the first dose reaches the spark plug in the time $t_d \approx 0.7$

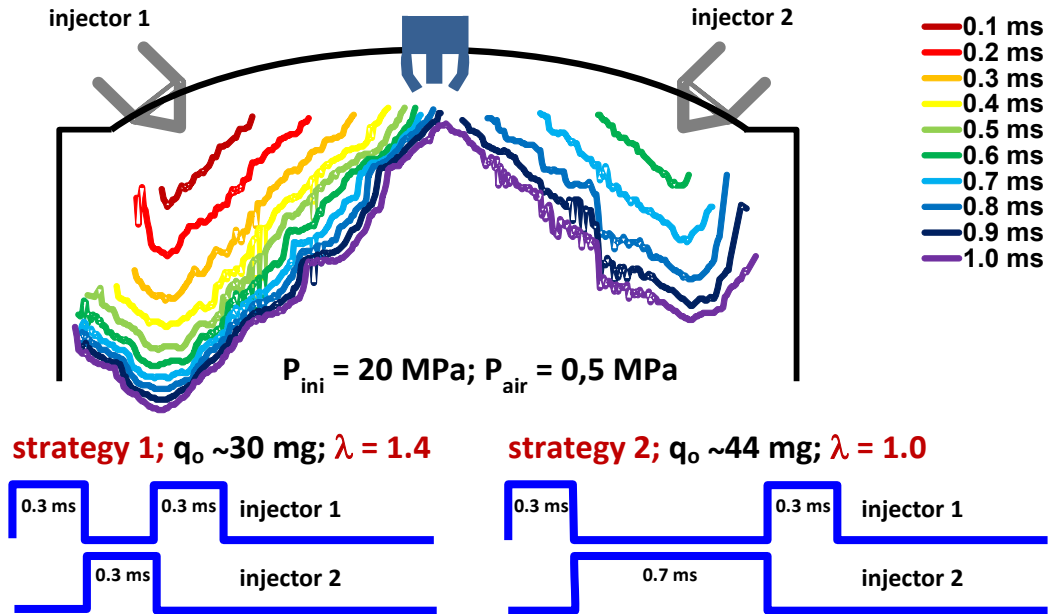


Figure 6: The injection strategies: stream development and fuel doses

4.2 Combustion process

The working cycle was realized at the end of compression with the pressure 2.0 MPa, that is in conditions equivalent to the medium loads of charged combustion engine with a gasoline direct injection. In the first strategy the summary dose was 30 mg and the resulting mixture was characterized by the air fuel ratio equaled $\lambda = 1.4$. In the second injection strategy the air fuel ratio equaled $\lambda = 1.0$ with the summary dose 44 mg. The characteristic indicators of RCM during the 10 following cycles using the second strategy are presented in Figure 7. The pressure waves with reference to volume, piston rod and delay time were compared. The pressure values are very similar in all 10 cycles. The lowest value equals 57.5 bar and is 7% lower than the maximum. The covariance indicator $CoV(P_{max})$ equaled 2.13% which means high repeatability of combustion process.

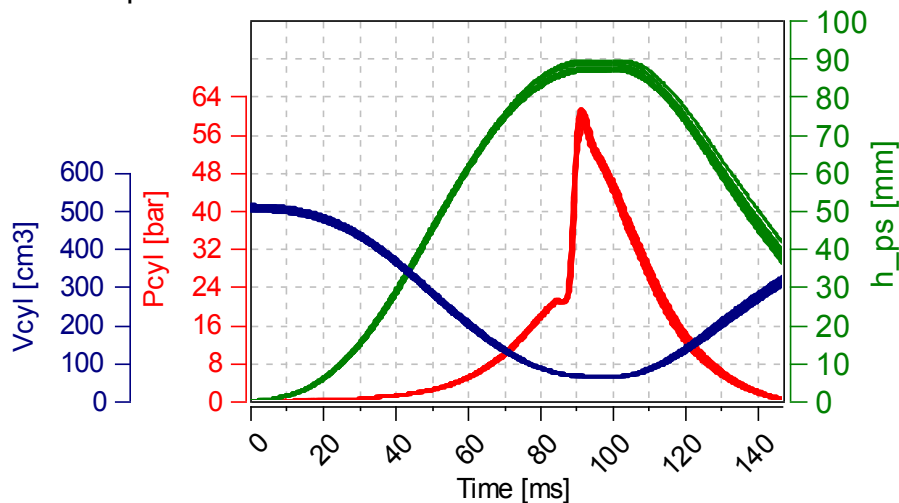


Figure 7: The repeatability of the measurements of the combustion pressure, piston stroke and cylinder capacity for 10 consecutive cycles of operation of RCM.

4.3 The research of combustion of small and big doses

The combustion research with two injection strategies was conducted with the same initial conditions. The air with atmospheric pressure $P_o = 1.018$ bar was compressed. The compression ratio was $\varepsilon = 9$. The time of the combustion start $SoC \approx 0,088$ s and the time of the maximum pressure $aP_{max} \approx 0.092$ s were obtained in both injection strategies. The example cycles of combustion in both strategies are presented in Figure 8. The combustion of higher dose causes 66 % higher pressure increase equaling $dP/dt = 10.5$ bar/s. The 22 % higher combustion pressure equaling $P_{max} = 61.23$ bar relative to 50.38 bar was obtained for the higher fuel dose as well. The combustion of the higher fuel dose causes 36 % higher maximum heat release equaling 735 J relative to 542 J (with a low fuel dose). The 37.5 % higher heat release during the usage of the strategy with longer injector opening time equaling 1848 J was obtained relative to the first strategy where heat release equals 1344 J. The heat release speed is 78 % higher with higher fuel dose and equals $dQ \approx 320$ J/ms.

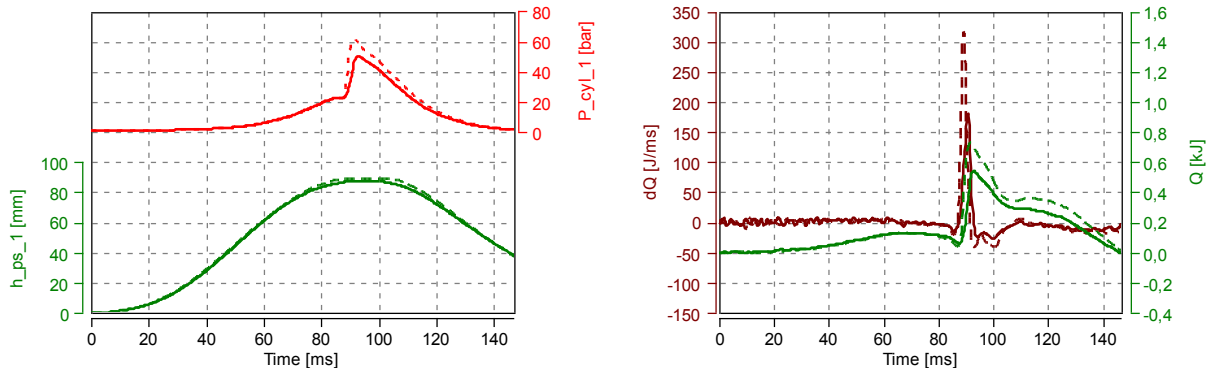


Figure 8: The combustion pressure and the heat release: continuous line – low dose (30 mg), dotted line – high dose (44 mg)

4.4 Combustion process

The exemplary courses of flame propagation with two injection strategies are presented in Figure 9. The usage of the higher fuel dose makes it possible to obtain a greater area of flame distribution (Figure 9b) and a higher intensity of its luminance. For both strategies the greatest flame areas in the time 2.5-3.0 ms after the start of combustion were observed.

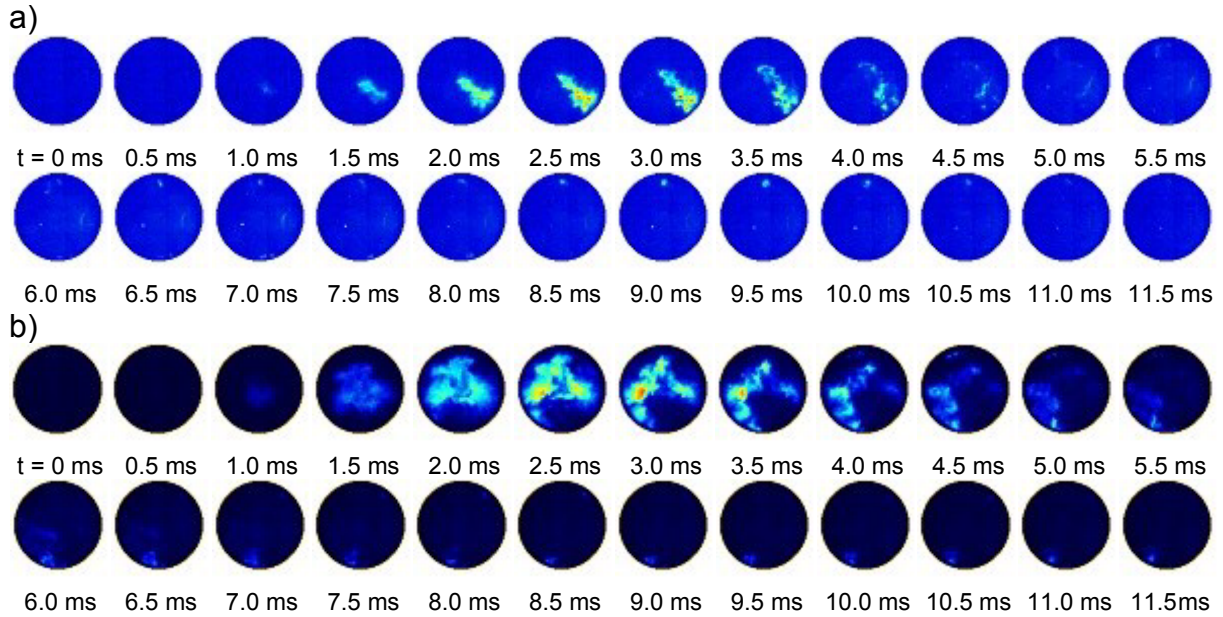


Figure 1:

Figure 9: The flame propagation with multi-injection: a) $q_o = 30$ mg; b) $q_o = 44$ mg

The analysis of the flame propagation area of the combustion chamber is presented in Figure 10. The start of combustion with both injection strategies is similar and equals about 1 ms since the start of compression. The flame of near-stoichiometric mixture combustion fills almost the whole combustion chamber. Its filling share equals 90 % and is 3 times higher than the flame area with a lean mixture.

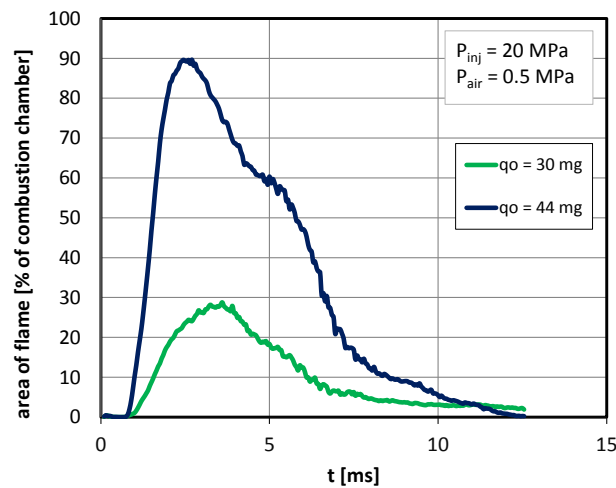


Figure 10: The flame area during combustion with different injection strategies

The full flame temperature analysis is presented in Figure 11. The flame temperature range with both injection strategies reaches values up to 3000 K. The flame temperature of the highest area share comprises within the range 1600-2000 K. The flame of this temperature range also lasts the longest during the combustion with both injection strategies. The usage of a higher dose causes occurrence of a greater flame area for the whole temperature range. The combustion time analysis on the basis of the flame propagation indicates two times longer combustion process of a greater fuel dose. The flame with temperature over 2000 K occurs relatively shortly (in the middle part of its duration) irrespectively of the total combustion time and the applied fuel dose.

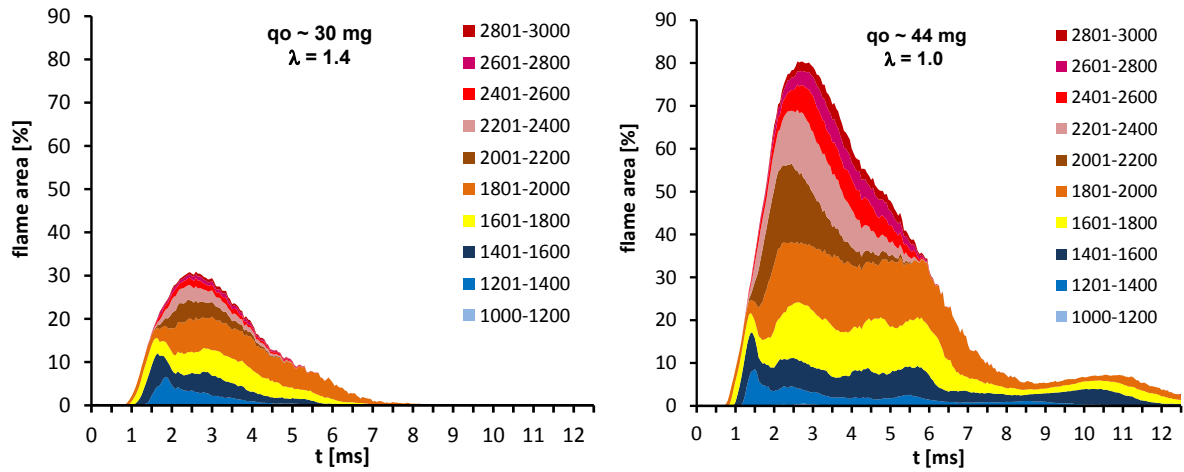


Figure 11: The analysis of flame distribution in combustion of lean and reach mixture

The detailed values of the flame propagation in the temperature ranges are presented in Figure 12. During the combustion of both mixture types, the highest value of the flame area is obtained for the 1801-2000 K temperature range. The second dominant temperature range is the 1601-1800 K one. It means that the temperature within the 1601-2000 K range has the highest share during the combustion of the mixtures created as a result of the proposed fuel injection strategies.

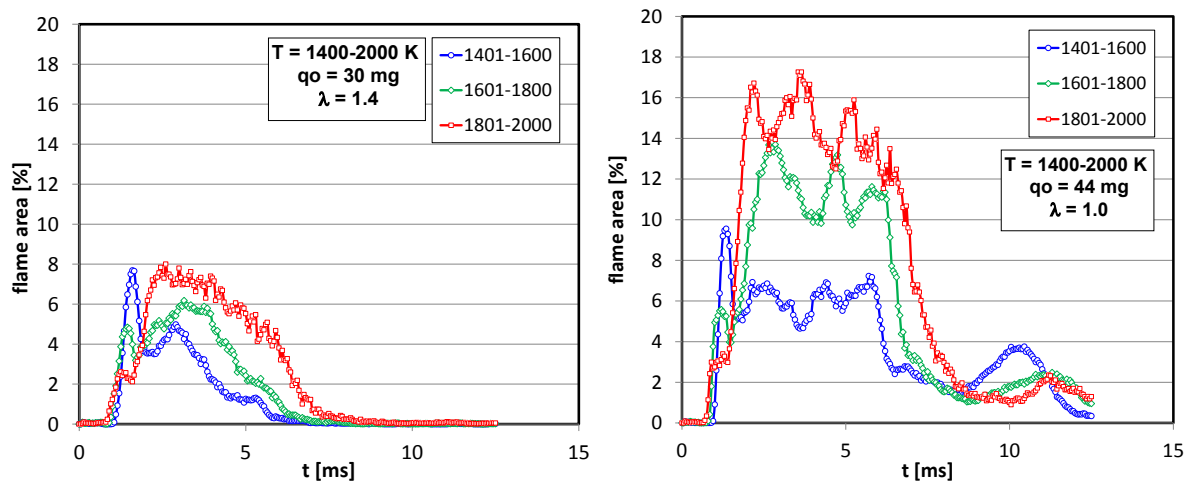


Figure 12: The temperature ranges division during combustion

5. Summary and conclusion

RCM as a tool for investigations is highly useful. The usage of RCM by optical access allows recording phenomena such as flame propagation, fuel distribution during injection and temperature distribution in the combustion chamber. This type of research is of a paramount importance nowadays when emission standards demand from internal combustion engine to be possibly efficient and environmental friendly. During the investigations high recurrence of combustion cycle were obtained. It is important information, as RCM allows achieving one combustion process at one test only therefore, the result of the research is possible to compare with other measuring points.

Both strategies achieved SoC and aP_{max} in comparable times since the cycle start, yet the pressure value and the increase speed were higher for the second strategy with a bigger fuel dose. The second strategy was also characterized by a bigger flame area in a combustion chamber and by higher luminescence intensity. The maximum temperature was approximate for both strategy types, but with reference to the flame area all ranges of temperature had bigger area for the second strategy.

References

- [1] Borowski P., Pielecha I., Comparative analysis of fuel penetration and atomization with the use of two angularly arranged injectors in the Rapid Compression Machine and Constant Volume Chamber. ILASS Americas 26th Annual Conference on Liquid Atomization and Spray Systems, Portland, 18-21 May 2014.
- [2] Bueschke, W.; Skowron, M.; Pielecha, I.; Borowski, P.; Cieřlik, W.; Czajka, J.; Stanowisko do optycznych badań parametrów strugi wtryskiwanego paliwa. In: Logistyka 6/2014
- [3] Jelitto Ch. Numerische Auslegung eines neuen Brennverfahrens für Benzin-Direktein-spritzung. Dissertation. Der Otto-von-Guericke-Universität Magdeburg, Fakultät für Maschinenbau; 2004
- [4] Larsson A., Optical Studies in a DI Diesel Engine. SAE Paper 1999-01-3650.
- [5] Light spectrum <http://midcurrent.com/flies/shining-a-light-on-uv-materials/>
- [6] Pielecha I. Modeling of gasoline fuel spray penetration in SIDI engines. International Journal of Automotive Technology; 2014; Vol. 15, No. 1, pp. 47-55. De Risi, A.; Donato, T.; Laforgia, D.; Optimization of the combustion chamber of direct injection diesel engines. In: SAE Technical Paper 2003-01-1064,
- [7] Pielecha I, Borowski P. Investigations of the Multiple Fuel Injection and Atomization with the Use of Two Outward-Opening Injectors. SAE International 2014; 2014-01-1402.
- [8] Pielecha I., Borowski P., Czajka J., Wislocki K.: Spray Analysis Carried Out With the Use of Two Angularly Arranged Outward-Opening Injectors, 25th Conference on Liquid Atomization and Spray Systems, ILASS USA, Pittsburg, USA 5-8.05.2013

The Authors:

Prof. DSc. DEng. Krzysztof Wiślocki, Poznan University of Technology,
Faculty of Machines and Transport, Poznan

DSc. DEng. Ireneusz Pielecha, Poznan University of Technology,
Faculty of Machines and Transport, Poznan

MSc. Przemysław Borowski, Poznan University of Technology,
Faculty of Machines and Transport, Poznan

MSc. Wojciech Bueschke, Poznan University of Technology,
Faculty of Machines and Transport, Poznan

MSc. Wojciech Cieślík, Poznan University of Technology,
Faculty of Machines and Transport, Poznan

MSc. Maciej Skowron, Poznan University of Technology,
Faculty of Machines and Transport, Poznan

Licence:

This document is licensed under the Creative Commons Attribution 3.0 DE License
(CC-BY 3.0 DE): <http://creativecommons.org/licenses/by/3.0/de/>

Efficiency Benefits of Optimising Downsized Boosted Engines for High Octane Fuel

Ben Leach
Richard Pearson
John Williams
Rana Ali

Abstract

Engine downsizing is a key approach employed by many vehicle manufacturers to improve engine efficiency and help meet CO₂ emissions targets. For gasoline engines reducing swept volume while increasing specific output can significantly reduce frictional and pumping losses in operating areas commonly encountered in legislative drive cycles. Optimising the engine design for use with a fuel with an increased research octane number (RON) allows the adoption of a higher compression ratio which can result in thermodynamic efficiency benefits and a reduction in CO₂ emissions and fuel consumption.

To quantify the benefits of this approach a prototype 1.2l 3-cylinder turbocharged gasoline engine with a maximum BMEP of 30 bar was installed on an engine test bed and its operation optimised across a range of compression ratios and fuel octane numbers. In addition the optimised engine was installed into a VW Passat vehicle and its emissions performance was assessed over a several legislative and pseudo real world drive cycles. Finally a numerical vehicle model was used to quantify the impact of compression ratio and fuel octane on drive cycle exhaust emissions.

It was found that simultaneously increasing the compression ratio from 10.2:1 to 12.2:1 and fuel octane number from 95 RON to 102 RON resulted in efficiency improvements of between ~4% and ~15% depending on operating point. This translated to a ~5% improvement in vehicle efficiency when operated over a range of drive cycles.

1. Introduction

The European Commission has declared a long-term target of reducing greenhouse gas emissions by 80%-95% relative to 1990 levels by 2050. To comply with this desire GHG emissions from transport are required to reduce by approximately 60% in the same time scale. There are additional aspirations to halve the use of conventionally fuelled cars in urban transport by 2030 and to phase out their use in cities by 2050.

To progress these objectives CO₂ emissions targets for passenger cars have been set, enforced by significant fiscal penalties for non-compliance. For 2015 (phased in from 2102) the target for the fleet-average emissions of new vehicle registrations is 130 gCO₂/km, with adjustments made based on the average mass of these vehicles for each manufacturer.

The replacement of larger displacement naturally aspirated gasoline engines with smaller pressure-charged alternatives (so-called 'downsizing') is key approach used by manufacturers improve engine efficiency and meet CO₂ emissions targets. These engines have increased susceptibility to abnormal combustion phenomena such as knock due to the high brake mean effective pressures which they are required to generate. This ultimately limits fuel efficiency benefits by demanding use of a lower geometric compression ratio and sub-optimal late combustion phasing at the higher specific loads experienced by these engines. The lower expansion ratio and retarded combustion in turn increase the exhaust gas temperature, which often leads to a need to add extra fuel that cannot be fully combusted in order to cool and protect engine components from thermal damage. Optimizing the engine design for use with a fuel with an increased research octane number (RON) allows the adoption of a higher compression ratio. This gives thermodynamic efficiency benefits at lower loads whilst mitigating the compromise in combustion phasing at high loads and reducing the requirement for over-fuelling. These synergies allow reductions in CO₂ emissions and fuel consumption in both legislative drive cycles and real world driving.

Significant synergies of turbocharging with direct-injection of fuel into the engine cylinder (1-4) have led to the combination of these two technologies being more prevalent as the specific torque and power targets for engines increases. Injecting fuel during the intake stroke after exhaust valve closure allows high valve overlap at low engine speeds to be applied in order to increase the compressor surge margin and the increased knock protection which results from direct-fuel injection can convert this additional air supply into high torque. The increased knock protection also allows higher compression ratios to be exploited than those used on port-fuel injected engines or less retarded combustion event phasing for the same compression ratio. The less retarded combustion phasing and / or greater expansion ratio leads to cooler exhaust gas temperatures thus reducing the requirement for over-fuelling at high loads and engine speeds for component protection. Higher compression ratio leads to part-load fuel economy benefits but the main benefit of downsizing on legislative drive cycles (which are predominantly low or medium load cycles) comes from load shifting on the engine operating map for a given vehicle road load. This reduces the pumping and friction losses which are more significant at lighter loads.

Increasingly aggressive downsizing is being used or proposed in order to push the mean engine operating point to higher efficiency regions of the load / speed map (5). This increase in specific torque and power is leading to increased stressing of the air-fuel charge mixture with respect to abnormal combustion events such as knock and pre-ignition leading to mega-knock. In a recent study related to the engine described in (5) Remmert et al. (6) concluded that the trend for continued engine downsizing will increase the potential performance benefit to be gained from knock resistant fuels. As the specific output of gasoline engines is increased, the area of the engine operating map in which the engine is knock-limited also increases. The choice of compression ratio for high part-load efficiency and the compromise with combustion phasing and the requirement to over-fuel at full-load becomes a more complex problem. This study investigates the synergistic benefits in energy efficiency of optimizing aggressively downsized engines for high octane fuel. Figure 1.1 illustrates ways in which optimizing an engine for fuel of an increased octane number can benefit efficiency and performance. The various benefits are described in detail in later sections of the paper. Also shown are typical regions of operation for a vehicle over the NEDC and in typical on road operation.

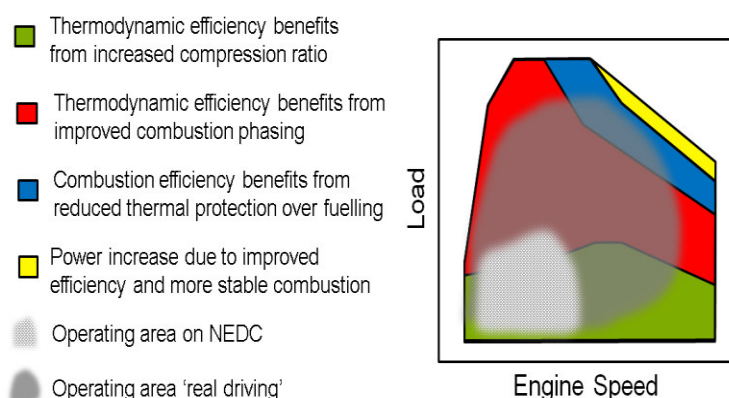


Figure 1.1: Benefits in engine efficiency and performance from optimizing for increased fuel octane number.

2. Engine and test bed fuel octane and compression ratio study

2.1 Engine build and installation

A prototype 1.2l 3-cylinder spark-ignition engine detailed in Table 2.1 was installed on an instrumented engine dynamometer as shown in Figure 2.1. Further details of the base engine are given in (7). During testing the engine was operated on the combinations of compression ratio and fuel octane number shown in Table 2.2 with the engine operational limits shown in Table 2.3 applied. The changes to compression ratio were achieved by varying the depth of the piston bowl. An example of each of the piston variants used is shown in Figure 2.2. Considering the rated BMEP of the engine even the base case compression ratio of 10.2:1 is considerably higher than the production turbocharged GDI engines shown in Figure 2.3.

Type/Swept Volume	Prototype In-Line-3 TC DI spark-ignition, 1.2l
Compression Ratio	Varied throughout programme – see Table 2
Maximum BMEP	30 bar
Maximum Power	120 kW
Maximum Torque	286 Nm
Turbocharger	BMTS prototype single scroll single stage
ECU	MAHLE Powertrain Flexible ECU
Injector	Solenoid multi hole, centrally mounted

Table 2.1: Engine specification

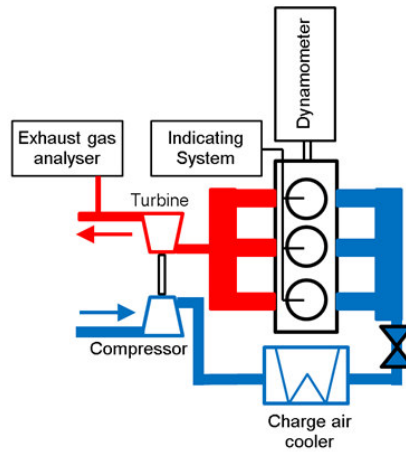


Figure 2.1: Schematic of the engine and experimental setup



Figure 2.2: Examples of the pistons used during testing to vary compression ratio. From left to right 10.2:1, 11.2:1 and 12.2:1

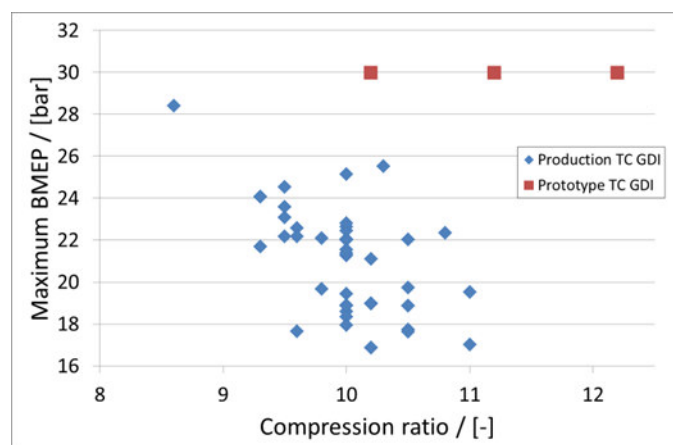


Figure 2.3: Compression ratio and maximum BMEP of production and prototype TC GDI engines

2.2 Test fuels

The engine was tested with the 2 fuels detailed in Table 2.2. The 95 RON fuel was a reference fuel intended to represent a gasoline that might be found in the European market. The 102 RON fuel was selected to represent a high performance road fuel that might be offered in the European market. The specification of both fuels fell within EN228 limits for European gasoline.

Fuel				Compression ratio
RON	MON	O ₂ Content (%)	LHV (MJ/kg)	
95	85	1.7	42.25	10.2:1
				11.2:1
				12.2:1
102	89	2.3	41.93	10.2:1
				11.2:1
				12.2:1

Table 2.2: Matrix of fuels and compression ratios tested

2.3 Engine performance optimisation

Gasoline vehicles in the current market often have a knock control system to allow a vehicle to adapt its performance to the various fuel grades encountered in the market as well as providing emergency engine protection. Typically the control system will be calibrated so that on a high octane fuel no knocking is encountered under normal conditions. However if a lower octane grade is used knocking may be detected and the control system will retard the spark timing in discrete steps until knock is avoided. The resulting delayed combustion will increase the exhaust gas temperature and so the engine control unit (ECU) may instruct the injection system to add extra fuel to each cylinder in order to provide engine thermal protection for components such as the pistons, the exhaust manifold, the turbocharger turbine housing or the turbocharger

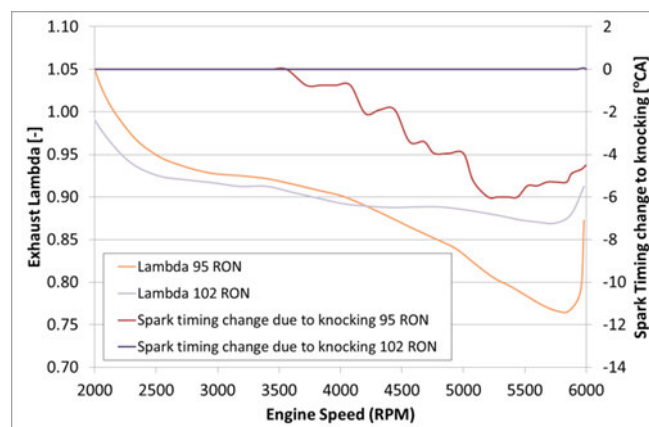


Figure 2.4: Spark timing and lambda response to fuel octane of a 1.4l EU4 emissions level vehicle fitted with an active knock control system

turbine wheel. This will reduce the efficiency and performance of the engine since the additional fuel is not converted into work - it is used only for cooling the critical engine components described above. Figure 2.4 illustrates this response to fuel octane number in terms the ignition timing and lambda (actual air-fuel ratio / stoichiometric air-fuel ratio) of a 1.4l vehicle of EU4 emissions compliance level with a peak BMEP of 21.5 bar during a full-load acceleration test.

For this study, no active knock control system was employed. Instead, for each combination of fuel and compression ratio the ECU control parameters were individually optimised at each operating point according to the criteria in Table 2.4 and while operating within the limits defined in Table 2.3. Peak knocking pressure was determined using the following manipulation of in-cylinder pressure data. The cylinder pressure from each cycle was sampled 0.1 °CA intervals from the period 10 - 70 °CA ATDC in the expansion stroke and passed through a 4 kHz high pass filter before being rectified. The maximum amplitude of this signal was termed the peaking knocking pressure for that cycle. In knock limited regions spark timing was adjusted to keep the average peak knocking pressure below the engine speed dependant limits detailed in Table 2.3.

2.4 Engine Testing

Each fuel and compression ratio combination was run with its specific optimised control parameters over a matrix of steady state points encompassing the engine's entire speed/load range. At each point once stable operation was achieved in-cylinder pressure and exhaust emissions data was collected in addition to fuel flow, engine speed, torque and key pressures and temperatures around the engine. Turbocharger speed was also recorded. The in-cylinder pressure data was processed to derive parameters including IMEP, CoV of IMEP, 10, 50 and 90% mass fraction burned CA, rate of pressure rise and average maximum cylinder pressure.

From this data, for each of the 6 compression ratio – fuel combinations, various full operating area maps were constructed including fuel consumption, combustion phasing / duration, maximum cylinder pressure, and CO₂ emissions.

Compressor outlet air temperature	200°C
Turbocharger Speed	Development limit = 225k rev/min Application limit = 210k rev/min
Turbine entry temperature	980 °C
Max. average cylinder pressure	120 bar
Max. rate of cylinder pressure rise	6 bar/°CA
Combustion Stability	Full load : COV IMEP 4% Part load: SDev IMEP 0.15 bar
Knock	Peak knocking pressure of ≤ 0.9 to 5.5bar (varying with engine speed)
Pre-Ignition	<0.2% of cycles

Table 2.3: Applied engine operating limits

Spark timing	Set to optimum (MBT or knock limited timing as appropriate)
Air/Fuel equivalence ratio	EGT<980 °C outside: $\lambda = 1$ EGT=>980 °C: $\lambda < 1$ as required to observe limit Scavenging region: $\lambda > 1$
Valve timing	Mapped, not varied between cases
Fuel injection rail pressure and SOI	Mapped, not varied between cases
Intake plenum air temperature	Controlled to 40 °C via test bed liquid to air charge cooler

Table 2.4: Engine and test bed operating parameters

3. Results and discussion

3.1 Brake efficiency

The brake efficiency of an IC engine is primarily determined by its thermal efficiency, combustion efficiency, fuel properties, frictional losses and pumping work. In the present study, while the pumping work and friction remained largely unchanged for each operating point, changes to the compression ratio and fuel properties and the associated re-optimisation of combustion phasing and air-fuel ratio resulted in significant changes to the combustion and thermal efficiencies.

Figure 3.1 shows whole area speed/load maps of brake efficiency for the prototype engine when operated on various fuel and compression ratio combinations. In general the charts show that peak efficiency is achieved around the middle of the operating map. Across the engine speed range heat losses and friction dominate the level of efficiency achieved. At low speed heat losses are high due to the time available per cycle for heat transfer to the engine structure. Engine friction increases as engine speed increases so at high speed frictional losses limit the efficiency. On the load axis

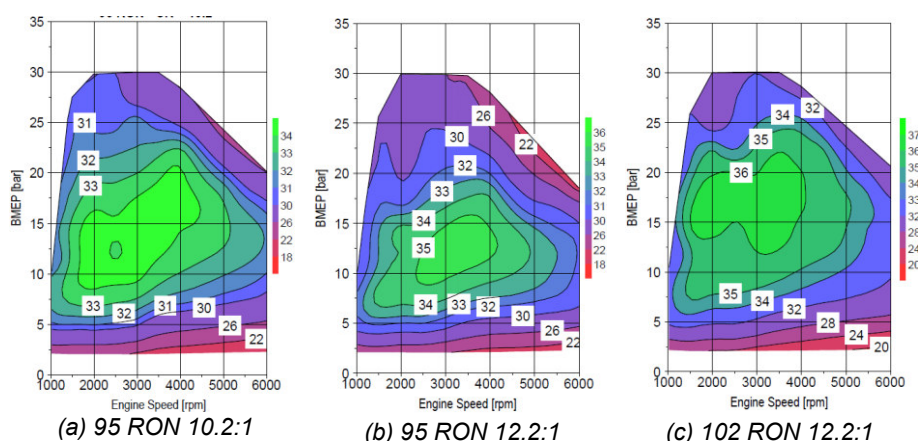


Figure 3.1: Engine brake efficiency (%) when operating with various fuels and compression ratios

pumping losses due to throttling dominate at low load. At high load high peak pressures increase the propensity for knocking and to avoid this combustion is retarded and as a result efficiency is reduced. In the high load/high speed region the combination of low heat losses and retarded combustion due to knocking can result in exhaust gas temperatures that breach the thermal limits of critical exhaust components such as the turbocharger. While the engine normally operates at $\lambda = 1$ to ensure optimal operation of the three way catalyst, in areas where thermal limits might be exceeded extra fuel is added which results in λ is being reduced below stoichiometric and the latent heat of the extra fuel and subsequent change in the ratio of specific heats cools the gas and protects the engine. However, since the extra fuel cannot fully take part in combustion much of it is not converted into work and thus efficiency is reduced.

Comparison of Figures 3.1 (a) and (b) shows the effect of increasing compression ratio from 10.2:1 to 12.2:1 when operating on 95 RON fuel. It is noted that at loads of up to around 10-15 bar BMEP increasing the compression ratio improves brake efficiency. This is because the gas is expanded over a greater volume and pressure / temperature range so more of the fuel energy can be converted to useful work. This can be seen by examining the lower load region of Figure 3.2 (a) which shows that when increasing the compression ratio the average maximum cylinder pressure increases by around 5 bar. However, at loads beyond this the fuel is not able to resist auto-ignition at the higher temperature and pressures generated and combustion phasing must be retarded to avoid engine damage from knocking combustion and thus efficiency is reduced. Figure 3.3 (a) shows the changes to combustion phasing required to avoid knocking when increasing compression ratio from 10.2:1 to 12.2:1 and operating on 95 RON fuel. Here combustion phasing is expressed as the crank angle value (CA) where 50% of the fuel mass has burned, and referred to as MFB50. The plot shows that at loads up to around 6-10 bar BMEP combustion phasing is the same for both compression ratios because the optimal values can be achieved for both cases.

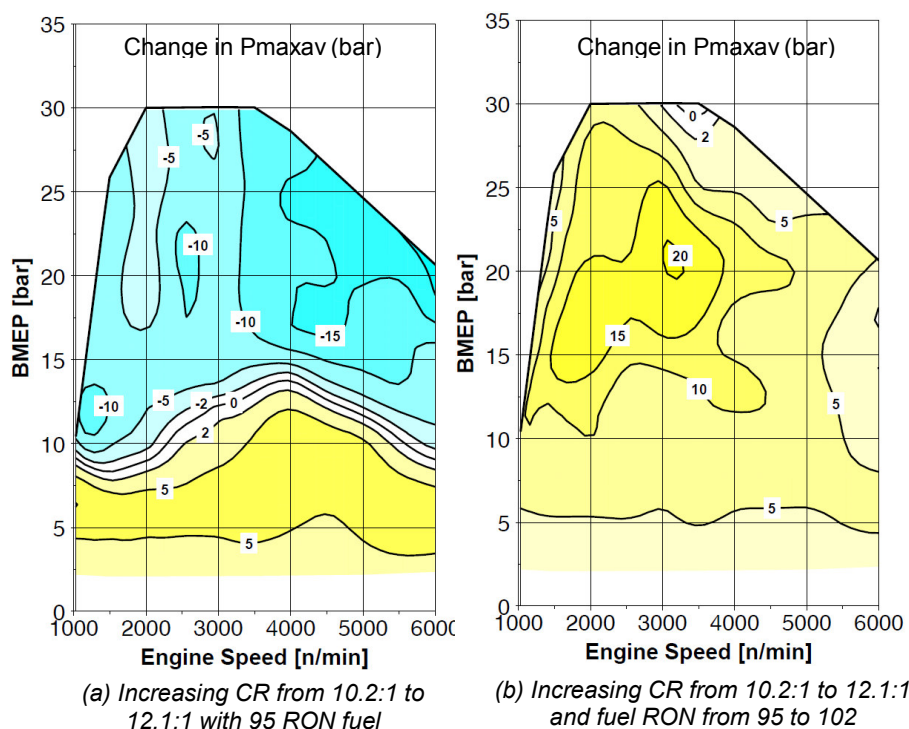


Figure 3.2: Effect of compression ratio and fuel RON on maximum average cylinder pressure P_{maxav} (bar)

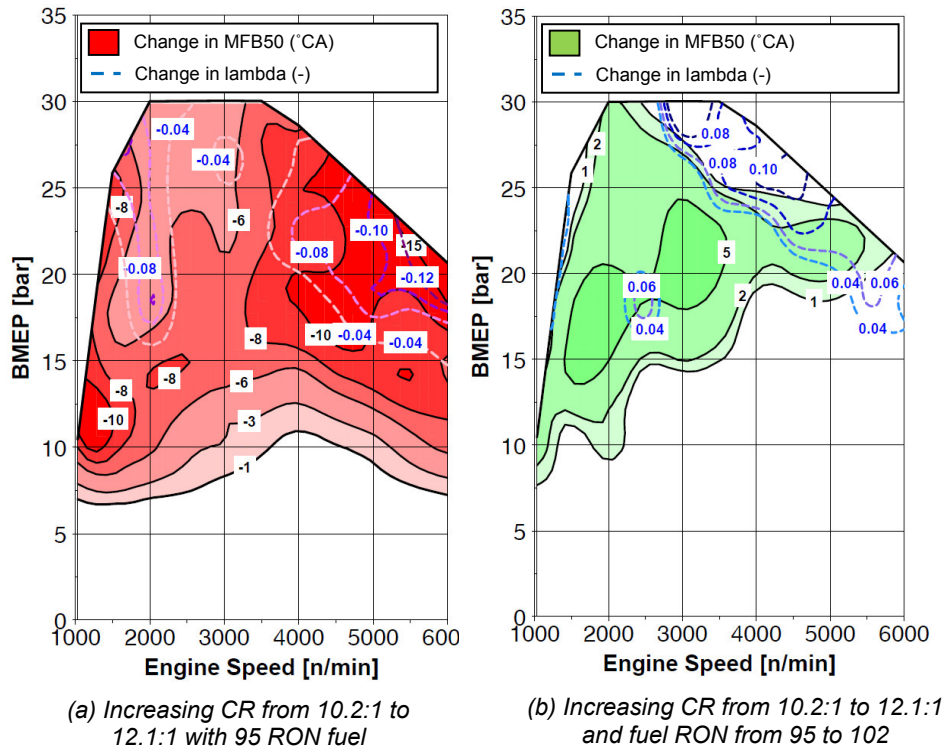


Figure 3.3: Effect of compression ratio and fuel RON on MFB50 and lambda

As the load rises the combustion phasing must be retarded from its optimum value to avoid knocking, with up to 15°CA extra retard required in the high CR case. The corresponding reduction in average peak pressure of up to 15 bar is shown in Figure

3.2 (a). As already discussed the retarded combustion causes the exhaust gas temperature to increase and so in high speed/high load regions extra fuel was added in order to cool the gas to avoid exceeding the thermal limits of the turbocharger. Figure 3.3 (a) shows that lambda was reduced by up to 0.12 in the high speed/high load regions in order to cool the gas and avoid exceeding the thermal limits of the turbocharger detailed in Table 3. The corresponding effect on efficiency is clearly visible in Figure 3.1 (b).

Figure 3.3 (a) also shows small variations in lambda at high load around 2000 rev/min although the target was lambda = 1. Close scrutiny of the test data showed that for the 2 test points in this region control of the lambda value was poor. These operating points are on the edge of the region where the engine is operated in 'scavenging' mode where control of lambda is complex due to high levels of air that short circuit combustion (8). A more comprehensive explanation of these issues is given in (9). Although unintentional the impact of this on peak pressure, combustion phasing and efficiency can be seen in Figures 3.2 (a), 3.3 (a) and 3.1 (b) respectively.

Comparing Figure 3.1 (a) and 6 (c) illustrates the effect on engine efficiency from simultaneously increasing fuel RON from 95 to 102 and the compression ratio from 10.2:1 to 12.2:1. As well as an increase in peak efficiency the higher RON and CR result in efficiency improvements across the entire operating map. This is because the increased knock resistance afforded by the high octane fuel allows more optimal combustion phasing to be maintained despite increased cylinder pressures as shown in Figures 3.3 (b) and 3.2 (b) respectively. Figure 3.3 (b) shows that in the lower region

of the map combustion phasing is at parity for both cases since both configurations can achieve optimal values. However, in the mid speed/load region combustion could be advanced by up to 5°CA (and thus be maintained closer to optimal) compared to the low RON and CR case further improving efficiency. In the high load and speed area combustion phasing is very similar for both cases. This is because the latent heat of extra fuel added for component protection in the 95 RON/10.2:1 case (see Figure 3.3 (b)) drops the maximum cylinder pressure (see Figure 3.2(b)) and reduces the propensity for knocking.

3.2 Impact of compression ratio and fuel RON on vehicle efficiency

Following the engine test bed study the prototype engine was installed into a D-segment vehicle with a mass of approximately 1600kg. Data from subsequent chassis dynamometer testing was used in combination with a vehicle simulation model and engine test bed data to assess the impact of the hardware, software and fuel changes on vehicle efficiency over various homologation and pseudo real world drive cycles listed in Table 3.1. Figure 3.4 shows the time velocity profiles of the NEDC and real world cycles used. All drive cycles were based on publically available data except for the real world cycle which was derived from data collected by the test house during actual road driving.

Data presented in this section includes full engine operating area speed/load maps with brake thermal efficiency benefits for selected fuel and compression ratio combinations compared to the 95 RON/10.2:1 case. Also included on the diagrams is the relative fuel consumption for the selected drive cycles. This was achieved by

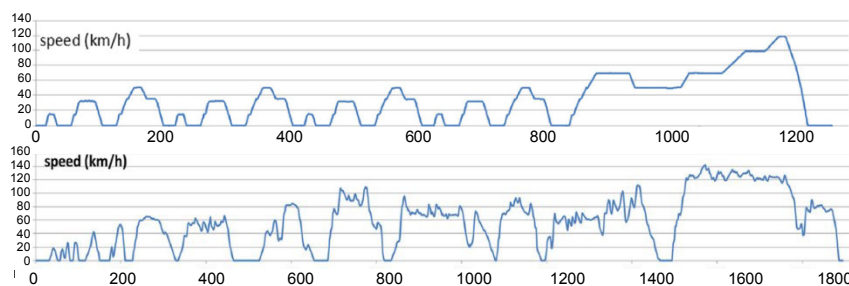


Figure 3.4: NEDC (top) and real world cycle (bottom)

binning the total mass of fuel used at discrete engine operating points throughout the cycle which are represented on the charts by the relative volume of circles at each location. This allows the characteristics of the selected drive cycles in terms of engine operating point to be visualised.

Table 3.1 shows the changes in efficiency over various drive cycles when the compression ratio and fuel octane number are varied as predicted by the vehicle simulation model. In each case a positive number represents the percentage improvement in efficiency of moving from a lower to higher compression ratio and/or fuel RON.

	Brake efficiency benefit (%)				
	Fuel RON		Compression ratio		RON and CR
Fuel RON	102 Vs 95	102 Vs 95	95	102	102 Vs 95
Compression ratio	10.2:1	12.2:1	12.2:1 Vs 10.2:1	12.2:1 Vs 10.2:1	12.2:1 Vs 10.2:1
NEDC	0.14	1.81	3.39	5.06	5.20
WLTP	0.17	1.78	2.93	4.54	4.72
ARTEMIS	0.35	1.88	2.97	4.50	4.85
US06	0.44	2.22	2.47	4.25	4.69
'Real World'	1.56	4.07	1.28	3.78	5.35

Table 3.1: Efficiency benefits of fuel RON and compression ratio combinations over various drive cycles

3.2.1 Effect of compression ratio on efficiency

Figure 3.5 (a) shows the percentage improvement in efficiency across the engine map when moving from a compression ratio of 10.2:1 to 12.2:1 when operating on 95 RON fuel. Also shown on the plot is the relative fuel usage on the NEDC and real world cycles. The plot shows that the 2 drive cycles exercise very different areas of the engine map due to the differing speeds and rates of acceleration required as shown in Figure 3.4. As discussed in the previous sections and shown in Figure 3.5(a) in the lower half of the engine map there is an efficiency benefit from increasing the compression ratio. Since the engine consumes most of the fuel required to drive the NEDC in this region an efficiency benefit of over 3% is realised as shown in Table 3.1. However, over the aggressive real world drive cycle a significant amount of fuel is consumed in areas where increasing the compression ratio reduces engine efficiency, and hence the net benefit in this case is limited to around 1%.

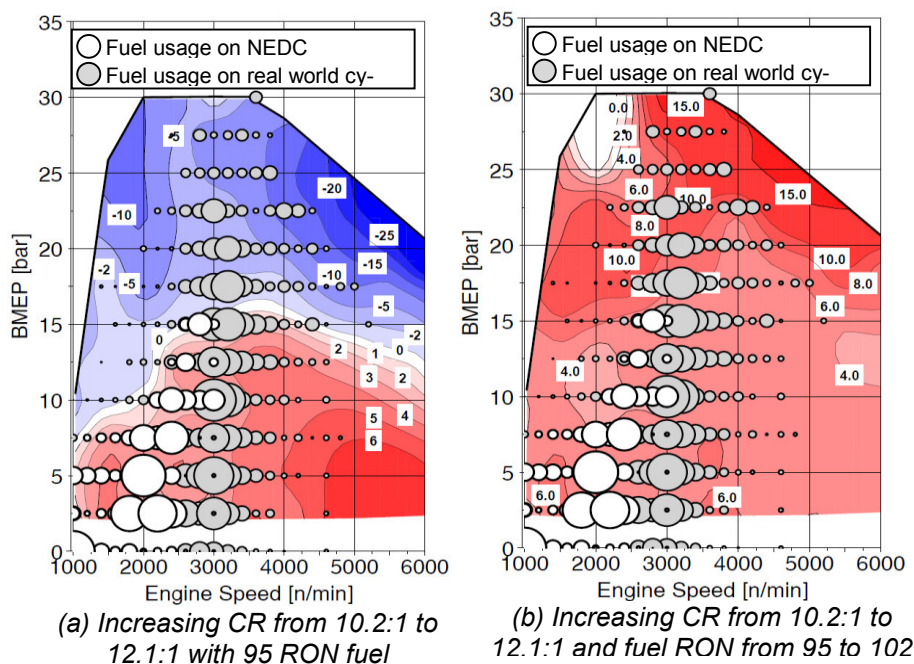


Figure 3.5: Effect of compression ratio and fuel RON on engine efficiency (%) and relative fuel consumed over NEDC and real world drive cycles

3.2.2 Effect of fuel octane and compression ratio on efficiency

Figure 3.5 (b) shows how engine efficiency is affected when the compression ratio and fuel RON are increased simultaneously. The chart also shows the relative mass of fuel consumed when operating over the NEDC and aggressive real world cycle. Over the whole engine map significant benefits are realised and so efficiency improvements of 5.2% and 5.35% are achieved over the NEDC and aggressive real world cycle respectively. The benefits are slightly greater over the higher load real world cycle because the greatest efficiency benefits are achieved at high load.

4. Conclusions

- Optimizing downsized gasoline engines for high octane fuel by specifying an increased geometric compression ratio can increase their efficiency across all areas of the engine operating map. This can lead to significantly increased efficiency which translates to reduced drive cycle CO₂ emissions and real world fuel consumption.
- Increasing the compression ratio from 10.2:1 to 12.2:1 on 95 RON fuel could improve brake efficiency by around 5% at low loads. However, at high speed and load efficiency can be reduced by over 25%.
- Simultaneously increasing the compression ratio from 10.2:1 to 12.2:1 and fuel octane number from 95 RON to 102 RON resulted in BSFC improvements of between approximately 5% and 15% depending on operating point.
- In knock limited regions thermal efficiency is dependent on fuel octane number (RON). Elsewhere efficiency is generally directly related to compression ratio.
- The level of over-fuelling for engine thermal protection and consequential loss of combustion efficiency at high load can be significantly reduced by increasing fuel octane number.

References

- [1] Wirth, M., Mayerhofer, U., Piöck, W.F., and Fraidl, G.K., "Turbocharging the DI gasoline engine", SAE Technical Paper 2000-01-0251, 2000
- [2] Ranini, A. and Monnier, G., "Turbocharging a gasoline direct injection engine", SAE Technical Paper 2001-01-0736, 2001
- [3] Lang, O., Geiger, J., Habermann, K., and Wittler, M., "Boosting and direct injection – synergies for future gasoline engines", SAE Technical Paper 2005-01-1144, 2005
- [4] Turner, J., Pearson, R., and Kenchington, S., "Concepts for improved fuel economy from gasoline engines". International Journal of Engine Research, vol. 6, pp. 137-157, 2005
- [5] Turner, J.W.G. et al., "Ultra Boost of economy: extending the limits of extreme downsizing", SAE Technical Paper 2014-01-1185, 2014.. DOI: 10.4271/2014-01-1185
- [6] Remmert, S., Cracknell, R., Head, R., Schuetze, A., Lewis, A., Akehurst, S., Turner, J., and Popplewell, A., "Octane response in a downsized, highly boosted direct injection spark ignition engine", SAE Technical Paper 2014-01-1397, 2014. DOI: 10.4271/2014-01-1397
- [7] Miller, J., Taylor, J., Freeland, P., Warth, M., et al. "Future Gasoline Engine Technology and the Effect on Thermal Management and Real World Fuel Consumption" SAE Technical Paper 2013-01-0271, 2013. DOI: 10.4271/2013-01-0271
- [8] Dr. Dirk Andriesse, Emilio Comignaghi, Gennaro Lucignano, Aldo Oreggioni et al., "The New 1.8 l DI Turbo-Jet Gasoline Engine from Fiat Powertrain Technologies" 17. Aachener Kolloquium Fahrzeug- und Motorentechnik, 2008
- [9] Leach, B., Pearson, R., Ali, R., and Williams, J., "CO₂ Emission Reduction Synergies of Advanced Engine Design and Fuel Octane Number," SAE Technical Paper 2014-01-2610, 2014, doi:10.4271/2014-01-2610

Definitions/abbreviations

ATDC	After top dead centre
BMEP	Brake mean effective pressure
BMTS	Bosch MAHLE turbo systems
BSFC	Brake specific fuel consumption
CA	Crank angle
CoV	Coefficient of variation
CR	Compression ratio
DI	Direct-fuel injection
ECU	Engine control unit
EU	European union
EGT	Exhaust gas temperature
GHG	Greenhouse gas
IC	Internal combustion
IMEP	Indicated mean effective pressure
LHV	Lower heating value
MBT	Minimum advance for best torque

MFB	Mass fraction burned
MY	Model year
NA	Naturally aspirated
NEDC	New European drive cycle
PI	Port-fuel injection
Pmaxav	Maximum average cylinder pressure
RON	Research octane number
SDev	Standard deviation
SI	Spark ignition
SOI	Start of injection
TC	Turbocharged
TDC	Top-dead-centre

Acknowledgements

The authors would like to thank staff at MAHLE Powertrain Ltd for their work presented in this paper.

The Authors:

Dr. Ben Leach, BP International Ltd., Pangbourne, UK

Dr. Richard Pearson, BP International Ltd., Pangbourne, UK

Dr. John Williams, BP International Ltd., Pangbourne, UK

Mr. Rana Ali, BP International Ltd., Pangbourne, UK

Licence:

This document is licensed under the Creative Commons Attribution 3.0 DE License (CC-BY 3.0 DE): <http://creativecommons.org/licenses/by/3.0/de/>

Fuel Requirements in a Downsized, Highly Boosted DISI Engine

Roger Cracknell
Sam Akehurst
Sarah Remmert
Andrew Lewis
Karl Giles
Rishin Patel
Andrew Popplewell
James Turner

Abstract

Market demand for high performance gasoline vehicles and increasingly stringent emissions regulations are driving the development of highly downsized, boosted direct injection engines.

Inter-cooling in boosted engines and the introduction of cooled EGR can lead to a much lower temperature for a given pressure in a real engine as compared to the test conditions in the CFR engine used to define the RON and MON octane rating scales. This divergence between fuel knock rating methods and fuel performance in modern engines has previously led to the development of an engine and operating condition dependent scaling factor, K , which allows for extrapolation of RON and MON values. Downsized, boosted DISI engines have been generally shown to have negative K -values when knock limited, indicating a preference for fuels of higher sensitivity and challenging the relevance of a lower limit to the MON specification.

The ULTRABOOST engine is an inline-4 downsized, highly boosted prototype DISI engine designed to achieve a 35% reduction in CO₂ emissions whilst maintaining performance of a production V8. The fuel appetite of the ULTRABOOST engine is discussed in the context of an emerging overall understanding of fuel requirements for highly boosted DISI engines.

1. Introduction

Recent trends in gasoline spark-ignition (SI) engine development have been driven by the balance between customer demand for vehicle performance and meeting increasingly ambitious global targets for fleet-average CO₂ emissions - such as 130 g/km by 2015 and 95 g/km by 2020 in Europe [1]. A key area of engine research hence relies on improving combustion efficiency and reducing losses to meet fuel consumption targets without compromising performance. Though various technologies have been developed to this aim, the use of more aggressively downsized and boosted engines is a major industry trend that enables improved efficiency at a given engine torque and speed via reduced friction and pumping losses, achieved by operating the engine at a higher specific output [2].

Engine knock occurs when the end-gas in the combustion chamber auto-ignites ahead of the flame front. It leads to pressure oscillations, which if severe enough can cause damage to the engine. Modern vehicles are fitted with a knock sensor, which can automatically retard the timing at which the spark fires in the engine cycle, thereby avoiding the knock. However, retarding the spark in this way leads to a loss of engine efficiency, since the movement of the piston during the power stroke of the engine is no longer synchronized with the expansion of the hot gases.

A fuel's knock resistance is historically characterised by the research octane number (RON) and motor octane number (MON) as determined in a Cooperative Fuels Research (CFR) engine test that dates back to the 1930s. RON and MON are assigned by determining the volume percent of iso-octane in a binary mixture with n-heptane (the resulting mixture being known as a primary reference fuel (PRF)) which has the same propensity to knock at a given engine compression as the real fuel. The MON test uses a higher temperature, lower manifold pressure and higher engine speed condition than the RON test.

For a real gasoline, the autoignition delay time (as measured in a shock tube or rapid compression machine) decreases monotonically with increasing temperature. However for the PRF fuels, there is a region of the curve in which the autoignition delay actually increases with increased temperature; this is a phenomenon known as "Negative Temperature Coefficient" (NTC) behaviour. Unfortunately this NTC region corresponds with the temperature and pressure regime found in the RON and MON tests. The presence of the pronounced NTC behaviour in the primary reference fuels is the main reason why the RON of a real fuel is typically around 10 numbers higher than the MON [3].

Inter-cooling in boosted engines and the use of cooled EGR can lead to a much lower temperature for a given pressure in a real engine as compared to a CFR engine. These differences in pressure and temperature regimes can lead to subtle but important differences in the chemical reactions that lead to gasoline auto-ignition. In particular it is the relative difference between the behaviour of a real gasoline and the PRFs that is critical. A gasoline with a high sensitivity ($S = \text{RON} - \text{MON}$) is frequently found to be more resistant to autoignition than would be predicted by the RON values in regimes that are at a lower temperature than an octane test in a CFR engine.

A practical approach to quantify the octane appetite of modern engines [4,5] is to define an octane index (OI) as a linear combination of RON and MON with an engine condition dependent weighting factor, K, such that

$$OI = K \times MON + (1-K) \times RON \quad (1)$$

This can also be written as

$$OI = RON - KS \quad (2)$$

where S is the sensitivity (RON-MON). The K-value is thought to be dependent only on the in-cylinder temperature and pressure conditions in the end-gas prior to the onset of auto-ignition.

Mittal and Heywood [6] have shown a progressive decrease in K over the last 50 years and results obtained by Shell on passenger vehicles from the last 20 years suggest that the best fit for OI is to have K less than zero, which means mathematically that for a given RON, a high MON value can indeed be disadvantageous.

In addition to achieving improved performance through exploiting high RON and high sensitivity fuels, performance benefits can also be derived from other fuel properties, such as fuel laminar burning velocity [7-9]. This mechanism relies on fuel properties influencing the engine's ability to achieve the optimal combustion phasing at a given spark timing for maximum thermodynamic work on the engine.

The ULTRABOOST engine is an inline-4 downsized, highly boosted prototype DISI engine designed to achieve a 35% reduction in CO₂ emissions whilst maintaining performance of a production V8. The fuel appetite of the Ultraboost engine is discussed in the remainder of this report in the context of an emerging overall understanding of fuel requirements for highly boosted DISI engines.

2. The ULTRABOOST Project

2.1 ULTRABOOST Engine

The "ULTRABOOST" project was a collaborative research programme co-funded by the Technology Strategy Board (now Innovate UK), Jaguar Land Rover, University of Bath, Shell Global Solutions, Lotus Engineering, GE Precision Engineering, CD-Adapco, Imperial College London, and the University of Leeds. The objective of the project was to develop a downsized, boosted engine technology capable of achieving a 35% CO₂ emissions reduction over the New European Drive Cycle (NEDC) in a 2013MY Range Rover, whilst maintaining performance relative to a baseline naturally aspirated V8 production engine (AJ133) used in the equivalent 2010 vehicle [10].

Specific details of ULTRABOOST engine design are given in references [11-16]. An inline-4 cylinder, 2.0 L (60% downsized) engine was constructed from one bank of the baseline AJ133 5.0 L, naturally aspirated V8 engine. To meet the performance target, the engine was required to meet a 35 and 25 bar BMEP target at 3000 and 2000 rpm, respectively, requiring air charging up to 3.5 bar absolute.

The details of the ULTRABOOST engine and University of Bath test cell are given in Table 1 and the engine installed on the dynamometer is shown in Figure 1.

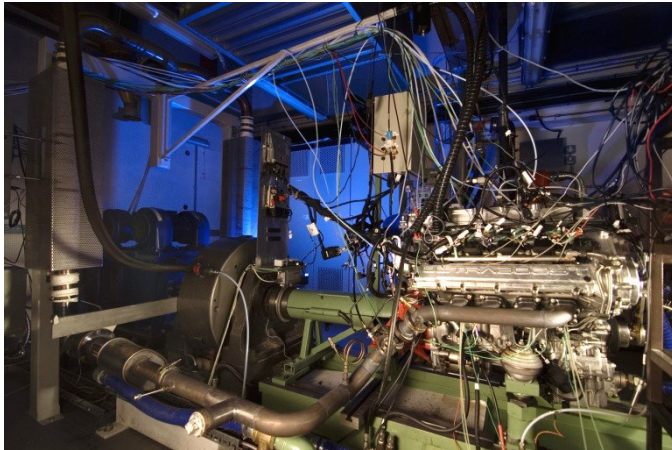


Figure 1: ULTRABOOST Engine on the dynamometer at the University of Bath

Engine Details	
Engine Type	4 cylinder in-line, 4 valves per cylinder
Capacity (cc)	1991
Bore (mm)	83
Stroke (mm)	92
Compression Ratio	9.0:1
Firing Order	1-3-4-2
Construction	All-aluminium AJ133 cylinder block (right bank)
Combustion System	Pent-roof combustion chamber Asymmetrical central DI and spark plug High-tumble intake ports Auxiliary port-fuel injection (not used in these experiments)
Valve Train	Chain-driven double overhead camshafts, fast acting dual continuously variable camshaft phasers (DCVCP) Cam profile switching (CPS) tappets on inlet and exhaust
Specific Power	142 (kW/l) @ 6500 rpm
Specific Torque	255 (Nm/l) @ 3500 rpm
Maximum BMEP	~35 bar @ 3500 rpm and ~25 bar @ 1000, 6500 rpm
Other	External cooled EGR, Water cooled exhaust manifold 130-145 bar peak pressure limit
Engine Test Facilities	
Dynamometer	Twin dynamometer arrangement (AVL 215kW AC dynamometer and Froude AG250 Eddy current dynamometer)
Emissions Bench	MEXA 7000 Series with EGR
Cylinder Pressure Sensors	Kistler type 6054 (air cooled)
Cylinder Pressure Acquisition	AVL Indiset

Table 1: ULTRABOOST Engine and Test Facility Details [16]

2.2 Selected Results from ULTRABOOST Fuels Testing

As the ULTRABOOST engine is extremely downsized and heavily boosted, it is expected to have reduced in-cylinder temperature and increased pressure compared to current engines. It is therefore a key platform from which to understand the impact of fuel effects in emerging technologies - namely, (1) the impact of high RON fuels, (2) the impact of fuel sensitivity on auto-ignition resistance, and (3) the performance impact of fuels formulated for high laminar burning velocity.

This section presents some selected illustrative results from a series of reports [17-19] detailing experiments on 14 fuel formulations over 8 engine operating conditions. The octane appetite of the engine was determined from a sub-set of the fuels tested in which the RON and MON were decorrelated (see Figure 2).

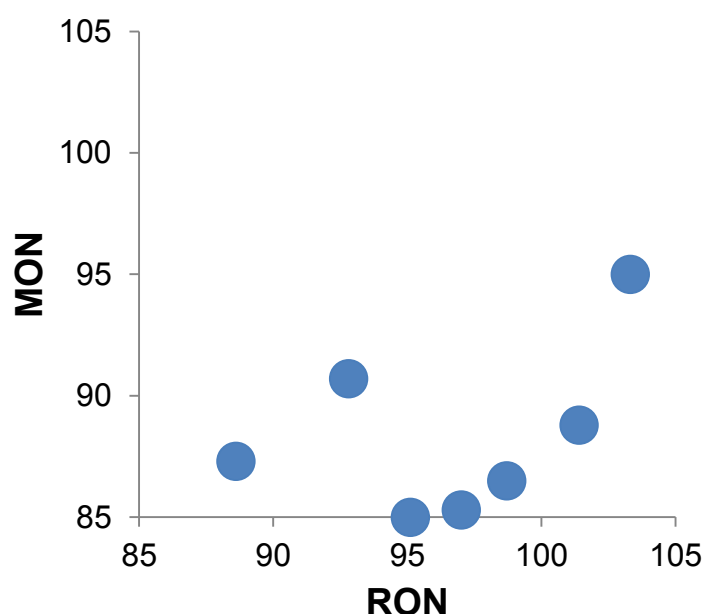


Figure 2: Octane Properties of the ULTRABOOST Fuels Matrix for K-value determination. The RON and MON values are decorrelated ($R^2=0.43$).

The results for the 2000rpm, 30 bar BMEP with 10% EGR condition are shown in Figure 3. It can be seen that there is no correlation between knock limited spark advance (KLSA) and MON, and only a limited correlation between KLSA and RON. If however KLSA is plotted against $OI=K \times MON + (1-K) \times RON$, then the best fit value is found to be $K=-1.1$ [18]. This is amongst the most negative K-values ever reported reflecting the extreme levels of charge pressure employed in this engine.

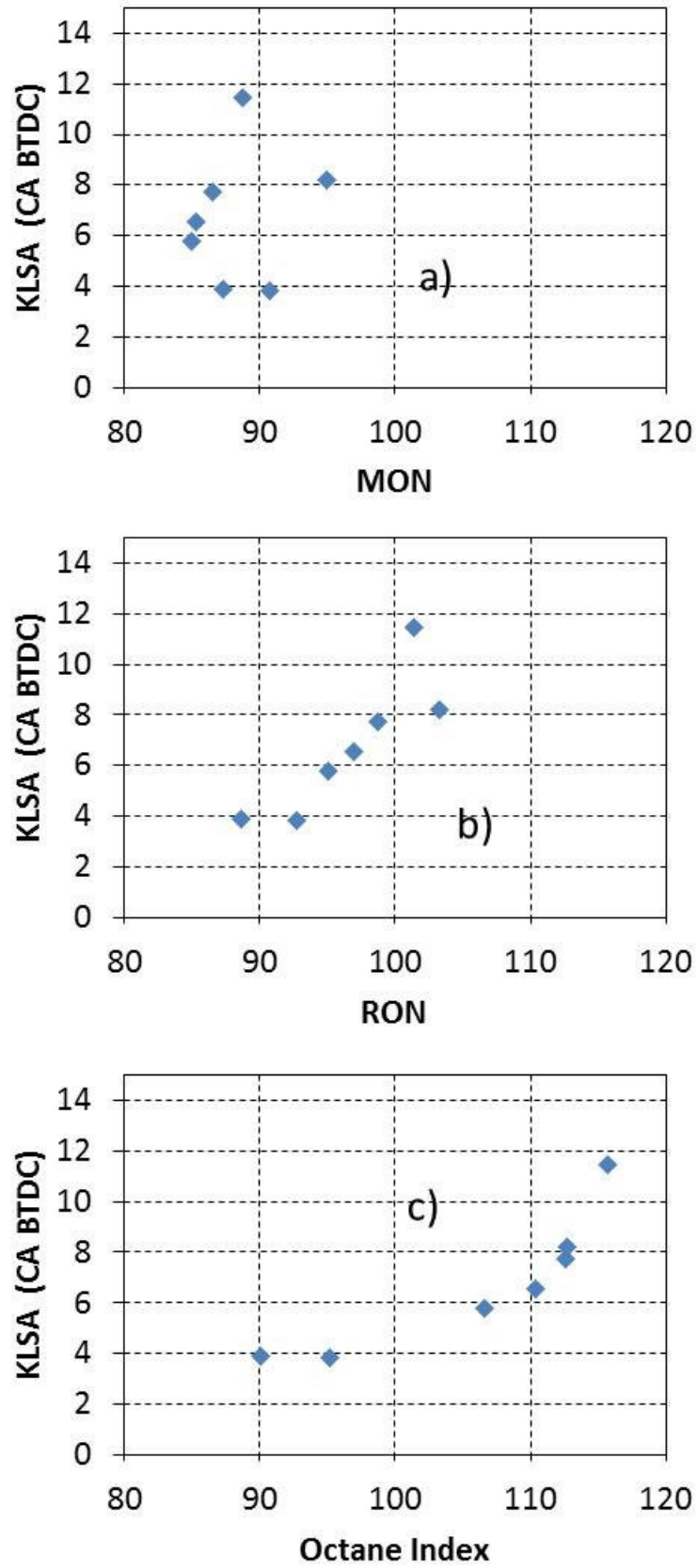


Figure 3: KLSA versus octane number: 2000rpm, 30 bar BMEP, 10% EGR. The spark advance correlates best with Octane Index evaluated with $K=-1.1$ in the expression $OI=K \times MON + (1-K) \times RON$, as shown in 3c.

The comparison shown in Table 2 provides an important illustration as to why the K-value matters by comparing two fuels from within the octane matrix: Fuel A has a higher RON than fuel B, but the spark cannot be advanced as much for Fuel A as for Fuel B, resulting in a lower BMEP. Fuel B has a much lower MON than fuel A. Under the specific conditions investigated (2000 rpm, 30 bar BMEP (approx.) 0% EGR), K was determined to be -0.85 which means from equation 2 that Fuel B has a higher octane index than fuel A which is consistent with the superior anti-knock performance.

In general the ULTRABOOST engine was operating in the plateau region of the BMEP versus spark-timing curve [17, 19], suggesting there is additional scope for further downsizing and compression ratio increase.

	A	B	Difference (B-A)
RON	103.3	101.4	-1.9
MON	95	88.8	-6.2
S (RON-MON)	8.3	12.6	4.3
OI (calc. with $K=-0.85$)	110.4	112.1	-1.7
KLSA (CAD BTDC)	3.8	4.5	0.7
BMEP (bar)	29.7	30.0	0.8%

Table 2: Comparison of Fuel A and Fuel B at KLSA (2000 rpm, 30 bar BMEP [approx.], 0% EGR)

In addition to the determination of K-value via a decorrelated matrix, an alternative approach was taken which allows the K-value to be determined directly from the engine pressure trace using chemical kinetic models for a surrogate gasoline and primary reference fuels [20]. The results for the ULTRABOOST engine confirm that the pressure/ temperature regime is consistent with a highly negative K-value [18], although the methodology does show some sensitivity to the specific chemical kinetic mechanisms used in the simulation [21].

Another two fuels, E and F, were tested to investigate the engine response to fuel laminar burning velocity, S_L (Fuel E - high S_L ; Fuel F - low S_L). Although it is possible to formulate high octane, high S_L fuels, Fuels E and F were not formulated to have matched auto-ignition properties in this study. To evaluate the impact of S_L on BMEP, these fuels are therefore only compared at fixed spark timings (see Table 3).

Speed/Load Point	Spark Timing chosen for comparison: (CA BTDC)	% Increase in BMEP	% Decrease in Burn Duration (CA50-CA10)
2000 RPM 30 bar BMEP 0% EGR	1.5	1.25	10.95
2000 RPM 30 bar BMEP 10% EGR	2.7	1.33	12.60
3000 RPM 26 bar BMEP 10% EGR	10.5	2.35	18.32

Table 3: Results comparing the benefit of high (Fuel E) versus low (Fuel F) laminar burning velocity fuel formulations on fixed spark timing combustion duration and performance

In Table 3 it can be seen that a higher laminar burning velocity results in reduced combustion duration which in turn manifests itself in improved BMEP, showing that the higher the value of S_L the greater the efficiency of the engine due to a shift in peak pressure towards a more-optimized phasing in the cycle.

3. Conclusions

The ULTRABOOST concept engine, as a prototype for emerging, downsized, highly boosted SI technologies, provided an excellent platform from which to understand trends regarding the impact of various fuel properties on engine performance. An extensive matrix of fuels was screened, with a focus on understanding the impact of fuel RON, fuel sensitivity, and fuel laminar burning velocity.

For the regions where the engine was most knock limited, the greatest spark advance was achieved with fuels of both high RON and high sensitivity (RON-MON).

Inter-cooling in boosted engines and the use of cooled EGR can lead to a much lower temperature for a given pressure in a real engine as compared to a CFR engine. A K-value of -1.1 was determined for one full load point, indicating that the thermodynamic conditions in the ULTRABOOST engine are a very long way from the RON and MON CFR engine tests. This is amongst the most negative values ever reported and is consistent with the extreme levels of boosting in the ULTRABOOST engine.

In general the ULTRABOOST engine was found to be operating in the plateau region of the BMEP versus spark-timing curve, suggesting there is additional scope for further downsizing and compression ratio increase.

Fuel laminar burning velocity was also shown to be another important factor in determining engine efficiency.

References

- [1] European Commission, "Climate Action: Reducing CO₂ emissions from passenger cars," http://ec.europa.eu/clima/policies/transport/vehicles/cars/index_en.htm, Jan. 2013.
- [2] Davies, T.; Cracknell, R.; Lovett, G.; Cruft, L. et al.: Fuel Effects in a Boosted DISI Engine, SAE Technical Paper 2011-01-1985, 2011
- [3] Leppard, W.: The Chemical Origin of Fuel Octane Sensitivity, SAE Technical Paper 902137, 1990
- [4] Kalghatgi, G.T: Fuel Anti-Knock Quality - Part I. Engine Studies, SAE Technical Paper 2001-01-3584, 2001.
- [5] Kalghatgi, G.T: Fuel Anti-Knock Quality - Part II. Fuel Anti-Knock Quality- Part II. Vehicle Studies - How Relevant is Motor Octane Number (MON) in Modern Engines? SAE Technical Paper 2001-01-3585, 2001.
- [6] Mittal, V.; Heywood J.B: The Shift in Relevance of Fuel RON and MON to Knock Onset in Modern SI Engines Over the Last 70 Years, SAE 2009-01-2622, 2009.
- [7] Cracknell, R.F; Prakash, A.; and Head, R.: Influence of Laminar Burning Velocity on Performance of Gasoline Engines., SAE Technical Paper 2012-01-1742, 2012
- [8] Cracknell, R.F; Head, R.; Remmert, S.; Wu, Y.; Prakash, A.; Luebbers, M.: Laminar Burning Velocity as a Fuel Characteristic: Impact on Vehicle Performance, Proceedings of I.Mech.E Internal Combustion Engines: Performance, Fuel Economy and Emissions, 27-28 November 2013, London 2013, Woodhead Press
- [9] Cracknell, R.F.; Remmert, S.; Prakash, A.: Evaluating Fuel Laminar Burning Velocity as a Parameter in Performance of Spark Ignition Engines, Fisita World Automotive Congress, 2-6 June 2014, F2014-CET-0332.
- [10] Sandford, M.; Page, G.; and Crawford, P.: The All New AJV8," SAE Technical Paper 2009-01-1060, 2009
- [11] Salamon, C.; McAllister, M.; Robinson, R.; Richardson, S.; Martinez-Boats, R.; Romagnoli, A.; Copeland, C.; and Turner, J.: Improving Fuel Economy by 35% through combined Turbo and Supercharging on a Spark Ignition Engine, presented at the 21st Aachen Colloquium Automobile and Engine Technology, Germany, October 8-10, 2012.
- [12] Giles, K.; et al.: The effect of advanced combustion control features on the performance of a highly downsized gasoline engine. Presented at the 34th FISITA World Automotive Congress, Beijing, China, 27th - 30th November 2012.
- [13] Carey, C.; McAllister, M.; Sandford, M.; Richardson, S.; et al: Extreme Engine Downsizing," Innovations in Fuel Economy and Sustainable Road Transport, Institution of Mechanical Engineers, 8 - 9 November 2011, Pune, India.

- [14] Lewis, A.G.; et al: Observations on the measurement and performance impact of catalyzed vs. non catalyzed EGR on a heavily downsized DISI engine” SAE Technical Paper, 2014-01-1196, 2014
- [15] Turner, J.W.G., et al.: Ultra Boost for Economy: Extending the Limits of Extreme Engine Downsizing, SAE Technical Paper, 2014-01-1185, 2014
- [16] Turner, J.W.G.; Popplewell, A.; Richardson, S.; Lewis, A.G.; Akehurst, S.; Brace, C.J.; and Bredda, S.W.: Ultra Boost for Economy: realizing a 60% downsized engine concept, presented at the Institute of Mechanical Engineering Internal Combustion Engines: Performance, Fuel Economy and Emissions, UK, 27-28 November, 2013.
- [17] Remmert, S.; Cracknell, R.F; Head, R.; Schuetze, A. et al.: Octane Response in a Downsized, Highly Boosted Direct Injection Spark Ignition Engine, SAE Technical Paper 2014-01-1397, 2014
- [18] Remmert, S.M.; Campbell, S.B.; Cracknell, R.F.; Schuetze, A.; Octane Appetite: The Relevance of a Lower Limit to the MON Specification in a Downsized, Highly Boosted DISI Engine, SAE Technical Paper 2014-01-2718, 2014
- [19] Campbell, S.B; Remmert, S.M Cracknell, R.F.; Schuetze, A.B; Warnecke, W.; Lewis, A.; Akehurst, S.; Turner, J.; Patel, R.: Popplewell, A: Fuel Effects in a Downsized, Highly Boosted Direct Injection Spark Ignition Engine presented at the 23rd Aachen Colloquium Automobile and Engine Technology, Germany, October 6-8, 2014
- [20] Davies, T.; Cracknell, R.; Head, B., Hobbs, K. et al.: A new method to simulate the octane appetite of any spark ignition engine, SAE Technical Paper 2011-01-1873, 2011
- [21] Somers, K.; Curran, H.J.; and Cracknell, R.F.: Simulating the octane appetite of SI engines: the influence of chemical mechanisms. Presented at 7th European Combustion Meeting, Budapest, Hungary, 30Mar - 2Apr 2015

The Authors:

Prof. Roger Cracknell, Shell Global Solutions, Manchester, UK

Dr Sarah Remmert, Shell Global Solutions, London, UK

Dr. Andrew Lewis, Dr. Sam Akehurst, Mr Karl Giles, Prof. Jamie Turner,
University of Bath, Bath, UK

Dr. Rishin Patel, Mr. Andrew Popplewell, Jaguar Land Rover, Whitley, Coventry, UK

Licence:

This document is licensed under the Creative Commons Attribution 3.0 DE License
(CC-BY 3.0 DE): <http://creativecommons.org/licenses/by/3.0/de/>

Optical analysis of combustion chamber and fuel spray interaction in terms of chamber geometry modification and injection parameters change

Krzysztof Wiślocki
Ireneusz Pielecha
Przemysław Borowski
Wojciech Bueschke
Wojciech Cieślik
Maciej Skowron

Abstract

The compatibility of combustion system elements has got crucial influence on the most of important engine indicators, which effect emission of regulated pollutants. The optimal combination of combustion chamber geometry and conditions in it, with injection factors is the necessary goal to reach highest possible efficiency and low emissions.

The analysis bases on the variation of three main parameters groups: selection of the combustion chamber dimensions, conditions in chamber and injection parameters. In the first group diameter, total depth, bottom and bowl lip of the chamber were changed. Conditions in the chamber are characterized by the charge pressure, which in real engine depends on boost pressure. From the injection point of view, fuel pressure and the injector opening time were regulated and compared for two different nozzles.

Concerning the investigation results an influence of geometrical and combustion system parameters regulation on spray and piston bowl interaction is concluded and compared to the actual state of art.

1. Introduction

Problems described in this paper concern processes of injection, fuel spray formation and air-fuel mixture creation. As it is observed in last years, increasingly intensive development of internal combustion engines is strongly associated with application of modern solutions of direct fuel injection, multi-injection strategies of fuel supply and cylinder charge stratification. To achieve good results in engine performance with good agreement with emission standards an optimal interaction of mixture creation process with combustion chamber geometry is necessary. Such problem seems to be most important in CI engines where fuel sprays injected with very high pressure (today already over 2500 bar) reach big velocities and penetration. In relatively small combustion chambers still not evaporated fuel can easily reach the chamber wall and may cause the burning of fuel film on the wall without sufficient air access. This results in higher PM emission in most cases.

In multi-injection strategies time of injection of partial fuel doses has an essential meaning. By this time and number of individual injection events the stratification of the mixture along combustion chamber will be defined. When the combustion chamber is located mainly in the piston bowl, to keep most fuel in it, the late injection should be preferred.

As we can notice, in mixture creation processes many parameters are playing significant role. There are mainly: injection pressure, cylinder back pressure, number and cross-section areas of injection orifices, distance from injector to chamber walls and shape of piston bowl.

The authors of this paper decided to perform the investigations for determination of the dependency of fuel distribution in the combustion chamber and in piston bowl from injection pressure and timing, back pressure and from piston bowl shape. Main concept of test bed design and results of preliminary investigations in this research area were already discussed in papers [6],[4],[2].

2. Main objective of research

The main intention of investigation undertaken by the authors was to detect and describe the influence of the pressure of the injected fuel and fuel spray propagation on its interaction with the combustion chamber walls at different piston positions which resulted from the time of injection. The scientific aim of the research was to answer questions about the distribution of fuel in the combustion chamber in the piston bowl and over the piston crown and to describe the qualitative and quantitative relations of the interactions between fuel spray and combustion chamber walls at different fuel pressures and back pressures inside the combustion chamber. The research also aimed at exploring the properties of the injected fuel under cold start. While conducting the tests the temperature of the walls of the combustion chamber inside the piston and the temperature of the air in the test chamber were 30°C.

The main problem of research was to recognize the fuel spray behavior in combustion chamber located in piston bowl. For sure such behavior is strongly dependent on the injection control parameters like injection pressure, injection duration, chamber back pressure, as well as geometrical shape of the bowl, especially shape and dimensions of the bowl upper edge. Location of fuel spray against the bowl edge depends on the time of injection which defines the distance between piston and cylinder head bottom plate and injector nozzle with orifices. One of the objectives resulting from the above

research problem definition was to estimate an influence of defined parameters groups on filling of combustion chamber area with fuel spray and time of reaching the piston wall by fuel stream. For detection of this influence some specific indicators were defined and have been determined in the investigations as functions of process duration. They were: fuel spray front velocity, spray penetration, area of spray (area occupied by liquid fuel, fuel droplets) and time of reaching the walls by the fuel spray. The history of development of the area of spray was being compared to the area of combustion chamber located in the piston bowl and between piston crown and cylinder head. The achieved results for various bowl shapes (denoted by letters N, P, K) and for two various injectors have been compared each other. To perform research and to determine expected values and indicators of the processes the special test-bed was designed and constructed.

3. Methodology

3.1 Test stand

The authors decided to perform the investigations on the experimental way with application of the independent test-stand equipped with special research chamber where it would be possible to mount piston crown and injector inside it, and to observe and record high speed movies from fuel spray behavior when injected into the piston bowl. For this purpose a constant volume chamber (CVC) was used where a modified piston was fitted. The chamber allows optical access from all sides, as shown in the Figure 1. The technical parameters of the test chamber have been presented in Table 1. Its operation is possible using air or nitrogen (or other gases) and investigation process is fully automatically controlled. The chamber has been equipped with two electronically controlled valves which ensure effective charge exchange.

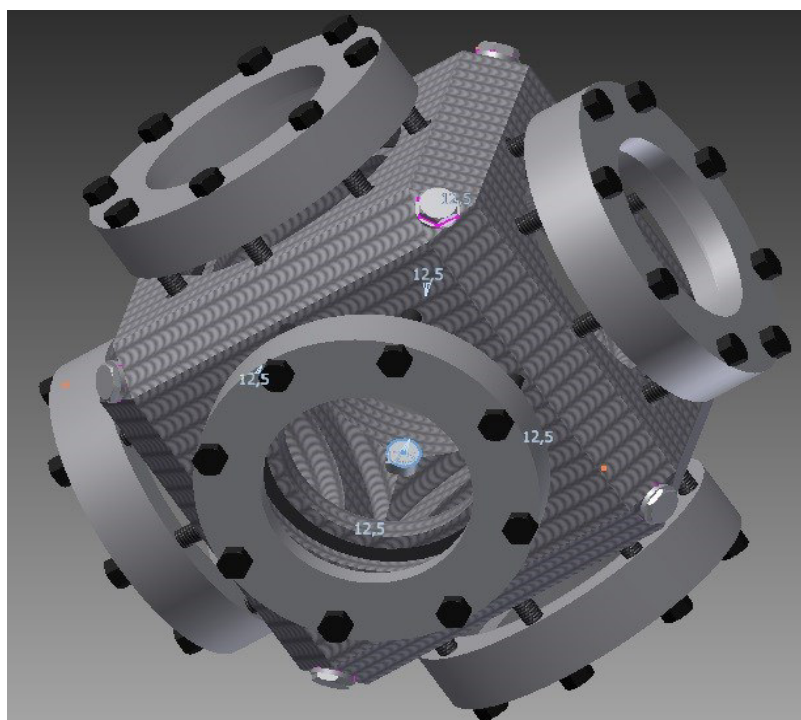


Figure 1: A View of the model of Constant Volume Chamber used in the investigations

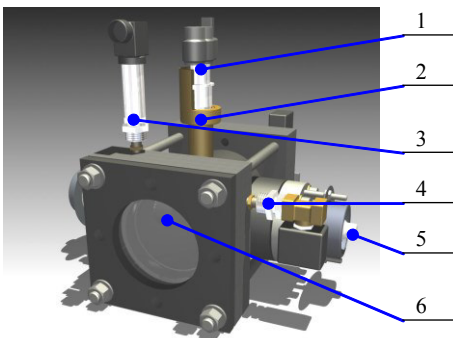
Chamber	Outer cell	Material (ø × H)	Steel (110 mm × 400 mm)	 <p>1 – injector, 2 – injector housing, 3 – air pressure sensor, 4 – electromagnetic wastegate valve, 5 – lighting, 6 – quartz glass window</p>
	Inner core	Material (ø × H)	Steel (90 mm × 350 mm)	
		Volume	2200 cm ³	
	Accessible pressure		0–4.5 MPa	
Heater	Air	External heating	20–100°C	
	Fuel	Heating injector	20–200°C	
Windows	Material/thickness		Quartz glass/30 mm	
Injector	Injection	Pressure	30–200 MPa	
		Duration	0.2–1.0 ms	
		Fuel	Diesel	
	Injector type	Common Rail	Electromagnetic, 1-dose, 0.17 mm	
Light	Type	2 × Halogen Lamp	24 V; 250 W, angle 30°	

Table 1: Technical data of Constant Volume Chamber [6]

Inside the chamber the piston crown is mounted. In the piston a cut has been made into a part of its crown (Figure 2), which allowed optical access to the edge of the combustion chamber inside the piston. A sufficiently intense illumination was obtained through lighting of the chamber from two sides. The perpendicular placement of the camera against the lighting allowed filming of the area where the fuel spray hits the edge of the combustion chamber inside the piston.

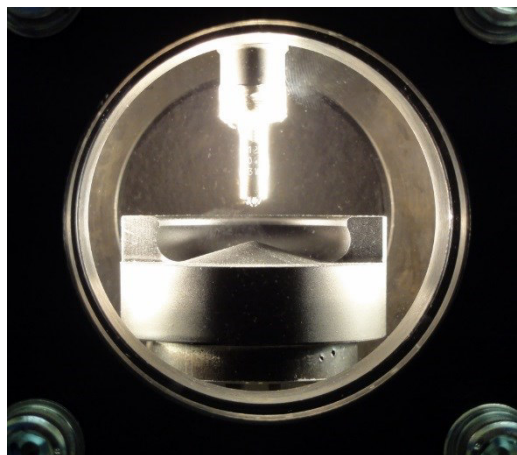


Figure 2: View of the test chamber with a cut of piston crown and injector mounted inside

3.2 Assumptions and its justification

For analyzing of fuel spray behavior when injected into the piston bowl a single spray should be observed and filmed. It does mean that from the 7 or 9 sprays from more-hole injector only one spray should be extracted. In other case the observed phenomenon of single spray behavior will be distorted by other sprays and its picture will be covered by the fuel cloud from them. In this case a technical problem appears: how to get one spray from multi-hole injector preserving the same parameters of injection pressure, spray velocity and penetration like in all other sprays. For investigations the electromagnetic injectors have been used.

In the case of discussed investigation a few specific assumption have been adopted. For defined measuring points in research engine defined by engine speed and load some characteristic parameters have been measured or calculated, as shown in the table 2. For injection pressures given in the table the jewels specific time of injection has been adjusted for getting the expected fuel dose q_{MI} . These measurements have been repeated for 3 injectors denoted as A, B, C. These parameters stand as the basis for investigation in Constant Volume Chamber, where the observations of fuel spray development and penetration have been performed, Fig. 3.

Point No	Engine speed, n	Torque T_o	Injection pressure, P-inj	Fuel dose q_{MI}	Cylinder pressure at main dose, P-cyl	Distance: injector-piston X
-	1/min	N·m	bar	mg	bar	mm
1	1375	35	470	8,37	46	20,247
2	1400	80	1000	18,21	64	20,945
3	1700	60	1100	13,86	55	21,874
4	2000	80	1350	19,09	63	22,662
5	2400	130	1650	30,19	83	29,183
6	1950	25	470	7,03	40	23,798
7	1500	130	1300	30,69	88	20,843

Table 2: Engine operating parameters in the selected load points

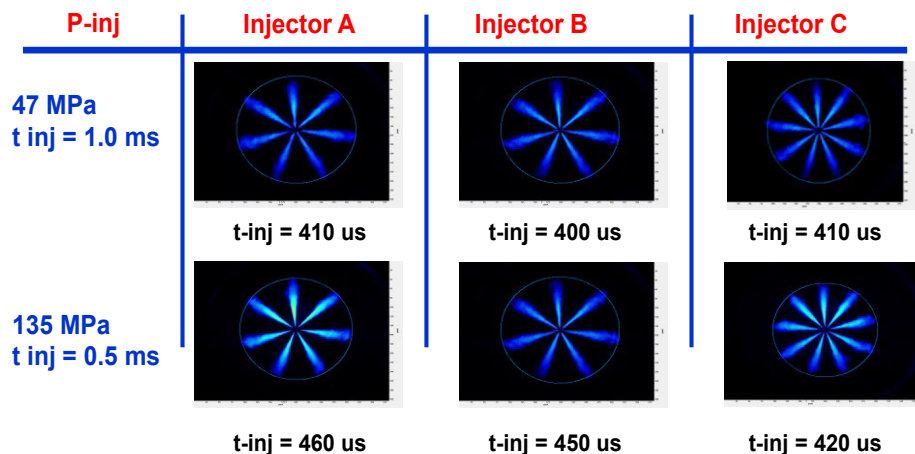
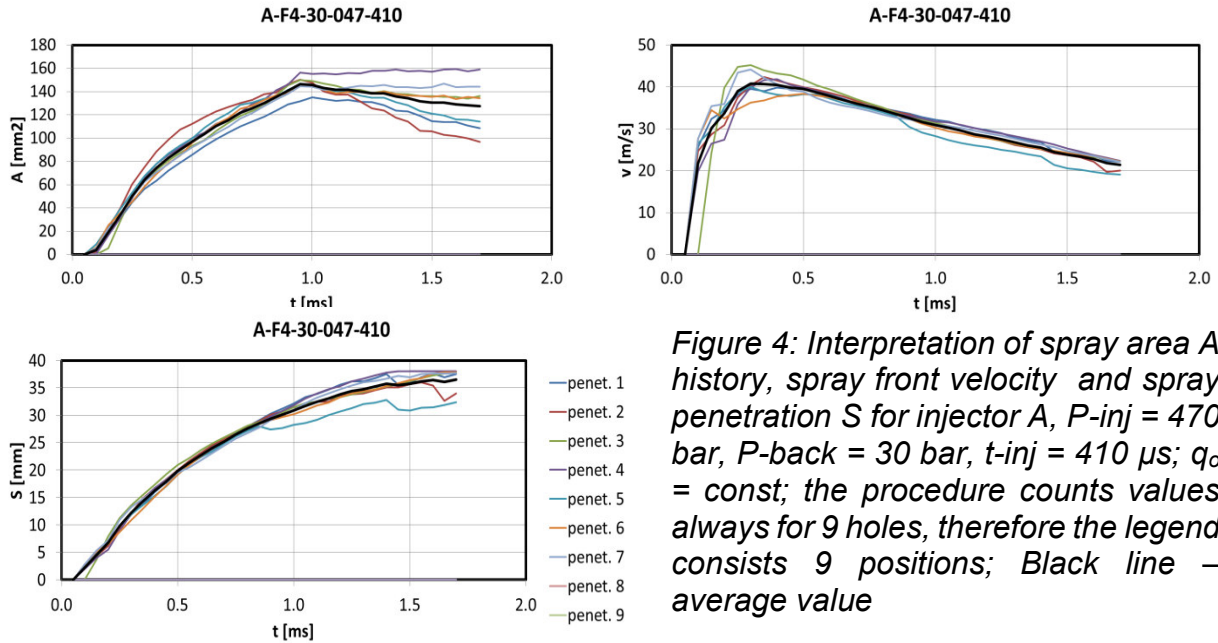


Figure 3: Fuel sprays from 7-hole injector (A, B) and 9-hole injector (C)

Results of these observations made it possible to evaluate spray penetration history for every single spray and for every investigation case defined by injection pressure and duration. Based on the statistic analysis of achieved results a single average spray with its penetration history for given values of injection pressure and duration was extracted, Fig. 4.



To get the possibility to observe single spray behavior all other holes in injector nozzle had to be closed. Multiple injections would have resulted in overlapping of the subsequent fuel doses and a reduction of the quality of the footage. Additionally, the analysis of the obtained footage would have been more difficult due to the interactions between the fuel doses.

For this purpose technology of laser welding of the holes has been applied where the laser beam energy had to be carefully adjusted for providing good quality of the internal sealing surface of the needle sit. In the case being described here good tightness of welded holes has been reached after few trials, Fig. 5.

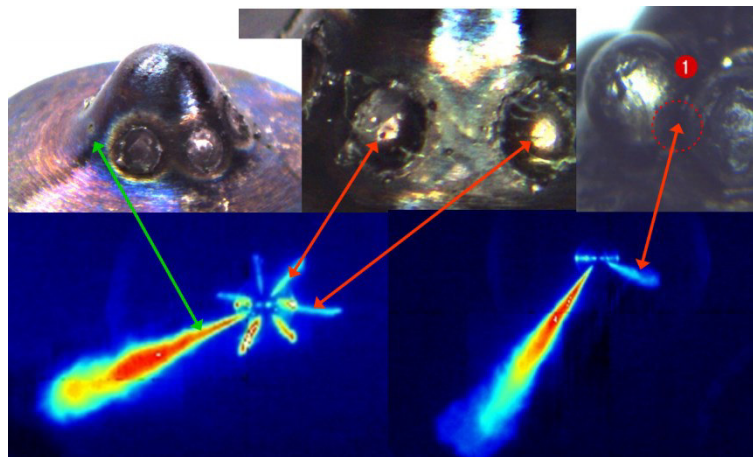


Figure 5: Preparation of injector nozzle for single spray injection by welding of other 6 holes; problems with leaks of welded holes can be noticed

For getting the single spray behavior (velocity, penetration, area) similar to the one extracted from multi-hole injector both injector pressure and injection duration had to be adjusted. Taking into consideration the Bernoulli equation of the fuel outflow from injector nozzle it was stated that injection duration should be preserved as long as in real engine and the fuel quantity from 1 hole should correspond to fuel dose in the engine divided by the number of holes. To get expected fuel doses from one hole the injection pressure had to be lowered more than two times, in exemplary case from 470 to 220 bar (first row). It could be explained that the fuel pressure drop in multihole injector is probably faster and deeper, as for 1-hole injector; for 1-hole injector the injection pressure should be kept lower for getting comparative quantities of fuel, in this case 1.2 mg.

After adjustment of control parameters the single spray penetration history (B1) has been compared with average spray from multi-hole injector (B), Fig. 6. Very good agreement concerning spray penetration (Fig. 6a) in the whole time of injection has been stated. In the spray velocity (Fig. 6b) the initial values were higher, but it is probably due to the effect of averaging of values from 7 sprays (black line) and of faster pressure drop in the nozzle when injected from more holes. It seems to be confirmed by bigger area of fuel cloud what suggests better atomization due to higher pressures at the start of injection in the nozzle with one hole.

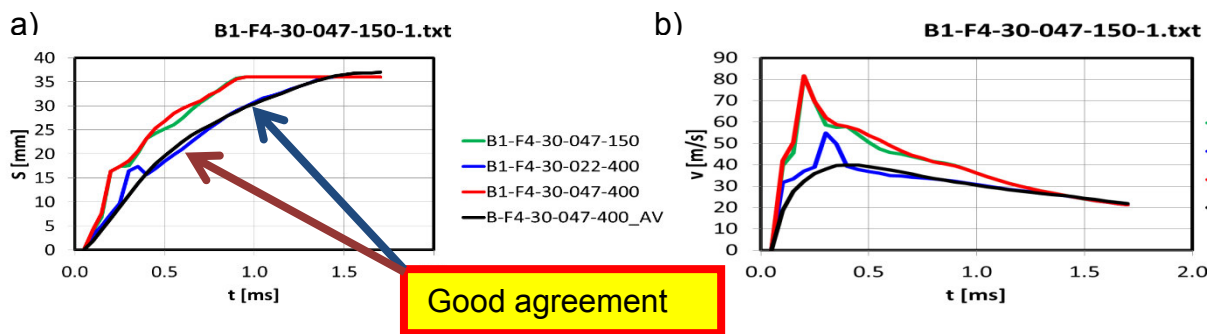


Figure 6: Comparison of spray penetration history (a) and spray front velocity (b) of single spray injection (B1, other holes welded) with average spray from multi-hole injection (B..._AV); notation: B1-F4-30-047-150: injector B, 1 hole, type of fuel, 30-back pressure in bar, 047 – P_{inj} =470 bar, 150 – injection duration ins

3.3 Investigation range and methodology

The above discussed assumptions and adjustment of operation parameters allow to begin main investigation procedure. Investigations were performed only for injection of main dose; pre-injection and post-injection were not taken into consideration because of relative small spray penetration and bigger distance of piston from injector nozzle and from injector to chamber walls. For injection process the interaction with walls of the bowl in piston and with edge of the bowl have been investigated and the fuel distribution in combustion chamber was determined with the use of fuel spray penetration history, spray front velocity and area of the atomized fuel cloud. The observed processes were recorded with the frequency of 10,000 frames per second (FPS). The observations were performed for an injection of a single fuel dose that lasted $t = 0.6$ ms, which allowed a comparison of the research material.

Investigations have been performed for different pistons and piston bowls (differing eq. with bowl edge), various distances between piston and injector, various values of back

pressure and charge temperature. Tests were performed at fuel injection pressures of $P_{inj} = 210, 220, 390, 400, 480, 580$ bar and at various values of air backpressure in the chamber (40, 46, 64, 55, 63, 83 bar). For the comparison of results the cases with injection duration of 300, 350, 400, 420 and 450 μs were used.

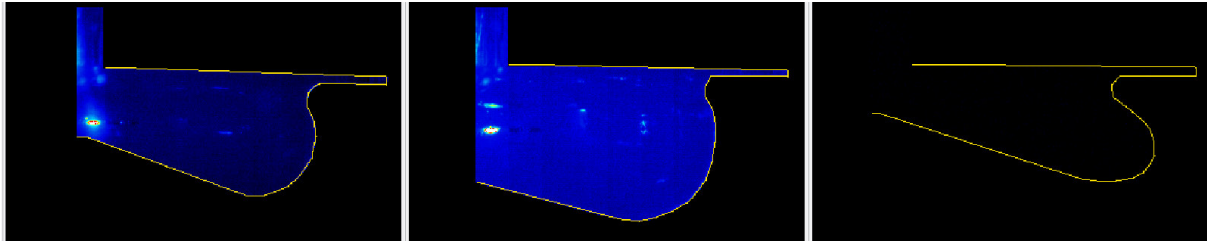


Figure 7: Shapes of various piston bowls used for this research: N, P, K

4. Interpretation of results

4.1 Results of optical observations

For the selected research cases defined by type of injector, piston bowl shape, injection pressure, injection duration and cylinder back pressure the optical observations have been recorded with the frequency of 10th FPS and analyzed with time interval 400 or 600 μs in the time range from SOI up to 7000 μs . On the movies the cloud of fuel droplets which creates the fuel spray can be observed, its penetration toward bowl walls and area covered by this cloud. The camera applied in this research records the light reflected by fuel droplets and the intensity of luminance recorded here depends on the concentration of liquid fuel particles. On this basis the fuel droplets concentration and distribution in the chamber can be evaluated from the analysis of luminance in every point of the picture (pixel).

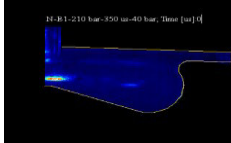
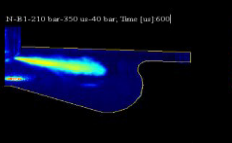
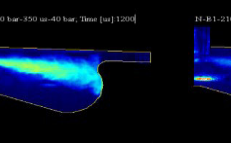
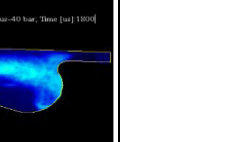
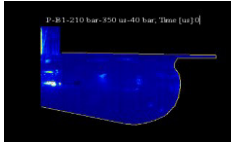
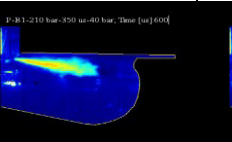
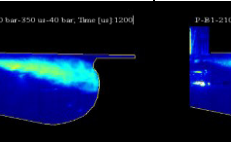
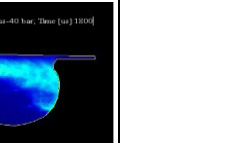
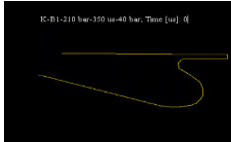
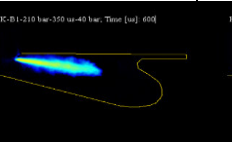
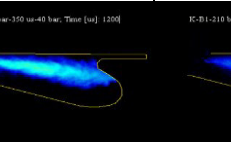
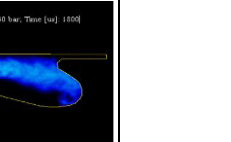
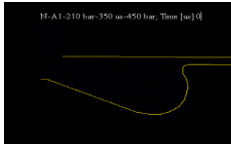
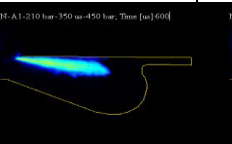
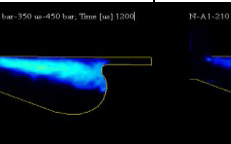
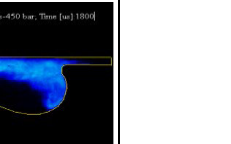
Piston type	Time after SOI = 0 μs	= 600 μs	= 1200 μs	= 1800 μs
N Injector B				
P Injector B				
K Injector B				
N Injector A				

Figure 8: Spray penetration in following injection phases for various bowl shapes (N, P, K), for 2 injectors (B, A) for bowl N; $P_{inj} = 210$ bar, $t_{inj} = 350$ μs , $P_{back} = 40$ or 45 bar

Very brief comparison of recorded pictures was demonstrated in the Fig. 8. It can be noticed that fuel spray meets the wall almost in all cases later than after 600 μs and earlier than 1200 μs . For sure higher injection pressure causes earlier touching the wall, later for bowl shapes K and P. Any significant influence of cylinder backpressure on the time of touching the wall was not observed. The results achieved from the movies discussed here were summarized in Fig. 9.

These movies were used for evaluation of spray penetration velocity and the area covered by the fuel cloud (A) for all investigated cases. The area A in each time was calculated by counting of pixels of defined luminance, multiplied by the area of individual pixel (here $17 \times 17 \mu\text{m}$) and summarizing them. The result was divided by the area of the whole chamber for calculation of the chamber share occupied by the fuel cloud.

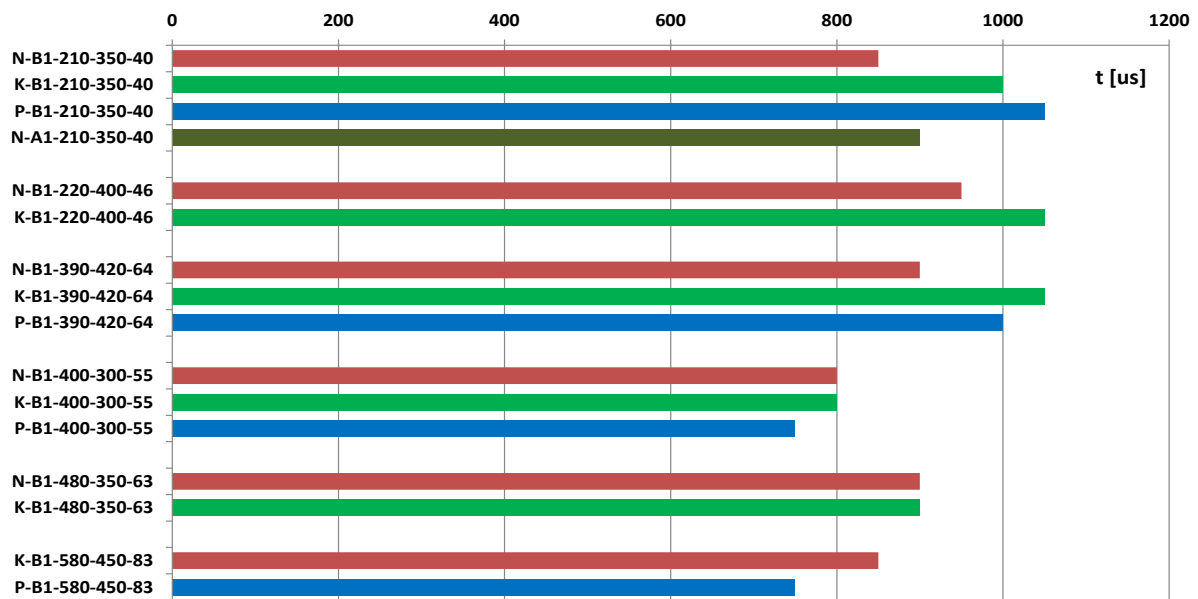


Figure 9: The comparison of the time from SOI to meeting the chamber wall for different bowl shapes and injection parameters

4.2 Fuel distribution in the chamber

The share of combustion chamber occupied by fuel cloud depends on injection pressure and injection duration as well as on the bowl shape. For the case when injection pressure was adjusted for 390 bar, injection duration 420 μs and back pressure 64 bar this share for bowl shapes N, P, K can be seen in 0One can noticed that maximal value reached after almost 7 ms is between 65 and 75% of whole volume of chamber. Higher values were achieved for piston bowls N and K. Faster fuel distribution along the chamber was achieved earlier for the bowl K.

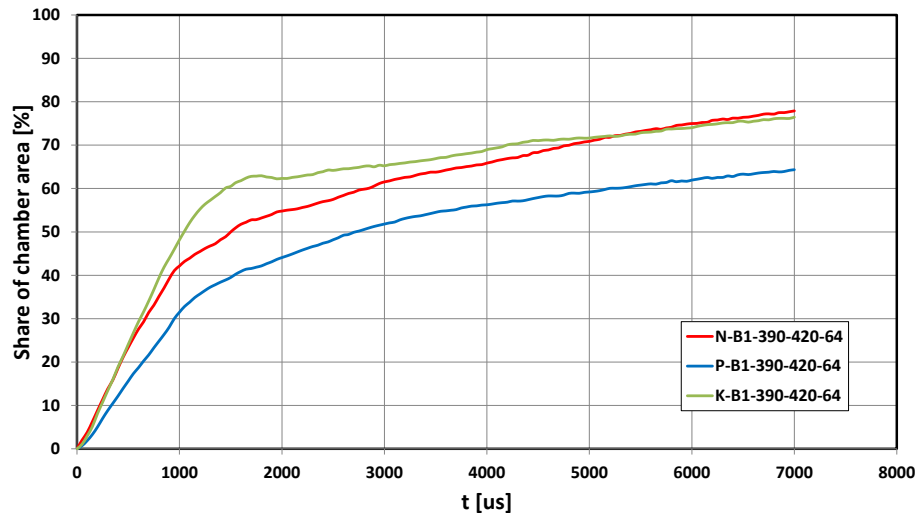


Figure 10: Share of combustion chamber occupied by fuel cloud against the time of the process for 3 bowl shapes (N, P, K); ($P_{inj} = 390$ bar, $t_{inj} = 420$ μ s, $P_{back} = 64$ bar)

For the shorter injection duration (300 μ s) and a little lower back pressure (55 bar) the fuel distribution in the chamber seems to be similar to the case before. The slide difference is in higher value of the maximal fuel cloud share (over 80%) for the bowl K, 0For bowls N and K the share of 60% is being achieved earlier in this case, shortly after 1 ms.

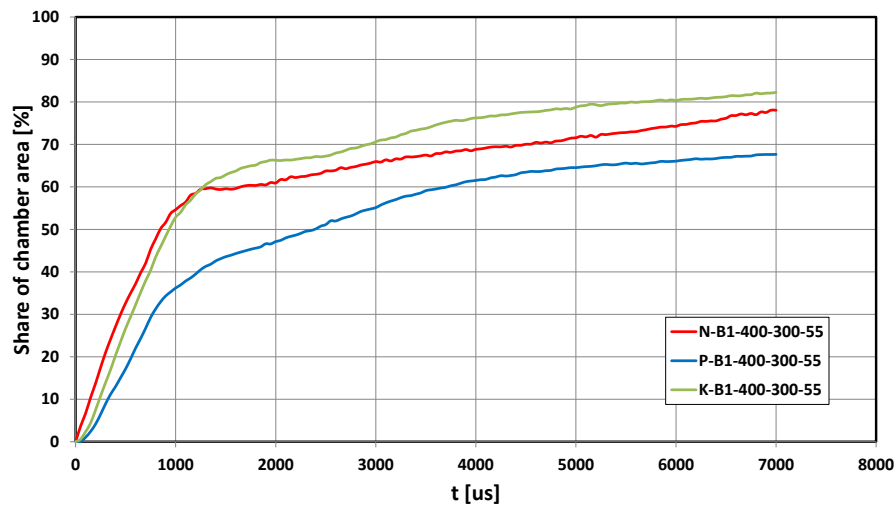


Figure 11: Share of combustion chamber occupied by fuel cloud against the time of the process for 3 bowl shapes (N, P, K); ($P_{inj} = 400$ bar, $t_{inj} = 300$ μ s, $P_{back} = 55$ bar)

Very similar results were achieved for the case with even higher injection pressure (480 bar), little longer injection duration (350 μ s) and higher back pressure (63 bar). The share of 70% was reached after first 1.5 ms for bowl K. In the same time the share of 60% was reached in bowl N.

Similar investigations were performed for injection pressure raised to 580 bar and back pressure – to 83 bar. The results for bowl P and K were shown in 0For this case the share of combustion chamber occupied by fuel cloud was higher, up to 85–90% after 7 ms of the process duration. Also here the fuel distribution in the chamber was higher for bowl K than for bowl P.

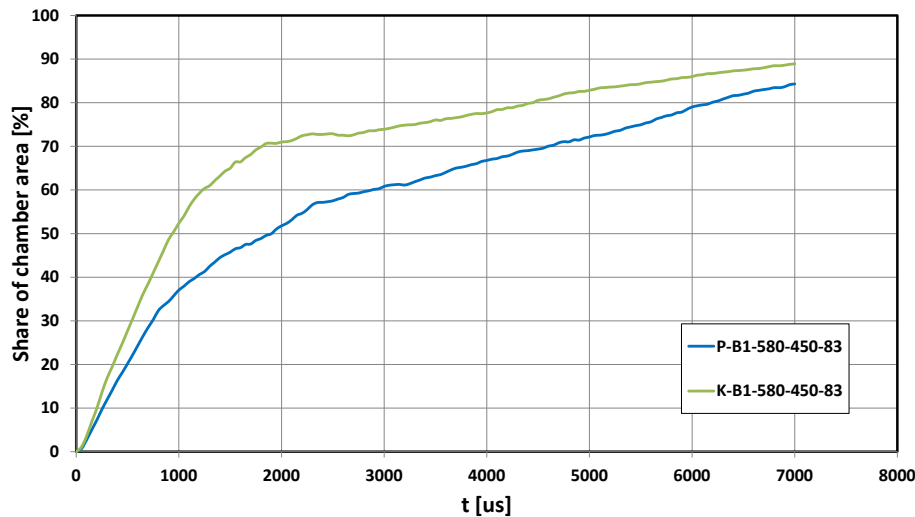


Figure 12: Share of combustion chamber occupied by fuel cloud against the time of the process for 3 bowl shapes (N, P, K); ($P_{inj} = 580 \text{ bar}$, $t_{inj} = 450 \mu\text{s}$, $P_{back} = 83 \text{ bar}$)

5. Discussion of results

Results of investigations performed in this work confirmed that too early injection into the combustion chamber may cause the intensive fuel penetration into the chamber between piston crown and cylinder head. Such case was recorded for piston bowl N, injector B1, injection pressure 210 bar, injection duration 350 μs , back pressure 40 bar. In this situation higher HC and CO emission can be expected, as already pointed out in the literature [1]. There are some methods to avoid this situation:

- to delay SOI to inject directly into the bowl;
- to increase the injection pressure;
- to change the direction of injection more toward the inside of the bowl.

In real engine the increasing of injection pressure can be applied for lower engine loads and middle engine speeds together with higher supercharging pressure. If additional charging is expected which leads to higher effective compression ratios, the piston bowl type P would be proposed for lowering of the geometrical compression ratio in the engine.

From the other point of view the bowl type K seems to be beneficial because of its bigger diameter and lower depth. The lower relation between chamber wall surface and chamber volume (s.c. A/V -ratio) leads to higher thermal efficiencies of energy conversion due to the reduced heat loss through the walls. However, bigger penetration of fuel onto cylinder walls can increase CO and HC emissions.

Application of piston bowl with bigger diameter will lead to delayed fuel interaction with the chamber walls, what gets his special meaning for higher injection pressures and bigger fuel doses. Conclusions published in the paper [5] suggest that the chamber of this type shows some positive properties, but is not optimal according the efficiency of energy conversion. Here the impact of some specific parameters of the chamber on emissions has been studied, Fig. 13.

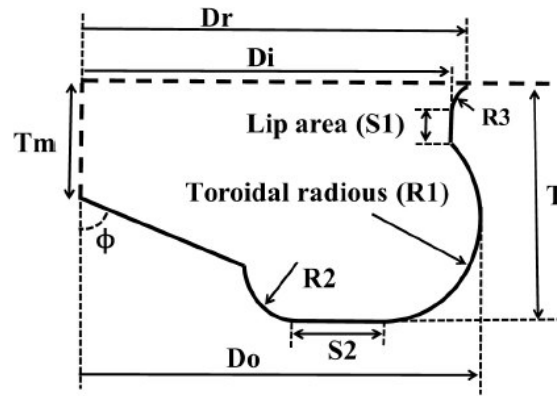


Figure 13: Specific parameters of the combustion chamber located in the piston bowl; T_m – bowl depth in the piston center, T – bowl maximal depth, D_r – bowl auxiliary diameter, D_o – maximal diameter inside the bowl, D_i – bowl internal diameter [5]

The piston type K has the bowl with relatively big auxiliary diameter. Authors of the work [5] suggest that bigger diameter D_r leads to lower emissions of exhaust toxic compounds, what illustrates the Fig. 14. Application of the bowl of such shape does not exclude high thermal efficiency of energy conversion.

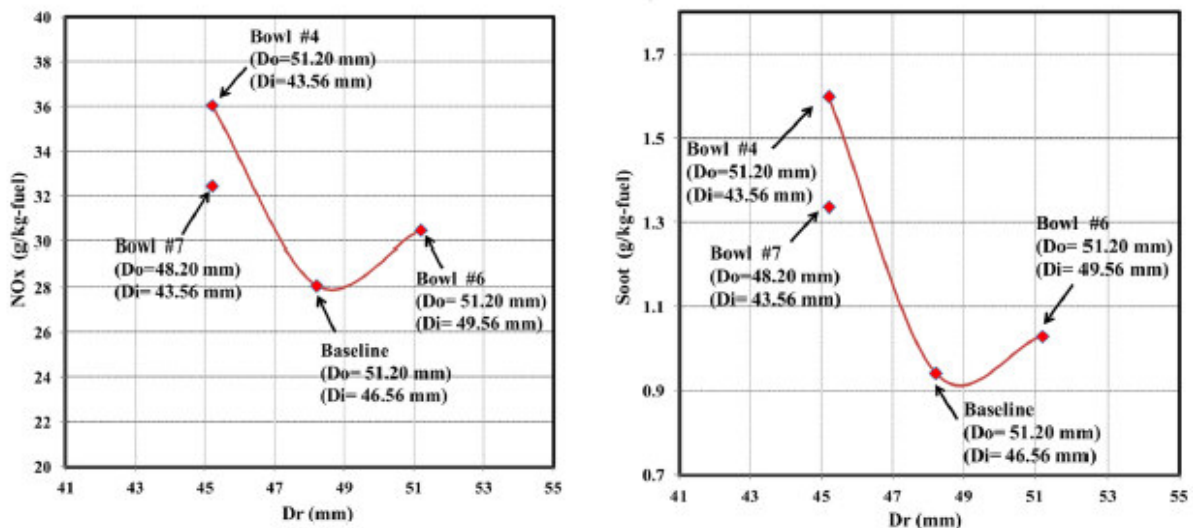


Figure 14: Influence of bowl auxiliary diameter on NO_x and soot emissions [5]

6. Summary and conclusion

In the paper the methodology and results of investigations of the impact of piston bowl shape and injection parameters on fuel distribution in the chamber have been presented. With the application of the techniques of optical observations and of analysis of recorded movies the fuel distribution in the chamber can be detected, validated and interpreted. For a proper mixture creation and its distribution along the chamber some comparative indexes can be used.

The work presented here will be continued for determining of the impact of fuel distribution in the chamber on the engine operating indexes and emission of toxic compounds. For this case the research engine should be used where the injection parameters will be adjusted in accordance with the piston bowl mounted inside.

References

- [1] Genzale C.L., Reitz R.D., Musculus M.P.B., Optical diagnostics and multi-dimensional modeling of spray targeting effects in late-injection low-temperature diesel combustion, SAE Paper 2009-01-2699, 2009.
- [2] Idzior M., Pielecha I., Stobnicki P., Czajka J., Badania i analiza wpływu ciśnienia wtrysku na rozpylenie paliwa w komorze o stałej objętości/*Research and analysis of the influence of the injection pressure on spraying fuel in the constant volume chamber*. Combustion Engines 2013, 154(3), PTNSS-SC-149.
- [3] Inagaki K., Mizuta J., Fuyuto T., Hashizume T., Ito H., Kuzuyama H., Kawae T., Kono M., Low emissions and high-efficiency diesel combustion using highly dispersed spray with restricted in-cylinder swirl and squish flows, SAE Paper 2011-01-1393, 2011.
- [4] Kałużny J., Czajka J., Pielecha I., Wisłocki K., Investigations of the fuel injection and atomization with the use of laser illumination/*Badanie wtrysku i rozpylenia paliwa z wykorzystaniem oświetlenia laserowego*. Combustion Engines 2013, 154(3), PTNSS-SC-072.
- [5] Mobasheri R., Peng Z., Analysis of the effect re-entrant combustion chamber geometry on combustion process and emission formation in a HSDI diesel engine, SAE Paper 2012-01-0144, 2012.
- [6] Wisłocki K., Pielecha I., Czajka J., Stobnicki P., Experimental and numerical investigations into diesel high-pressure spray wall interaction under various ambient conditions. SAE 2012 International Powertrains, Fuels & Lubricants Meeting, SAE Paper 2012-01-1662, 2012.

The Authors:

Prof. DSc. DEng. Krzysztof Wisłocki, Poznan University of Technology,
Faculty of Machines and Transport, Poznan.

DSc. DEng. Ireneusz Pielecha, Poznan University of Technology,
Faculty of Machines and Transport, Poznan.

MSc. Przemysław Borowski, Poznan University of Technology,
Faculty of Machines and Transport, Poznan.

MSc. Wojciech Bueschke, Poznan University of Technology,
Faculty of Machines and Transport, Poznan.

MSc. Wojciech Cieślak, Poznan University of Technology,
Faculty of Machines and Transport, Poznan.

MSc. Maciej Skowron, Poznan University of Technology,
Faculty of Machines and Transport, Poznan

Licence:

This document is licensed under the Creative Commons Attribution 3.0 DE License (CC-BY 3.0 DE): <http://creativecommons.org/licenses/by/3.0/de/>

Nozzle geometry impact on spray, ignition and combustion of large fuel injection jets

Fabian Pinkert
Ibrahim Najjar
Martin Drescher
Christian Fink
Horst Harndorf

Abstract

This work deals with the experimental analysis of the impact of different spray hole geometries on the fuel injection and combustion process of a medium speed diesel engine. By means of a newly developed injection and combustion test chamber it was for the first time possible to investigate the whole spray pattern of multi-hole nozzles of this size. The measurement results include data on the spray penetration and spray cone angle at non-vaporizing, vaporizing and reactive conditions, comprising also information on ignition location and Flame Lift-Off length of the combusting diesel spray.

1. Introduction

Since the tightening of emission limits for ship propulsion systems by the IMO (International Maritime Organization), engine process related as well as engine external measures for emission reduction are being focused by research activities in recent years. Several strategies are being pursued in order to fulfil the limits: One method aims at reducing the emission formation by combining an exhaust gas recirculation with an optimization of the fuel injection system. Another method is to develop exhaust gas after treatment systems for ships. Both Methods are impeded mainly by the demand for heavy fuel capability of the propulsion system. Another Method has gained popularity in the recent years: By changing the fuel type from diesel and heavy fuel oil to liquefied natural gas, many problems of the emission generation are circumvented. A technically mature lean combustion concept is capable of meeting the emission limits and appeals to ship operators due to the recent price development of natural gas.

IMO – Tier III emission limits demand a lowering of NO_x-Emissions within the emission control areas (ECA) by 75% compared to IMO-Tier II. At the same time the fuel sulphur content has to be abided, as can be seen in *Figure 1*. While until now heavy fuel oil was typically used within the ECAs, from 2015 the sulphur limit can only be met through the use of distillate fuels. Particulate emissions are not strictly regulated, however in many harbors and especially in passenger shipping a visible exhaust plume is not tolerated.

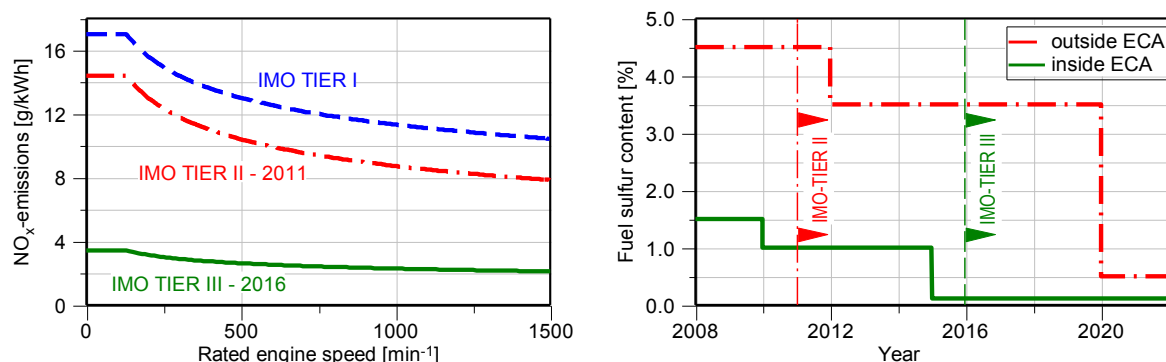


Figure 1: NO_x emission and fuel sulphur limits for ship propulsion systems

The high potential of EGR to lower the NO_x-emissions is known especially from land based applications of higher speed engines. Studies on medium speed ship engines [9] have shown that IMO-TIER III limits can be reached by the application of EGR. At the same time, however, a strong increase in soot emissions is observed. According to common perception this increase can be controlled by raising the injection pressure and applying a post injection strategy [5], [10]. Yet, the HFO capability complicates the development of appropriate injection systems, so that geometric variations of the injection nozzle as a means to influence the emission generation will become more important in the future.

No extensive research has been conducted so far concerning the influence of nozzle hole geometry on mixture formation in corresponding engines due to the comparatively low requirements for ship diesel engines by the emission legislation so far. Now, however, these options as well are expected to yield a potential for in-engine reduction of

emissions. Therefore, an experimental and numerical analysis of the injection and mixture formation for varying nozzle and hole geometries is an important basis for the development of future generations of large engines.

Within in the scope of the BMWi founded joined research project FAME (Fuel and Air Management for Emission reduction) the partners AVL Deutschland GmbH, Caterpillar Motoren GmbH und CO. KG, L'Orange GmbH, WTZ Roßlau gGmbH and the LKV of the University of Rostock study different nozzle geometries systematically using an injection chamber, a single cylinder research engine and 3D-CFD-Calculations. The present work is concerned with an experimental analysis of the spray penetration, evaporation characteristics and the ignition process. For this purpose, optical methods have been applied to injection sprays from differently shaped nozzles in a high-temperature, high-pressure injection chamber.

2. Methods

2.1 Test rig

The object of the study is the single-circuit common rail injector by L'Orange GmbH depicted in figure 2. It is being deployed in a medium speed diesel engine with 320mm bore and a rated cylinder power of 500 kW. In the present case the injection rate has been adapted to fit a single cylinder research engine with 240mm bore. In principle, the functionality of the injector is comparable to conventional car and truck solenoid injectors. What sets the injector apart is its heavy fuel oil capability, necessitating a spatial separation of the solenoid from the pilot valve as well as the cooling with lube oil. For the investigations injection pressures of 1000 bar, 1400 bar and 1600 bar have been used. The high pressure line and the pressure accumulator correspond to the serial engine setup ensuring a high degree of transferability of the results.

The impact of the nozzle geometry was analyzed on the basis of three different spray hole geometries and two spray hole diameters (Table 1, Figure 2). The geometries include a cylindrical ($K=0$) and two conical ($K=3$, $K=6$) 8-hole test nozzles. All nozzles have been adjusted to the same flow rate by a hydro-erosive treatment.

Nozzle	K-Factor	# of Bores	Q100 [ml/min]	$R_{IN}[\mu m]$	$D_{OUT}[\mu m]$
K0N8	0	8	6600	65	384
K3N8	3	8	6600	165	348
K6N8	6	8	6600	134	346

Table 1: Analyzed nozzles and corresponding discharge hole geometry

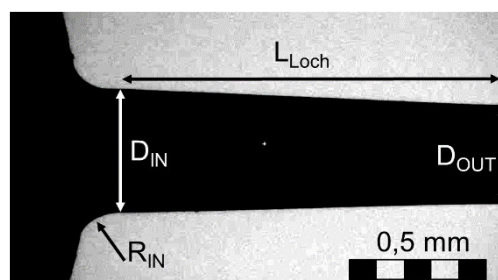


Figure 2: Photograph of the cast of the K6 nozzle

The spray diagnostics measurements were performed at a new high pressure high temperature spray chamber designed specifically for large injectors at the Institute of Piston Machines and Internal Combustion Engines in Rostock, Figure 3. The chamber allows the analysis of fuel sprays at engine like conditions. It features a 300 mm diameter quartz glass window allowing the observation and analysis of all spray jets of medium speed diesel engines.

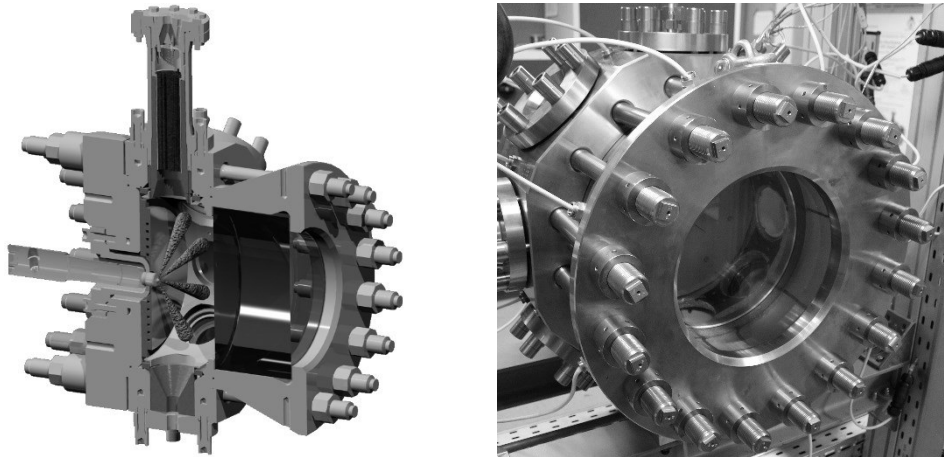


Figure 3: Section of the CAD model of the high pressure high temperature chamber (left) and photograph of the test rig after installation (right)

2.2 Measurement technique

In order to separate the influence of the combustion process during mixture formation, experiments at non-evaporative-cold, evaporative-inert and evaporative-reactive conditions were carried out.

In the experiments, inert conditions have been implemented using nitrogen as the ambient gas in the chamber. The visualization of the liquid and gaseous fuel mixture zones is done by means of a combined schlieren-/scatterlight method. Figure 4 shows a representative picture sequence of an injection process at evaporative, inert conditions. The liquid fuel phase of the jets appears blue and the gaseous fuel phase shady-black in the pictures. Based on the images, typical spray parameters such as penetration length and spray cone angle are calculated and analyzed for each nozzle geometry and boundary condition.

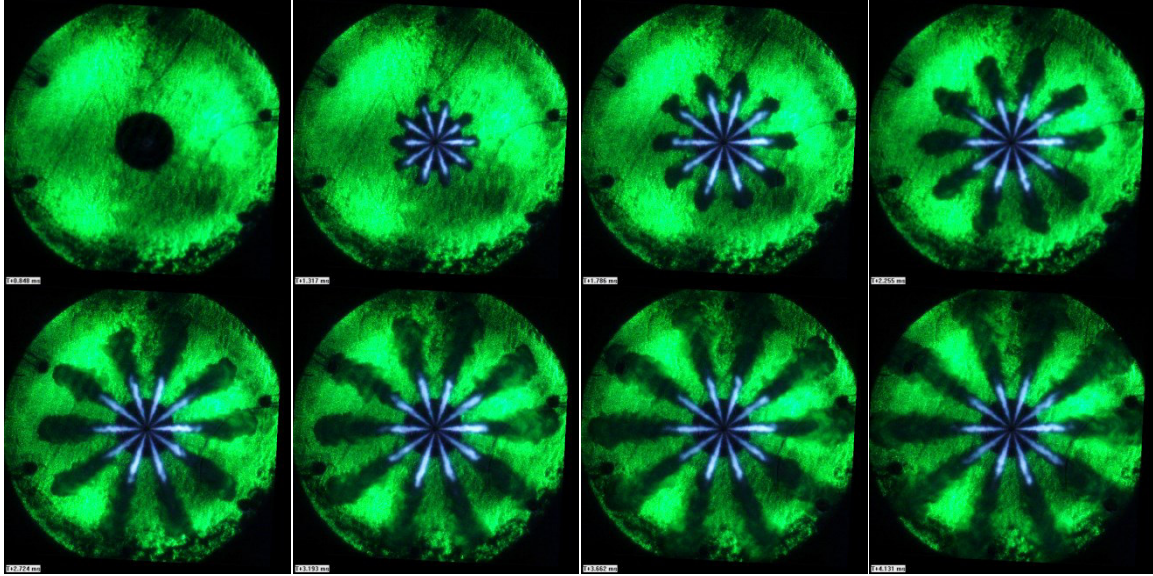


Figure 4: Picture sequence of a fuel injection process at $T_{Gas} = 850\text{ K}$, $\rho_{Gas} = 14.2\text{ kg/m}^3$, $p_{Rail} = 1400\text{ bar}$ with a temporal separation of $470\mu\text{s}$ visualized by a combined schlieren-/scatterlight setup at evaporative, inert conditions

Reactive conditions are brought about by applying air as ambient gas or air with increased nitrogen content in order to simulate “EGR-conditions”. Thereby a variation of the oxygen concentration, i.e. 21% and 16%, and its impact on the ignition process can be estimated and compared between the different nozzle geometries. Figure 5 illustrates a series of typical schlieren images taken at reactive conditions. In the pictures the propagation of the fuel jets (schlieren) as well as the combustion process (soot radiation) can be observed. This technique even allows the visualization of the very early stages of heat release, also called cold flame reactions. The small amount of heat changes the refractive index only slowly, leading to the disappearance of schlieren in the corresponding spray region. This phenomenon can be observed in the third image of the series in Figure 5.

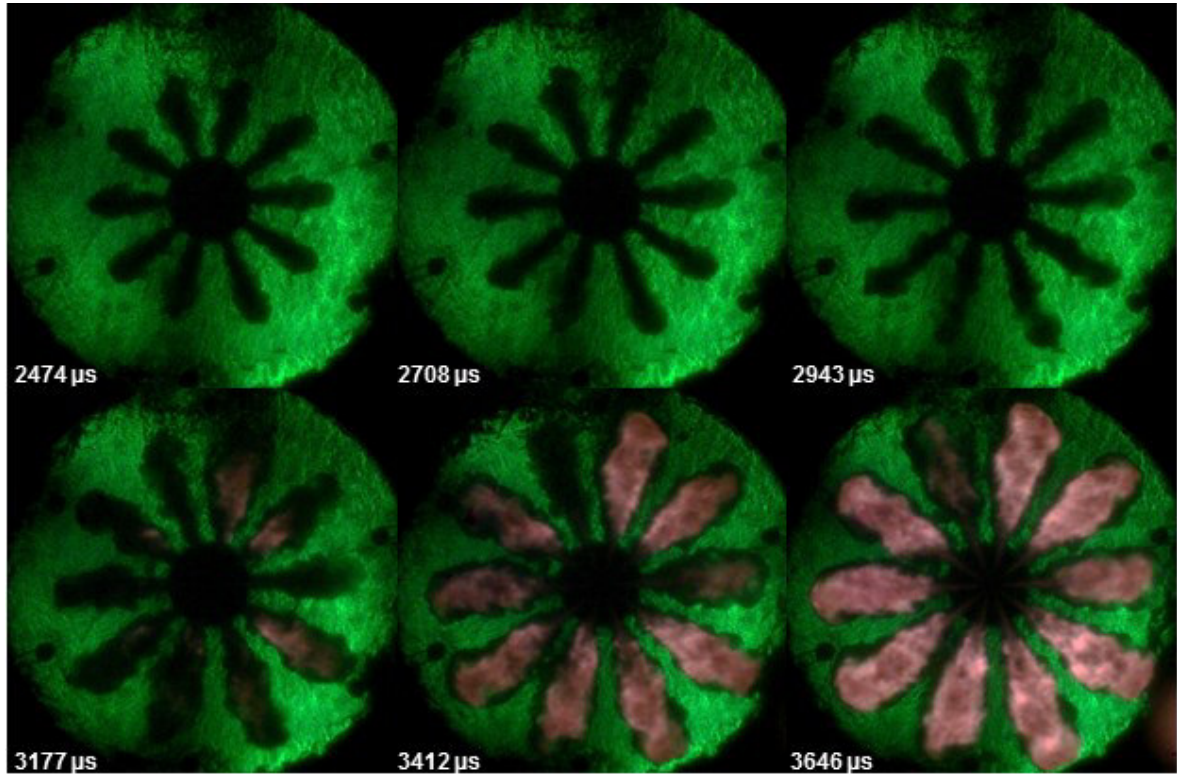


Figure 5: Picture sequence of a fuel injection process at $T_{Gas} = 800\text{ K}$ and $\rho_{Gas} = 14.2\text{ kg/m}^3$ visualized by a schlieren-/scatterlight setup at evaporative, reactive conditions

2.3 Test procedure and data processing

For the investigation of nozzle geometries, the ambient density and temperature, as well as the rail pressure were varied. The actuation timing was kept constant for all nozzles and rail pressures, allowing the formation of a stationary state of the jet. This approach results in a variable injection mass for different rail pressures. However this is assumed to have no impact on the spray specific results presented here. The investigated measurement points are presented in table 2. For each point, at least 10 repetitions were recorded, which leads to a database of 80 sprays for the 8 hole nozzle.

Parameter	Measurement Points
Gas Temperature [K]	300; 800; 850
Gas Density [kg/m ³] for hot conditions	7,1; 14,2
Gas Density [kg/m ³] for cold conditions	14,2; 28,4; 42,6
Rail pressure [bar]	1000; 1400; 1600
Injector actuation time [ms]	4

Table 2: Overview of the examined measurement points

In order to reduce the raw video data to comparable scalar values, self-developed algorithms in Matlab were used. Using color and intensity based thresholds as well as filters examining the texture of the image, the extend of the liquid and gaseous fuel phase are identified. The subtraction of the preceding image allows the exclusion of changes in the image background. Morphologic operators serve to suppress image artefacts. The algorithm is applied to all measurement repetitions separately. The identified areas are saved and measured to obtain parameters like spray penetration, volume, cone angle and the ignition cites.

Due to the temperature dependence of the electromagnetic radiation emitted by all matter, it is possible to infer the temperature of the combustion from the soot incandescence. This temperature dependence of the specific spectral emission is described by Planck's law. The law is valid only for black bodies. Real bodies emit a smaller amount of radiation, which is given by the emission factor ϵ . The emissivity is a function of the wavelength and also depends on the surface of the body.

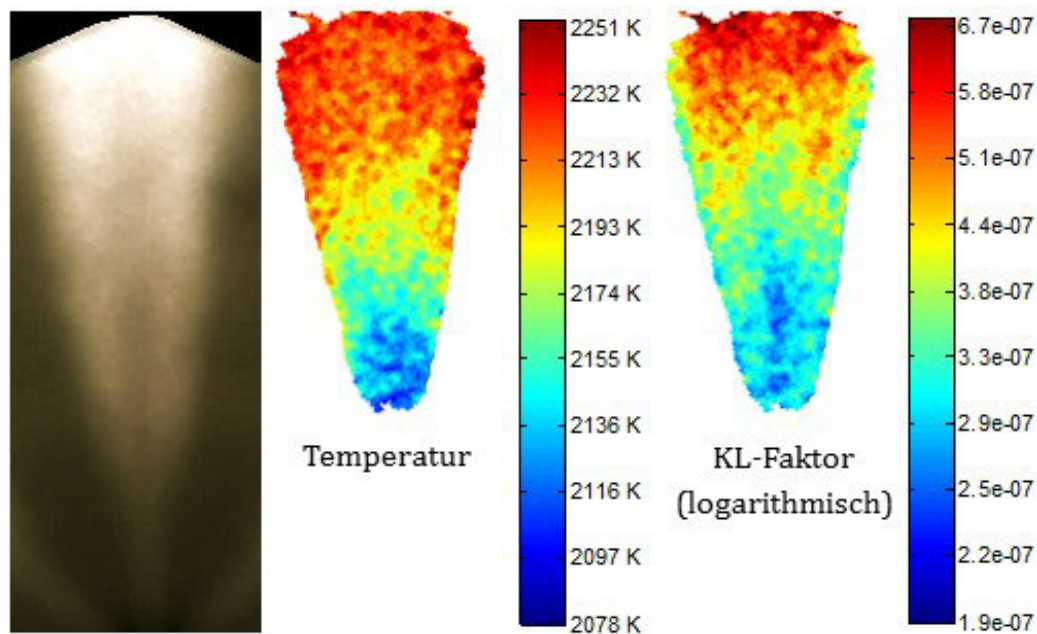


Figure 6: Comparison of the visible soot incandescence and the derived fields of temperature and KL-factor of the K6 Nozzle at $p_{Rail} = 1600$ bar, $\rho_{Gas} = 14,2$ kg/m³, $T_{Gas} = 850$ K in air. The distribution of the KL-factor uses a logarithmic color scale.

The temperature measurement using an RGB camera is closely related to the 2 color spectrometry. This later technique relies on narrow band filters to obtain the emission of the body at two discrete wavelengths. The temperature is derived from the quotient of these values. The knowledge of the emissivity is not necessary as long as it is not strongly wavelength dependent. Due to the color filters in the Bayer matrix, the RGB camera measures the electromagnetic radiation in three broad wavelength bands. The method relies on the integration of the theoretical emission over the relevant limits using a model of the emission and the transmission. In the present case not a body but a cloud of soot particles is measured, which is accounted for by the emission model. The calculation method used here is based on a model by Schmidradler [12], allowing to derive not only the soot temperature but also the amount of soot (KL-Factor) as can be seen in figure 6.

3. Results

3.1 Spray break up at cold conditions

Figure 7 shows the influence of a variation of the gas density on spray penetration and cone angle of the K3 nozzle. As expected, the penetration speed is slower at higher densities, while the cone angle increases significantly. This behavior corresponds to the experience with diesel sprays of smaller high speed engines. In a similar manner figure 8 shows a comparison of the three analyzed nozzles at non evaporating conditions. The comparison of the penetration doesn't show significant differences. According to Najar et al. [7] the spray tip penetration length at a given boundary conditions depends only on the flow rate of the single nozzle hole. Since the flow rate of the K0, K3 and K6 nozzle is the same, there very little difference in the spray tip penetration. An impact of the nozzle shape on penetration by means of the conicity has not been detected.

However, with respect to the spray cone angle significant influences of the nozzle hole conicity can be derived. The maximum cone angle was observed for the K6-geometry while K0 and K3 behave very similar. These results are also obtained at varying boundary conditions as can be seen in figure 9. The presented cone angles are calculated from the average values of the stationary spray. Considering similar penetration lengths the spray cone angle directly influences the spray volume, and thus, the amount of entrained ambient gas in the spray.

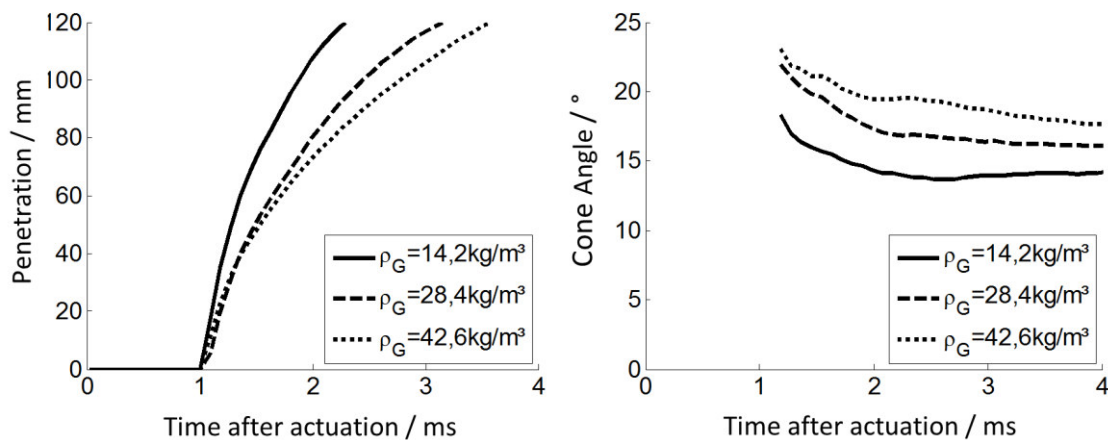


Figure 7: Penetration and spray angle of the K3 nozzle in dependence of the gas density at $p_{Rail} = 1600 \text{ bar}$. The gas density has a strong influence on the spray break up

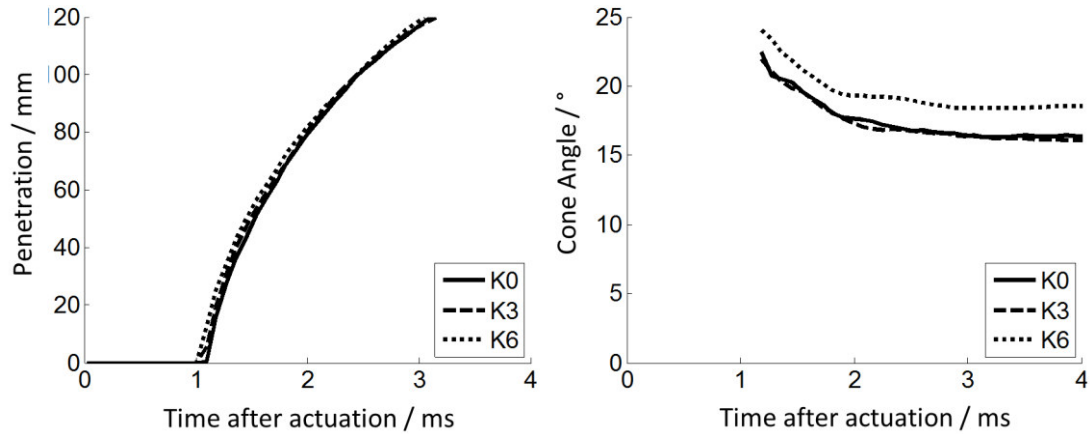


Figure 8: Nozzle comparison by means of penetration and spray angle at $p_{Rail} = 1600$ bar und $\rho_{Gas} = 28,4 \text{ kg/m}^3$. The conicity has only marginal influence on the penetration, but strongly affects the spray cone angle.

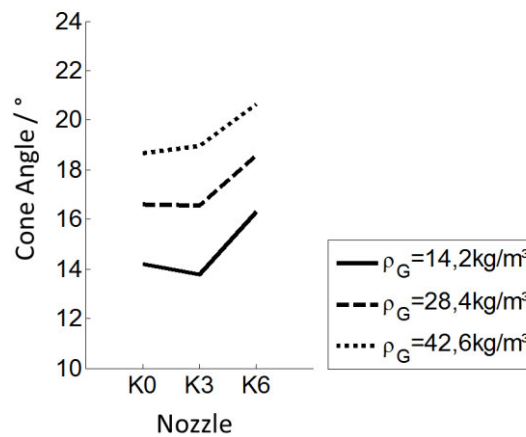


Figure 9: Overview of the measurement results for the liquid cone angle at $p_{Rail} = 1600$ bar. The K0 und der K3 Nozzle exhibit a stronger influence of aerodynamic forces compared to the influence of the geometry. The K6 nozzle has the highest cone angle for all tested operating points.

3.2 Vaporization

Figure 10 demonstrates the image quality for the spray visualization under evaporating ambient conditions in the new spray chamber. The image shows the mean image of all repetitions at one operating point overlaid with the individual contours of the liquid and gaseous spray.

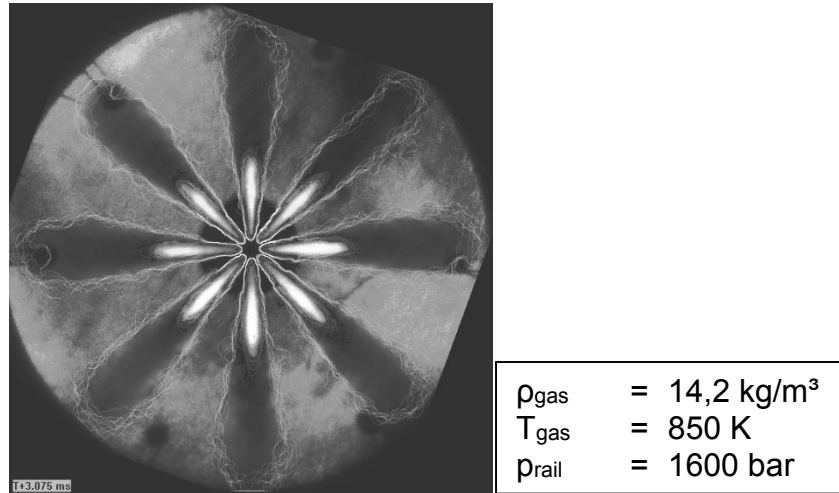


Figure 10: Representative, mean schlieren-/scatterlight image of the evaporating spray of the K6 nozzle and computer detected contours of the individual events at 2893 μs after injection start. The fluid phase is depicted in white; the gaseous phase is depicted in black.

Through these measurements it is for the first time possible to evaluate the spray symmetry of a large diesel injector under evaporating ambient conditions. For this purpose Figure 11 shows the maximum penetration of the liquid fuel for all operating points and all sprays in a polar plot.

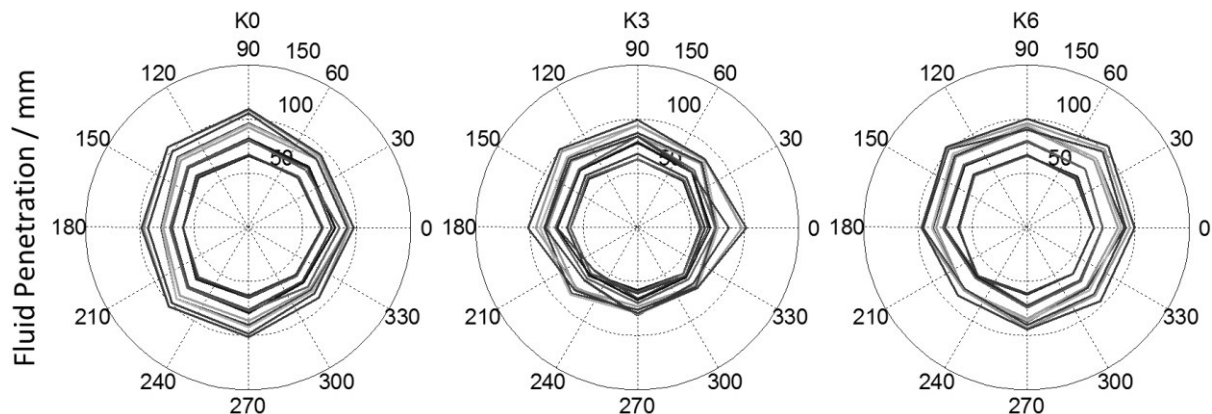


Figure 11: Analysis of the symmetry of evaporation of the test nozzles using the maximum liquid penetration. The presentation of all operating points in different line colors gives a qualitative measure of spray symmetry

The asymmetrical evaporation of the sprays of the K3 nozzle is evident. A comparison of all measured nozzles (not shown here) confirms the origin of the differences is not caused by a systematic influence of the test rig, like the temperature distribution in the chamber.

Gas temperature and gas density have a considerable influence on the maximum liquid penetration length. As already reported from smaller nozzles [2], [6], [8] also the large nozzles used in this work show a maximum liquid penetration length that is not exceeded during the ongoing injection process. Analyzing the gaseous spray penetration, the gaseous spray cone angle and the volume of the mixture zone it can be derived that the gas density is clearly the dominating parameter influencing the gaseous spray

characteristics. This conclusion is confirmed by gaseous spray cone angle measurement results of all six nozzle geometries as shown in figure 12. A very similar behavior at evaporative conditions was detected compared to cold conditions (figure 9). The attained behavior at the comparably low gas densities applied at evaporative conditions supports this hypothesis.

Figure 12 one more time highlights the influence of the gas density on the spray cone angle. For all the nozzles an angular increase of 2.5° is observed when doubling the gas density. Comparing the nozzles between each other, the largest spray cone angle is reached for the K6-nozzle, closely followed by the K0-nozzle. The K3-nozzle always shows the smallest spray cone angle at a given boundary condition.

The most common value to characterize the evaporation of a fuel injection jet is the maximum liquid penetration length. A short penetration length implies a better mixing of the fuel with the ambient gas, leading to an increased transport of energy from the gas to the fuel droplets compared to a spray with long liquid penetration length. As can be seen in figure 12, the maximum liquid penetration lengths were obtained for the K0-nozzle, followed by the K6-nozzle. The shortest penetration lengths have been observed for the K3-nozzle. Considering the fact that the K3-nozzles also showed the smallest spray cone angle, this is in contradiction to the expectation since the overall entrained mass of air into the spray is supposed to be smaller than for the other nozzle geometries.

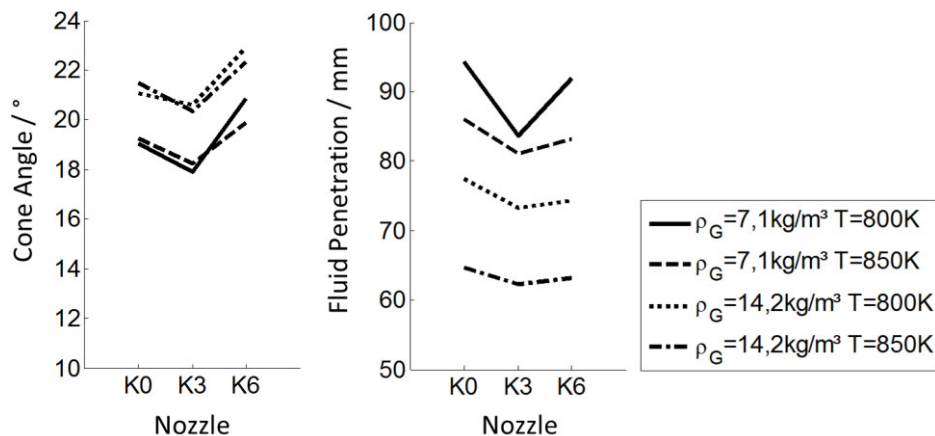


Figure 12: Overview of measurement results of the gaseous cone angle and the maximum liquid penetration at evaporating ambient conditions at $p_{Rail} = 1600 \text{ bar}$. The relation of the spray angles amongst each other is similar to the results at cold ambient conditions

According to the concepts of different authors [3], [6], the larger spray cone angle entrains more ambient air into the spray. This provides a larger heat flux for the evaporation of the fuel and is reflected in a smaller liquid penetration length. The nozzles K0 and K6 in comparison abide this rule. The nozzle K3 on the other hand exhibits the smallest cone angle as well as the smallest liquid penetration, hinting at the influence of other effects on the spray breakup and vaporization.

3.3 Ignition and combustion

At reactive ambient conditions, the times of the first soot incandescence, from now on called “ignition times” as well as the distance from the nozzle of the sooting stationary flame, from now on called “flame lift-off” were evaluated. The “ignition times” therefore do not represent the start of the chemical chain reaction, but none the less provide important information about the fuel distribution in the early phases of the combustion. Figure 13 shows an image sequence of the ignition as well as a fully developed flame. In the first image of the sequence, the ignition time can be seen on the left. In order to allow a comparison of the nozzles under realistic conditions, an exhaust gas recirculation (EGR) was simulated in the chamber. For this purpose the chamber was operated using a nitrogen enriched mixture with an oxygen content of 16%.

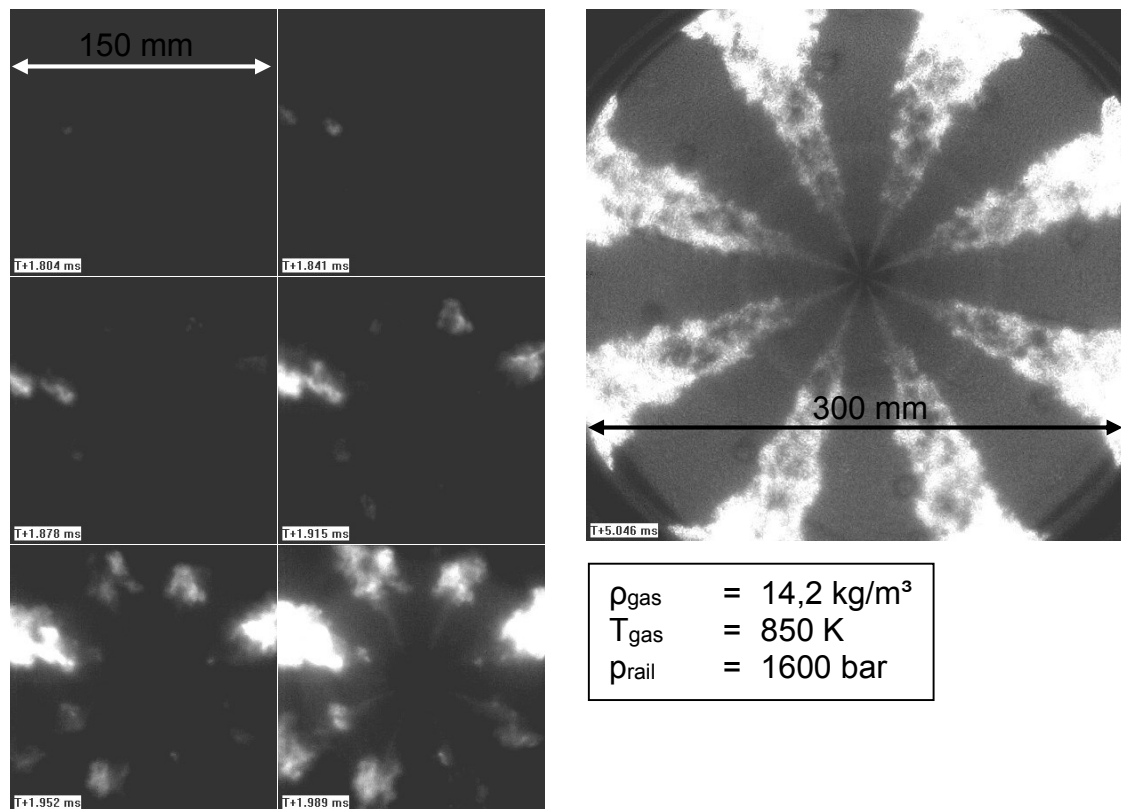


Figure 13: Image sequence of ignition with $\Delta t = 37\mu\text{s}$ (left) and fully developed combustion (right) of the K0 nozzle.

The results of the obtained flame-lift-off lengths of the different nozzles at non-EGR and EGR-conditions are presented in figure 14. According to the expectations an increase in rail pressure causes a longer lift-off length. Moreover, it can be seen that the reduced oxygen atmosphere leads to a considerable increase of the lift-off length. The observed behavior of the tested nozzle geometries correlates closely with the characteristics of the maximum liquid penetration length, being however more distinctive at simulated EGR-conditions. The shortest flame-lift-off is detected for the K3-nozzle at most conditions, followed by K0 and K6, showing the largest lift-off in all test cases.

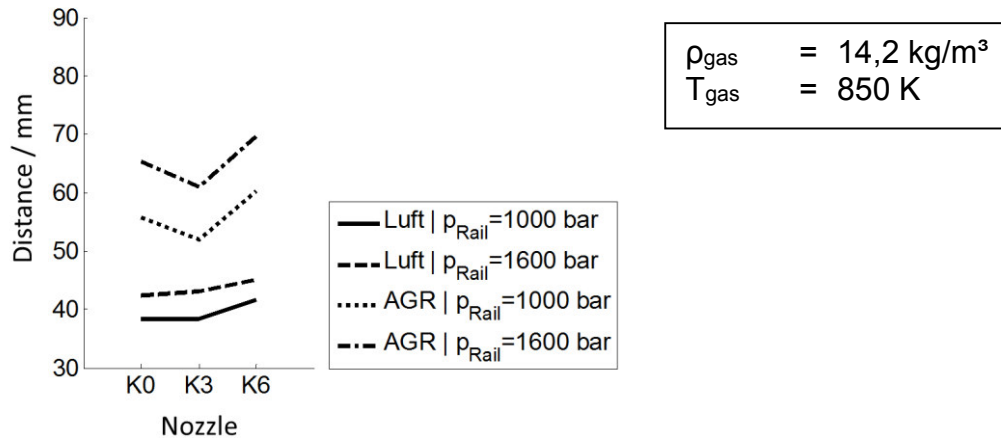


Figure 14: Average distance to the nozzle of the sooting flame (Flame Lift-off) after reaching a steady state under atmospheric (air) and reduced oxygen (EGR) conditions. Under EGR-conditions the K3 nozzle exhibits a different behavior than the K0 and K6 nozzle.

This observation is also supported by the results of the ignition location measurement in figure 15. With the exception of the EGR measurement point at a rail pressure of 1600 bar the results of the two measurement methods are very similar. This outlier is caused by the stochastic nature of the processes and the comparably small database for the ignition measurement, since here only one of the 8 sprays provides data.

The effect of an increase in rail pressure from 1000 bar to 1600 bar leads to a larger offset of the ignition from the nozzle, which is confirmed by Bertsch [1]. The increase of the FLO as a result of increasing rail pressure and lower oxygen content is also mentioned in the Literature [4].

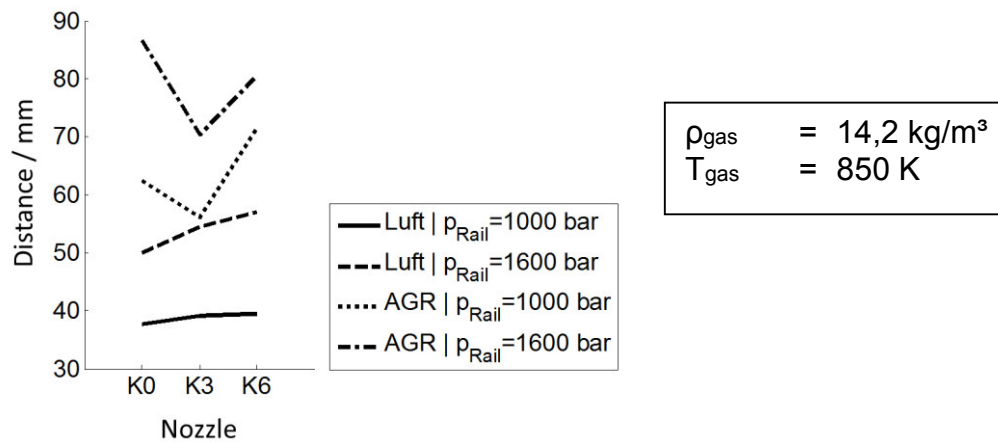


Figure 15: Average distance of first soot incandescence under atmospheric (air) and reduced oxygen (EGR) conditions.

By means of the pyrometric interpretation of the combustion measurements it is possible to estimate the temperature and the amount of the visible soot at the outer regions of the combustng spray. Figure 16 shows the temporal distribution of the temperature and the KL-factor as a measure for the soot concentration in the jet of the K6N8-nozzle. The first interpretable signal is achieved 2.9 ms after start of injector actuation. Because of fuel-rich conditions in the inner spray core a high amount of soot is detected within the spray which further spreads through the spray until it reaches the tip.

The maximum amount of soot is detected 4.8 ms after start of injector actuation. The temperature increases during the injection process and reaches a stationary condition at about 5 ms. An almost linear temperature gradient along the spray axis can be observed. Only after complete closing of the needle a strong raise of temperature in the whole spray region accompanied with an upstream propagation of high soot concentrations is detected. This process is followed by a decrease of the soot concentration since the rate of soot oxidation exceeds the soot generation.

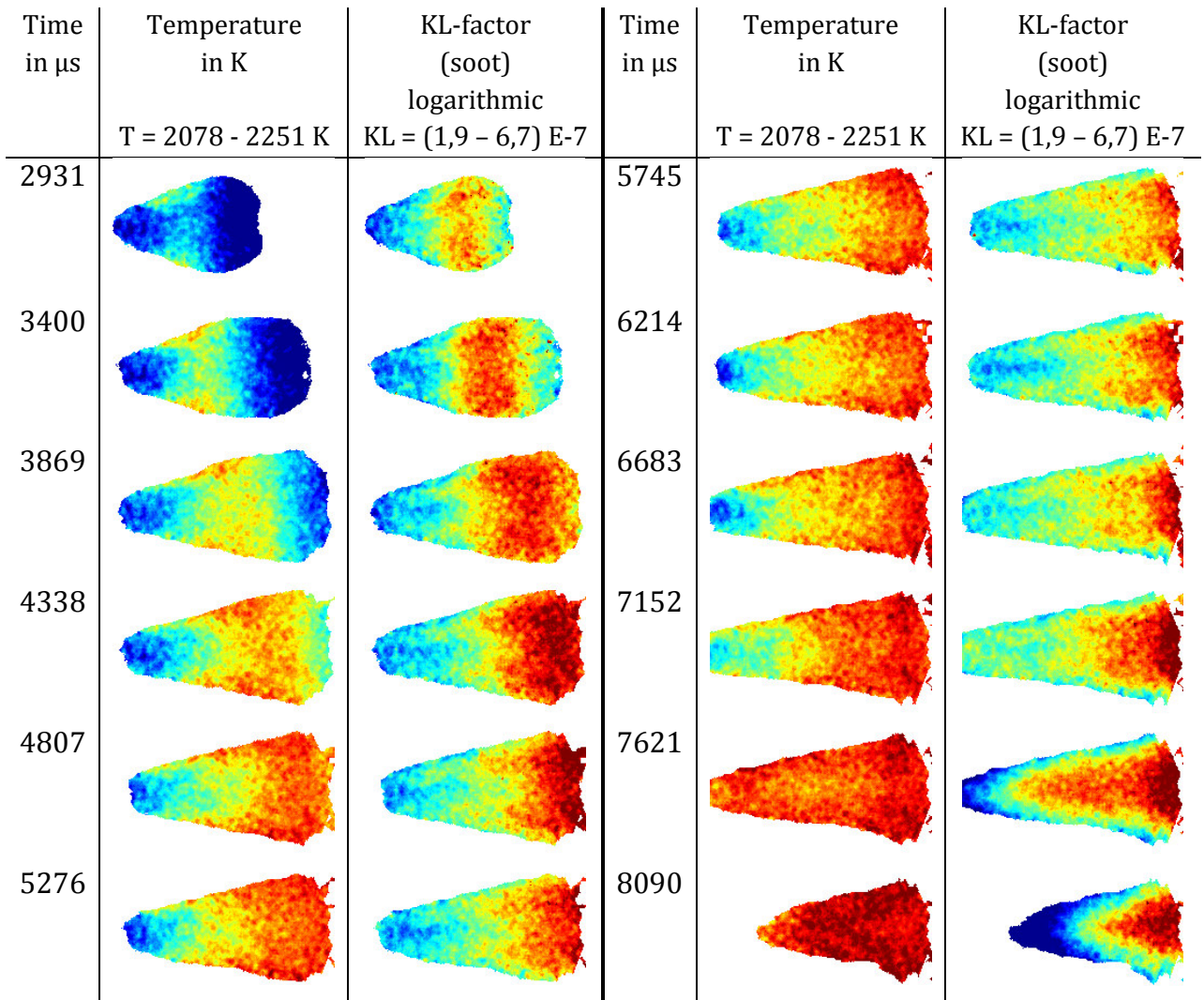


Figure 16: Image sequence of temperature and soot quantity of the combustng spray of the K6N8 nozzle at $p_{Rail} = 1600$ bar, $\rho_{Gas} = 14,2$ kg/m³, $T_{Gas} = 850$ K, in air. The images show values averaged over all measurements and all jet. The color scale is given in figure 6.

Aiming at a more simplified comparison of the two-dimensional temperature and KL-factor distribution, reduced scalar values are calculated based on the approach from Schmidradler [12]. The reduction is done on the basis of the frequency of occurrence of the temperature values.

The comparison of the temporal development of temperature and KL-factor between the three nozzles can be seen in figure 17. Under EGR conditions the temperature differences are on the order of 50 K. Especially in the second half of the combustion, deviations between the nozzles are clearly visible. The chart of the KL-factor shows

especially at the beginning of the combustion a clear dependency on the nozzle geometry. In the following plateau the differences between the nozzles become negligible.

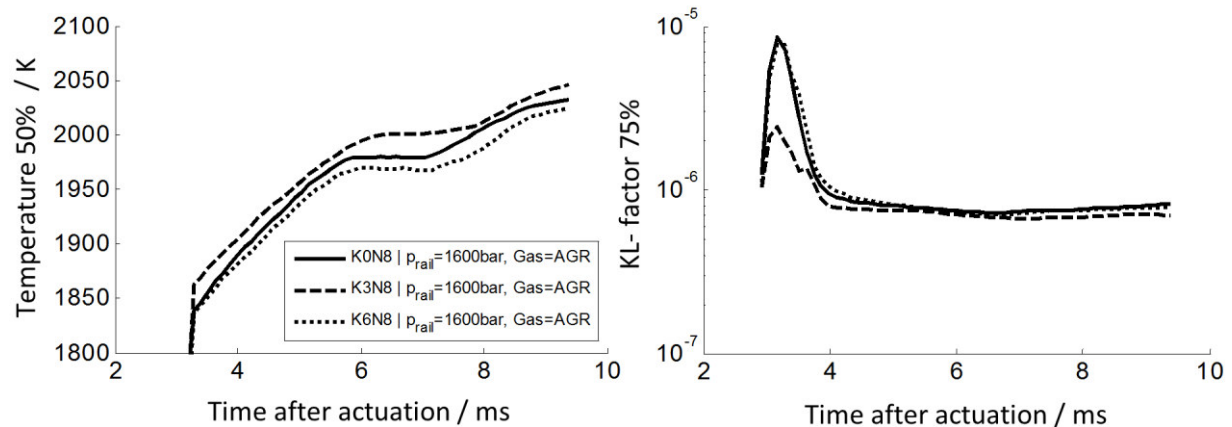


Figure 17: Representation of the influence of the nozzle geometry on the combustion, by the means of the temperature and the KL-factor.

An overview on the temperature and KL-factor results is given in figure 18. First of all it can be highlighted that the application of simulated EGR-conditions causes a decrease of combustion temperature of approximately 200 K. At the same time significantly increased soot concentrations are detected.

The influence of the spray hole type becomes especially relevant at simulated EGR-conditions. The highest calculated temperature of the combusting spray coincides with the lowest soot concentration for the K3-nozzle. However, at non-EGR-conditions the calculated results indicate a different behavior. It is to be evaluated in future investigations if the attained results can be confirmed by additional measurement methods and if the applied method to determine the temperature and soot concentration proves to be applicable for combusting sprays in high-pressure, high-temperature injection chambers.

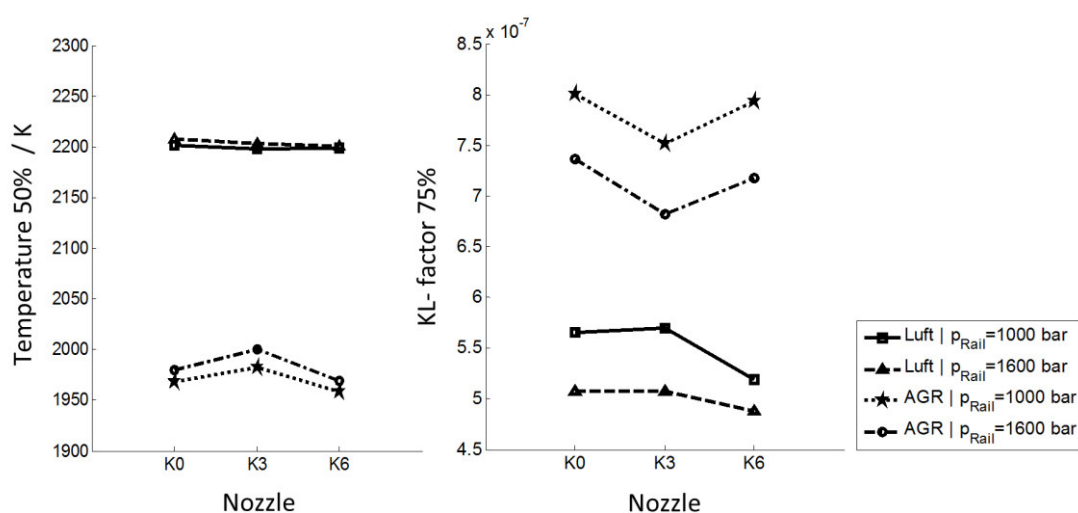


Figure 18: Overview of the Temperature and the KL-factor for all nozzles and operating points.

4. Discussion

As has been known from other studies, the conicity of the nozzle holes has a very complex influence on spray break up, mixture preparation and the combustion. The reasons for this complex behavior lie in the inner nozzle flow and its influence on the spray, the most important effects including the generation of eddies and cavitation, the mean discharge velocity and the radial gradient of the velocity at the edge of the emerging jet. These effects were studied among others by Qin [11]. They depend heavily on geometric features like the inlet radius R_{IN} and the orifice diameter D_{OUT} . A description of the smaller spray angle of the K3 nozzle, as determined in the current investigation, is possible by implicating all geometric features and will be discussed in further publications.

The larger distance of the ignition with higher conicity in air operation is attributed to the higher mean discharge velocity. An interesting characteristic of the ignition and combustion of the K3 nozzle becomes evident when changing to EGR operation. In an air atmosphere the ignition sites lie closer to each other. By trend the K3 nozzle ignites farther from the nozzle. At simulated EGR atmosphere all nozzles ignite significantly farther from the injector. The influence of the lower oxygen content on the K0 and the K6 nozzles is larger, leading to a comparably lower ignition distance of the K3 nozzle. A similar observation can be made for the FLO. The K3 nozzle has the lowest FLO length under EGR operation suggesting that the mixture is flammable sooner for this geometry. The extraordinary behavior of the K3 nozzle was also shown in single cylinder engine tests by the project partner WTZ Roßlau. Here, in particular at higher loads under EGR operation, the K3 nozzle was shown to produce less soot than the K0 and the K6 nozzle.

5. Summary

In the framework of the research project FAME the impact of different fuel injection nozzle geometries of a medium speed diesel engine on injection, mixture formation and the combustion process was investigated. For this purpose a new injection chamber was designed, allowing for the first time the observation of the complete spray pattern of large injectors under engine like conditions. The obtained results reveal that especially at evaporative and reactive conditions differences between the nozzles have been observed which were not seen at cold, non-evaporative conditions. With the measurement results a basis of data was generated providing new insight into the complex relations between nozzle geometry and diesel engine combustion process. It is shown that the nozzle geometry has a considerable potential to influence the mixture formation and combustion process, and thus, the emissions of large diesel engines. A targeted design of nozzle hole geometries for a specific application, however, still requires additional research and novel investigation methods particularly in the dense spray region and the combusting spray.

Acknowledgements

The results presented in this paper have been obtained in the framework of the associated research project FAME, "Fuel and Air Management for Emission reduction" (03SX292C). The authors gratefully wish to acknowledge the funding by the German Federal Ministry of Economics and Energy (BMWi).

Thanks are also due to the project partners AVL Deutschland GmbH, Caterpillar Motoren GmbH & Co. KG, L'Orange GmbH and WTZ Roßlau gGmbH for the good cooperation.

References

- [1] BERTSCH, DIETMAR: Experimentelle Untersuchungen zum Einfluss gemischbildungsseitiger Massnahmen auf den Zündprozess, Verbrennung und Schadstoffbildung an einem optisch zugänglichen DE-Dieselmotor, Karlsruhe, Univ., Diss., 1999, 1999
- [2] BLESSING, M: Untersuchung und Charakterisierung von Zerstäubung, Strahlausbreitung und Gemischbildung aktueller Dieseldirekteinspritzsysteme, Universität Stuttgart, 2004
- [3] FINK, CHRISTIAN: Experimentelle Analyse von Einspritz- und Gemischbildungsvorgängen an schweröltauglichen Common-Rail-Injektoren mittelschnelllaufender Schiffsdieselmotoren, 2011
- [4] FISCHER, DIPL-ING SEBASTIAN: Bewertung relevanter Einflussgrößen beim Pkw-Dieselmotor auf die Emissionsreduktion durch Höchstdruckeinspritzung
- [5] GÄRTNER, U ; WERNER, P ; KOCH, T: Wohin mit dem Ruß? – Grundlagen der passiven und thermischen Regeneration von Dieselpartikelfiltern im Nutzfahrzeug. In: FAD-Konferenz. Dresden, 2007
- [6] NABER, JEFFREY ; SIEBERS, DENNIS L.: Effects of Gas Density and Vaporization on Penetration and Dispersion of Diesel Sprays (SAE Technical Paper Nr. 960034). Warrendale, PA : SAE International, 1996
- [7] NAJAR, IBRAHIM ; FINK, ING CHRISTIAN ; PINKERT, FABIAN ; HARNDORF, ING HORST: Development of an Application-Oriented Model to Predict Fuel Spray Penetration in a Combustion Chamber. In: MTZ worldwide Bd. 75 (2014), Nr. 12, S. 50–54
- [8] PAUER, T: Laseroptische Kammeruntersuchungen zur dieselmotorischen Hochdruckeinspritzung – Wirkkettenanalyse der Gemischbildung und Entflammung, Universität Stuttgart, 2001
- [9] PÜSCHEL, M ; DRESCHER, M ; BUCHHOLZ, B ; SCHLEMMER-KELLING, U ; HARNDORF, H: Abgasrückführung am mittelschnelllaufenden Common-Rail-Schiffsdieselmotor zur Erreichung der IMO Tier III. In: 13. Tagung Der Arbeitsprozess des Verbrennungsmotors. Graz, 2011
- [10] PÜSCHEL, M ; STÖBER-SCHMIDT, C.-P.: Mehrfacheinspritzstrategien zur Reduzierung der Partikelemissionen an Großmotoren im AGR-Betrieb. In: Die Zukunft der Großmotoren II. Rostock, 2012
- [11] QIN, JIAN-RONG ; DAN, TOMOHISA ; LAI, MING-CHIA ; SAVONEN, CRAIG ; SCHWARTZ, ERNEST ; BRKYLIK, WALTER: Correlating the diesel spray behavior to nozzle design : SAE Technical Paper, 1999
- [12] SCHMIDRADLER, DIETER: Temperaturmessung im Verbrennungsraum eines Dieselmotors mittels RGB-Kamera. 1999, TU Wien

The Authors:

Dipl.-Ing. Fabian Pinkert, Universität Rostock, Rostock

Ing. Ibrahim Najar, Universität Rostock, Rostock

Dipl.-Ing. Martin Drescher, Universität Rostock, Rostock

Dr.-Ing. Christian Fink, Universität Rostock, Rostock

Professor Dr.-Ing. Horst Harndorf, Universität Rostock, Rostock

Licence:

This document is licensed under the Creative Commons Attribution 3.0 DE License (CC-BY 3.0 DE): <http://creativecommons.org/licenses/by/3.0/de/>

Influence of the spray hole geometries on cavitation formation inside diesel injector nozzles

Hauke Hansen
Sven Jollet
Dirk Niemeyer
Lennart Thimm
Friedrich Dinkelacker

Abstract

The detailed geometry of high pressure diesel injector nozzles is expected to have sensitive influence on the spray break up and the succeeding mixing with air and combustion. In this work five different geometries of spray nozzles are compared experimentally as well as with three-dimensional numerical simulation methods. For that two bottle shaped nozzles, one laval nozzle, one conical nozzle and a standard reference nozzle of typical heavy duty engine injector size are investigated, all with the same overall flow rate. Experimentally the KUP value (transition to cavitation flow) as well as the spray injection process and the spray cone angle are compared. Both simulation and KUP experiments show that the nozzle geometries have a significant effect on the cavitation formation, being in accordance with each other. The behavior of the spray cone angle and spray penetration is in accordance with the expectation that cavitation increases the turbulence inside the nozzle and increases the spray cone angle while decreasing the spray injection length. Only the laval shaped nozzle behaves significantly different. Here simulation indicates super cavitation taking place behind the narrow cross section, reducing both the cone angle and the injection length.

1. Introduction

The detailed geometry of high pressure diesel injector nozzles has significant influence on the spray break up and the succeeding combustion. Even modern high pressure injection systems still provide a potential to reduce the emissions and the fuel consumption. Especially the nozzle of a diesel injector is crucial for the mixture formation, ignition and combustion. However, the details of these influences are not known yet. Today's injector nozzles are built with cylindrical or conical spray holes. In the following investigation two bottle shaped and a laval nozzles are compared with a conically shaped and a standard reference nozzle of typical size for application in heavy duty engines. It is expected that the differently shaped spray holes lead to different cavitation behavior, different inner flow field within the nozzle and that they affect the spray break-up and the succeeding mixing process.

In this work both numerical simulation methods as well as experimental investigations in a high pressure injection chamber have been conducted. The aim is to study the behavior of the small scale transient flow inside the diesel injector nozzle in relation with the resulting spray processes outside the injector (Figure 1).

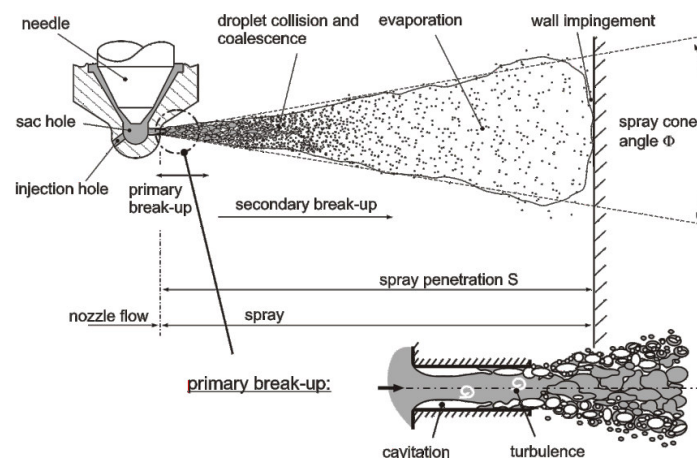


Figure 1: Schematic illustration of the relationships between the injector flow and the spray breakup [1]

The flow inside the nozzle is studied with the help of three-dimensional numerical simulation methods, based on computational fluid dynamics (CFD), where the focus is set on the multi-phase modelling, the cavitation modelling and the numerical computation of the transient processes, including moving meshes. A multiphase model (Mixture multiphase model) and a cavitation model (Zwart-Gerber-Belamri-cavitation model) have been combined to analyze the internal flow and cavitation for the different nozzle hole geometries.

Experimentally the effects of cavitation formation are investigated with the measurement of the cavitation transition point (KUP - Kavitations-Umschlags-Punkt). The trends are compared with the CFD simulation of the inside flow. Furthermore, the spray behavior concerning spray angle, penetration speed and depth is determined experimentally. It is of special interest whether a direct influence of the cavitation behavior inside the nozzle on the spray behavior behind the nozzle can be seen. The basic theory expects that cavitation produces additional turbulence inside the nozzle flow, which leads to increased spray cone angles.

2. Approach details

Simulation approach

The numerical simulation of the flow inside the injection nozzle is based on the three-dimensional simulation of the temporally averaged mass and momentum balances (Reynolds averaged Navier-Stokes equation) with the approach of computational fluid dynamics [3]. Only the special models are mentioned in the following. For this study the multiphase processes are treated with the so called „Mixture” model [2][3]. Here the multiphase flow is described by a mixing approach where the mass conservation

equation is formulated for the total mixture density $\rho_{mix} = \sum_N (\alpha_N \rho_N)$ and

the mixture velocity $u_{i,mix} = \sum_N ((\alpha_N \rho_N u_{i,N}) / \rho_{mix})$, with the volume fraction α_N of either gas phase or liquid phase, leading to:

$$\frac{\partial}{\partial t}(\rho_{mix}) + \frac{\partial}{\partial x_i}(\rho_{mix} u_{i,mix}) = 0 \quad (1)$$

The momentum equations are similarly based on these mixture quantities and include a mixture viscosity η_{mix} and the drift velocity $u_{i,dr,N} = u_{Ni} - u_{i,mix}$ between the phase N and the mixture. Also an energy equation is taken into account [3].

For the application in two-phase models essentially the mass transfer rate R between the liquid and the gas phase is needed, which for the flow inside the nozzle is related to cavitation. The simulations are based on the Zwart-Gerber-Belamri cavitation model [4]. This model assumes large vapour bubbles of equal size. Mass transfer is based on the change in mass of a unit of vapor bubbles with the number of bubbles per volume of fluid n_B , the bubble surface $4\pi R_B^2$, the vapor density α_v and the bubble radius growth rate dR_B/dt . For the evaporation caused by cavitation, the vapour fraction α_v is replaced by $\alpha_{nuc}(1-\alpha_v)$, indicating the importance of nucleation for vapour bubble appearance with α_{nuc} being the density of the nuclei. Introducing an evaporation coefficient F_e and a condensation coefficient F_c the transfer rates for cavitation R_e or condensation R_c are given for the Zwart-Gerber-Belamri cavitation model with

$$R_e = F_e \frac{3(\alpha_{nuc}(1-\alpha_v))\rho_v}{R_B} \sqrt{\frac{2(p_v - p_h)}{3\rho_l}} \quad \text{if } p_h \leq p_v, \quad (2)$$

$$R_c = F_c \frac{3\alpha_v\rho_v}{R_B} \sqrt{\frac{2(p_v - p_h)}{3\rho_l}} \quad \text{if } p_h \geq p_v. \quad (3)$$

being based on the difference between local hydrostatic pressure p_h and vapor pressure p_v . The bubble radius $R_B = 10^{-6} \text{ m}$, the nucleation sites with $\alpha_{nuc} = 5 \cdot 10^{-4}$, the evaporation coefficient with $F_e = 50$ and the condensation coefficient with $F_c = 0.01$ are hold constant for the calculations [3].

Measurement of the cavitation transition point

For the experimental characterization of the cavitation tendency of injectors the so-called cavitation transition point value is commonly determined (KUP). For the determination, the difference of rail pressure p_R and back pressure p_G is varied, usually being described with the normalized K_i quantity.

$$K_i = \sqrt{\frac{p_R - p_G}{p_R}} \quad (4)$$

Near the KUP value (Figure 2), cavitation inside the nozzle narrows the flow cross-section of the nozzles and limits the flow rate. If the K_i value is higher, the cavitation tendency of the nozzle is lower.

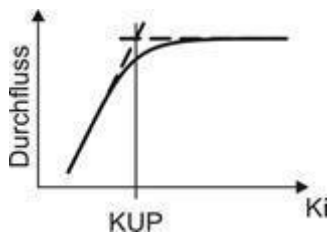


Figure 2: Cavitation tendency of nozzles

The ideal approach to investigate the correlation between inner flow, cavitation and resulting spray behavior would be based on the measurement of the cavitation inside transparent nozzles. This approach, however, is so far only possible for simply shaped nozzles and for injection pressures up to about 700 bar [5][6][7]. For complex shaped nozzles with higher injection pressure, instead the tendency for cavitation is investigated with the cavitation transition point method (KUP method), being compared with detailed three dimensional computational fluid dynamics simulation.

The resulting spray behavior is investigated experimentally with optical measurements of the macroscopic spray visualization methods. For that an isothermal high pressure injection chamber is used (Figure 3). The inside of the chamber is illuminated by a LED-ring. Light which is reflected by the fuel drops gets recorded by a high speed camera ("Phantom V711" with a 50 mm objective). This method results in high-contrast pictures, in which the shape of the spray can be observed against a dark background. The geometry of the spray is automatically analyzed by software.

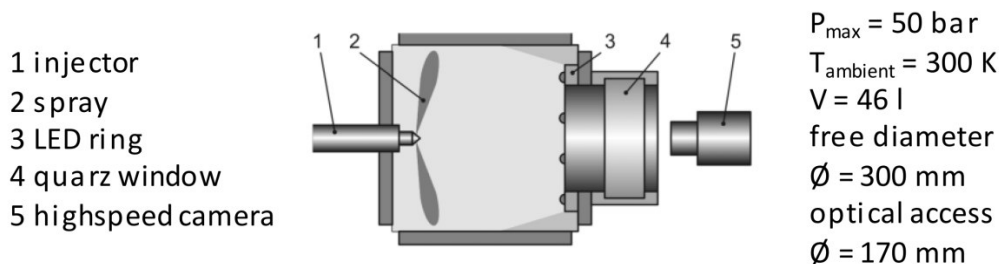


Figure 3: Setup of isothermal high pressure injection chamber [8]

The geometric parameters of the spray are spray symmetry, spray cone angle, penetration depth and penetration speed. It can be assumed that these quantities are directly related to the inner flow of the injector nozzle and its affinity for cavitation. Different spray breakup mechanisms are shown in Figure 4. With increasing flow velocity, increased turbulence can be assumed. Internal cavitation is expected to increase the degree of turbulence significantly more, such that the radial velocity component of the spray increases and increased spray cone angle is expected.

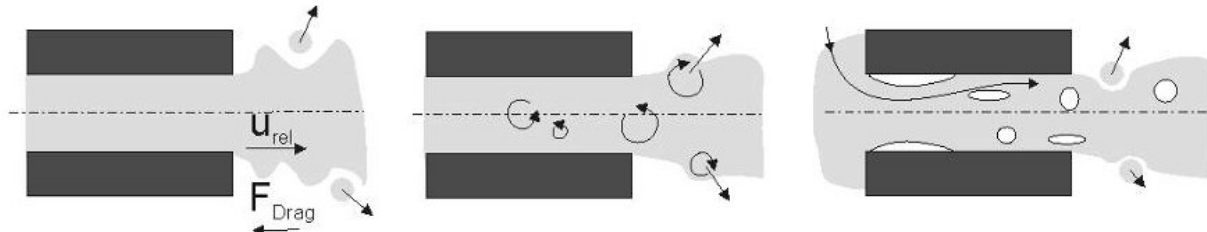


Figure 4: Relation between flow speed and spray breakup [9]

Within this study five different nozzle shapes have been investigated, where the injection rates of the different nozzle geometries are matched to each other. These are two bottle shaped nozzles with a longer and a shorter thin neck, a laval shaped nozzle, a conically shaped nozzle with a conical factor $k = 1,5$, and a standard reference nozzle with cylindrical shape of typical size for application in heavy duty engines.

The studies have been done for different injection pressures of 800, 1400, 2200 bar and a chamber back pressure of 26 bar with density 30 kg/m³. The gas density is desired to be similar to that of an internal combustion engine during its compression stroke. This is important to have a comparable break-up behavior. In the following, essentially the results from 1400 bar injection pressure are discussed.

3. Results of the cavitation transition point measurements and the simulation

In Figure 5 the measured cavitation transition points (KUP value) are shown in the left column, while on the right side the corresponding simulation results of the injector flow are presented. Here, a cross section through the upper half side of the injector flow is shown, with the symmetry axis on the lower margin, the injector needle on the left side, the sack hole on the lower right side and one of the eight injector nozzle holes leading to the upper right side. For the fluid flow the predicted phase is shown, being dark grey for the liquid phase and white for the gaseous phase.

The comparison of the normalized cavitation transition point measurements and the simulation of the multiphase flow show a good matching (Figure 5). The simulations of those geometries without significant cavitation tendency have a higher measured Ki -value than the geometries with more cavitation tendency.

The conical and the bottleneck long nozzles predict a Ki -value higher than 0.95, which means a low cavitation tendency. In the associated simulations no significant cavitation can be noticed. The experiments with the bottleneck short nozzle give a lower Ki -value which is not fully following the expectation as the simulation shows no cavitation areas. The cylindrical nozzle causes moderate cavitation with a Ki -value greater than 0.85. The simulation of the cylindrical geometry shows also cavitation in the nozzle, which corresponds to the measurement. The lowest Ki -value is measured by the laval nozzle. This value is about 0.74 and reflects the cavitation behavior of the nozzle. Both in the measurement and the simulation this geometry shows the strongest cavitation tendency.

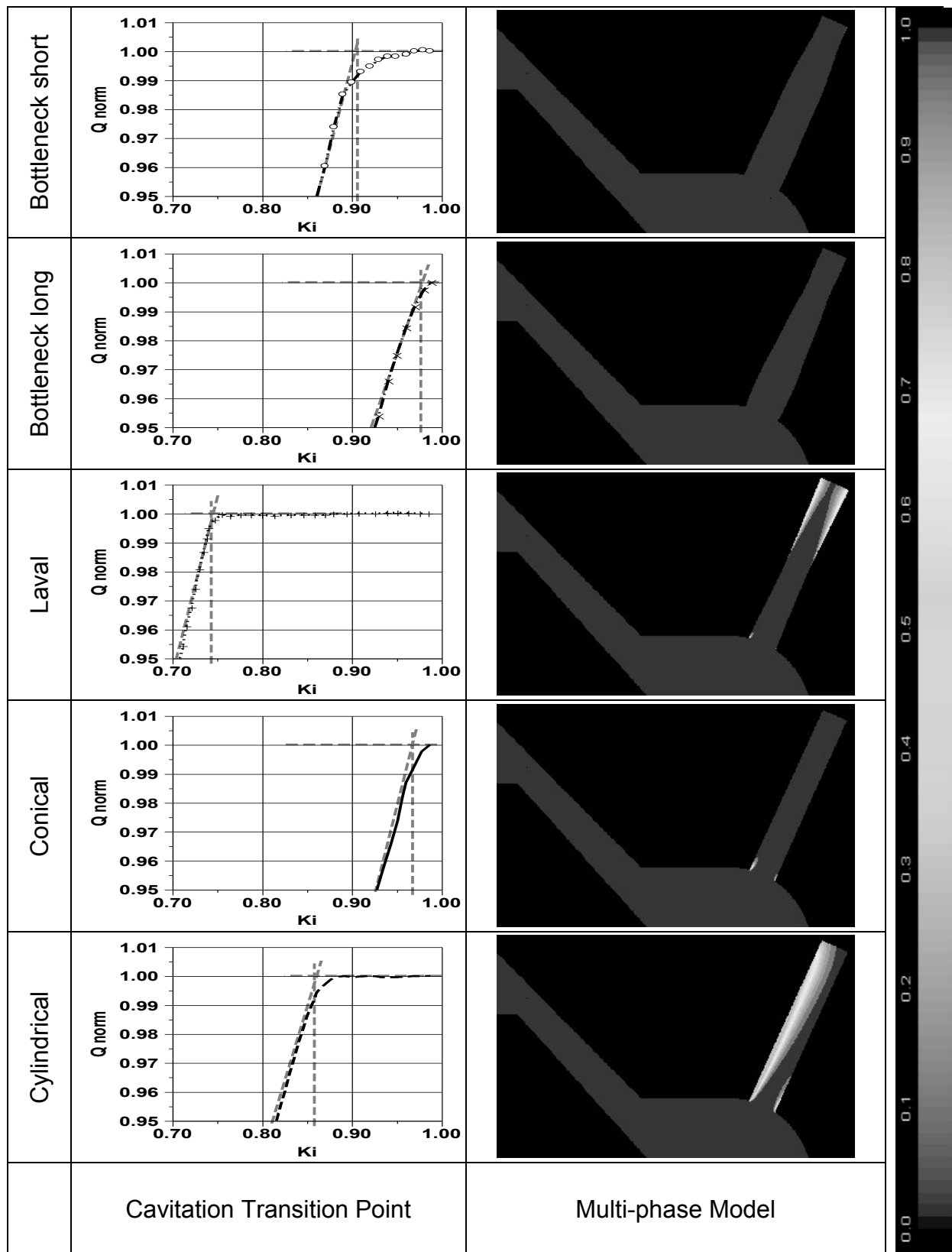


Figure 5: Comparison of the cavitation transition point measurements and the simulation of the liquid phase of different geometries

4. Spray geometry measurements

The evaluation of the spray geometry parameters is shown in Figure 6. The fuel was injected under an injection pressure of 1400 bar with an injection period of 1 ms.

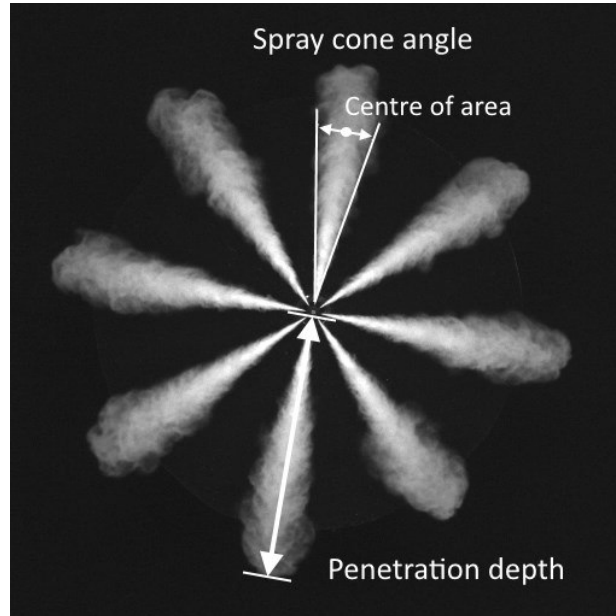


Figure 6: Measured parameters of the spray shape

In Figure 7 the measured spray cone angles for all investigated nozzle shapes at 1400 bar are shown. A higher spray cone angle is related to a stronger spray break-up. The highest measured spray cone angle is generated by the cylindrical geometry. The following sequence is the bottleneck short, the bottleneck long and the conical geometry with decreasing cone angles. The laval nozzle shows the lowest spray cone angle of the measured nozzles.

Figure 8 compares the spray penetration of the measured geometries. As expected the sprays with a higher cone angle have a shorter penetration depth. Because of the larger volume of the fuel droplets in a wider scattered spray angle, the spray is slowed down earlier and reaches less penetration. Here the laval nozzle shows a special behavior. It has both the smallest spray cone angle and the shortest penetration depth.

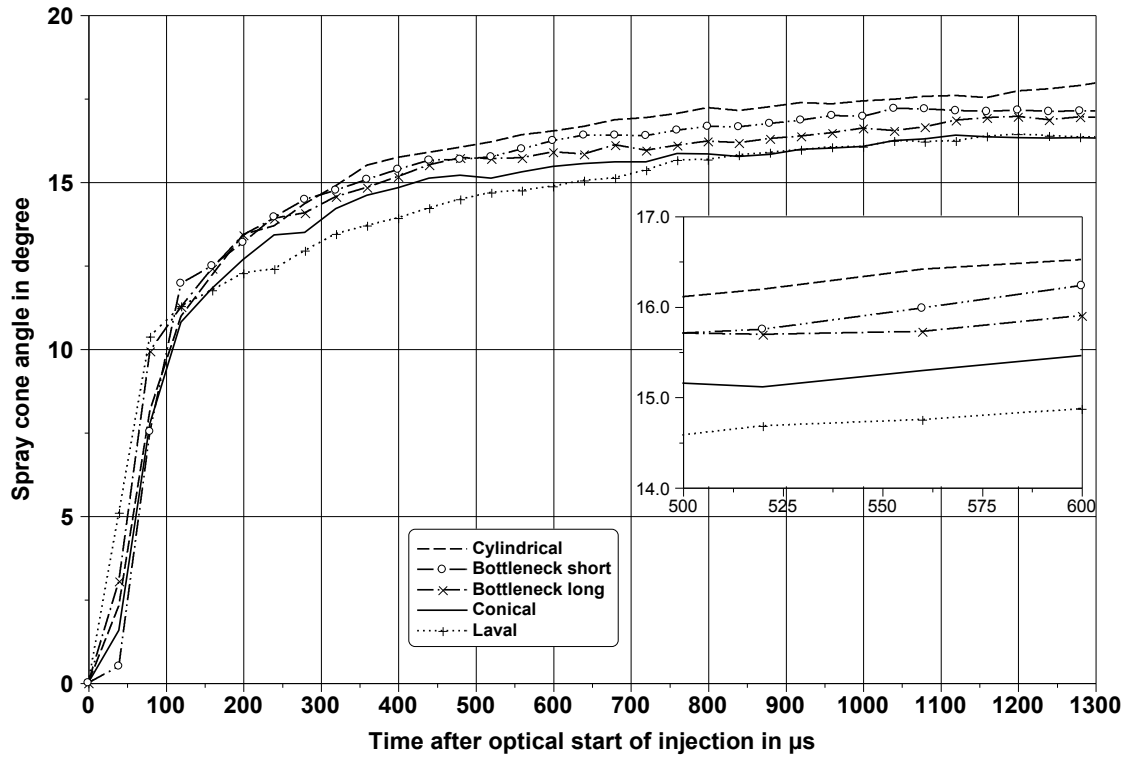


Figure 8: Measurements of the spray cone angle of different nozzle geometries at 1400 bar injection pressure

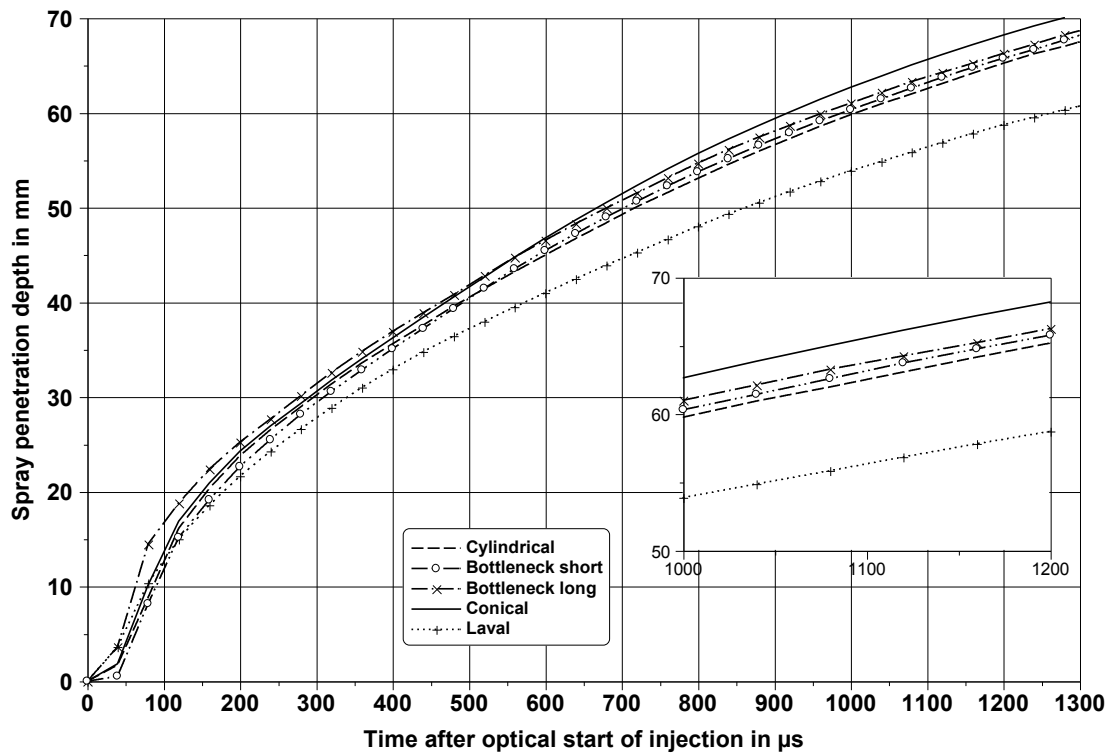


Figure 8: Measurements of the spray penetration depth of different nozzle geometries at 1400 bar injection pressure

5. Discussion

The results of the high pressure chamber measurements show a connection between cavitation tendencies of the nozzles and the strength of the spray break-up. The nozzles with the lowest, both simulated and measured, cavitation tendency are producing the smallest spray cone angle. The K_i -values of the measured nozzle holes can be directly transferred to the spray cone angle and the penetration depth. However the laval nozzle is outstanding. Although its K_i -Value is the lowest of the investigated geometries, it has the smallest spray cone angle and the lowest penetration depth. An explanation for this uncommon behavior can be found from the simulation. In Figure 5 it is shown that for the 1400 bar injection pressure case a large cavitation area is formed. This area extends from the narrow part of the spray hole to the outlet. This so called super cavitation leads to a reduced effective outer diameter of the nozzle. This distinct cavitation inside the nozzle hole leads to a constriction of the stream by a cavitation film around the nozzle wall, guiding the spray within. Because of the reduced effective outer diameter of the nozzle, this leads to a smaller spray cone angle. As the total injection rates of the different nozzle geometries are matched to each other, this should lead to an increased penetration depth. Apparently it has the shortest spray length measured. Possibly due to the raised turbulence of the stream by the appearance of the larger cavitation area, the strong cavitation in this nozzle type leads to smaller fuel droplets in a denser and compact spray with reduced momentum and shorter penetration length.

Further measurements showed a different spray behavior at lower injection pressures for the laval shaped nozzle. In this case an increased spray cone angle has been measured. The simulation shows that for lower fuel velocity the flow follows the diverging contour of the nozzle more closely and the cavitation area is reduced near the outlet, resulting in enhanced radial momentum and increased spray cone angle. This could be of interest for engine application and requires further investigation.

6. Conclusion

The spray measurements and determinations of cavitation transition points of the investigated nozzle geometries have been compared to "Mixture" multiphase model simulations with a Zwart-Gerber-Belamri cavitation model. These simulations are displaying the different cavitation tendencies of the investigated nozzle hole geometries. Furthermore the cavitation transition point measurements are verifying the results of these simulations. In addition to this the spray has been investigated in a high pressure chamber under constant temperature conditions. The results of these experiments are showing a clear tendency towards a higher spray cone angle and a shorter penetration depth with an increasing cavitation tendency. A supporting influence of the cavitation to the spray breakup is visible. Only the results of the laval nozzle do not fulfill the first expectations that a high tendency of cavitation leads to a high spray cone angle and a short penetration depth. The explanation for this behavior is given by the CFD-simulation, which shows super cavitation. This cavitation area is responsible for a smaller effective outlet diameter of the nozzle hole and therefore a smaller spray cone angle is observed.

Conclusively the used simulation model has the ability to specify the cavitation tendency of different nozzle geometries. The produced spray break-up is not only determined by its general cavitation tendency, but by the shape and local appearance of cavitation bubbles.

Acknowledgement

The nozzles of this work have been supplied by Dr. J. Seebode, IAV (Ingenieurgesellschaft Auto und Verkehr) Gifhorn. The KUP measurements have been done by IAV.

References

- [1] Baumgarten, C.: Mixture Formation in Internal Combustion Engines. Springer, Berlin, 2006
- [2] Brennen, C. E.: Fundamentals of Multiphase Flow. Cambridge University Press, 2009
- [3] ANSYS, Inc.: ANSYS FLUENT Theory Guide. Release 13.0, 2012
- [4] Zwart, P.J., and Gerber, A.G., and Belamri, T.: A Two-Phase Flow Model for Predicting Cavitation Dynamics. In: Fifth International Conference on Multiphase Flow. Yokohama, Japan, 2004
- [5] Jollet, S., Heilig, A., Bitner, K., Niemeyer, D., Dinkelacker, F.: Comparison of experiments and numerical simulations of high pressure transparent injection nozzles. In: 25th European Conference on Liquid Atomization and Spray Systems. Chania, Crete, 2013
- [6] Jollet, S.: Experimentelle und numerische Untersuchungen der instationären dynamischen Innenströmung in Dieselinjektoren. Dissertation, Leibniz Universität Hannover, PZH Verlag, 2014
- [7] Heilig, A.: Untersuchungen des Primärzerfalls von Hochdruckdieselsprays mittels optischer Messtechnik. Dissertation, Leibniz Universität Hannover, PZH Verlag, 2013
- [8] Heilig, A., Kaiser, M., Dinkelacker F.: Spray Analysis and Comparison of Diesel and Biodiesel-Methanol Blends. In: 24th European Conference on Liquid Atomization and Spray Systems. Estoril, Portugal, 2011
- [9] Zigan, L.: Kraftstoffeinfluss und Spraymodellierung. In: Grundlagen und moderne Anwendungen der Verbrennungstechnik. Eds. Dinkelacker, F., Zigan, L., Leipertz, A., ESYTEC Erlangen, 2012, p. 469

The Authors:

Dipl.-Ing. Hauke Hansen, Institute of Technical Combustion, Hanover

Dr.-Ing. Sven Jollet, Paul Scherrer Institute, Villigen

Dirk Niemeyer, Institute of Technical Combustion, Hanover

Dipl.-Ing. Lennart Thimm, Institute of Technical Combustion, Hanover

Prof. Dr. Friedrich Dinkelacker, Institute of Technical Combustion, Hanover

Licence:

This document is licensed under the Creative Commons Attribution 3.0 DE License (CC-BY 3.0 DE): <http://creativecommons.org/licenses/by/3.0/de/>

Simulation of auto-ignition behaviour for varying gasoline engine operating conditions

Karl Georg Stapf
Benjamin Reis

Abstract

Gasoline engine knock still persists as a major task for modern combustion engine development. Increasing power densities by downsizing lead to an increased knock tendency. A prediction of the presence of pre-ignition and knocking should be possible already during the early development process of an engine.

The present report introduces an approach for the quantification of knock occurrence within gasoline engines by solving a knock integral of the ignition delay time of the unburned mixture. The approach covers a wide range of engine operating conditions and mixture characteristics like relative air/fuel ratio and residual gas mass content as well as octane number or ethanol content.

The presented auto-ignition model is validated against fundamental homogeneous reactor experiments. Furthermore it is used as part of 0D thermodynamic simulations of a current gasoline combustion system to be validated and to assess parameter studies of different engine parameter variations.

As an outlook, the coupling of the model to 1D and 3D CFD simulations is described.

1. Introduction

Modern gasoline engines are characterized by downsizing, turbo charging, direct injection and valve train variability. Rising requirements regarding fuel consumption have led to engines with increased power density. Following this trend, the relevance of knock phenomena is increasing, too. Abnormal combustion is advantaged by high compression end temperature and pressure. Furthermore, fuel quality and composition have an impact on auto-ignition.

A prediction of the presence of pre-ignition and knocking should be possible already during the early development process of an engine. Therefore, several approaches are used today to set up models with different levels of detail that should resolve auto-ignition phenomena. A classification into three groups is possible according to Spicher and Worret [1] with increasing computational demand:

- Empirical models
- Reduced low temperature reaction kinetics
- Detailed low temperature reaction kinetics

In this report the authors focus on the first group of empirical models. Here, the knock integral according to Livengood and Wu [2] is a widely used measure to predict auto-ignition by utilizing the ignition delay time τ of the mixture. Empirical models are highly advantageous in terms of calculation time. The accurate prediction of the ignition delay time is crucial for the quality of the results of this approach.

Douaud and Eyzat [3] have proposed an empirical correlation for the ignition delay time that is still in use today. It incorporates the thermodynamic state in terms of pressure and temperature of the unburned regime as well as the octane number of the fuel. However, the residual gas mass fraction is not resolved. More recent developments use a three stage Arrhenius approach to predict ignition delay times of hydrocarbon fuels with negative temperature coefficient (NTC) behaviour more accurately as a single stage correlation is limited here [4,5,6]. The ignition process is subdivided into three reaction regimes. These regimes account for low, medium and high temperature auto-ignition reaction kinetics. Furthermore, formulations for residual gas content are introduced and real fuels are modelled by mixtures of primary reference fuels PRF. Kalghatgi et al. [7] extend the PRF mixture by toluene to TPRF.

The herein presented auto-ignition model also uses a three stage Arrhenius approach that is adapted for gasoline surrogate fuels. A mixture of primary reference fuels as well as ethanol is used. A validation of the approach is done by comparison of ignition delay times from shock tube measurements. The model is coupled towards a 0D thermodynamic simulation software to analyse a state-of-the-art gasoline combustion system.

2. Methodology

Auto-ignition is calculated here by the Livengood-Wu integral according to Equation 1 [2]. If the integral reaches unity auto-ignition of the unburned regime is expected. As can be seen in the equation the ignition delay time τ is necessary to predict auto-ignition correctly.

$$p = \int \frac{1}{\tau} dt \quad (1)$$

Therefore, an empirical correlation is used to determine the ignition delay time properly depending on:

- End gas pressure
- End gas temperature
- Relative air/fuel ratio
- Residual gas mass fraction
- Fuel quality

Following [3,4,5,6] the correlation has to resolve the thermodynamic boundaries pressure p and temperature T within the end gas as well as mixture properties in terms of the relative air/fuel ratio λ and residual gas mass fraction x_{rg} . Finally the fuel quality has to be accounted for which is done here by characterizing fuel quality in terms of the research octane number RON by a mixture of primary reference fuels PRF and an additional ethanol content. Here, the vector \mathbf{X} defines the composition of the fuel as molar fractions.

$$\tau = f(p, T, \lambda, x_{rg}, \mathbf{X}) \quad (2)$$

The auto-ignition model uses a three stage Arrhenius approach to determine the ignition delay τ of each fuel component accurately. Hydrocarbon fuels tend to show a negative temperature coefficient (NTC) linked to chain branching and chain breaking reactions during the auto-ignition process. In this regime, ignition delay time increases with temperature while it decreases in general. The three stages represent low, medium and high temperature reaction kinetics. As shown in [4], the low and medium temperature chemistry are expected to occur sequentially while high temperature chemistry occurs parallel, see Equation 3. The fuel quality is modelled by a primary reference fuel PRF containing n-heptane C₇H₁₆ and iso-octane C₈H₁₈. Furthermore the surrogate fuel can contain ethanol C₂H₅OH to represent for example E10 fuel, see Equation 4. Here, X_i is the molar fraction of each species i and \exp is an empirical constant.

$$\frac{1}{\tau} = \frac{1}{\tau_{low} + \tau_{medium}} + \frac{1}{\tau_{high}} \quad (3)$$

$$\tau_{mix} = \sum X_i^{\exp} \sum \frac{\tau_i}{X_i^{\exp}} \quad (4)$$

Equation 5 shows the utilized correlation for the ignition delay time with the empirical constants A, B, C, D, E and N for one specie and a single temperature regime.

$$\tau_i = A_i p^{N_i} (1 + x_{rg})^{C_i} \exp\left((1 + x_{rg})^{D_i} \frac{B_i}{T}\right) \left(\frac{1}{\lambda}\right)^{E_i} \quad (5)$$

Figure 1 shows a comparison of different methodologies to predict auto-ignition within a gasoline combustion engine for a single operating point. The left bar represents a simulation with detailed reaction kinetics which was validated against test bench measurements. This type of simulation is most detailed but also much more time consuming than the presented approach. It belongs to the above stated third group of models. The herein proposed integral approach with a fixed parameter set for gasoline fuel as well as with a correlation for variable RON are not able to match the reference simulation with reaction kinetics as can be seen by the two bars in the middle of the figure. The thermodynamic boundaries are not sufficient for the correct prediction of auto-ignition over the complete engine operating range. Only the right bar which incorporates also mixture in terms of relative air/fuel ratio and residual gas mass fraction can reproduce the reference simulation in good agreement.

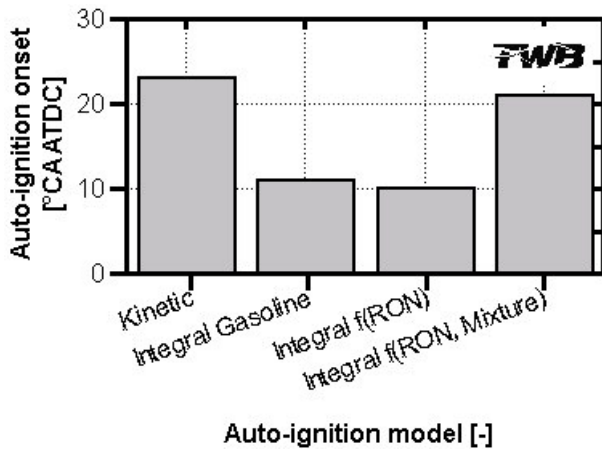


Figure 1: Calculated auto-ignition onset, reaction kinetics results compared to Livengood-Wu integral

The auto-ignition model is incorporated into an in-house 0D simulation tool for the analysis of the high pressure cycle of an internal combustion engine which is called engine process model (EPM). The crank train kinematics bore, stroke, con rod length and piston offset are used to reproduce piston work. Furthermore, wall heat losses dQ_w are modelled by Hohenberg's approach [8] for the heat transfer coefficient α_w . The model uses either a user defined transient trace of burned heat release dQ_b or an empirical fit to account for the spark ignited combustion. These boundaries form the Equations 6 to 9.

$$\frac{dp}{dt} = \left(-p \frac{dV}{dt} \left(1 + \frac{c_v}{R} \right) - dQ_w + dQ_b \right) \frac{R}{V c_v} \quad (6)$$

$$\frac{dT}{dt} = \frac{1}{mc_V} \left(-p \frac{dV}{dt} - dQ_w + dQ_b \right) \quad (7)$$

$$\frac{dQ_w}{dt} = \alpha_w A (T - T_w) \quad (8)$$

$$\alpha_w = 0.013 V^{-0.06} p^{0.8} T^{-0.4} (c_m + 1.4)^{0.8} \quad (9)$$

During flame progress, the cylinder is divided into burned and unburned regime by a two zone model. The calculation of ignition delay time and hence auto-ignition is only utilized within the unburned regime of the cylinder. The two zone approach is coupled via pressure and delivers an unburned and burned temperature for each regime respectively. Figure 2 shows the temperature traces of the 0D approach in comparison to 3D CFD combustion simulation results. The unburned temperature trace shows a minor increase due to pressure increase by flame propagation. The very fast 0D approach matches the much more detailed 3D approach well.

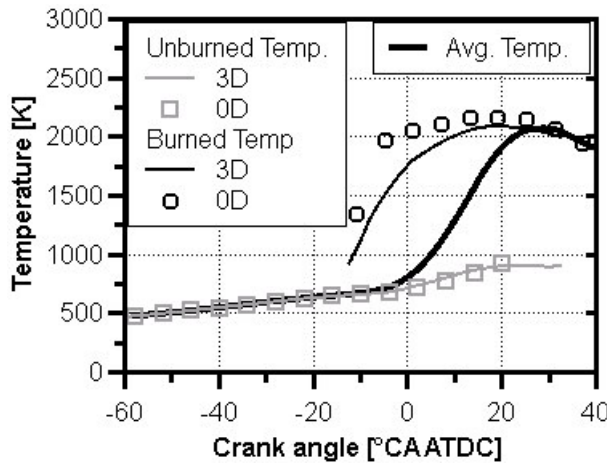


Figure 2: Comparison of unburned and burned temperature, 0D results from presented approach and 3D CFD results

3. Validation of ignition delay times

The results of homogeneous reactor ignition delay time experiments are used to validate results of the auto-ignition model. The following section shows a comparison of the simulation results produced by the 0D auto-ignition model with test bench results from literature. Corresponding experimental values were extracted from proceedings of Fieweger et al. [9] and Ciezki et al. [10].

Figure 3 shows the simulated ignition delay time for a mixture of iso-octane (RON100) compared to corresponding results from shock-tube experiments from [9]. The relative air/fuel ratio is varied starting from $\lambda = 0.5$ for a rich mixture over $\lambda = 1.0$ for a stoichiometric mixture and ending at $\lambda = 2.0$ for a lean mixture. Only one pressure level of 40 bar is investigated here.

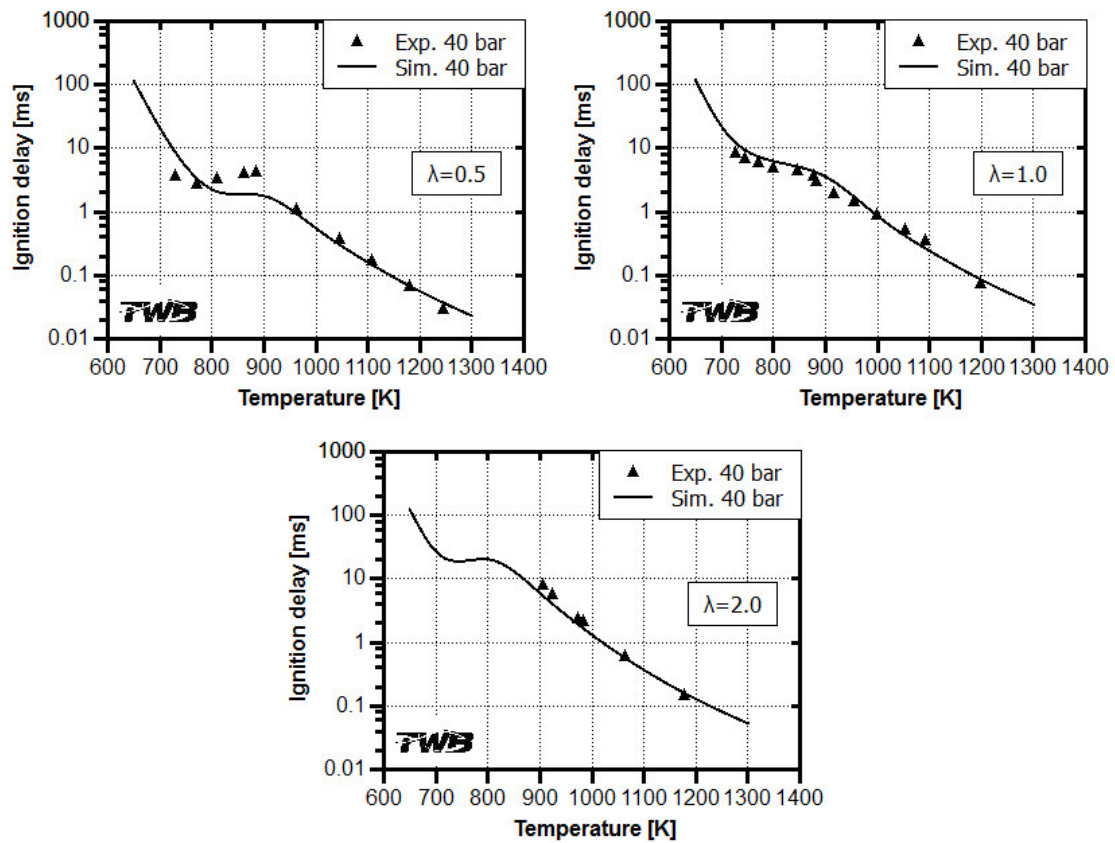


Figure 3: Ignition delay times of iso-octane, simulated and experimental [9] results

As one can see there is a good agreement between the 0D simulation results and the experimental findings. Especially under high temperature conditions test bench and simulation results match very good. Only the rich mixture results for $\lambda = 0.5$ differ more significantly in the low temperature range between $750 \text{ K} \leq T \leq 900 \text{ K}$.

In either case the dependence of the ignition delay time on temperature becomes clear. In general, increasing temperature leads to decreasing ignition delay time. The NTC behaviour of iso-octane can be seen in the temperature range between $700 \text{ K} \leq T \leq 900 \text{ K}$ in both simulation and experiment.

In Figure 4 n-heptane (RON0) is investigated under low and high pressure terms. Experimental data have been taken from [10]. The NTC effect, as already stated above, can be observed here as well. However, the RON0 mixture shows a more distinctive increase of the ignition delay time within the NTC regime than the RON100 fuel. For the stoichiometric air/fuel ratio of $\lambda = 1.0$ both simulation and experiment do correlate in a very good manner. The correlations of rich and lean relative air/fuel ratios seem to be clearly weaker at first sight. Nevertheless a good trend can be achieved for all relative air/fuel ratios, especially under high temperature conditions. Here, the impact of the pressure can be seen clearly. A decrease of the pressure level leads to an increase of the ignition delay time.

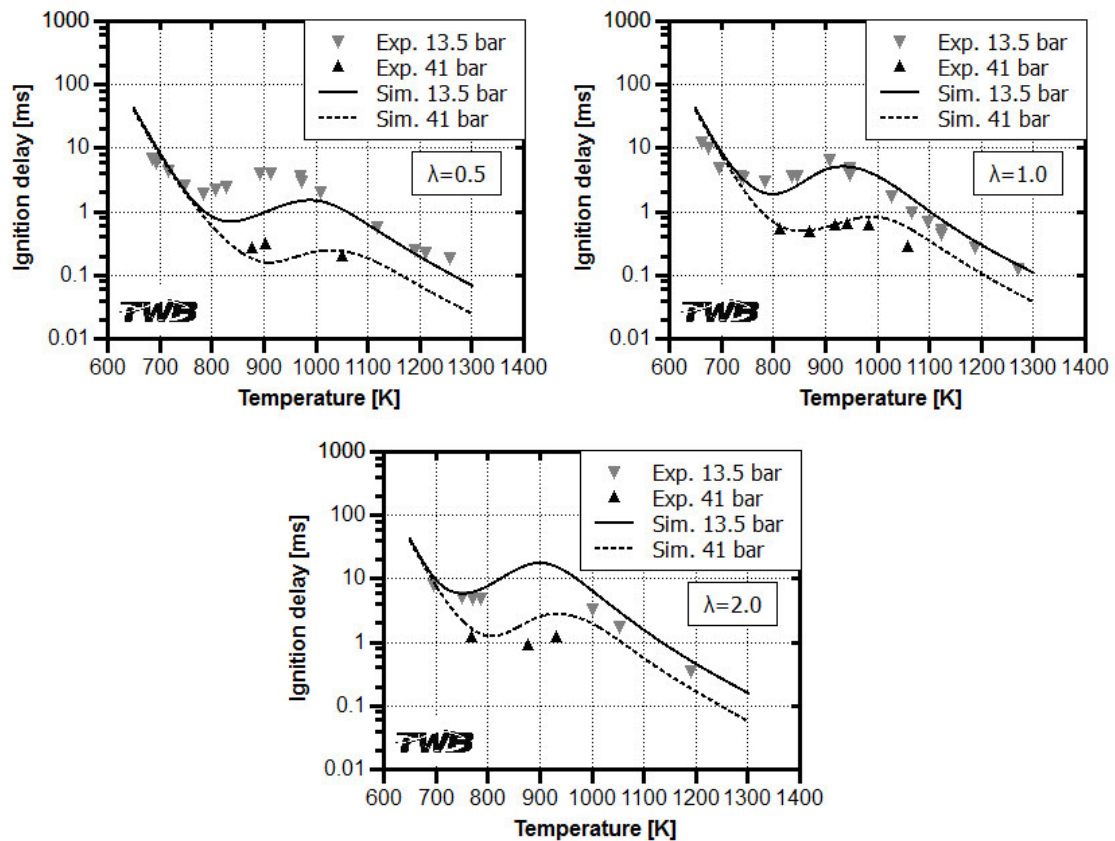


Figure 4: Ignition delay times of *n*-heptane, simulated and experimental [10] results

4. Ignition delay time maps of surrogate fuels

The presented auto-ignition model is used to analyse the ignition delay times of typical engine fuels like RON95 or E10. Therefore, real fuels are modelled by surrogates containing iso-octane, *n*-heptane and ethanol. In the following contour plots in Figure 5 the ignition delay time calculated utilizing the Livengood-Wu integral is depicted as a function of pressure and temperature. Therefore, ignition delay time calculations as stated above are utilized for numerous pressures and temperatures. These investigations are performed for the fuel qualities RON0, RON100 and RON95. Additionally, the impact of an admixture of 10 percent ethanol to the RON95 fuel which is used here as surrogate for E10 fuel on the ignition delay is analysed.

Especially for RON0 a very distinctive NTC behaviour can be identified inside the temperature range $800 \text{ K} \leq T \leq 1050 \text{ K}$ over the whole pressure range. For RON100 the NTC can only be observed at low pressure and temperature values. RON95 just shows a slight increase in ignition delay time for matchings of low temperature and low pressure. The additional content of 10 percent ethanol in the E10 fuel affects the ignition delay time only in the mid temperature range and high pressures where ignition delay times are increased.

Regarding ignitability of the compared fuel qualities the auto-ignition model properly shows the RON0 mixture (*n*-heptane typically used as diesel surrogate) being more ignitable than the RON100 fuel (iso-octane typically used as gasoline surrogate).

Especially for low temperatures the RON0 fuel is more than one-tenth lower concerning ignition delay time than the gasoline fuels RON100, RON95 and E10.

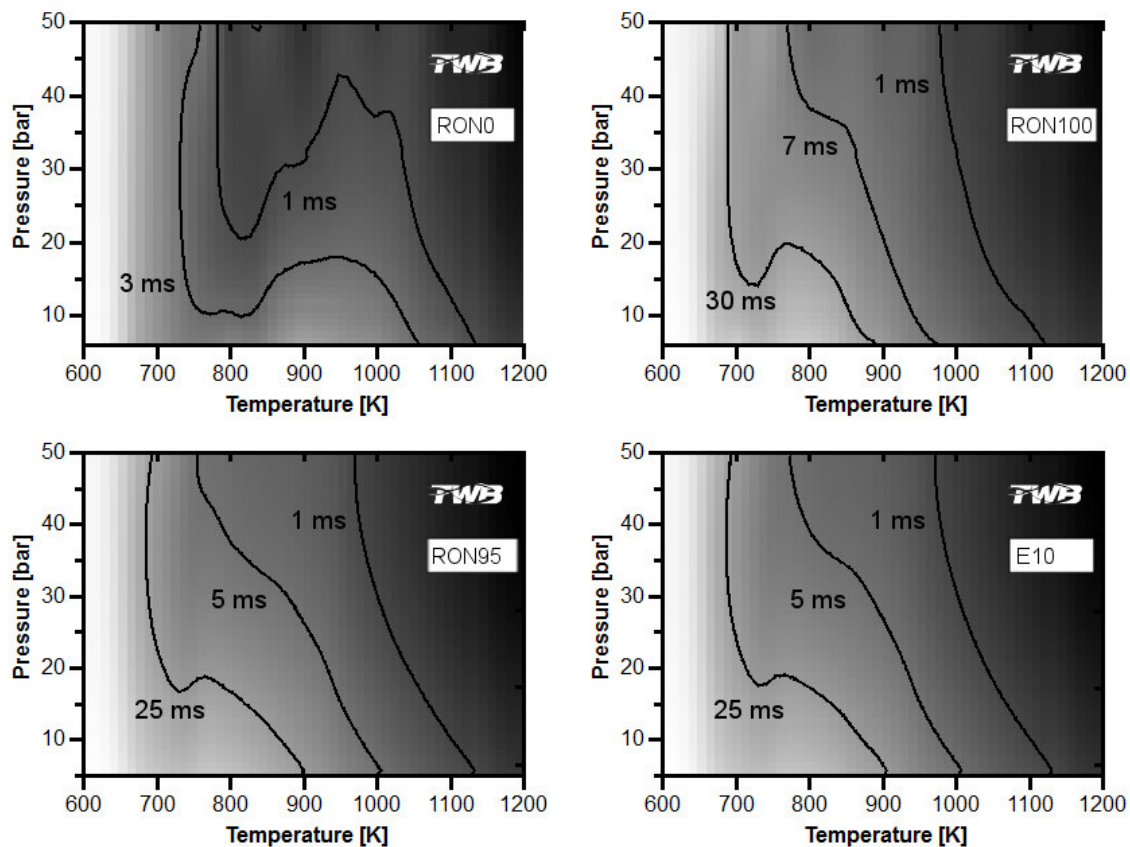


Figure 5: Ignition delay time map for RON0, RON100, RON95 and E10

5. Variation of engine parameters

The following section summarizes different parameter studies that are known to have a major impact on the appearance of auto-ignition phenomena and knocking within an internal combustion engine. For this purpose the impact of the compression ratio and the intake pressure as well as the cylinder wall temperature and engine speed is analysed. The auto-ignition model in conjunction with the 0D simulation tool EPM are utilized. Spark timing during the engine cycle is adjusted in the simulation to keep the nominal value of the Livengood-Wu integral constant and smaller than unity.

5.1 Compression ratio and fuel quality

The investigation of variable compression ratio has been made for several fuel qualities RON95, RON85 and E10 while the geometrical compression ratio ε was varied from 10 to 12. Basically, the 0D simulation properly points out that due to higher compression ratios a steady increase in spark timing to later timings has to be realised to keep the auto-ignition probability in terms of the Livengood-Wu integral constant and also keep the indicated mean effective pressure (IMEP) constant. This may be recognized by appropriate delayed in-cylinder pressure rises in Figure 6. For instance, spark timing of RON95 has to be set at 11 °CA BTDC, 7 °CA ATDC and 3 °CA ATDC for the tested compression ratios 10, 11 and 12, respectively. E10 does not differ much from the behaviour of pure RON95 fuel and shows only a slightly earlier spark timing of about 1 °CA. In contrast, RON85 needs a certain shift of spark timing to later crank angles of approximately 10 °CA to keep the knocking integral at constant level which can be related to its higher ignitability. As a consequence, this leads to lower maximum pressure levels and thus lower released energy and efficiency.

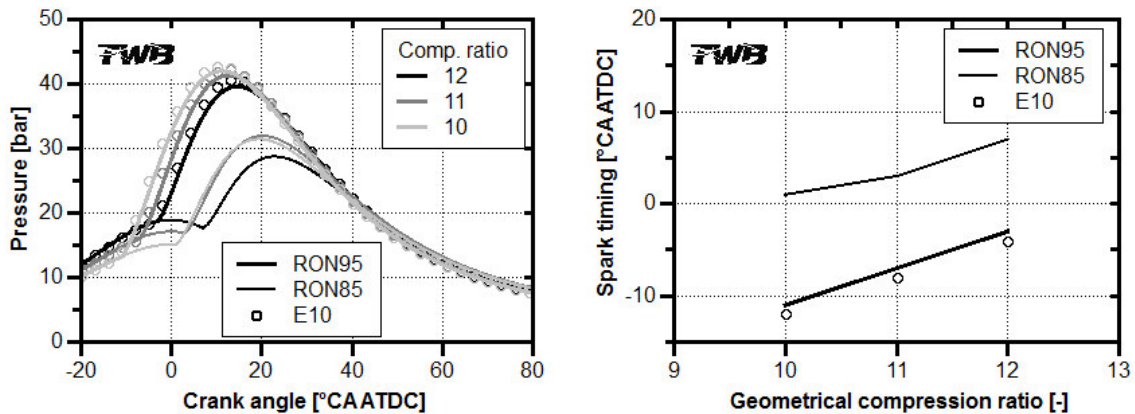


Figure 6: Pressure traces and spark timing for different compression ratios and fuel qualities; IMEP and Livengood-Wu integral kept constant

5.2 Intake pressure

For the following parameter variations the fuel quality is kept at RON95. The geometrical compression ratio $\varepsilon = 11$ and the relative air/fuel ratio $\lambda = 1.0$ are analysed. For the intake pressure variation also the intake temperature T_{in} is kept at a constant value of $T_{in} = 300$ K. Varying the intake pressure over a range from 0.7 bar to 1.0 bar and hence varying the engine load accordingly reveals a high sensitivity of the needed spark timing to keep the Livengood-Wu integral at constant level. An intake pressure of 0.7 bar results in a spark timing of 7 °CA BTDC. According to higher intake pressures the spark timing of the engine needs to be moved to later crank angles up to 6 °CA ATDC for $p_{in} = 1.1$ bar. The corresponding pressure traces and spark timings can be seen in Figure 7.

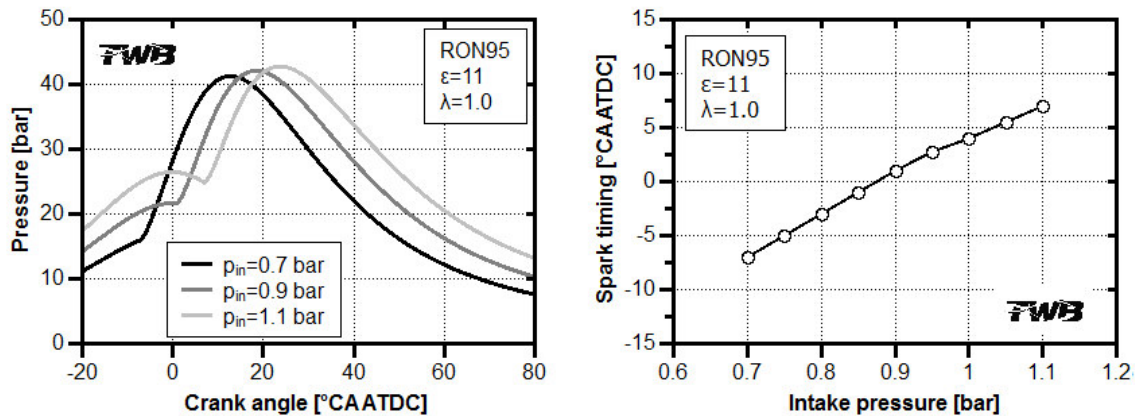


Figure 7: Pressure traces and spark timing for varying intake pressures; intake temperature and Livengood-Wu integral kept constant

5.3 Wall temperature

Regarding wall temperatures of the combustion chamber as another determining factor the following analysis points out that higher temperatures imply a higher risk of auto-ignition or knocking. To keep the operating conditions in terms of IMEP and Livengood-Wu integral constant, spark timing has to be moved to later crank angles for rising wall temperatures. Figure 8 shows the in-cylinder pressure traces for different wall temperatures as well as the according spark timing. An increase of the wall temperature T_{wall} from 373.15 K to 473.15 K may result in a retarded spark timing by 6 °CA. However, the delayed combustion goes along with lower maximal pressure values.

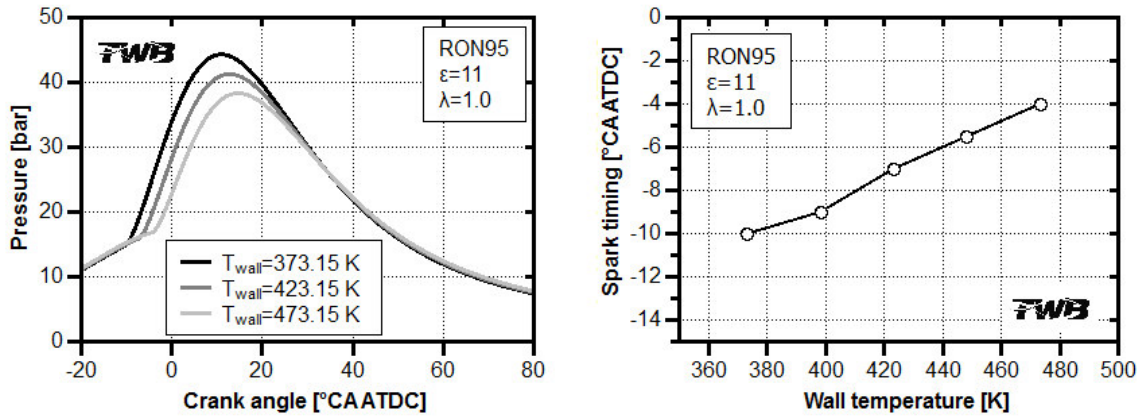


Figure 8: Pressure traces and spark timing for varying wall temperatures; IMEP and Livengood-Wu integral kept constant

5.4 Engine speed

Finally, engine speed n is varied regarding the impact on auto-ignition tendency. Therefore, a range from $n = 1500$ 1/min to $n = 5000$ 1/min is considered keeping IMEP and intake temperature constant. The 0D simulation points out that generally with an increased engine speed spark timing can be shifted towards earlier timings. The residence time of the unburned end gas is reduced. Under the assumption of constant thermodynamic boundary conditions this can be used to utilize earlier spark timing.

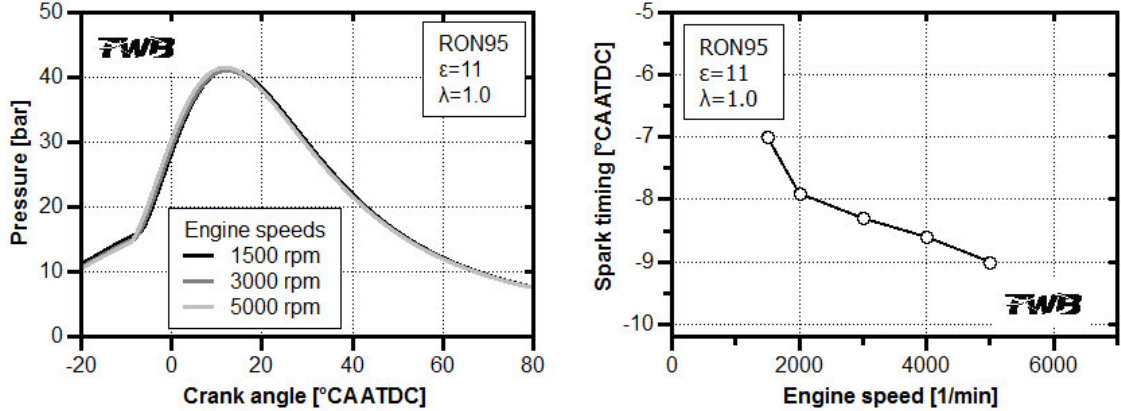


Figure 9: Pressure traces and spark timing for varying engine speeds; IMEP, intake temperature and Livengood-Wu integral kept constant

6. Conclusion and outlook

In this report the prediction of auto-ignition phenomena using an empirical correlation of the ignition delay time and an in-house 0D simulation tool is investigated. Appearance of auto-ignition is described by the knock integral according to Livengood and Wu. The integral, however, is strictly coupled to the mixture's ignition delay time. For that reason, an empirical three stage Arrhenius approach representing low, medium and high temperature reaction kinetics is introduced and implemented in the simulation code.

In the following the quality and performance of the herein mentioned 0D simulation tool is analysed. For validation purposes, simulated ignition delay times are compared to experimental data from literature. It can be shown that a very good agreement is achieved between simulation and appropriate test bench results. Even chain branching and chain breaking effects which result in the typical NTC behaviour of hydrocarbon fuels for internal combustion engines are determined in a proper way.

Ignition delay times under several pressure and temperature conditions are illustrated for different fuel qualities. Here, different characteristics concerning NTC behaviour and ignitability of the considered fuel qualities can be pointed out.

Finally, a selection of parameters affecting auto-ignition within an internal combustion engine have been varied in between realistic engine operating conditions. Here, changes of compression ratio, fuel quality as well as intake pressure, wall temperature or engine speed and their effects on auto-ignition and thus required spark timings for steady engine conditions are discussed.

The coupling of the auto-ignition model and the 0D code EPM presented here is a very fast possibility for the analysis of engine operation in terms of auto-ignition and knocking. However, 1D and 3D CFD (Computational Fluid Dynamics) simulation codes are standard nowadays in the engine development process and enable further insights into the engine processes. A coupling of the auto-ignition model to these kind of simulations were already established. Especially the incorporation of the model to the 3D CFD code OpenFOAM is utilized in further research activities of the authors [11,12].

References

- [1] Spicher, U., Worret, R.: Entwicklung eines Kriteriums zur Vorausberechnung der Klopfgrenze. In: Abschlussbericht zum FVV-Vorhaben Nr. 700, 2001
- [2] Livengood, J.C., Wu, P.C.: Correlation of Autoignition Phenomena in Internal Combustion Engines and Rapid Compression Machines. In: 5th International Symposium on Combustion, p. 347, 1955
- [3] Douaud, A.M., Eyzat, P.: Four-Octane-Number Method for Predicting the Anti-Knock Behaviour of Fuels and Engines. In: SAE technical paper 780080, 1978
- [4] Yates, A., Swarts, A., Viljoen, C.: Correlating Auto-Ignition Delays And Knock-Limited Spark-Advance Data For Different Types Of Fuel. In: SAE technical paper 2005-01-2083, 2005
- [5] Vandersickel, A.: Two Approaches to Auto-Ignition Modelling for HCCI Applications. In: Dissertation, ETH-Zürich, 2011
- [6] Ritzinger, J.: Einfluss der Kraftstoffe RON95, Methan und Ethanol auf Flammenausbreitung und Klopfverhalten in Ottomotoren mit Abgasrückführung. In: Dissertation, ETH Zürich, 2013
- [7] Kalghatgi, G.; Babiker, H.; Badra, J.: A Simple Method to Predict Knock Using Toluene, N-Heptane and Iso-Octane Blends (TPRF) as Gasoline Surrogates. In: SAE technical paper 2015-01-0757, 2015.
- [8] Hohenberg, G.F.: Experimentelle Erfassung der Wandwärme in Kolbenmotoren. In: Habilitationsschrift, TU Graz, 1980.
- [9] Fieweger, K., Blumenthal, R., Adomeit G.: Self-Ignition of S.I. Engine Model Fuels: A Shock Tube Investigation at High Pressure. In: Combustion and Flame 109: 559-619, 1997
- [10] Ciezki, H., Adomeit, G.: Shock-tube investigation of n-heptane-air-mixtures under engine relevant conditions. In: Combustion and Flame 93:421-433, 1993
- [11] Stapf, K.G.; Paczko, G.; Peters, N.: Computational analysis of the interrelation of mega-knock phenomena and charge motion. In: XIIth Congress Engine Combustion Processes, 12.-13.03.2015, Ludwigsburg
- [12] Stapf, K.G.; Paczko, G.; Peters, N.: Simulation of Mega-Knock Probability in Highly Boosted Direct Injection SI Engines. In: Symposium for Combustion Control, 17.-18.06.2015, Aachen

The Authors:

Dr.-Ing. Karl Georg Stapf, Ingenieurbüro TWB, Fulda

M.Sc. Benjamin Reis, Ingenieurbüro TWB, Fulda

Licence:

This document is licensed under the Creative Commons Attribution 3.0 DE License (CC-BY 3.0 DE): <http://creativecommons.org/licenses/by/3.0/de/>

Investigations of Diesel Spray structure using Spray Momentum Measurements and link to injector performance

Gavin Dober
Christophe Garsi
Nouredine Guerrassi
Thomas Leonard

Abstract

An experimental and analysis technique is developed and presented for a Diesel Spray Momentum Measurement Device. The influence of various measurement parameters including: sensor size, sensor distance and rail pressure, are presented. Further the method for analysis of the collected data is also investigated including: normalization, filtration, averaging, spatial momentum profile interpretation.

The importance of the momentum measurements in injector design and development is then demonstrated with two analysis tasks. The first is to compare and contrast the performance of two different injector designs, with different needle motion behavior. The second task is to compare and contrast the performance of two different nozzle designs. Both designs have tapered hole shapes and have the same discharge coefficient (C_d) at 100 bar although one design achieves this with hydro-erosive grinding and another without hydro-erosive grinding.

The spray momentum measurements are compared and correlated with various other injector and spray measurements for an appropriate interpretation of the results and to demonstrate the unique capabilities of the device. Comparison is made to hydraulic rate of injection data; spray visualization of the near nozzle spray structure and combustion results.

1. Introduction

A continuing advancement of diesel fuel injection systems is required to meet future more stringent vehicle emissions regulations for particulate and NO_x as well as demands for lower fuel consumption and CO_2 . There have been substantial advances in fuel injection technology providing the capability for much higher fuel injection pressures that together with high levels of EGR and multiple injection strategies have allowed combined reductions in engine-out emissions of NO_x and soot as well as low levels of combustion noise and high specific power outputs [1, 2, 3]. Common rail injection systems [3] currently provide the best blend of injection flexibility and spray generation efficiency.

The design of the diesel fuel injector and its nozzle has also been the subject of continuous design and development improvement processes which to date have targeted more efficient conversion of rail pressure energy into spray energy, and precise control of fuel metering into the cylinder. Future developments for fuel injection equipment will move beyond these simple bulk characteristics of the spray into the structure of the spray itself, how it is evolving both spatially and over time.

Such an optimization process presents a difficult challenge in measurement. As the spray is optically dense it is difficult to measure beyond a simple spray dispersion angle. There has been some success to measure with high energy X-rays [7]. However such measurements are enormously expensive, provide qualitative data and are subject to interpretation. What is needed is a quantitative tool to make spatial and temporal measurements of sprays under realistic injection conditions.

This paper details the latest efforts at Delphi to measure and characterize diesel sprays from common rail diesel fuel injection equipment using spray momentum measurements. It will detail the measurement process, the sensitivity of the results to standard engine variables such as backpressure and rail pressure, and illustrate the differences between different injectors and between different nozzle designs.

2. Theory of Spray Momentum Measurements

There have been numerous publications to date measuring the spray momentum in a diesel fuel jet [1, 2, 3]. These momentum measurement devices are based on the theory that a spray is directed against a target surface and the force that is generated on the surface is measured. The target must be designed such that the spray is deflected perpendicular to its axis such that the net axial momentum of the deflected spray becomes 0. In such a situation the change in momentum at the target position is equal to the momentum of the free spray.

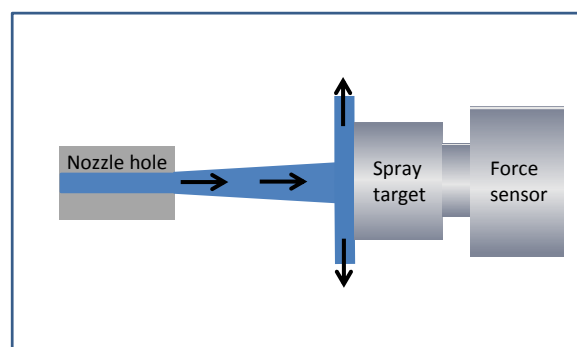


Figure 1: Target is designed to deflect the spray perpendicular to the spray axis.

If the momentum flux is measured in conjunction with the mass flow then a measurement of the mass weighted velocity of the spray can be determined. This velocity can be divided by the Bernoulli velocity to give a momentum efficiency (η_n) characteristic of the nozzle/injector. η_n is similar although not the same as nozzle C_d . It is argued as well that η_n is more representative of the combustion behavior of a particular nozzle as it is directly related to the mixing energy per unit mass of injected fuel.

$$C_d = \dot{m} / \dot{m}_{th} = \dot{m} / (\rho_{fuel} \cdot Area_{hole} \cdot U_{th}) \quad (1)$$

$$U_{th} = \sqrt{2(P_1 - P_2) / \rho_{fuel}} \quad (2)$$

$$\eta_n = \frac{M \dot{m}}{M \dot{m}_{tham}} = \frac{F_p}{(\dot{m} \cdot U_{th})} \quad (3)$$

$$C_d = C_a \times C_v = C_a \cdot \eta_n \quad (4)$$

Delphi's older device [3] was capable of making simultaneous momentum flux and mass flow measurements under fixed needle lift conditions. However, in order to investigate the impact of needle motion, high rail pressure and gas density, a new momentum measurement device has been commissioned at Delphi. Unfortunately, the simultaneous measurement of fuel mass flow is not easily made at high pressures, for short injections and when there is high gas density in the measurement chamber. So, momentum force measurements must be compared to hydraulic rate of injections made on a separate test apparatus. This can become a source of error.

3. Description of the Spray Momentum Measurement Device

The spray momentum measurement device is well described in other publications [4, 6]. Only a brief overview of the apparatus will be given here. A sectional view of the test equipment is given in Figure 2. In brief, the design is such that the injector is fixed and the target and chamber are free to move around the injector. The target can be moved through 360° of θ , 100° of Φ , and 5-80 mm of z . The gas in the chamber is nitrogen to suppress any chance of combustion, and can be raised to 80 bar. It is not possible to heat the gas in the chamber, and so spray measurements are made under non-evaporating conditions.

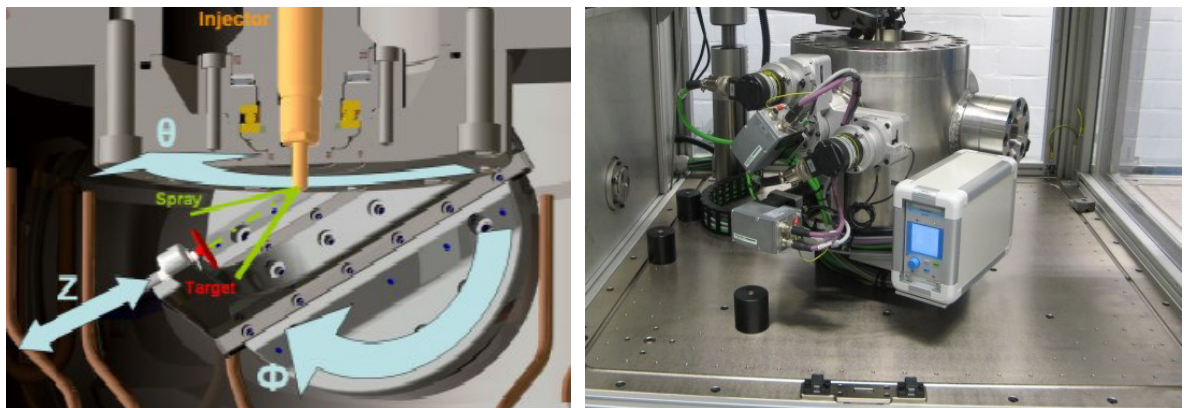


Figure 2: Momentum Measurement Device sectional view (left) [5, 6] and external picture (right).

4. Measurement Technique

4.1 Data Processing

Certain processing of the data is required to get a sensible measurement signal which can be used for injector or nozzle comparison exercises. The process for measurement of the total momentum of a complete injection event is illustrated in Figure 3. Multiple traces are collected at a specific frequency. The first few injections are not recorded as they may vary slightly from the steady state values due to differences within the injector in component temperature, fuel gas content, friction, injector back-leak pressure and temperature. It may be observed that the raw injection traces show a significant amount of noise in the range of 25kHz. This must be removed with a low pass filter. The use of such a filter limits the resolution of features of interest that may be explored. The measurement sensor is also seen to drift, both between measurements and during measurements. Corrections for both drifts are necessary. The rail pressure has also a significant impact on the momentum measured as it impacts both fluid velocity and mass flow rate. The relationship between rail pressure and momentum is linear and a normalization by the rail pressure before the start of injection reduces the dispersion between results. After applying all these corrections, the signal repeatability is excellent and as a final step ensemble averaging can be used to give a highly accurate representative trace for a single spray hole.

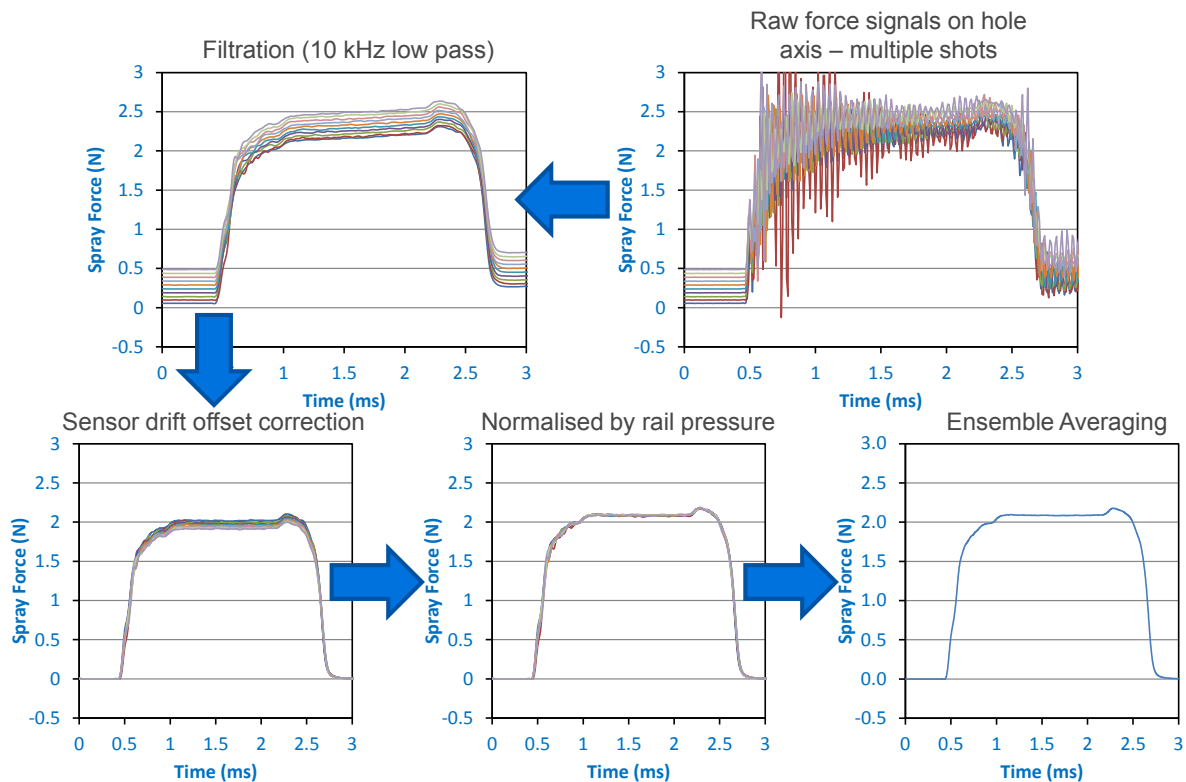


Figure 3: Example of the data processing method. Raw momentum signals are filtered, corrected for sensor drift, normalized by rail pressure and ensemble averaged.

4.2 Comparison of ROI and Momentum Signal

This momentum signal can be interpreted directly in much the same way as a rate of injection (ROI) from an injection analyzer. A comparison of the two signals is made in Figure 4. It should be noted that the momentum signals have been re-phased to account for the spray transit times from the nozzle to the measurement sensor. We can observe that the ROI varies with the square root of the pressure, while the momentum signal varies linearly with pressure. Several interesting features can also be observed on both signals. At 1, the end of needle lift is identified. This is associated with a nozzle pressure increase and consequently an increase in both ROI, velocity and momentum. At 2, the start of needle closing is also associated with an increase in the nozzle pressure and a further increase in the ROI, velocity and momentum. At 3, the gas has an impact on the end of injection as it smooths the decay in momentum rate. This feature increases in magnitude with higher momentum chamber gas densities.

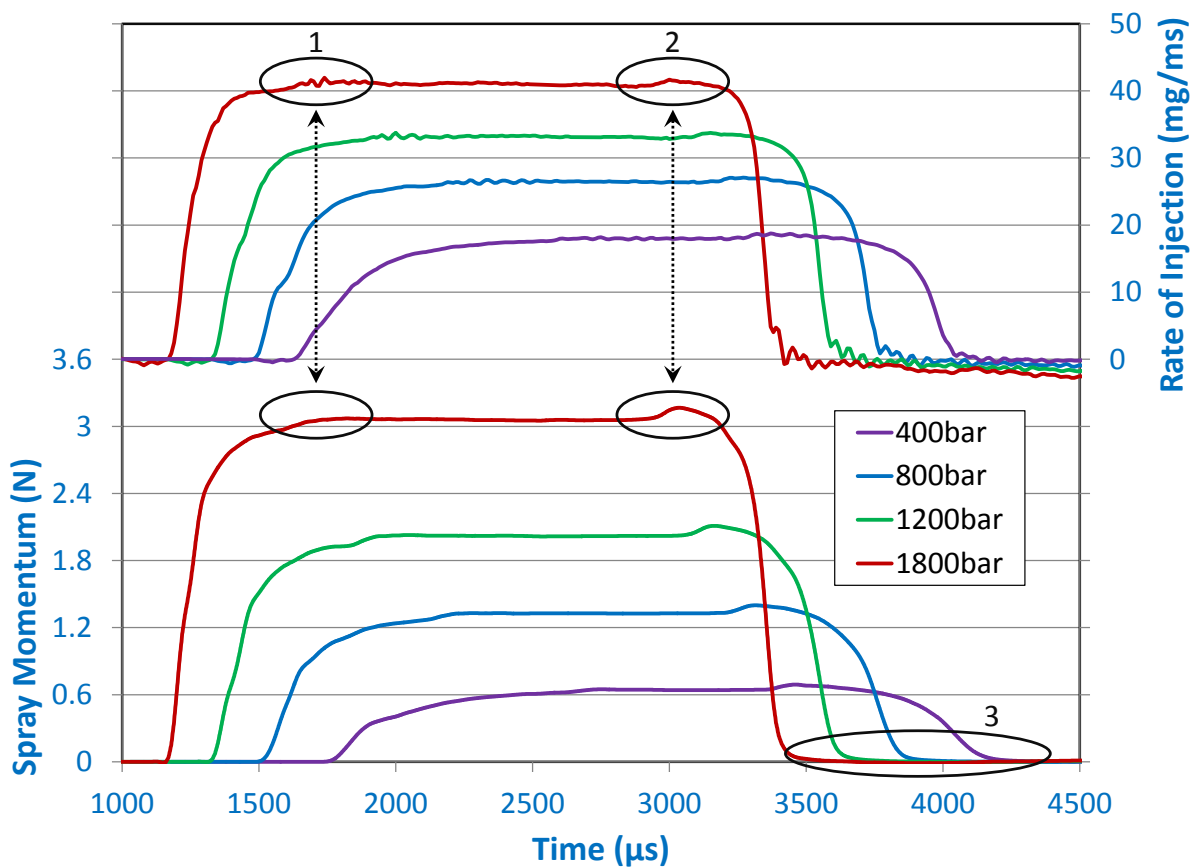


Figure 4: Rate of Injection (BP = 50 bar), vs Momentum Spray Force (BP = 0 bar). Signals have been phased to align the start of the injection.

4.3 Individual spray assessment

One of the benefits of these spray momentum measurements over standard injection rate measurements is that flow or momentum variability can be investigated in great detail. Values are available for each spray hole and for each shot. This is illustrated in Figure 5 below. We can observe that while the shot-to-shot performance of the injector is very well controlled, there are significant hole-to-hole differences. The variation shown illustrates a particularly bad nozzle sample. The possible causes for this variation are either a difference in diameter, difference in nozzle hole C_d , an eccentricity of the nozzle needle or a combination of these factors.

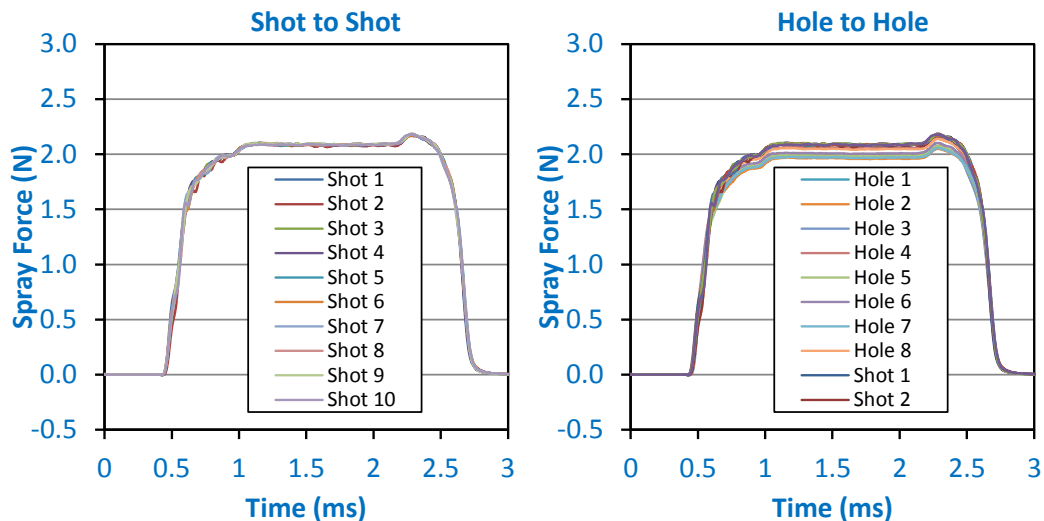


Figure 5: Shot-to-Shot (left) and Hole-to-Hole (right) $RP = 1200$ bar, 2.0 ms injection duration.

4.4 Spray targeting and shape

One of the key parameters for injector nozzle design is the spray cone angle, sometimes referred to as the vertical spray targeting. Engine performance and emissions are very sensitive to this parameter. Typically, $>1^\circ$ difference in the spray targeting is detectable in engine emissions. By moving the sensor position, the point at which the spray misses the target can be identified and from this, the spray targeting can be calculated. A high level of accuracy of $<0.5^\circ$ is possible. The favored definition at Delphi for the spray targeting is to find the angles at which 50% of the maximum momentum force is measured on either side of the spray and assume that the targeting lies at the midpoint of these two angles. This definition identifies the angle where 50% of the spray momentum lies on either side.

A spray dispersion angle may also be calculated using thresholds based on the maximum force value. The momentum measurements provide an almost unique possibility to measure the vertical dispersion angle of the spray on standard multi-hole nozzles. This is not generally possible using spray visualization. The dispersion angle is strongly linked to spray penetration rate, and at least at full load, a compact narrow spray is desired for best performance.

As the target is moved out from under the spray then the rate of change of the force on the sensor is an indication of the spray force profile. It should be noted that this is not the actual spray force profile, but is nevertheless useful to identify asymmetry in the spray and hole-to-hole or injector-to-injector differences in spray structure.

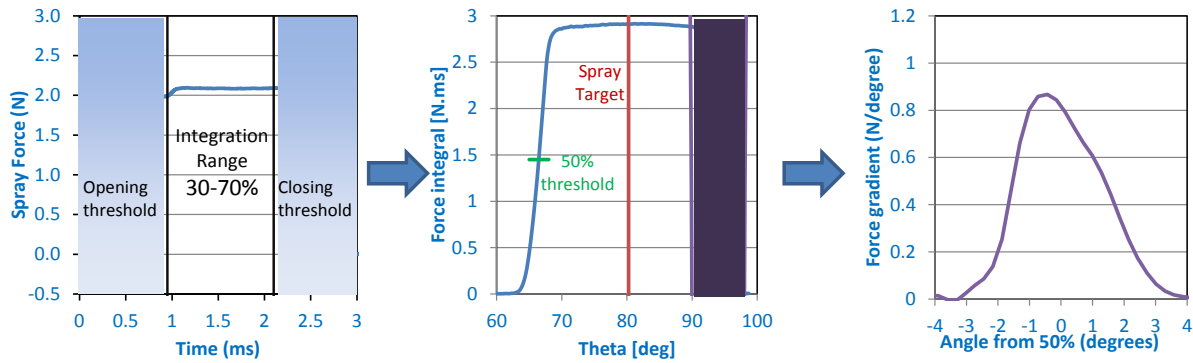


Figure 6: Instantaneous force signal is integrated over a defined time window (left). This integral is measured at a range of spray target positions (center). The derivative of this profile gives an indication of the spray force distribution (right).

A time windowing is also generally used to either isolate the structure of the spray at full lift, or to track the evolution of the spray parameters through the injection event. This is interesting as the needle lift is known to have a strong impact on the spray formation. Such a temporal processing of the spray macroscopic parameters is seen in Figure 7. It is observed that both early and late in the injection event, at low needle lifts, the spray width is almost doubled. There are additionally slight variations in the spray targeting at the beginning and the end of the injection event, but these are generally $<1.0^\circ$.

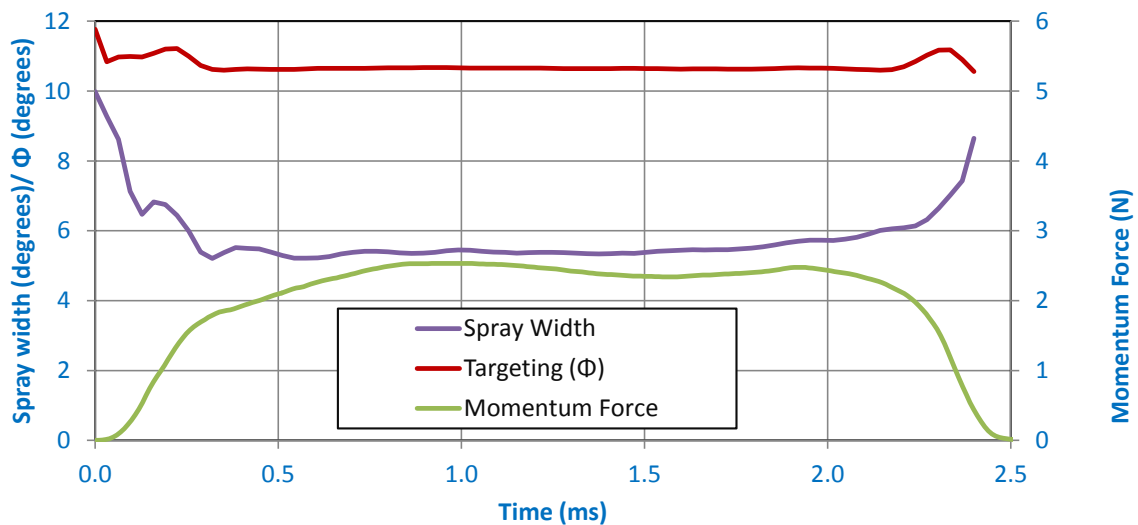


Figure 7: Sensor = 5 mm; RP = 1200 bar; BP = 0 bar; Evolution of Spray targeting and Vertical Dispersion angle with time during an injection event.

This capability for measurement of the macroscopic properties of spray momentum, targeting and dispersion angle is very interesting. It is envisaged that such knowledge will enable injector/nozzle designs which can optimize the spray structure differently at the different periods during the injection event.

4.5 Spray Sensor Size

For an accurate indication of the force profile through the spray, a much smaller sensor must be used. In the tests presented here, a 1 mm diameter sensor was available. Such a sensor is not normally large enough to capture all of the spray from one hole, but neither is it so small that it directly measures the spray force at a particular location. Depending on the distance the target is from the injector, the rail pressure and the gas backpressure, the spray width may be between 0.5 and 10 mm. This means that the sensor averages the local force over its measurement area.

It is possible to reconstruct the exact force profile through the spray if we make some assumptions about the shape of the spray. Figure 8 illustrates the relationship between the real spray force profile for different sensor diameters. When spray width is large (50% max-force value width > 2 sensor diameters) then the measured force signal is very similar to the actual force profile and can be interpreted directly. However, when the spray width and the sensor width are similar in size (<1.5 times diameter), the differences between the measured signal and the actual profile are great and the challenge to reconstruct the spray is difficult and prone to significant error. It is noted that various assumptions about spray symmetry and shape are required to make the reconstruction which are not easily validated.

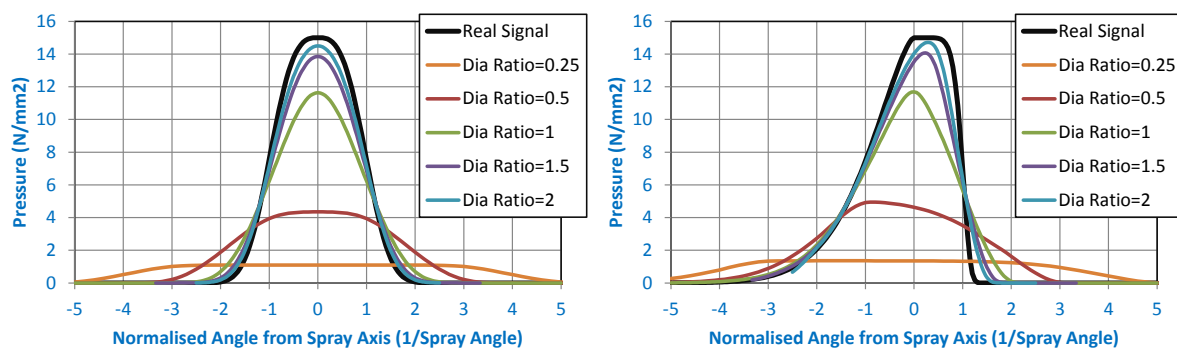


Figure 8: Comparison of the real force profile through a spray with the measured force profile. An assumed ideal signal is taken and the measurement signal is simulated. Symmetric Profile (left) and Asymmetric Profile (right).

In Figure 9, a range of force profiles can be seen at different distances from the spray hole. In this case the spray width of 8° is only 1.5 times larger than the sensor width of 5.7° @ 10 mm. At 20 mm it is ~3 times larger than the sensor width and very closely resembles the real spray profile. It is noted that the 20 mm signal appears to have a wider structure than at 10 mm, even though the impact of the sensor size would be expected to give the opposite effect. This difference can be attributed to the changing structure of the spray as it develops. Over time there is more momentum exchange with the gas and hence diffusion of the spray profile. At 30 mm the strength of the momentum signal has dropped so significantly that only a very poor signal to noise ratio is available.

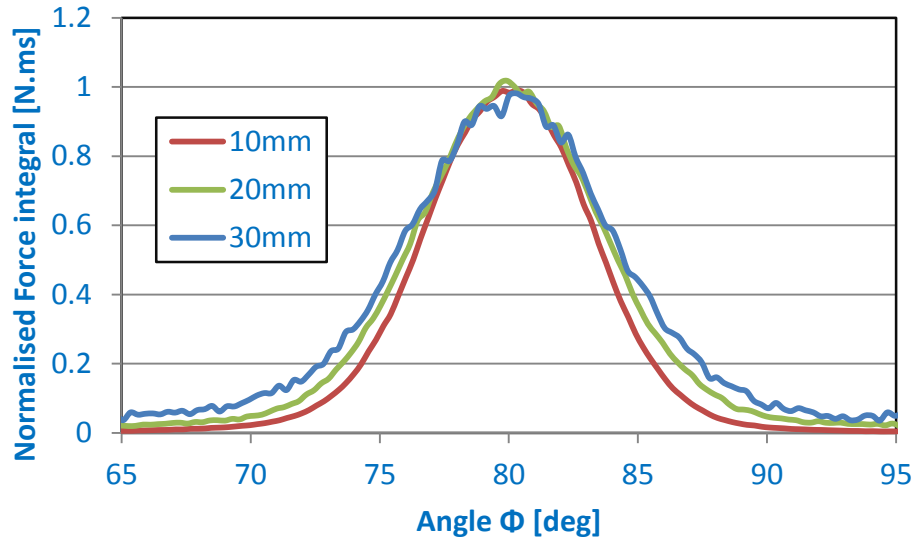


Figure 9: Sensor = 1 mm; RP = 1200 bar; BP = 50 bar; Z = 10, 20 and 30 mm. As the distance increases, the ratio of sensor size and spray width changes; also the force profile tends to spread due to the liquid-gas momentum exchange.

4.6 Chamber Backpressure

The backpressure in the chamber controls some aspects of the flow through the nozzle, but mainly influences the spray breakup. It is well known that the spray dispersion angle increases with backpressure. There is also a significant transfer of momentum from the spray to the gas and then to the sensor. This has a damping effect on the momentum signal. However, such conditions are much more realistic of true engine operating conditions, and hence the momentum measurements are particularly useful for the investigation of spray development or for the measurement of spray structure for CFD model calibration. If we look at Figure 10, it is noticeable that the backpressure reduces the peak momentum force. The momentum at the hole exit varies linearly with delta pressure but there is also a further reduction in the spray force due to the liquid-gas momentum exchange. Backpressure also reduces the opening rate and the closing rate. The momentum profile is much more significantly affected at low rail pressure than at high pressure. Finally, it adds an oscillation in the momentum force during the needle opening. It is believed that this oscillation is due to the generation of an aerodynamic vortex early in the injection event [5].

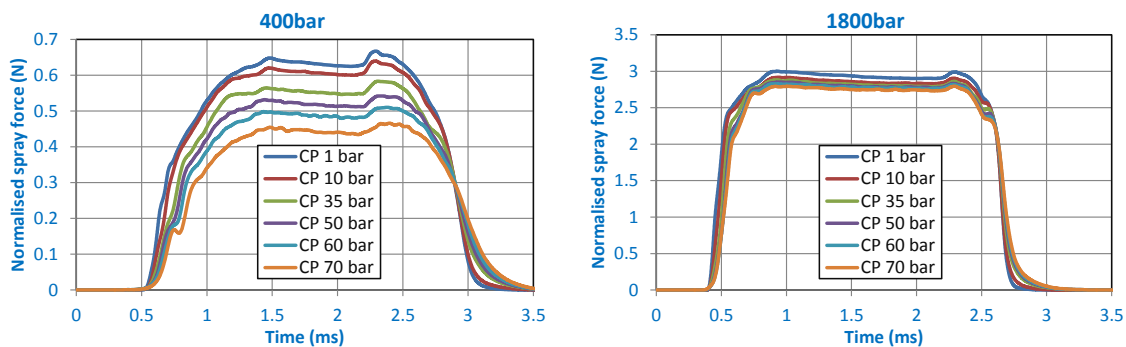


Figure 10: Sensor = 5 mm; Z = 10 mm; RP = 400 bar (left); RP = 1800 bar (right). Variation of chamber backpressure (1 → 70 bar).

5. Injector Comparison

So how can the momentum measurements help in the injector development process? How can it help to identify and diagnose injector functional differences and how they relate to spray behavior and to combustion? Figure 11 illustrates a typical comparison between two injectors with very different needle motions. The signal features associated with the needle motion are clearly visible. Inj-A has a very fast needle motion which is nearly independent of rail pressure and Inj-B is a fast servo injector with a needle lift stop. The much faster velocity of the needle of Inj-A is clearly captured by the momentum profile. Also captured is the higher momentum at full needle lift which indicates a higher injection velocity. This is due to lower internal pressure losses within Inj-A.

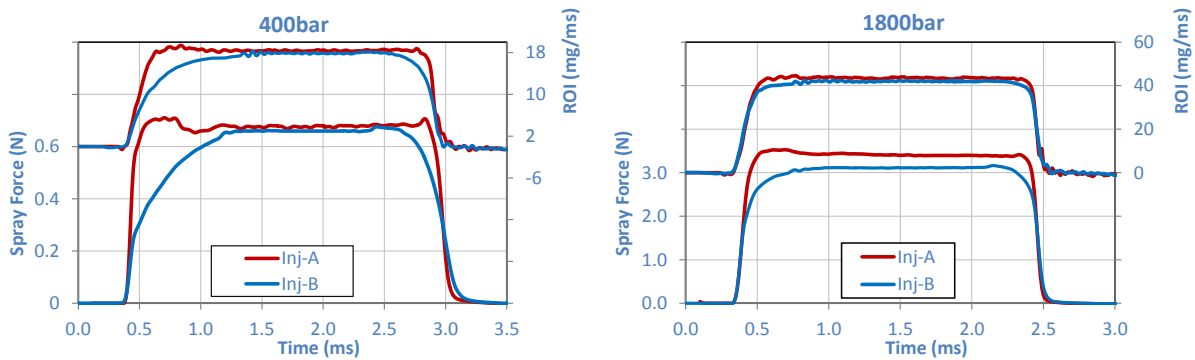


Figure 11: Comparison of Spray Force and Rate of Injection at high and low Rail Pressure. Sensor = 5 mm; BP = 0 bar.

This fast needle motion gives a very square injection rate which has been frequently correlated and understood to improve air-fuel mixing and reduce smoke. This effect is illustrated in Figure 12. In conjunction with the square injection rate is a squarer heat release rate (HRR). This has a negative impact on noise which is also illustrated in the combustion results.

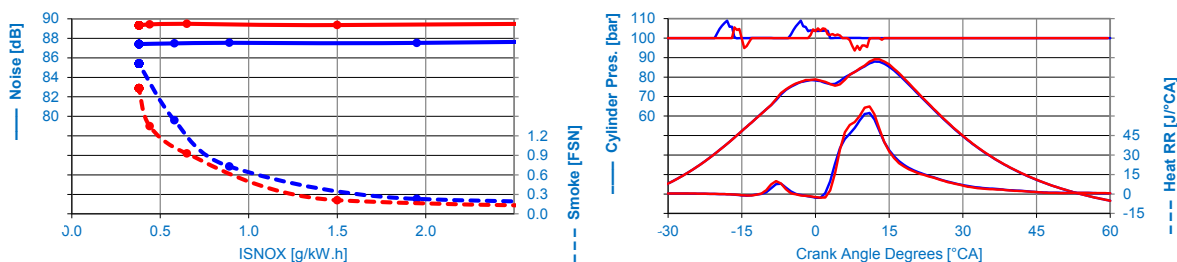


Figure 12: Comparison of Inj-A (red) and Inj-B (blue) at 2000rpm, 9bar IMEP, pilot+Main calibration. EGR variation.

6. Nozzle Comparison

The measurements can also be used to more closely investigate nozzle spray structure, which can be influenced by the geometry of the spray holes, sac or the needle. By way of example, two different nozzles A and B with the same C_d at 100 bar are presented. Nozzle A has both hole taper and hydro-erosive grinding and is called honed. Nozzle B only has hole taper and is called unhoned. Nozzle flow tests seen in Figure 13 identified that these nozzles have completely different C_d behavior versus rail pressure.

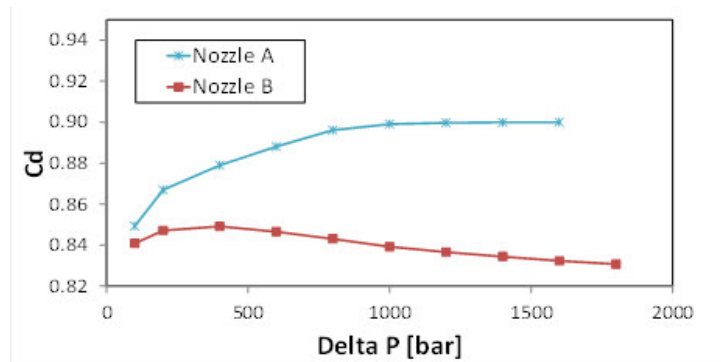


Figure 13: C_d taken from experimental measurement on a nozzle flow rig; the injector needles were removed; backpressure set to 5 bar; nozzle A is honed, and nozzle B is un-honed. Evolution of C_d with rail pressure is quite different.

The honed and un-honed nozzles were also investigated with phase contrast X-ray imaging Figure 14. This technique allows the spray structure in the near nozzle area to be investigated in great detail. An interesting phenomenon which the imaging revealed was that the flow behavior at full lift was completely different between the two injectors. The un-honed injector had a random structure with a wide dispersion angle, while the honed injector showed a narrow laminar breakup structure. It was also observed at low needle lifts both early and late in the injection event that the sprays became very similar.

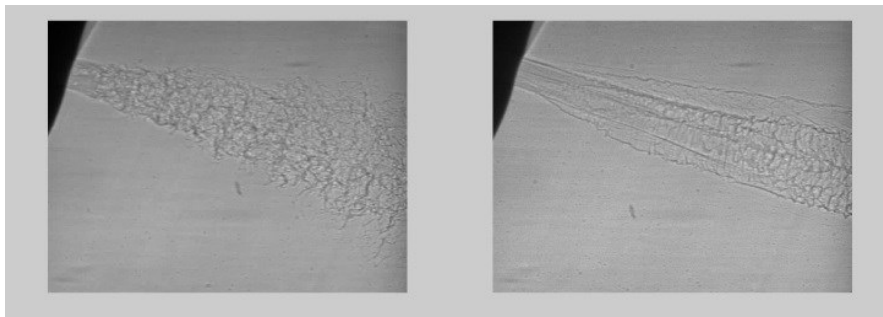


Figure 14: Phase Contrast X-ray images of spray structure at the hole exit, $RP = 1200$ bar, $BP = 0$ bar and full needle lift conditions. Left: un-honed; Right: honed. [7]

Figure 15 shows the momentum measurements for the same two injectors. On the left we see the gradient of the total momentum force for an injection event as the sensor is rotated through the spray. The higher peak spray force, and total force from the honed injector is obvious. It is also observed that the honed injector is significantly narrower than the un-honed injector. Further an asymmetry of the spray is evident with the un-honed injector. This asymmetry is caused by the sharp entry radius on the un-honed nozzle hole creating a recirculation region on the upper side of the hole near this corner. In Figure 15 on the right, we see the evolution of these properties of momentum and dispersion angle with time through the injection event. As with X-ray images, we see that at full lift the dispersion angle is narrower for the honed injector, but at the beginning and end of injection there is little difference between the two injectors.

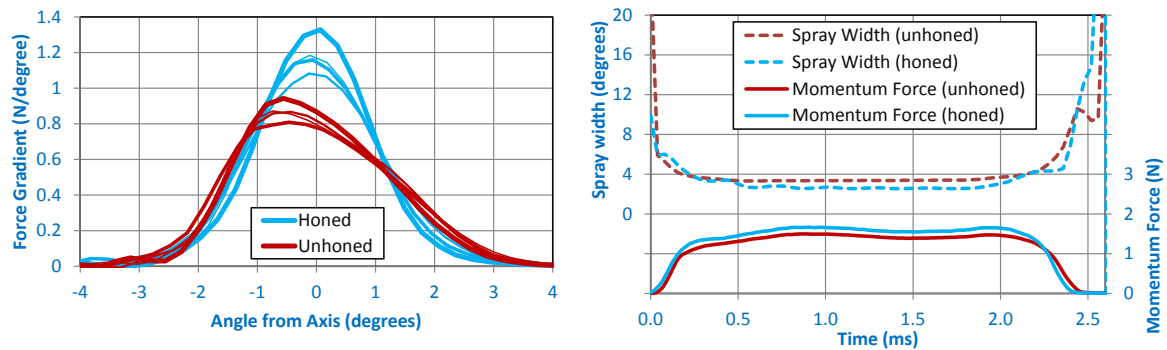


Figure 15: Sensor = 5 mm; z = 10 mm; RP = 1200 bar; BP = 0 bar; various holes shown. (left); Time windowing is used to show how the momentum force, and spray dispersion angle differ between each nozzle and throughout the injection event.

The combustion performance of these same two injectors with honed and un-honed nozzles is given in Figure 16. We note that the C_d effect is a first order effect, and can be seen very clearly in the results. At low loads and low rail pressures, the C_d is similar and the performance is also similar. However, at high loads the C_d is quite different and the honed injector has also a narrower more penetrating spray. These differences impact the available power, both the exhaust temperature and the smoke. The C_d difference can be interpreted as a measure of how efficiently the nozzle converts the rail pressure energy into spray momentum. As such, the performance difference is equivalent to a rail pressure change where a 5% difference in C_d would lead to a ~10% difference in effective rail pressure.

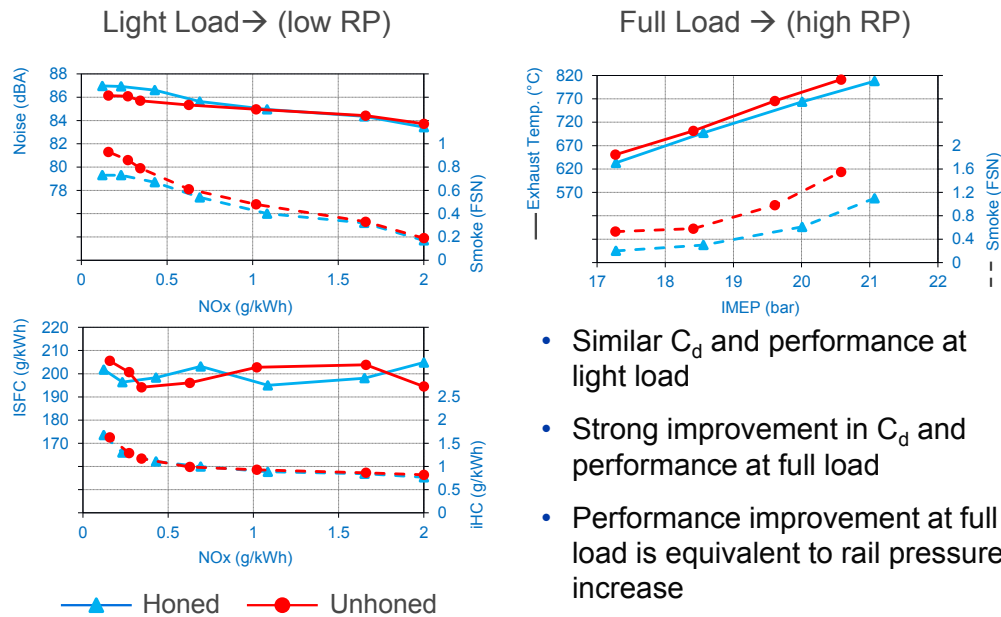


Figure 16: Comparison of combustion results with the honed and un-honed injectors.

7. Conclusions

An experimental and analysis technique has been developed and presented for diesel spray momentum measurement. The influence of various measurement parameters including: sensor size, sensor distance and rail pressure were presented. The technique for measurement and interpretation of high quality data has also been described. The data has also been compared with hydraulic and spray data.

The importance of the momentum measurements in injector design and development were then demonstrated with two analysis tasks comparing different injector designs and different injector nozzle designs. The momentum measurement technique was capable to differentiate between the injector and nozzle designs. Notably, it shows unique capabilities to investigate the diesel spray structure, in a vertical plane and to investigate the evolution of this structure with time throughout an injection event.

It is expected that this new momentum measurement technique will prove highly useful in Delphi's continuing efforts to develop and improve diesel fuel injection equipment to meet the challenges of customer performance and an increasingly stringent regulatory environment.

References

- [1] J. M. Desantes, R. Payri, F. J. Salvador, J. Gimeno.; Measurements of Spray Momentum for the Study of Cavitation in Diesel Injection Nozzles; SAE2003-01-0703.
- [2] J. M. Desantes, R. Payri, F. J. Salvador and J. Gimeno; Prediction of Spray Penetration by Means of Spray Momentum Flux; SAE2006-01-1387.
- [3] Godfrey Greeves, Gavin Dober, Simon Tullis, Nebojsa Milovanovic and Stefan Zuelch; Nozzle Momentum Efficiency Definition, Measurement And Importance For Diesel Combustion; ILASS 2008; Sept. 8-10, 2008, Como Lake, Italy; ILASS08-A033.
- [4] Lucio Postrioti, Francesco Mariani, Michele Battistoni and Alessandro Mariani; Experimental and Numerical Evaluation of Diesel Spray Momentum Flux; SAE2009-01-2772.
- [5] J. Ernst; T. Hergemoeller; F.P. Gulde; Analysis of Diesel Spray Momentum in the Near Field of the Nozzle; Diesel Powertrains 3.0, Montabaur, October 28-29, 2014.
- [6] C. Ungaro; A. Mariani; In-depth investigations of diesel injectors by means of spray momentum measurements for tailored analysis and further optimization; Diesel Powertrains 3.0, Montabaur, October 28-29th 2014.
- [7] Lai M., Wang F., Xie X., Shi J., Dober G., Guerrassi N., Meslem Y., "Correlating the Nozzle Flow to Spray and Primary Breakup using Visualization and Multi-phase Simulation," in SIA, Rouen, France, 2014.

The Authors:

Dr.-Ing. Gavin Dober, Delphi Automotive Systems, Luxembourg

Dipl.-Ing. Christophe Garsi, Delphi Automotive Systems, Luxembourg

Dr.-Ing. Nouredine Guerrassi, Delphi Automotive Systems, Luxembourg

Dipl.-Ing. Thomas Leonard, Delphi Automotive Systems, Luxembourg

Licence:

This document is licensed under the Creative Commons Attribution 3.0 DE License (CC-BY 3.0 DE): <http://creativecommons.org/licenses/by/3.0/de/>

Development of an optical sensor for determination of swirl level in diesel engines

Robin Vanhaelst
Jakub Czajka

Abstract:

In this paper the systematic development of an optical swirl sensor to measure the swirl ratio in an operating serial turbocharged DI-diesel engine is described. The optical sensor detects the visible light of the combustion, in particular the emission of the sooting flame in a wavelength range from 600 nm up to 1000 nm. The acceptance angle is so small that the soot clouds from every spray can be detected as they are being turned under the optical sensor by the swirling flow. In a first part the new optical probe method was validated on a transparent engine by comparison with high speed video recordings. In the second part several hardware variations were made on a serial DI-diesel engine which was equipped with a variable swirl valve. The influence of the opened- and closed swirl valve constellation and the piston geometry on the swirl ratio was measured with the optical probe technique. The results were compared with a zero dimensional simulation model.

There was a good agreement between the swirl measurements and the 0D-model. The optical swirl sensor has proven to be a powerful tool to optimise the combustion process. Without any modifications on the cylinder head, the effect of application parameters and hardware parts on the swirl strength can be quantified for all engine loads and speeds

1. Introduction

The importance of the air swirl flow motion on the internal combustion process of the DI Diesel engine has been known since the first engines were built. The exhaust gas emissions and the fuel consumption in DI Diesel engines are governed by the interaction of the swirl flow with the high pressure fuel injection. An improved understanding of the swirl flow field during the combustion process can lead to a better compromise between the exhaust gas emissions and the fuel consumption [1], [2], [3]. The level of swirl can enhance the combustion process in several ways. With a high swirl flow, the rates of air/fuel mixing are increased. This allows shortening the burning duration and a more isochoric combustion, which leads to an improved specific fuel consumption [4]. The higher mixing rates can also cause a reduction in the smoke emissions [5]. In the literature can be found that this is due to a reduced soot formation by the higher mixing rates [6], [7]. Another phenomenon causing lower soot emissions is the enhanced late-cycle oxidation [8]. The higher burning rates, with larger swirl numbers, lead to higher NO_x emissions. A high swirl combustion system has a higher egr tolerance and is therefore a good compromise in relation to NO_x- and soot emissions [9].

Several physical mechanisms by which a swirl flow can influence the entire combustion process are found in the literature:

1. Improving the early air entrainment into the injected fuel jet and reducing the spray penetration. The fuel spray is deflected and there is improved overall air utilization with high fuel/air mixing rates [7].
2. Increasing the air flow over- and in the piston bowl and improving the evaporation and mixing rates [10].
3. Increasing the late-cycle turbulence as a result of the stored kinetic energy of the swirl flow. This leads to a better mixing of the burned combustion mixture and residual oxygen in the cylinder [11].
4. During the reversed squish flow period there is an enhanced turbulence generation. The squish is thereby defined as the radially inward gas motion that occurs toward the end of the compression stroke [1].
5. Increasing the in-cylinder heat transfer, thereby lowering the mean gas temperature and increasing the wall heat losses [12].
6. Raising the gas exchange losses at high swirl rates, because of the reduced cylinder mass and increasing the effective fuel consumption [3].
7. Improving the specific power output by an optimal swirl application at full load [3].

The optimal swirl level in every load point is required to fulfil present and future legislative requirements.

The DI Diesel engine used for the measurements is equipped with a variable swirl valve, which allows varying the swirl intensity. When the swirl valve is closed, only the tangential intake port is through-flown and a very high swirling flow is induced. The swirl valve can be opened continuously. When both intake ports are open, only a low swirl is generated. In figure 1 the egr-trades for the load point at 1500 rpm and a mean effective pressure of 3 bar, which is characteristic for the first phase in the European driving cycle, for different swirl valve positions are shown. In the NO_x-soot trade on the left side of figure 1, the immense influence of the swirl valve position can be seen. The soot emissions can be reduced from 1,1 to 0,18 at a NO_x level of 50 ppm by closing the swirl valve. The hydrocarbon and carbon monoxide emissions increase by closing the swirl valve. The specific fuel consumption shows little reaction by closing the swirl

valve, only at the completely closed swirl valve position there is a very large increase of the specific fuel consumption. When the swirl valve is closed from the 60°- to the 90°-position and the swirl number after Toppelmann [1] is increased from 0,6 to 0,9, the soot emissions can be reduced from 0,5 to 0,18. The disadvantage of the higher swirl intensity can be seen on the right side of figure 1. The specific fuel consumption is increased by an almost 15 g/kWh. Such deterioration usually leads to a fuel increase of 0,1 l up to 0,3 l in the European driving cycle.

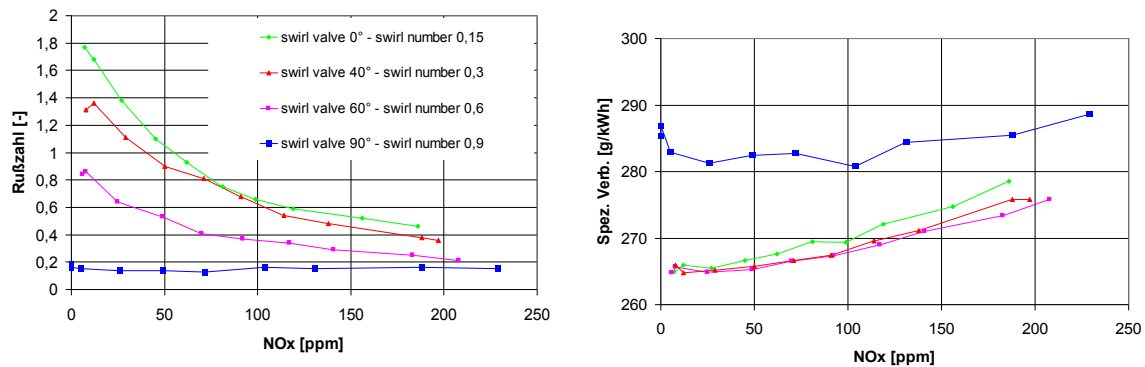


Figure 1: Effect of a swirl and egr variation at 1500 rpm and $p_{me}=3$ bar on the NOx and soot emissions (left side), Effect of a swirl and egr variation at 1500 rpm and $p_{me}=3$ bar on the NOx emissions and the specific fuel consumption (right side)

These measurements show the conflict between the reduction of the exhaust gas emissions and fuel consumption. Therefore, new measurement methods which allow detailed insights in the governing processes are needed. A contribution to this demand is the development of the so called “optical swirl sensor”.

2. Definition and mathematical modelling of the swirl ratio

Swirl measurements have become an established process in the development of diesel engines. Usually, the swirl flow induced from the intake ports of a cylinder head is determined. The charge motion in the cylinder is very complex. Simplified it can be described by the swirl or tumble number. The model presented in this article computes the swirl development during the induction stroke. It also calculates the swirl modification during the compression stroke. The model considers the influence of the camshaft (valve lift timing), the crankshaft kinematics and the piston bowl geometry. This allows a comparison between measured and simulated swirl numbers.

2.1 Swirl Measurement

Steady state test rigs are used for swirl measurement. A common technique uses a paddle wheel mounted on the cylinder axis. The measured quantity is the rotation speed of the paddle.

Another possibility is to use an impulse swirl meter to determine the total torque induced in the cylinder. This technique has superseded the paddle wheel and is therefore used to give the start values for swirl computation during induction stroke.

[1] In general, the swirl number is defined as:

$$D = \frac{\varpi_{air}}{\varpi_{engine}} = \frac{\varpi_{air}}{2 \cdot \pi \cdot n} \quad (1)$$

Since the engine speed n is known, one has to compute the angular velocity ϖ_{air} . With the assumption of a solid body rotation, the angular velocity can be written as:

$$\varpi_{air} = \frac{2 \cdot M}{\dot{V} \cdot \rho \cdot r^2} = \frac{8 \cdot M}{\dot{m} \cdot d^2} \quad (2)$$

In general, the result of a swirl measurement is the torque which is also dependent of the valve lift. In order to model the swirl generation in the cylinder with more accuracy, the torque and the mass flow rate values have to be determined for the complete valve lift curve. To do so, equation (2) has to be changed in:

$$\varpi_{air} = \frac{8}{d^2} \cdot \frac{\int_{IVO}^{IVC} M \cdot d\alpha}{\int_{IVO}^{IVC} \dot{m} \cdot d\alpha} = \frac{8}{d^2} \cdot \frac{\sum_{IVO}^{IVC} M \cdot \Delta\alpha}{\sum_{IVO}^{IVC} \dot{m} \cdot \Delta\alpha} \quad (3)$$

During the compression stroke it is possible to model the swirl evaluation with or without friction losses. For simplification the following derivations neglect friction. Then, the conservation law of angular momentum yields:

$$\begin{aligned} \frac{dL}{dt} &= 0 \\ L &= const. \end{aligned} \quad (4)$$

The angular momentum L is defined as:

$$\begin{aligned} L &= J_{air} \cdot \varpi_{air} = const. \\ J_1 \cdot \varpi_1 &= J_2 \cdot \varpi_2 \end{aligned} \quad (5)$$

Since the charge motion is modelled without friction, there is no change in angular momentum. The angular velocity increases because the moment of inertia of the rotating air is decreasing as the piston moves from bottom dead centre to top dead centre. Therefore, we have to compute, the change of inertia over the crank angle from BDC to TDC.

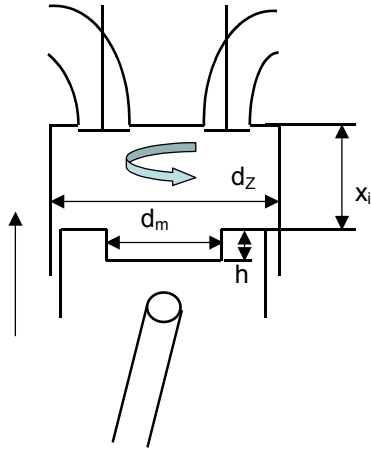


Figure 2: Swirl modification during compression stroke

The moment of inertia of the rotating air according to the figure 2 becomes:

$$J_i = J_{BDC} \cdot \frac{\frac{x_i}{h} \cdot \left(\frac{d_m}{d_z}\right)^4}{\frac{x_i}{h} \cdot \left(\frac{d_m}{d_z}\right)^2} \quad (6)$$

Figure 3 shows the swirl evaluation during induction and compression stroke. From BDC to TDC the moment of inertia changes with the factor $(d_m/d_z)^2$. Therefore, the angular velocity ω_{air} increases by the factor $(d_z/d_m)^2$. In an operating engine the observed increase in swirl is less due to wall friction and other factors.

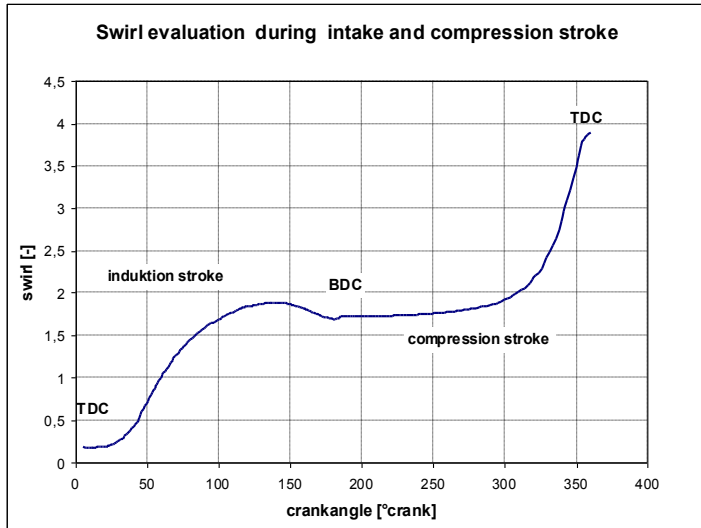


Figure 3: Computed swirl number during induction and compression stroke

In the future the model will consider wall friction during compression stroke. Under this condition equation 4 becomes:

$$\frac{dL}{dt} = -M_r \quad (7)$$

Looking at equation 6 the angular momentum is no longer constant. The friction moment has to be calculated with respect to the time. The transformation of equation 6 leads to:

$$\begin{aligned} \frac{d(J \cdot \varpi)}{dt} &= -M_r \\ J_i \cdot \varpi_i &= -\int M_r \cdot dt + J_{i+1} \cdot \varpi_{i+1} \end{aligned} \quad (8)$$

This equation has to be solved iterative, because the term M_r depends on the angular velocity (ϖ).

3. The optical swirl measurement system

The optical swirl measurement system is derived from the Kistler 2-color method system, which is available on the market [13]. The system is adapted to measure the swirling flow in the combustion chamber.

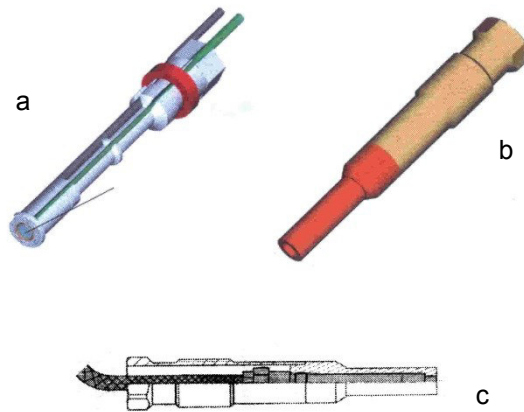


Figure 4: The optical swirl sensor: (a) optical fibre with quartz glass window; (b) adapter; (c) the sensor mounted in the adapter

The technical specifications of the components are described in [14]. The swirl sensor operates motionless and doesn't interfere with the combustion process. The miniaturised optical sensor shown in figure 4a is mounted in an adapter (figure 4b) and placed in the glow plug bore of the engine and replaces the standard glow plug. The complete measurement system is shown in figure 5. The measurement system consists of a front end quartz glass lens (a) and an optical fibre (b) to lead the light to an optical detector unit (c). The optical detector unit is a photo diode which transforms the emitted light intensity into an electrical current. This signal is recorded by the data acquisition system Indicom (d). The optical sensor detects the visible and near infrared light of the combustion, in particular the emission of the sooting flame in a wavelength range from 600 nm up to 1000 nm.

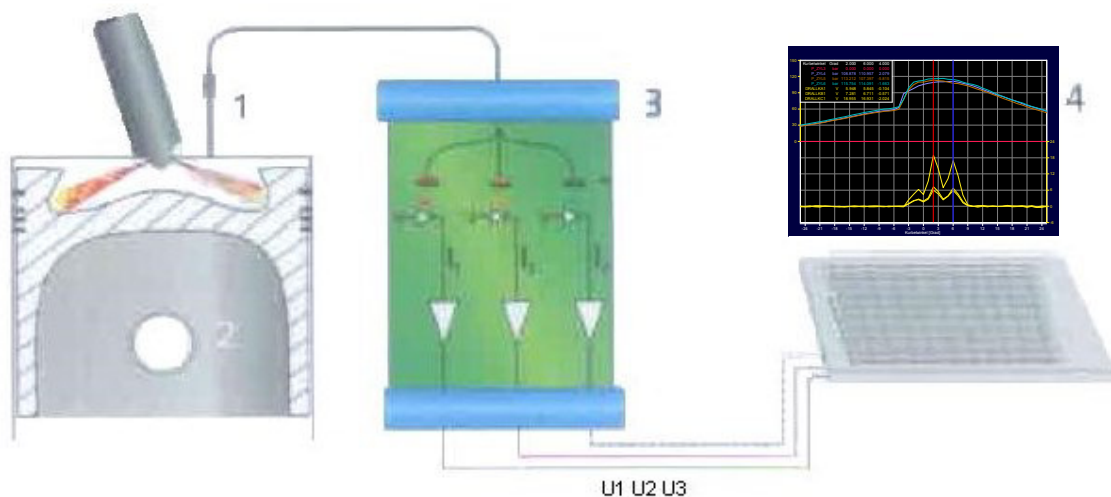


Figure 5: The optical swirl system with (a) swirl sensor; (b) optical fibre (c) optical signal amplifier; (d) data acquisition system

The acceptance angle had to be reduced to an absolute minimum. In this way it is possible to correlate a signal intensity peak with a single sooting coil. The design of the optical glass lens in combination with a suitable adapter allowed realising an acceptance angle of about 1 degree.

The system was adapted in order to obtain the maximum light intensity of the sooting flames. Therefore, the optical filters of the standard system were removed and the broadband light emissions in the visible range were captured. The signal intensity could be increased significantly in this way.

Due to the small acceptance angle the soot clouds from every spray can be detected as they are being turned under the optical sensor by the swirling flow. At high swirl, the single-cycle signal trace shows a high first maximum during the flame development and two or three succeeding smaller relative maxima when the soot clouds from windward neighbouring sprays pass the detection cone of the sensor.

In the figure 6 an image of the combustion chamber shows the sooting flames, the sensor position, the geometric angle between the coils and the swirl direction. The single sooting spray coils, who have there origin in the injector nozzle holes, can be seen very clearly.

The sooting flames are detected as they pass the narrow observation area of the optical sensor. The emitted light intensity increases rapidly, as the sooting flame passes the detector.

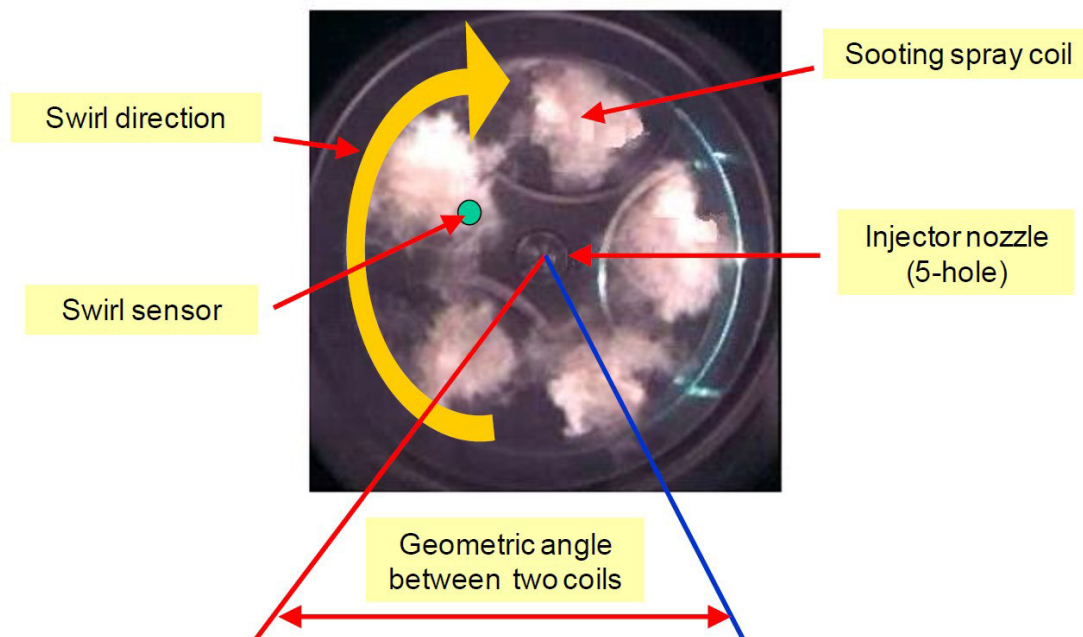


Figure 6: Image of the combustion chamber showing the sooting flames, the sensor position, the geometric angle between the coils and the swirl direction

Since the light intensity is proportional to the current, a peak in the measured signal trace can be observed. When more than one burning spray coil passes the detector, more peaks are detected. With the aid of the high resolution data acquisition system the time lap for two coils to pass the swirl sensor can be recorded, this is shown in figure 7.

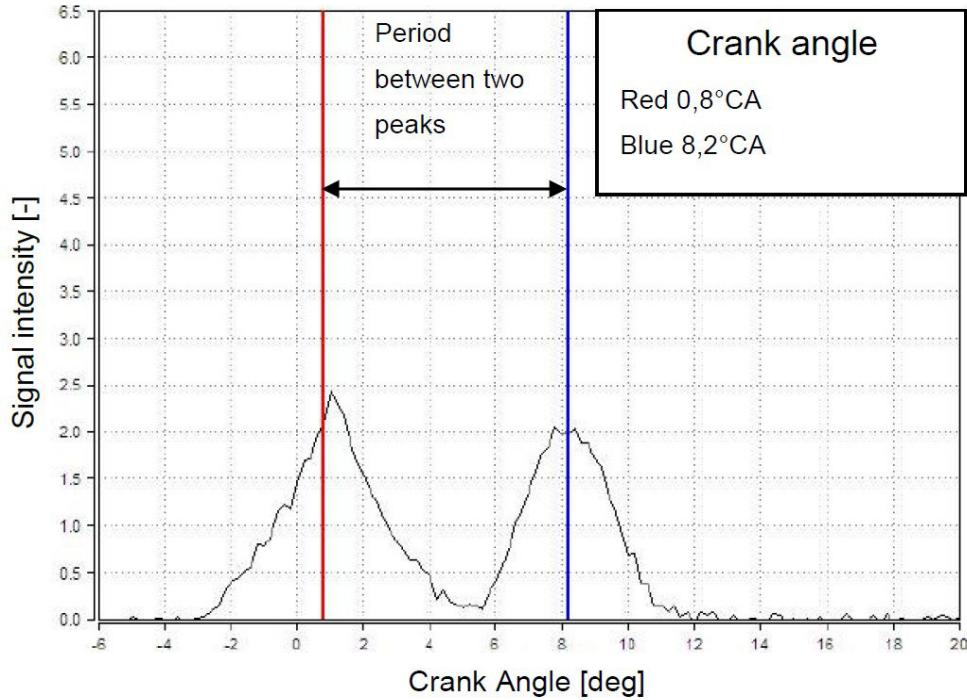


Figure 7: The measured signal of the optical swirl sensor with the time period between the two signal peaks

When the time period between two signal peaks is known, as well as the geometric angle between the spray coils, then the swirl ratio can be calculated by the equation:

$$S = \frac{\omega_s}{\omega_E} = \frac{\text{geometric angle between the injector holes [deg]}}{\text{time period between two peaks [deg]}} \quad (9)$$

The geometric angle between the coils is a production feature of the injector nozzle and can be determined from the construction drawings.

4. Validation of the swirl sensor on an optical engine

The optical probe system has been validated on an “optical engine”, an engine with optical access to the combustion chamber via a quartz glass window in the bottom of the piston bowl and by a mirror inserted into the piston from the side. The principal design of the optical DI-diesel engine was outlined in more detail in a previous paper by Hentschel [15]; the validation procedure should be described here just briefly. For a deeper view on the validation results refer to Hentschel et al. [16] or Czajka et al. [17].

Different optical techniques have been used to analyse the development of the in-cylinder swirl flow. Firstly, a particle image velocimetry (PIV) system was applied to the research engine and the swirl flow development during intake and compression stroke was measured. The engine was motored and the measurements were performed in a plane parallel to the cylinder head and about 10 mm below it. Measurements close to TDC were not possible later than 30 deg CA before TDC because at that time, due to compression, the temperature inside the combustion chamber was so high that all types of oil seeding evaporate. The field of view is located above the piston crown and contains both the piston bowl and part of the squish area. PIV was used to analyse the in-cylinder intake flow and the development of the swirl on a cycle-averaged basis. [17] As shown on the left side of figure 8 a well-defined swirl flow field is developed at 90 deg CA before TDC. It looks very similar to a solid body rotation.

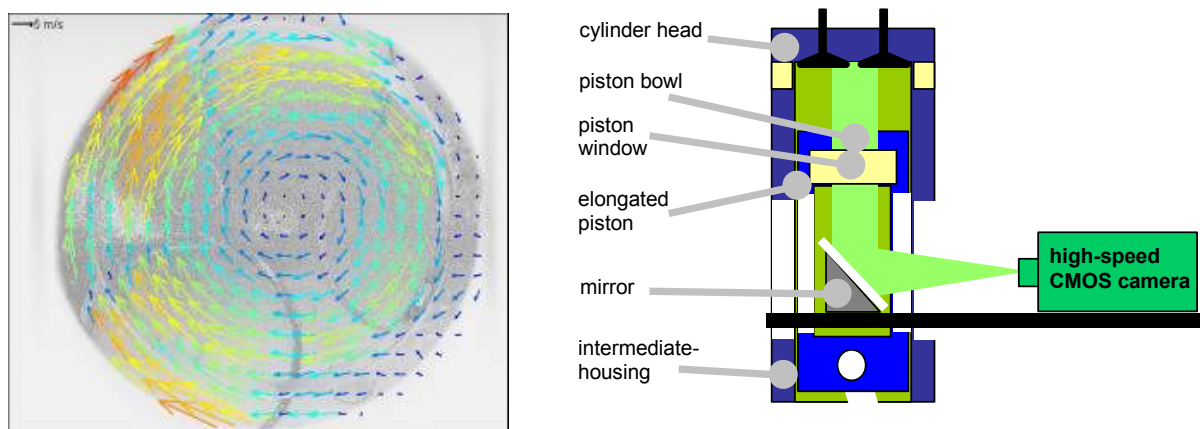


Figure 8: Fully developed swirl flow during compression stroke (left side), setup for high-speed video measurements on the DI diesel engine (right side)

Secondly, a high-speed video (HSV) technique with a framing rate of one frame per deg CA of the engine is applied to record both the flame propagation and the movement of soot clouds in the swirl flow inside and above the bowl-shaped combustion chamber. The setup for HSV is sketched on the right side of figure 8. A modern colour HSV CMOS camera with a high spatial and temporal resolution was used to get one frame per deg CA at the required engine speeds. A typical sequence of HSV frames taken in a single engine cycle is shown in Figure 9. Every second frame of the video sequence has been skipped in the presentation. The influence of the in-cylinder swirl on the movement of the soot clouds can be clearly seen.

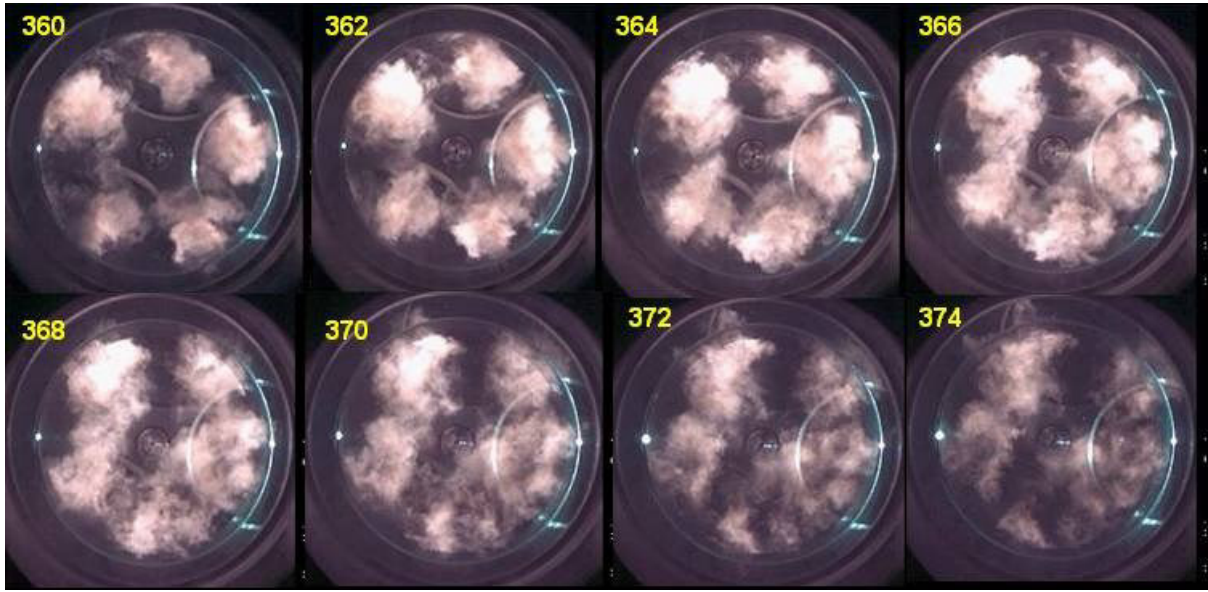


Figure 9: HSV frames of swirling soot clouds in the engine cylinder 5-hole injector; numbers indicate °CA; 360°CA=TDC

For a clearer separation of the flame clouds, a 5-hole injector was used for this visualisation. Succeeding frames are evaluated two-by-two by a full-field correlation in a polar-coordinate system to achieve the characteristic number of the swirl strength and its development during a single combustion cycle. Evaluation of the images is meaningful after auto-ignition and first flame development have finished and the resulting soot clouds move in the swirling flow field. At the end of combustion, about 40 deg CA after TDC, the soot is oxidised or cooled down and is no longer visible. The accuracy of this procedure is high enough to resolve even the light decrease in swirl strength during the engine cycle after TDC.

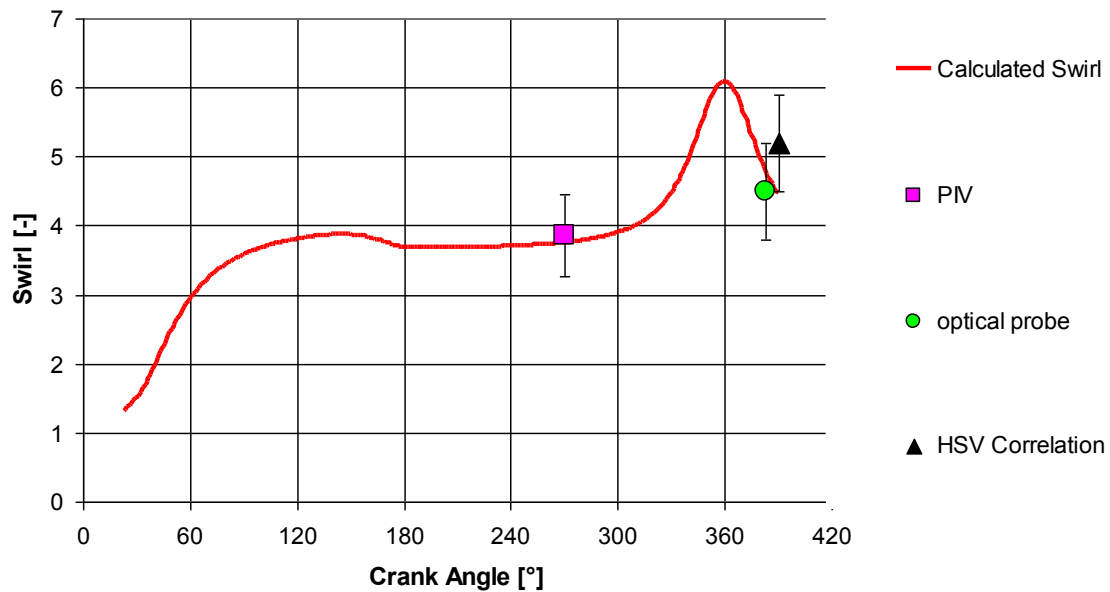


Figure 10: Swirl flow development in an optical engine at 1200 rpm numerical simulation and data achieved by different experimental techniques

In the figure 10 the three swirl results from the different optical measuring techniques, i.e. PIV, HSV and optical probe, are summarised. The simulated swirl ratio for every crank angle position is also included in the figure 10.

The real swirl in the cylinder differs from the solid-body-type swirl assumed for the HSV correlation evaluations. The position of the optical probe is defined by the glow plug bore. At this location, the tangential flow component is slightly lower compared to the cylinder-averaged flow velocity. The positive results on the optical engine confirmed the functionality of the optical swirl sensor.

5. Experimental results

After a thorough validation of the optical swirl sensor on the optical engine, the sensor was applied on a full serial turbocharged DI-diesel engine.

The injection system is a common rail system with rail pressures up to 1600 bar, and the nozzle used is equipped with 8 injection holes. The engine was equipped with a variable swirl valve in the spiral intake port.

When the swirl valve is opened, both ports (the spiral- and tangential port) are flown through. This leads to a high flow charge coefficient and a low swirl number.

By closing the variable swirl valve, the intake charge is forced to flow through the tangential intake port, causing a higher swirl number.

Since only one intake port is being operated, the charge coefficient is reduced in this case. The behaviour of the cylinder head was measured on the Tippelmann test rig, the results are shown in figure 11:

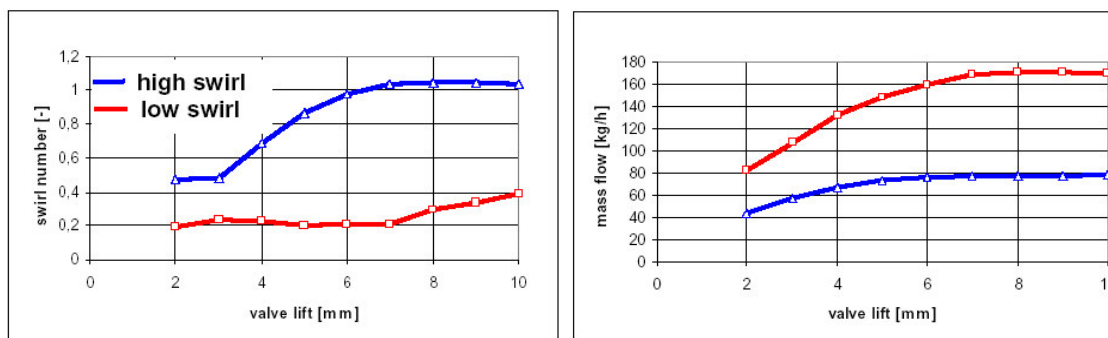


Figure 11: Swirl number of the cylinder head from the steady-state Tippelmann test rig; blue line: high swirl case, red line: low swirl case (left side), Mass flow of the cylinder head from the steady-state Tippelmann test rig; blue line: high swirl case, red line: low swirl case (right side)

5.1 Influence of the injector

The optical swirl sensor has to deliver plausible results under all operating conditions. This means that the optical peak to peak signal has to be a measure for the swirl flow in the top dead center. It is expected that the injection affects the swirl only weakly. Only in that case the optical method to measure the swirl and the tangential velocity in an operating engine is robust enough for multiple application purposes. A possible way to investigate this behavior is by setting the (swirl) air system as a constraint and by varying the injector properties [19].

The table 1 shows the injector variants which were chosen to examine the influence of the injection rate on the swirl flow.

Number of Holes	Qhyd [cm ³ /60s]	ks-Factor	Hole Diameter [μm]
8	900	2,5	145
9	500	5	90
10	700	5	95

Table 1: Injector variants for the measurements

The k factor of an injector nozzle is defined as $k \equiv \frac{D_I - D_E}{10}$ where D_I is the nozzle inlet diameter and D_E is the nozzle exit diameter in microns. The symbol s states that the inlet holes are rounded by a hydro-erosive fluid. The operating point was at 1500 1/min and a mean effective pressure of 6,3 bar without egr. The injected fuel mass was about 20 mg. The start of injection for the three injectors was 12° before the TDC with a rail pressure of 800 bar. The injectors with 8 and 10 holes were also measured in a high pressure chamber with similar ambient conditions as in the TDC of a serial engine. This means with the same pressure (80 bar) and temperature (900 °C) boundaries. A fragment of the experiment is shown in Figure 12:

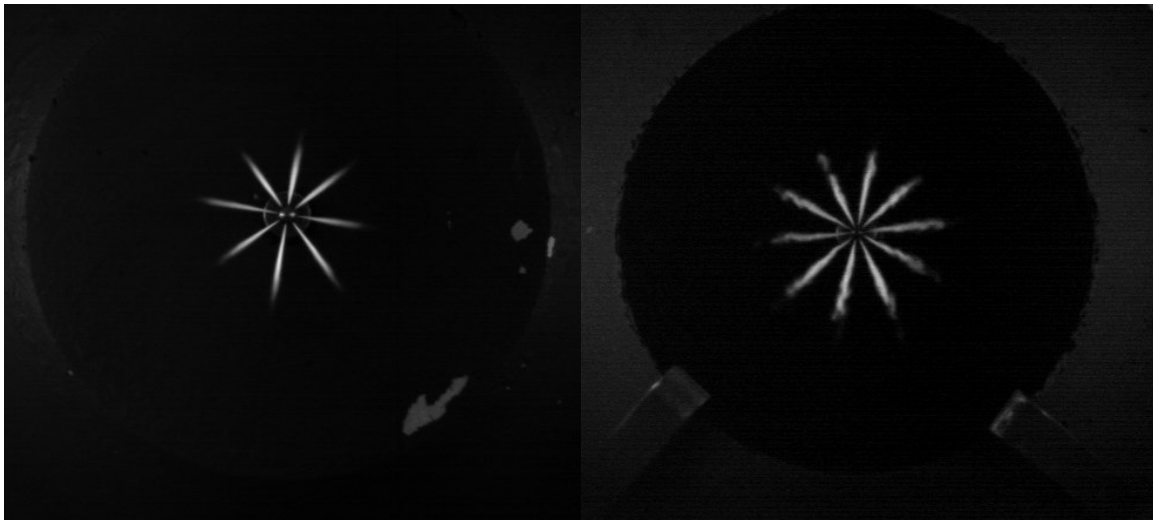


Figure 12: high pressure chamber images for an injected fuel mass of 20 mg at a rail pressure of 800 bar in a nitrogen surrounding atmosphere of 80 bars and 900°C for an 8-hole injector (on the left) and a 10 hole injector (on the right).

The high speed images of the pressure chamber show the significant differences between the two injectors. The physical processes as the liquid atomization, the droplet break up, the droplet-droplet interaction, the droplet size distribution, the droplet evaporation are responsible for the different spray penetrations and spray outlines of the 8- and 10-hole injector in Figure 12. This measurement shows very impressively how different the spray characteristics of the examined injectors are.

The measurements at the full serial engine, equipped with the optical swirl sensor are shown in Figure 13. The first measurement was made for the closed swirl valve constellation. For an 8 hole injector the spray angle is 45 degrees, for the 9 hole injector the spray angle is 40 degrees and for the 10 hole injector the spray angle is 36 degrees. Other properties as the hydraulic mass flow, the ks-factor and the hole diameter are not required for the calculation.

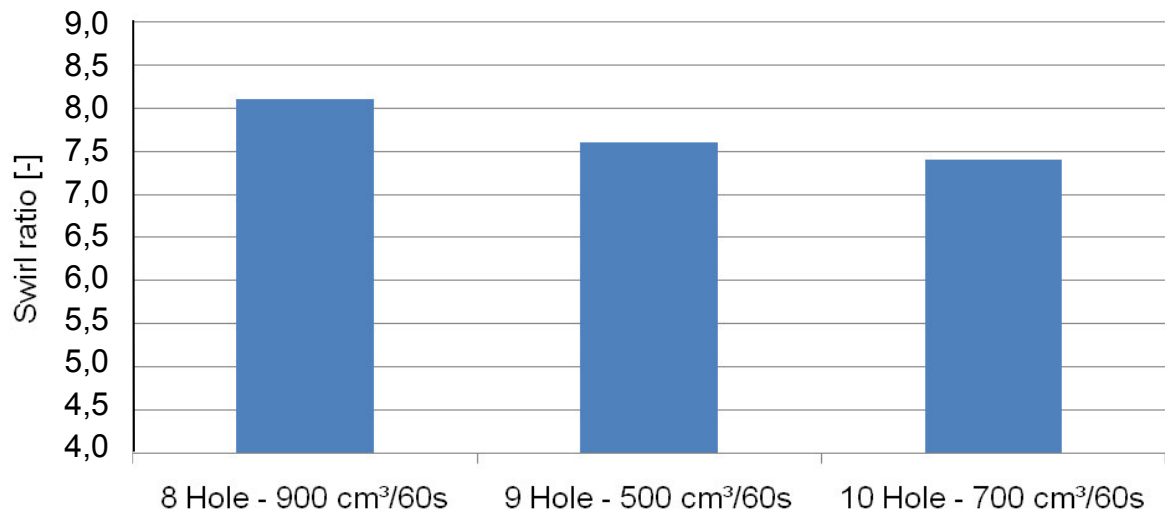


Figure 13: Measured swirl ratio with the swirl sensor for the investigated injectors of table 4 for a closed swirl valve.

From the Figure 13 can be seen that the injector type properties can have no significant influence on the flow field in the top dead center. The swirl numbers are all in the same measuring swirl ratio range of $7,5 \pm 1,0$.

The same measurements were made for an opened- and a half opened swirl valve positions. The results are shown in figures 14 and 15:

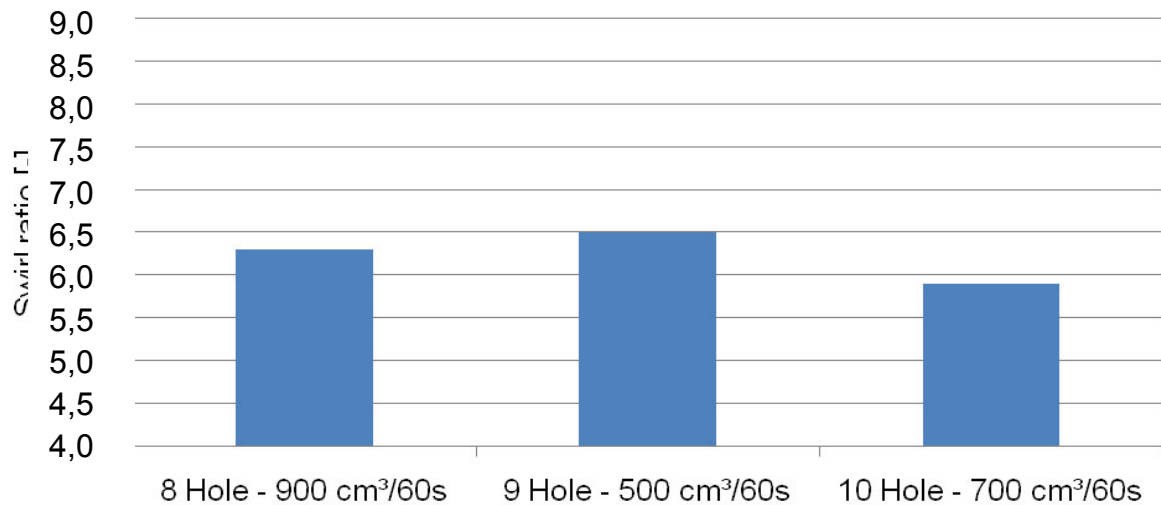


Figure 14: Measured swirl ratio with the swirl sensor for the investigated injectors of table 1 for a half opened swirl valve (45°).

Also at a half opened swirl valve the swirl ratio is only weakly influenced by the injector characteristics. The swirl ratio in Figure 14 lies for all the injectors in the range of $6 \pm 1,0$.

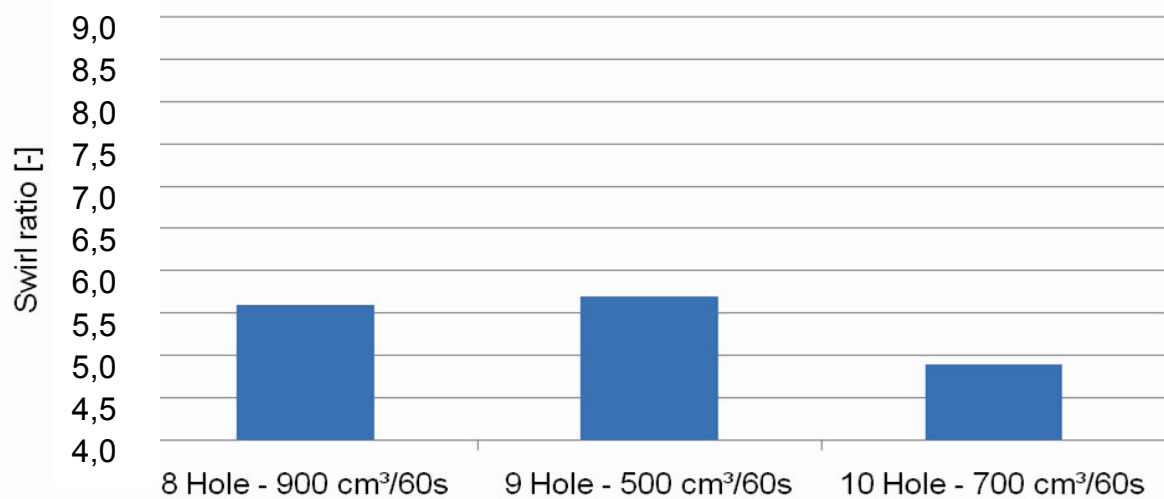


Figure 15: Measured swirl ratio with the swirl sensor for the investigated injectors of table 4 for a closed swirl valve (45°).

The measured swirl ratio for an opened swirl valve constellation is, as in the last cases, nearly independent of the injector or spray coil properties. This can be deduced from the Figures 13, 14 and 15.

The spray of a high pressure injection has a very high turbulent kinetic energy. The air flow velocities are very low in comparison to the droplet velocities in the injected fuel spray. During the injection period, the air flow field is disturbed. This was also observed and measured in [20]. The measurements with the optical swirl valve show very clearly, that after the injection period the swirl air flow is preserved. The measured swirl intensity in the TDC is not influenced by the way the fuel is injected in the combustion chamber. The hole number, the hydraulic flow, the ks-factor cause a completely different droplet penetration, droplet size distribution. The course of the turbulent kinetic energy is for the three injector variants completely different. As soon as the injection is terminated the turbulent kinetic energy decays rapidly. After this point the evaporated droplets, the combustion mixture and the observed sooting flame follow the swirl air flow field.

This experiment with different injector nozzle geometries delivers the essential proof that the air flow field is sufficiently independent of the injection quantities. That means that the optical swirl sensor, which detects the rotation of the sooting flame, is a suitable measurement technique to determine the swirl ratio in an operating engine.

5.2 Influence of the piston bowl geometry

The design of the piston bowl has also an influence on the swirl ratio in the TDC. It is generally accepted that a smaller piston bowl diameter increases the swirl ratio at the TDC. This knowledge can be gained from 0D- and 3D-simulation.

The optical swirl measurement technique allows measuring the influence of different piston bowl geometries on the swirl ratio in a real operating engine. Therefore, three piston variants were operated in the turbocharged DI-diesel engine.

The sensor was mounted in the glow plug bore, without any mechanical changes of the cylinder head. The technical drawings of the pistons are shown in the figures 16, 17 and 18:

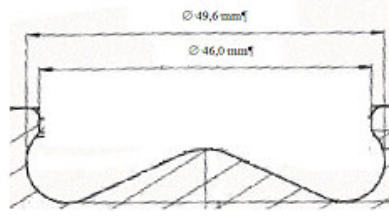


Figure 16: Piston bowl geometry A, with a piston bowl diameter of 49,6mm and a piston bowl neck diameter of 46mm

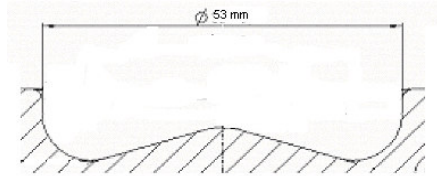


Figure 17: Piston bowl geometry B, with a piston bowl diameter of 53 mm

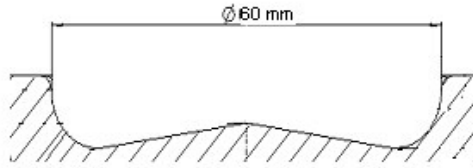


Figure 18: Piston bowl geometry C, with a piston bowl diameter of 60 mm

The three piston bowls were investigated on the same engine at 1500 rpm and 6,2 bar mean effective pressure, without egr and a start of injection of 12° before the TDC. The swirl valve position was varied for the three pistons from completely closed to completely opened.

The rotation air impulse is being compressed from the cylinder diameter to the piston bowl diameter. It can be proven from the equation 6 that the moment of inertia of the charge about the cylinder axis for a bowl-in-piston combustion chamber can be written as [12]:

$$J_i = \frac{m_{cyl} d_z^2}{8} \left[\frac{(x_i / h) + (d_M / d_z)^4}{(x_i / h) + (d_M / d_z)^2} \right] \quad (10)$$

The air mass in the cylinder has an influence on the moment of inertia and is being taken in account by the contribution m_{cyl} . At the TDC the distance to the cylinder head is zero. The equation can therefore be reduced to:

$$J_{TDC, x=0} = \frac{m_{cyl} d_z^2}{8} \quad (11)$$

According to this equation the swirl ratio in the TDC will drop about 24% with the 53 mm (piston bowl B) in comparison to the piston with a bowl diameter of 49,6 mm and a neck diameter of 46 mm (piston bowl A). The swirl ratio of the variant 3, with piston bowl diameter of 60 mm, will decrease about 42%.

The problem with the equation 10 is that the actual piston bowl geometry as designed in figure 15 cannot be taken in account, because only one value is considered for the piston bowl – and piston bowl neck diameter.

The measurement results of the three piston variants are shown in the figure 19.

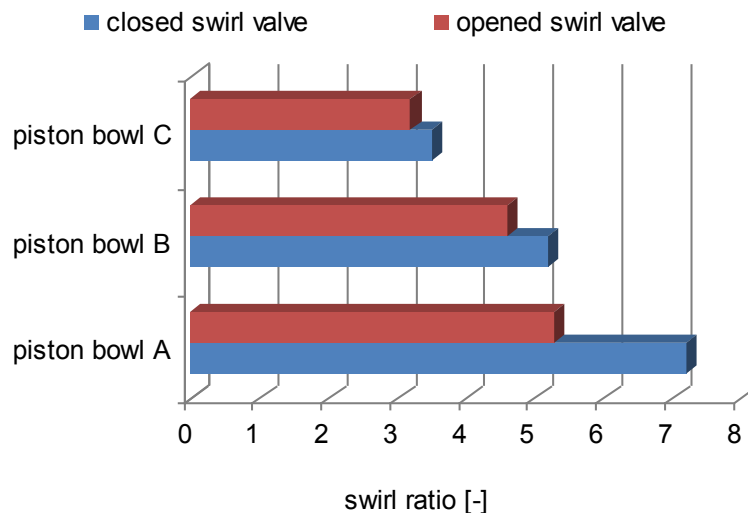


Figure 19: Measured swirl ratios for three different pistons with an opened and a closed swirl valve constellation

The measurements shown in the figure 19, confirm the predicted decrease of the high swirl ratio when the piston bowl diameter is enlarged. By increasing the piston bowl diameter from 49,6mm to 53mm, the swirl ratio is reduced from 7,2 to 5,2. This is a decrease of about 28%, predicted was a swirl reduction of 24%. Considering the measurement tolerances and the plain 0-Dimensional model, this is a good approximation. The swirl ratio is ratio is reduced from 7,2 to 3,5 between the piston bowl geometries A and C, this represents a reduction in swirl ratio of about 51%. The equation 10 derived a prediction of 42%. The same measurements were made for the low swirl case with an opened swirl valve. As expected the swirl ratios in the figure 19 are lower than those of the closed valve measurements. Also the drop of swirl ratio between the variants is smaller than in the case above. Between the piston bowl geometries A and B the swirl ratio is reduced by 13% and between the geometries A and C by 31%. It can be observed, that in the low swirl case the measured drop in swirl ratio is lower than the predicted values. In the high swirl case the decay of swirl ratio is higher than calculated by equation 10. This could be explained by the simplification of the 0D-models, where the dissipation effects are neglected. Another factor which can lead to inaccurate results are the boundary conditions of the input data in the 0D-model. The Tippelmann test rig delivers mass flow and swirl number under steady state conditions. The 0D-model uses this information together with the valve lift timing to calculate the in-cylinder-mass and the rotation impulse. All the instationary gas flow effects as pressure waves in the intake system, the real boost pressure, turbulent intake flow effects, etc. are neglected.

6. Conclusion

The exhaust gas emissions and the fuel consumption in DI-diesel engines is governed by the interaction of the swirling flow with the high pressure fuel injection. An improved understanding of the swirling flow field during the combustion process can lead to a better compromise between the exhaust gas emissions (i.e. soot, NO_x, HC and CO) and the fuel consumption

It is generally accepted that the piston bowl geometry and the swirl valve position influence the swirl ratio of a DI-diesel engine. The effect of these variations can be modelled with a 0D or 3D model. In these models numerous assumptions, for example the estimation of the turbulence factor, the friction coefficient, have to be made. The validation of such empirical factors is made on special steady state test rigs or on optical engines.

The goal of this work is to develop a measuring technique to determine the swirl ratio in a full serial DI-diesel engine. The result is an optical swirl sensor which can be easily mounted on a series production engine by just replacing the glow plug.

In the validation experiments the formation of the swirl flow in the cylinder during the compression stroke and the swirl strength during the combustion process have been analysed by means of different optical methods, PIV, a HSV correlation method, and the optical probe technique. The methods complement each other. PIV measurements have been performed during the intake and compression stroke, but not later than 30°CA before TDC. The application of the HSV correlation method and the optical probe technique are restricted to the combustion phase when bright soot clouds are present. For PIV and HSV correlation an optical engine with large scale optical access to the combustion chamber is required. The validation results have shown that the optical probe is well suited to measure the in-cylinder swirl during combustion.

In this work the influence of the swirl valve position and the piston bowl geometry in a full DI-diesel engine on the swirl strength is examined. For the piston bowl variation there was a good correlation between the 0D model and the optical swirl results.

The 0D model was not fully able to reproduce the measurements of the low swirl case. The optical swirl measurement system allows detecting the inaccuracies in the 0D model and gaining deep insights in the tangential flow field during the combustion phase.

The system can be used to study the influence of hardware parts and engine applications on the swirling flow in a DI-diesel engine. These results allow achieving an optimised configuration in relation to the raw exhaust gas emissions and fuel consumption.

The swirl sensor has been found to be a powerful tool to optimise the swirl strength in the development process for future low emission DI-diesel engines.

7. Acknowledgements

The Authors would like to thank Dr.-Ing. Dieter Karst of the Fa. Kistler Instruments for his contribution and efforts to adapt and optimise the measurement technique for optical swirl measurements. We would also like to thank Dr. rer. nat Werner Hentschel, Dipl.-Ing. Christian Müller, Dipl.-Ing. Bernd Hahne, Dr.-Ing. Emanuela Montefrancesco, Dr.-Ing. Gerhard Ohmstede, Dipl.-Ing. Stefan Schmerbeck, Dipl.-Ing. Gerald Block of the Volkswagen R&D and Prof. Krzysztof Wislocki of the TU-Poznan for their support and the numerous discussions about the internal combustion process.

Nomenclature

CA	Crank Angle
DI	Direct Injection
egr	exhaust gas recirculation
HSV	High Speed Video
IVO	inlet valve opening
IVC	inlet valve closing
m	mass flow rate [kg/s]
m_{cyl}	air mass in the cylinder [kg]
M	total torque [Nm]
M_r	Friction moment [Nm]
PIV	Particle Image Velocimetry
V	volumetric flow rate [m ³ /s]
TDC	Top Dead Center
α	Cam shaft angle
ρ	Density in the cylinder [kg/ m ³]
ω_{air}	Angular velocity [1/s]

References

- [1] Tippelmann G.,
A new method of investigation for swirl ports. SAE Technical Paper Series 770404, 1977.
- [2] Heywood, J.B.
Internal Combustion Engine Fundamentals, McGraw-Hill, 1988
- [3] Vanhaelst, R., Analysis of the swirl flow in DI-Diesel engines, ISBN 978-83-87433-80-2, Ars Nova, Poznan 2014
- [4] Zikoridse, G.
Einspritzdüsen mit variablem Drall – ein vielversprechendes Konzept zur aktiven Beeinflussung der Strahleigenschaften
5. Dresdner Motorenkolloquium, 2007
- [5] Dürnholz, M., Stommel, P.
Untersuchung des Potentials der Brennverfahrensparameter Drall und Einspritzung zur Erfüllung zukünftiger Anforderungen an hochaufgeladene Dieselmotoren mit direkter Kraftstoffeinspritzung
Forschungsberichte Verbrennungskraftmaschinen; Abschlußbericht, FVV, 1999
- [6] Van Gerpen, J., Huang, C., Borman, G.
The effects of swirl and injection parameters on diesel combustion and heat transfer, SAE Technical Paper 850265, 1985
- [7] Binder, K, Hilburger, W.
Influence of the relative motions of air and fuel vapor on the mixture formation processes of the direct injection diesel engine
SAE Technical Paper 810831, 1981

- [8] Zillmer, M.
Stickoxid- und Rußbildung bei dieselmotorischer Verbrennung
Dissertation, Technischen Universität Carola-Wilhelmina zu Braunschweig,
1998
- [9] Timoney, D.J.
A simple technique for predicting optimal fuel air conditions in a direct injection
diesel engine with swirl
SAE Paper 851543, 1985
- [10] Greeves, G., Wang C.H.T., Kyriazis, G.A.
Inlet port design and fuel injection rate requirements for direct injection diesel
engines; VDI-Berichte, No. 370, 1980
- [11] Fansler, T.D., French, D.T.
Swirl, Squish and turbulence in stratified engines: Laser velocimetry
measurements and implications for combustion
SAE Technical Paper 870371, 1987
- [12] Van Gerpen, JH, Huang, C, Motooka, H.
The effects of swirl and injection parameters on diesel combustion and heat
transfer
SAE Technical Paper 850265, 1985
- [13] Kunte S, Boulouchos K, Hentschel W, Kallmeyer F, Cavalloni C, Karst D.
Optical indicating on combustion engines with smallest sensors.
Proc. 10. Symp The Working Process of the Internal Combustion Engine, Graz,
2005.
- [14] Wolter T.;
Optische Dralluntersuchung an einem TDI®, Diploma Thesis, R&D Volkswagen
AG, 2006, in German, not published
- [15] Hentschel W.
Modern tools for diesel engine combustion investigation. 26. Symp (Int) on
Combustion / The Combustion Institute, Naples, pp 2503-2515, 1996.
- [16] Hentschel W., Ohmstede G., Block G., Vanhaelst R., Schmerbeck S., Czajka J.,
Wislocki K., Karst D.
Multiple swirl flow analysis in a direct- injection diesel engine. Proc. 12. Int.
Symp. on Flow Visualization, 10.-14. Sept. 2006, Göttingen
- [17] Czajka J.
Zur Bestimmung des Dralls in Diesel Brennverfahren. Diploma thesis, VW
Wolfsburg / TU-Poznan, 2005, in German, not published.
- [18] Steiger W., Kohnen C.
New combustion systems based on a new fuel
- [19] Boecking, F., Dohle, U.; Hammer, J.; Kampmann, S.
Pkw-Common-Rail-Systeme für künftige Emissionsanforderungen
MTZ 07, 2005, pp. 552-557
- [20] Möser, P., Hentschel, W.
Development of a Time Resolved Spectroscopic Detection System and Its
Application to Automobile Engines
SAE Technical Paper, 961199, 1996

The Authors:

Prof. Dr.-Ing. Robin Vanhaelst, Ostfalia, UAS, Wolfsburg

Dr.-Ing. Jakub Czajka, Poznan University of Technology, Poznan

Licence:

This document is licensed under the Creative Commons Attribution 3.0 DE License (CC-BY 3.0 DE): <http://creativecommons.org/licenses/by/3.0/de/>

Diesel Engine Performance Mapping Using the Stochastic Reactor Model

Michal Pasternak
Andrea Matrisciano
Fabian Mauss

Abstract

A simulation process has been developed for the prediction of Diesel engine performance and exhaust emissions for a wide range of loads and speeds. Engine in-cylinder processes are calculated using a zero-dimensional (0D) probability density function (PDF)-based direct injection stochastic reactor model (DI-SRM). A skeletal chemical reaction mechanism of n-heptane is used for the modelling of hydrocarbon fuel oxidation and emission formation. The locality of turbulence and chemistry interactions, which govern the in-cylinder mixture inhomogeneity, rate of heat release (RoHR) and emission formation in Diesel engines, is accounted for by the modelling of the crank angle dependent mixing time. The predictive character of modelling has been achieved by parameterising the mixing time history with engine design parameters such as speed, load and fuel injection strategy. Thanks to detailed chemistry consideration, the nonlinearity of reaction kinetics that influences on local RoHR and pollutants formation is taken into account. This is beneficial for an accurate extrapolation of the simulations beyond the engine operating points used for model training, and hence, it enables one to simulate complete engine performance maps for combustion progress, exhaust NO_x and indicated mean effective pressure. Low computational cost, insight into the locality of mixture formation along with the detailed chemistry consideration, and the predictive character of simulations are main features of the proposed method

1. Introduction

Besides experimental works, the development of internal combustion engines benefits from numerical simulations. Among the available simulation methods (see, e.g., [[1]-[2]]), various forms of zero-dimensional (0D) models are frequently used. On the one hand, 0D modelling ensures overall simplicity of simulations and low demand for computational cost, which makes the method suitable for various type engine parametric studies. In particular the 0D models are well suited for the simulation of in-cylinder processes within one-dimensional (1D) tools for full cycle performance studies. On the other hand, 0D formulation prevents an accurate modelling of the three-dimensional (3D) character of chemistry and turbulence interactions that characterise the combustion process of Diesel engines. As a consequence, strong local inhomogeneity of the in-cylinder mixture for temperature and equivalence ratio cannot be captured accurately, yielding inhibited prediction of engine exhaust emissions.

In the context of this challenge, as a separate variant of 0D engine modelling can be considered the stochastic reactor model (SRM) [[3]-[5]], which is built on a probability density function (PDF) approach [[6]-[7]]. The distinguishable features of the 0D SRM are (1) the use of detailed chemical reaction mechanisms for the simulation of fuel oxidation and emission formation, and (2) the capability of modelling, in high resolution, the local inhomogeneity of the in-cylinder mixture in species mass fractions and temperatures, which makes the method relevant to represent the effects of non-premixed combustion in Diesel engines. Hence, as far as the representation of the in-cylinder mixture is concerned, the SRM can be located in between quasi-dimensional and 3D computational fluid dynamics (CFD) models.

The specific objectives of the current paper is to introduce a simulation process that is built around the DI-SRM, and is tailor-made for the prediction of Diesel combustion, exhaust NO_x emission, and indicated mean effective pressure (IMEP) at wide range of engine speeds and loads. The paper is organized as follows. After an introductory section, the DI-SRM and the modelling concept of the volume-averaged representative mixing time are described. Subsequently, mixing time parameterisation with known engine design parameters is introduced, which underlays the simulation process presented. Next, simulation results are presented and the performance of the method, along with possible future developments is discussed.

2. Modelling

The modelling is based on the 0D DI-SRM [[5], [8]] employing the crank angle (CA) dependent mixing time model [[10], [12]]. Following these references, in this section are repeated basic information about the DI-SRM for readability of the paper.

2.1 Direct Injection Stochastic Reactor Model

The DI-SRM is a 0D model of physical and chemical processes occurring during the Diesel engine cycle. It is formulated within the PDF approach to turbulent reacting flows [[6]-[7]] that enables the exact treatment of chemical reactions. The DI-SRM considers gas inside the cylinder as an ensemble of notional particles. The particles can mix with each other and exchange heat with the cylinder walls. Each particle has a chemical

composition, temperature and mass, that is, each particle represents a point in phase-space for species mass fraction and temperature. These scalars are treated as random variables and can vary within the cylinder. They determine composition of the gas mixture and are described using PDF distributions. The in-cylinder mixture is thus represented by a PDF in gas-phase space and the particles are realizations of the distributions. The solution for scalars, temperature and species mass fraction is obtained from the PDF transport equation [[14]]. The changes of the PDF are due to (1) chemical reactions, (2) convective heat loss, (3) volume changes due to piston motion, (4) fuel injection, and (5) turbulent mixing. These processes are calculated sequentially using the Monte Carlo particle method [15] with the operator splitting technique [[15]].

2.2 Representative Mixing Time Model

Mixing between particles represents the turbulence effects, and in this work it is modelled based on the coalescence-dispersion (CD) type mixing model [[16]]. The modelling of mixing is reduced to the description of the evolution of particles in the gas-phase to mimic the composition change of real fluid particles due to mixing caused by the turbulence in the turbulent flow. The evolution of particles depends on the mixing model applied, and the history of mixing time. The mixing time governs the intensity of mixing between the particles that in turn decides about the inhomogeneity of the in-cylinder mixture in temperature and species concentration. Hence, the mixing time is responsible for representing the interactions between chemistry of emission formation and turbulent flow. These interactions govern the autoignition process and consequently influence the combustion rate and pollutants formation.

The mixing time is a main input parameter for the DI-SRM, and it must be modelled because 0D models cannot consider for 3D geometry influence on the mixing process. In the present study, the time dependent mixing time model is used. The model distinguishes (for an engine operated with single fuel injection) between four different phases as sketched in Figure 1. The phases are denoted by τ_0 , τ_1 , τ_2 , and τ_3 , and on a crank angle (CA) basis they correspond to different engine in-cylinder processes.

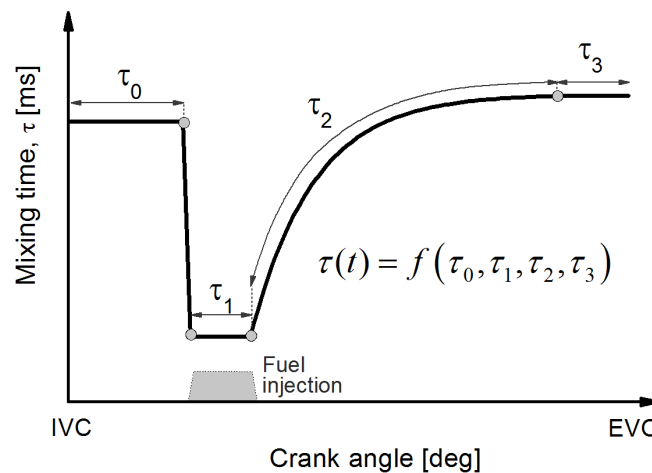


Figure 1: Concept of modelling the volume-averaged mean representative mixing time for the DI-SRM simulations of Diesel engines with single fuel injection

Loosely, the phase τ_0 describes mixing from the intake valve closure (IVC) to start of injection (SOI), the phase τ_1 corresponds approximately to the fuel injection duration, the τ_2 is mainly associated with the diffusive part of combustion, and the phase τ_3 describes the late combustion phase until the exhaust valve opening (EVO). Each phase is considered as a modelled parameter in terms of the duration on CA basis and the value of the mixing time; the slope of the linear functions corresponding to τ_0 , τ_1 , and τ_3 may also change. The τ_2 is modelled as an exponential decay of the form: $\tau_2 \propto \exp(-Bt)$, where t is a time in CAD and B is a constant given as $B = \ln(t_{1/2})$, and $t_{1/2}$ denotes the time needed for the mixing time in τ_2 to reach one half of its final value (before the begin of the τ_3).

Determining mixing times τ_0 , τ_1 , τ_2 , and τ_3 in each section defines the global mixing time (τ) that is treated as a volume averaged representative mixing time and is needed as an input for the DI-SRM.

Besides the mixing time τ_0 , τ_1 , τ_2 , and τ_3 , the presented modelling requires also the determination of start of vaporization (SOV) that influences the anchorage of the entire mixing time profile. In the DISRM used in the present work, the mass of injected fuel is assumed to vaporize instantaneously at the moment of injection and no separate vaporization model is employed [[5], [15]]. This implies the fuel injection discharge curve to represent the vaporisation rate rather than injection rate. Hence, from the modelling point of view, and after the calibration, the SOI becomes the SOV and the EOI becomes the end of vaporisation (EOV). This simplified modelling approach is application tailored. Depending on the conditions inside the cylinder, mainly temperature at the moment of injection, the rate of fuel injection may not necessarily reasonably mimic the rate of fuel vaporisation. For this reason, in this work as a rule of thumb the SOV being derived from the SOI is a calibrated parameter. In practise, the calibration reads to moving the complete injection rate profile towards EVO, until the simulated start of combustion (SOC) matches the targeted value.

2.3 DI-SRM Parameterisation

The turbulent mixing time can be defined as a ratio between the integral length scale of the largest eddies in the flow and velocity fluctuation [26, 27]. Velocity fluctuations and length scales depend on the flow conditions and hence, they are affected by engine geometry and operating conditions such as speed (n), the amount of injected fuel (m_f), pressure under which the fuel is injected, and the start and rate of fuel injection. These are denoted here as *engine design parameters* and are known during the calibration. The parameterisation of the temporal changes of mixing time with engine design parameters should enable the prediction of the mixing time history in advance to simulations. The remaining DI-SRM parameters, such as the number of notional particles (NP), the number of cycles (NC) from which mean-value properties are computed, the time step (Δt), and the stochastic heat transfer constant (C_h) can be estimated before simulations [[8]]. Therefore, mixing time is the only parameter that needs determination for the prediction of engine performances at wide range of operation. The concept is schematically illustrated in Figure 2.

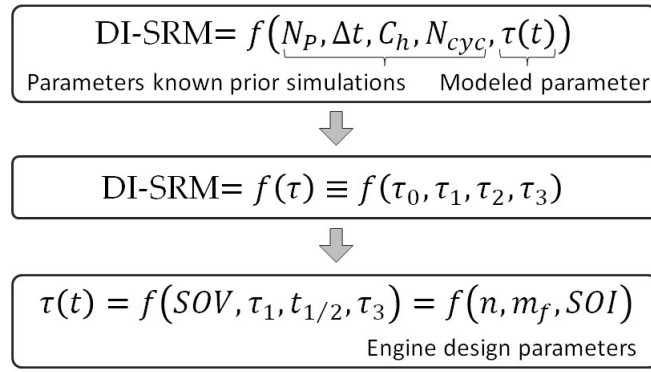


Figure 2: Parameterisation of the DI-SRM for engine performance mapping

For engines operated with single fuel injection further simplifications frequently apply to the derivation of the mixing time history (see, e.g. [[8]]). If τ_0 influences very little the results then it can be assumed to be equal τ_3 . If the engine is operated with short fuel injection then frequently τ_1 can be modelled as constant value linear function. A practical consequence of these assumptions is that the temporary change of mixing time history can be fully determined by optimising only four parameters of the mixing time.

$$\begin{aligned}\tau(s) &\equiv f(SOV, \tau_1, t_{1/2}, \tau_3) = f(n, m_f, SOI) \\ \tau(s) &\equiv f(SOV, \tau_1, t_{1/2}, \tau_3) = f(n, m_f, SOI)\end{aligned}\tag{1}$$

Here, engine speed (n), mass of injected fuel (m_f) and SOI have been selected for correlating to the mixing time (Figure 2). These parameters are henceforth denoted as engine design parameters. The effects of fuel injection pressure p_{inj} , which also has a strong impact on fuel air mixing, has been indirectly considered by having the effects due to SOI, m_f and injection rate. The solution of Eq. 1 is denoted as the parameterisation of the DI-SRM using tabulated mixing time, and it is discussed in Section 4.

3. Computational Setup

3.1 Test Engine and Experimental Data

Simulation results refer to a direct injection (DI) Diesel fuelled engine. The engine has a bore 81 mm, stroke 95.5 mm and compression ratio 15.3, and was operated with single fuel injection. Measurements data are for four different speeds and loads (here represented by the m_f), and for five different SOI locations for each pair of n and m_f . At each operating point (OP) the engine was operated at 20% EGR. The resulting matrix contains 80 operating points in total that are presented in Figure 3.

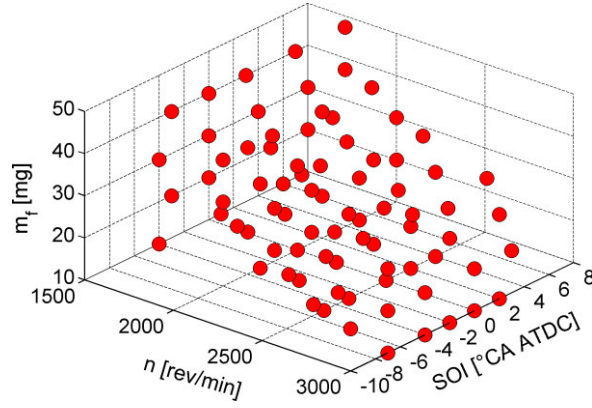


Figure 3: Reference experimental-based engine operating points

3.2 The DI-SRM Setup

Following findings from our previous works, the in-cylinder mixture has been discretized into 1000 particles. Calculations were carried out with 0.5 CAD time step. Mean in-cylinder performance parameters, such as pressure, RoHR, and NO_x concentration, were computed from 30 consecutive cycles. A reaction mechanism of n-heptane was used as Diesel surrogate. The mechanism was extracted from the Primary Reference Fuel (PRF) model developed in [[19]]. To simulate engine exhaust NO_x emission, the thermal mechanism of NO formation from [[20]] has been added. The resulting mechanism contains 28 species and 58 forward and backward reactions. The selection of the small size mechanism was driven by the demand for low computational cost that is beneficial at early stages of simulation method development that requires extensive calculations.

4. Mixing Time Tabulation

The preliminary investigations indicate that the effects of changes of n , m_f and SOI on the mixing time profile $\tau(t)$ (cf. Eq. 1) can be deduced based on the results from the DI-SRM calibrated at nine operating points; three different n and m_f , and three different SOI locations for each pair of n and m_f . The selection of the points is conceptually presented in Figure 4. These points are henceforth denoted as training operating points.

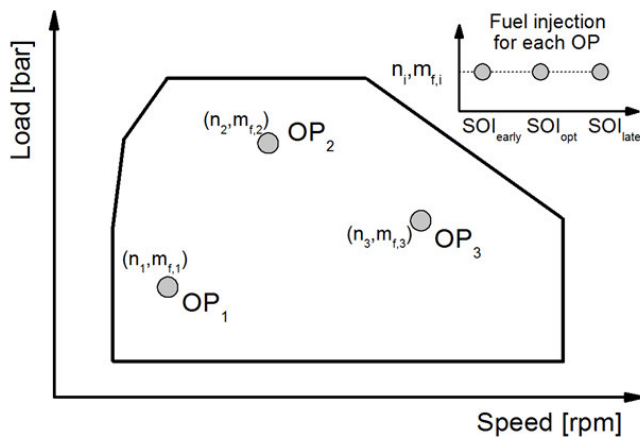


Figure 4: Selection of operating points for mixing time parameterisation

The mixing time was calibrated separately for each training OP using an automated procedure from [[8]]. Six tracking parameters were selected to evaluate quality of the training process of the mixing time. The combustion progress is represented by CA_{10} , CA_{50} , CA_{90} and p_{max} , where 10, 50 and 90 denote respectively CAD where 10%, 50% and 90% of the energy has been released due to combustion. The parameters CA_{10} , CA_{50} , and CA_{90} are indicators of the occurrence of the SOC and EOC, respectively. The IMEP is regarded as an overall indicator of engine performance during the closed part of the engine cycle. The formation of NO_x was controlled based on the concentration computed at EVO.

A separate calibration of the DI-SRM at the selected operating points leads to a set of single solutions for given engine design and mixing time parameters. The results have scatter character that can be treated as a manifold of solutions. To obtain a single solution for Eq. (1), first the mutual interactions were distinguished between the mixing time parameters (SOV , τ_1 , $t_{1/2}$, τ_3) and engine design variables (n , m_f , SOI). Subsequently, the obtained dependencies were approximated by polynomials. The resulting dependencies are presented in Figure 5.

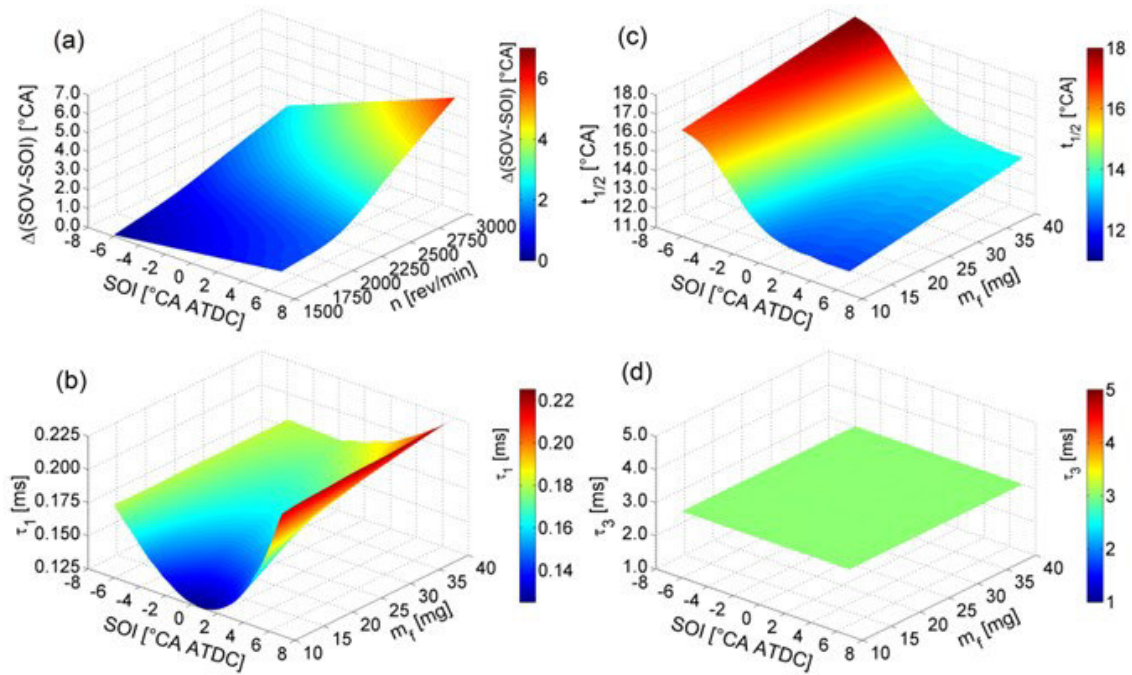


Figure 5: Dependencies between mixing time model parameters: $\Delta(SOV-SOI)$ (a), τ_1 (b), $t_{1/2}$ (c) and τ_3 (d), and engine design variables (n , m_f , SOI)

The surfaces of the modelled mixing time parameters were obtained through the interpolation in between the results obtained during the separate calibration of the mixing time at the training points. For operating conditions exceeding the values of SOV, m_f , τ_1 , $t_{1/2}$ and τ_3 obtained during the training process, the dependencies were extrapolated. Furthermore, in Figure 5, instead of a correlation for the absolute values of SOV the correlation for the difference SOV-SOI is presented. This is more general representation since it directly indicates for the calibration range of the SOV, and makes the correlation independent on the location of the SOI.

The location of SOV depends on n and does not depend on m_f . The changes of the SOV as a function of the SOI have linear character; the SOV moves towards the later CA as the SOI is retarded. Delaying the SOI towards the expansion stroke implies the fuel injection occurs in a bigger volume, and lower pressure and temperature. Lower temperature in the combustion chamber decreases the heat transfer between the injected fuel droplets and the surrounding gas. This slows down the fuel vaporization process. As a result, the effective distance, on CA basis, between the SOV and SOI increases; for a given SOI, higher engine speed implies relatively more time passes until the SOV timing.

The parameters τ_1 and $t_{1/2}$ have the strongest impact on the results. With respect to SOI and m_f changes, the τ_1 can be modelled by second order polynomials. In turn, the $t_{1/2}$ can be modelled by fourth order polynomial with respect to the SOI changes, and by linear function with respect to m_f changes. The values of $t_{1/2}$ were optimized having determined SOV, τ_3 and τ_1 . Hence, the dependency for $t_{1/2}$ is considered as the closure to other parameters of the mixing time. Mixing time τ_1 decides about the mixing during the fuel injection and vaporization, air-fuel mixture preparation and early combustion phase. Intensity of these processes depends on the volume in which they occur. For very early or late fuel injection, mixing occurs in a relatively large volume when compared to the volume at top dead centre (TDC). In consequence, the kinetic energy from fuel injection is relatively faster dissipated at these extreme CA positions. During simulations this corresponds to lower probability that all particles will mix with each other and implies longer τ_1 in these regimes. In contrast, for the SOI located around the TDC there is a higher probability that more particles mix with each other that implies shorter τ_1 . This interaction is reflected in the modelled profile of τ_1 (Figure 5b) that in some extend follows a trajectory of the in-cylinder volume change.

Mixing time τ_3 describes mixing over just a few CA, shortly before EVO (cf. Figure 1). In comparison to τ_1 or $t_{1/2}$, it does not have significant influence on the overall results. Hence, it was kept unchanged, and equal 3.1 ms (found during the preliminary calculations), for all operating points. The assumption that $\tau_0 = \tau_3$ (see Section 2.2), implies that τ_0 is also equal 3.1 ms for this particular engine operation.

5. Performance of the Method

5.1 Combustion and NO_x Emission

In Figure 6 histories of the in-cylinder pressure and RoHR, and NO_x concentration at EVO are analysed for $n=2000$ rev/min, $m_f=10$ mg and SOI=0 CAD ATDC. The results from this operating point are considered as representative for OPs used to develop the dependencies in Figure 5.

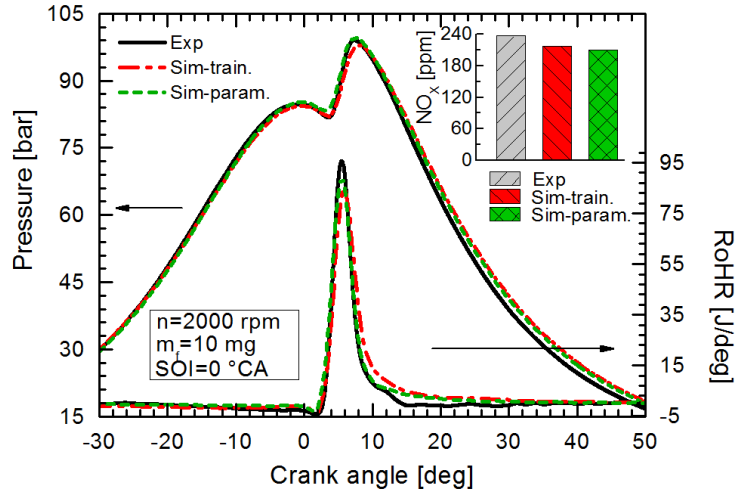


Figure 6: Experimental in-cylinder pressure, RoHR, and NO_x at EVO compared to the results from the trained (-train.) and parameterised (-param.) DI-SRM

Overall, the simulated in-cylinder pressure and RoHR agree between both simulation methods, and match accurately the experimental data. The concentration of NO_x at EVO is also predicted reasonably well by both methods, but the parameterised mixing time model provides slightly less accurate results than the trained model.

Similarly accurate results, in terms of the in-cylinder pressure and RoHR have been obtained at operating points that did not participate in the mixing time training. Concentration of NO_x at EVO for these points have been usually, predicted slightly less accurate. This is attributed to the reconstruction process of mixing time profiles and is discussed in next section. Exemplary results are presented in Figure 7 for $n=3000$ rev/min, $m_f=30$ mg and SOI=-7 CAD ATDC.

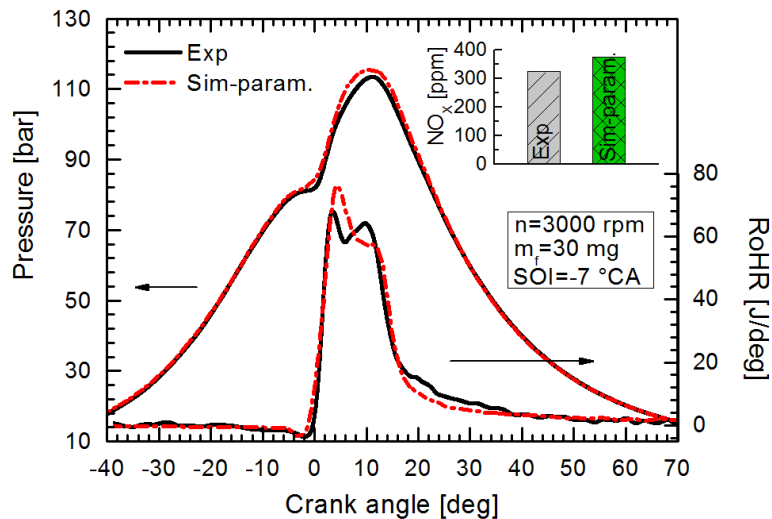


Figure 7: Experimental in-cylinder pressure, RoHR, and NO_x at EVO compared to the DI-SRM simulations employing the parameterised (-param.) mixing time

5.2 Reconstructed Mixing Time and NO_x Formation

The dependencies for mixing time parameters in Figure 5 are valid with a certain tolerance. Hence, at the verification operating points the reconstructed mixing time profiles may slightly differ from the calibrated profiles. Possible small discrepancy might be important for predicting NO_x that is more sensitive to the local changes of mixture composition than the integral properties such as in-cylinder pressure or RoHR. As an example are analysed mixing time profiles corresponding to the simulations in Figure 6. For the considered OP, the combustion process occurs mainly between 1 °CA and 15 °CA ATDC (Figure 6). In this regime both calibrated and parameterised mixing time profiles are very similar to each other (Figure 8). As a result, correspondingly good agreement is observed for in-cylinder pressure and RoHR histories that also match the experimental data. After approximately 10 °CA ATDC both profiles begin to differ. This difference has no negative impact on the in-cylinder pressure and RoHR since the main phase of combustion has ended at this CA. However, it may influence on NO_x that can still be formed in this regime due occurrence of local zones inside the cylinder with high temperature.

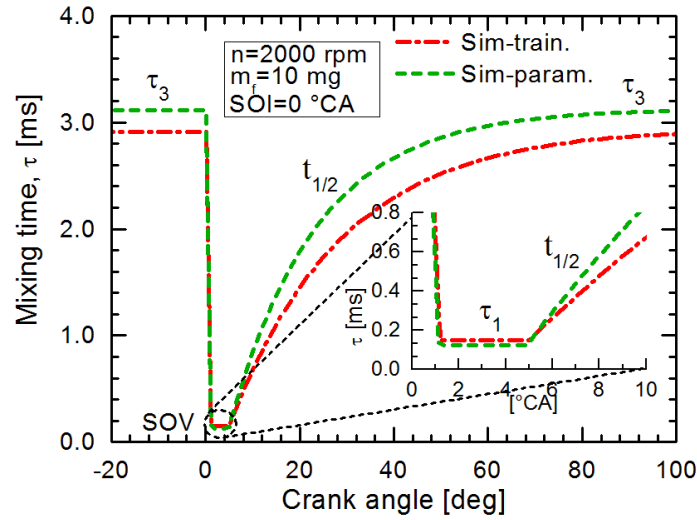


Figure 8: Calibrated and parameterised mixing time histories

The influence of the mixing time on local in-cylinder temperature (T) and equivalence ratios (ϕ) is presented in Figure 9 for both mixing time histories. The results are shown for 18 °CA ATDC.

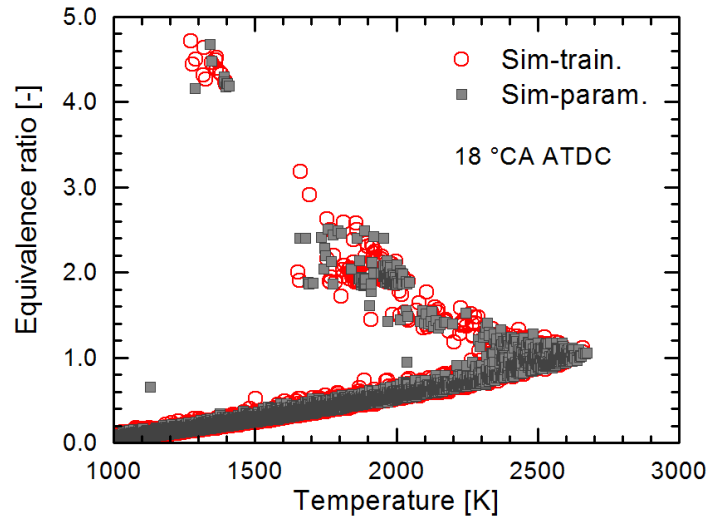


Figure 9: Local temperatures and equivalence ratios from DI-SRM particles at 18 °CA ATDC and using trained and parameterised mixing time histories

At the selected location the in-cylinder pressure and RoHR history agree well (Figure 6), though there is already a visible difference between both mixing time histories (Figure 8). The overall trend of particle based ϕ - T values are similar for both mixing time histories, but the difference in spread is also evident. It is expected that these differences influence on the local rates of formation of NO and NO₂ (see, e.g. [[23]]), on a rich side in particular, that results in different NO_x concentration at EVO.

6. Results for the Complete Engine Matrix

Overall, and for all considered operating points (Figure 3), best results have been obtained for CA_{10} , CA_{50} and p_{max} (Figure 10). For these parameters, the coefficient of determination R^2 (see, e.g., [30]), exceeds 0.95. For CA_{90} the $R^2=0.655$, and the obtained results are more spread than for CA_{10} , and CA_{50} ; there is an offset between the results that indicates a tendency for longer combustion duration by simulations.

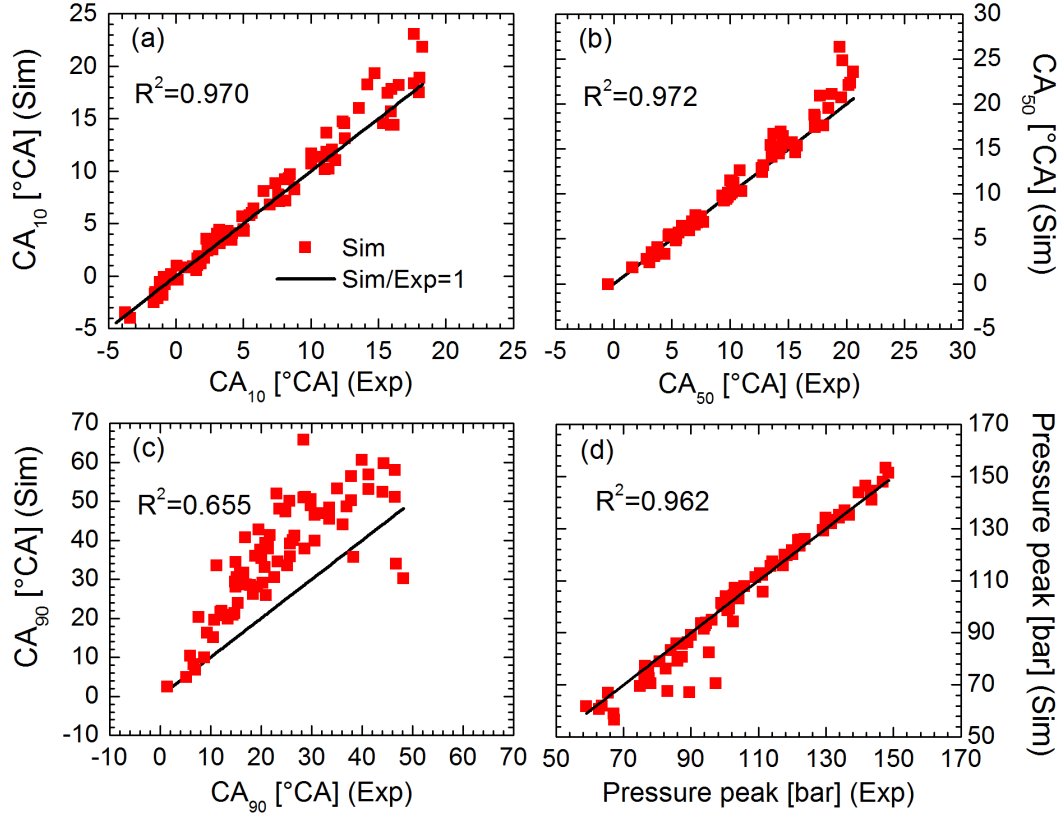


Figure 10: Prediction of the combustion progress: CA_{10} (a), CA_{50} (b), CA_{90} (c) and maximum in-cylinder pressure (d) for operating points from the matrix in Figure 3

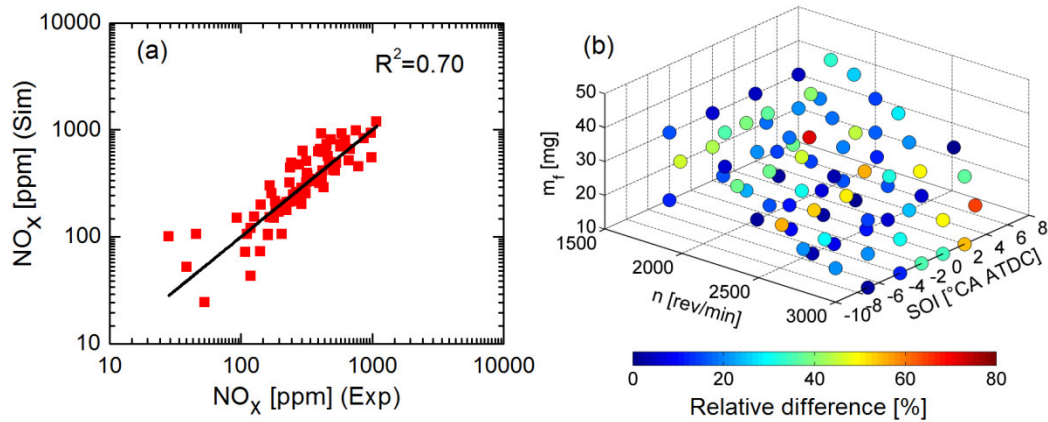


Figure 11: NO_x concentrations at EVO for operating points from the matrix in Figure 3; correlation between the simulated and the experimental data (a), and accuracy of the prediction (b)

For NO_x (Figure 11) the $R^2=0.70$ and the accuracy of results is still regarded as acceptable. Good agreement between the simulated and the experimental values of

$CA_{10,50,90}$ and p_{max} (Figure 10) yielded good agreement in IMEP. Figure 12 presents exemplary results for different SOI locations and different pair of n and m_f .

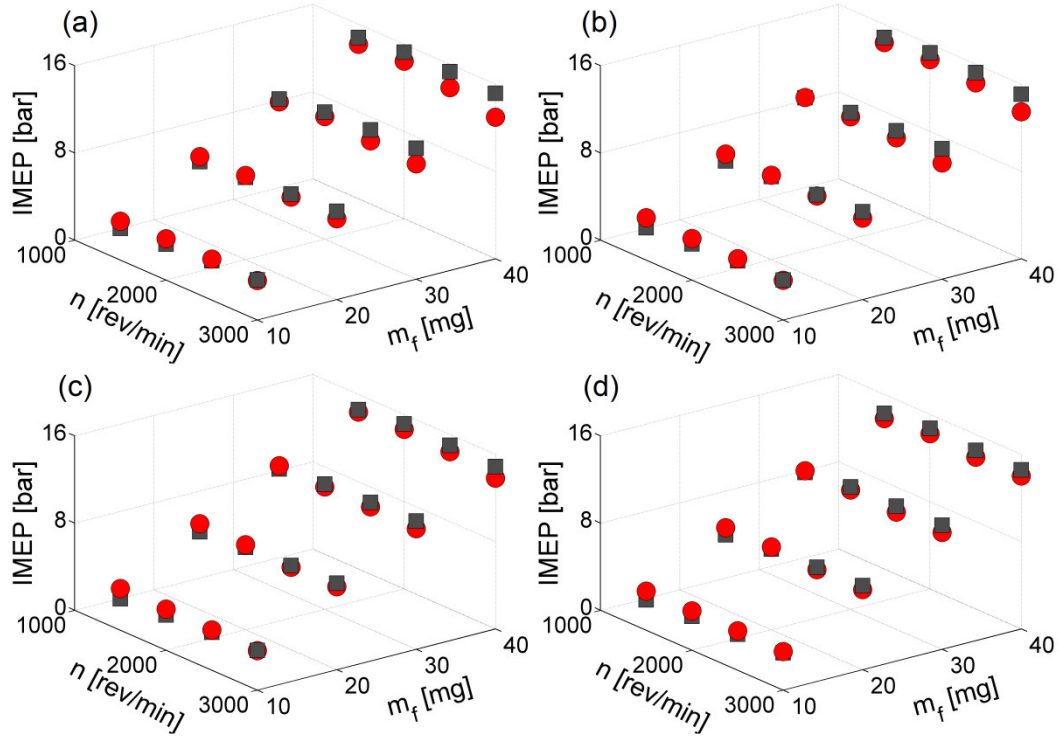


Figure 12: Comparison between the simulated (circles) and experimental-based (squares) IMEP for different SOI such that $SOI(a) < SOI(b) < SOI(c) < SOI(d)$ in CAD ATDC and for each pair of n and m_f

7. Computational Cost

Using the 28-species reaction mechanism and running simulations parallel on 10 nodes with 16 CPUs each (Opteron 2378@2.4 GHz processors from the year 2008) the complete DI-SRM model can be calibrated at single operating point from scratch within approximately 4.6 hours. Once for a given engine the correlations for mixing time have been determined, the time needed to calculate engine performance at single operating point decreases to approximately 26 minutes.

8. Summary

A method has been developed for the simulation of Diesel engine performance parameters and exhaust emission at full load and speed ranges. The method employs the DISRM that is built on a probability density function approach for modelling of turbulent flow with reactions. The following is indicated by the obtained results.

1. In terms of in-cylinder pressure, RoHR, NO_x at EVO and IMEP, accurate results can be obtained from the DI-SRM by calibrating only the volume-averaged and crank angle dependent mixing time. For a Diesel engine operated with single fuel injection, the setup of mixing time can be simplified to the determination of only up to four parameters. These are: SOV, τ_1 , $t_{1/2}$ and τ_3 (cf. Figure 1).
2. The parameters governing the mixing time (SOV, τ_1 , $t_{1/2}$ and τ_3) can be parameterised with known engine design parameters such as n , SOI and m_f . The SOV depends on the SOI and engine speed, and is not sensitive to the load changes. In contrast, τ_1 and $t_{1/2}$ depend on SOI and m_f and are not sensitive to n changes. Parameter τ_3 is less influential than other three, and frequently it can be assumed constant regardless to engine speed and load changes.
3. Most accurate results are obtained for combustion progress parameters, CA_{10} , CA_{50} and p_{\max} that correspond to most accurate results for histories of the in-cylinder pressure and rate of heat release with the R^2 coefficient exceeding 0.95. Lower accuracy has been achieved for CA_{90} ($R^2=0.65$) and the concentration of NO_x at EVO ($R^2=0.70$). In comparison to the combustion parameters (CA_{10-90}), the formation of NO_x is more sensitive to the locality of the mixing process due to the modelled mixing time.

The method described in this paper has been applied to a Diesel engine operated with single fuel injection. However, the used concept of the volume-averaged and crank angle dependent mixing time was already applied to an engine operated with double fuel injections [[22]]. Hence, it is expected that the presented method is of general purpose, but more proof calculations are still to be carried out. Similarly, validity of the obtained correlations between the mixing time parameters and the engine design variables, for other engines and operating conditions is still to be verified. The proposed method of mixing time parameterisation has been validated in simulating combustion and NO_x formation. The method is expected to remain valid also for simulating unburned hydrocarbons and soot from Diesel engines, if more detailed Diesel surrogate is applied. These aspects of modelling and simulations are subjected to on-going investigations and will be considered for future publications.

References

- [1] Rychter, T., and Teodorczyk, A., 1990. Modelowanie matematyczne roboczego cyklu silnika tłokowego. PWN Warszawa.
- [2] Merker, G., Schwarz, C., Stiesch, G., and Otto, F., 2006. Simulating Combustion. Simulation of Combustion and Pollutant Formation for Engine-Development. Springer-Verlag Berlin Heidelberg.
- [3] Su, H., Vikhansky, A., Mosbach, S., Kraft, M., Bhave, A., Kim, K., Kobayashi, T., and Mauss, F., 2006. "A Computational Study of an HCCI Engine with Direct Injection During Gas Exchange". Combust. Flame, 147(1-2), pp. 118–132.
- [4] Su, H., Mosbach, S., Kraft, M., Bhave, A., Kook, S., and Bae, C., 2007. "Two-stage Fuel Direct Injection in a Diesel Fuelled HCCI Engine". SAE Paper 2007-01-1880.
- [5] Tuner, M., Pasternak, M., Mauss, F., and Bensler, H., 2008. "A PDF-Based Model for Full Cycle Simulations of Direct Injected Engines". SAE Paper 2008-01-1606.
- [6] Pope, S., 1985. "Pdf Methods for Turbulent Reactive Flows". Prog. Energy Combust. Sci., 11(2), pp. 119–192.
- [7] Haworth, D., 2010. "Progress in Probability Density Function Methods for Turbulent Reacting Flows". Prog. Energy Combust. Sci., 36(2), pp. 168–259.
- [8] Pasternak, M., Mauss, F., Janiga, G., and Thevenin, D., 2012. "Self-Calibrating Model for Diesel Engine Simulations". SAE Paper 2012-01-1072.
- [9] Pasternak, M., Mauss, F., Matrisciano, A., and Seidel, L., 2012. "Simulation of Diesel Surrogate Fuels Performance under Engine Conditions using 0D Engine – Fuel Test Bench". Proc. COMODIA Conf.
- [10] Pasternak, M., Mauss, F., Perlman, C., and Lehtiniemi, H., 2014. "Aspects of 0D and 3D Modeling of Soot Formation for Diesel Engines". Combust. Sci. and Tech., 186(10-11), pp. 1517–1535.
- [11] Pasternak, M., Mauss, F., and Bensler, H., 2009. "Diesel Engine Cycle Simulations with a Reduced Set of Modeling Parameters Based on Detailed Kinetic". SAE Paper 2009-01-0676.
- [12] Pasternak, M., Mauss, F., and Lange, F., 2011. "Time Dependent Based Mixing Time Modelling for Diesel Engine Combustion Simulations". Proc. ICDERS Conf.
- [13] Kraft, M., 1998. Stochastic Modelling of Turbulent Reacting Flow in Chemical Engineering. VDI Verlag.
- [14] Balthasar, M., Mauss, F., Knobel, A., and Kraft, M., 2002. "Detailed Modeling of Soot Formation in a Partially Stirred Plug Flow Reactor". Combust. Flame, 128(4), pp. 395–409.
- [15] Loge AB, 2013. LOGEsoft v1.0. User Manual.
- [16] Curl, R., 1963. "Dispersed Phase Mixing: I. Theory and Effects in Simple Reactors". AIChE J., 9(2), pp. 175–181.
- [17] Peters, N., 1992. Fifteen Lectures on Laminar and Turbulent Combustion. ERCOFTAC Summer School, Aachen.

- [18] Maigaard, P., Mauss, F., and Kraft, M., 2003. "Homogenous Charge Compression Ignition Engine: A Simulation Study on the Effect of Inhomogeneities". J.Eng. Gas Turb. Power, 125(2), pp. 466–471.
- [19] Tsurushima, T., 2009. "A New Skeletal PRF Kinetic Model for HCCI Combustion". Proc. Comb. Inst., 32(2), pp. 2835–2841.
- [20] Smith, G., Golden, D., Frenklach, M., Eiteener, B., Goldenberg, M., Bowman, C., Hanson, R., Gardiner, W., Lissianski, V., and Qin, Z., 2000. GRI-Mech 3.0. http://www.me.berkeley.edu/gri_mech/.
- [21] Ratner, B., 2011. Statistical and Machine-Learning Data Mining: Techniques for Better Predictive Modeling and Analysis of Big Data, Second Edition. Taylor & Francis.
- [22] Pasternak, M., and Mauss, F., 2013. "Aspects of Diesel Engine In-Cylinder Processes Simulation using 0D Stochastic Reactor Model". Proc. ICEP Conf. ISBN 78-3-8169-3222-2.
- [23] Pasternak, M. and Mauss, F., 2013 Simulation of Fuel Effects under Diesel-Engine Conditions using 0D-Fuel-Test Bench. Berichte zur Energie- und Verfahrenstechnik (BEV), ISBN 3-931901-87-4.

The Authors:

Dipl.-Ing. Michal Pasternak, Loge GmbH, Technology and Research Center
Burger Chaussee 25, 03044 Cottbus, Germany

M.Sc.-Ing. Andrea Matrisciano, Chalmers University of Technology,
Department of Applied Mechanics, Horsalsvägen 7a 412 96 Göteborg, Sweden

Prof. Dr.-Ing. Fabian Mauss, Brandenburg University of Technology,
Division of Thermodynamics/Thermal Process Engineering,
Siemens Halske Ring 8, 03046 Cottbus, Germany

License:

This document is licensed under the Creative Commons Attribution 3.0 DE License (CC-BY 3.0 DE): <http://creativecommons.org/licenses/by/3.0/de/>

Modeling of Spray Combustion under Diesel Engine Conditions

Harry Lehtiniemi
Anders Borg
Fabian Mauß

Abstract

Several models for ignition, combustion and emission formation under Diesel engine conditions for multi-dimensional computational fluid dynamics have been proposed in the past. It has been recognized that the use of a reasonably detailed chemistry model improves the combustion and emission prediction especially under low temperature and high exhaust gas recirculation conditions.

The coupling of the combustion chemistry and the turbulent flow can be achieved with different assumptions. In this paper we investigate a selection of n-heptane spray experiments published by the Engine Combustion Network (ECN spray H) with three different combustion models: well-stirred reactor model, transient interactive flamelet model and progress variable based conditional moment closure. All models cater for the use of detailed chemistry, while the turbulence-chemistry interaction modeling and the ability to consider local effects differ.

The same chemical mechanism is used by all combustion models, which allows a comparison of ignition delay, flame stabilization and flame lift-off length between the experiments and the results from simulations using the different combustion models. The investigated parameters influence the predictions of computational fluid dynamics simulations of Diesel engines. This study indicates that the most reasonable behavior with respect to ignition, flame stabilization and flame structure is predicted by the progress variable based conditional moment closure model.

1. Introduction

One of the challenges in turbulent combustion modeling is the closure of the highly non-linear chemical source term. The capacity of today's computers limits the use of Direct Numerical Simulation (DNS) which resolves all relevant time- and length scales associated with turbulence, spray, and combustion chemistry to study small computational domains and to model the combustion chemistry with small and simplified chemical mechanisms. Therefore, not all time- and length scales are resolved in industrial CFD simulations and appropriate closures of terms resulting from averaging procedures are required. In this paper the discussion is restricted to treatment of the reactive scalars and the chemical source term in the context of Reynolds-Averaged Navier-Stokes (RANS) computational fluid dynamics (CFD) simulations.

Turbulence causes fluctuations of the reactive scalars and the state variables. One of the challenges when modeling turbulent reactive flows lies in the closure of the chemical source term. Approximating the chemical source term using cell mean quantities may cause a deviation in ignition, combustion, and emission prediction between experiments and simulations due to the exponential nature of the reaction rates. Two main modeling approaches have been developed in the past, attempting to overcome this difficulty: models based on a presumed probability density function (PDF), and models based on transported PDF. Further in-depth discussion on the challenges of turbulent combustion modeling can be found in Refs. [1-3].

To treat the chemical source term without the consideration of any fluctuations, a so-called well-stirred reactor (WSR) closure, is still a commonly used method. It is therefore of interest to perform an investigation to study the influence of the closure of the chemical source term on measurable spray flame properties such as ignition delay time and flame lift-off length, in order to choose the appropriate combustion model for emission formation studies. The Engine Combustion Network (ECN) [4] provides an experimental database containing experimental data for spray ignition and combustion under engine relevant conditions. The spray H experiments refer to n-heptane sprays and in this paper three different combustion models have been applied to study n-heptane spray ignition and combustion at three different operating points.

Although some of the n-heptane spray experiments were reported in the literature by Pickett et al. in e.g. [5] about a decade ago, they receive continued attention of the combustion modeling community. Approaches to combustion modeling, where the chemistry is solved on-line with the flow calculation, as well as tabulated chemistry based methods have been proposed and used to model the experiments. Recent modeling efforts where the combustion chemistry is solved on-line include i.a. WSR [6,7], partially stirred reactor (PaSR) [8], volume reactor fraction model (VRFM) [9], interactive flamelets [9], conditional moment closure (CMC) [10,11] and transported PDF (t-PDF) [12]; and recent studies of tabulated chemistry approaches include i.a. efforts based on homogeneous auto-igniting reactor tabulation [13] and various approaches based on flamelet tabulation [14,15].

Of particular interest, related to the topic of this paper, are the studies presented by Kösters et al. [9], Bolla et al. [11], Bhattacharjee and Haworth [12]; and Egüz et al. [14].

Kösters et al. [9] investigated seven different spray H operating points at constant ambient temperature at different levels of ambient oxygen and density. They used the same CFD software with three different combustion models: WSR, VRFM and the interactive flamelet model. They observed that although all models could predict ignition delay trends and lift-off length trends correctly, the choice of turbulence-chemistry interaction model affects results and flame structure. They concluded that turbulent combustion model development towards a model which can account for both non-premixed and premixed turbulent combustion is required. Moreover, considering the choice of chemical mechanism, Kösters et al. [9] used a reduced chemical mechanism containing 35 species and 80 reactions, and suggest that the choice of chemical mechanism is likely to have an impact on the modeling results.

Bolla et al. [11] investigated the influence of turbulence-chemistry interaction on soot predictions employing the CMC and WSR models, using a chemical mechanism with 22 species and 18 global reaction steps coupled with a simplified soot model. They found that turbulence-chemistry interaction is not significantly affecting the ignition delay time prediction or the soot distribution for these cases, although the flame structure appears to be better predicted by the CMC model. They found however that CMC better captures the physics of a spray flame having much shorter injection duration than the spray H cases and advocate the use of CMC in order to obtain accurate predictions.

Bhattacharjee and Haworth [12] presented a comparison between t-PDF and WSR for a variation of spray H operating conditions with different ambient temperature, density and ambient oxygen level. They used a reduced chemical mechanism containing 40 species and 165 chemical reactions, and noticed differences in prediction of ignition delay time, lift-off length and flame structure although experimental trends were possible to capture with both models. One important finding is that the deviation between t-PDF and WSR predictions increases with lower temperature, density and ambient oxygen level, indicating that turbulence-chemistry interactions are important when the ignition delay time is long.

Egüz et al. [14] investigated spray H at constant ambient temperature and density, but different levels of ambient oxygen, using different strategies for flamelet generated manifold (FGM) tables and incorporation of the effect of turbulence fluctuations through the mixture fraction variance. They produced FGM tables with homogeneous, auto-igniting constant pressure reactors and through the calculation of auto-igniting counterflow diffusion flames at different strain rates using a chemical mechanism consisting of 137 species and 633 reactions. The auto-ignition process was parameterized using the FGM strategy and mapped using look-up tables of different sizes. It was noticed that uniformly spaced table grids are exhibiting much worse accuracy than non-uniform table grids, even with a high number of uniformly placed grid points. Moreover it was shown that the incorporation of turbulence fluctuations shortens the lift-off length for both the homogenous reactor table and the igniting counterflow diffusion flame table. The ignition delay time appears to be slightly shorter with the homogeneous reactor table if the influence of turbulence fluctuations is considered than if it is omitted – although the difference could be considered negligible – while the ignition delay time obtained with the igniting counterflow diffusion flame table seems unaffected by the consideration of turbulence fluctuations.

The aforementioned studies indicate that there is an influence of the choice of how turbulence-chemistry interactions are modeled – and that the choice of chemical mechanism affects the results. Clearly, the choice of CFD software, grid resolution and turbulence model and spray model will influence the results. In the investigation presented in this paper the detailed n-heptane mechanism developed by Seidel et al. [16], containing 349 species and 3686 reactions, was used for all calculations. Three different combustion models, sharing the same chemistry solver from the LOGEsoft package [17] were used: WSR, transient interactive flamelet model (TIF), and progress-variable based conditional moment closure using a transient flamelet library (LTIF-CMC). The combustion models were implemented in the CFD software STAR-CD [18] through user coding.

This paper is organized as follows: first the experimental test cases and the CFD setup are discussed; subsequently the combustion models are presented followed by a presentation and analysis of the simulation results. The paper is closed with conclusions.

2. Test Cases and CFD Setup

As test cases three spray H cases from the Engine Combustion Network [4] were selected. The experiments were performed at Sandia National Laboratories, using their high-temperature/high-pressure constant volume vessel [5]. The vessel is cubical with an edge length of 108 mm and the injector is placed such that fuel injection occurs along the center axis when a single-hole nozzle is used. For the spray H experiments, n-heptane was injected into the vessel through a single-hole nozzle, $d = 100 \mu\text{m}$, the injection duration was around 6.8 ms and the injection pressure around 150 MPa. Since it may be expected that the influence of the combustion model becomes more pronounced at low ambient density than at high ambient density due to slower evaporation and slower reaction rates, the 14.8 kg/m^3 ambient density experiments were considered in this work. Further details of the experiments can be found at the ECN website [4]. Table 1 shows which operating conditions were chosen as test cases.

Case	Amb. Temperature [K]	Amb. Oxygen [mol-%]	Pressure [MPa]
1	800	21	3.3
2	1000	21	4.2
3	1200	21	5.0

Table 1: Test cases.

The commercial CFD software STAR-CD v. 4.22 [18] was used to resolve the turbulent flow-field. The standard $k - \varepsilon$ – turbulence model was used, with the constant $C_{\varepsilon 1} = 1.52$. The turbulent Schmidt and Prandtl numbers were set to $Sc_t = Pr_t = 0.9$. The spray modeling was performed with standard STAR-CD models: the “effective” nozzle model with the nozzle diameter set such that the experimentally found discharge coefficient was considered; the Reitz-Diwakar models for atomization and break-up were used with their default STAR-CD parameters. Turbulent dispersion was considered, however the collision modeling was switched off. Evaporation, mass transfer and momentum transfer were modeled with standard STAR-CD practice [18]. The MARS (monotone advection and reconstruction scheme) discretization scheme,

which is a second order accurate scheme, was used for all scalars, enthalpy, turbulence and momentum; and the central differencing scheme was used for the continuity equation. The “chemico-thermal” form of the enthalpy equation was solved, and user coding was activated in order to calculate combustion chemistry, thermodynamic properties and source terms.

The computational grid was constructed as an axisymmetric wedge mesh with dimensions 108 mm × 60.9 mm × 6°. The wedge was elongated in radial direction in order for the wedge to represent the appropriate fraction (1/60) of the volume of the cubical vessel. The grid contained totally 22680 cells, of which 19440 were used to build a uniform mesh with edge length 0.33 mm along the spray axis and 20 mm outwards in radial direction. The remaining 3240 cells were distributed uniformly in axial direction, with an edge length of 1 mm, and non-uniformly in radial direction with increasing edge length towards the wall. This mesh is slightly coarser than the uniform mesh with cells having an edge length of 0.25 mm used by Egüz et al. [14], but finer than the mesh used by Bolla et al. [11] and as fine as the meshes used by Kösters et al. [9] and Bhattacharjee and Haworth [12]. The meshes employed in Refs. [9,12] were reported to be non-uniform, with an edge length of 0.3 mm close to the nozzle, resulting in a lower total number of grid cells compared to the mesh used for the present work.

The initial pressure and temperature were set according to nominal conditions for each case. The velocity field was initialized as quiescent. The turbulent kinetic energy was initialized to $k = 0.735 \text{ m}^2/\text{s}^2$ based on the velocity field induced by the mixing fan in the experimental setup, and the dissipation of turbulent kinetic energy was initialized to $\varepsilon = 10.1 \text{ m}^2/\text{s}^3$.

3. Combustion Modeling

In this section the different combustion models used in the present work are introduced. All combustion models used the same detailed chemical mechanism for n-heptane containing 349 species and 3686 reactions. The reader is referred to the paper written by Seidel et al. [16] for further details concerning the development and validation of the n-heptane chemistry.

3.1 Well-Stirred Reactor Model

The transport equation for a reactive scalar (e.g. chemical species) reads after Favre averaging and after invoking the usual assumptions for RANS modeling:

$$\frac{\partial \bar{\rho} \tilde{Y}_\alpha}{\partial t} + \nabla \cdot (\bar{\rho} \tilde{\mathbf{v}} \tilde{Y}_\alpha) - \nabla \cdot (\bar{\rho} D_t \nabla \tilde{Y}_\alpha) = \bar{\rho} \tilde{\omega}_S \delta_{\alpha\beta} + \bar{\rho} \tilde{\omega}_\alpha, \quad (1)$$

with the first term on the right-hand-side being the spray source term, which has a contribution to the fuel species (β) only, and the last term on the right-hand-side is the chemical source term. The treatment of the last term depends on the combustion model choice. As mentioned in the introduction, this term is calculated with the cell mean species mass fractions and thermo-chemical state in the WSR model. This treatment of the chemical source term is one major drawback of the WSR model. One advantage is that the model is extremely simple to implement. A typical strategy is to let the flow solver handle the spatial transport terms and the spray term, and leave the

chemical source term treatment to a dedicated chemistry solver. The larger the chemical mechanism is the higher is the computational cost of the transport part and the cost of solving the chemistry. The computational time required by the transport part is approximately linearly proportional to the number of species in the mechanism, while the computational cost of solving the chemistry step depends highly on the implementation strategy and the numerical solution algorithms employed in the ordinary differential equation (ODE) solver. To reach acceptable simulation wall-clock time, and to facilitate the use of large, detailed chemical mechanisms, parallelization and a load-balancing strategy coupled with an adaptive clustering method as described by Perlman et al. [19] are used with an optimized ODE solver [17] for the simulations in this paper. As clustering parameters, mixture fraction and chemical enthalpy (enthalpy of formation) were chosen for the present study.

3.2 Transient Interactive Flamelet Model

The flamelet model, described extensively by Peters in Refs. [1,20], assumes that a turbulent flame can be described by an ensemble of laminar, one-dimensional flame structures, so called flamelets. The main feature of the flamelet model is that it allows de-coupling of the turbulent flow-field and the combustion chemistry. After a coordinate transform from physical space to flamelet space, it may be observed that the reactive scalars are possible to express as a function of mixture fraction, Z , and scalar dissipation rate, χ . For turbulent non-premixed combustion the flamelet method provides the possibility to consider sub-grid-scale effects, and the effect of turbulence on the evolution of the chemistry. Mixture fraction is defined here as mass originating from the fuel stream:

$$Z = \frac{\dot{m}_F}{\dot{m}_F + \dot{m}_{Ox}}. \quad (2)$$

The scalar dissipation rate is defined as:

$$\chi \equiv 2D_Z(\nabla Z)^2. \quad (3)$$

Assuming unity Lewis numbers, performing the coordinate transform, and neglecting the coordinate directions tangential to the stoichiometric mixture fraction isosurface, the equation solved for species conservation in flamelet space reads:

$$\rho \frac{\partial Y_\alpha}{\partial \tau} = \frac{\rho \chi}{2} \frac{\partial^2 Y_\alpha}{\partial Z^2} + \rho \dot{\omega}_\alpha. \quad (4)$$

It can be observed here that the term including scalar dissipation rate acts as a diffusion term in mixture fraction space. The implementation of the TIF solver and its coupling with the flow solver are discussed in detail in Ref. [21] why only a brief description is provided below.

Since the evolution of the chemistry is solved in flamelet space, there is no need to transport any species in the flow-field. Instead, mixture fraction and its variance are transported. Their respective transport equations can be expressed as:

$$\frac{\partial \bar{\rho} \tilde{Z}}{\partial t} + \nabla \cdot (\bar{\rho} \tilde{\mathbf{v}} \tilde{Z}) - \nabla \cdot (\bar{\rho} D_t \nabla \tilde{Z}) = \bar{\rho} \dot{\omega}_s \quad (5)$$

$$\frac{\partial \bar{\rho} \tilde{Z}''^2}{\partial t} + \nabla \cdot (\bar{\rho} \tilde{\mathbf{v}} \tilde{Z}''^2) - \nabla \cdot (\bar{\rho} D_t \nabla \tilde{Z}''^2) = 2 \bar{\rho} D_t (\nabla \tilde{Z})^2 - \bar{\rho} \tilde{\chi} + \overline{\rho \dot{\omega}_{s,Z''^2}}. \quad (6)$$

It may be noticed that Eq. (5) contains the spray evaporation source term on the right-hand-side, while Eq. (4) was derived assuming that mixture fraction is a conserved scalar. Recently, Olguin and Gutheil [22] presented a derivation of the flamelet equations where the influence of the spray source term on the flamelet structure is considered. However, for the application considered in this paper, which employs a multiple flamelet strategy, the influence of the evaporation source term on the flamelet structure is neglected. Borghesi et al. [10] investigated the influence of the spray source terms in the CMC equation when studying the spray H flames, and found that there was a small effect due to the spray terms in the CMC equation on the ignition delay time, but hardly any effect on the flame structure and the flame stabilization mechanism. Therefore, it is assumed that an inclusion of the spray source term in the flamelet equation would not significantly impact the results obtained with the transient interactive flamelet method. The last term on the right-hand-side of the mixture fraction variance transport equation, Eq. (6), contains $\dot{\omega}_{s,Z''^2}$, which is short-hand for the mixture fraction variance source due to spray evaporation. This term is modeled following the approach proposed by Hollmann and Gutheil [23].

The mean scalar dissipation rate is modeled according to:

$$\tilde{\chi} = c_\chi \frac{\tilde{\varepsilon}}{\bar{k}} \tilde{Z}''^2 \quad (7)$$

with $c_\chi = 2$.

In the TIF approach, multiple interactive flamelets are solved following a fuel-based splitting strategy. The implementation allows for using any number of flamelets. For each flamelet, a flamelet marker transport equation is solved, similar to the mixture fraction equation. The individual flamelet probabilities are thus obtained using the flamelet markers and the mixture fraction. Each flamelet is advanced interactively with the flow-field, but their scalar dissipation rate histories will be different, and the probability to find individual flamelets will be different in different locations of the flow-field. Scalar dissipation rate is modeled in mixture fraction space using the inverse complementary error function [20], and the magnitude of the scalar dissipation rate profile is given by the conditional scalar dissipation rate. The scalar dissipation rate treatment for the individual interactive flamelets is described in Ref. [21]. An overview over different multiple flamelet strategies is presented in the same reference.

Since no species are transported, the thermodynamic state in the flow-field is updated using the mixture fraction, mixture fraction variance, and the flamelet markers. In order to obtain density, specific heat and enthalpy, the appropriate quantities present in the solution of the interactive flamelets are integrated by the mixture fraction PDF (assumed to be a beta-pdf determined by the mixture fraction and its variance), and weighted by the flamelet probabilities. Chemical species are retrieved in a similar manner for post-processing purposes.

Different from the WSR model, TIF caters for the possibility to model turbulence-chemistry interaction. The effects of turbulence and flow-field inhomogeneities affect the solution of the combustion chemistry through the scalar dissipation rate. The local thermo-chemical state in a grid cell in the flow-field is given by the mixture fraction and the mixture fraction variance – which are the parameters defining the shape of the mixture fraction PDF – and the flamelet probabilities.

In the present paper 50 interactive flamelets were used and each new flamelet inherited its initial state from the previous flamelet.

3.3 Progress Variable Based Conditional Moment Closure

For an in-depth description of the CMC model the reader is referred to the review paper by Klimenko and Bilger [24] and the book chapter by Kronenburg and Mastorakos [25]. The authors of this paper have previously presented a method for performing CMC for only a progress variable [26], which allows for the use of arbitrarily large chemistry within the CMC modeling framework. The progress variable is chemical enthalpy (enthalpy of formation) and it has previously been found that it accurately describes the low-temperature and high-temperature reactions. Since the number of transported scalars is drastically decreased thanks to the use of a progress variable, the CMC can be performed on the same grid as used for the flow-field solution. This method – LTIF-CMC – is pursued in this paper and it is described briefly below.

Different from the flamelet model, where a coordinate transform from physical space to flamelet space is performed, the CMC model considers that the instantaneous value of a reactive scalar Y can be decomposed according to:

$$Y = Q(Z(\mathbf{x}, t), \mathbf{x}, t) + Y'' \quad (8)$$

where Q is the conditional average and Y'' the conditional fluctuation.

Let $Q = \langle \rho Y(\mathbf{x}, t) | Z(\mathbf{x}, t) = \eta \rangle / \langle \rho(\mathbf{x}, t) | Z(\mathbf{x}, t) = \eta \rangle$, i.e. Q is the Favre conditional average of the reactive scalar Y . The conditioning variable is the mixture fraction, and η is the mixture fraction sample space. Using the methods in Ref. [24] the following transport equation for the conditionally averaged scalar is derived:

$$\frac{\partial Q}{\partial t} + \langle \mathbf{v} | \eta \rangle \cdot \nabla Q = \frac{\langle \chi | \eta \rangle}{2} \frac{\partial^2 Q}{\partial \eta^2} + \langle \dot{W} | \eta \rangle + e_y \quad (9)$$

It may be noted that the first two terms on the right-hand-side of Eq. (9) are reminiscent of the right-hand-side of the flamelet equation, Eq. (4). The CMC equation dictates however that the problem is five-dimensional: time, space (three coordinate directions) and mixture fraction.

The terms in Eq. (9) involving conditional averages require modeling. In the implementation used for the simulations in this paper a linear model is applied for the conditional velocity. Since the CMC grid is the same as used by the CFD solver, the conditional scalar dissipation rate profile is determined in each grid cell by calculating the scalar dissipation rate conditioned on $Z_{max}/2$ and applying the inverse

complementary error function profile. This procedure is similar to the amplitude mapping closure (AMC) [27]. The source term for the progress variable is closed to first order, and for each grid point in mixture fraction space, the source term is retrieved from a transient flamelet look-up table as function of mixture fraction, scalar dissipation rate, pressure, enthalpy and the current value of the progress variable. The e_y -term is modeled with the gradient transport hypothesis. The details of the numerical implementation of Eq. (9) in a finite-volume CFD solver are omitted for brevity of the paper, however it needs to be pointed out that the part of the differential operator involving transport and source in mixture fraction space is handled by the same transient “flamelet” solver as used in the TIF approach. The terms involving spray sources are omitted from Eq. (9), following the findings for spray H discussed in Ref. [10].

In practice, the mixture fraction and its variance equation are solved according to Eq. (5) and Eq. (6), together with the conditional average of the progress variable on the mixture fraction sample space grid. If 51 sample space points in mixture fraction are used, then the total number of transported scalars is $2 + 51 = 53$, which is much less than if the conditional averages of all of the species in the chemical mechanism would be solved – for chemical the mechanism employed in this paper, the total number of transported scalars would be $2 + 51 \times 349 = 17801$ and already the computational cost of the transport would be prohibitive for practical RANS application.

The state variables are updated for each cell using the cell local state of the conditionally averaged progress variable, cell local scalar dissipation rate and the mixture fraction PDF. Species mass fractions for species of interest are mapped from the CMC solution in the same manner. Different from the interactive flamelet model, the CMC method is able to account for cell local effects on the combustion chemistry. Both the flamelet model and the CMC model consider transport across the mixture fraction iso-lines. In the CMC method employed here, this transport is computed at grid cell level based on the cell local scalar dissipation rate, whereas in the flamelet model the transport in mixture fraction space is calculated based on an averaged scalar dissipation rate for the different flamelets. Moreover, the CMC equation includes spatial transport along the mixture fraction iso-lines, which can be argued to account for (turbulent) flame propagation. It is complex to include such effects in the flamelet model, i.e. curvature effects and transport tangential to the mixture fraction iso-surface which was selected for the flamelet transform [28].

Different from the WSR and TIF models, where the combustion chemistry is solved on-line, LTIF-CMC relies on tabulated chemistry. For each investigated operating condition a look-up table was constructed by pre-calculating flamelet structures for different scalar dissipation rates in the interval $0.05 - 1000 \text{ s}^{-1}$. The progress variable was discretized using a non-uniform grid. The grid was determined using an automated procedure for each case with a measure based on the gradient and the curvature of the progress variable. This methodology ensures that no important features of the ignition process, or of the transition towards equilibrium, are overlooked by the tabulation process. The inclusion of the scalar dissipation rate as a look-up parameter is one major difference against other tabulated chemistry models which are based on tabulation of homogeneous auto-ignition and models which omit the effect and influence of scalar dissipation rate on chemical reaction rates.

4. Results

The results obtained with the different simulation approaches are described in this section. The analysis here is restricted to the following properties: (1) ignition delay time and maximum temperature; (2) flame development; and (3) lift-off length. The simulated ignition delay time and the flame-lift off location are defined following the ECN [4] modeling standard. The ignition delay is defined as first time at which the Favre averaged OH mass fraction reaches 2 % of the value after a stable flame is established; and the lift-off length is defined as the first down-stream location where the Favre averaged OH mass fraction reaches 2 % of its domain maximum.

The ignition delay times, and the lift-off lengths, determined for all spray flames at 4 ms after start of injection are listed in Table 2.

	Case 1 (800 K)	Case 2 (1000 K)	Case 3 (1200 K)
Exp. LOL / ign.del	46 mm / 1.65 ms	17 mm / 0.53 ms	10 mm / 0.27 ms
Sim. WSR	49 mm / 1.69 ms	29 mm / 0.55 ms	16 mm / 0.25 ms
Sim. TIF	42 mm / 1.95 ms	23 mm / 0.59 ms	0 mm / 0.28 ms
Sim. LTIF-CMC	38 mm / 1.65 ms	18 mm / 0.48 ms	11 mm / 0.29 ms

Table 2: Comparison between experimental and simulated lift-off length and ignition delay time for the three test cases.

Figures 1-3 show the development of maximum Favre averaged OH mass fraction and temperature in the computational domain for the three test cases. A different time axis was chosen for each case, in order to better see the global differences and similarities between the different combustion models. As expected, the maximum temperature and maximum OH mass fraction agree well between the TIF and LTIF-CMC models while the maximum temperature and OH is substantially higher in all simulations employing the WSR model. This is explained by the fact that the WSR model does not consider any sub-grid scale effects. TIF and LTIF-CMC consider the effect of turbulence on the reaction rates through the scalar dissipation rate, and the unconditional averages of all properties are obtained through the use of a presumed PDF based on mixture fraction and its variance.

Comparing the ignition delay times, it can be observed that all models are able to follow the experimental trends. The difference in ignition delay time prediction is rather small between the different models. Investigating the ignition process and flame stabilization event, it was found that for all models, ignition was predicted in the rich mixture downstream of the injector for case 2 and case 3. The ignition event was followed by a “flame propagation” event along the stoichiometric mixture fraction iso-surface with the WSR and LTIF-CMC models. The TIF model showed instead an effect of the flamelet discretization and no clear flame propagation was predicted by the TIF model.

The case with lowest temperature and longest ignition delay time, case 1, showed a different behavior depending on the combustion model. The WSR model predicted ignition in the vicinity of stoichiometric mixture at the jet tip, followed by an equally fast upstream reaction front propagation in the rich mixture as along the stoichiometric mixture fraction iso-surface. In contrast, the LTIF-CMC model predicted ignition in the lean mixture at the jet tip. After ignition, the LTIF-CMC model predicted an upstream movement of the reaction front along the stoichiometric mixture fraction iso-surface. The TIF model also predicted ignition in the lean mixture at the jet tip. The upstream

movement of the reaction front showed clearly an effect of the progress of individual flamelets and no distinct flame propagation was observed.

Figure 4 and Figure 5 show simulation results for mixture fraction, temperature, OH mass fraction (OH is a high temperature chemistry indicator) and CH₂O mass fraction (CH₂O is a low temperature chemistry indicator) at $t = 4$ ms for Case 1 and

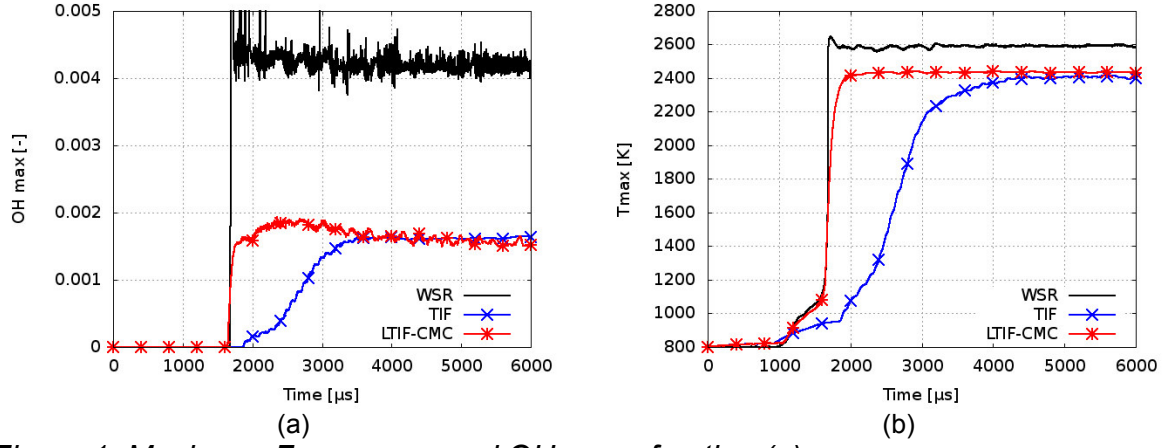


Figure 1: Maximum Favre averaged OH mass fraction (a) and temperature (b) for Case 1.

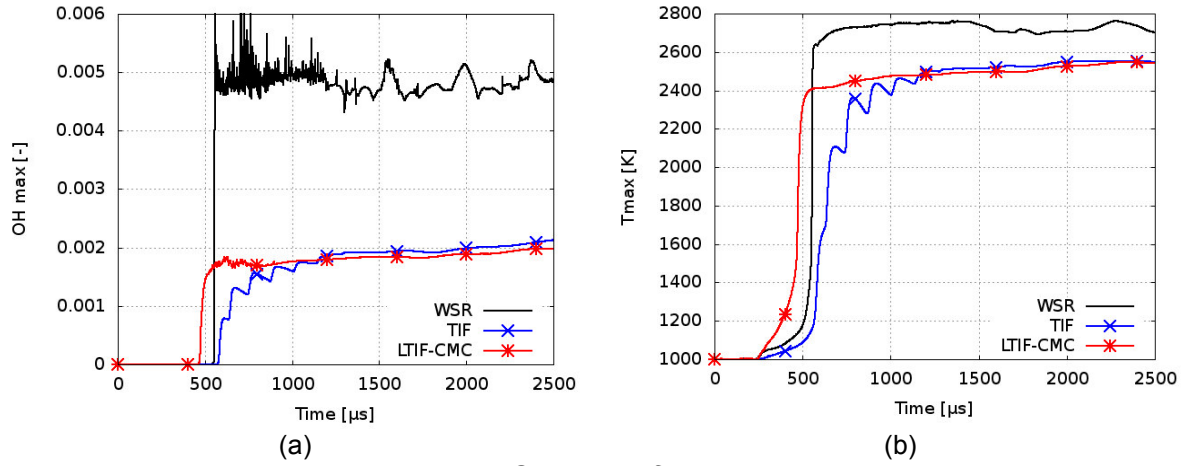


Figure 2: Maximum Favre averaged OH mass fraction (a) and maximum temperature (b) for Case 2.

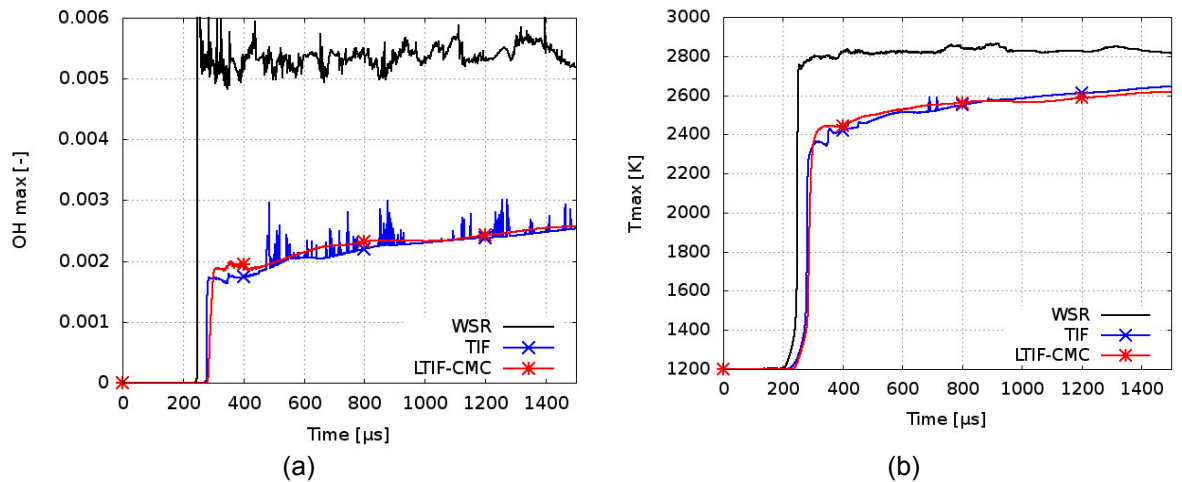


Figure 3: Maximum Favre averaged OH mass fraction (a) and maximum temperature (b) for Case 3.

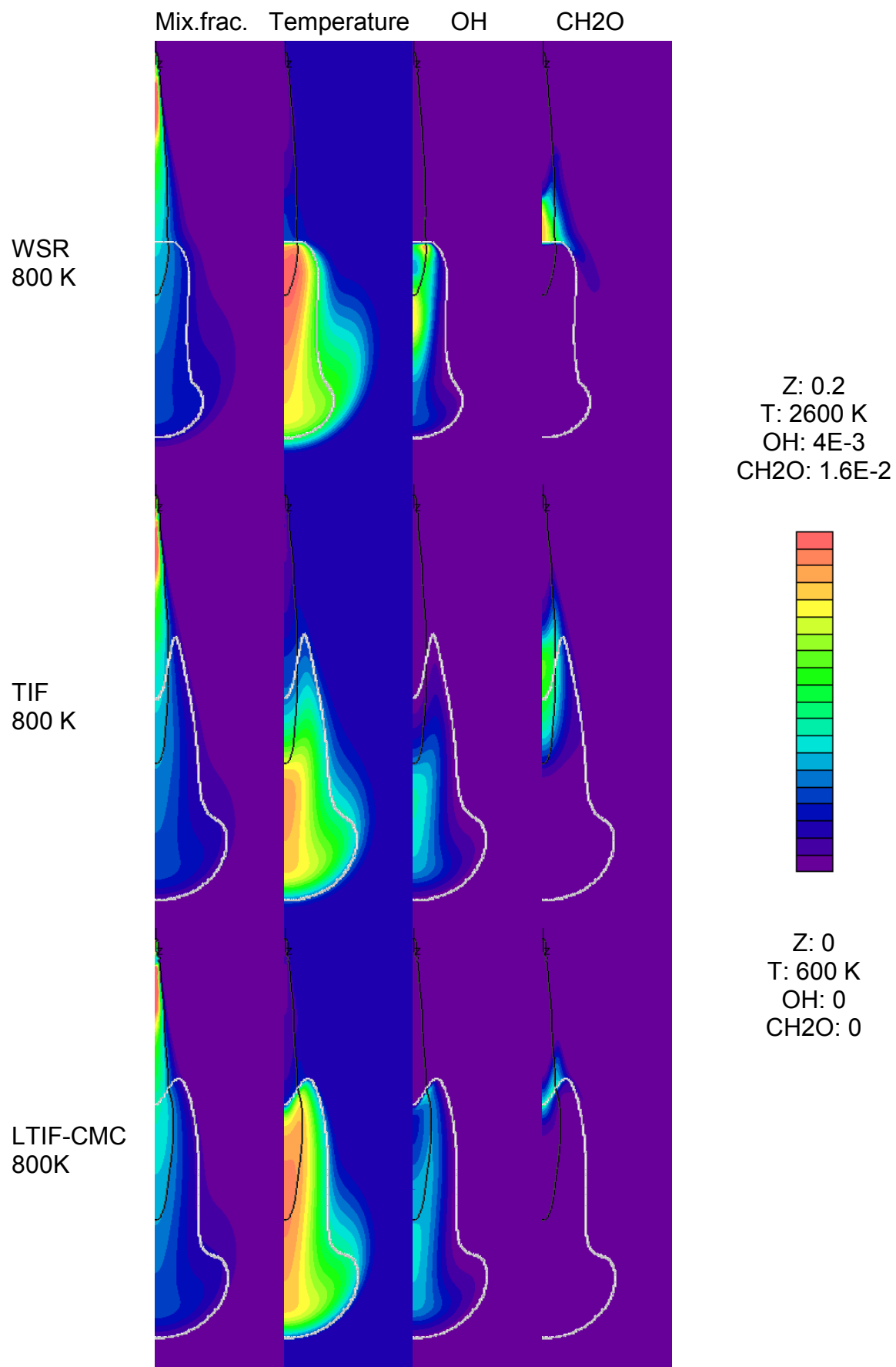


Figure 4: Section plots at 4 ms after start of injection depicting mixture fraction, temperature, OH mass fraction and CH2O mass fraction for Case 1.

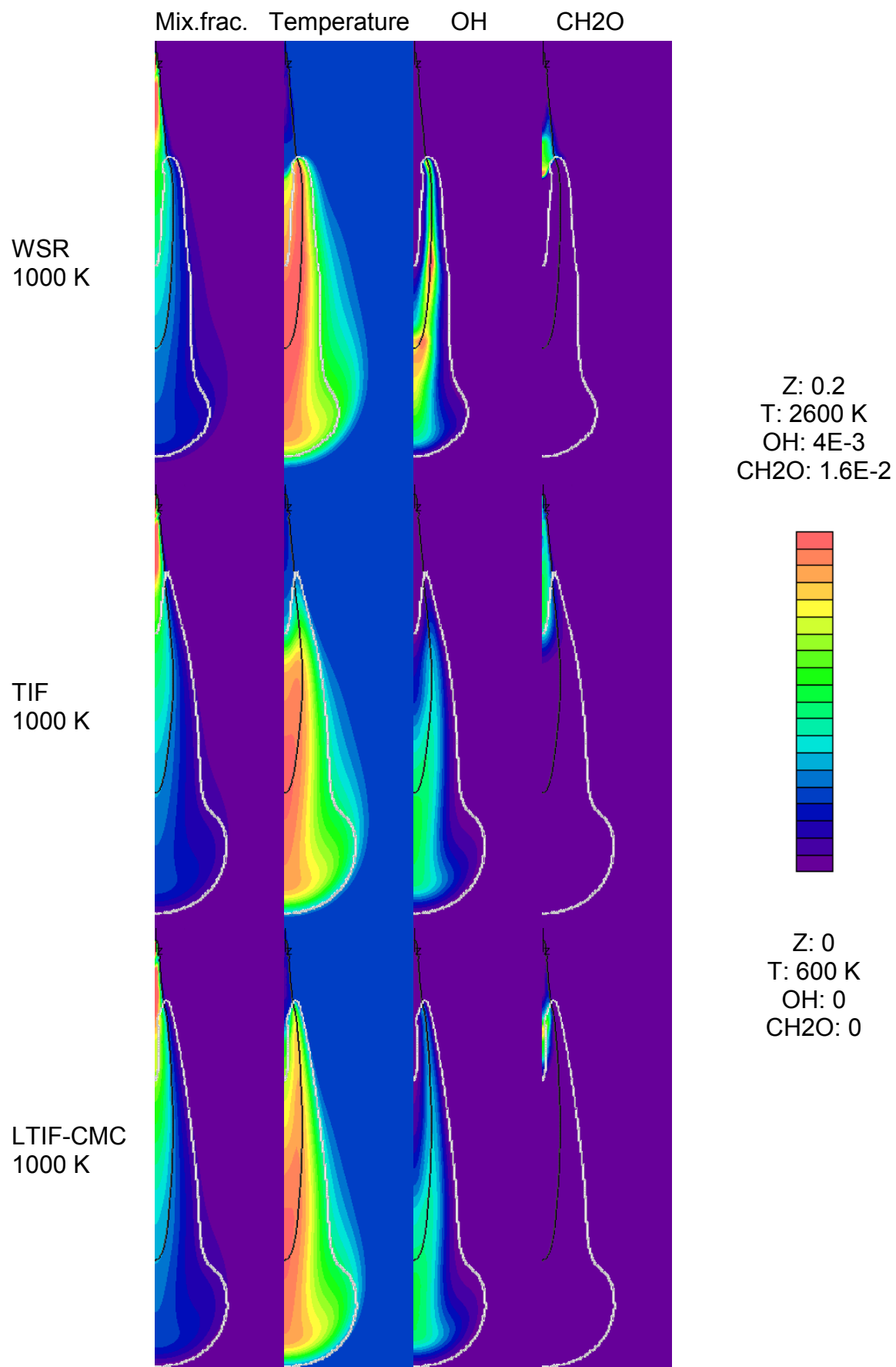


Figure 5: Section plots at 4 ms after start of injection depicting mixture fraction, temperature, OH mass fraction and CH2O mass fraction for Case 2.

Case 2 respectively. The same color scale is used for all combustion models, and in all figures, the stoichiometric mixture fraction iso-surface is drawn as a black line, and the 2 % maximum OH iso-surface is drawn as a white line. The WSR and LTIF-CMC models predict a high OH concentration at the flame base, and a distinct region with high CH₂O concentration upstream of the region with high OH concentrations. The occurrence of CH₂O upstream of the high-temperature chemistry region has also been observed in the experiments. The TIF model, on the other hand, predicts a rather diffuse OH cloud, with the maximum OH concentration in the center of this cloud for both cases. The CH₂O region predicted by the TIF model occurs upstream of the region with high OH concentration. However, for the 800 K case the CH₂O penetrates far downstream, through the 2 % maximum OH mass fraction border. For the 1000 K case, CH₂O is observed close to the nozzle. This is a result of the mixture fraction PDF – fuel vapor exists close to the nozzle – and the fact that the flamelets have had enough time for the low temperature reactions to start. Similar results as for Case 2 are found for Case 3 (1200 K) and not shown here. For Case 3, no lift-off could be predicted with TIF and 50 interactive flamelets. A higher number of interactive flamelets would be needed for lift-off prediction.

Comparing the ignition event, flame stabilization and flame structure predicted by the different models, it seems the most reasonable results are obtained with the LTIF-CMC model. The influence of turbulence-chemistry interaction on the flame structure has been shown to be of importance in [10,12].

Different from the FGM based model with sub-grid scale fluctuations [14], and the t-PDF model [12], the lift-off distance was generally found to be shorter with the LTIF-CMC model than with the WSR model. This is in-line with the findings presented in [11], where the CMC calculation with online chemistry predicted shorter lift-off lengths than the WSR model. It can be noted that the implementation used here, and the implementation in [11] closes the chemical source term to first order. The closure of the chemical source term might influence the prediction of the lift-off distance.

In order to facilitate a comparison of computational efficiency, all cases were run using five cores on a Dell Precision workstation with dual Intel Xeon E5-2670 v2 ten-core CPUs. The wall-clock time required by the LTIF-CMC model was 15 h, TIF with 50 interactive flamelets required 79 h and the WSR model required 29 h. The higher computational cost of the TIF model is explained by the use of 50 flamelets, which in the end leads to the need to solve more “reactors” than when using WSR with clustering. The performance of the on-line chemistry combustion models (TIF and WSR) is good, considering the size of the chemistry (349 species, 3686 reactions).

5. Conclusion

Three different ECN spray H (n-heptane) cases were investigated using a detailed n-heptane mechanism and three different combustion models: well-stirred reactor (WSR) model, transient interactive flamelet (TIF) model and progress variable based conditional moment closure (LTIF-CMC).

The ignition delay was predicted close to what has been experimentally observed. The influence of turbulence-chemistry interaction was found to only have a minute effect on the ignition delay prediction of the cases investigated here. It is likely, that other cases, at lower temperatures and lower levels of ambient oxygen, will show a higher sensitivity to turbulence-chemistry interaction effects on the ignition delay time. Flame development and structure were found to be affected by the capability of turbulence-chemistry interaction modeling.

The most advanced model, LTIF-CMC, showed best predictions of lift-off length, flame stabilization and flame structure for all cases investigated. Future application concerning emission prediction will employ LTIF-CMC for a wider range of operating conditions and different fuels.

Acknowledgements

Dipl.-Ing. Cathleen Perlman, LOGE AB, is thanked for assistance with the MPI parallelization; Dipl.-Ing. Lars Seidel at LOGE GmbH is thanked for providing the chemical mechanism; and Dr. Rajesh Rawat, CD-adapco, is thanked for providing the STAR-CD license used for this study.

References

- [1] N. Peters. Turbulent Combustion. Cambridge University Press, Cambridge, 2000.
- [2] N. Peters. "Multiscale combustion and turbulence", Proc. Combust. Inst. 30(1):1-25, 2009.
- [3] S. B. Pope. "Small scales, many species and the manifold challenges of turbulent combustion", Proc. Combust. Inst. 34(1):1-31, 2013.
- [4] <http://www.sandia.gov/ecn/>, accessed May 2015.
- [5] L. M. Pickett, D. L. Siebers and C. A. Idicheria. "Relationship between ignition processes and the lift-off length of diesel fuel jets", SAE Technical Paper 2005-01-3843, 2005.
- [6] G. Vishwanathan and R. D. Reitz. "Development of a practical soot modeling approach and its application to low-temperature diesel combustion", Combust. Sci. and Tech. 182:1050-1082, 2010.
- [7] K. M. Pang, M. Jangi, X.-S. Bai and J. Schramm. "Evaluation and optimization of phenomenological multi-step soot model for spray combustion under diesel engine-like conditions", Combust. Theory Model. 19(3):279-308, 2015.

- [8] F. Peng Kärholm, F. Tao and N. Nordin. "Three-dimensional simulation of diesel spray ignition and flame lift-off using OpenFOAM and KIVA-3V codes", SAE Technical Paper 2008-01-0196, 2008.
- [9] A. Kösters, A. Karlsson, M. Oevermann, G. D'Errico and T. Lucchini. "RANS predictions of turbulent diffusion flames: comparison of a reactor and a flamelet combustion model to the well stirred approach", *Combust. Theory Model.* 19(1):81-106, 2015.
- [10] G. Borghesi, E. Mastorakos, C. B. Devaud and R. W. Bilger. "Modeling evaporation effects in conditional moment closure for spray autoignition", *Combust. Theory Model.* 15(5):725-752, 2011.
- [11] M. Bolla, D. Farrace, Y. M. Wright, K. Boulouchos and E. Mastorakos. "Influence of turbulence-chemistry interaction for n-heptane spray combustion under diesel engine conditions with emphasis on soot formation and oxidation", *Combust. Theory Model.* 18(2):330-360, 2014.
- [12] S. Bhattacharjee and D. C. Haworth. "Simulations of transient n-heptane and n-dodecane spray flames under engine-relevant conditions using a transported PDF method", *Combust. Flame* 160:2083-2102, 2013.
- [13] J. Campbell, A. D. Gosman and D. Hardy. "Analysis of premix flame and lift-off in diesel spray combustion using multi-dimensional CFD", SAE Technical Paper 2008-01-0968, 2008.
- [14] U. Egüz, S. Ayyapureddi, C. Bekdemir, B. Somers and Ph. de Goey. "Manifold resolution study of the FGM method for an igniting diesel spray", *Fuel* 113:228-238, 2013.
- [15] C. Bajaj, M. Ameen and J. Abraham. "Evaluation of an unsteady flamelet progress variable model for auto-ignition and flame lift-off in diesel jets", *Combust. Sci. Technol.*, 185:454-472, 2013.
- [16] L. Seidel, K. Moshhammer, X. Wang, T. Zeuch, K. Kohse-Höinghaus, F. Mauß. "Comprehensive kinetic modeling and experimental study of a fuel-rich, premixed n-heptane flame", *Combust. Flame* 162(5):2045-2058, 2015.
- [17] LOGE AB. LOGEsoft, <http://www.loge.se/Products/Products.html>
- [18] CD-adapco. Methodology – STAR-CD version 4.22, 2014.
- [19] C. Perlman, K. Fröjd, L. Seidel, M. Tunér and F. Mauß. "A fast tool for predictive IC engine in-cylinder modeling with detailed chemistry", SAE Technical Paper 2012-01-1074, 2012.
- [20] N. Peters. "Laminar diffusion flamelet models in non-premixed combustion", *Prog. Energy Combust. Sci.* 10:319-339, 1984.
- [21] H. Lehtiniemi, Y. Zhang, R. Rawat, F. Mauß. "Efficient 3-D combustion modeling with transient flamelet models", SAE Technical Paper 2008-01-0957, 2008.
- [22] H. Olguin and E. Gutheil. "Influence of evaporation on spray flamelet structures", *Combust. Flame* 161(4):987-996, 2014.
- [23] C. Hollmann and E. Gutheil. "Modeling of turbulent spray diffusion flames including detailed chemistry", *Proc. Combust. Inst.* 26:1731-1738, 1996.

- [24] A. Y. Klimenko and R. W. Bilger. “Conditional moment closure for turbulent combustion”, Prog. Energy Combust. Sci. 25:595-687, 1999.
- [25] A. Kronenburg and E. Mastorakos. “The conditional moment closure model”, In: T. Echehki and E. Mastorakos (eds.): Turbulent combustion modeling – Advances, new trends and perspectives, Fluid mechanics and its applications 95, pp. 91-117, Springer, Dordrecht, 2011.
- [26] H. Lehtiniemi, A. Borg and F. Mauß. “Conditional moment closure with a progress variable approach”, Paper MS 2-3, COMODIA, Fukuoka, Japan, 2012.
- [27] E. E. O’Brien and T.-L. Jiang. “The conditional scalar dissipation rate of an initially binary scalar in homogenous turbulence”, Phys. Fluids A 3(12):3121-3123, 1991.
- [28] A. Scholtissek, W. L. Chan, H. Xu, F. Hunger, H. Kolla, J. H. Chen, M. Ihme and C. Hasse. “A multi-scale asymptotic scaling and regime analysis of flamelet equations including tangential diffusion effects for laminar and turbulent flames”, Combust. Flame 162(4):1507-1529, 2015.

The Authors:

Dr.-Ing. Harry Lehtiniemi
 LOGE AB
 Ideon Science Park Beta 2
 SE-22370 Lund
 Sweden

Dipl.-Ing. Anders Borg
 LOGE AB
 Ideon Science Park Beta 2
 SE-22370 Lund
 Sweden

Prof. Dr.-Ing. Fabian Mauß
 Thermodynamics and Thermal Process Engineering
 Brandenburg University of Technology – BTU Cottbus
 Siemens-Halske-Ring 8
 DE-03046 Cottbus
 Germany

Licence:

This document is licensed under the Creative Commons Attribution 3.0 DE License (CC-BY 3.0 DE): <http://creativecommons.org/licenses/by/3.0/de/>

Experimental investigations of a dual-fuel combustion system for passenger car Diesel engines with gasoline and Diesel fuel

Benedikt Heuser
Florian Kremer
Stefan Pischinger
Hans Rohs
Bastian Holderbaum
Thomas Körfer
Christof Schernus

Abstract

Dual-fuel combustion was studied in experiments on a modern single cylinder Diesel engine (SCE) for passenger car applications. Gasoline RON95 E10 was used as fuel for port fuel injection (PFI), and EN590 Diesel B7 for direct injection (DI).

Generally, soot emissions are found to be substantially lower in dual-fuel operation than for conventional direct injection compression ignition (DICI). But to overcome the drawback of a significantly increased heat release rate in highly premixed combustion at high load, the amount of premixed fuel at full load has to be limited. At lower to middle part load, however, increased homogenization was found to be beneficial against steep combustion pressure gradients.

The high sensitivity of combustion to air- and fuel-path variations motivated a detailed parameter study in a medium operation at $n = 1500$ 1/min and IMEP = 6.8 bar point using Design of Experiments (DoE). It was possible to achieve almost soot and NOx free combustion along with very smooth pressure gradients accepting a small penalty against conventional DICI combustion of up to approximately 2% lower efficiency caused by more incomplete combustion.

1. Introduction

Today, researchers go to great lengths to minimize pollutant and Greenhouse gas (GHG) emissions within the transportation sector. Compared to spark ignition (SI) engines, compression ignition (CI) engines feature a higher thermodynamical efficiency, but at the same time require intense aftertreatment of the exhaust gas in order to meet latest standards. Therefore, a Diesel Oxidation Catalyst (DOC) for the oxidation of hydrocarbons (HC) and carbon monoxide (CO) is used. Tailpipe emissions of nitrogen oxides (NO_x) are prevented by utilization of e.g. a NO_x Storage Catalyst (NSC) or a Selective Catalytic Reduction (SCR) catalyst. Emitted particulate matter (PM) is reduced by a Diesel Particulate Filter (DPF). Next to these aftertreatment systems, engine-out emissions have to be reduced by in-cylinder measures as well. NO_x is formed at high combustion temperatures and air-excess. Therefore, exhaust gas is recirculated (EGR) into the combustion chamber in order to reduce the combustion temperatures and oxygen concentration and lower therefore NO_x emissions. However, this measure – if no countermeasures are applied – typically reduces the amount of oxygen mass available in the cylinder as well and thus worsens the soot oxidization. It is well known, that soot emissions can effectively be reduced by lowering the local equivalence ratio Φ at the start of combustion (SOC). For this reason, several combustion concepts that propose a more homogenous mixture at SOC, like Homogenous Charge Compression Ignition (HCCI) or Partially Premixed Compression Ignition (PPCI), have been suggested to achieve overall lower engine-out emissions [1,2,3]. As an optimum fuel for such combustion concepts an auto-ignition quality between Diesel and gasoline fuel is suggested [4].

Besides increasingly stringent emissions legislations, another challenge arises with the increasing energy demand. The worldwide demand of liquid fuels is constantly increasing, but within the last decade, the share of gasoline is declining in favor of Diesel fuel. In the future, this trend is expected to become even more intense due to efficiency increase and the fact that passenger cars with Diesel engines will have a bigger market share: The sale of gasoline is predicted to be reduced by 10 % within the next three decades, while Diesel demand will increase by up to 84 % within the same time, resulting in a rise of Diesel market share of above 60 % [5]. Thus, the already existing imbalance of production and demand for both Diesel and gasoline will exist beyond 2025 [6]. With the shifted market share of gasoline and Diesel, the price for Diesel fuel is expected to increase significantly. For both reasons, the more stringent emission legislation and the existing fuel imbalance, an effort is made to utilize more volatile fuels in Diesel engines. [7,8,9]

It is still challenging to utilize these combustion concepts within the whole engine load range. On the one hand, HCCI typically causes very high heat release rates (HRR), and thus steep cylinder pressure gradients, resulting in both poor acoustics and insufficient transient response. On the other hand, combustion concepts with highly homogeneous mixtures suffer from high levels of unburned hydrocarbon (HC) and carbon monoxide (CO) emissions, particularly in the low load regime. Therefore, another combustion concept was sought after that combines both a low PM/NO_x-trade-off and low HC- and CO emissions. Consequently, a combustion strategy was proposed that utilizes a port fuel injection (PFI) of a low-reactivity fuel and direct injection (DI) of a fuel with high reactivity. It could be proven, that this dual-fuel operation allows the control of the overall mixture reactivity and therefore the load-dependent combustion phasing. Hence, this in-cylinder fuel blending with early injection of the reactive fuel was called “Reactivity Controlled Compression Ignition”

(RCCI) by Kokjohn et al. [10]. The RCCI concept provides a better controllability of combustion compared to e.g. (dual-fuel) HCCI and PCCI. It also contributes to very low PM- and NO_x emissions for both light-duty (LD) and heavy-duty (HD) engines at various loads [11,12,13]. In addition to the reduction in regulated pollutants, very high gross thermal efficiencies in HD engines above 60% were reported. This is mostly caused by reduced wall heat losses due to lower combustion temperatures. [14]

In this study dual-fuel operation with Diesel and gasoline fuel was investigated in detail. The investigated loads range from low part load up to rated torque and rated power. During these experiments, the gasoline mass fraction varied from 0% to 90% m/m. The engine-out NO_x emissions were controlled via high EGR-rates and met EU-6.1 legislation for all part load points. In order to preclude effects of, for example, retarded combustion on efficiency and emissions, the center of combustion (CA50) was kept constant and independent of the gasoline mass share. In addition to the investigations with Diesel pilot injection, investigations with a very early Diesel injection were performed at an medium load point with an engine speed of $n = 1500$ rpm and an engine load of IMEP = 6.8 bar. The investigations with early Diesel injection will be referred to as “RCCI” in the following. At full load operation, gasoline mass fraction was increased until a given maximum cylinder pressure rise rate was reached.

2. Methodology

In the following subsection, the characteristics of the utilized fuels, the specifications of the engine, and the measurement devices will be introduced.

2.1 Fuel characteristics

For PFI, a conventional EN228 gasoline RON95 E10 was selected. For DI, standard EN590 Diesel pump fuel was chosen. The physical characteristics of the fuels are given by Table 1.

	EN 590 Diesel	EN 228 Gasoline
Carbon mass fraction / %	84.47	82.97
Hydrogen mass fraction / %	13.27	13.48
Oxygen mass fraction / %	2.26	3.56
Density (25 °C) / kg/m ³	820	733.6
Boiling temperature / °C	170-350	28-188
Vapour pressure (20 °C) / kPa	<0.1	68.9
Specific enthalpy of vaporization / kJ/kg	358	420
Stoichiometric air requirement / 1	14.8	14.0
Lower heating value / MJ/kg	42.8	42.1
Research octane number (RON)	-	96.3
Cetane Number (CN)	53	-

Table 2: Properties of the investigated fuels

2.2 Single cylinder Diesel research engine

The engine that was used for this study is a single cylinder engine (SCE) with a displacement of 0.39 l. The fuel injection equipment (FIE) for direct injection (DI) is near to series production, state-of-the-art and features an injection pressure up to 220 bar. For PFI a series production Bosch valve was used. The engine control unit is based on a Rapid Control Prototyping (RCP) computer enabling a free determination of the injection parameters for both DI and PFI. The engine features a maximum specific power output of 80 kW/l with peak firing pressures of 190 bar. Due to intense charge-air and exhaust gas recirculation (EGR) cooling the engine meets EU-6 NO_x-level while simultaneously achieving low particulate matter (PM) emissions even in pure Diesel operation. For dual-fuel operation, the piston bowl geometry was not adjusted. Thus, the piston has a ω -shaped reentrant bowl with a volume of 21.6 cm³. The squish height is 0.78 mm and the compression ratio results in $\epsilon = 15:1$. A more detailed description of the engine can be found in [15]. The main engine specifications are given in Table 2.

	Unit	
Displacement	cm ³	390
Stroke / bore	mm	88.3 / 75
Compression ratio	-	15:1
Max. cylinder pressure	bar	190
Fuel injection equipment DI	-	Bosch Piezo Common Rail System
Max. injection pressure DI	bar	2200
Nozzle DI	-	8 hole, 109 μ m hole diameter, 153°
PFI Valve	-	E14, type E (2-spray),
Boosting	-	Max. 3.8 bar abs.

Table 3: Engine specifications

2.3 Investigated load regime

This study focuses on the application of a dual-fuel approach for a LD-engine as it is used for passenger cars. Therefore, almost the whole engine load regime was investigated, covering low part load operation to full load operation. For all engine loads, an optimization of the engine calibration was carried out with Diesel only in previous studies [16]. For the initial characterization of dual-fuel operation, most of the calibration parameters such as boost pressure, DI rail pressure, and center of combustion (CA50) were kept constant at part load operation. Table 3 summarizes the main engine settings at part load operation. The transition of the EU-6.1 NO_x-level of 80 mg/km into g/kWh for the four stationary load points is explained in [16].

Speed, load	CA50	Rail press. DI	Boost press.	Charge air temp.	Exh. gas press.	EU-6.1 NO _x level
rpm, bar	°CA bTDC	bar	bar	°C	bar	g/kWh
1500, 4.3	-6.6	720	1.07	25	1.13	0.2
1500, 6.8	-5.8	900	1.50	30	1.60	0.2
2280, 9.4	-9.2	1400	2.29	35	2.39	0.4
2400, 14.8	-10.8	1800	2.6	45	2.8	0.6

Table 4: Investigated part load points and engine calibration

The maximum engine power and torque is limited by the Filter Smoke Number (FSN), exhaust gas temperature, and peak firing pressure (PFP). These limits as well as the further calibration parameters (rail pressure, boost pressure etc.) were adapted from current state-of-the-art applications. The most important calibration parameters as well as the restraints at full load are presented in Table 4.

Speed	IMEP (in DICI)	Boost press.	Exh. gas press.	Rail press.	Charge temp.	Max. FSN	Max. exh. temp.	Max. cyl. pressure
rpm	bar	bar	bar	bar	°C	-	°C	bar
1000	13.8	1.5	1.9	1000	35	2.6	850	130
2000	26.1	2.45	2.46	1800	46	1.7	850	160
3000	28.5	2.7	3.2	2000	53	2.5	850	190
4000	26.0	3.0	3.9	0200	60	2.8	850	190

Table 4: Engine calibration and restrictions at full load operation

Figure 1 shows the investigated part and full load points within the range of the whole engine map.

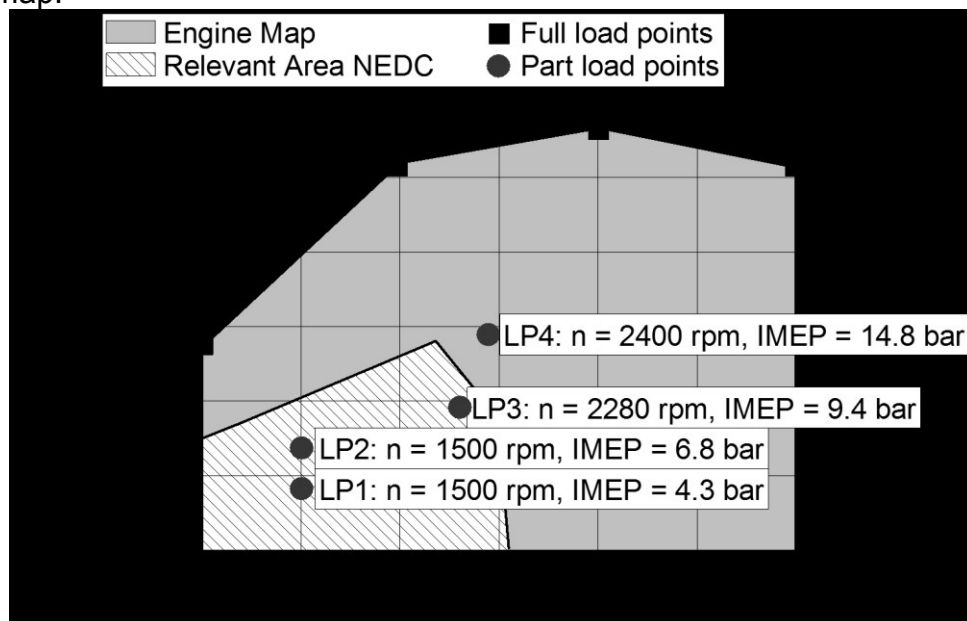


Figure 1: Investigated engine load points

2.4 Measurement equipment

Regulated and unregulated emissions, i.e. CO, CO₂, HC, NO_x and PM are measured at engine exhaust by means of following sampling systems:

- HC: Flame ionization detector (Rosemount NGA 2000)
- O₂: Paramagnetic oxygen analyzer (Rosemount NGA 2000)
- CO: Infrared gas analyzer (Rosemount NGA 2000)
- CO₂: Infrared gas analyzer (Rosemount NGA 2000)
- NO_x: Chemiluminescence analyzer (Eco Physics 700 EL ht)
- PM: Filter paper method (AVL 415S)

For the HC emissions, it was assumed that all HCs are present as propane (C₃H₈). During low load operation, the extraction site for exhaust gas is located in the exhaust gas manifold. During medium to high load operation, it is placed downstream of the back pressure valve due to high exhaust gas back pressure and exhaust gas temperatures. The sampling lines are heated up to 180 °C for the HC, CO, and NO_x measurements to avoid condensation. The sample line of the Smoke Meter is heated to 75 °C. The EGR-rate is calculated based on the molecular CO₂ concentration in the intake manifold and the exhaust gas. The fuel consumption of both gasoline and Diesel fuel is measured by a Coriolis-type fuel flow meter. An ultrasonic gas meter “Flowsic” by Sick is utilized to measure air volume flow. Taking into account the air temperature and its water content the air mass flow is calculated. The boost pressure can be adjusted independently by an external three-stage charging system which also provides low intake air temperatures via three charge air coolers that are in series connection. An electric, position controlled EGR-valve is used for adjusting the EGR-rate. The exhaust gas backpressure is controlled by two valves in the exhaust gas track. A water-cooled piezoelectric pressure transducer by Kistler (6041A) is utilized for measurement of the cylinder pressure. FEV’s “Combustion Analyzing System” (CAS) records the cylinder pressure trace. It is used for determination of combustion related parameters such as CA₅₀. All pressures are recorded in increments of 0.5 crank angle degrees (°CA) except the cylinder pressure, which is recorded at 0.1 °CA. Indicated values, such as indicated mean effective pressure (IMEP) and displayed cylinder pressure traces, are recorded as an average of 50 cycles unless stated otherwise. The position of the crank angle and the differentiation between high pressure phase and gas exchange phase is measured by a crank angle sensor and an additional sensor at the intake camshaft. For calculation of burning rates, ignition delay, etc., the FEV software “Engine Process Optimization System” (EPOS) V4 was utilized. The ignition delay of the fuel is deduced from the time difference of the in-cylinder pressure rise due to ignition (5% of fuel mass converted) and the start of direct fuel injection (SODI). The time lag between the start of injector energizing (SOE) and SODI is 160 μs, almost independently of the injection pressure.

3. Test results and discussion

Within this section, the experimental test results at part load and full load operation are presented.

3.1 Diesel pilot injection strategy

In the investigations with Diesel pilot injection, the standard calibration was kept constant independent of the gasoline mass fraction. The gasoline mass fraction was continuously increased until the combustion either became very unstable or until the premixed fuel ignited before Diesel fuel was injected. For limitation of the mechanical stress, another boundary was the maximum pressure rise rate (MPRR) that was set to 15 bar/°CA independent of the engine load conditions. This section is divided into part load operation and into full load operation.

3.1.1 Part load investigations

Figure 2 shows the results of the part load investigations. In Figure 3 exemplary cylinder pressure traces, apparent heat release rate, cumulative normalized heat release and the energizing of the Diesel injector are given. The traces show the findings with conventional DICI operation and with the maximum gasoline mass fraction that could be achieved in these tests. Additionally, the gasoline mass fraction that is between 0% and the corresponding maximum of each load point is shown.

The findings in the lowest load point at an engine speed of $n = 1500$ rpm and an IMEP of 4.3 bar are displayed in black color. Because the particulate emissions in this load point are already very low (even with conventional DICI), there is no further benefit of a higher premixing by the addition of gasoline. See the upper left graph. Unfortunately, the emissions of unburned hydrocarbons (HC) and carbon monoxide (CO) continuously rise to the sevenfold with 55.7% m/m gasoline compared to pure Diesel operation. This was observed in previous studies as well. This is believed to be the result of fuel that is trapped in crevices and parasitic volumes [17]. Since the overall temperature level is low at this engine operating condition, the fuel cannot be oxidized during the exhaust stroke. This directly causes a drop in efficiency up to 2.9%, while the losses caused by incomplete combustion increase. The NO_x emissions have been controlled via the EGR-rate to be compliant to the EU6 legislation. However, the EGR-rate required to meeting the desired NO_x emissions slightly decreases with increasing gasoline mass fraction, which can be attributed to an overall reduced reactivity of the mixture. The lower reactivity also results in a continuous reduction of the maximum pressure rise rate (MPRR) with higher gasoline mass fraction. As it can be concluded from both Figure 2 and Figure 3, the start of energizing of the Diesel injector (SOE) has to be advanced with higher gasoline mass portion in order to maintain a constant CA50. With 55.7% m/m gasoline, the SOE is as early as -26°CA aTDC. Despite the high homogeneity, the apparent heat release rate (HRR) and the pressure rise rate (PRR) are rather low. Moreover, when comparing the rates of heat release, it is obvious that the influence of the gasoline fraction is non-linear. Even with 28% m/m gasoline, it is hard to make a distinction between the corresponding burning function and that of DICI. However, in the present study a gasoline mass fraction of 55.7% was considered as maximum, even though the covariance of IMEP (COV) was well below the 5% border what is considered as engine misfiring [18]. The reason rather is that with the reported gasoline portion the CA50 could not be controlled anymore and combustion is retarded.

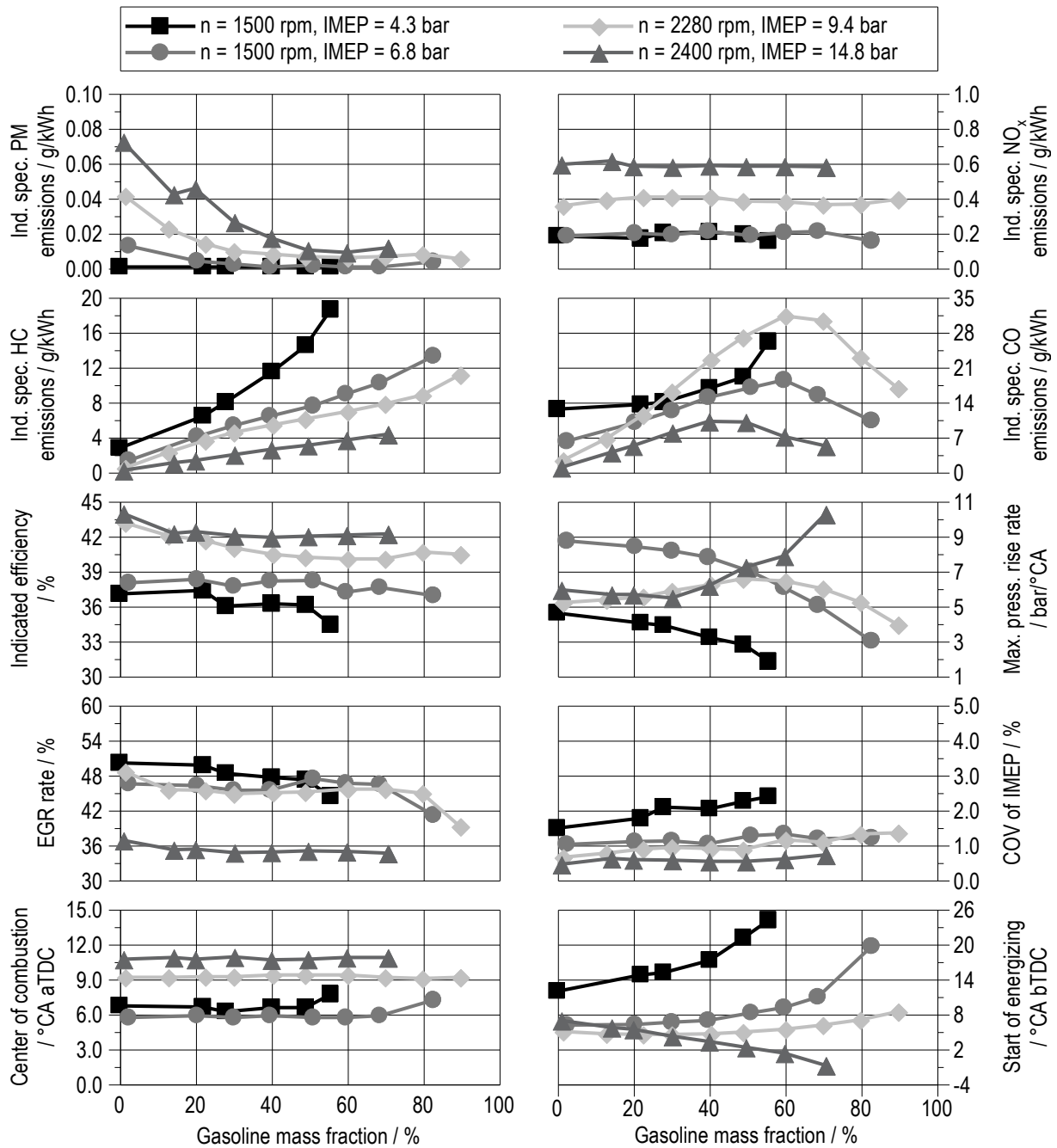


Figure 2: Experimental test results at four different engine load points: Gasoline mass fraction sweeps with constant engine-out NO_x emissions and constant center of combustion

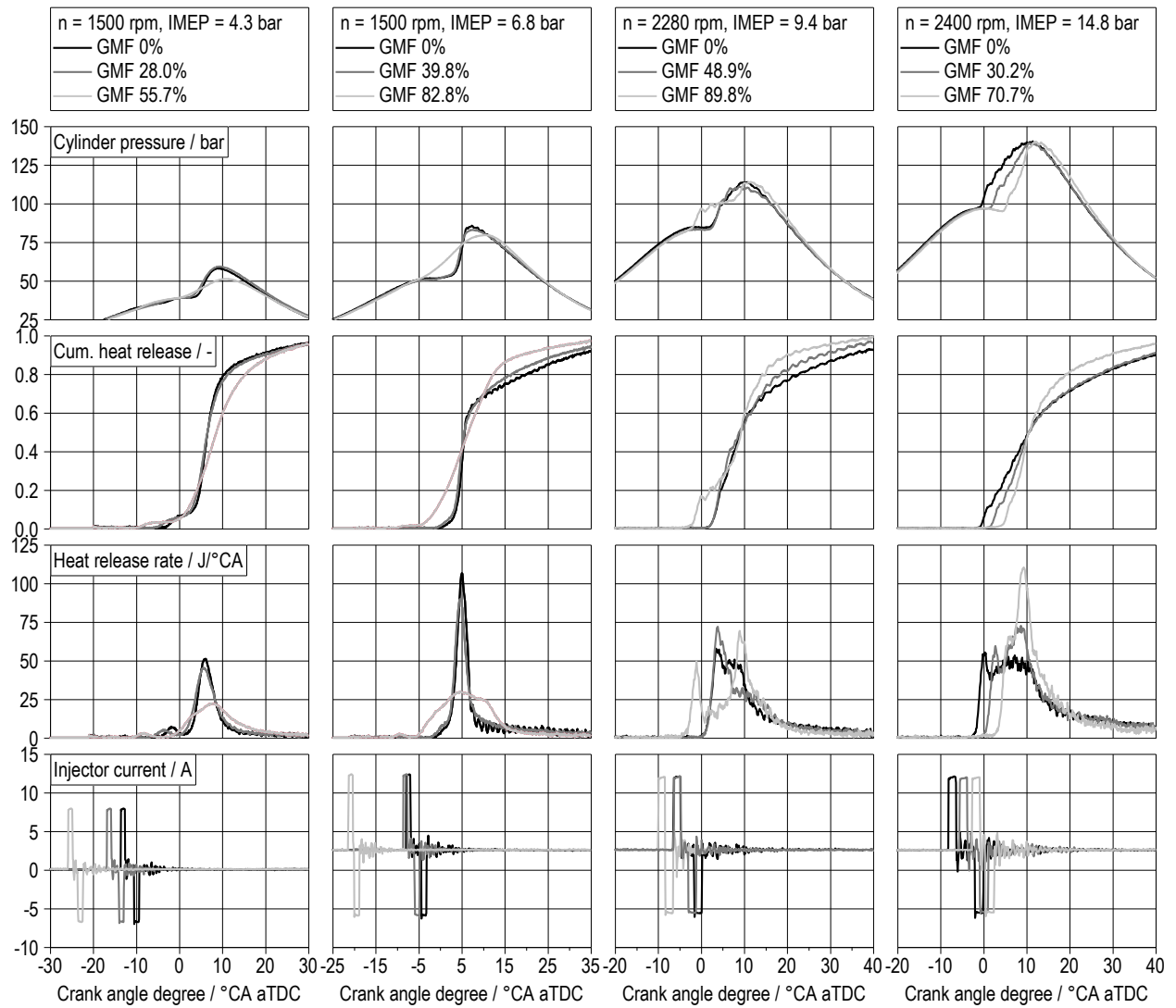


Figure 3: Cylinder pressure trace, cumulated normalized heat release, apparent heat release rate and DI injector current for all part load points and different gasoline mass fractions (GMF)

In the second load point at same engine speed but slightly higher load of IMEP = 6.8 bar, a benefit of a higher premixing in terms of an improved soot/NO_x-trade-off can be observed. With a share of 20% m/m gasoline, a substantial reduction of 70% of soot emissions can be observed. However, the overall soot emissions can be considered low with DICI as well. The NO_x emissions were regulated to meet EU6 legislation. Similar to the lower load point, the HC emissions rise continuously with increasing gasoline mass fraction. Contrary to that, CO emissions initially increase linearly with up to a gasoline mass fraction of 59.7%, and then decline with a further increase of gasoline mass fraction. Whereas the majority of the unburned fuel origins from crevices and parasitic volumes, CO emissions are mainly caused by flame quenching. With higher share of the premixed fraction, CO emissions start to rise. However, increasing the gasoline mass fraction results in an increase in the equivalence ratio of the premixed cylinder charge as well. Thus, at a certain equivalence ratio, quenching is reduced due to a more stable combustion in the fully premixed zones. Considering the EGR-rate and the oxygen content of the recirculated exhaust gas, in this very high load

point the equivalence ratio is increased from $\phi = 0.339$ to $\phi = 0.385$ when increasing the gasoline mass fraction by 9% to 58.7%.

The indicated efficiency in this load point remains almost constant and is not influenced by variations of the fuel mass fractions. Thus, higher losses due to incomplete combustion are compensated for by faster combustion. The combustion duration (5% to 90% fuel mass conversion) is 21°CA with 82.8% m/m gasoline, and ~30°CA in with 100% m/m Diesel. Consequently, the 95% mass fraction burned is achieved earlier in the cycle with high gasoline mass fraction (see Figure 3, second column) which results in reduced thermal exhaust losses ($\Delta T = 15.41$ °C). Additionally, lower combustion peak temperatures due to lower HRR might lower wall heat losses as well.

With respect to the MPRR the same observations can be made as for the lower load point with an IMEP of 4.3 bar. The reactivity of the mixture is continuously decreased with an increase of the gasoline mass fraction. Thus, with the highest gasoline mass fraction of 82.8%, the MPRR is lower by almost 5 bar/°CA in comparison to DICI operation. As it can be concluded from the second column in Figure 3, the cylinder pressure trace is very smooth since the pressure gradient during combustion is very similar to that during the compression stroke. The reason is in the very low maximum HRR of 36.6 J/°CA compared to 108.9 J/°CA in DICI operation, respectively 94.9 J/°CA with a gasoline mass fraction of 39.8%.

To summarize the findings in the two lowest load points, it can be said that with an increase in gasoline mass fraction the Diesel direct injection has to be significantly advanced in order to maintain the desired combustion phasing. The early Diesel injection and the high gasoline mass fraction lead to a high homogeneity in the mixture, and simultaneously to a substantially reduced reactivity of the mixture. In literature, this is often referred to as “Reactivity Controlled Compression Ignition” (e.g. [12, 13]). During the investigations at the engine this combustion concept has shown a high sensitivity on both variations in the air and in the fuel path, as it will be discussed later in this paper.

In gray line color, the results of the gasoline mass fraction sweep at an engine speed of $n = 2280$ rpm and load of IMEP = 9.4 bar are given. Again, an increased share of premixing enables an improved soot/NO_x-trade-off. However, the saturation in soot reduction is achieved already with 49.8% m/m gasoline. At EU6 NO_x-level the corresponding FSN is 0.11, compared to 0.68 in DICI operation. With regard to HC- and CO emissions the same observations can be made as for the previously discussed load point #2 with $n = 1500$ and IMEP = 6.8 bar. HC emissions continuously incline with higher premixing, but CO emissions reach a maximum at a gasoline mass fraction of 60% and then decrease with a further increase of the premixed air/fuel fraction. Compared to the lower load point, the equivalence ratio is lower (transition from $\phi = 0.28$ to $\phi = 0.317$). The reason that this equivalence ratio is already sufficient to reduce the quenching effect may be due to higher temperatures and pressure in the cylinder at this load point.

The indicated efficiency shows a remarkable drop of up to 3.8%. Again, losses caused by incomplete combustion rise due to higher emissions of HC and CO. In addition, and in contrast to the previous discussed load points, the maximum heat release increases with higher gasoline portions. The combination of both results in the most significant reduction in efficiency that is observed during this test bench campaign. The efficiency again rises with higher gasoline mass fractions, when a decline in CO emissions and HRR can be observed and thus the related losses are being reduced.

The MPRR increases slightly in this load point with increasing premixed combustion. As already mentioned, the maximum increase when compared to DICI is 1.26 bar/°CA, which can be considered as moderate. When evaluated according to the FEV method

[19], the combustion noise increases by 1.2 dB(A). The increase in MPRR is caused by slightly higher HRR as displayed in the graph in the third row and column of Figure 3. Moreover, by the given plots of the HRRs a transformation of the combustion with varying gasoline portion can be observed. With ~50% gasoline mass fraction, the combustion trace is quite similar to that of DICl operation, and shows only a more distinct peak of premixed combustion and little less mixing controlled combustion. With ~90% gasoline, the combustion can clearly be separated into three phases: First, a peak with a medium HRR which is caused by the Diesel fuel combustion can be seen. In succession, relatively low HRRs can be observed which are caused by a turbulent combustion of the premixed fuel. The HRRs are below that of the Diesel fuel combustion, since the reactivity in this mixture is rather low. This is due to the fact that the air-excess ratio (λ) is $\lambda = 2.1$ and thus beyond the upper flammability limit of ~1.4. While the in-cylinder temperatures and pressures keep increasing due to combustion of the premixed fuel, another distinct peak in HRR becomes evident. The cause for this second peak was investigated in more detail via simulation and is discussed within the next subsection. In this load point, a higher share of premixed fuel requires and adjustment in Diesel DI in order to maintain a constant CA50. However, when compared to the lower load points, the required advancing is very low.

The highest part load point that was investigated within this study is characterized by an engine speed of $n = 1500$ rpm and a load of IMEP = 14.8 bar. Here, the soot reduction at constant NO_x emissions is most remarkable. With a substitution of 60% m/m Diesel fuel by gasoline, the soot emissions could be reduced by almost 90%. However, this is at the cost of elevated HC- and CO emissions, and even more disadvantageously, significantly elevated PRRs. Compared to DICl, the MPRR is higher by 1.94 bar/°CA at 60% m/m gasoline (see), and the combustion noise is increased by 3.8 dB, which equals more than a doubling in the perceived noise emissions. Overall, in this engine-load point, using dual-fuel combustion with a high premixing is critical in terms of PRR. Contrary to the other load points, the HRR and thus the PRR continuously rises with increasing premixing. Despite low equivalence ratio of the premixed fuel of maximum $\phi = 0.338$, the mixture is highly reactive due to very high in-cylinder temperatures and pressure. Therefore, the gasoline portion was limited to 70.7%, since with slightly higher gasoline contents the mixture started to ignite before the Diesel fuel was injected. In order to keep the CA50 at 10.8 °CA aTDC, the Diesel injection had to be retarded. This trend can be observed by the lower right graph in Figure 3. With 70.7% gasoline the HRR is almost a single, distinct peak. The HRR shows a maximum of 120 J/°CA°, caused by self-ignition of the unburned gasoline fuel. This is discussed in the following subsection.

3.1.2 Full load results

In addition to part load operation, dual-fuel combustion was investigated at full load conditions as well. The target at full load was to achieve the highest possible IMEP at given constraints. In this study, the constraints were exhaust gas temperature, FSN, MPRR and peak firing pressure (PFP) (see Table 4). First, conventional DICl operation was investigated, and in a second step gasoline was introduced. In dual-fuel combustion mode, the gasoline portion was limited mainly by the MPRR. The results at all four engine speeds are depicted in Figure 4.

As it can be concluded from Figure 4, in dual-fuel operation the same IMEP as in DICl operation was achieved. However, the achieved gasoline mass fraction at all engine speeds is significantly lower compared to the part load investigations. Due to higher

boost pressures, higher charge temperatures and an overall richer mixture, the premixed charge was very much prone to auto-ignition

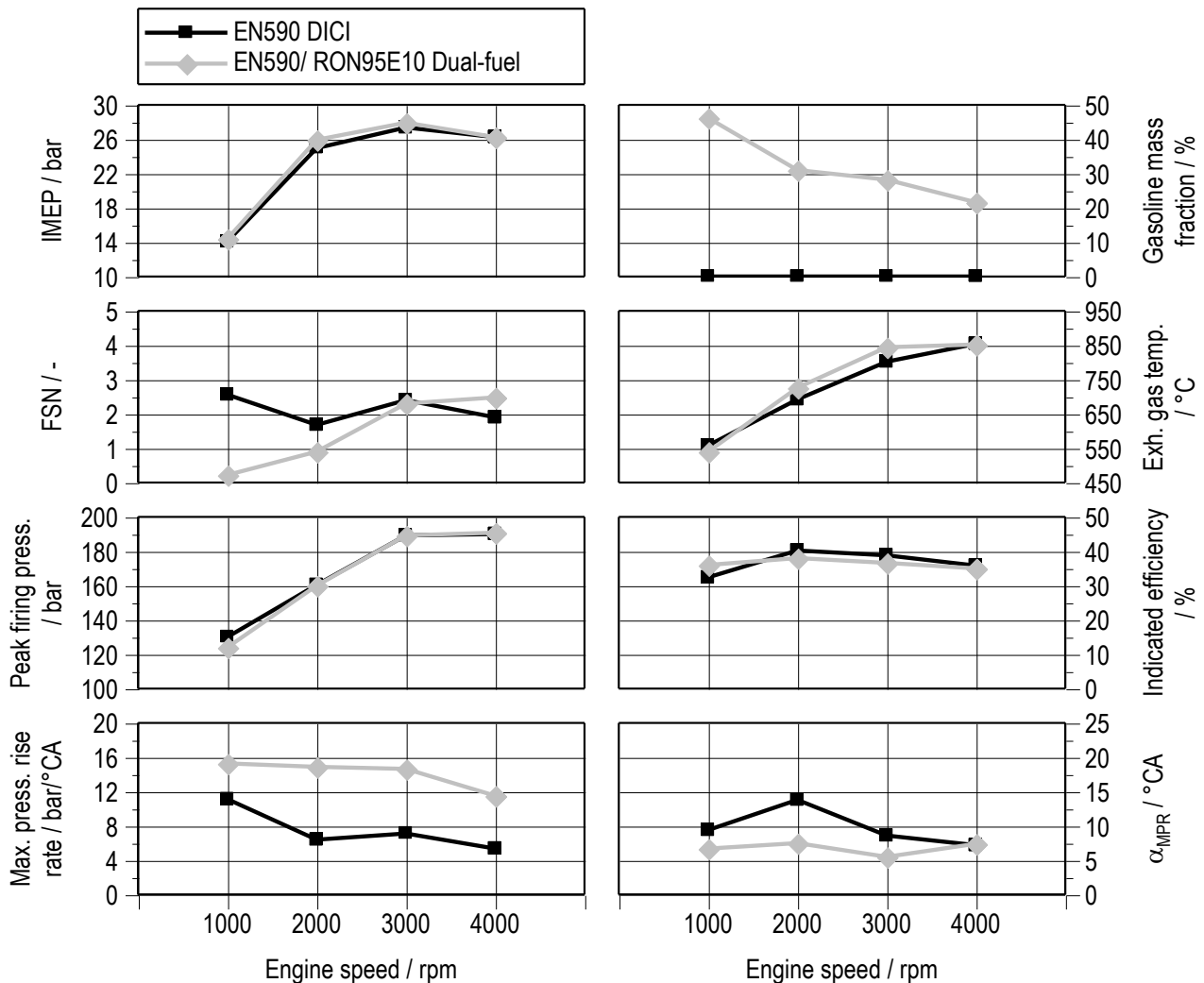


Figure 4: Full load test results for DICl and dual-fuel operation at four engine speeds

Due to this and the limit in MPRR, the highest gasoline content of 46.1% was achieved at an engine speed of $n = 1000$ rpm. In order to maintain a $MPRR = 15 \text{ bar/}^\circ\text{CA}$, the gasoline mass fraction had to be decreased with increasing engine speed. Therefore, with regard to emissions, there is no benefit of dual-fuel combustion to be observed at high engine speeds. Only at engine speeds up to $n = 2000$ rpm a reduction in FSN can be achieved with higher premixed combustion: at an engine speed of $n = 1000$ rpm the FSN can be reduced by 2.33 units, whereas at $n = 2000$ rpm soot emissions are lowered from 1.68 to 0.89. At $n = 3000$ rpm soot emission are almost equal in both DICl and dual-fuel operation. Finally at $n = 4000$ rpm, the FSN is even slightly higher in dual-fuel than in DICl operation. This might be caused by the slightly lower air-excess ratio, what is given in dual-fuel operation $\lambda_{DF} = 1.139$ and in DICl operation $\lambda_{DICl} = 1.183$. With only a small amount of fuel being premixed at this high engine speed, the soot oxidation seems to be worsened by the lower amount of oxygen available in the combustion chamber. With regard to efficiency at full load operation for both combustion concepts DICl and dual-fuel, no clear trend can be observed. Moreover, at all engine speeds the observed differences are quite small.

To summarize the findings of the experimental study with Diesel pilot injection, it can be stated that with conventional gasoline RON95E10 a benefit in the soot/NO_x-trade-off can be achieved almost over the whole engine load range. At low engine loads, this benefit is rather small due to overall low soot emissions. In high engine loads, a substantial benefit can be achieved, but here one has to cope with high pressure gradients due to rapid combustion of the premixed charge. At medium engine loads, it was found that the gasoline mass fraction can be extended to above 80% without considerably sacrificing efficiency or combustion noise. However, to maintain a constant combustion phasing, the Diesel DI had to be advanced significantly. This leads to a very homogenous mixture with rather low reactivity due to high portions of the low reactivity fuel and a local low equivalence ratio. This combustion system has been proven to be very sensitive to variations in e.g. boost pressure and gasoline mass fraction. For this reason, intense investigations by means of Design of Experiment (DoE) have been carried out. These results are presented within the next section.

3.2 Reactivity Controlled Compression Ignition

With high shares of gasoline, the combustion is highly sensitive on particularly EGR-rate, boost pressure and gas temperature on the one hand, and gasoline mass share, start of Diesel direct injection (SODI) and injection pressure on the other hand. Therefore, more detailed investigations have been performed at a medium load point with an engine speed of $n = 1500$ rpm and an engine load of IMEP = 6.8 bar. In this load point, the effect of variations in the Diesel DI is given exemplarily by Figure 5.

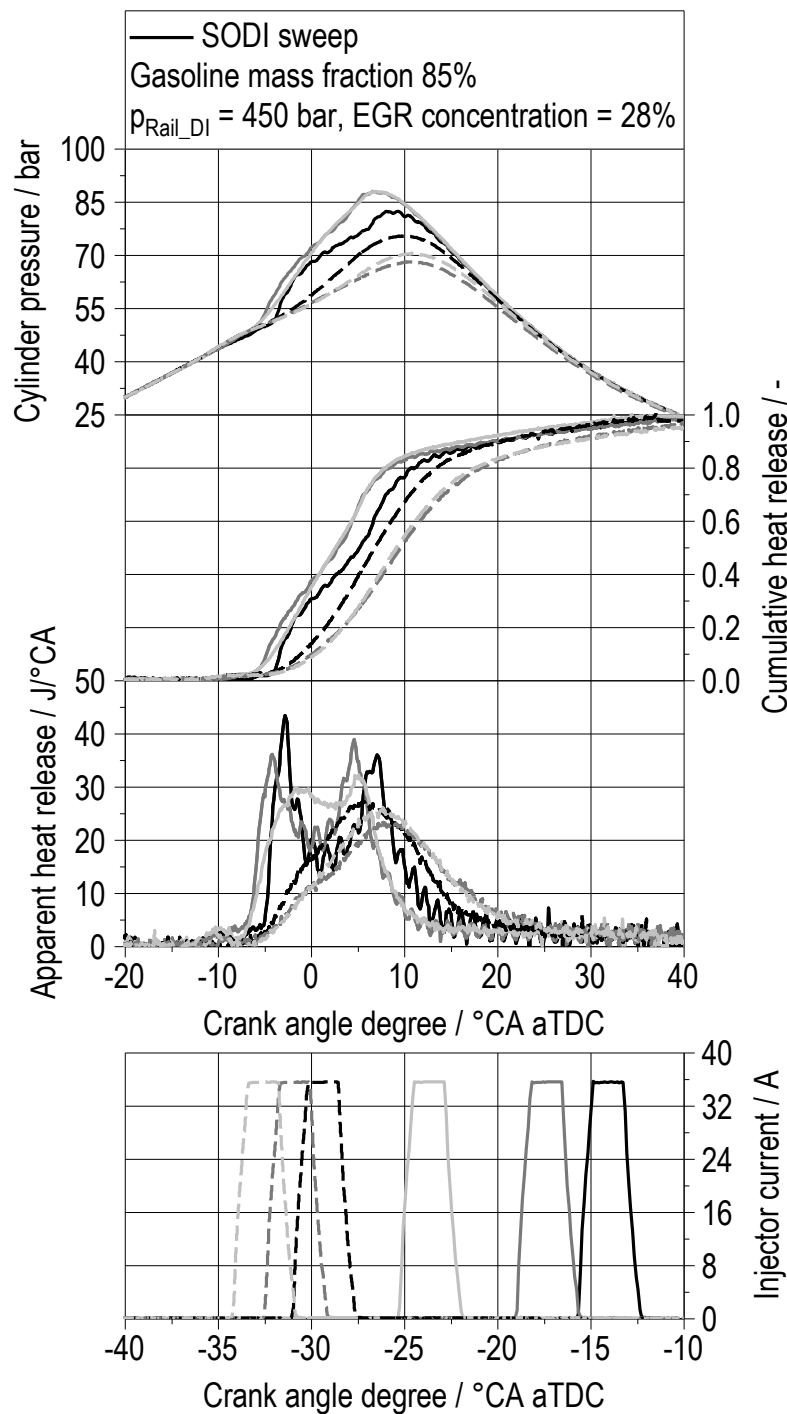


Figure 5: Cylinder pressure trace, cumulative heat release, HRR and injector current for different start of energizing times for Diesel DI

The corresponding engine calibration is given by Table 2. The only differences are in the reduced rail pressure for DI of $p_{\text{Rail_DI}} = 450$ bar, since the injection events have been very early and extreme wall wetting should be prevented. Moreover, in these experiments a constant EGR-rate of 28% was applied. The reason for this constant EGR-rate was not the control of NO_x emissions, but rather to avoid very steep pressure gradients.

Investigations via DoE's have been carried out in this load point. For the test plan, the models were setup to be V-optimal, pure cubic and without constraints. For both the air and the fuel path a test plan was created with three variable inputs. The boundaries

for both tests are provided by Table 4 and Table 5. In order to maintain a constant scavenging gradient during the tests, the differential pressure between intake and exhaust runner was set to 100 mbar.

	Minimum	Maximum
Engine speed / rpm	1500	
IMEP / bar	6.8	
Rail pressure / bar	450	
Start of energizing DI / °CA aTDC	-35	
Gasoline mass fraction / %	85	
EGR concentration / %	0	20
Boost pressure / bar	1.3	1.8
Temperature downstream charge air cooler / °C	25	65

Table 5: Boundary conditions and ranges of the variability in the air path for creation of the DoE test plan

	Minimum	Maximum
Engine speed / rpm	1500	
IMEP / bar	6.8	
EGR concentration / %	0	
Temperature downstream charge air cooler / °C	30	
Boost pressure / bar	1.5	
Exhaust back pressure / bar	1.6	
Rail pressure / bar	300	1200
Start of energizing DI / °CA aTDC	-28	-42
Gasoline mass fraction / %	70	85

Table 6: Boundary conditions and ranges of the variability in the fuel path for creation of the DoE test plan

During the previous engine investigations, a gasoline mass fraction of 85% has proven to be close to the critical limit for RCCI operation. With higher shares combustion became very unstable. Therefore, the gasoline portion was kept constant at 85% in order to ensure sufficient combustion stability during the tests of variability in the air path. For the investigations of variability in the fuel path, the gasoline portion was varied from 70% to 85% m/m.

Below in Table 6 and Table 7 the statistics and model qualities for all models created based on variability in the air and fuel path are given. Overall, the qualities of the models are sufficient for interpretation of the model outputs. Unfortunately, the quality of the model of the indicated efficiency is too bad, so that a discussion of the efficiency is postponed.

	Center of combustion	MPRR	Ind. spec. CO	Ind. spec. HC	Ind. spec. NO _x
Model points	21	21	22	21	20
Model coefficients	9	12	13	10	7
R ²	0.9799	0.9834	0.9862	0.9757	0.9741
LOF	0.3291	0.174	0.9027	0.051	0.3156
Model quality	0.5275	0.3682	0.3511	0.1912	0.154
Validation quality	0.8191	0.84	0.9741	0.8671	0.8236

Table 7: Statistics of models created for variability in the air path

	Center of combustion	MPRR	Ind. spec. CO	Ind. spec. HC	Ind. spec. NO _x
Model points	21	21	22	21	20
Model coefficients	9	12	13	10	7
R ²	0.9799	0.9834	0.9862	0.9757	0.9741
LOF	0.3291	0.174	0.9027	0.051	0.3156
Model quality	0.5275	0.3682	0.3511	0.1912	0.154
Validation quality	0.8191	0.84	0.9741	0.8671	0.8236

Table 8: Statistics of models created for variability in the fuel path

To improve the model's qualities and to reduce the uncertainties, some measurements had to be removed. Those measurements obviously have been outliers. The modeling results are presented in Figure 6 for variability in the air path, and in Figure 7 for variability in the fuel path. Since three-dimensional plots are often confusing, here a different way of representing is chosen. Even though three model inputs are considered, only two inputs are displayed for each graph. To present the influence of the third variable, each graph is shown four times with different values of the third model parameter. By doing this, the influence of the EGR-rate respectively the rail pressure can be assessed in a discrete way. From the first through the fourth row, the value of EGR-rate and rail pressure increase.

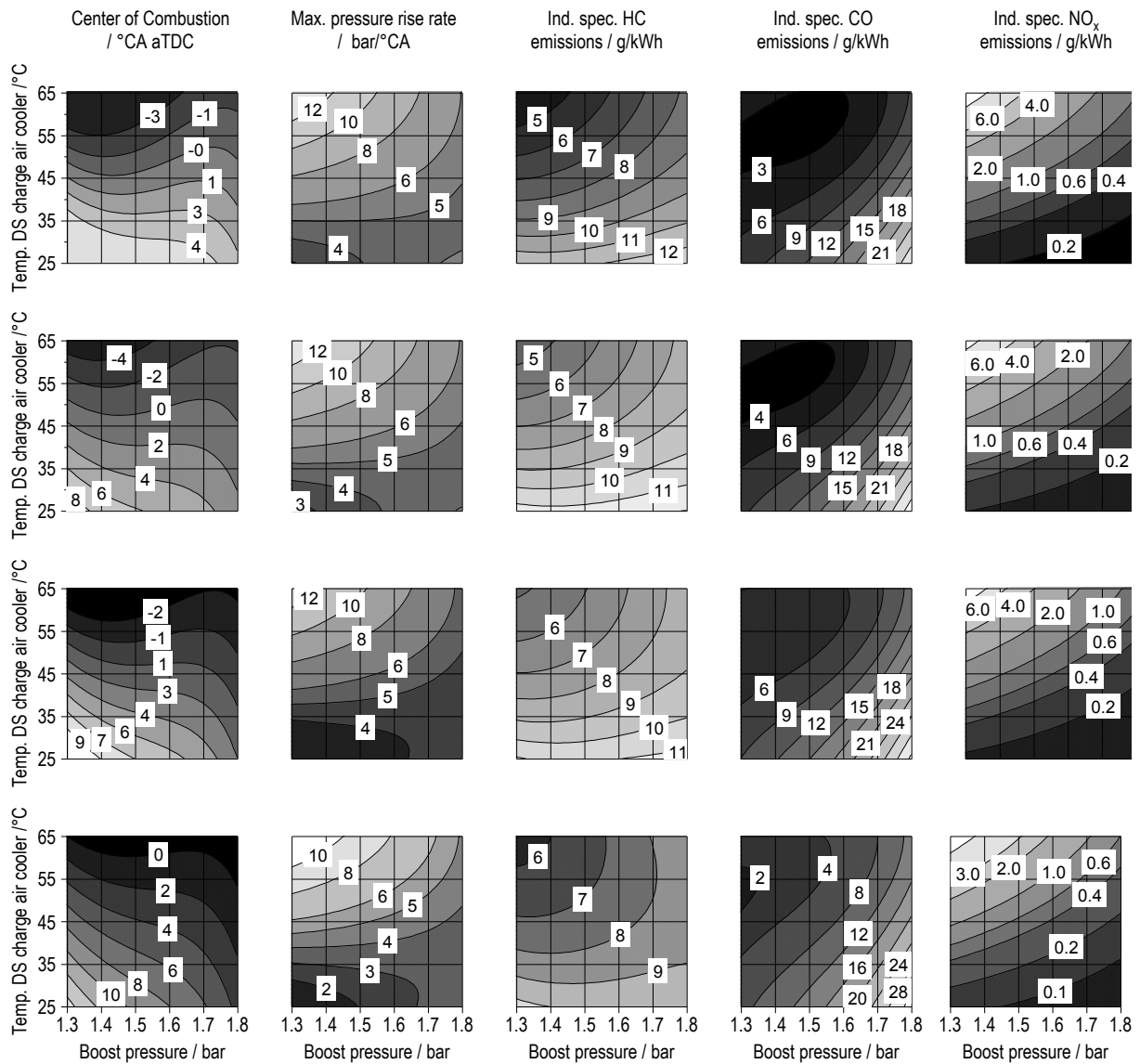


Figure 6: Modelling results for center of combustion, maximum pressure rise rate, indicated specific HC-, CO- and NO_x emissions for variations in the air path. From the first row to the fourth row the EGR-rate is 0%, 5%, 10%, and 20%

In each row of Figure 7, the modeling results for the center of combustion, the maximum pressure rise rate and the indicated specific emissions of HC, CO and NO_x are shown. Soot emissions are not discussed here, since the maximum value that was found during the RCCI investigations was 0.008 g/kWh. Thus, all RCCI measurements can be considered as soot-free. From the first to the fourth row the EGR-concentration increases from 0% to 20%. Looking at the CA50 in the left column, it is obvious that the CA50 is retarded with higher EGR-concentration. This is plausible and often observed for conventional DICl operation as well, since the higher share of inter gas causes on the one hand a pressure and temperature decrease due to higher specific heat capacity than ambient air, and on the other hand reduces the available amount of oxygen. Similarly, an increase in gas temperature yields an increase in mixture reactivity. Thus, with constant SODI, the CA50 is advanced when the temperatures is elevated. An increase in boost pressure has two counter-acting effects. A higher intake

pressure results in a higher temperature and pressure during the compression stroke, and thus typically in a higher reactivity of the mixture. However, a higher boost pressure also causes a more diluted mixture, which may result in similar effects as discussed in the presentation of the part load results with Diesel pilot injection. A more diluted mixture typically shows lower reactivity. For this reason, the effect of a higher boost pressure is non-linear, but in general a higher boost pressure results in a retarded CA50.

The same observations can be made for the MPRR. With high mixture reactivity, steep pressure gradients are observed. Thus, highest MPRR are caused by high charge air temperatures, low EGR-concentrations and low boost pressure.

The trends in HC- and CO emissions are very similar, since both are driven by the same parameters and opposed to the trend in NO_x emissions. With relatively low mixture reactivity, a rather slow and retarded combustion is predicted. Thus, the combustion temperatures are quite low the oxidation of HC and CO is worsened. However, formation of NO_x requires high temperatures of 2250K. Therefore, the highest NO_x emissions coincide with advanced CA50 and steep pressure gradients, where simultaneously low HC- and CO emissions occur.

To summarize the findings of the investigations with variability in the air path, it can be concluded that both - charge air temperature and pressure - have a significant impact on combustion performance and emissions of HC, CO and NO_x. The influence of the EGR-rate on the discussed parameters is not as dominant, but the reader has to keep in mind that the range of EGR-concentration is rather narrow and has been varied from 0% to 20%.

In Figure 7 the model findings with variability in the fuel path are shown. The investigated parameters are equal to those discussed above in. Overall, the impact of the injection pressure on combustion and emissions performance in RCCI operation is rather low. However, with high injection pressure, problems with oil dilution may occur specifically when the Diesel fuel jets hit the cylinder wall. This is caused by the very early injection timings when the thermodynamic conditions are low, due to mean pressure and temperature of the charge in the cylinder.

The impact of SODI on the CA50 is given in the left column and on the MPRR in the second column. The variation in SODI by 14°CA is found in the CA50 as well. As already briefly described at the beginning of this subsection, an early SODI leads to an overall more homogenous mixture. The air-excess ratio within the Diesel spray becomes higher, and thus local temperatures during combustion drop. The lower temperatures result in lower energy available for starting the chain reaction of gasoline combustion. Thus, the CA50 is significantly retarded with an advanced Diesel fuel injection, and simultaneously the MPRR is substantially reduced.

The same observations can be made for variations in the gasoline mass fraction. The higher the gasoline share, the later the CA50 and the lower the MPRR.

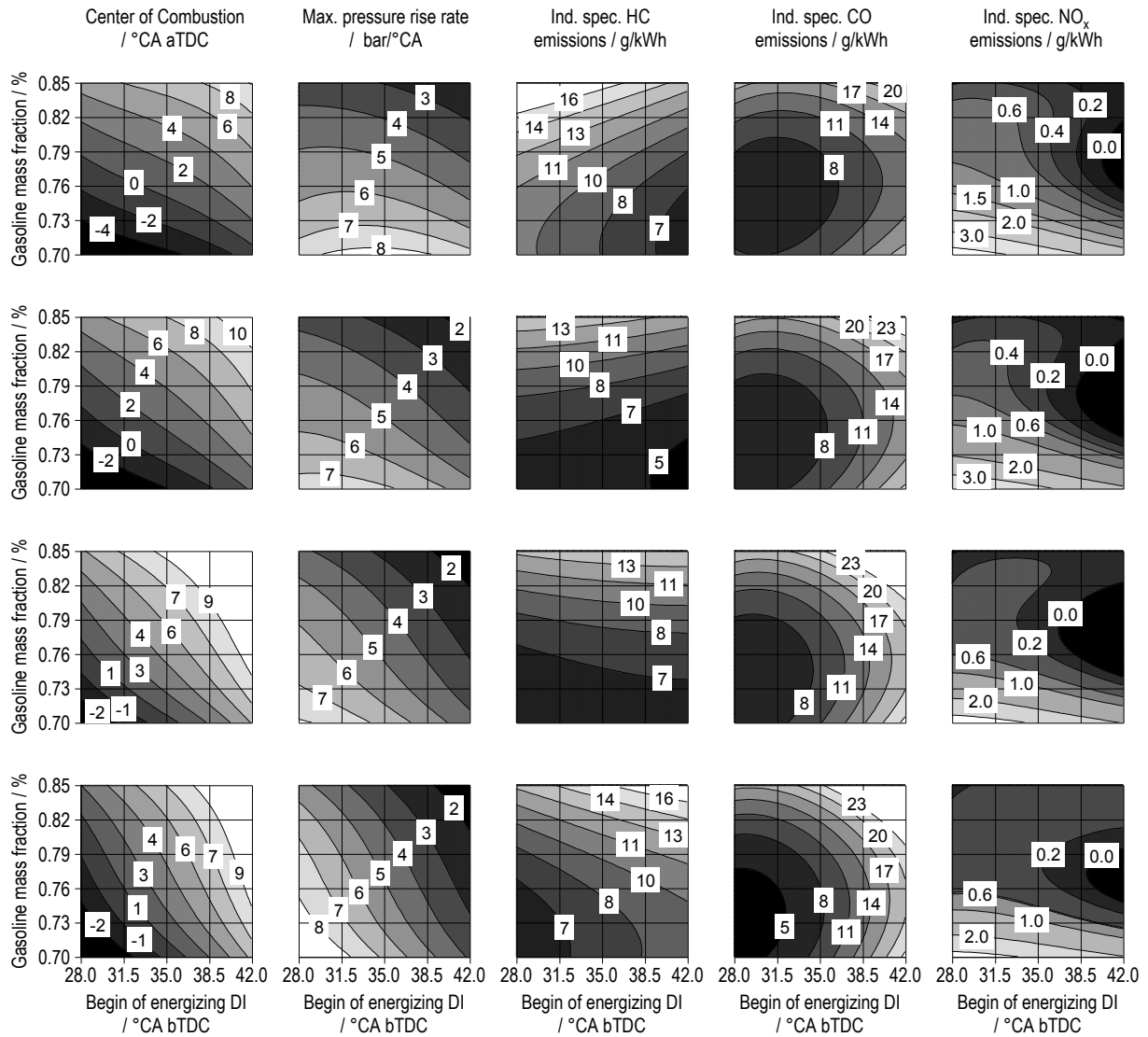


Figure 7: Modelling results for center of combustion, maximum pressure rise rate, indicated specific HC-, CO- and NO_x emissions for variations in the air path. From the first row to the fourth row the injection pressure is 300 bar, 600 bar, 900 bar, 1200 bar

With regard to the emissions, observations that have been made during the discussion of the Diesel pilot injection can be confirmed here. The HC emissions are mainly driven by the gasoline portion. The HC emissions originate from unburned fuel trapped in the crevices. The drivers that influence the HC emissions seem to be others, since there is no linear correlation between gasoline mass share and magnitude of CO emissions. However, a general trend of increasing CO emissions with higher gasoline portions can be observed as well. But simultaneously, the impact of SODI is very distinct. Due to the shell-shaped iso-contour line, a dominant source cannot be identified. When looking at the NO_x emissions, the main driver again is the gasoline mass fraction, but the effect is almost exponential. With early SODI and high gasoline mass share, NO_x emissions below 0.2 g/kWh can be achieved even without the need of EGR. However, reducing the gasoline mass share by 15% and injection late (-28°CA aTDC), NO_x emissions increase by the 20-fold. Here again, a rapid combustion with early CA50 leads to high temperatures and thus high formation of NO_x.

4. Summary and Conclusion

In this study, dual-fuel combustion of gasoline RON95E10 (EN228) and Diesel fuel (EN590) was investigated. The utilized engine features a displacement of 0.39l and thus is designed for passenger car applications. The load regime covered low part load operation at 4.3 bar IMEP up to rated power and rated torque with a corresponding IMEP of 27 bar. Independent of the engine load, an improvement in indicated efficiency cannot be reported. This might be mainly caused by the disadvantageous volume/surface ratio, since many other researchers have attributed improvements in efficiency to reduced wall heat losses.

With Diesel pilot injection, at part load operation a stable combustion with up to 90% m/m gasoline could be achieved at medium engine loads. The soot/NO_x-trade-off could be improved by increasing the premixed burn fraction. However, this improvement is not linear, and, depending on the engine load, different gasoline mass fractions are needed to reach the maximum improvement. At low to medium part load operation it was necessary to advance the start of the Diesel injection significantly. The overall increased homogeneity caused a reduction in maximum pressure rise rates, but combustion showed an enormous dependence on various parameters regarding the air and fuel path. At high and full load operation, the gasoline mass fraction was limited by auto-ignition of the premixed cylinder charge. In two load points a three-step combustion was observed, which can be divided into Diesel fuel combustion, diffusive combustion of the gasoline fuel, and a second peak in heat release rate. Simulations could prove that the second peak in the heat release rate is caused by auto-ignition of the remaining unburned gasoline.

At full load operation, the same IMEP in dual-fuel operation could be achieved as in conventional Diesel-only operation. Due to given constraints such as maximum pressure rise rate and peak firing pressure, at maximum low end torque the gasoline mass share was limited to 50%. With this amount of premixed fuel, the Filter Smoke Number could be reduced by 2.33 units at same IMEP. However, with increasing load and speed, the maximum achieved gasoline mass share dropped to 20% at rated power. Here, no benefit in terms of emissions or efficiency could be gained.

Due to the high sensitivity of combustion and emissions on variations in the air and fuel path at part load, investigations have been performed by means of Design of Experiment. Two test plans have been created that took into account three inputs each. The EGR-concentration, the boost pressure, and the charge air temperature have been considered as variations in the air path. For the fuel path, the gasoline mass fraction, the start of energizing of Diesel injection and the injection pressure has been varied.

With regard to the air path, it was demonstrated that the mixture reactivity is dominantly influenced by the intake air temperature and the boost pressure. The effect of EGR that was varied from 0% to 20% had minor influence. Overall, a higher temperature and lower boost pressure increases the reactivity, advances the center of combustion, and increases the pressure rise rates and consequently combustion temperatures along with NO_x emissions. Simultaneously, these measures reduce HC- and CO emissions.

With regard to the fuel path, it can be concluded that the gasoline mass share and the start of Diesel direct injection have the main influence on combustion and emission rather than the Diesel injection pressure. Again, the higher the mixture reactivity the higher the pressure rise rate and the NO_x emissions. Whereas CO emissions were found to be influenced by both gasoline mass share and start of Diesel injection, the HC emissions are mainly depending on the gasoline mass share.

Overall, for such a dual-fuel approach for port fuel injection a fuel characterized by superior anti-knock characteristics is desired. At medium to high load conditions, extreme pressure rise rates have been observed due to auto-ignition of the remaining unburned gasoline fuel. At low part load operation, where rather HC- and CO emissions are challenging than the soot/NO_x-trade-off, still high shares of a highly reactive fuel can be introduced into the cylinder via direct injection, as long as the main focus is on regulated emissions.

5. Outlook

In upcoming test campaigns, fuels with improved anti-knocking behavior such as the biomass-derived molecules 2-methylfuran and 2-butanone will be investigated. Another measure to reduce the pressure gradients might be a lower compression ratio, since this causes a lower in-cylinder temperature and pressure before and during combustion. Moreover, a different DI nozzle will be investigated with a reduced number of nozzle holes. In doing so, the ignition sources are reduced, which might prevent auto-ignition of the premixed charge.

Acronyms

Acronym	Explanation	Unit
λ	AFR relative to stoichiometric AFR , air excess ratio	
AFR	Air-to-fuel mass ratio	
aTDC	After TDC	
BDC	Bottom Dead Center	
bTDC	Before TDC	
CA	Crank Angle	
CA50	Center of Combustion, i.e. CA of 50% fuel MF burned	°CA aTDC
CI	Compression Ignition	
DI	Direct Injection	
DICI	Direct Injection Compression Ignition	
DOC	Diesel Oxidization Catalyst	
DoE	Design of Experiments	
DPF	Diesel Particulate Filter	
EGR	Exhaust Gas Recirculation	
EN	European Norm	
FIE	Fuel Injection Equipment	
FSN	Filter Smoke Number	
GHG	Greenhouse gas	
GMF	Gasoline MF	1, %
HC	Hydrocarbon(s)	
HCCI	Homogenous Charge Compression Ignition	
HD	Heavy-Duty	
HRR	Heat Release Rate	
IMEP	Indicated Mean Effective Pressure	bar, N/m ²
LD(V)	Light-Duty (Vehicle)	
LOF	Lack of fit	
MF	Mass Fraction	1, %
MPRR	Maximum Pressure Rise Rate	bar/ °CA
n	Engine speed	1/min
NEDC	New European Driving Cycle	
NSC	NO _x Storage Catalyst	
PCCI	Premixed Charge Compression Ignition	
PFI	Port Fuel Injection	
PFP	Peak Firing Pressure	bar
PM	Particulate Matter	
PPCI	Partially Premixed Compression Ignition	

Acronym	Explanation	Unit
PRR	Pressure Rise Rate	bar/ °CA
R ²	Coefficient of determination	
RCCI	Reactivity Controlled Compression Ignition	
RCP	Rapid Control Prototyping	
RON	Research Octane Number	
rpm	Revolutions per minute	
SCE	Single Cylinder Engine	
SCR	Selective Catalytic Reduction	
SI	Spark Ignition	
SOC	Here: Start of Combustion	
SODI	Start Of Direct fuel Injection	°CA
SOE	Start Of injector Energizing	°CA
TDC	Top Dead Center	

References

- [1] Bression, G., Soleri, D., Savy, S., Dehoux, S., et al., "A Study of Methods to Lower HC and CO Emissions in Diesel HCCI," SAE Int. J. Fuels Lubr. 1(1):37-49, 2008
- [2] Dec, J.E., "Diesel-Fueled HCCI Engines" from "Homogenous Charge Compression Ignition (HCCI) Engines," SAE International, Warrendale, PA, ISBN 978-0-7680-1123-4, 2003
- [3] Hanson, R., Splitter, D., and Reitz, R., "Operating a Heavy-Duty Direct-Injection Compression-Ignition Engine with Gasoline for Low Emissions," SAE Technical Paper 2009-01-1442, 2009, doi: 10.4271/2009-01-1442
- [4] Bessonette, P., Schleyer, C., Duffy, K., Hardy, W., et al., "Effects of Fuel Property Changes on Heavy-Duty HCCI Combustion," SAE Technical Paper 2007-01-0191, 2007, doi:10.4271/2007-01-0191
- [5] Exxon Mobil, "The Outlook for Energy: A View to 2040", 2015, http://cdn.exxonmobil.com/~media/Reports/Outlook%20For%20Energy/2015/2015-Outlook-for-Energy_print-resolution.pdf
- [6] Rose, K.D., "Fuel Quality Issues and European Research", JATOP Conference, 2012
- [7] Cracknell, R., Ariztegui, J., Dubois, T., Hamje, H. et al., "Modelling a Gasoline Compression Ignition (GCI) Engine Concept," SAE Technical Paper 2014-01-1305, 2014, doi:10.4271/2014-01-1305.
- [8] Rose, K., Ariztegui, J., Cracknell, R., Dubois, T. et al., "Exploring a Gasoline Compression Ignition (GCI) Engine Concept," SAE Technical Paper 2013-01-0911, 2013, doi:10.4271/2013-01-0911.
- [9] Chang, J., Kalghatgi, G., Amer, A., Adomeit, P. et al., "Vehicle Demonstration of Naphtha Fuel Achieving Both High Efficiency and Drivability with EURO6 Engine-Out NOx Emission," SAE Int. J. Engines 6(1):101-119, 2013, doi:10.4271/2013-01-0267.
- [10] Kokjohn, S., Hanson, R., Splitter, D., and Reitz, R., "Experiments and Modeling of Dual-Fuel HCCI and PCCI Combustion Using In-Cylinder Fuel Blending," SAE Int. J. Engines 2(2):24-39, 2010, doi:10.4271/2009-01-2647.
- [11] Desantes, J., Benajes, J., García, A., and Monsalve-Serrano, J., "The role of in-cylinder gas temperature and oxygen concentration over low load reactivity controlled compression ignition combustion efficiency," Energy (2014), <http://dx.doi.org/10.1016/j.energy.2014.10.080>
- [12] Splitter, D., Hanson, R., Kokjohn, S., and Reitz, R., "Reactivity Controlled Compression Ignition (RCCI) Heavy-Duty Engine Operation at Mid-and High-Loads with Conventional and Alternative Fuels," SAE Technical Paper 2011-01-0363, 2011, doi:10.4271/2011-01-0363.
- [13] Kokjohn, S., Hanson, R., Splitter, D., Kaddatz, J. et al., "Fuel Reactivity Controlled Compression Ignition (RCCI) Combustion in Light- and Heavy-Duty Engines," SAE Int. J. Engines 4(1):360-374, 2011, doi:10.4271/2011-01-0357
- [14] Hanson, R., Kokjohn, S., Splitter, D., and Reitz, R., "An Experimental Investigation of Fuel Reactivity Controlled PCCI Combustion in a Heavy-Duty Engine," SAE Int. J. Engines 3(1):700-716, 2010, doi:10.4271/2010-01-0864.

- [15] Muether, M., Lamping, M., Kolbeck, A., Cracknell, R. et al., "Advanced Combustion for Low Emissions and High Efficiency Part 1: Impact of Engine Hardware on HCCI Combustion," SAE Technical Paper 2008-01-2405, 2008, doi:10.4271/2008-01-2405.
- [16] Muether, M. „Einflüsse alternativer Kraftstoffe auf die dieselmotorische Verbrennung“, Ph.D. Thesis, RWTH Aachen University, 2009
- [17] Kim, D., Ekoto, I., Colban, W., and Miles, P., "In-cylinder CO and UHC Imaging in a Light-Duty Diesel Engine during PPCI Low-Temperature Combustion," SAE Int. J. Fuels Lubr. 1(1):933-956, 2009, doi:10.4271/2008-01-1602
- [18] Weall, A., Szybist, J., Edwards, K., Foster, M. et al., "HCCI Load Expansion Opportunities Using a Fully Variable HVA Research Engine to Guide Development of a Production Intent Cam-Based VVA Engine: The Low Load Limit," SAE Int. J. Engines 5(3):1149-1162, 2012, doi:10.4271/2012-01-1134
- [19] Alt, N.; Nehl, J.; Heuer, S., "Combustion Sound Prediction within Combustion System Development", SIA "Vehicle Comfort", 2004

The Authors:

Dipl.-Wirt.-Ing. Benedikt Heuser, Institute for Combustion Engines, RWTH Aachen University, Aachen, Germany

Dr.-Ing. Dipl.-Wirt.-Ing. Florian Kremer, Institute for Combustion Engines, RWTH Aachen University, Aachen, Germany

Prof. Dr.-Ing. Stefan Pischinger, Institute for Combustion Engines, RWTH Aachen University, Aachen, Germany

Dr.-Ing. Hans Rohs, FEV GmbH, Aachen, Germany

Dr.-Ing. Bastian Holderbaum, FEV GmbH, Aachen, Germany

Dipl.-Ing. Thomas Körfer, FEV Group Holding GmbH, Aachen, Germany

Dipl.-Ing. Christof Schernus, FEV GmbH

Licence:

This document is licensed under the Creative Commons Attribution 3.0 DE License (CC-BY 3.0 DE): <http://creativecommons.org/licenses/by/3.0/de/>

Investigation of the Combustion Process of a Small Direct Injection Spark Ignition Engine

Arne Siedentop
Jörn Schech
Andreas Bradenstahl
Peter Eilts

Abstract

This report presents results of the research project “GDI-Boundary Bore” funded by the Research Association for combustion engines, which has been carried out at the Institute of Internal Combustion Engines of the Technische Universität Braunschweig. Basing on extensive preliminary studies presented in [1, 2], two cylinder head concepts have been implemented to realise a small bore spark ignition engine with direct injection. This is on one hand a cylinder head concept with three valves and a lateral upright standing injector and on the other hand a 4V-concept with a lateral injector position under the intake port. The engine concepts have been realised with a bore diameter of 60mm and a stroke of 71mm.

As a consequence of the large scope of the experimental investigations, just a slight part of the results obtained with a thermodynamic and an optically accessible research engine is presented. The engine performance and the emission behaviour of the small direct injection spark ignition engine have been determined in a broad range of engine load and speed at the thermodynamic research engine. The main focus within the investigations was on the particulate emission behaviour. The level of these emissions could be improved significantly by variation of injection parameters like start of energization, injection pattern and by variation of the charge motion intensity. This article outlines the results with particle optimized application. Optical investigations of the inlet flow, the injection and the combustion help to get a deeper understanding of the measurements at the thermodynamic engine. 3D-CFD calculations of the mixture formation have been carried out to get a further insight into the mixture formation and to understand the emission behaviour.

With regard to the decrease of particulate emissions, the 3V-concept provides a higher potential but is more sensitive to the variation of application parameters like injection timing. Wall wetting may cause particulate emissions and oil dilution and hence be a limiting factor for the reduction of the bore diameter. Investigations of the mechanisms of wall wetting and related mixture formation as well as optimization to enhance the application span of the 3V concept have to be topic of further research.

1. Introduction

The focus of research and development of internal combustion engines has been led to the reduction of specific fuel consumption and pollutant emissions as a result of the long term trend of the oil price, higher ecological awareness and emission regulations. Various conceptions have been developed to reduce the fuel consumption of spark ignition engines. The combination of turbo charging and direct injection allows downsizing of the engine displacement at constant engine power. The engine efficiency rises at part load as a result of a higher mean effective pressure and thereby lower throttle and friction losses.

Very small cars, in Japan denoted as “Kei-Cars”, represent a market demand for small engines as conventional powertrain. This in combination with the emission regulations and the mentioned scenario of fuel consumption requires the development of small displacement spark ignition engines with direct injection. Thereby limits of the displacement of 660ccm and the engine power of 47kW are substantial parameters of the “Kei Cars”. In most cases a three cylinder in-line engine with a single cylinder displacement of 220ccm and manifold injection is used.

A reduction of car dimensions is to be expected in other markets as well, which leads to a reduction of the installed power of the combustion engine. Further on, an increasing hybridization has the same effect. This in combination with downsizing results in a reduction of the engine displacement and thus the bore diameter.

The risk of wall wetting increases with the application of direct injection with small cylinder dimensions, which may result in drawbacks concerning emissions, especially particulates. In addition liner wetting may increase the risk of oil dilution. Due to the benefits of onto the work process of internal combustion engines the direct injection should be used with cylinder dimensions expectable in future. This leads to the question which bore diameter is possible without drawbacks concerning emissions and oil dilution as a result of wall wetting.

2. Preliminary Studies

Preliminary CAD studies and 1D simulations for the determination of effective operation values have been carried out and are presented in [1, 2]. The boundary conditions of the investigation have been set as follows:

- Bore diameter: $56\text{mm} < d < 62\text{mm}$
- stroke to bore ratio: 0.9 to 1.2
- Engine displacement: $175\text{ccm} < V_D < 220\text{ccm}$
- Design point: 1500rpm, BMEP = 22bar
- Nominal speed: 5500rpm
- Specific power: 90kW/l
- Injector position: lateral and central
- Injector type: Multihole injector

An optimization of the arrangement of spark plug, injector, intake and exhaust valves has been carried out within the CAD studies to identify suitable cylinder head concepts. All investigated concepts are shown in figure 1. The evaluation and selection of the configurations for further investigations has been ensued based on the inner seat diameter of the intake valves and the eccentricity of the spark plug. Detailed results of the CAD studies can be obtained from [1, 2].



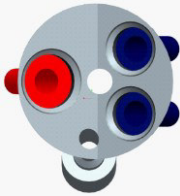

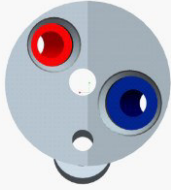
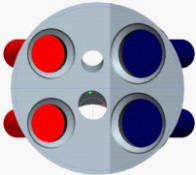
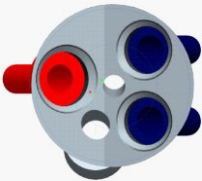

Lateral injector position	4V-concept	3V-concept (lateral mounted injector)	3V-concept (upright mounted injector)	2V-concept (decentral spark plug)	2V-concept (central spark plug)
					
Central injector position	4V-concept	3V-concept		2V-concept	
					

Figure 1: Cylinder head concepts investigated

2.1 Summary of 1D Simulation

The calculation of effective operation values shows most advantages for the 4V-concept with lateral mounted injector. The 3V-concepts feature just slight disadvantages compared to this concept. As a result of compared to the 4V-concept with identical injector position smaller valve diameters, the 3V-concept with lateral lying injector can be excluded from further investigations. Further on, the 4V-concept with central injector position shows no advantages. Based on these preliminary studies, the following cylinder head concepts have been selected to be realized for the test engine.

- 4V-concept with lateral lying injector position
- 3V-concept with lateral upright standing injector position

The drawbacks regarding effective operation values rise disproportionately with a bore diameter less than 60mm for all concepts. Hence a bore diameter of 60mm has been selected for further investigations. The most favourable stroke to bore ratio is dependent on the load point. Whilst a long stroke shows advantages at the design point it is adverse at rated output. As a result of the advantages at the design point and under consideration of an engine displacement suitable for automotive application the stroke has been selected to 71mm. In combination with a bore diameter of 60mm this yields to a single cylinder displacement of 200ccm.

3. Design

During the design process of the cylinder heads it has been considered, that the designs are usable for a full engine without substantial changes. Furthermore the use of a glass liner for the optical access has been taken into account. The requirements for this application are the following, [3]:

- Dry fire deck without coolant- or oil bores
- Larger bolt circle of the cylinder head screws due to the bigger wall thickness of the glass liner

The design of the cylinder head variants of the thermodynamic and the optical engine is mostly identical. The water jacket of the optical variant has been changed at the pent-roof cutout to avoid an opening of the water jacket. Further on, the lateral bore of the cylinder pressure sensor has to be omitted at the optical cylinder head as a result of the pent-roof cutout. More features of the cylinder head design are as follows:

- AISi10-alloy with T6-heat treatment
- Reproduction of the combustion chamber geometry at the casting with a steel core for an improved surface quality and strength
- Coated sand cores for intake and exhaust port
- Coolant inlet under the intake and exhaust port, coolant outlet at opposite side of the belt drive
- Segregated intake port with guide plate for generation of charge motion
- Valve actuation with roller cam followers with hydraulic valve clearance compensation

Since the geometry of the intake port of direct injection spark ignition engines has a direct effect on the mixture formation it has been optimized numerically concerning flow resistance and charge motion intensity. For the 3V-concept nearly same values compared to the reference engine (Volkswagen EA111, 125 kW) could be achieved. The steeper inclination of the intake port of the 4V-concept resulting out of the mounting position of the injector under the intake port leads to an approximately 10% lower intensity of the charge motion, compare figure 2. The intensity could have been increased with further adjustment of the geometry, but only in combination with the negative effect of an increased flow resistance.

The arrangement of injector and spark plug can be obtained from the half transparent illustration of the 3V-concept in figure 3. The injector position is lateral upright standing on the side of the exhaust valve. The figure shows the optical cylinder head variant. The pent-roof cutout, two grooves for the sealing of the glass liner, the bigger bolt circle and the adapted water jacket mentioned are good to be identified from the figure.

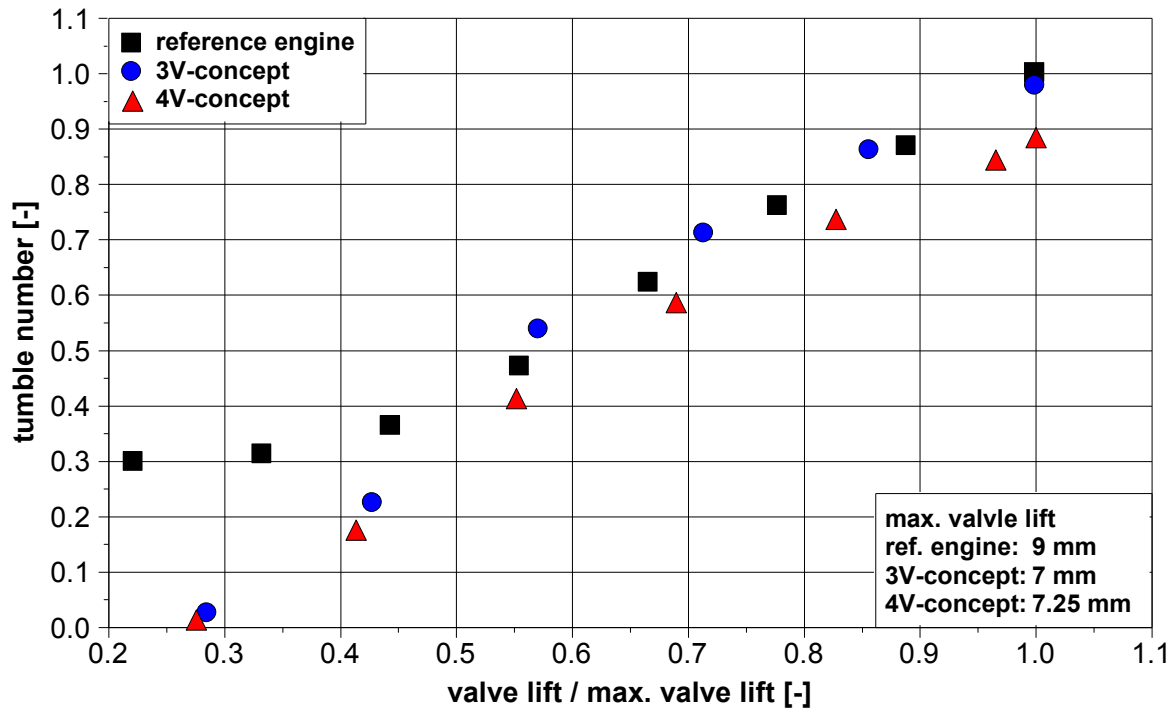


Figure 2: Comparison of calculated tumble numbers, [1]

Figure 4 shows the thermodynamic cylinder head of the 4V-concept in half transparent illustration. The illustration on the right side shows a cut through the middle plane of the cylinder head. Injector and spark plug are mounted in this plane. The spark plug is inclined about 5° into the direction of the exhaust valve to gain sufficient mounting space for the hydraulic valve clearance compensation elements on the intake side. This is as well valid for the 3V-concept. The bore for the high-pressure indication is shown on the left side. The mounting position is identical for both concepts.

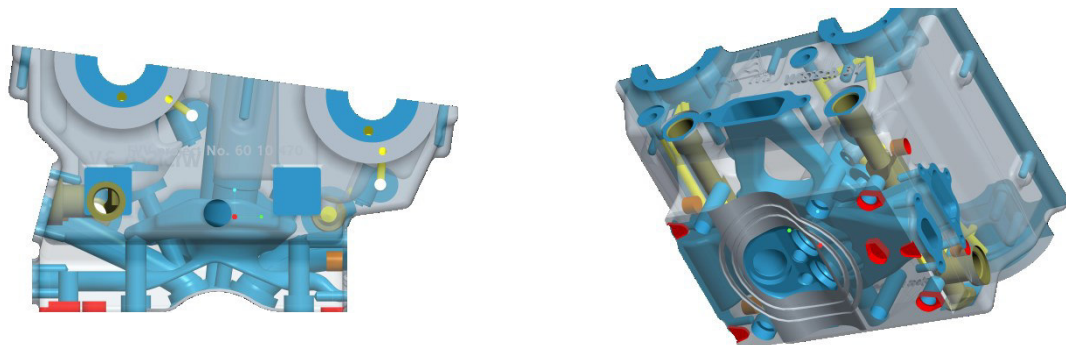


Figure 3: CAD prospect of the optical cylinder head of the 3V-concept

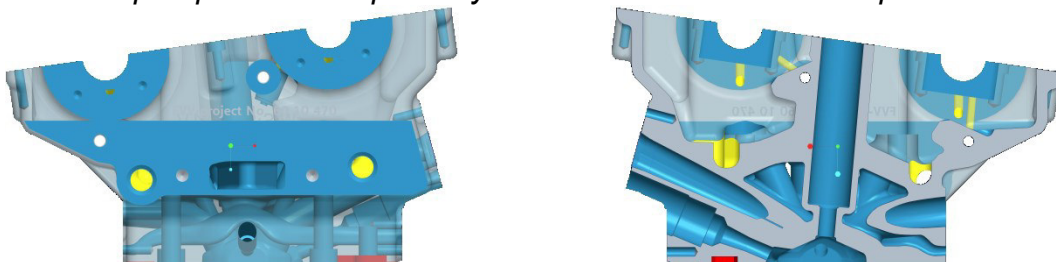


Figure 4: CAD prospect of the 4V-concept cylinder head for thermodynamic investigations

4. Experimental Engine and Setup

Both cylinder head concepts with different injector positions have been surveyed within the project at a thermodynamic and an optically accessible single cylinder research engine. The engine features a mass balancing of first and second order to minimize the vibrations during the optical measurements.

The engine is equipped with a high- and low-pressure indication as well as a high-pressure sensor for the indication of the pressure in the fuel rail. The generation of the fuel pressure is realised with an external pump driven by compressed-air. Coolant and fuel are conditioned by an external media conditioning system. Further measured variables are the fuel and air mass flow, the fuel/air ratio and all necessary temperatures for a thermodynamic analysis.

4.1 Injectors Investigated

For both cylinder head concepts two multihole injectors each have been provided by Robert Bosch GmbH. These injectors are of the type HEDV5 with laser drilled holes and differ concerning mass flow rate and spray layout. Figure 5 shows the spray layout of the injectors for the 3V-concept with specific parameters and figure 6 the layout of the 4V-concept injectors respectively.

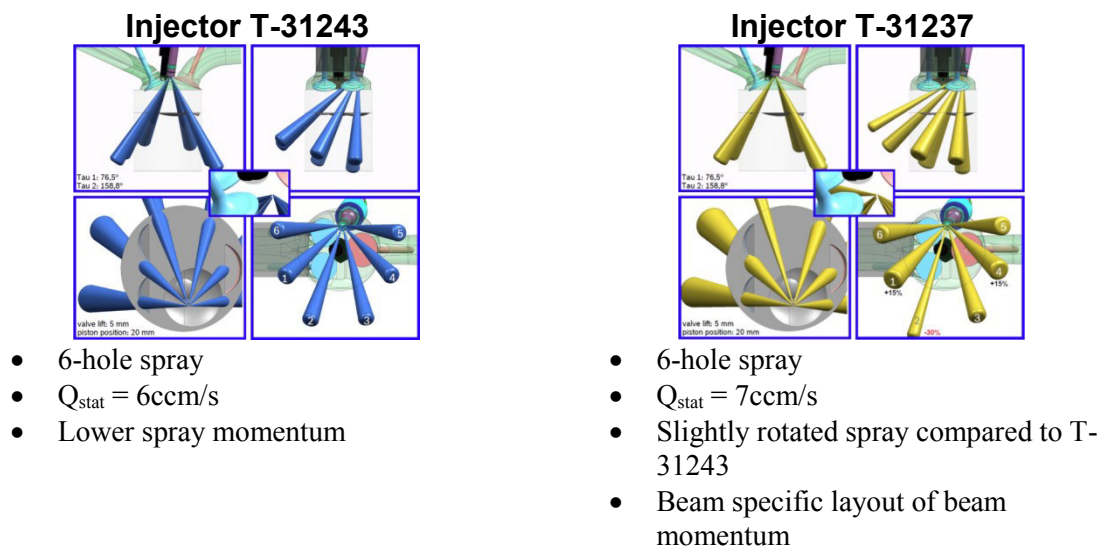


Figure 5: Investigated injectors within the 3V-concept, [4]

4.2 Exhaust Gas Measuring Technology

The metering of gaseous emissions has been done at all investigations with an exhaust gas measurement system of the type Horiba MEXA 7100 DEGR. For the characterization of particulate emissions two measurement systems have been used. This is on the one hand the filter smoke number obtained with a smoke meter AVL 415 SE and on the other hand the particle number concentration recorded with a particle counter of the type TSI 3790. For the dilution of the particle number concentration to a suitable range of values, a rotational dilution system of the type Matter MD19-3E has been applied.

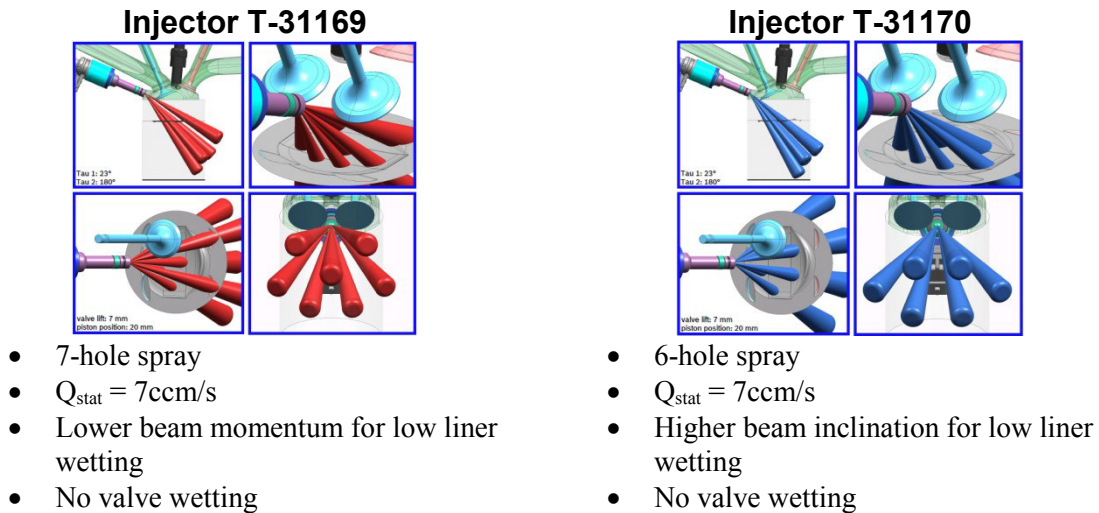


Figure 6: Investigated injectors within the 4V-concept, [5]

5. Thermodynamic Investigations

Application parameters like injection timing and pattern as well as the injection pressure have been varied within the investigations. The intensity of the charge motion has been varied by closing the lower section of the intake port. The load points investigated are shown in table 1 as well as the centre of heat release, which shows the highest efficiency. It has been determined within preliminary studies and kept constant during the investigations. The investigation of load points six and seven has been performed at the knock limit. For the evaluation of the results, criteria like the specific fuel consumption, engine smoothness and pollutant emissions have been used, whereby particulate emissions were the main criterion.

Table 2 shows the optimal application of the varied parameters regarding particulate emissions for the 3V-concept. Lowest particulate emissions have been obtained for both injectors with high injection pressure. High charge motion intensity shows advantages concerning particulate emissions. A reason for this effect may be an increasing evaporation rate and into the combustion chamber entrained liquid fuel from the intake valve [6, 7].

For injector T-31243 with reduced mass flow rate it is remarkable that the particulate optimal injection timing at load points one to five is at $190^\circ \text{CA b. TDCF}$. As a result of the position of the piston near the bottom dead centre the free length of the spray path maximises. The intake valves are almost closed. An interaction of the liquid fuel with the valves and the piston, which is a main source for particulate emissions [8, 9, 10], can be ruled out. On the contrary the time for the mixture formation is decreased resulting in a lower homogeneity of the mixture. With regard to particulate emissions this drawback is overcompensated by the lower wall wetting. Adverse effects of the late injection are higher specific fuel consumption and CO-emissions as a result of a lower homogeneity of the mixture, compare figure 7 and 8. Summarizing the investigations of injector T-31243 at part and medium load, it can be stated that the particulate emissions can be minimized by maximizing the free path length and hence avoiding a wetting of valves and piston.

Load point	Engine speed n in rpm	BMEP in bar	FMEP in bar	NMEP in bar (rounded)	Centre of heat release in °CA (ISFC-optimal)
1	1200	3.00	0.87	3.9	≈ 8
2	1800	3.00	0.99	4.0	≈ 9 – 10
3	1800	6.00	1.04	7.0	≈ 8 – 9
4	1800	10.00	1.12	11.1	≈ 9
5	2400	10.00	1.22	11.2	≈ 7 – 8
6	1500	22.00	1.33	23.3	knock limit
7	5500	19.65	1.95	21.6	knock limit

Table 1: Load points investigated

In contrast, an early injection is the particulate optimal application for injector T-31243 at full load since valve wetting cannot be avoided due to the necessary long injection duration. Multiple injections are not possible at rated output as a result of the minimal break time of 1.5ms required between two injections. The second injection would be timed into the compression stroke since the break time equals 50°CA at high engine speed. Further on, a charge motion has been neglected due to a high resulting demand of manifold pressure.

Load point	Injector T-31243				Injector T-31237			
	p _{Inj.} in bar	pattern	SOI in °CA b. TDCF	Tumble flap position	p _{Inj.} in bar	pattern	SOI in °CA b. TDCF	Tumble flap position
1	200	single	190	closed	150	double	323.3/ 300	closed
2	200	single	190	closed	150	double	329.6/ 260	closed
3	150	single	190	closed	200	double	311.9/ 190	closed
4	200	single	190	closed	200	single	300	open
5	200	single	190	closed	150	single	310	open
6	250	double	310/ 235	closed	250	single	270	closed
7	250	single	300	open	250	single	320	open

Table 2: Particulate optimal application parameters of the 3V-concept

The different spray layout of injector T-31237 results in a reduced interaction of the fuel spray with the intake valve. In particular the interaction of beams one and two (compare figure 5) with the inlet valve is reduced due to the compared to injector T-31243 slightly rotated spray layout. Since injector T-31237 has a higher mass flow rate it generates a spray with higher momentum and thus higher spray penetration.

Despite the higher mass flow rate, the injector shows particulate optimal behaviour at early injection timing. The early injection shows no drawbacks concerning the particulate emission behaviour due to the longer time for mixture formation. Furthermore the higher mass flow rate results in an approximately 10% to 15% shorter injection duration which additionally extends the time for mixture formation. A splitting

of the fuel mass into two injections and thus a lower liquid penetration length leads to lowest particulate emissions at load points one and two. At medium load it applies that the best particulate behaviour can be obtained with a single injection. It can be assumed that the shorter time for the mixture formation overcompensates for the effect of the lower liquid penetration length.

It can be summarized that a reduction of the liquid penetration length with a double injection and an as long as possible time for the mixture formation are the main factors for the level of the particulate emissions emitted with injector nozzle T-31237.

The particulate optimal application of the parameters varied is shown in table 3 for the 4V-concept. As well as for the 3V-concept lowest particulate emissions are obtainable with high injection pressure. The lowest level of particulate emissions could be obtained with an injection pressure of 200bar. Higher pressure leads to increased piston wetting and related drawbacks concerning particulate emissions. In comparison with the 3V-concept the range for an early injection is decreased by increasing piston wetting due to the mounting position of the injector. Advantageous of this injector position is, that no interaction between the liquid fuel and the intake valve occurs, which allows an injection into high velocities of the intake flow at maximum valve lift. The particulate optimal injection timing varies just slightly in the range from 285° to 255°CA b. TDCF, whereas for the 7-hole nozzle slightly later injection timings are favourable.

Load point	Injector T-31170				Injector T-31169			
	p _{Inj.} in bar	pattern	SOI in °CA b. TDCF	Tumble flap position	p _{Inj.} in bar	pattern	SOI in °CA b. TDCF	Tumble flap position
1	200	single	255	open	200	single	270	closed
2	200	single	255	open	200	single	285	open
3	200	single	270	open	150	single	285	open
4	200	single	255	closed	200	single	285	open
5	200	single	270	open	200	single	285	open
6	200	single	270	closed	200	double	285/ 250	open
7	200	single	300	open	250	single	290	open

Table 3: Particulate optimal application parameters of the 4V-concept

The influence of the intensity of the charge motion is not that distinct as for the 3V-concept. A comparison of the particulate optimal application of both concepts shows, that lowest particulate emission levels could be obtained with opened tumble flap. An increased charge motion seems to transport the fuel onto the walls especially at high injection pressure which results in related drawbacks concerning particulate emissions. A double injection compared to a single injection shows for both injectors no advantages concerning particulate emissions. It can be assumed, that the drawback of the lower time for the mixture formation is not compensated by the reduction of the penetration of the liquid fuel. The high number of holes in combination with the comparatively low static mass flow rates of the nozzles for both injectors leads to a sufficiently low momentum of the single beams whereas a wetting of the liner and the piston can be avoided largely by suitable injection timing. Multiple injections may lead, especially in combination with short injection durations, to an aggregation of fuel in the nozzle holes as a result of throttling points like the needle seat and nozzle holes. This aggregation of the fuel increases the risk of dropping [6]. Another drawback of multiple

injections is that the injection during the opening and closing of the injector does not take place with the full pressure which results in an increase of the droplet diameter with all its associated drawbacks concerning mixture formation [11, 12]. Figure 7 and 8 show a comparison of operating values and emission levels for both concepts and injectors.

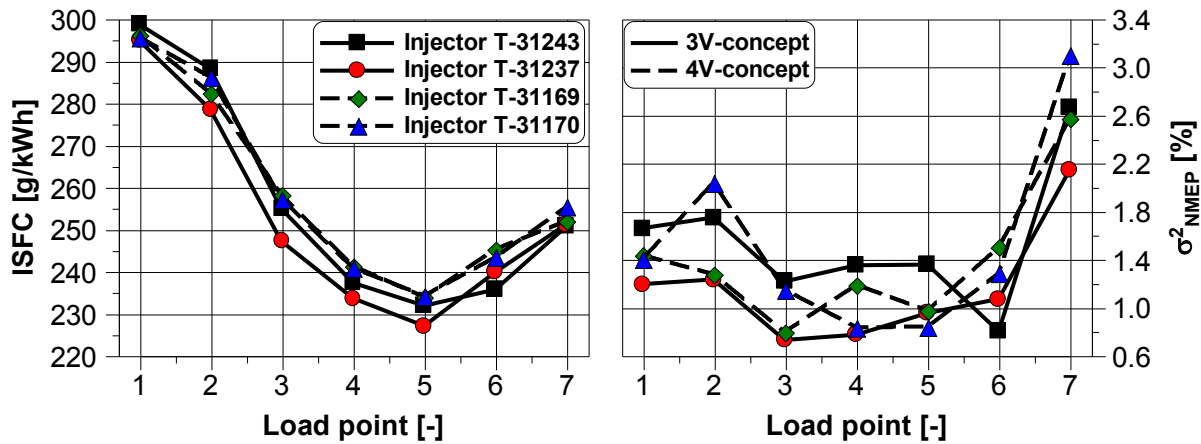


Figure 7: Operating values with particulate optimal application

The combination of the 3V-concept with injector T-31237 shows slightly lower indicated specific fuel consumption at part and medium load. The level obtained with injector T-31243 and the 4V-concept is comparable in these load points. The specific fuel consumption decreases with increasing load due to reduced gas exchange losses and is comparable with engines in series application. The fuel consumption increases at full load as a result of knocking and slight enrichment.

The operating smoothness characterised by a low variance of the net mean effective pressure is at a high level for both concepts with all injectors. The variance decreases with increasing load as a result of better conditions for ignition and combustion but increases sharply at rated output. While Injector T-31237 tends to show the highest operating smoothness, the other injector of the 3V-concept (T-31243) tends to show the lowest. A reason for the low operating smoothness could be found in high inhomogeneities of the mixture as a result of short time for the mixture formation, compare table 2.

An indication for the low fuel consumption with injector T-31237 can be obtained from the specific CO-emissions depicted in figure 8. These are except at load point five lower than with the other injector and concept respectively. This suggests a better homogeneity of the mixture and a higher quality grade of the combustion. The high CO-emission at load point five can be traced back to the low injection pressure of 150bar. The low pressure minimizes the particulate emissions at early injection at 310°CA b. TDCF but has a negative influence onto the homogeneity of the mixture and thus the CO-emissions. The bad mixture formation with injector T-31243 as a result of the late injection timing at 190°CA b. TDCF at load points one to five leads to high CO-emissions as can be seen in figure 8. The CO-emissions emitted with both 4V-concept injectors are on a high level especially at part load (load points one to three). The 4V-concept shows with both injectors at load point three to five lower HC-emissions as with the 3V-concept. Since HC-emissions are related to wall wetting [13] it can be assumed, that the combination of the mounting position of the 4V-concept injector and early injection timings leads for particulate optimal application to lower wall wetting at medium load.

Resulting out of high combustion and component temperatures at full load HC- and CO-emissions are on a low, NO_x-emissions on a high level at load points six and seven. The absolute levels of these gaseous emissions are comparable for both concepts and injectors.

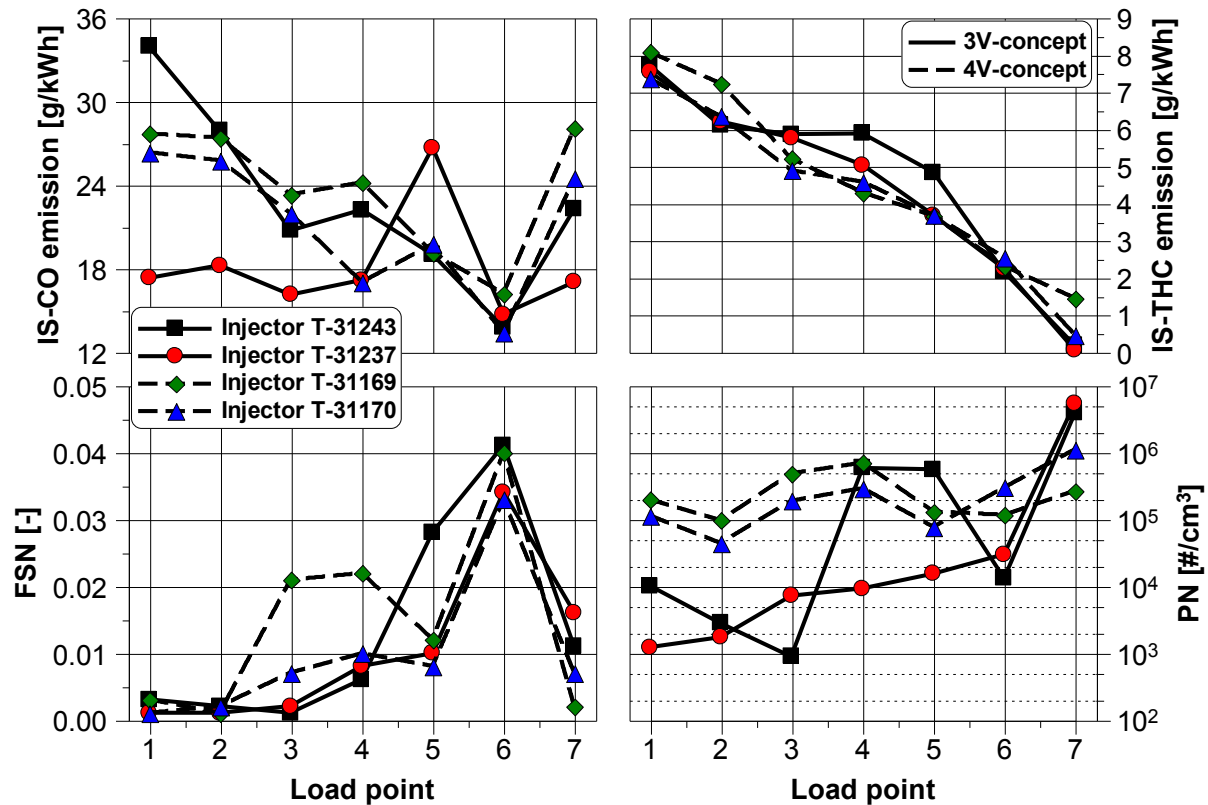


Figure 8: Emission levels with particulate optimal application

Concerning particulate emissions, the 3V-concept has advantages especially with injector T-31237. This combination shows just at load point three distinct and at full load (LP 6 and 7) slightly higher particulate emissions as with injector T-31243. The particle number concentration rises sharply at load points four and five for injector T-31243 with reduced mass flow rate. This results out of the late start of injection at 190°CA b. TDCF for avoiding valve wetting, which has in combination with longer injection duration at higher load drawbacks onto the homogeneity of the mixture.

For the 4V-concept advantages concerning particulate emissions could be obtained only at rated output. At part and medium load, the emission level shows to be above the level obtained with injector T-31237. The level decreases from load point one to two due to the increase of engine speed at constant load and hence a higher turbulence in the combustion chamber. The emission level increases with increasing load (load point two to four) as a result of higher injected fuel mass, which leads to wall wetting and reduced time for mixture formation. The 7-hole injector T-31169 shows higher emission levels at part and medium load compared to the other 4V-concept injector but has advantages at full load.

While at load point six a comparable filter smoke number could be obtained for both concepts, the 3V-concepts show lower particle number concentrations. The increased homogeneity of the mixture as a result of the closed tumble flap has a positive effect on the level of the particulate emission. In addition the long time for the mixture formation at low engine speed of 1500rpm is advantageous. The 3V-concept shows

higher values for the filter smoke number and higher particle number concentrations at rated output. It can be assumed that the homogeneity of the mixture is improved as a result of the mounting position of the injector in the middle plane of the combustion chamber.

It has been seen within all investigations that the particulate emission behaviour of the 4V-concept is more stable regarding the start of injection. The emission level increases merely for late injection timings due to higher inhomogeneities of the mixture. As opposed to this, the 3V-concept shows high dependency of the injection timing. Especially an interaction of the liquid fuel with the intake valves leads to increased particulate emissions. The highest particulate emission levels have been measured with valve wetting. The comparison of the investigations with particulate optimal application of the variation parameters shows nevertheless a high potential for the upright standing mounting position of the injector of the 3V-concept.

Figure 9 shows a comparison of operating values for both concepts at full load. The early centre of heat release results especially for the 3V-concept in advantages concerning the quality grade of the combustion process at the design point. A short burning duration in combination with an early centre of heat release leads to low exhaust gas temperatures, which allows almost stoichiometric combustion at all load points.

The short burning duration entails however high pressure gradients and thus high thermal and mechanical loading of the engine. The closed tumble flap and hence a high intensity of the charge motion results for the 3V-concept and injector T-31243 at the design point in a pressure gradient of $8.5\text{bar}/^\circ\text{CA}$. The early centre of heat release and the stoichiometric operation results for all concepts in low specific fuel consumption. The 3V-concept shows at the design point the lowest consumption due to an early and fast combustion.

Figure 10 shows a comparison of the centre of heat release at full load points within the FEV scattering range for an evaluation in comparison with engines in series application. At the design point the engine concepts investigated are located at the lower boundary of the scattering range, which shows the potential of the concepts especially of the 3V-concept. The investigated concepts are located at rated output in the upper range of the scattering range. This may be related to the comparatively high load at this load point.

6. Optical Investigations

Experiments at an injection chamber preceded the optical studies at the research engine. All injectors have been investigated in terms of liquid penetration length and spray cone angle. The experiments have been accomplished at room temperature with an ambient pressure varying between 0.5 and 5.0bar. As injection pressure 100bar up to 200bar has been used. These experiments were used for validation of 3D CFD calculations and provide for a better understanding of the injectors.

The operating points shown in Table 1 were given as reference for the optical investigations. Boundaries for an optical operation are a net mean effective pressure of 6bar, an exhaust temperature of 650°C as well as an engine speed of 3000rpm using a metal piston and 2500rpm using a glass piston respectively.

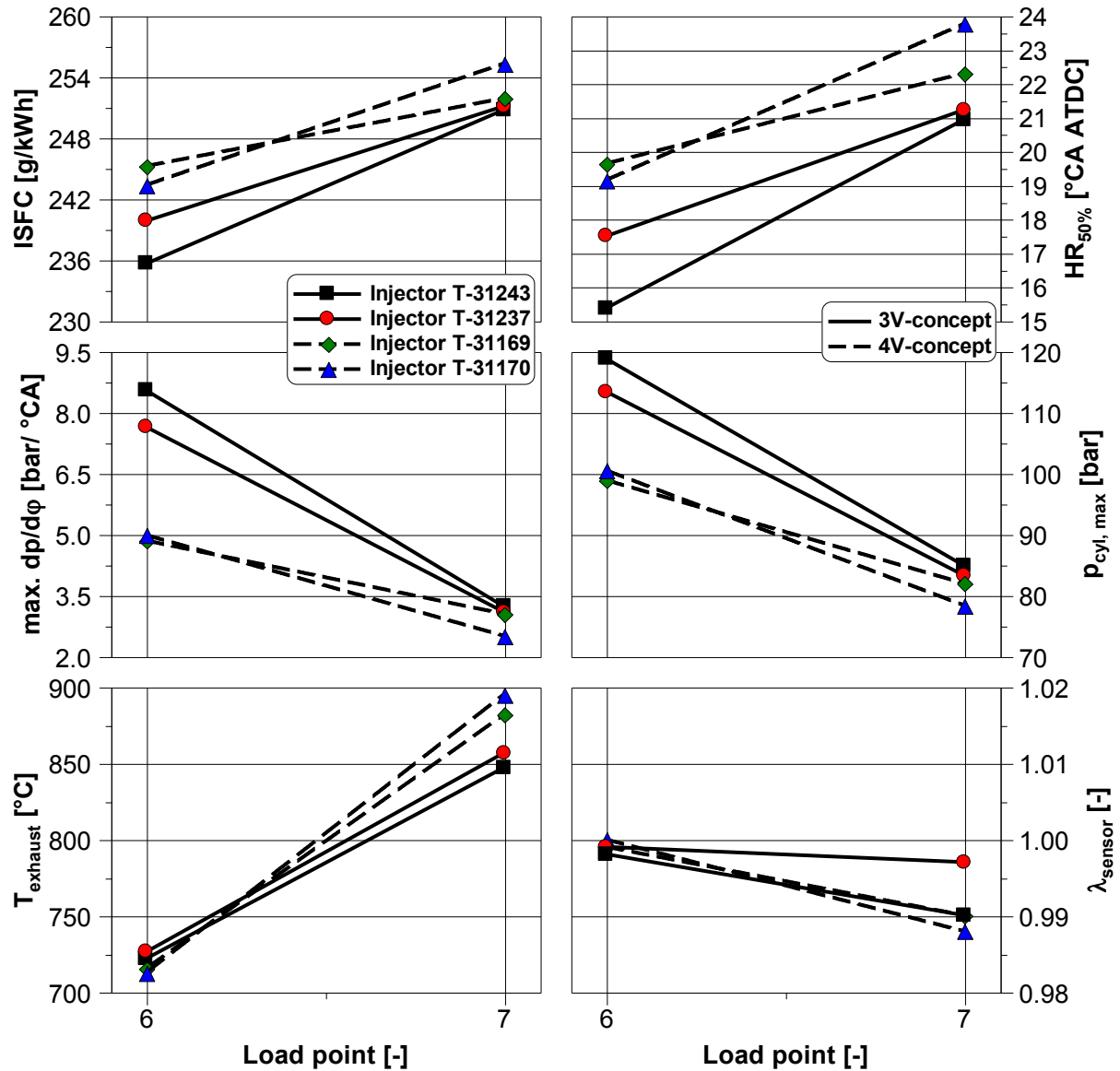


Figure 9: Operating values with particulate optimal application; load points 6 and 7

6.1 Investigation of the Inlet Flow

For the visualization of the in-cylinder flow by particle image velocimetry (PIV) a glass piston has been used to illuminate the seeding by laser light sheet. For the generation of the laser sheet a Nd:YAG double pulse laser with a wavelength of 532nm has been used. The light has been introduced perpendicularly into the combustion chamber. A CCD double-image camera with a band pass filter having a wavelength of 532nm has been mounted orthogonally to the light sheet. Seeding particles comprising of diethylhexyl sebacate have been used. The in-cylinder flow has been sampled from 330 to 30°CA b. TDCF with an increment of 10°CA, while each time step was recorded 30 times to eliminate turbulent fluctuations. The software DaVis of LaVision GmbH has been used for the calculation of the cross correlation and batch processing.

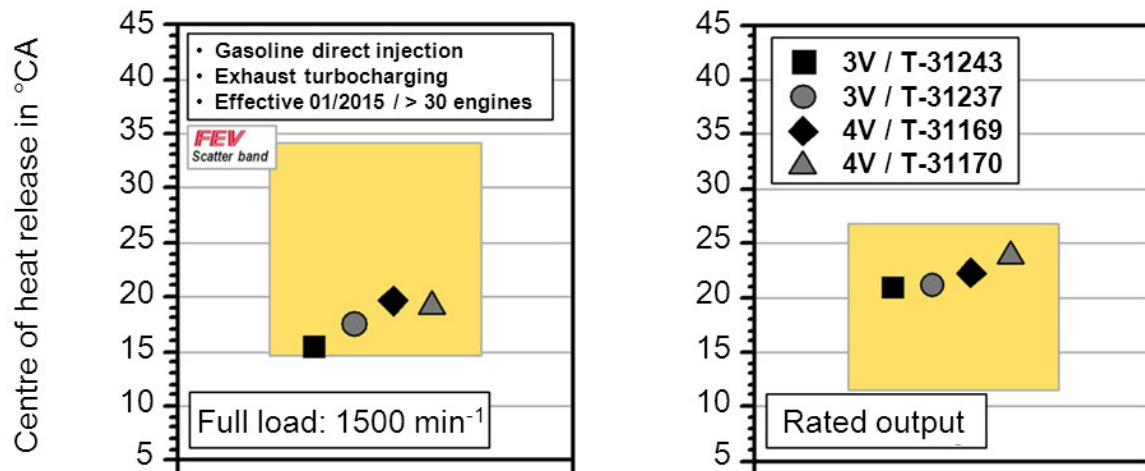


Figure 10: Centre of heat release of load points 6 and 7 within the scatter range of engines, [14]

The following figures are showing the inlet flow for both concepts with opened and closed tumble flap exemplarily at load point two at 260°CA b. TDCF. The inlet flow of the 3V-concept is shown in figure 11. The picture on the left side shows the flow with an open and the right side with a closed tumble flap. With an open tumble flap it can be seen, that the entire circumference of the valve is used for the flow into the combustion chamber. On contrary the valve is predominantly overflowed at the upper side of the valve with closed tumble flap, which results in a higher charge motion with the advantageous effect onto mixture formation.

The comparison of the inlet flow with opened and closed tumble flap of the 4V-concept is shown in figure 12. In comparison with the 3V-concept a similar flow structure but at a lower velocity level can be obtained. Thus, the intake port of the 4V-concept generally seems to generate lower charge motion. Further on, the effect of the tumble flap is not that distinct as for the 3V-concept.

6.2 Investigation of Injection and Combustion

For the examination of injection and combustion the compression pressure was determined to be equal to the pressure obtained within thermodynamic measurements. Due to the lower compression ratio of $\epsilon = 8.73$ the manifold pressure has to be increased, resulting in an increase in air and injection mass. This leads to longer injection duration and in terms of the small bore diameter to an increase of wall wetting. Isooctane has been used as fuel to reduce the fouling of the glass liner. Further on, oil and coolant temperatures of 60°C had to be used during the optical operation of the engine compared to temperatures of 90°C at thermodynamic operation.

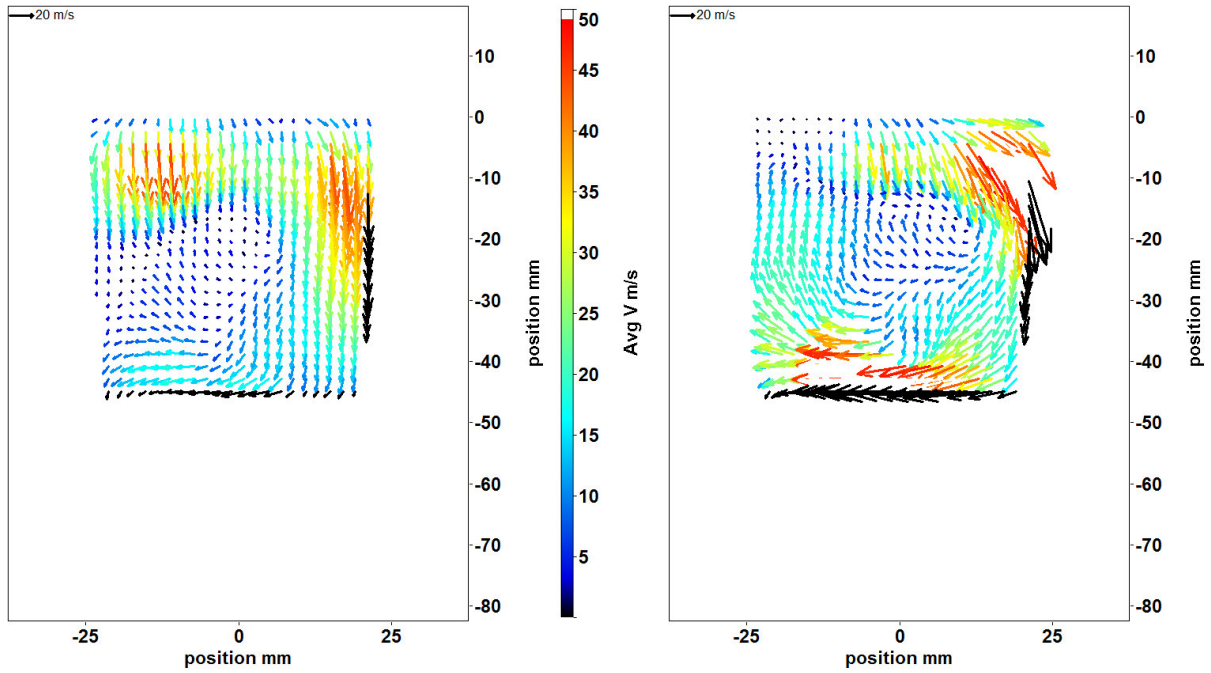


Figure 11: Comparison of the inlet flow with open (left) and closed (right) tumble flap; 3V-concept

The injection has been visualized by high-speed measurements based on the Mie theory. LED boards with a power of 120W each were used on both sides of the glass liner for integral illumination. The high-speed camera was of the type Redlake HG-100K, which has a resolution of 8-bit. The engine cycles have been recorded with a sampling rate of 2°CA , which results in the exposure ratios shown in table 4.

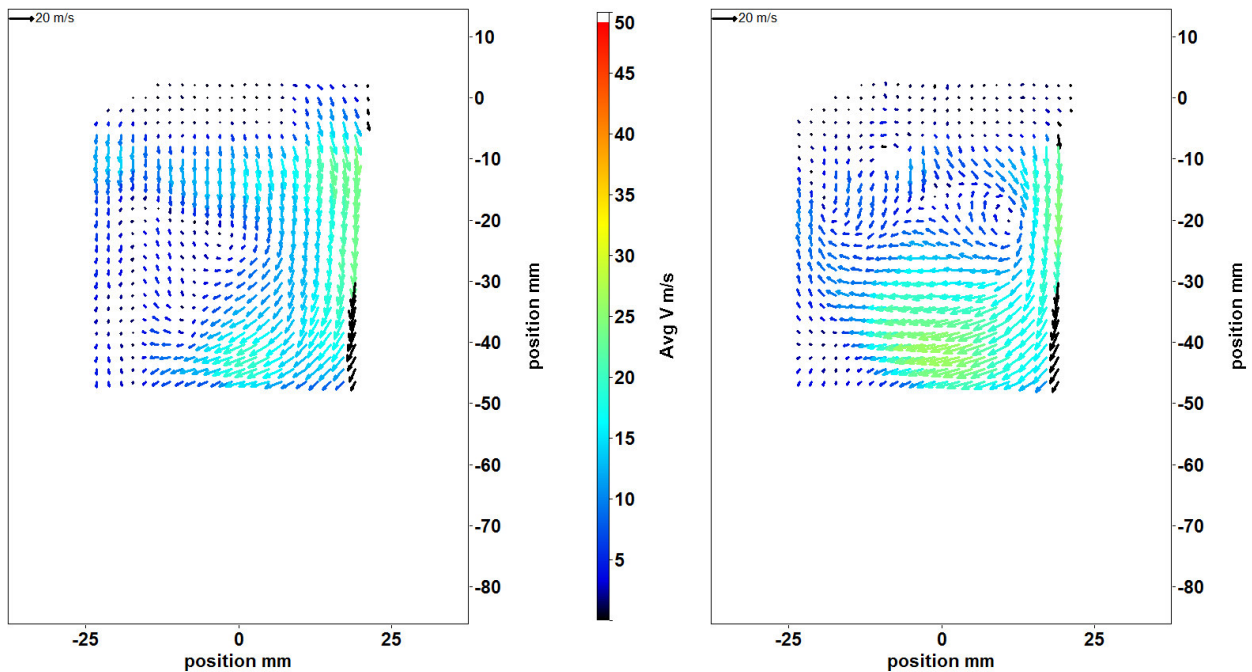


Figure 12: Comparison of the inlet flow with open (left) and closed (right) tumble flap; 4V-concept

Engine speed in rpm	Exposure rate in Hz
1200	3600
1800	5400
2400	7200

Table 4: Exposure rate of the high speed camera

To maintain a constant image size a resolution of 544 x 368 pixels has been chosen. Ten consecutive cycles have been recorded at each operation point in order to eliminate cyclical fluctuations by averaging. Further on, the measurement of the motored engine operation at the same load point has been subtracted from the raw images to eliminate reflections and other background noise.

Within the optical investigations all variation parameters like the injection pressure, injection timing and intensity of the charge motion as well as the injector layout have been varied according to the thermodynamic investigations. Due to high thermal loading just load points one to three could be investigated optically. At load point three, the ignition timing had to be shifted to late injection to comply with the operating parameters of the optical engine.

Figure 13 shows the best operation point of the thermodynamic experiments in optical mode at load point 2 of the injector T-31243. The figure shows the injection at crank angle $184^{\circ}\text{CA} \leq \varphi \leq 162^{\circ}\text{CA}$ b. TDCF. The 6-hole injector has a lower flow rate compared to injector T-31237, so the spray momentum is reduced to decrease wall wetting. The longer triggering time associated leads to wall wetting even at best operation point. Furthermore, a slight wetting of the intake valves could be obtained.

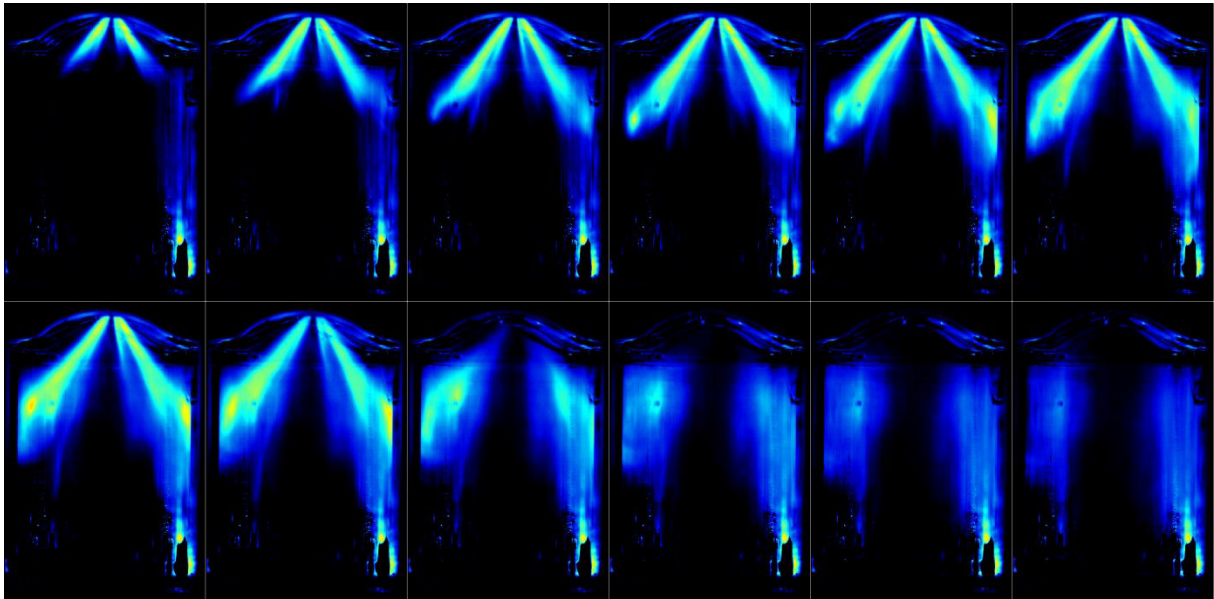


Figure 13: Injector T-31243, closed tumble flap, $p_{inj.} = 200\text{bar}$, $OE = 190^{\circ}\text{CA}$ b. TDCF

Figure 14 and 15 are showing the injection of particulate optimal double injection at load point two with injector T-31237. Injector T-31237 differs from injector T-31243 by its hole-individual mass flow rate and slightly rotated spray to avoid wetting of the intake valves. Further on, its mass flow rate is increased, which reduces the trigger time. This results in a higher spray momentum, which is detrimental to the small bore diameter. A reduction of the liquid penetration length can be realized by multiple injections.

Figure 14 shows the first injection starting at 330°CA until 320°CA b. TDCF and figure 15 the second injection at crank angle $256^\circ\text{CA} \leq \varphi \leq 246^\circ\text{CA}$ b. TDCF. As a result of early injection timings the combustion chamber is shaded by the piston at near TDCF position. Due to this the spray is not illuminated very well by the LED light. Nevertheless it can be recognized, that the spray hits the piston and starting at 324°CA b. TDCF is deflected into the direction of the liner. An interaction with the inlet flow could not be proved for the first injection. However a sufficient time remains for the resulting wall film to evaporate off the piston. An interaction of the spray with the wall can be reduced with a double injection, especially in combination with the charge motion. In terms of wall wetting a closed tumble flap generally shows advantages at this load point, thus the increased wall contact of beam 5 is avoidable. The influence of injection timing has a big impact. Late injection timings are not desirable due to the reduced tumble motion.

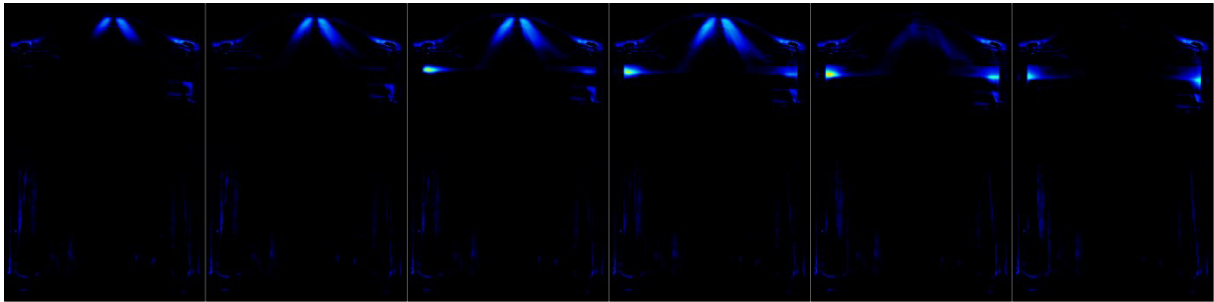


Figure 14: Injector T-31237, closed tumble flap, $p_{inj.} = 150\text{bar}$, $SOE_1 = 334^\circ\text{CA}$ b. TDCF

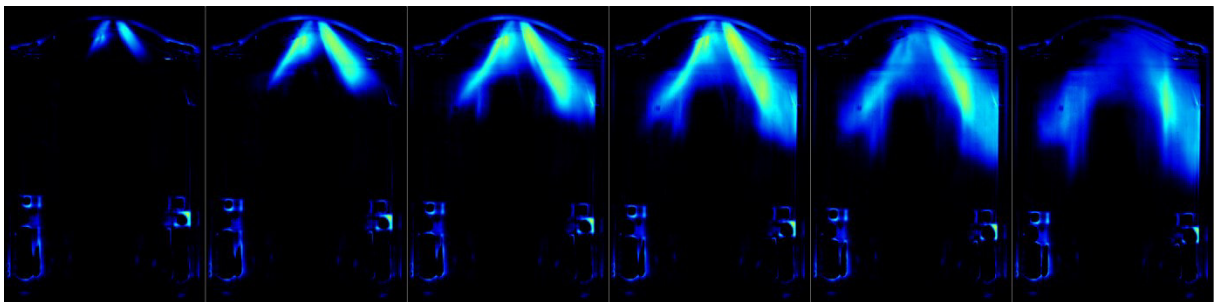


Figure 15: Injector T-31237, closed tumble flap, $p_{inj.} = 150\text{bar}$, $SOE_2 = 260^\circ\text{CA}$ b. TDCF

The layout of the injectors of the 4V-concept differs in the number of holes (7 versus 6 holes) and the inclination of the spray in the combustion chamber, compare figure 6. Due to the increase of the number of holes the single beam momentum is reduced, which leads to a lower liquid penetration length. The lateral layout of the injector is advantageous compared to the 3V-concept, since valve wetting is avoided.

Figure 16 shows a single injection with injector T-31169 and open tumble flap starting at 266°CA b. TDCF. It is shown, that no significant wall wetting occurs even by a single injection. Later injection timings have a negative effect due to increased wall wetting. Further, the results of the PIV measurements could be confirmed. A closed tumble flap showed no advantages regarding particulate emissions.

Within the optical investigations it has been shown that a double injection is preferable, since wall wetting could be avoided as well as less diffusive combustion could be obtained.

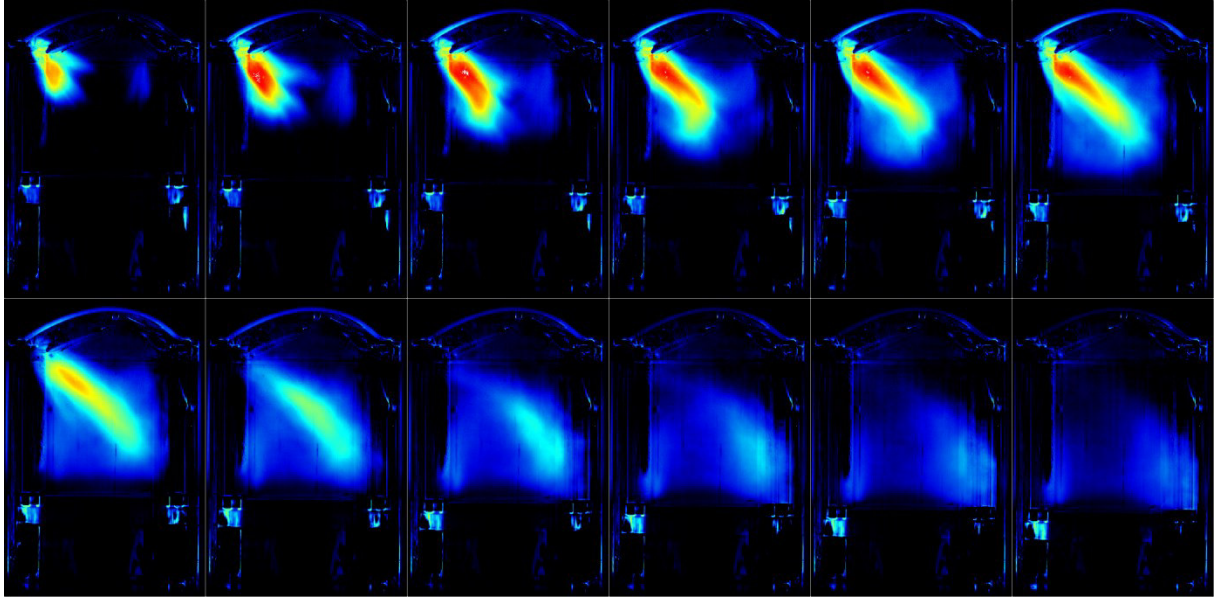


Figure 16: Injector T-31169, open tumble flap, $p_{inj.} = 200\text{bar}$, $SOE = 270^\circ\text{CA}$ b. TDCF

In Figure 17 a single injection with injector T-31170 and open tumble flap starting at 264°CA b. TDCF is shown. As well as for injector T-31169 no significant wall wetting occurs even by a single injection. Despite of this, the related combustion not illustrated in figure 17 shows to be slightly diffusive. Since injector nozzle T-31170 has less nozzle holes compared to injector T-31169 and thus a higher single beam momentum it is inclined further towards the piston to compensate the higher liquid penetration length.

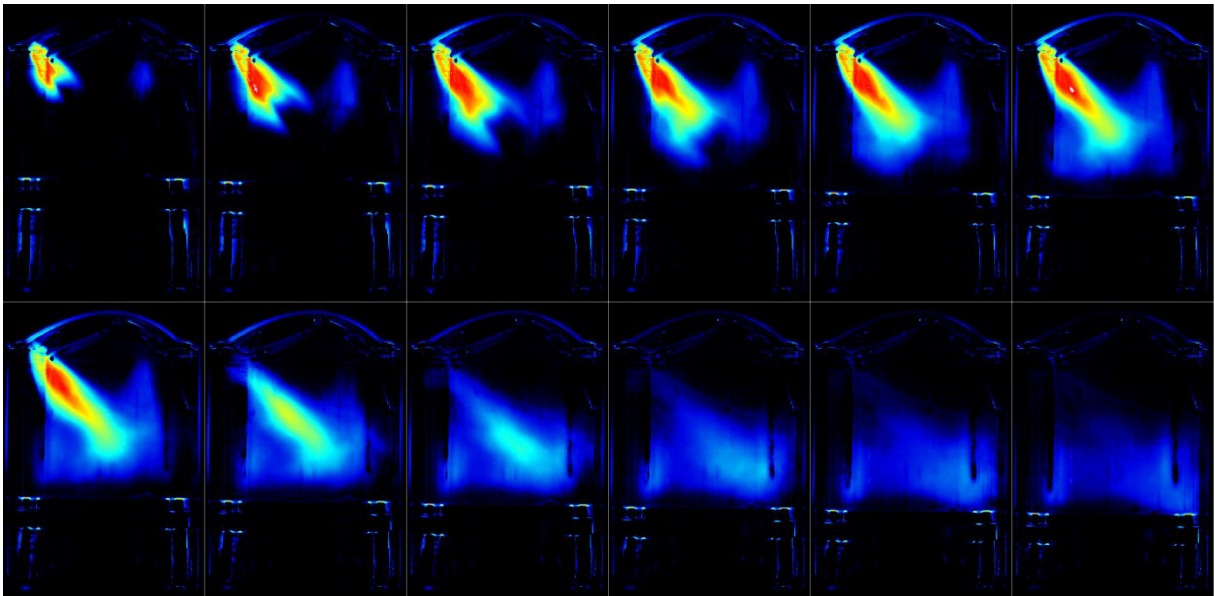


Figure 17: Injector T-31170, open tumble flap, $p_{inj.} = 200\text{bar}$, $SOE = 270^\circ\text{CA}$ b. TDCF

6.3 Summary of the Optical Investigations

Comprising both cylinder head concepts, it is noticeable that the 4V-concept shows low sensibility regarding the application parameters on injection, evaporation and combustion. Injector T-31169 shows the most stable results regarding this. The almost negligible influence of the closed tumble flap at the 4V-concept found at the thermodynamic engine has been confirmed using PIV and injection visualization. For the 3V-concept a strong dependency on the injection timing regarding particulate emissions has been ascertained within the thermodynamic investigations. On basis of the results of the optical investigations, valve wetting could be identified as a possible cause for the strong dependency of the injection timing.

7. Numerical Investigations

Numerical investigations of the mixture formation have been carried out to get a further insight into the processes in the combustion chamber and to identify sources for particulate and other emissions. The following section exemplarily shows results of the 3V-concept with Injector T-31243 at load point two (1800rpm, 4bar NMEP), open tumble flap and an injection pressure of 150bar. The particle number concentration, specific CO-emissions and the covariance of the net mean effective pressure are shown in figure 18 for an interpretation and transfer of the numerical results onto the results obtained at the thermodynamic engine. The particle number concentration decreases with later injection timing, while specific CO-emissions and the covariance of the net mean effective pressure increase with late injection at 530°CA.

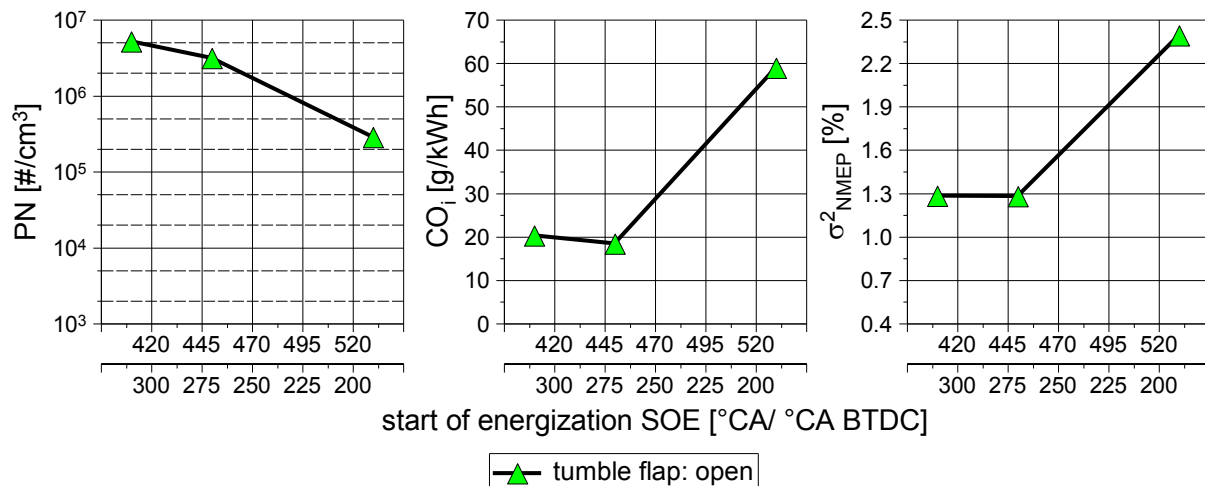


Figure 18: Load points investigated with CFD

7.1 Computational Model

The computational model used for the numerical investigation of the mixture formation is based on a coupled Euler-Lagrange method. Hereby the equations of the gas phase are solved with the element based finite volume method of the CFD code ANSYS CFX 14. The turbulence has been modelled with a standard k-ε turbulence model. Initial and boundary conditions have been obtained from 1D calculations performed as part of a pressure analysis. Isooctane has been used as modelling fuel for the liquid phase. The

spray models have been calibrated based on the optical investigations carried out at the high pressure injection chamber.

As a result of the comparatively low free path length wall wetting occurs and thus the modelling of the wall film has to be considered within the computational model. Two models have been used for the calculation of the results presented in this article. This is on the one hand the “stick-to-wall” model where the entire fuel mass which has been in interaction with the wall is impinged into the wall film and on the other hand the model of Elsässer, which considers droplet reflection and breakup [15, 16, 17].

7.2 Results

Figure 19 shows curves of tumble number and turbulence kinetic energy at three different injection timings. The wall film has been modelled within these calculations with the model of Elsässer. It is shown, that the injection timing has a direct effect onto the intensity of the charge motion. While an early and a mid-injection has a supporting effect, it is reduced by a late injection. The levels of the peak values reached at around 655°CA are in line with the order of the injection timing. Since the charge motion decomposes into turbulence, a lower charge motion at late injection results in a lower turbulence kinetic energy. This is the case especially for the late injection at 530°CA, which shows disproportionally lower turbulence energy compared to the other calculations.

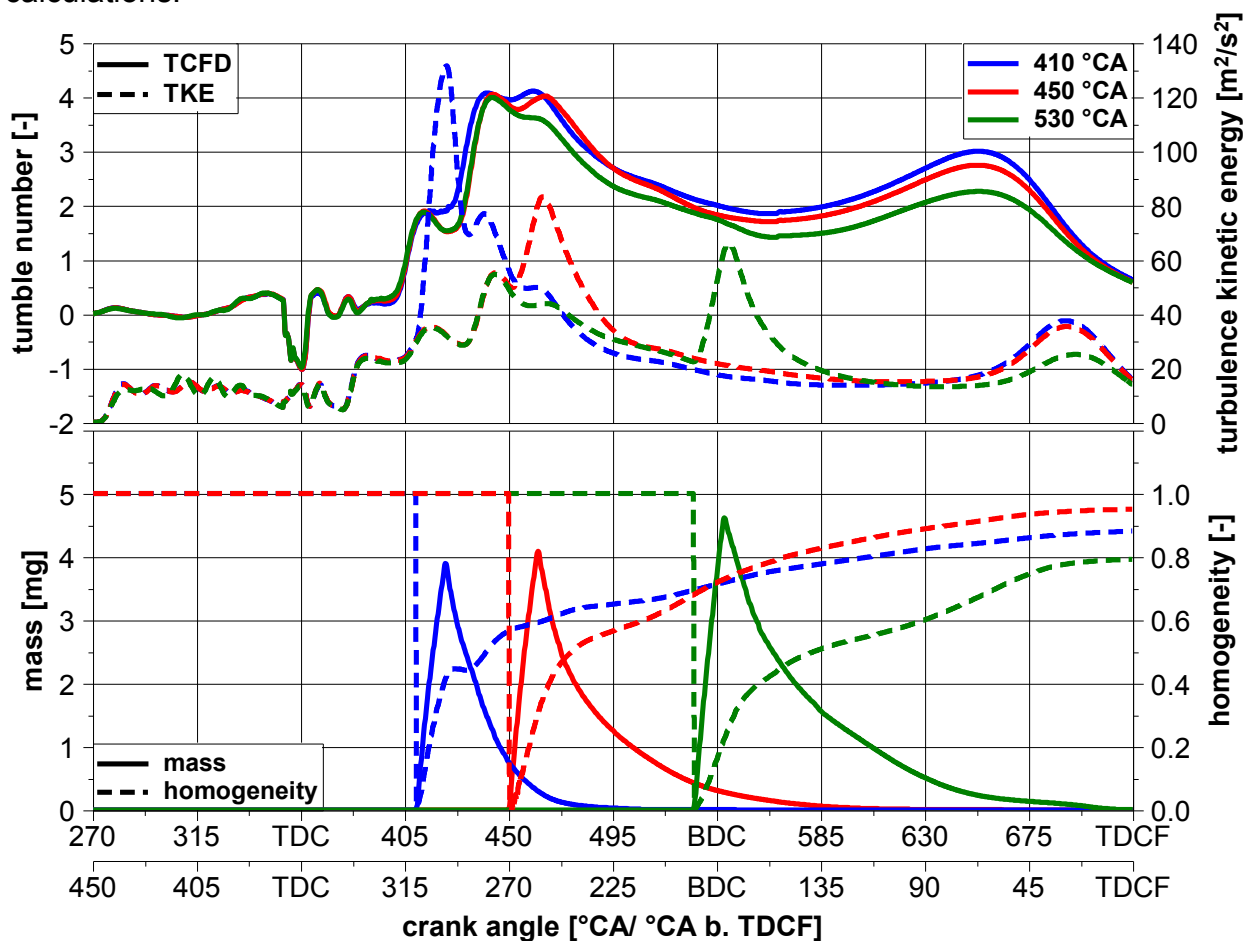


Figure 19: Tumble number, turbulent kinetic energy, liquid mass and homogeneity for various injection timings at load point 2

As evaporation and mixture formation are related to the charge motion and the turbulence it is necessary to investigate the effect of the injection timing. For this, figure 19 shows as well curves of the liquid fuel mass and the homogeneity of the mixture. The homogeneity is an index based on the ratio of the volume weighted average absolute deviation of the fuel mass fraction to its average value and is defined as follows [18].

$$H = 1 - \left(\frac{e}{2 \cdot \overline{m}_f} \right) \quad (1)$$

$$\overline{m}_f = \frac{1}{V_{ges}} \cdot \sum_{i=1}^N (m_{f,i} \cdot V_i) \quad (2)$$

$$e = \frac{1}{V_{ges}} \cdot \sum_{i=1}^N (|m_{f,i} - \overline{m}_f| \cdot V_i) \quad (3)$$

It can be obtained from the curves of the liquid fuel mass that the time for the evaporation of the fuel increases with later injection timings. This in combination with the shorter time for mixture formation leads to a lower homogeneity of the mixture. The best homogeneity could be reached with an injection at 450°CA, which is a result of the injection into a strong charge motion due to high velocities at maximum valve lift. A comparison of these results with the results obtained experimentally depicted in figure 18 shows that the calculated trends of homogeneity and turbulent kinetic energy are in line with the trends of CO-emissions and covariance of the net mean effective pressure. On the contrary the particle number concentration measured shows an opposing trend. Hence the high particle number concentration at early injection could not be explained with the homogeneity of the mixture.

Investigations of the wall film have been done for the injection timings at 410°CA and 530°CA to identify sources of these particulate emissions. The stick to wall model has been used in these calculations, since this represents the worst case regarding the wall film mass. Figure 20 shows curves of liquid fuel mass and wall film mass for both injection timings.

For an early injection at 410°CA it is shown that a substantial part of the liquid fuel forms a wall film. This wall film is located primarily on the piston. Whereas most of the wall film evaporates during the intake and compression stroke, still a slight unevaporated part remains on the piston at ignition timing. The burnup of this wall film with the related local shortage of oxygen could be a source for particulate emissions. In contrast, no wall wetting could be ascertained for an injection at 530°CA. Thus particulate emissions at this injection timing are a result of local rich zones due to inhomogeneities of the mixture, compare figure 19. Further numerical investigations have shown that valve wetting occurs for an injection at 450°CA, which might be the source of particulate emissions.

7.3 Summary of the Numerical Investigations

Possible sources for particle emissions could be identified with numerical calculations of mixture formation. While a liquid wall film may be the reason of particulate emissions for an early and mid-injection, at late injection a poorly mixed mixture could be obtained. These inhomogeneities might be an explanation for the increased CO-emissions and combustion instabilities at late injection.

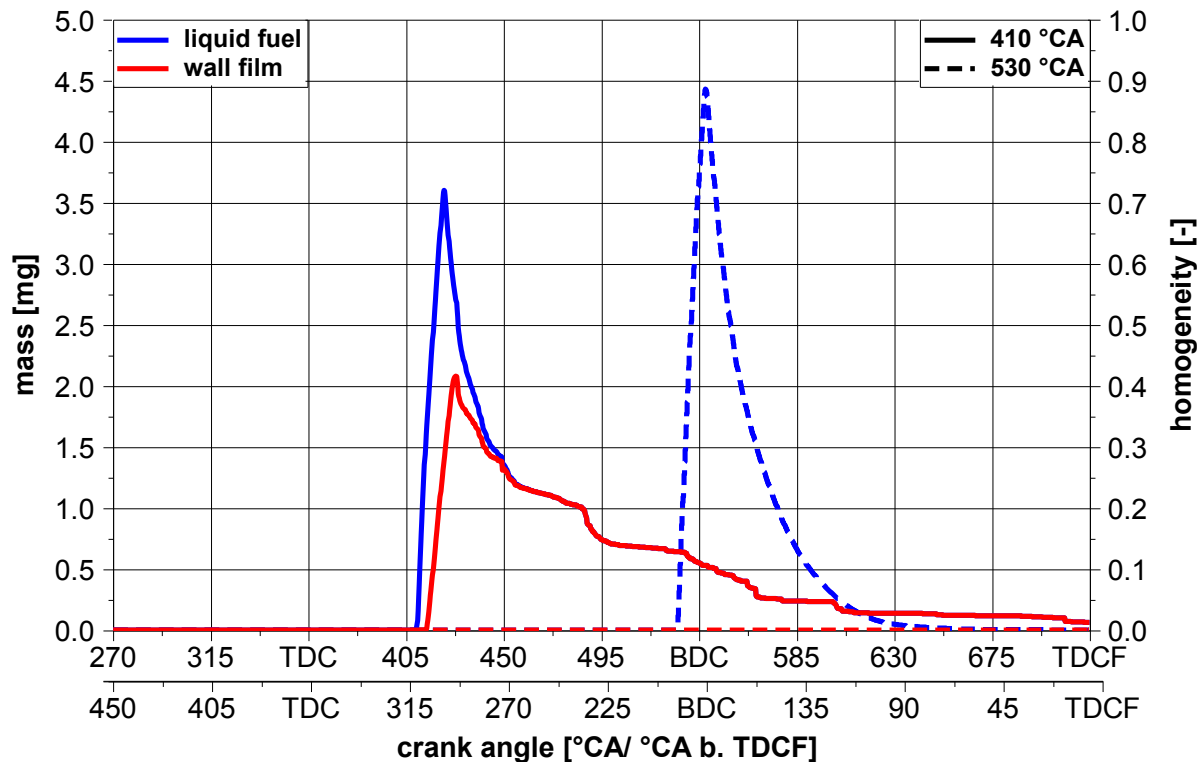


Figure 20: Liquid fuel and wall film mass for early and late injection at load point 2

8. Summary and Outlook

Suitable cylinder head concepts for a small direct injection spark ignition engine have been defined within preliminary CAD studies preceding the investigations outlined in this article. Further on, 1D-simulations have been carried out to evaluate effective operating values of these concepts for various bore/stroke combinations. Two concepts with different injector positions have been selected for an implementation of engine prototypes. Within the design process of the cylinder heads demands of manufacturing processes and minimal wall thicknesses due to mechanical strength have been considered. The geometries of the intake port and the water jacket have been optimised with 3D CFD calculations.

The operating and emission behaviour of the cylinder head concepts have been determined by extensive studies at a thermodynamic engine in a wide range of load and speed. Two injectors have been available for each cylinder head concept. The focus within these investigations has been especially on particulate emissions. Investigations at an optically accessible engine like the visualization of the inlet flow by Particle Image Velocimetry and high speed visualization of the injection by Mie scattering as well the combustion have been carried out to get an insight into the

processes in the combustion chamber. Accompanying numerical calculations of the mixture formation helped to identify sources for particulate emissions and for a deeper understanding of the results obtained at the thermodynamic and optical engine. Due to the high number of variants, the engine performance and emission level of the small bore direct injection spark ignition engine concepts could be investigated just in principle. The investigations illustrate however a great potential of these engine concepts.

Operating points with higher load and for the 3V-concept especially the rated output have shown to be critical regarding particulate emissions, since valve wetting cannot be avoided as a result of long injection durations. According to the present results wall wetting does not seem to be a bigger problem than with large bore engines. Oil dilution as a result of wall wetting could however be a limiting factor for the reduction of the bore diameter. Comparing both investigated concepts, the 3V-concept provides higher potential regarding lower particulate emissions but is more sensitive to application parameters like injection timing.

Investigation of the effects of wall wetting and related mixture formation as well as reducing the sensitivity of the 3V-concept should be the topic of future research. A resulting question is, whether a central injector position leads to an improved mixture formation as indicated in [19]. This is especially the case since both concepts show a very low tendency to knocking, indicating a tolerance for a decentralized spark plug. Further on, the low tendency to knock provides the potential to increase the mean effective pressure which offers the possibility to use the engine as powertrain for higher vehicle classes. Another open question is the small influence of the charge motion obtained at the 4V-concept.

References

- [1] Schech, J.; Siedentop, A.; Wiebe, A.; Eilts, P.: Zwischenbericht: GDI-Grenzdurchmesser. In: FVV-Herbsttagung 2012, Heft R 560, Dortmund, 2012.
- [2] Schech, J.; Siedentop, A.; Herbst, F.; Wiebe, A.; Eilts, P.: Conceptual Design of Small Direct-Injection Spark-Ignition Engine Concepts by Use of CAE-Tools. SAE Technical Paper: 2012-32-0066, 2012.
- [3] AVL LIST GmbH: AVL Customized Transparent Single Cylinder Engine - Design & Layout Cylinder Head Interfaces, Graz, 2011.
- [4] Robert Bosch GmbH: Spray Targeting Study 3V, FVV-Projekt TU Braunschweig, 2012.
- [5] Robert Bosch GmbH: Spray Targeting Study 4V, FVV-Projekt TU Braunschweig, 2012.
- [6] Koch, T.; Spicher, U.; Kubach H.; Dageförde, H.: Untersuchung von Maßnahmen zur Reduktion der Partikel-Anzahlmissionen bei Otto-DI-Motoren. In: FVV-Herbsttagung 2013, Heft R 564, Bad Neuenahr, 2013.
- [7] Lauer, T.: Einfluss der Ladungsbewegung auf Gemischbildung und Entzündung bei Otto-Motoren mit homogenen Brennverfahren. In: Bde. %1 von %2 VDI Fortschritt-Berichte Reihe 12, Nr. 647, VDI Verlag GmbH, Wien, 2007.
- [8] Drake, M. C.; Fansler, T. D.; Solomon, A. S.; Szekely, G. A.: Piston Fuel Films as a Source of Smoke and Hydrocarbon Emissions from a Wall-Controlled Spark-Ignited Direct-Injection Engine. SAE Technical Paper: 2003-01-0547, 2003.
- [9] Hertler, D.: Partikelemission von Ottomotoren mit Direkteinspritzung: Experimentelle Charakterisierung des Einflusses der Kraftstoffaufbereitung und Verbrennung. Dissertation, Technische Universität Darmstadt, Darmstadt, 2012.
- [10] Kaden, A.; Altenschmidt, F.; Gildein, H.; Kraus, E.; Schaupp, U.; Prilop, H.: Die Analyse der Rußentstehung mittels optischer Messtechnik und CFD-Simulation an einem aufgeladenen Ottomotor mit Direkteinspritzung. In: 9. Internationales Symposium für Verbrennungsdiagnostik, Baden-Baden, 2010.
- [11] Stach, T.; Schlerfer, J.; Vorbach, M.: New Generation Multi-hole Fuel Injector for Direct-Injection SI Engines - Optimization of Spray Characteristics by Means of Adapted Injector Layout and Multiple Injection. SAE Technical Paper: 2007-01-1404, 2007.
- [12] Piock, W.; Hoffmann, G.; Berndorfer, A.; Salemi, P.; Fusshöller, B.: Strategies Towards Meeting Future Particulate Matter Emissions Requirements in Homogeneous Gasoline Direct Injection Engines. SAE Technical Paper: 2011-01-1212, 2011.
- [13] Suck, G.: Untersuchung der HC-Quellen an einem Ottomotor mit Direkteinspritzung. Dissertation, Otto-von-Guericke-Universität Magdeburg, Magdeburg, 2001.
- [14] Dieterich, C.: Email message, January 29th 2015.
- [15] Mühlbauer, M.: Modelling wall interactions of a high-pressure, hollow cone spray. Dissertation, Technische Universität Darmstadt, Darmstadt, 2009.

- [16] Elsässer, G.: Experimentelle Untersuchung und numerische Modellierung der freien Kraftstoffstrahlausbreitung und Wandinteraktion unter motorischen Randbedingungen. Dissertation, Karlsruhe, 2001.
- [17] ANSYS, Inc.: ANSYS CFX-Solver Theory Guide. Release 14.0, 2011.
- [18] Munnannur, A.; Cremeens, C. M.; Liu, Z. G.: Development of Flow Uniformity Indices for Performance Evaluation of Aftertreatment Systems. SAE Technical Paper: 2011-01-1239, 2011.
- [19] Lehrheuer, B.; Hoppe, P.; Günther, M.; Pischinger, S.: CO₂-Reduzierung durch kleinen Hubraum in Kombination mit Biokraftstoffen. In: MTZ - Motortechnische Zeitschrift, pp. 66-73, 2014.

The Authors:

Dipl.-Ing. Arne Siedentop, Institute of Internal Combustion Engines,
Technische Universität Braunschweig, Braunschweig

Dipl.-Ing. Jörn Schech, Institute of Internal Combustion Engines,
Technische Universität Braunschweig, Braunschweig

Dipl.-Ing. Andreas Bradenstahl, Institute of Internal Combustion Engines,
Technische Universität Braunschweig, Braunschweig

Prof. Dr.-Ing. Peter Eilts, Institute of Internal Combustion Engines,
Technische Universität Braunschweig, Braunschweig

Licence:

This document is licensed under the Creative Commons Attribution 3.0 DE License (CC-BY 3.0 DE): <http://creativecommons.org/licenses/by/3.0/de/>

Zero-Dimensional Analysis of Spark Ignition Engines with High Variability under Transient Conditions

Thorben Walder
André Casal Kulzer
Michael Bargende

Abstract

With the upcoming introduction of more dynamic test procedures (e.g. WLTP) and the approaches to take real driving emissions into account [1], more detailed investigation of the transient behavior is essential to fulfill the stringent legislation in the future.

In the past decades several measurement technologies and methods to analyze transient events were developed and published. These analyses aim at gaining more detailed information about the course of single work cycles within changing boundary conditions. In order to enable a cycle-based evaluation of control strategies of internal combustion engines under transient operation conditions, a zero-dimensional approach of pressure analysis (gas exchange and high pressure cycle) is chosen in this paper.

Starting with a synopsis of the past publications on this topic, the developed methods will be discussed on the basis of a load step. For experimental investigations a 3.6 liter V6 spark-ignition direct-injection turbocharged engine was chosen, which is equipped with variable valve lift on the intake including asymmetric lift profiles and variable valve timing on the intake and the exhaust [2].

To calculate the correct burn rate under transient conditions, the determination of the cycle-based fresh air charge and residuals mass is crucial. In addition to the crank-angle-based quantifiable pressure in the intake and the exhaust port the corresponding temperature is required to calculate the correct fresh air charge. Due to the high frequency of variation which is caused by reverse flow of residual gas, the inlet temperature is barely measurable, since the resolution of available thermocouples is limited by their thermal inertia and convective heat transfer. Because crank-angle-based temperatures are typically unknown, zero-dimensional gas exchange calculations often use a mean intake temperature, which is adapted in such a way that the difference between the calculated cylinder fresh air charge and the measured integral (engine) reference air mass is minimized. Without crank-angle-based measuring of all intake and exhaust pressures, the adaptation also includes uncertainties regarding the unequal distribution of the air charge between the cylinders. Since there is no measurable reference air mass for single-cycle-based investigations, it is not possible to adapt the mean intake temperature in transient events [3]. The present paper describes a model which enables a zero-dimensional approach to calculate the crank angle resolved intake temperature. For accurate validation of the model, the experimental setup includes twelve piezoresistive absolute pressure sensors to measure all gas exchange pressures on the chosen six cylinder engine. Subsequent to the description of the method and its validation, the results of the calculation of a load step will be discussed. In addition, the major quantities of the transient single cycle analyses will be compared to the corresponding quantities extracted from stationary measurements.

1. Introduction

Since the problem of air pollution was detected in Los Angeles in the fifties, emission control regulations have been introduced by governments throughout the whole world [4]. At least since the first oil crisis in the seventies and the growing interest in energy conservation which that caused, legislators have been monitoring vehicles' fuel consumption. Because transient events (i.e. operation conditions with changing engine speed and load) outweigh stationary operation under normal driving conditions [5], the analysis of transient events has come into the focus of scientific study. With the upcoming introduction of more dynamic test procedures (e.g. WLTP) and the approaches to take real driving emissions into account [1], more detailed investigation of the transient behavior is essential to fulfill the stringent legislation in the future. Transient events are characterized by an engine control that is to some degree open-loop because any controller will be less effective since the required feedback signal is always time-delayed. The aim of analyzing transient events should be to thermodynamically assess the operation strategy of all actuators, their interactions as well as their impact on the engine process. As soon as the impact is known the operation strategy of all actuators can be optimized either to achieve an improvement in the fuel consumption, the emissions or in the torque response. Because transient operations can cause high variation in the measurement variables within a very short time, high resolution analysis up to cycle-based analysis is preferable. This requires the highest level of performance of the measurement technologies as well as of the analysis methods themselves.

In the past decades several measurement technologies and methods to analyze transient events were developed and published. The present paper starts with a survey of literature regarding the analysis of transient events. In the course of this survey the published literature is summed up in a framework of methods. Based on this the chosen method of a zero-dimensional pressure analysis is presented. The requirements for this method and the influencing factors on its accuracy as well as some new approaches to utilize the analysis successfully under transient conditions are described. Finally the accuracy of this approach is discussed using an example for a load step with constant engine speed.

2. Literature Survey and Framework of Analysis Methods

Although the previously published literature has quite different priorities, it is possible to categorize them into a common framework based on the utilized type of method, see figure 1. The utilized methods can be divided in the established classes of the analysis of integral and differential quantities. The analysis of differential quantities can be subdivided in zero-, one- and three-dimensional analysis. Although the level of detail increases in the order of the enumeration, at the same time the complexity and thus the effort of these investigations increases relative to the augmentation of findings disproportionately.

As early as 1979 [5] described a method that allows the differences in the transient fuel consumption of internal combustion engines with different mixture preparation systems (carburetor and port fuel injection (PFI)) to be quantified using a dynamometer and an engine test bench. In addition to a vane anemometer for measuring the air mass flow a Pierburg flowmeter (PLU 103-75) is used to determine the fuel mass flow. Thus integral quantities are considered. Even though it has more historical

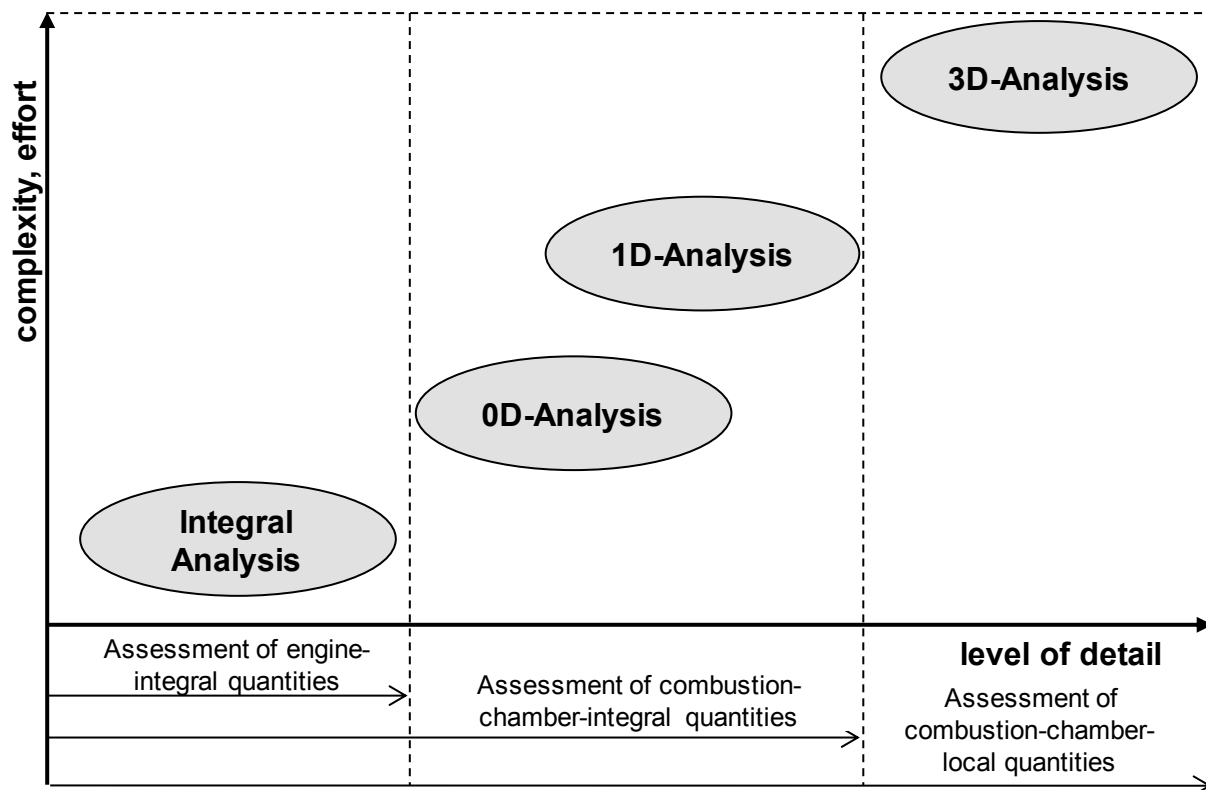


Figure 1: Framework of analysis methods (stationary and transient)

relevance, it should be mentioned for the sake of completeness that in this comparison the PFI-engine achieved better transient fuel consumption in the NEDC even though it had some drawbacks in the stationary part-load fuel consumption. Those advantages in the transient fuel consumption are attributed to fact that the carburetor system has no fuel cut-off capability.

To determine the cycle-resolved air/fuel ratio investigation of different methods are carried out in [3, 6] on a single cylinder research engine and on a PFI series production 4-cylinder spark-ignition engine, which has no variabilities in the air path [7]. Both integral measuring technology methods as well as zero-dimensional calculations on the basis of indicated cylinder and manifold pressures are considered in this investigation. The determination of the air/fuel ratio is divided in the determination of the air/fuel ratio before, in and after the cylinder, as these may differ in transient events. The authors come to the conclusion that only single integral quantities before and after the cylinder are detectable by measurement. Thus the injected fuel mass can be determined by measuring the injection timing and the decision whether the engine is running with a lean or rich air/fuel ratio can be achieved using a binary lambda sensor. At low engine speeds ($n < 2000$ RPM) the cycle-resolved air/fuel ratio after the cylinder can be determined using a wide range lambda sensor. In order to determine the cycle-resolved air/fuel ratio in the cylinder a method is presented that initially calculates a cylinder air mass using the indicated low pressures that are acquired at the intake and exhaust port of one cylinder. The air/fuel ratio in the cylinder is determined in a subsequent burn rate analysis from the converted amount of fuel in combination with the information on whether the air/fuel ratio after the cylinder is rich or lean. The authors state that the average temperature of the intake mass flow must be determined iteratively to calculate the fresh air charge of the cylinder correctly. Since there is no possibility of iteration or inlet temperature adaptation in the analysis of transient events (initial and final conditions of one cycle differ and there is no suitable reference air

mass), this method can deliver inaccurate results regarding dynamics. The need for the iterative determination of the average temperature of the intake mass flow is also described in [8].

In [9] an energy-based cycle-resolved method for determining the air/fuel ratio is presented in which initially the composition of the cylinder charge (fresh air, residual gas, ...) is calculated on the basis of indicated pressures before and after the cylinder. The calculation is carried out using an estimated air/fuel ratio before the cylinder. Subsequently the air/fuel ratio in the cylinder is determined in a burn rate analysis by adapting the air/fuel ratio until the ratio of the burned mass and the total mass equals one. Because there are respectively one solution for a lean and one solution for a rich air/fuel ratio, a fuzzy logic based approach is presented that allows making a statistically correct rich-lean decision on the basis of several interrelated cylinder pressure-based criteria. This zero-dimensional method is applied to a transient event in which the fuel mass is reduced at constant speed and throttle position.

The warm-up and transient behavior of a PFI spark-ignition engine with an electromechanical valve train is investigated in [10]. In this paper, different valve lift and timing strategies were assessed to reduce the increased hydrocarbon emissions that typically occur during cold-start operation as well as positive and negative load steps in a PFI engine. To calculate the cycle resolved hydrocarbon masses Fast-FID concentration measurement was used in combination with an unspecified gas exchange analysis.

One-dimensional pressure trace analysis of transient events on the basis of indicated pressure traces is the object of investigation in [11]. This method is applied to a load step of a two-stage turbocharged, direct-injection 4-cylinder prototype gasoline engine with variable compression in [12]. For the investigations one cylinder of the engine is equipped with a piezoelectric pressure sensor in the intake and exhaust manifold respectively. Based on a polytropic pressure correction of the in cylinder pressure the indicated intake pressure is corrected in a way that in cylinder pressure and intake pressure match while the intake valve is opened. The offset of the indicated exhaust pressure is adapted to match measured and calculated indicated mean effective pressure. Subsequent to the determination of the air and residual gas masses the air/fuel ratio inside the cylinder is determined from the released energy per cycle and the heating value of the used fuel. The released energy is derived from the calculated burn rate. The requirement of a binary decision regarding the air/fuel ratio, which is stated in [3, 9], as well as the consideration of incomplete combustion is not mentioned in this publication.

In [13] a local crank-angle-resolved air/fuel ratio is determined for transient events of a direct-injected spark-ignited engine using an optical sensor system [14, 15] that is integrated in the spark plug. Thus the impact of different operating parameters on the mixture formation at the location of the spark plug can be quantified. The optical sensor system is based on the infrared absorption method, which allows the measurement of hydrocarbon concentration in the absorption path. The basics of deriving a local in-cylinder air/fuel ratio from the hydrocarbon concentration are outlined in [16, 17]. By assuming an adiabatic compression to determine the crucial trace of in cylinder temperature and neglecting the fuel and residual mass, a local relative air/fuel ratio can be calculated. The absolute local lambda has to be derived from a correlation of the relative in-cylinder air/fuel ratio with a measured air/fuel ratio in the exhaust system. However it is noted that an error in the calculation of the in-cylinder temperature of 10 K results in a deviation of the air/fuel ratio of 0.02 [17]. While using a representative air/fuel ratio after the cylinder to calibrate the absolute in-cylinder lambda, it has to be assumed that the mixture in the combustion chamber is completely homogenized.

During calibration with a total air/fuel ratio measured in the exhaust of all cylinders, it also has to be assumed that there is no uneven distribution of air/fuel ratio among the cylinders if not all cylinders are equipped with the optical measurement system. Since spatially resolved sizes are considered this method can be classified as a three-dimensional approach.

By combining the described optical sensor system with a fast emission measurement system that is applied to one cylinder of the engine, different load changes are investigated regarding the optimization of emissions in an hybrid electric vehicle context in [18]. For this purpose, an engine is operated on an engine-in-the-loop test bench, which is coupled with a driving simulator. This setup makes it possible to simulate real driving maneuvers at the test bench. It is stated that rapid changes in the accelerator pedal position and thus high dynamic changes in the engine load have the greatest impact on the emission formation under real driving conditions. Thus, the impact of different strategies for smoothing engine torque response rates in combination with a virtual electric motor on the emissions is investigated for load steps with constant engine speed. Using the same experimental setup the development of gaseous and particulate emissions is studied in [19] for changes in the engine load without considering a hybrid context.

A zero-dimensional approach for a burn rate analysis while starting a combustion engine is described in [20, 21]. In [22] the effects of wall heat transfer while starting a direct injection spark ignition engine are investigated. Besides the already presented publications, there are a number of other investigations on the subject of real-time zero-dimensional analysis based on measured in-cylinder pressures, e.g. for purposes of engine control [23, 24, 25, 26, 27, 28].

Considering today's high quality of engine control, the previously published studies emphasize that it is not sufficient to analyze integral quantities in order to achieve substantial improvement in transient events. In fact, single suboptimally controlled working cycles lead to significant deterioration in transient emissions or even fuel consumption. The requirement for a state-of-the-art transient analysis method must therefore be to identify those non-optimal working cycles and to explain the occurring physical effects, so that it is possible to enable the control units in an adequate way. Accordingly, the only capable methods are the zero-, one- or three-dimensional analysis of differential quantities. Due to the favorable effort-to-findings ratio a zero-dimensional approach has been adopted in this paper.

The zero-dimensional pressure trace analyses described in previously publications have in common that the crank-angle-resolved temperature that corresponds to the measured indicated low pressures is not known. Thus the determination of the cylinder air mass and the air/fuel ratio is only possible by adapting the mean intake temperature. The use of the previously published methods to analyze transient effects can lead to inaccurate results. Considering state-of-the-art engines with highly variable valve trains makes these uncertainties even worse, because the attempt to achieve maximum dethrottling by realizing high rates of residual gas reverse flow leads to quite high differences in the intake temperature profile in different operating points. The present paper describes a model which enables a zero-dimensional approach to calculate the crank-angle-resolved intake temperature. Using this model a zero-dimensional approach can be used to analyze transient events with high dynamics.

3. Test Engine and Experimental Setup

For the development of the method described in this paper a direct-injected turbocharged 3.6-liter V6 spark-ignition engine was chosen, figure 2. The engine is equipped with hydraulic camshaft actuators on the intake and exhaust side. On the intake camshaft an asymmetric lift profile is applied, in which one intake valve per cylinder has a constant maximum valve lift of 2.5 mm and the second valve has a variable valve lift that can be switched either to 3.6 mm or 10.3 mm using the Porsche VarioCam Plus System [2]. The asymmetric lift profile causes an intense charge motion which improves the combustion stability. Therefore it is possible to realize high residuals fractions to achieve maximum dethrottling without compromising the running smoothness of the engine.



Figure 2: Engine used for this work [2]

For the purposes of transient investigation the test engine was equipped with extensive measurement technology. Piezoelectric pressure sensors (type 6052, Kistler) were applied in order to measure the in-cylinder pressure. Since the combustion chamber wall temperature changes within transient events, it was measured with thermocouples 2 mm beneath the surface at each cylinder at a representative position in order to take the correct wall heat losses into account. The representative positions were determined based on the results of preliminary test. The intake port and exhaust manifold of each cylinder were equipped with piezoresistive absolute pressure sensors (intake: type 4005 V200S, exhaust: 4075 V200S with cooling adapters, both Kistler). In addition two thermocouples were placed in close vicinity to each pressure sensor. Respectively one thermocouple was applied in order to measure the fluid temperature and another thermocouple to measure the wall temperature.

4. Zero-Dimensional Pressure Analysis of Single Cycles

Since the conditions at cycle start and end may differ for transient events, the pressure analysis of single cycles under varying conditions is generally characterized by the fact that there are no possibilities for iteration and adaptation [3]. However, the prerequisite for the correct calculation of the burn rate of each cycle remains the most precise possible knowledge of the cylinder mass and their composition. The application of the “conventional” low-pressure-based methods (described in chapter 2 and schematically shown in figure 3 left side) to calculate the cycle-resolved cylinder mass and composition under transient conditions can lead to errors, since the adaptation of the averaged inlet temperature is limited to a certain

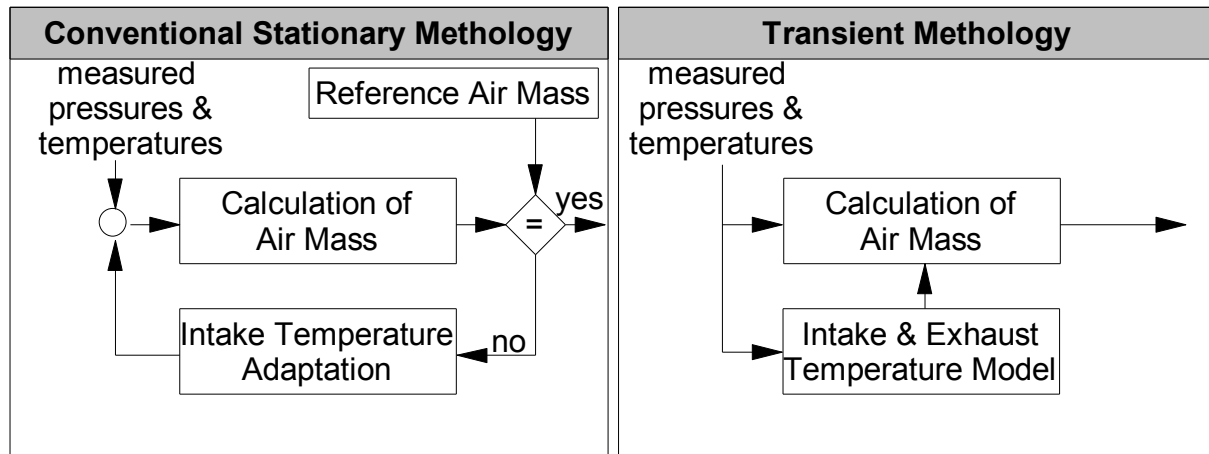


Figure 3: Schematic diagram showing the zero-dimensional calculation of the trapped air mass

extent. In order to investigate any random transient event, the relevant physical phenomena that have an impact on the gas exchange must be integrated into a model that does not require adaptation (figure 3, right side).

The next sections will describe the factors which influence the low-pressure-based air mass calculation as well as the influencing factors on the determination of the reference air mass that is used to validate the model. Subsequently the particularities of signal processing of single cycles are described before the physical model which is developed in this work is introduced. The calibration and validation of this model is subject of the last section of this chapter.

4.1 Influencing Factors on the Low-Pressure-Based Air Mass Calculation

To determine the quality of a low-pressure-based air mass calculation, the results have to be compared to a reference air mass. Figure 4 shows the influencing factors on the quantities to be compared. A widely used means of determining the reference air mass is to multiply the air/fuel ratio derived from exhaust emission concentration measurement using Brettschneider's equation, the measured fuel mass flow and the stoichiometric air/fuel ratio, which has to be determined in a fuel analysis. For the interpretation of the comparison between the calculated and the reference air mass it is important to note that the reference air mass is also subject to tolerances of the measurement systems and methods used for its determination. Thus the comparison of the calculated and reference air mass shows the sum of errors of both methods.

Under the assumption of quasi-stationary change of state the equation for isentropic compressible flow through a flow restriction is used to calculate an air mass based on low-pressure-traces measured in the intake and exhaust in close proximity to the combustion chamber (see equation 1). This requires precise measurement of the used pressures and temperatures. Potential thermal drift of the applied low pressure sensors has to be avoided by appropriate calibration. Furthermore, the effective valve lift and timing should be known. On the one hand, the effective valve timing is determined by the reference cam positions and on the other hand, by the current position of the camshaft adjuster. The engine used for the investigations published in this paper features a position detection of the camshaft, which uses Hall-effect sensors and

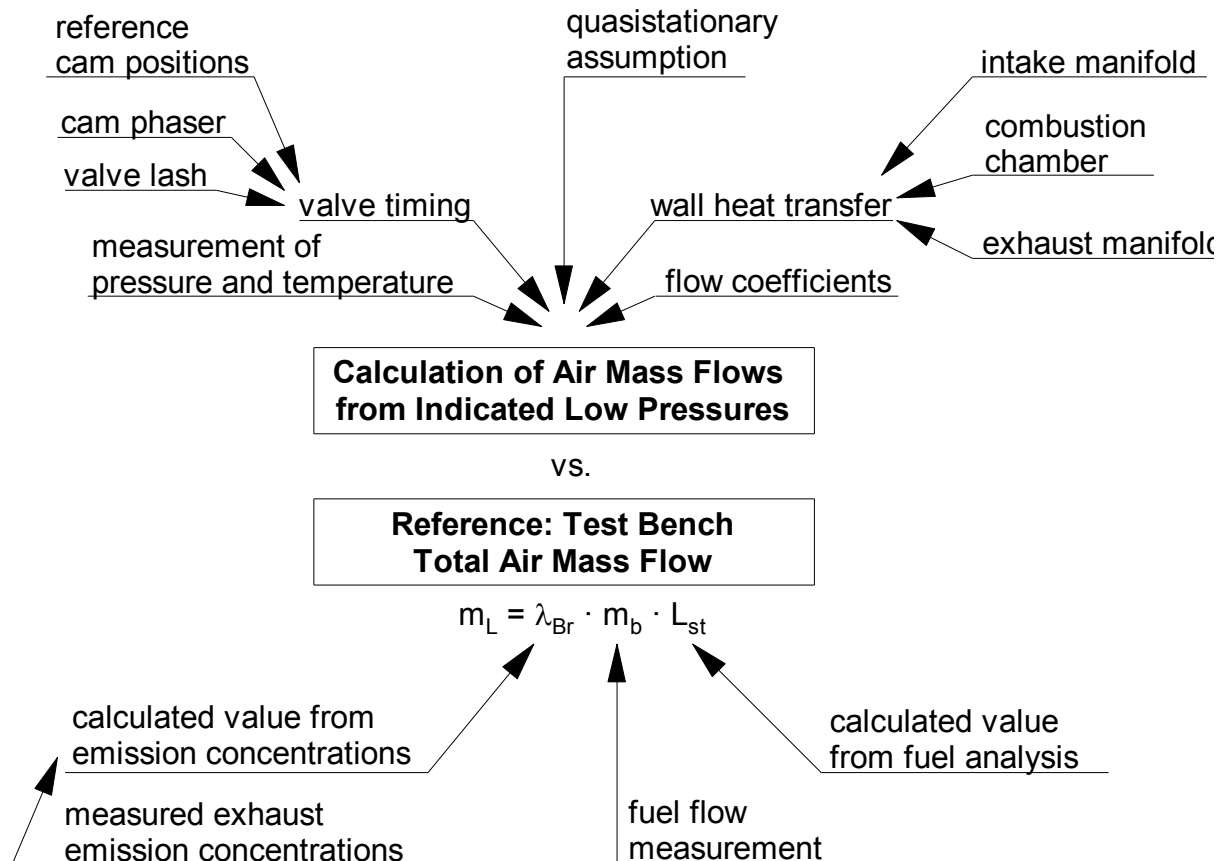


Figure 4: Comparison of the influencing factors on the determination of the reference and the low-pressure-based air mass flow

a sensor wheel. The reference camshaft positions were measured before the tests were carried out. In addition, the hydraulic lash adjuster has an impact on the effective valve timing, since the gradient of the valve lift is quite small at the end of the cam. In addition to the effective valve lift and timing, the flow coefficients should be known as a function of valve lift. The flow coefficients are experimentally determined on a flow test rig on which only flow through the cylinder head without the piston is measured. Finally the heat transfer of the fluid to the surrounding walls has to be taken into account. Besides the heat transfer in the combustion chamber, also the heat transfer in the intake and exhaust port has to be considered.

4.2 Signal Processing of Measured Pressures for Single Cycle Analysis

For single-cycle-based pressure analysis under transient conditions, special care has to be taken for the signal processing since it is not possible to use crank-angle-based pressures which are averaged over a certain number of cycles. The aim of the signal processing is to extract the highly dynamic useful signal while removing high frequency parasitic parts of the signal, which could cause numerical disturbance that would change the results of the pressure analysis. The analysis method described in this paper is not intended for real-time processing. Thus it is possible to create a FIR (finite duration impulse response) low-pass filter which has no impact on the phase characteristic of the signal by processing the data forward and then backward through the same filter [29]. In the following section the choices of expedient filter

characteristics (stop and pass frequency) is discussed using an arbitrary picked measured single cycle pressure trace. The frequency responses of the chosen filters are shown in figure 5.

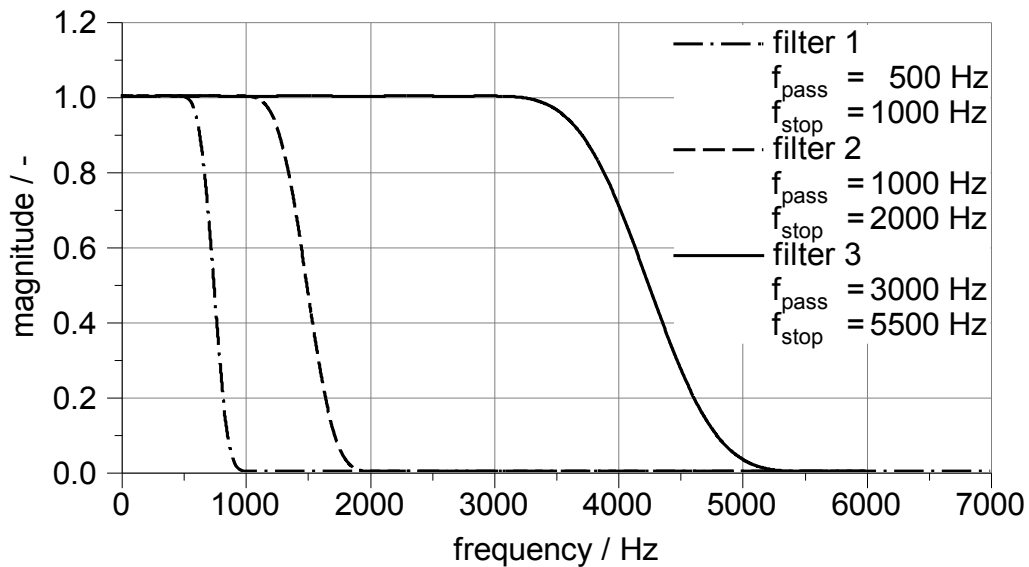


Figure 5: Frequency response of the chosen FIR low-pass filters

The frequency response of filter 1 rejects high frequencies above 1000 Hz (stop frequency) and passes only frequencies below 500 Hz with an unaffected magnitude (pass frequency), whereas filter 3 has its pass frequency at 3000 Hz and its stop frequency at 5500 Hz. With a pass frequency of 1000 Hz and a stop frequency of 2000 Hz filter 2 reflects a compromise between filter 1 and 3. Figure 2 shows a measured single cycle in-cylinder pressure trace as well as the same signal processed with the filters described above. The left-hand side of the figure shows the pressure signals around the gas exchange bottom dead center of the piston. In this area the raw signal is very noisy. This is physically not plausible. Filter 3 barely affects the measurement noise. Using filter 1 and 2 considerably reduces the noise, whereby the low-pass effect

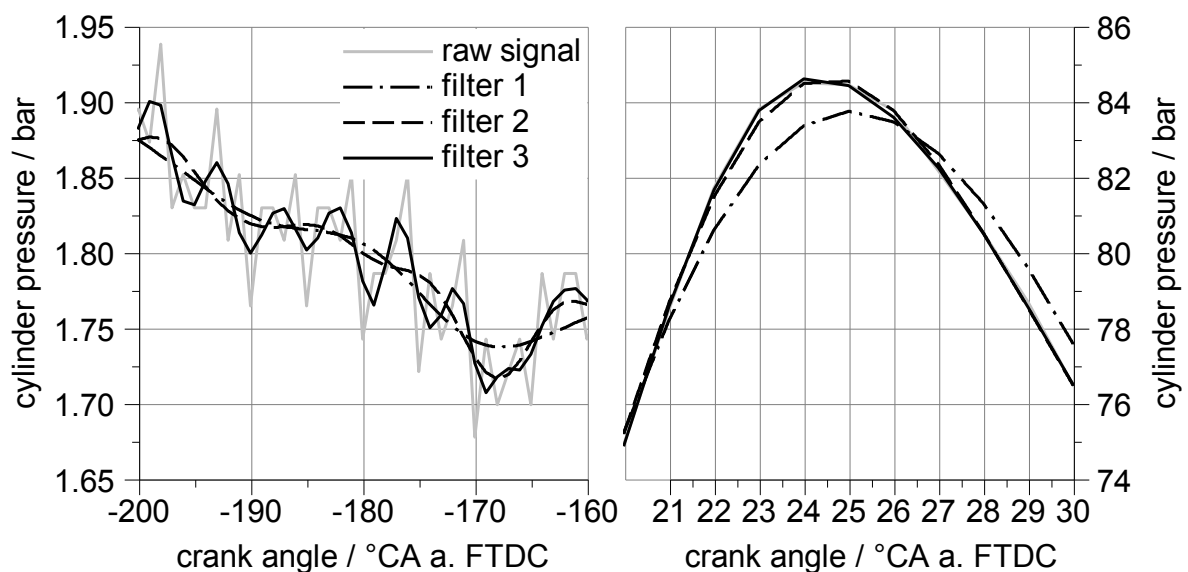


Figure 6: Raw and processed cylinder pressure signals

of filter 1 is so intense that especially around -170°CA significant divergence (approximately 20 mbar) between the useful measured signal and the processed

signals is caused. This divergence becomes even more significant in the area of the maximum cylinder pressure, which is shown on the right hand side in figure 2. The maximum divergence of 1.48 bar is not acceptable since it would affect the calculation of the burn rate. The divergences between the useful signal and the signals processed with filter 2 and 3 are very small. In total the characteristic of the frequency response of filter 2 seems to be the best, so these filter characteristics were used for the following investigations.

4.3 Adaptation-Free Zero-Dimensional Calculation of Air Mass under Consideration of Mixture and Heat Transfer Effects in the Intake and Exhaust Port

In zero- and one-dimensional analysis the mass flows through the intake and exhaust valve are calculated using the equation for isentropic compressible flow, equation 1. According to equation 1 the mass flow through a valve is a function of the effective flow area $A_{valve,eff}$, the pressure upstream p_1 and downstream p_2 of the valve, the temperature upstream the valve T_1 as well as a function of the properties of the fluid upstream the valve represented by the specific gas constant R and the isentropic exponent κ .

$$\frac{dm}{dt} = \begin{cases} A_{valve,eff} \cdot \frac{p_1}{\sqrt{R \cdot T_1}} \cdot \sqrt{\frac{2 \cdot \kappa}{\kappa - 1} \left[\left(\frac{p_2}{p_1} \right)^{\frac{2}{\kappa}} - \left(\frac{p_2}{p_1} \right)^{\frac{\kappa+1}{\kappa}} \right]} & \forall \frac{p_2}{p_1} < \left(\frac{2}{\kappa + 1} \right)^{\frac{\kappa}{\kappa-1}} \\ A_{valve,eff} \cdot \frac{p_1}{\sqrt{R \cdot T_1}} \cdot \left(\frac{2}{\kappa + 1} \right)^{\frac{1}{\kappa-1}} \cdot \sqrt{\frac{2 \cdot \kappa}{\kappa + 1}} & \forall \frac{p_2}{p_1} \geq \left(\frac{2}{\kappa + 1} \right)^{\frac{\kappa}{\kappa-1}} \end{cases} \quad (1)$$

Due to backflow of residual gas from the combustion chamber high temperature gradients may occur in the intake port. These temperature gradients are barely measurable, since the resolution of available thermocouples is limited by their thermal inertia and convective heat transfer. Nevertheless, the exact knowledge of the crank-angle-resolved fluid temperatures in the intake port is essential for adaptation-free precise calculation of mass flow (see equation 1). Due to the expanding burned mixture high temperature gradients also occur in the exhaust port. If there is backflow from the exhaust port into the combustion chamber the proper consideration of the temperatures in the exhaust port is also relevant for the determination of the cylinder mass. However, since the zero-dimensional consideration of the effects in the exhaust port can be done analogous to those in the intake port, in this chapter what is described with reference to the intake port is generally valid. With this model it is possible to calculate the crank angle resolved temperature in the intake port. The relevant quantities of the model are shown schematically in figure 7. The known thermodynamic system of the combustion chamber is extended with the thermodynamic system of the intake port, which is described by the properties of its temperature T_{im} and pressure p_{im} as well as its volume V_{im} and mass m_{im} . The intake port pressure can be directly measured with the low-pressure indication at crank-angle resolution. The system combustion chamber and intake port are linked to each other by a flow of enthalpy - $dH_{im,out} = dH_{cyl,in}$, which is determined by the mass flow through the intake valves


$$\frac{dU}{dt} = \frac{dQ}{dt} - p \cdot \frac{dV}{dt} + \sum_i \frac{dm_i}{dt} \cdot h_i \quad (2)$$
$$\frac{\partial U}{\partial m} \cdot \frac{dm}{dt} + \frac{\partial U}{\partial c_v} \cdot \frac{dc_v}{dt} + \frac{\partial U}{\partial T} \cdot \frac{dT}{dt} = \frac{dQ}{dt} - p \cdot \frac{dV}{dt} + \sum_i \frac{dm_i}{dt} \cdot h_i \quad (3)$$

309

$$u \cdot \frac{dm}{dt} + m \cdot c_v \cdot \frac{dT}{dt} = \frac{dQ}{dt} - p \cdot \frac{dV}{dt} + \sum_i \frac{dm_i}{dt} \cdot h_i \quad (4)$$

Solving equation 4 for the rate of change of the temperature, the general differential equation of the temperature in open systems is obtained.

$$\frac{dT}{dt} = \frac{\frac{dQ}{dt} - p \cdot \frac{dV}{dt} + \sum_i \frac{dm_i}{dt} \cdot h_i - u \cdot \frac{dm}{dt}}{m \cdot c_v} \quad (5)$$

Because of constant intake port volume, the differential equation of the rate of change of the temperature in the intake port can be written in the form of equation 6:

$$\frac{dT_{im}}{dt} = \frac{\frac{dQ_w}{dt} + \frac{dm_{im,in}}{dt} \cdot h_{im,in} - \frac{dm_{im,out}}{dt} \cdot h_{im,out} - u_{im} \cdot \frac{dm_{im}}{dt}}{m_{im} \cdot c_{v,im}} \quad (6)$$

In equation 6 the exchange of masses of the intake manifold and the intake port are described by $\frac{dm_{im,in}}{dt}$ and the exchange of masses of the intake port and the combustion chamber is described by $-\frac{dm_{im,out}}{dt} = \frac{dm_{IV}}{dt}$. Because there is no modelling of the intake manifold in zero-dimensional pressure analysis, a reasonable assumption has to be made in order to calculate the mass flow $\frac{dm_{im,in}}{dt}$. It proves to be appropriate to assume that the outflowing volume is directly replaced, i.e. the volumetric flow into the intake port corresponds directly to the volumetric flow out of the intake port at each point of time $\dot{V}_{im,in} = \dot{V}_{im,out}$. The specific internal energy and enthalpy as well as the specific heat are described according to the caloric approach published in [30] depending on the respective associated temperatures and compositions. Due to the backflow of residual gas caused by a high ratio of pressure between combustion chamber and intake port, the change of temperature of the residual gas which is expanding to the intake port has to be considered in order to calculate the flow of enthalpy correctly. Since the time of the change of state is very small and because it is difficult to obtain information about friction losses, the temperature change caused by the expansion is assumed to be isentropic. To describe the predominantly convective heat transfer in the intake manifold $\frac{dQ_{w,im}}{dt}$ a Newtonian approach is considered in equation 7:

$$\frac{dQ_{w,im}}{dt} = \alpha_{im} \cdot A_{im} \cdot (T_{im} - T_{im,w}) \quad (7)$$

where α_{im} is the convective heat-transfer coefficient, A_{im} is the surface of the intake port and $T_{im,w}$ is the intake port wall temperature which is measured for each cylinder. The investigations carried out show that the wall temperature in the intake port is similar to the cooling water outlet temperature, so that this quantity can be used as a first approximation if there is no measurement available. In order to determine the heat-transfer coefficient a correlation between Nusselt number and Reynold number can be established according to [31]:

$$Nu = K \cdot Re^b \quad (8)$$

Where the constant K equals 0.0483 and the exponent b equals 0.783. For description of pipe flow, Nusselt number is defined as:

$$Nu = \frac{\alpha \cdot d}{\lambda_f} \quad (9)$$

In equation 9 d describes the pipe diameter and λ_f describes the thermal conductivity of the fluid. For pipe flow the Reynolds number is defined as the quotient of the fluids density ρ , the velocity of the fluid v , the pipe diameter d and the dynamic viscosity μ of the fluid.

$$Re = \frac{\rho \cdot v \cdot d}{\mu} \quad (10)$$

Substituting equation 9 and 10 in equation 8 and solving for the heat-transfer coefficient:

$$\alpha = \frac{K \cdot \lambda_f}{d} \cdot \left(\frac{\rho \cdot v \cdot d}{\mu} \right)^b \quad (11)$$

For the case of the intake port considered here, the convective heat transfer coefficient is calculated by assuming the simplification that the flow velocity can be calculated as

$$v_{im} = \frac{|\dot{m}_{im}|}{\rho_{im} \cdot A_{im}};$$

$$\alpha_{im} = \frac{K \cdot \lambda_{f,im}}{d_{im}^{b+1}} \cdot \left(\frac{4 \cdot |\dot{m}_{im}|}{\pi \cdot \mu_{im}} \right)^b \quad (12)$$

where $|\dot{m}_{im}|$ describes the absolute value of the averaged mass flow in the intake port, which is derived from the arithmetic averaging of $\frac{dm_{im,in}}{dt}$ and $\frac{dm_{im,out}}{dt}$. The diameter d_{im} describes a characteristic diameter, which must be chosen in such a way that the wall heat transfer of the modeled stationary flow in a straight pipe equals the wall heat transfer resulting from the transient flow through the complex intake port geometry. According to [32] the thermal conductivity λ_f and the dynamic viscosity μ of the relevant fluids can be calculated using equations 13-16:

$$\lambda_{f,air} = 3.17 \cdot 10^{-4} \cdot T^{0.772} \quad (13)$$

$$\lambda_{f,stoich. \text{ burned mixture}} = 2.02 \cdot 10^{-4} \cdot T^{0.837} \quad (14)$$

$$\mu_{air} = 0.612 \cdot 10^{-6} \cdot T^{0.609} \quad (15)$$

$$\mu_{stoich. \text{ burned mixture}} = 0.355 \cdot 10^{-6} \cdot T^{0.679} \quad (16)$$

Due to the fact that both air and burned mixture occur in the intake port, the values of the thermal conductivity and the dynamic viscosity are averaged according to the corresponding mass fractions. The impact of deviation from the stoichiometric air/fuel ratio is neglected. It can be concluded that the wall heat transfer coefficient is mainly influenced by the velocity of the fluid. Since the mass flow is a result of the calculation, the wall heat transfer can be adjusted by adjusting the characteristic diameter. To account for systematic errors in the calculation, e.g. errors resulting from the assumption of stationary turbulent flow, a correction factor can be applied, which

evenly affects all operating points. A factor that depends on the operating point is unsuitable since physical causality and thus the capability of analyzing transient events would be lost.

4.4 Calibration and Validation of the Adaptation-Free Gas Exchange Analysis

In this section first the mode of operation of the model described in section 4.3 is discussed on the basis of part load operating point chosen as an example. Subsequently the results of the validation are presented and compared with results that can be achieved without explicit consideration of the effects in the intake and exhaust port.

As stated in section 4.3 the temperature trace in the intake port depends on the incoming and outgoing enthalpy flows, the internal energy of the system as well as the wall heat flow. Therefore in addition to the characteristic diameter of the intake port d_{im} , which influences the wall heat flow, the mass of the intake port and thus its modeled characteristic volume is a relevant parameter that affects the trace of the temperature. To illustrate these effects, the left side of figure 8 shows a parameter variation of the intake port volume at constant characteristic diameter and the right side shows a parameter variation of the characteristic intake port diameter at constant volume. The parameter variation was carried out using measurement data of a part load operating point at 2000 RPM. The upper graphs show a family of curves of the calculated intake port temperature. The resulting quantities of trapped fresh air and air/fuel ratio in the combustion chamber are shown as a function of the respective variation parameters in the lower graphs. It is seen that a reduction of the modeled intake port volume causes a higher peak temperature. Since the enthalpy flow of the residual gas that flows from the combustion chamber into the intake port is only a function of the ratio of the pressures p_{im} and p_{cyl} as well as the temperature T_{cyl} and the fluid properties inside the combustion chamber, the enthalpy flow of the residual gas is constant for each variation of the intake port volume. However, a reduction of the intake port volume results in a decrease of the internal energy by decreasing the mass of the fluid inside the intake port. Hence a reduction of the intake port volume results in a higher mixing temperature. As soon as the flow direction is reversed due to the pressure conditions, this higher mixing temperature decreases faster for the same reason. In addition the wall heat transfer is increased due to the higher difference of fluid temperature and wall temperature. The increased heat transfer is clearly illustrated in the area between the calculated intake port temperature and the measured average intake wall temperature $T_{w,im,meas}$. The lower graph shows that the air/fuel ratio becomes leaner by decreasing the modeled intake port volume due to the fact that the calculated trapped fresh air mass increases. Although the mass flow into the combustion chamber decreases due to the higher intake temperature at the beginning, this lower mass flow is overcompensated subsequently due to lower temperatures in combination with higher mass flows through the more and more opened intake valve (cf. equation 1). Thermodynamically considered, the higher rate of wall heat transfer decreases the enthalpy flow of the residual gas and hence this results in a lower temperature and thus higher trapped air mass at intake valve closing. The graph on the right shows the influence of the characteristic diameter on the calculated air mass and air/fuel ratio. In comparison to the modeled intake port volume, the influence of the intake port diameter is relatively low. The reason is that due to the relatively low mass flow at the considered operating point the heat transfer coefficient is relatively low. Hence the influence of the characteristic diameter on the wall heat

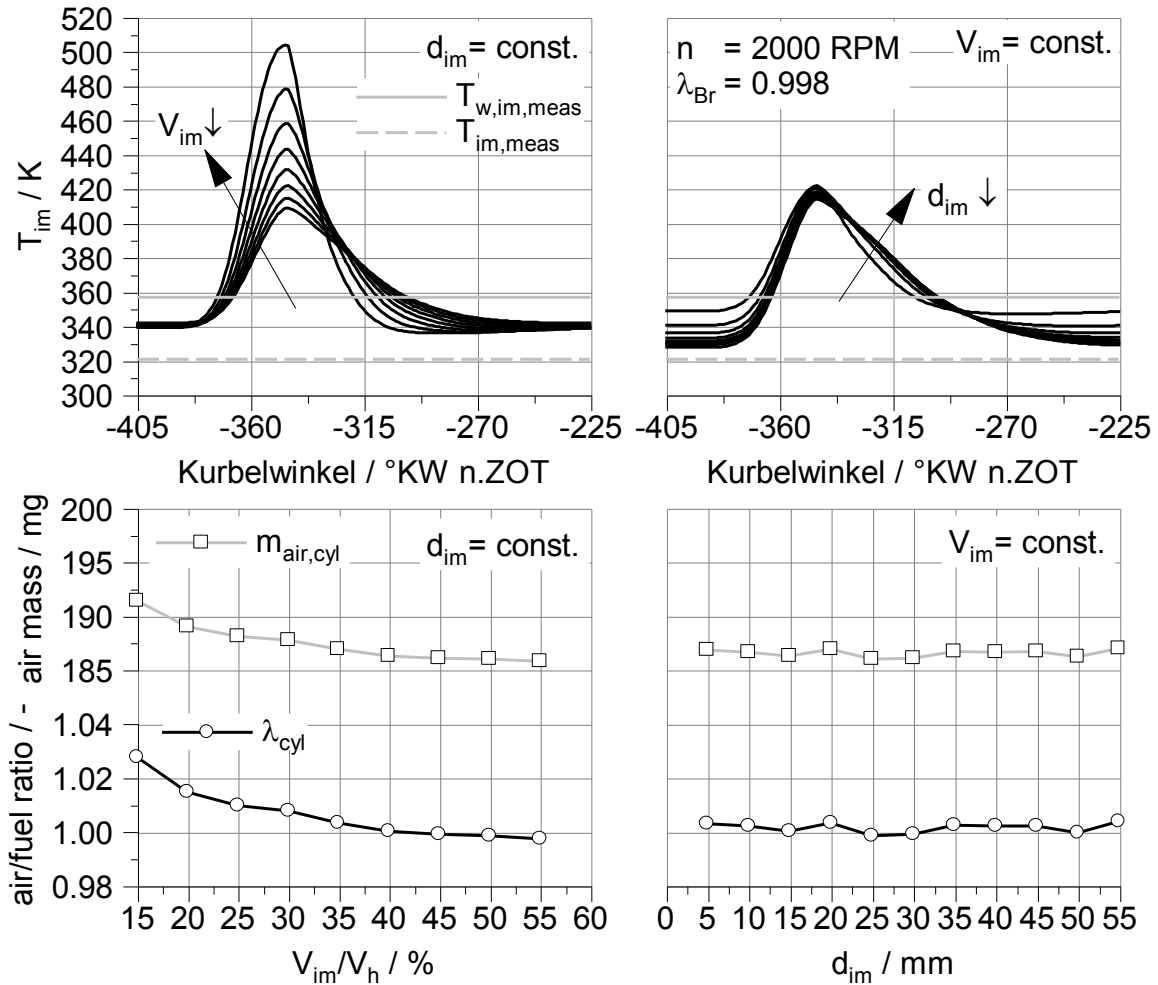


Figure 8: Influence of the modeled intake port volume and diameter

transfer is relatively low compared to the influence of the temperature difference. Thus the calculated trapped fresh air mass is almost constant over the entire parameter variation. A detailed analysis of the enthalpy flows shows that the effects of increased wall heat transfer out of the fluid while fluid temperatures are higher than the wall temperature at the beginning are almost completely compensated by the correspondingly stronger heat transfer into the fluid, while fluid temperatures are lower than the intake port wall temperature. The influence of the characteristic diameter is all the more important as the heat transfer coefficient increases due to higher mass flows, e.g. with increase of the engine load. Figure 8 also shows the fluid temperature $T_{im,meas}$ which is measured in the intake port with a 1.5 mm diameter thermocouple. Due to the high rates of change of the fluid temperature and thus the small amount of time for the heat transfer from the fluid to the thermocouple as well as the thermal inertia of the thermocouple itself, the magnitude of this measured tip temperature of the thermocouple is less than the average value of the calculated temperatures. The use of such a constant, time-averaged thermocouple temperature leads to errors in the calculation of fresh air mass, since a mass-flow-average fluid temperature would have to be used to calculate the correct fresh air mass. This will be shown as a part of the following model validation.

In order to validate the model also with consideration of possible unequal distribution of the cylinders to each other, all cylinders of the test engine were equipped with high- and low pressure sensors. Thus, it is possible to sum up all calculated air mass flows

$\dot{m}_{air,cyl,i}$ and thereby they can be directly compared to the overall reference air mass flow $\dot{m}_{air,ref}$, determined at the test bench. The relative deviation Δm_{GEA} shows the sum of errors of both methods, equation 17.

$$\Delta m_{GEA} = \frac{\sum_{i=1}^Z \dot{m}_{air,cyl,i} - \dot{m}_{air,ref}}{\dot{m}_{air,ref}} \cdot 100 \quad (17)$$

Figure 9 shows the validation on the basis of a load sweep at 2000 RPM. In addition to the results which can be obtained using the intake model described in section 4.3, the results of the gas exchange calculation using the respectively measured intake port temperatures and using the measured intake manifold temperature are illustrated too. The relative deviation Δm_{GEA} , the residual gas fraction as well as the trapping ratio are shown as a function of the indicated mean effective pressure. It can be seen that the measured air mass and the air mass calculated by using the intake port model with a constant characteristic diameter and volume fluctuate in a range of $\pm 2.5\%$ around each other. If this comparison is carried out at different measurements of the same load sweep, it seems to be confirmed that a tolerance of $\pm 2.5\%$ equals the overall accuracy of the whole calculation and measurement chain. Nevertheless some systematic influences can be identified based on the validation. Especially in the operation range of scavenging ($x_{trapped} < 100\%$) it can be seen that the relative deviation Δm_{GEA} decreases almost continuously. The possible reasons for that are numerous. For example the assumption of perfect mixing of fresh air and residual gas during scavenging inside the combustion chamber might be flawed because there might be a short-circuit flow of fresh air from the intake valve directly through the exhaust valve. Due to the possible lower temperature of flow through the exhaust valve the overall mass flow could increase (cf. equation 1). In addition, it must be questioned whether the flow coefficients measured only separately for the opened intake or

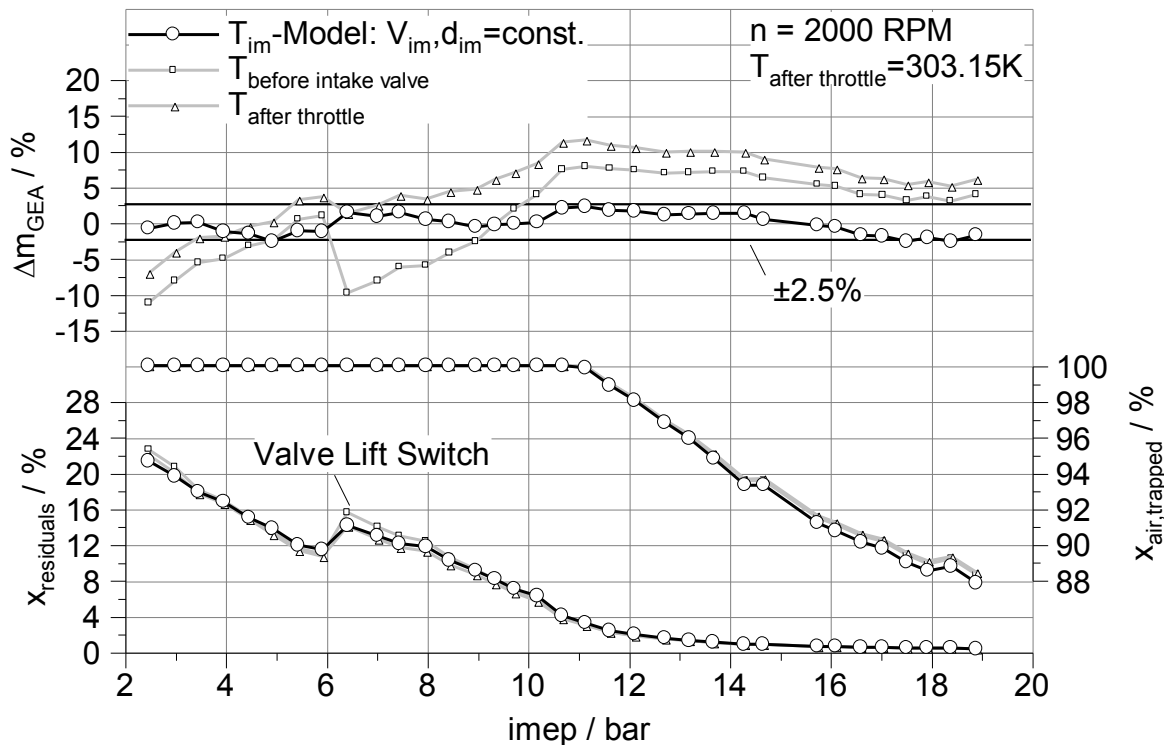


Figure 9: Comparison of calculation results using the intake port model and measured temperatures

exhaust valve without considering the piston are valid for the flow regime occurring

during scavenging. Besides these errors there could also be a systematic error in the measurement of emission concentration, due to high rates of change of the concentrations at the sampling point as a result of the scavenging. A measurement error in the emission concentrations in turn would lead to errors in the calculation of the air/fuel ratio based on Brettschneider which could cause errors in the reference air mass. The investigation of those phenomena with both experiments and simulations should be subject of future research. However, the accuracy achieved with the intake port model can be considered sufficient for the investigation of transient events carried out in this work. This is particularly true if the results obtained by using the intake port model are compared to the results of calculation using the respectively measured intake port temperature or the intake manifold temperature measured directly after the throttle. Figure 9 shows that using the measured temperature in the intake manifold at low loads, a too low air mass is calculated as the enthalpy flow of the residual gas is not reduced due to wall heat transfer. The calculated air mass using the temperature measured with a thermocouple in the intake port is even lower, since the measured intake port temperature is even higher than the intake manifold temperature. After switching the valve lift, the calculated air mass using the intake manifold temperature continues to grow until it reaches its maximum deviation of about 12 % compared to the reference air mass at an indicated mean effective pressure of about 11 bar. This is attributable to the missing consideration of heating of the fluid due to wall heat transfer in the intake port. The usage of the temperature measured in the intake port results in a too low calculated air mass after valve lift switching due to the fact that the measured temperatures in the intake port increase significantly after switching the valve lift. While the load increases the relative deviation Δm_{GEA} increases too until it, following the general trend of all simulations, declines again with decreasing trapping ratio. Although there are deviations in the calculated air mass, the calculated quantities of trapping ratio and residual gas fraction that are crucial for a burn rate analysis are on a similar level as the results of the calculation using the intake port model. The maximum deviation of the trapping ratio is 0.42 (intake port temperature) or 0.57 percentage points (intake manifold temperature) and the maximum deviation of the residual gas fraction is 1.37 or -0.14 percentage points. Due to the significant deviations between the calculated and the reference air mass measured temperatures should not be used for pressure analysis of transient events, since the deviations would cause errors in the calculation of the burn rate. However, using the presented intake port model all relevant physical phenomena can be considered without adaptation. Hence the model enables an optimal calculation of the cycle-resolved air mass even under transient conditions, which will be shown in an example in chapter 5 for a load step.

5. Single-Cycle Pressure Analysis under Varying Conditions using the Example of a Load Step

For the analysis of transient events, it is useful to measure a couple of cycles under stationary boundary conditions. On the one hand, this has the advantage that there is always a reproducible initial state while repeating the measurement of the transient event for the purpose of validation. On the other hand, it is possible to initialize the pressure analysis, since iterations are possible even for single-cycles during stationary operation. In the present case, therefore, a stationary cycle measured before the start of the transient event is iterated in the gas exchange calculation until both the cylinder mass and their composition are constant in subsequent calculation procedures. With knowledge of this cylinder mass the gas exchange analysis of the next cycle is then

started at the point when the exhaust valve opens without any further iteration. Once the cylinder mass and composition for each cycle is known from the gas exchange analysis, the burn rate analysis can be done. Since the aim of this work is to derive global energy-related statements concerning the combustion chamber, a single-zone approach is chosen. The wall heat transfer is calculated according to the model of Woschni [33]. In order to take account of the real caloric properties of the cylinder charge the approach developed by Grill [30] is used. The amount of energy which is conserved in the carbon monoxide, the hydrocarbon and the hydrogen exhaust emissions is considered according to an approach published by Bargende [34]. In this approach the amount of energy of carbon monoxide and hydrogen emissions is calculated using the approximation equation for the conversion efficiency according to Vogt [35] by determining the air/fuel ratio used in the Vogt equation as a function of the carbon monoxide emissions. This function is derived from a chemical equilibrium calculation using an approach that takes ten chemical compounds into account. In addition to that, the calculations in this work also consider the improvement to the Vogt approximation equation presented by [30] as well as a specific adaptation of the chemical equilibrium calculation for the fuel being used. The pressure offset correction of the in-cylinder pressure signal is done by adjusting the offset iteratively so that the burn rate equals zero until ignition [36]. Before the results obtained by the use of the transient pressure analysis are described in this work, the quality of the analysis shall be discussed. A fundamental criterion to assess the quality of a pressure analysis is the so-called burn energy balance, equation 18.

$$\eta_{Br} = \frac{\int_{start}^{end} \dot{Q}_B d\varphi}{m_b \cdot H_u - Q_{HC,CO,H_2}} \cdot 100 \quad (18)$$

The energy balance is calculated by dividing the released amount of energy which is determined from the pressure analysis $\int_{start}^{end} \dot{Q}_B d\varphi$, and the maximum amount of energy which is available for the combustion. The amount of energy which is available for the combustion is calculated by subtracting the energy content of the fuel $m_b \cdot H_u$ and the amount of energy conserved in the exhaust emissions Q_{HC,CO,H_2} . According to [37] a burn energy balance of 95-105 % can be considered very well within the achievable accuracy for the pressure analysis of measured pressure profiles of spark-ignition engines for stationary operating points that are averaged over 250 cycles. However, a frequency distribution of the burn energy balance is the result while analyzing single-cycles instead of averaged pressure profiles. Figure 10 shows the frequency distribution of the burn energy balance that is obtained from the pressure analysis of the load step where 100 cycles per cylinder were analyzed. It can be seen that the averaged value of the burn energy balance is 96.5 % and thus the analysis is valid according to [37]. In order to assess the mean value and the shape of the distribution of the transient analysis, figure 10 also shows the frequency distribution of the burn energy balance of a pressure analysis of 10 steady-state operating points of a load-sweep, in which 100 single-cycles were analyzed per cylinder and per operating point. The load-sweep was measured at the same engine speed (2000 RPM) as the load step. The mean value of the burn energy balance of the stationary pressure analysis is 99.5 % and thus it is even more close to the optimum. Nevertheless the

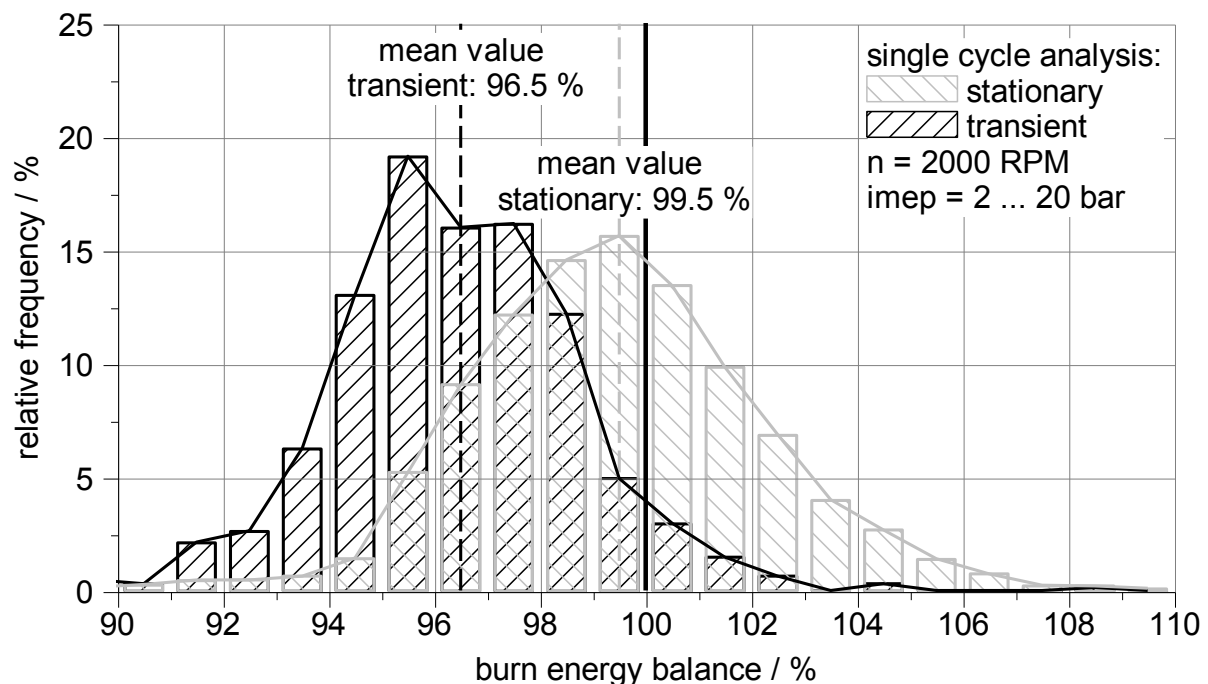


Figure 10: Frequency distribution of burn energy balance from single cycle analysis. Load step with 100 cycles analyzed vs. 10 stationary operating points with 100 cycles analyzed.

shape of the stationary distribution equals the shape transient distribution which is another indication of the validity of the transient analysis. Possible causes of the deviation of the distributions may be the response time of the exhaust gas analyzers used, the possible error propagation in the gas exchange calculation, the missing possibility of numerical iteration while analyzing transient events as well as the smaller sample size of the transient analysis. In addition, a changed behavior of the pressure sensors caused by the rapid change in the surrounding conditions could have an effect on the burn energy balance.

Figure 11 shows some selected quantities resulting from the transient pressure trace analysis of a load step from part load to full throttle operation as a function of time. Starting at a stationary operation point with a brake mean effective pressure of 2 bar, the load step was carried out with constant engine speed of 2000 RPM. In addition to the single-cycle values of each cylinder, the moving average of each quantity is illustrated, too. In order to achieve a certain degree of comparability a quasi-stationary comparison value is also shown in the graphs. The quasi-stationary comparison value is obtained from linear interpolation using the transient indicated mean effective pressure as well as a map of the respective quantity that was obtained from stationary measurement with an increment of 0.5 bar mean effective pressure. Even during steady state operation, a relatively large spread in the center of the combustion $mfb_{50\%}$ can be seen. The relatively large spread is caused by the high rate of residual gas $x_{residuals}$ in combination with the early closing of the intake valve (small lift of the intake valves, Miller combustion principle), which contributes to the maximum possible dethrottling of the gas exchange and thus contributes to low fuel consumption at part load. By opening the throttle at the beginning of the load step, the intake manifold pressure and thus the cylinder air mass increases. The increasing intake manifold pressure also leads to a significant reduction in the residual gas mass. As a

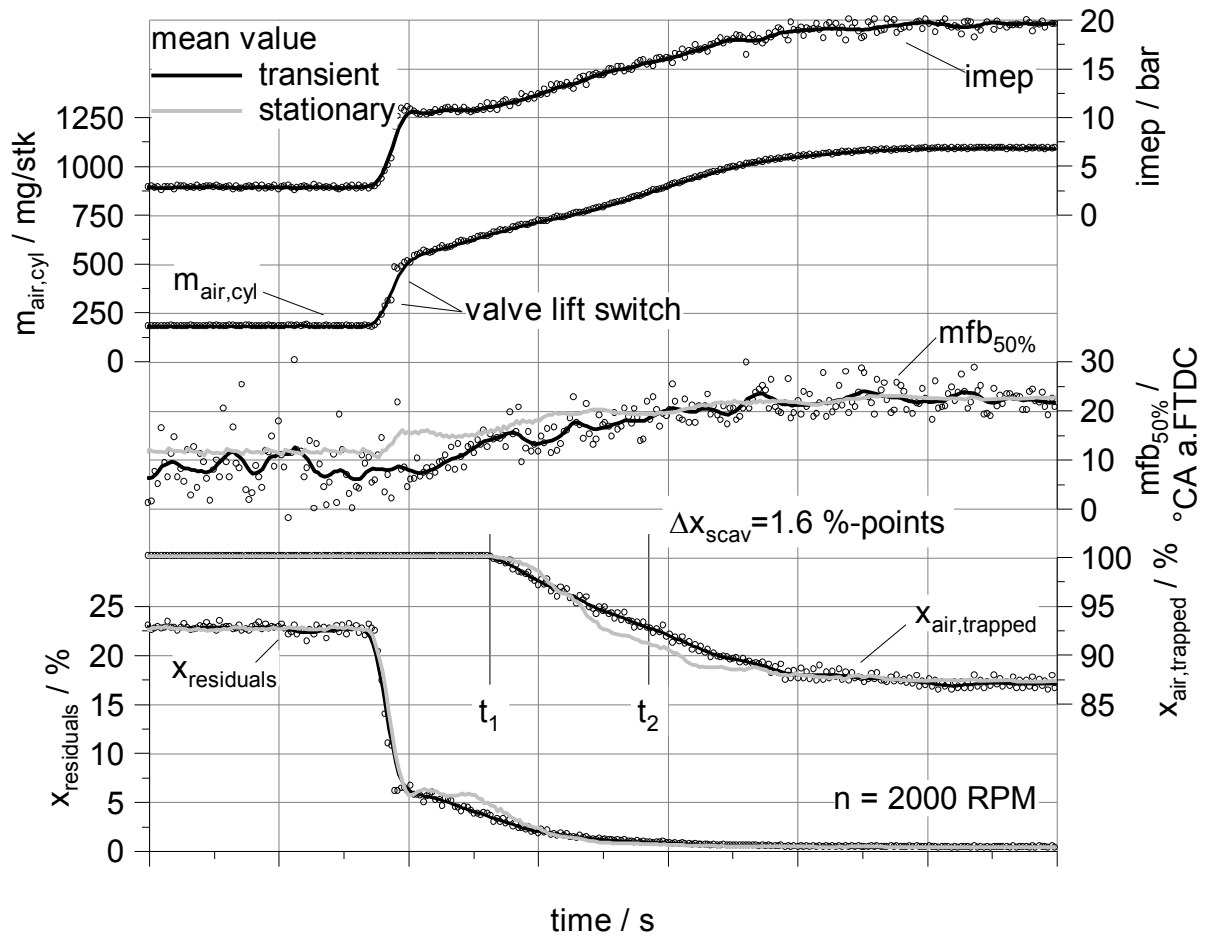


Figure 11: Selected quantities from a transient pressure analysis of load step

result of the lower pressure ratio between the combustion chamber and intake manifold, less residual gas mass flows back into the intake manifold and is subsequently aspirated back in (reaspirative residual gas). After the start of the load step, the cam of one intake valve per cylinder is switched to large valve lift upon reaching the applied load threshold. The switch of the valve lift can be seen in the gap that occurs in the calculated air mass as well as in the indicated mean effective pressure. As a result of the now later intake valve closing, the higher charge motion and the resulting higher turbulent kinetic energy in the combustion chamber at ignition angle, the significantly reduced residual gas rate as well as the higher cylinder pressures, the spread in the center of combustion is reduced significantly. Except for the first cycles after opening the throttle the moving average of the center of combustion follows the quasi-stationary comparison value. After the engine has reached its natural aspirated full load, it starts with scavenging operation at the time t_1 . The trapping ratio decreases during transient operation almost linearly until the boost pressure control intervenes and adjusts a constant intake manifold pressure by opening the wastegates. Due to the constant intake manifold pressure in combination with constant valve timing, the result is a constant trapping ratio. In comparison to the quasi-stationary trapping ratio there are differences which can especially be seen in the range of the time t_2 where the quasi-stationary trapping ratio is 1.6 percentage points less than the transient trapping ratio. To explain this difference, an exemplary gas exchange cycle of cylinder 5 taken out of the transient event is compared to the corresponding quasi-stationary cycle in figure 12. In addition to the pressure traces in

the cylinder and in the intake and exhaust port, the valve lift and the calculated mass flows are shown.

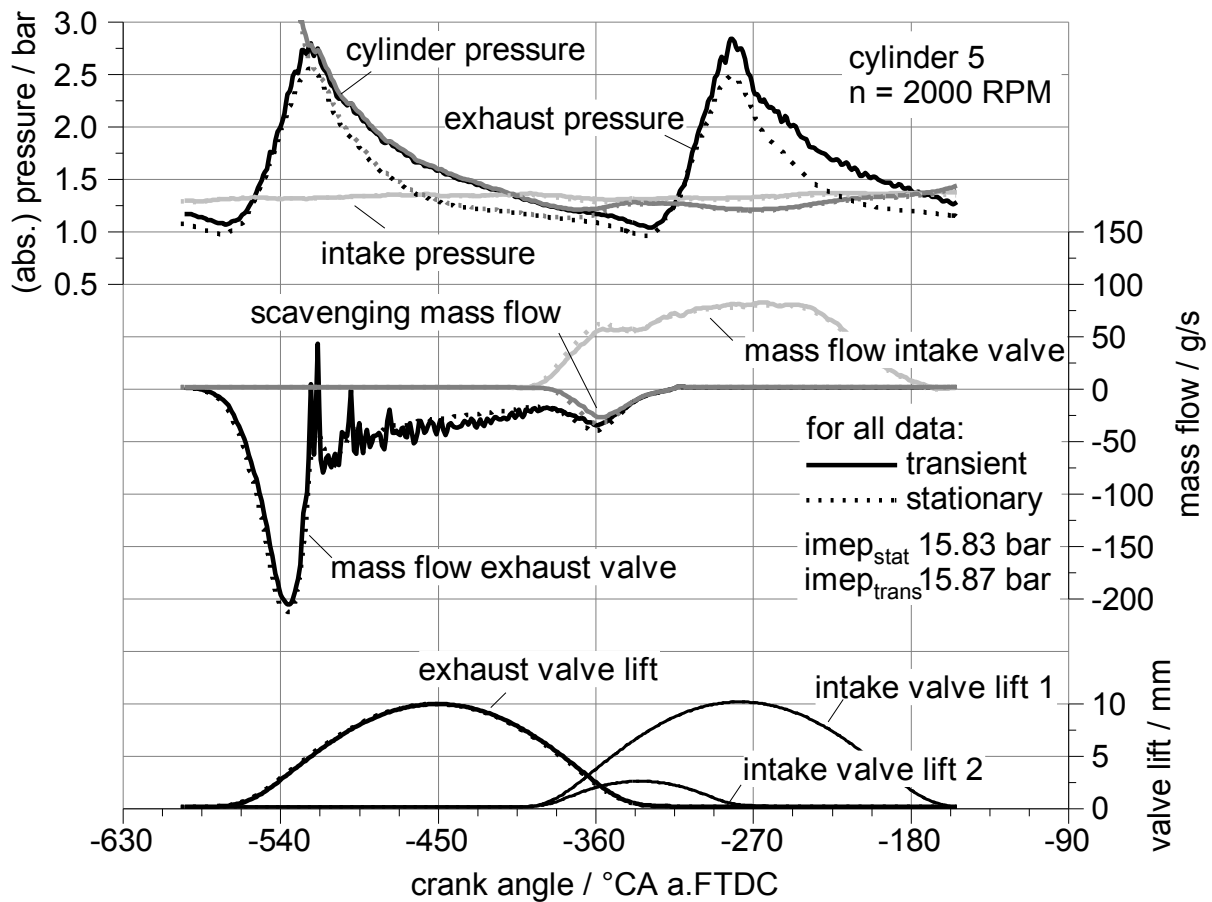


Figure 12: Comparison of the gas exchange cycle at the time t_2 and the corresponding quasi-stationary cycle

It can be seen that the pressure in the exhaust port in the case of the transient event is significantly higher than the pressure in the quasi-stationary comparison cycle, although the intake pressures as well as the valve timings are comparable. The increased level of pressure can be explained by the wastegate that is closed during boost pressure build up. As a result of the stationary lower exhaust pressure the amount of stationary scavenged mass is higher than the transient one, which can be seen in figure 12 from the higher scavenging mass flow during valve overlap. After the exhaust valve is closed, the intake mass flows are almost equal, resulting in a similar cylinder fresh air mass. Accordingly the trapping ratio is lower in case of the quasi-stationary comparison cycle. Because the calibration of engine control units is done by using stationary measurement data, the presence of such phenomena can lead to inaccuracies in the pilot mixture control. Against the background of increasingly stricter legal constraints such transient phenomena should be considered during the calibration process.

6. Summary and Outlook

In the present study the zero-dimensional approach for transient pressure analysis has been developed further. The key challenge for a zero-dimensional transient pressure analysis is the cycle-resolved, adaptation-free determination of the fresh air mass. For this, a zero-dimensional thermodynamic substitute model was developed. The substitute model enables the adaptation-free determination of fresh air mass on the basis of a crank-angle-resolved calculation of intake port temperature. Based on the stationary validation it was demonstrated that the sum of errors between calculated and measured reference air mass is below $\pm 2.5\%$. The quality of the transient pressure analysis was discussed with reference to the frequency distribution of the burn energy balance compared to the frequency distribution of an analysis carried out at stationary single-cycles. It can be concluded that the transient pressure analysis provides valid results, even under consideration of the quality criteria for stationary analysis of averaged pressure traces. Based on the shown analysis of an exemplary load step it can be seen that the usage of the presented transient pressure analysis allows to quantify the cycle-resolved cylinder mass and composition as well as its thermodynamic state in the best possible way. The pressure analysis can therefore be used in the development process to assess the thermodynamic impact of different actuation strategies as well as the thermodynamic impact of changes in the hardware on any transient event. In addition, besides valuable information for the calibration of the engine control unit, necessary input parameters for three-dimensional analysis can be derived. Thus, for example, the restrictions for the determination of the local air/fuel ratio in the combustion chamber according to [16, 17] could be mitigated, because both the entire cylinder mass as well as the temperature profile is determined in the transient pressure analysis.

Symbols

A	Area
$A_{valve,eff}$	Effective flow area
b	Exponent
c_v	Specific heat at constant volume
d	Diameter
f	Frequency
H_u	Heating value
H	Enthalpy
h	Specific enthalpy
K	Konstant
L_{st}	Stoichiometric air/fuel ratio
m	Mass
$mfb_{50\%}$	Mass fuel burned
n	Engine speed
Nu	Nusselt number
p_1	Pressure upstream a valve
p_2	Pressure downstream a valve
p	Pressure
R	Specific gas constant
Re	Reynolds number
Q	Heat flow
T	Temperature
T_1	Temperature upstream a valve
t	Time
U	Internal energy
u	Specific internal energy
V	Volume
v	Velocity
x	Fraction / ratio
Z	Number of cylinders
α	Convective heat transfer coefficient
κ	Isentropic exponent
λ_f	Thermal conductivity
λ	Air/fuel ratio
μ	Dynamic viscosity
ρ	Density
φ	Crank angle

Subscripts

<i>air</i>	Air
<i>b</i>	Fuel
<i>Br</i>	Brettschneider
<i>cyl</i>	Cylinder, combustion chamber
<i>f</i>	Fluid
<i>GEA</i>	Gas exchange analysis
<i>h</i>	Displacement
<i>im</i>	Intake manifold
<i>in</i>	Ingoing
<i>L</i>	Air
<i>leak</i>	Leakage
<i>meas</i>	Measured
<i>out</i>	Outgoing
<i>ref</i>	Reference
<i>scav</i>	Scavenging
<i>st</i>	Stoichiometric
<i>w</i>	Wall

Abbreviations

<i>a.FTDC</i>	After firing top dead center
<i>CA</i>	Crank Angle
<i>FIR</i>	Finite duration impulse response
<i>imep</i>	Indicated mean effective pressure
<i>PFI</i>	Port fuel injection
<i>stk</i>	Stroke
<i>CO</i>	Carbon monoxide
<i>H₂</i>	Hydrogen
<i>HC</i>	Hydrocarbon

References

- [1] Vlachos, T. G.; Bonnel, P.; Perujo, A.; Weiss, M.; Mendoza Villafuerte, P.; Riccobono, F.: In-Use Emissions Testing with Portable Emissions Measurement Systems (PEMS) in the Current and Future European Vehicle Emissions Legislation: Overview, Underlying Principles and Expected Benefits. Warrendale, PA : SAE International, 2014
- [2] Bögl, A.; Hemminger, B.; Janssen, A.; Kerkau, M.; Kerner, J.; Kronich, A.; Schlüter, M.: Die neuen V6 Turbomotoren im Porsche Macan. In: 35. Internationales Wiener Motorensymposium, 2014, S. 197–222
- [3] Schmidt, C.; Hohenberg, G.: FVV Abschlussbericht über das Vorhaben Nr. 519: Arbeitsspielbezogenes Luftverhältnis. 1993
- [4] Pischinger, S.: Verbrennungskraftmaschinen II. 27. Auflage. Aachen : Lehrstuhl für Verbrennungskraftmaschinen RWTH, 2010
- [5] Kordon, H.: Instationäre Untersuchungen an Ottomotoren mit unterschiedlicher Gemischaufbereitung. Technische Universität Wien, Dissertation, 1979.
- [6] Schmidt, C.; Bargende, M.; Hohenberg, G.: Arbeitsspielbezogenes Luftverhältnis. In: Motorentechnische Zeitschrift, 57. Jahrgang (1996), Nr. 10, S. 572–578
- [7] Schwärzel, W.; Willenbockel, O.; Zwickwolff, E.: Der neue Zweiliter-Vierventilmotor von Opel. In: Motorentechnische Zeitschrift, 49. Jahrgang (1988), Nr. 4, S. 139–147
- [8] Köhler, U.; Bargende, M.; Schwarz, F.; Spicher, U.: FVV Abschlussbericht über das Vorhaben Nr. 740 : Entwicklung eines allgemeingültigen Restgasmodells für Verbrennungsmotoren. 2003
- [9] Pischinger, M.: Bestimmung des Verbrennungsluftverhältnisses von Einzelarbeitsspielen für Otto- und Dieselmotoren. Rheinisch-Westfälische Technische Hochschule Aachen, Dissertation, 1993.
- [10] Pischinger, S.; Salber, W.; Andrian, S. v.: FVV Abschlussbericht über das Vorhaben Nr. 647 : Warmlauf- und Instationärverhalten von Ottomotoren mit variabler Ventilsteuerung. 1998
- [11] Leifert, T.; Fairbrother, R.; Nevado, F. M.: Durch Messung unterstützte thermodynamische Analyse von Zylinder internen Vorgängen unter transienten Bedingungen. In: 8. Internationales Symposium für Verbrennungsdiagnostik, 2008, S. 427–437
- [12] Leifert, T.; Nevado, F. M.; Fairbrother, R.; Prevedel, K.: Optimierung transients Vorgänge mit AVL-GCA an einem Otto-Motor hoher Flexibilität. In: 3. Tagung Motorprozesssimulation und Aufladung, 2011
- [13] Disch, C.; Pfeil, J.; Kubach, H.; Koch, T.; Spicher, U.; Thiele, O.: Experimentelle Untersuchungen zur Entwicklung des kurbelwinkelaufgelösten Brennraumluftverhältnisses im Transientbetrieb eines Ottomotors mit Direkteinspritzung. In: 7. MTZ-Fachtagung Ladungswechsel im Verbrennungsmotor, 2014

- [14] Berg, T.; Thiele, O.; Seefeldt, S.; Vanaelst, R.: Bestimmung der innermotorischen Gemischbildung durch optisches Indizieren. In: Motorentechnische Zeitschrift, 74. Jahrgang (2013), Nr. 6, S. 472–476
- [15] Berg, T.; Beushausen, V.; Thiele, O.; Voges, H.: Faseroptischer Zündkerzensensor zur Optimierung motorischer Brennverfahren. In: Motorentechnische, Zeitschrift 67 (2006), Nr. 6, S. 440–444
- [16] Grosch, A.; Beushausen, V.; Thiele, O.; Grzeszik, R.: Crank Angle Resolved Determination of Fuel Concentration and Air/Fuel Ratio in a SI-Internal Combustion Engine Using a Modified Optical Spark Plug. Warrendale, PA : SAE International, 2007
- [17] Thiele, O.: Faseroptische Gemischbildungsanalyse in Otto-Motoren bei direkteinspritzenden Brennverfahren. Universität zu Göttingen, Dissertation, 2004.
- [18] Disch, C.; Koch, T.; Spicher, U.; Donn, C.: Engine-in-the-Loop als Entwicklungswerkzeug für die Emissionsoptimierung im Hybridkontext. In: Motorentechnische Zeitschrift 75. Jahrgang (2014), Nr. 10, S. 70–78
- [19] Disch, C.; Pfeil, J.; Kubach, H.; Koch, T.; Spicher, U.; Thiele, O.; Donn, C.; Schyr, C.: Zyklusaufgelöste Verbrennungsprozessanalyse des transienten Betriebs an einem Ottomotor mit Direkteinspritzung. In: 11. Internationales Symposium für Verbrennungsdiagnostik, 2014, S. 141–155
- [20] Kulzer, A.: BDE-Direktstart : Startoptimierung eines Ottomotors mit Direkteinspritzung mittels eines thermodynamischen Motorsimulationsmodells. Universität Stuttgart, Dissertation, 2004.
- [21] Kufferath, A.; Lejsek, D.; Scherrer, D.; Kulzer, A.: Einsatz der Brennverlaufsanalyse im Motorhochlauf. In: Motorentechnische Zeitschrift, 67. Jahrgang (2006), Nr. 6, S. 434–438
- [22] Lejsek, D.; Kulzer, A.; Kufferath, A.; Hohenberg, G.; Bargende, M.: Berechnung des Wandwärmeübergangs im Motorhochlauf von DI-Ottomotoren. In: Motorentechnische Zeitschrift, 71. Jahrgang (2010), Nr. 4, S. 250–257
- [23] Hart, M.: Auswertung direkter Brennrauminformationen am Verbrennungsmotor mit estimationstheoretischen Methoden. Universität Siegen, Dissertation, 1999.
- [24] Jeschke, J.: Konzeption und Erprobung eines zylinderdruckbasierten Motormanagements für PKW-Dieselmotoren. Universität Magdeburg, Dissertation, 2002.
- [25] Jippa, K.-N.: Onlinefähige, thermodynamikbasierte Ansätze für die Auswertung von Zylinderdruckverläufen. Universität Stuttgart, Dissertation, 2003.
- [26] Gotter, A.: Brennraumdruckbasierte Motorsteuerung für Ottomotoren. Rheinisch-Westfälische Technische Hochschule Aachen, Dissertation, 2008.
- [27] Klein, P.: Zylinderdruckbasierte Füllungserfassung für Verbrennungsmotoren. Universität Siegen, Dissertation, 2009.
- [28] Becker, M.; Kienzle, D.; Shutty, J.; Wenzel, W.: Abschätzung von Parametern im Gaswechselfad per Zylinderdruck. In: Motorentechnische Zeitschrift, 73. Jahrgang (2012), Nr. 7-8, S. 586–590
- [29] Oppenheim, A. V.; Schafer, R. W.; Buck, J. R.: Discrete-Time Signal Processing. Upper Saddle River, New Jersey : Prentice Hall, 1998

- [30] Grill, M.: Objektorientierte Prozessrechnung von Verbrennungsmotoren. Universität Stuttgart, Dissertation, 2006.
- [31] Malchow, G. L.; Sorenson, S. C.; Buckius, R.: Heat Transfer in the Straight Section of an Exhaust Port of Spark Ignition Engine. Warrendale, PA : SAE International, 1979
- [32] Pflaum, W.; Mollenhauer, K.: Wärmeübergang in der Verbrennungskraftmaschine : Springer Verlag Wien, 1977
- [33] Woschni, G.: Die Berechnung der Wandwärmeverluste und der thermischen Belastung der Bauteile von Dieselmotoren. In: Motorentechnische Zeitschrift 31 (1970), Nr. 12
- [34] Bargende, M.; Burkhardt, C.; Frommelt, A.: Besonderheiten der thermodynamischen Analyse von DE-Ottomotoren. In: Motorentechnische Zeitschrift 62. Jahrgang (2001), Nr. 01, S. 56–68
- [35] Vogt, R.: Beitrag zur rechnerischen Erfassung der Stickoxidbildung im Dieselmotor. Universität Stuttgart, Dissertation, 1975.
- [36] Bargende, M.: Skript zur Vorlesung: Berechnung und Analyse innermotorischer Vorgänge. Universität Stuttgart, 2005
- [37] Merker, G.; Schwarz, C.; Stiesch, G.; Otto, F.: Verbrennungsmotoren : Simulation der Verbrennung und Schadstoffbildung. 3., überarbeitete und aktualisierte Auflage. Wiesbaden : B. G. Teubner Verlag / GWV Fachverlage GmbH, 2006

The Authors:

Thorben Walder, M.Sc., Dr. Ing. h. c. F. Porsche AG, Weissach

Dr.-Ing. André Casal Kulzer, Dr. Ing. h. c. F. Porsche AG, Weissach

Prof. Dr.-Ing. Michael Bargende, Forschungsinstitut für Kraftfahrwesen und Fahrzeugmotoren Stuttgart, Stuttgart

Licence:

This document is licensed under the Creative Commons Attribution 3.0 DE License (CC-BY 3.0 DE): <http://creativecommons.org/licenses/by/3.0/de/>

Real-time Capable 1-D Engine Simulation Model with the Fast Fourier Transformation (FFT) Concept

Aras Mirfendreski
Andreas Schmid
Michael Grill
Immanuel Kutschera
Michael Bargende

Abstract

Longitudinal models are used to evaluate different vehicle-engine concepts with respect to driving behavior and emissions. The engine is generally map-based. An explicit calculation of both fluid dynamics inside the engine air path and cylinder combustion is not considered due to long computing times. Particularly for dynamic certification cycles (WLTC, US06 etc.), dynamic engine effects severely influence the quality of results. Hence, an evaluation of transient engine behavior with map-based engine models is restricted to a certain extent. The coupling of detailed 1-D engine models is an alternative, which rapidly increases the model computation time to approximately 300 times higher than that of real time.

This paper presents a novel modeling concept for fast fluid mechanics calculation, which has been developed at AUDI AG in cooperation with the Institute of Internal Combustion Engines and Automotive Engineering at the University of Stuttgart. In many technical areas, the Fast Fourier Transformation (FFT) method is applied, which makes it possible to represent superimposed oscillations by their sinusoidal harmonic oscillations of different orders. For longitudinal dynamics simulations, this method is used to describe pressure pulsations of the fluid dynamics inside the engine air path. By renouncing an explicit calculation of the fluid dynamics, the computation time of the engine simulation model can be significantly decreased, whereby the quality of the fluid dynamics still remains through the application of pressure pulsations. Moreover, the engine model enables versatile use as it fulfills real-time capability, which is required for many applications such as HIL, OBD and function development for ECUs.

1. Introduction

According to the Fourier Theorem, any periodic signal $f(t)$ with a periodic time T can be expressed by a constant component and the sum of its infinite harmonic signals $h_n(t)$ and angular frequencies ω_n , differing in their amplitudes A_n and phases φ_n . The angular frequencies of the harmonics are multiples of the basic angular frequency $\omega_0 = 2\pi/T$. The total sum is also called the trigonometric sequence, or Fourier sequence, and is given by the following equation:

$$f(t) = c_0 + \sum_{n=1}^{\infty} [a_n \cos(n\omega_0 t) + b_n \sin(n\omega_0 t)] \quad (1)$$

The variables c_0 , a_n and b_n are known as Fourier coefficients. c_0 represents the average value (mean value) of the signal $f(t)$. If $f(t)$ is represented by an oscillating pressure signal $p(t)$, the variable c_0 represents the mean pressure of the pressure signal. Equation (1) can be simplified by using the following correlations:

$$a_n \cos(n\omega_0 t) + b_n \sin(n\omega_0 t) = c_n \sin(n\omega_0 t + \varphi_n) \quad (2)$$

with

$$c_n = \sqrt{a_n^2 + b_n^2} \quad (3)$$

and

$$\varphi_n = \arctan\left(\frac{a_n}{b_n}\right) \quad (4)$$

Equation (1) now can be transformed into the so-called spectral representation of the Fourier sequence:

$$f(t) = c_0 + \sum_{n=1}^{\infty} c_n \sin(n\omega_0 t + \varphi_n) \quad (5)$$

After executing the Fourier Analysis, a periodic signal $f(t)$ can be expressed by the following parameters [1]:

c_0	average value (mean value of signal $f(t)$)
$c_n = c_n(n\omega_0)$	amplitude spectrum
$\varphi_n = \varphi_n(n\omega_0)$	phase spectrum

2. Pressure pulsations of a V6-TDI

The following investigations are based on a current Audi V6-TDI engine. First, pressure pulsations inside the engine air path are examined, using a calibrated, detailed 1-D engine model. The pressure inside the exhaust manifold directly behind cylinder 1 is tapped and split into its spectral components by applying the Fourier Transformation. Afterwards, the gained Fourier coefficients (amplitude, phase and order) are

superimposed with the Reverse Fast Fourier Transformation Method (RFFT). The result of the RFFT is shown in Figure 1. The left column, starting from the top with a mean pressure signal, lists all harmonic pressure signals with decreasing amplitude height, gained from the FFT. The right column shows the results of the RFFT process. With each additionally superimposed harmonic pressure wave, the original pressure is approached. With five orders already, the original pressure pulsation can be reproduced up to a coefficient of determination R^2 of 97 %.

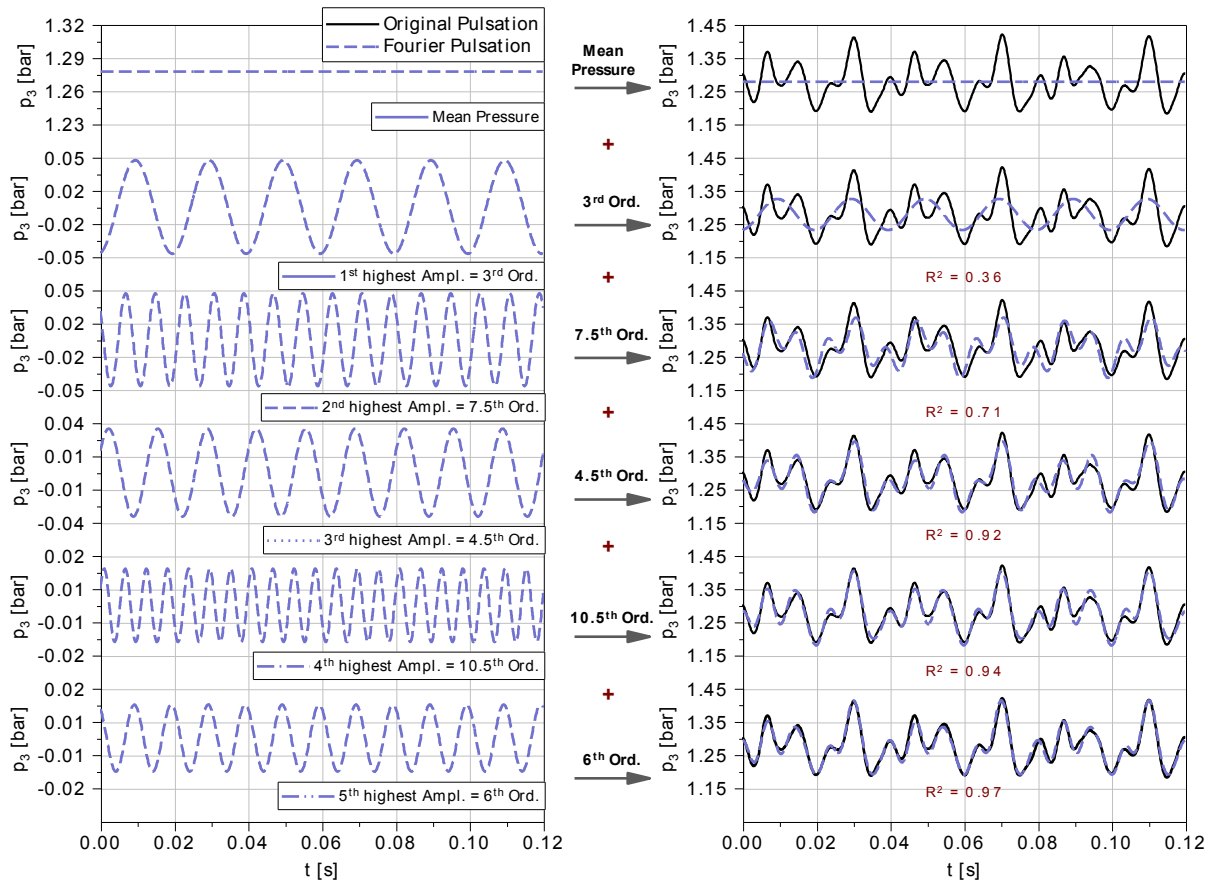


Figure 9: RFFT at cylinder 1 'Outlet' ($n = 1000$ RPM, IMEP = 3.93 bar)

Pressure pulsations inside the engine air path have a strong influence on the gas exchange and hence on the combustion. Furthermore, the turbocharger shows different behavior when being applied with pressure pulsations instead of a constant pressure. In order to be able to take these relevant effects into account, four nodes at which a pulsating pressure brings advantages in terms of higher realistic results are defined.

The nodes 'Cylinder In' und 'Cylinder Out' will ensure a correct calculation of the cylinder gas exchange. The nodes 'Compressor Out' and 'Turbine In' will lead to calculation of a much more accurate balance of the fluid dynamics outside the turbocharger boundaries.

By means of four chosen operating points, Figure 2 gives a good overview of how the coefficient of determination R^2 correlates with the number of superimposed harmonics for all four defined nodes.

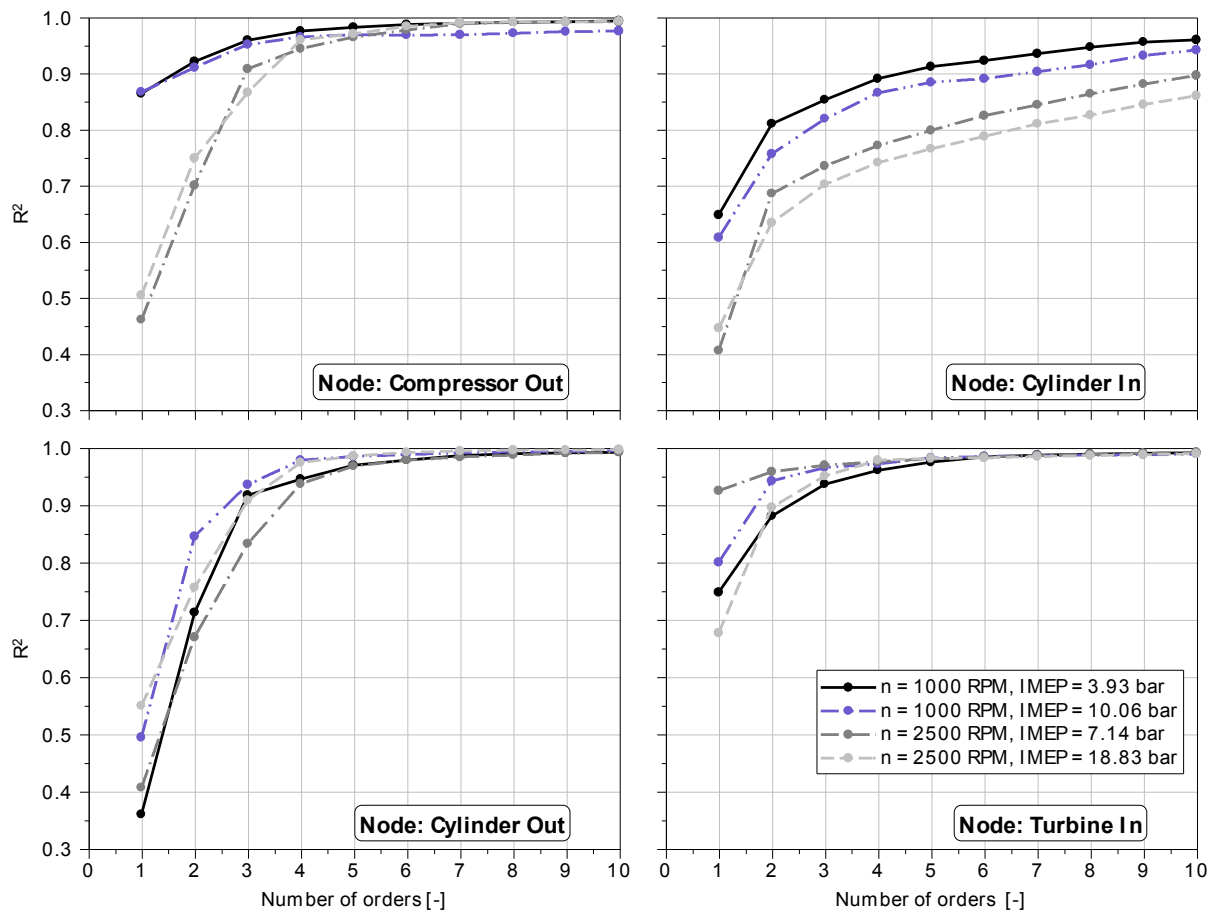


Figure 2: Coefficient of determination vs. number of orders for four predefined nodes

Figure 2 shows that the number of orders needed to obtain a certain value for the coefficient of determination clearly differs from node to node. “Cylinder In” is a conspicuous node, at which obviously a higher number of orders is required for obtaining result quality similar to the other nodes. The pressure pulsation inside the air path gets overlaid by for- and backward pressure feeds, which strongly depend on the engine geometry. A long air path, flow splits, filling and tangential intake manifolds, etc., cause many reflections inside the intake system. In contrast, the pressure pulsations at the other nodes can be quite well reproduced with 4 of the most important orders already. Additional harmonics here lead only to minor increase in quality.

For a quantification of the benefit a pulsating pressure brings compared to a non-pulsating pressure, the following examinations are presented. By way of example, Figure 3 (top left) shows the gas exchange loop for the operating point $n = 2500$ RPM, $\text{IMEP} = 18.83$ bar. When applying a mean pressure on both sides (intake and exhaust), deviations in cylinder pressure up to 350 mbar result at discrete times. With five applied orders of harmonic pressure signals, the gas exchange loop can be well reproduced. Figure 3 (bottom left) demonstrates the resulting error in volumetric efficiency after the gas exchange cycle which attains a value of 4 %. The operating point $n = 2500$ RPM at $\text{IMEP} = 18.83$ bar even shows that an insufficiently accurate pulsation (1st order) can have an adverse effect on the gas exchange and, thus, on the volumetric efficiency. Incorrect pressure pulsations during valve opening times principally change the cylinder charge. By superimposing further orders, the error can gradually be reduced.

The graph on the bottom right shows that the volumetric efficiency directly affects the maximal cylinder pressure during the combustion.

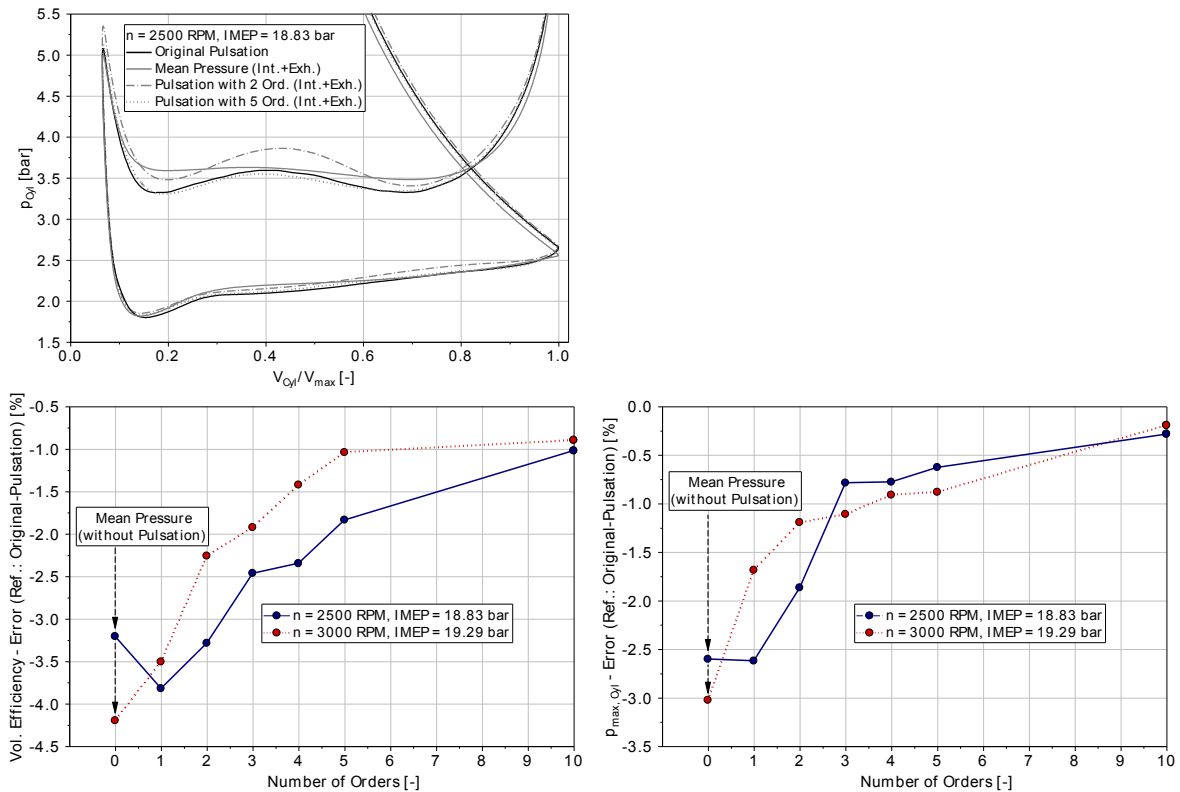


Figure 3: Model quality examinations: Internal engine

The same quantitative analyses are carried out on the turbocharger. Figure 4 (top left) shows the crank angle resolved turbocharger efficiency for $n = 2500$ RPM at IMEP = 18.83 bar. The efficiency of this operating point fluctuates in a maximum range of 26 %. The mass averaged efficiency is approximately 2 % lower than the time averaged efficiency. This indicates that a turbocharger applied by a mean pressure results in a higher mass flow. A different operating point is consequently tapped from a turbocharger map as can be seen in Figure 4 (top right). Hence, the turbocharger performance is overestimated. In the graph on the bottom left, it is evident again that the error in turbocharger efficiency can be eliminated using the FFT method [2].

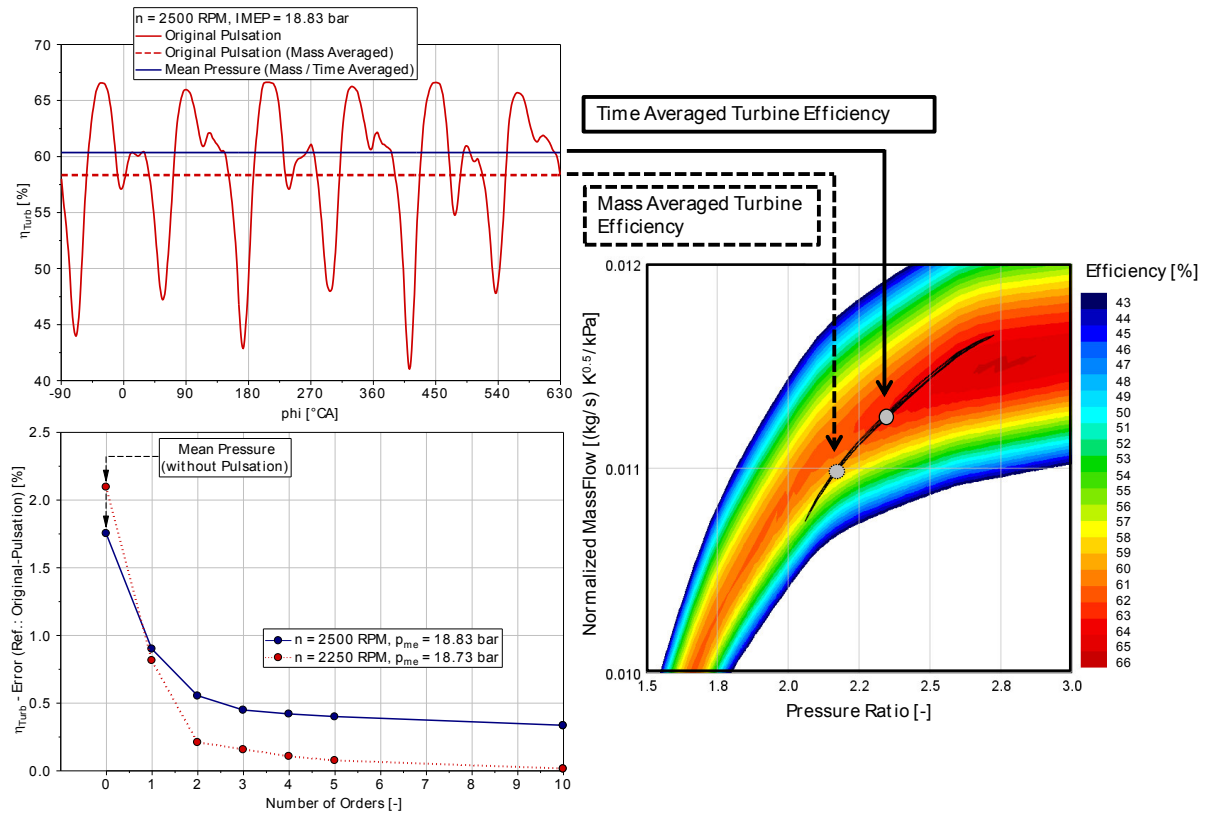


Figure 4: Model quality examinations: Turbocharger

3. Model architecture

The FFT model can be generated based on a detailed 1-D engine model or based on low pressure indication on an engine test bench. This way, an automated measurement process directly on the test bench will be possible. First, the air path of a detailed 1-D model must be reduced to spherical volume parts.

Figure 5 (left) shows an engine model reduced in its detailed air path. An explicit calculation of the fluid dynamics along the stream line, therefore, will not be performed here. Next, all cylinders are replaced by a representative single cylinder as exhibited in Figure 5 (right). Pressure pulsation on the intake side as well as on the exhaust side for cylinder 2-6 are copied and applied to the eliminated cylinder ports with respect to their firing angles. The output torque of cylinder 1 applied to the crank train is analogously taken into consideration.

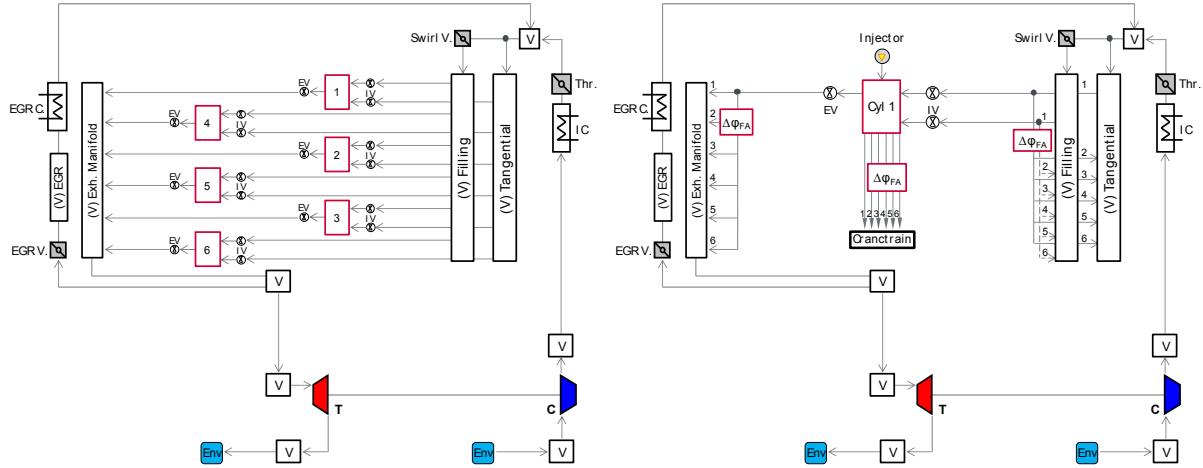


Figure 5: Volume-based engine model (left), cylinder reduction (right)

At the earlier predefined nodes, the model is split into several subsystems (Figure 6, left). Between the subsystems, an RFFT process with the FFT coefficients gained in a previous step can be performed (Figure 6, right).

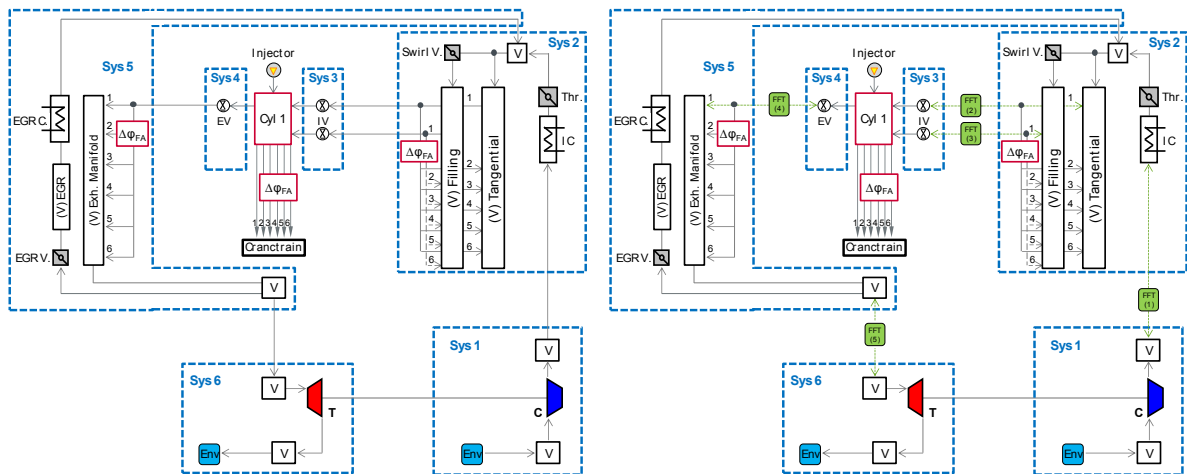


Figure 6: Model split into subsystems (left), application of Fourier coefficients at four predefined nodes (right)

The Fourier coefficients (phase-, order- and amplitude information) are placed in maps according to engine speed and current mean pressure (Figure 7, left). Now a connection of the subsystems is necessary to ensure mass continuity. This is done by a control strategy, which uses information over pressure, temperature and mass flow, shown in the right graph in Figure 7.

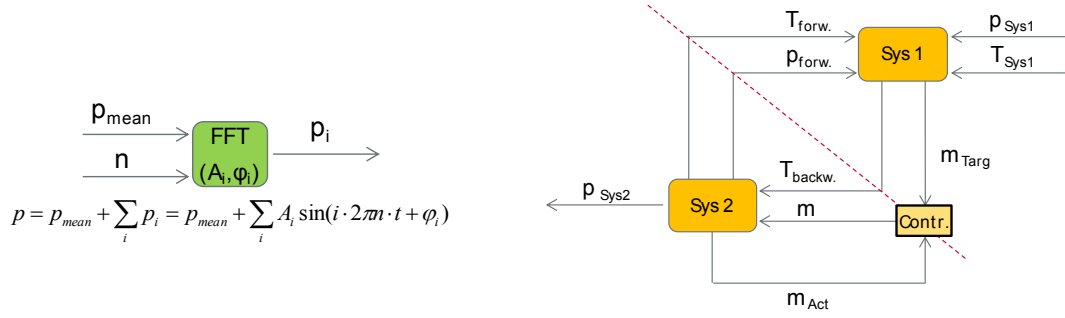


Figure 7: FFT module (left), physical controller (right)

The final system architecture of the FFT model is presented in Figure 8 (left). By means of this applied method a further advantage arises. Each subsystem is now available as an independent system. The numeric solution of each subsystem can, therefore, be chosen individually. For an optimization of the overall computation time, an optimal combination of implicit and explicit solvers can be chosen. By clustering, the potential of the computation time can be used more efficiently (Figure 8, right), which brings an increase of up to 400 % compared to a solution with a single explicit solver.

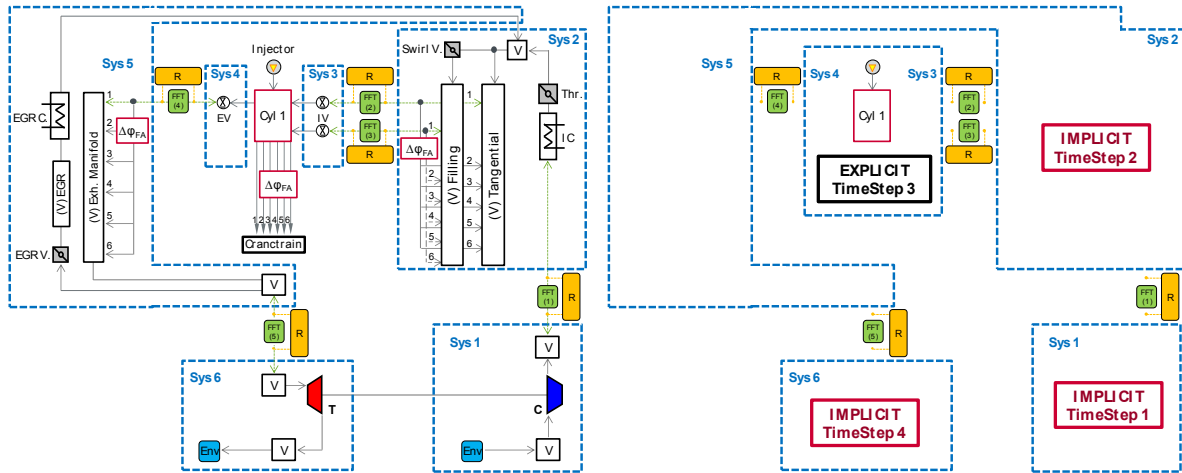


Figure 8: Connection of the air path by physical controllers (left), selection of individual solver types for each subsystem (right)

4. Results

Figure 9 shows the pressures for all four nodes for the stationary operating point $n = 2000$ RPM, IMEP = 10 bar. Theoretically, any number of orders can be stored in the model. However, an increasing number of computing operations increases the computation time. In order to minimize the computation load, the number of orders for each node is being limited so that for all operating points of the engine map a minimum coefficient of determination of 99 % is always guaranteed. Node 'Cylinder In' constitutes an absolute maximum number of orders in its extreme engine map range of 18.

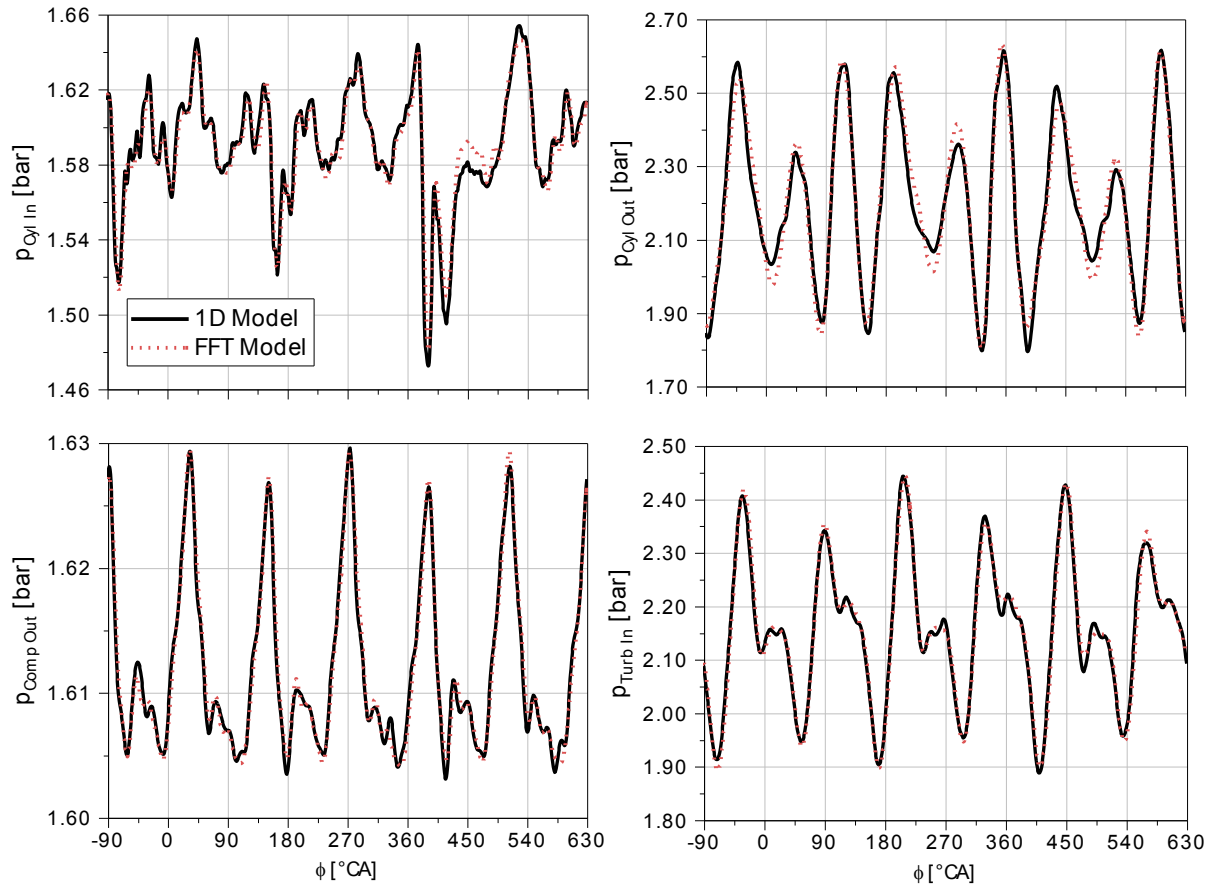


Figure 9: Model results ($n = 2000$ RPM, IMEP = 10 bar)

For the calculation of a stationary operating point inside or outside the range of embedded data points or for transient simulations, the determination of the Fourier coefficients will be done by a two-dimensional interpolation of the input parameters (engine speed and adjacent mean pressure).

For an evaluation of the interpolation quality, two exemplary operating points for a complex pressure pulsation of the cylinder intake pressure with a gap of 1000 RPM in engine speed and 390 mbar in mean pressure were chosen. The two left graphs in Figure 10 show the interpolation for the determination of phase and amplitude information for a number of orders.

The result in pressure pulsation from the interpolation of the Fourier coefficients is shown in the right graph. As evidenced, this methodology demonstrates an agreement in results compared to the original pressure curve at 1500 RPM, see dashed line. Averaging the pressure curves of the two boundary pressure curves, represented by the dotted line, would in comparison produce a result lower in quality.

In conclusion, it can be stated that due to its physical character, an interpolation of the Fourier coefficients leads to good quality.

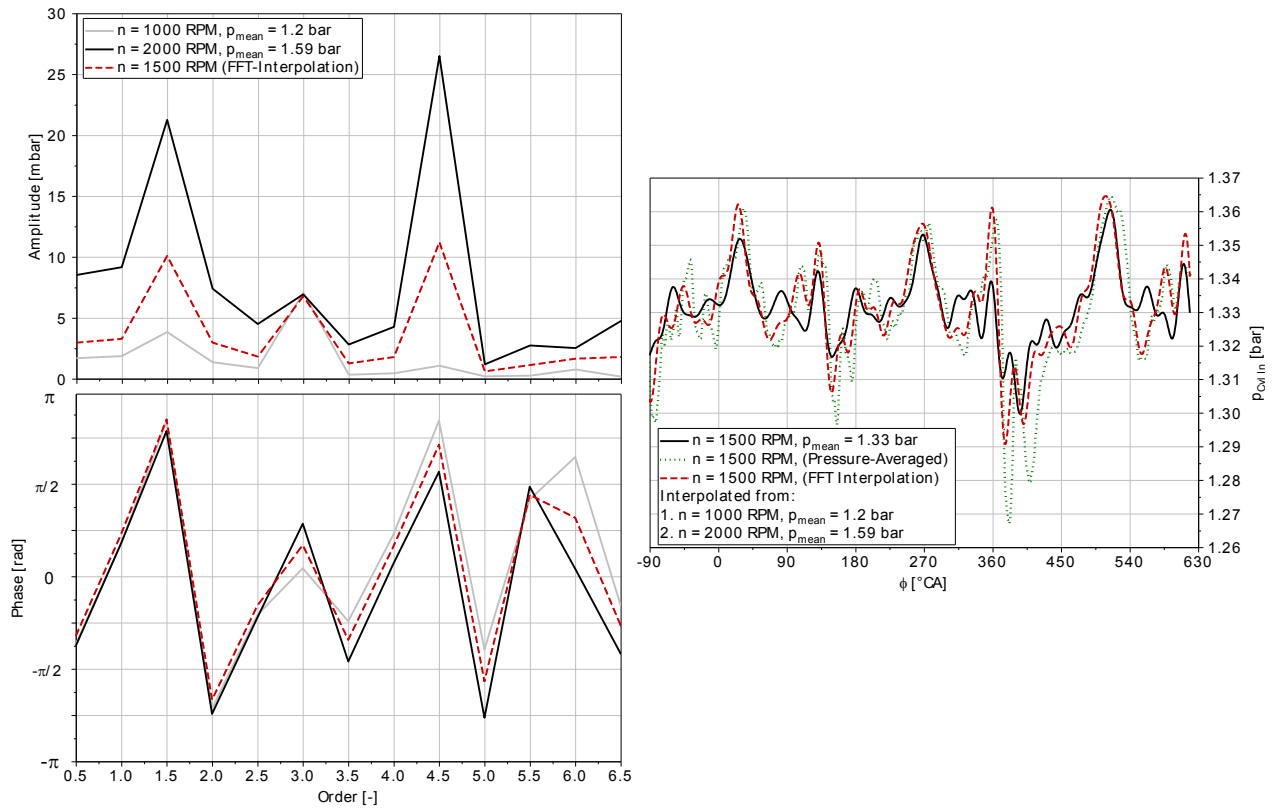


Figure 10: Interpolation quality of Fourier coefficients

Compared to the detailed 1-D engine model, the computation speed of the FFT model could be improved by a factor of 197 (real-time factor from 140 to 0.71) at 1000 RPM and by a factor of 93 (real time factor from 252 to 2.7) at 4000 RPM as shown in Figure 11. The results were determined on a computer with an i7-2.80 GHz processor.

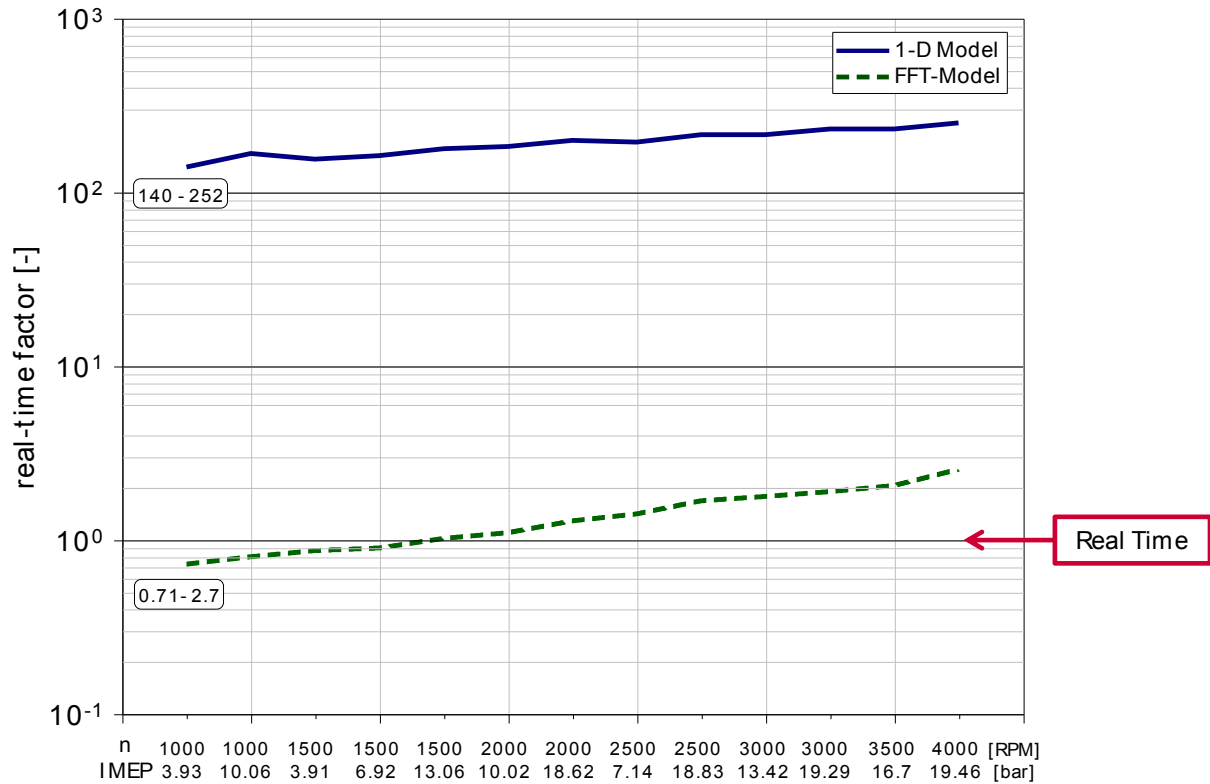


Figure 11: Computation speed

In summary, Figure 12 visualizes the properties of different model levels discussed in this paper and highlights the advantages of an FFT model compared to other model types. The table shows that an FFT model practically forms an optimal combination of a detailed model and a mean value model with respect to the quality of results. However, it remains restricted in predictability regarding geometry optimizations.













Properties Level	1D Geometry Optimization	1D Pressure Pulsation	Flow Volumes	Simulation Speed
1D Model				
Mean Value Model				
FFT Model				

Figure 12: Level of model details

5. Summary

In this paper a novel concept for an engine simulation model based on a mean value model was presented. Moreover, it was possible to generate pressure pulsations inside the engine air path by means of the FFT concept. The pressure pulsations were applied using the RFFT method at so-called ‘nodes’, where a pulsating pressure influences the inner motor behavior. The model still provides high computing speed, such as a mean value model, and represents pressure pulsations of a detailed 1-D engine model without an explicit calculation.

An individual choice of implicit and explicit solvers for each subsystem boosts the computation speed up to 400 %.

By coupling this model with a longitudinal model instead of using map-based engine models previously used, results of higher quality could be gained.

Moreover, the engine model enables versatile use as it fulfills real-time capability, which is required for many applications such as HIL, OBD and function development for ECUs.

References

- [1] Bossert, M.: Einführung in die Nachrichtentechnik. Oldenburg Wissenschaftsverlag, München, 2012
- [2] Pucher, H.; Zinner, K.: Aufladung von Verbrennungsmotoren. 4. Auflage, Springer Verlag, Berlin, 2012

The Authors:

Dipl.-Ing. Aras Mirfendreski, Universität Stuttgart, Institut für Verbrennungsmotoren und Kraftfahrwesen (IVK)

Dr.-Ing. Andreas Schmid, AUDI AG, Neckarsulm

Dr.-Ing. Michael Grill, Forschungsinstitut für Kraftfahrwesen und Fahrzeugmotoren Stuttgart (FKFS)

Dipl.-Ing. Immanuel Kutschera, AUDI AG, Neckarsulm

Prof. Dr.-Ing. Michael Bargende, Universität Stuttgart, Institut für Verbrennungsmotoren und Kraftfahrwesen (IVK)

Licence:

This document is licensed under the Creative Commons Attribution 3.0 DE License (CC-BY 3.0 DE): <http://creativecommons.org/licenses/by/3.0/de/>

Simulation of heat transfer with variation of the operating conditions

Volker Zeitz
Patrick Varga
Hermann Rottengruber
Helmut Tschöke
Jürgen Schmidt

Abstract

Based on the main engine parts a thermal network was created with the 1D simulation tool AMESim. The model consists of 18 lumped masses and the corresponding fluid volumes. Particular attention was paid to the combustion and friction approaches, because of their large influence to the warm-up phase of an engine.

The experimental investigations for model validation were carried out on a 2.0 l Diesel engine with direct injection. All in all there are 71 sensors installed in the engine. 27 of them were placed to the crank case and 22 to the cylinder head. The remaining sensors measure the temperatures and volumetric flow rates of oil and cooling water. All in all there is a good reproducibility for the measurements.

Some engine components were further subdivided considering characteristic geometrical parameter. In this way analyses of heat transfer in the engine and investigation for reducing the time of heating up of several parts in the model are possible. Moreover, temperature gradients in the engine were also taken into account for modeling the network. These gradients were detected through numerous measurements at the test bench.

Characteristic component and fluid temperatures of the model were used to validate the thermal network with measured temperature profiles at suitable measuring points. The accuracy of the results concerning the difference of simulation and measurement has been evaluated positively with statistical techniques for the investigated operation points. For them it can be concluded that all the approaches and assumptions are confirmed.

1. Motivation

Climate change and worldwide increasing energy requirements demand a re-thinking on the use of available resources. Future ambitions have to be the reduction of CO₂-emissions and a careful handling with finite fossil energy sources. The automotive segment contributes with a further optimization of conventional engines and the development of new drive concepts such as hybrid and electric drives.

Besides continuous improvements of mixture formations and combustion methods, thermal management is as well as subject of current research and development. The warming up of the engine is particularly important because there is a great potential for reducing fuel consumption and CO₂-emissions. Furthermore you have an increasing formation of HC and CO emissions caused by incomplete combustion. Especially for Diesel engines the formation of soot particles is of great importance. A further focus involves a reduction of friction losses through temporally und locally guided heat flows to friction points of the engine.

The aim of the project is to receive an engine simulation model for describing transient operating states as well as analyzing the heat flows with respect to time.

2. Modelling

In the following section the setting up of the simulation model and all the approaches used for the simulation will be described. This includes, in particular, the combustion process and several calculations for the friction.

2.1 Structure of the thermal network

Outgoing from a four-cylinder in-line engine a representative cylinder unit was built up to simulate the engine warm-up. This reduces simulation time and modeling effort. The simulation model consists of 20 lumped masses and corresponding capacities for the cooling water and the oil in the system. All the main components were taken into account such as cylinder head, crank case, crank shaft, piston and connecting rod.

Depending on the position of temperature sensors and regarding of thermodynamical coherences certain components were further subdivided (figure 1). For example the liner in the crank case was divided on the one hand into a section near the combustion chamber (BR) and an outer part (out) and on the other hand in several vertical segments.

In the lower part of the crank case was tried to model similar volumes for the upper and lower area of the main bearings to make statements about the heat flow rate. Whereas the cylinder head was divided into two lumped masses. The component 'cylinder head 1' gets all the influences of the cooling system and the friction from the valve train. The second component 'cylinder head 2' gets the heat from the combustion and is in contact with 'cylinder head 1' and the upper liner. A further subdivision of the cylinder head requires a significant effort, because of the complex geometry.

Every lumped mass in the system is described with its volume and its characteristic geometric measurements from the CAD. The physical properties are defined with temperature depending data for density, conductivity and specific capacity.

For the modeling the simulation tool LMS Imagine.Lab AMESim was used [1]. AMESim is a 1D simulation environment for modeling multidisciplinary systems and analyzing their properties. The software is based on the bond theory which describes continuous

and dynamic systems. Considering the causality of related components the power is defined as the product of effort and flux.

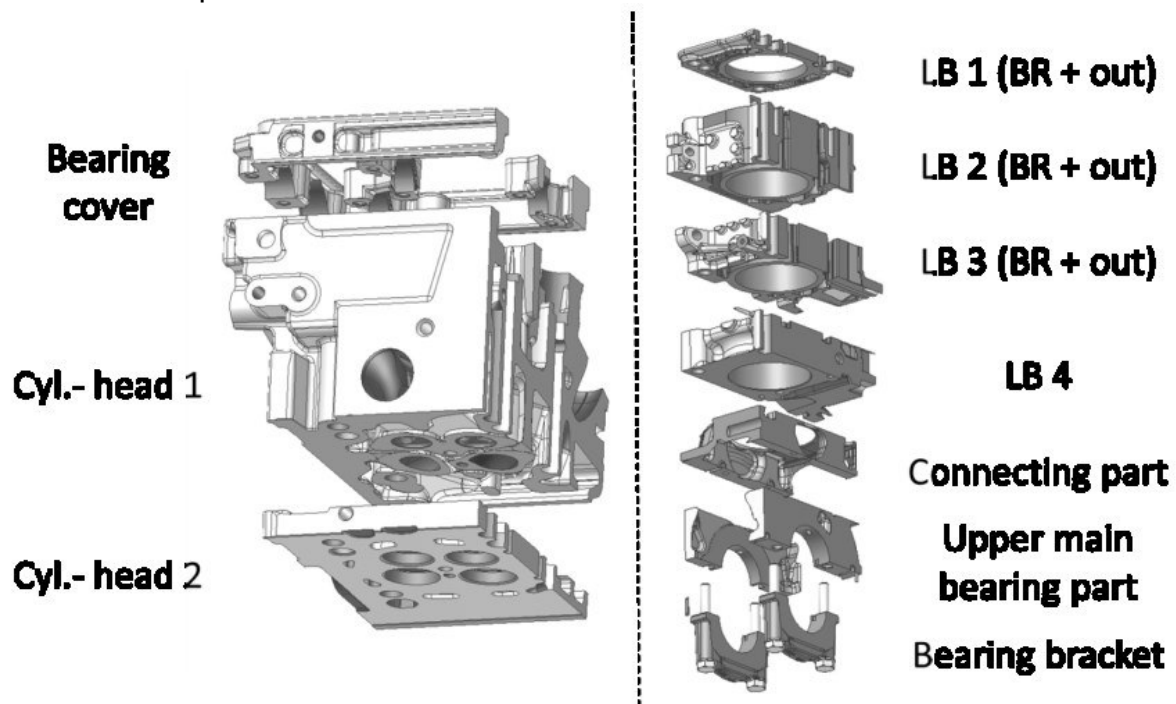


Figure 1: Subdivision of a representative cylinder unit

2.2 Fluid circuits

In view of the aim to describe the heat flow in the engine and partially missing possibilities for the validation, the cooling and lubrication circuits were modeled with a sufficient degree of detail.

Coolant

The cooling circuit is represented by a pump, a thermostat and an oil / coolant heat exchanger. The thermostat is described with its opening characteristic and the heat transfer between coolant and wax. The pump is defined by a data map. In addition the exact volume of coolant is taken into account.

A simplified cooler in the simulation model is a deviation to the experimental setup. In the model there is the assumption, that excess enthalpy of the fluid will be removed after opening the thermostat. The good correlation between measured and simulated temperatures of the cooling water strongly supports this approach (see figure 5).

Lubrication

The lubrication circuit consists of the oil pump, represented by a data map, the oil cooler and the exact volume of oil in the circuit. The most sensitive variables in the hydraulic system are volumetric flow rate and pressure in the pipes of cylinder head and crank case. Furthermore the flow rate and minimal height of lubricant with several bearing components can be explored. Unfortunately there are just a few possibilities to validate these results.

The heating of the oil in the lubrication circuit is caused mainly by friction in the system. Every time step friction is calculated with the actual oil temperature and then transferred to the corresponding components and the oil volume.

The cooling as well as the lubrication circuit offers the possibility for extensions with regard to the level of detail and the coupling with appropriate models.

2.3 Combustion

The heat release from the combustion process in the simulation model is taken into account with data maps. The heat flow rates averaged over a cycle are provided to the components closed to the combustion chamber depending on speed, torque and wall temperature.

In this work a phenomenological approach developed by Barba is used [2, 3]. This approach is a middle way between an empirical method and a CFD code. It is particularly suited for applications with common-rail Diesel engines and simulates besides the main injection several pilot and post-injections. The combustion behavior in high pressure phase can be built in dependence of the injected mass flow rate, characteristic parameters of the injector and state values from gas exchange. Validated for several operation points the approach can be applied to a wide load range with just one set of parameters. In terms of prediction accuracy it is a great advantage in comparison to empirical methods.

All in all the approach consists of several physical and chemical model parts considering all the steps of combustion. These involve in particular the injection and atomization, the development of the spray and the mixture formation, as well as the ignition and combustion.

2.4 Friction

The internal engine losses caused by friction attach high importance for the description of warm-up phase of an engine. Initial low oil temperatures and accordingly high viscosity lead to a significant heat input to the lubricant and the involved components. With regard to the fuel consumption there is a huge potential for savings through reducing the heating up time of the engine.

A differentiated consideration of single friction parts has the advantage that its respective influencing variables and target parameters can be identified and explored. For this purpose, there is more than just one approach for friction in this work.

For the determination of total friction the empirical approach for Diesel engines by Schwarzmeier is used [4, 5]. Based on a reference point from warm operating conditions the characteristic influencing parameters of piston group, main- and conrod bearings and the auxiliaries including the injection pump will be considered. These involve particular the mean piston speed, engine speed, torque and oil temperature.

The approach was adapted for the warm-up phase of the engine by fitting the corresponding coefficients with an evolutionary algorithm. The simulated values were validated with data from the test bench. The mean effective pressure is calculated by the difference of mean indicated and mean effective pressure (eq. 2.1).

$$p_{mr} = p_{mi} - p_{me} = \frac{1}{V_H} \oint p dV - \frac{2 \cdot \pi}{i} \cdot \frac{M_D}{V_H} \quad (2.1)$$

Piston group, crank shaft and valve train are the most significant friction parts in the system. The largest part of mechanical losses has the piston group with approximately 50 %. It can be subdivided into the contact between piston and liner, the conrod

bearings and the piston pins. Friction in the piston pin bearings can be neglected because there is low influence to the overall friction [6].

For the contact between piston and liner an empirical approach by Thiele for engine operating conditions will be used [6, 7, 8]. Based on a subdivision into piston rings and piston skirt an analysis of the influences of significant input parameters is possible. These involve lubricant properties, engine load and important design parameters such as tangential force of the piston rings, length of the skirt and piston mounting clearance. The estimation of friction in the main- and conrod bearings is based on DIN 31652 and VDI 2204 [9]. These standards will be used for calculation and designing of hydrodynamic bearings in steady operation. That method was chosen because of the simplification of a hydrodynamic lubrication in this study. This assumption implies that there is always a minimum thickness of lubricant between tribological contacts.

A large impact on friction in bearings have the properties of lubricant as well as design parameters such as width and diameter of a bearing and especially the relative clearance. All these factors are taken into account with this approach.

3. Experimental setup

The experimental studies were performed on a 2.0-liter 4-cylinder common-rail diesel engine with 103 kW from Volkswagen. The structure of the test bench was carried out according to the classic longitudinal arrangement.

Since the focus is on the investigation of the warm-up behavior, the test rig was placed on a vehicle-related build up.

The entire cooling system, the air intake and charge-air duct, as well as the oil circulation system were constructed with original car parts.

3.1 Overview of measurement sensors

On the test bench, 71 external and internal sensors have been installed to measure temperatures, pressures and flow rates. Figure 2 shows all external measurement points.

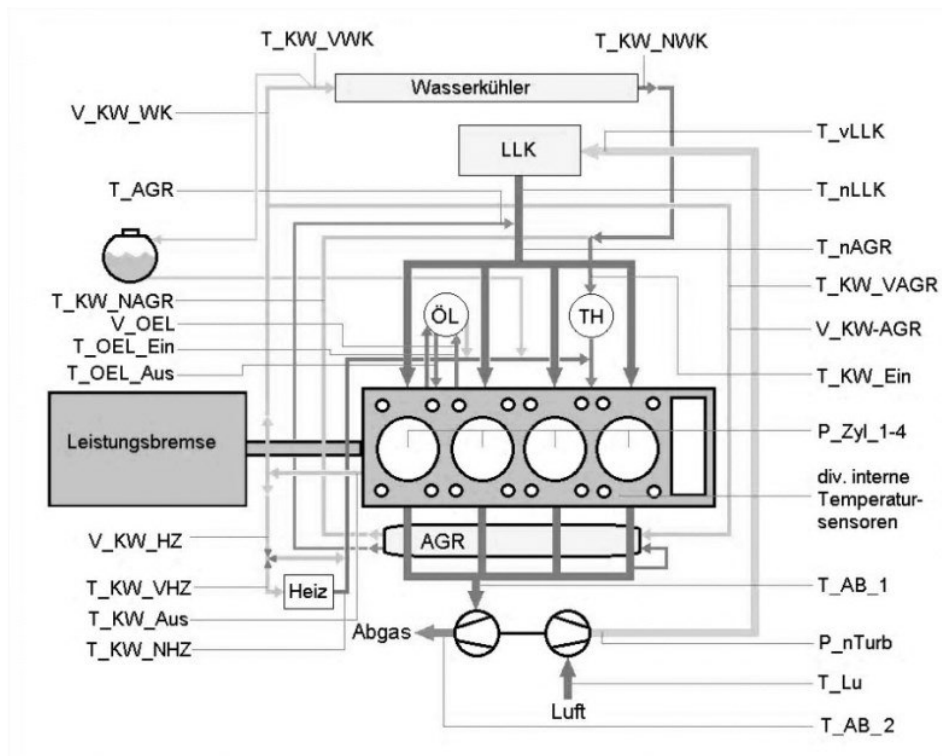


Figure 2: External points of measurement

Temperature measurement

A suitable method for measuring temperatures is important for describing the heating up of the engine. Besides high accuracy a wide dynamic range covering a wide temperature range and a high long-term stability are key requirement points. For the measurement of fluid temperature and component temperature Pt-100 thermocouples are used. In the area of hot gas, type K thermocouples were mounted.

Volumetric flow rate measurement

For the determination of the cooling water flow ultrasonic sensors of type DUK by the company Kobold are used. This acoustic measurement method based on the different acoustic wave propagation in a fluid, depending on the flow rate. The advantage of this procedure is the resistance-free measurement without reference to temperature and density of the fluid.

Pressure indication

For monitoring the combustion process and for the calculation of different combustion quantities, the cylinder pressure curve on the test vehicle is recorded with piezo-resistive pressure sensors.

3.2 Selection and identification of temperature measuring points

For a reliable statement about the warm-up behavior of an engine and the heating of the critical areas, it is important to have detailed knowledge of the temperature distribution and the corresponding heat fluxes. For this purpose it is necessary to measure the characteristic points in the engine, which have a high predictive value for the heating process. The measurement points for the control of the main component temperature and heat flux are located in the cylinder head, the cylinder block, and in the area of the camshaft and crankshaft.

Temperature measurement points - cylinder head and camshaft.

In the area of the cylinder head several measuring points were installed. Next to the upper and lower bearing portion of the camshaft, in the fire deck, just above the combustion chamber, and in the area of the cooling water additional sensors were placed.

Temperature measurement points crankcase and crankshaft

A similar approach is taken to the engine block. Besides a special attention to the bearing there are several temperature sensors along the cylinder liner (figure 3).

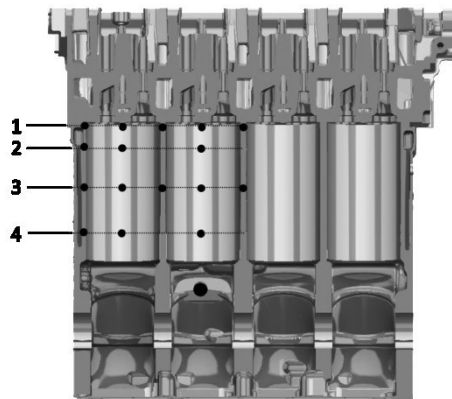


Figure 3: Temperature arrangement along the cylinder liners

The first measurement plane is 4 mm from the upper dead center, which corresponds to a crank angle of about 32 °. In this region, there is a high fuel conversion and thus a high heat input. The next measurement level is located at 40 mm, the area with the highest piston speed. Measuring plane three is placed at the level of the bottom dead center. A long piston exposure time suggests an increased heat input. In the last plane, which is 120 mm away from the cylinder head, there is only thermal conductivity to various components of the engine, including in the area of the main bearings.

3.3 Experimental procedure

The heating up process of the engine takes place according to the following pattern. The engine and its associated mass and the appropriate fluids have a temperature of approximately 20 °C at the time of the launch. For a stationary operation point the engine is warming up until reaching warm operating conditions. After that the engine is cooling down to ambient temperature and the procedure can start again.

All operating conditions that are examined on the test bench are shown in figure 4. Besides a wide load range presented as a variation of torque and engine speed within lower and upper limits, there 4 more characteristic operation points of the NEDC. Driving a transient cycle at the test bench is not possible.

All in all there is a good reproducibility for the measurements.

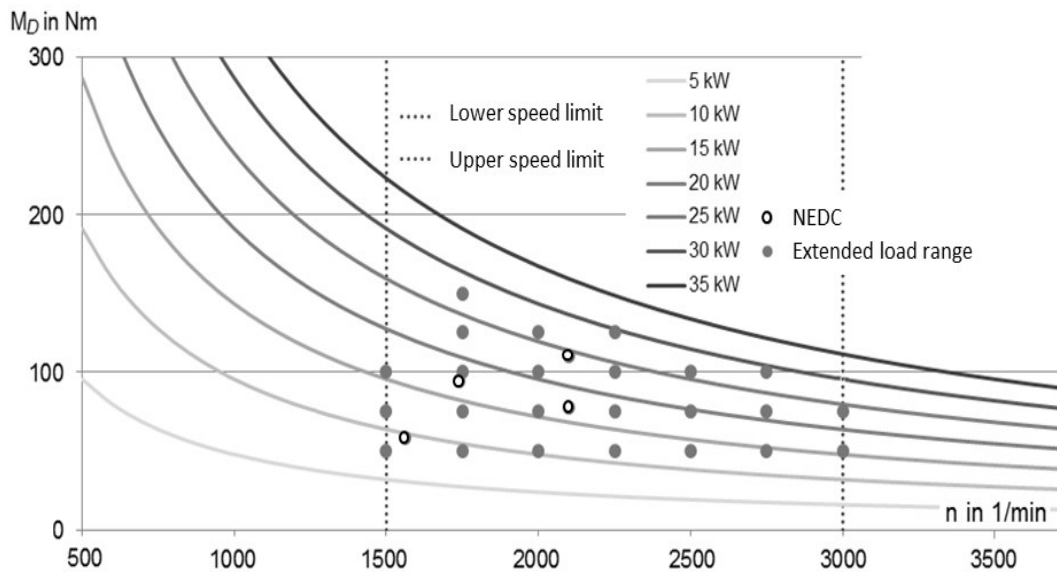


Figure 4: Characteristic diagram with all operation points

4. Model validation in the engine operation map

Comparison of temperature trends

The parameterization of the model was carried out using selected operating times. Figure 5 shows the corresponding profiles of heat (simulation and experiment) of a test run with 10 different component sensor readings.

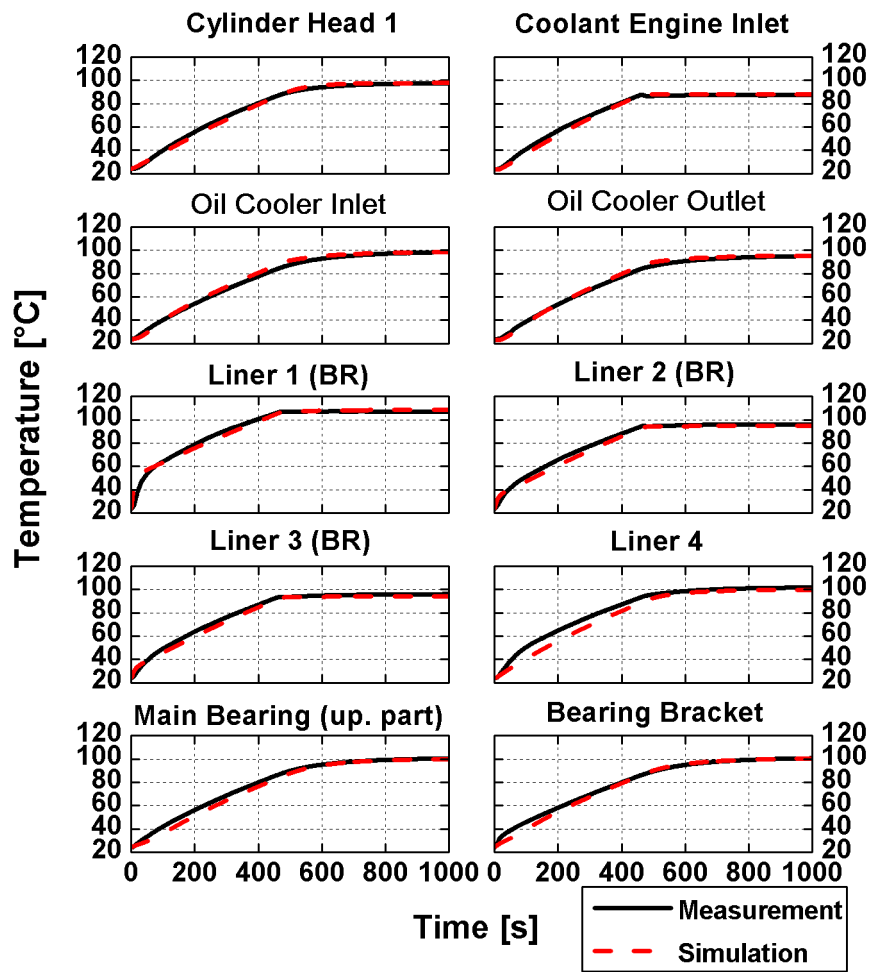


Figure 5: Comparison of simulation and measurement of selected components (operating point 2000 1/min and 50 Nm)

The coolant has significant influence on the warm-up behavior of the engine. A high flow rate within the Engine promotes the heat transfer with the adjacent components. These components then take the temperature characteristics of the coolant allowing a more even thermic transposition. This can be seen in cylinder head 1 and also near combustion chamber liner 1 in Figure 5. For additional validation, experiments were performed with a dynamic test run with 8 different component sensor readings (Figure 6).

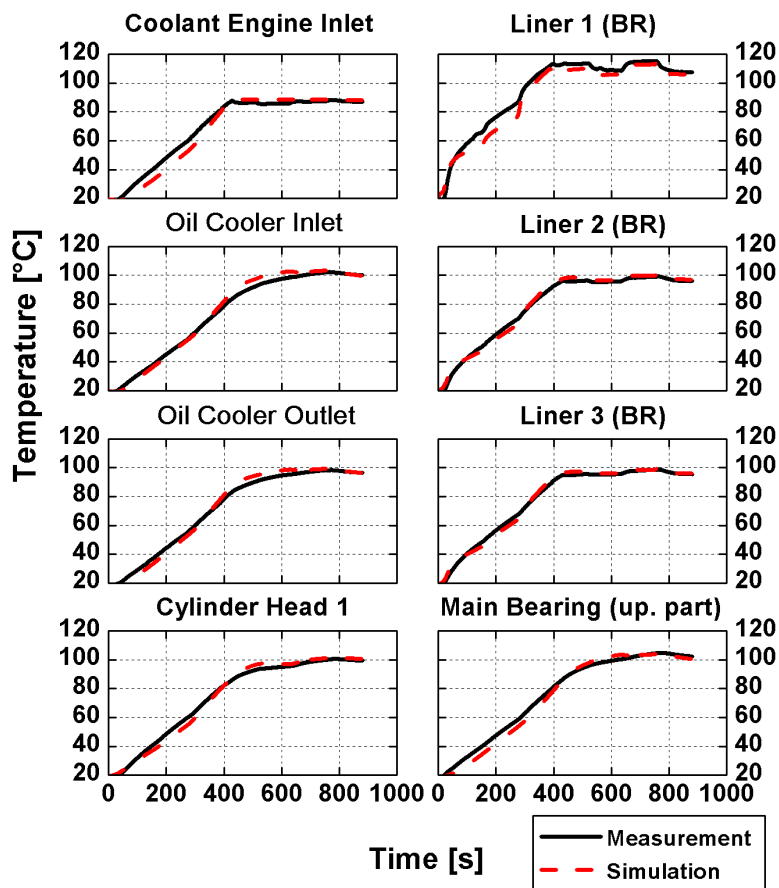


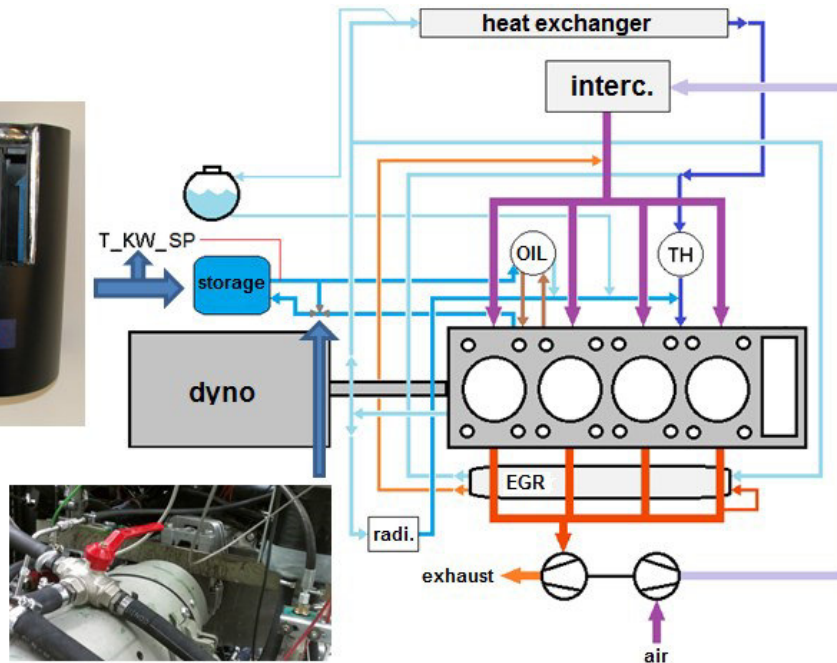
Figure 6: Comparison of measured and simulated temperature profiles under dynamic test run.

The results show that the coolants thermal behavior is reproduced with great accuracy to that of the simulation, even when the engine speed is changed. Overall, the simulated temperature curves, of all operating points, have an average standard deviation of 2-3 K.

4.1 Experiments with modified operating conditions

To ensure high quality results are obtained from the thermal network, the following experiments have been carried out with thermal management measures. This is intended to check the forecast ability of the simulation model and quantify the fuel saving effects. The following investigations were carried out:

- static coolant,
- variations of the coolant composition,
- variation of oil types,
- reducing the amount of oil,
- heat storage tank,
- external heat supply.



Test results (operating point 2000 1/min and 50 Nm)

349

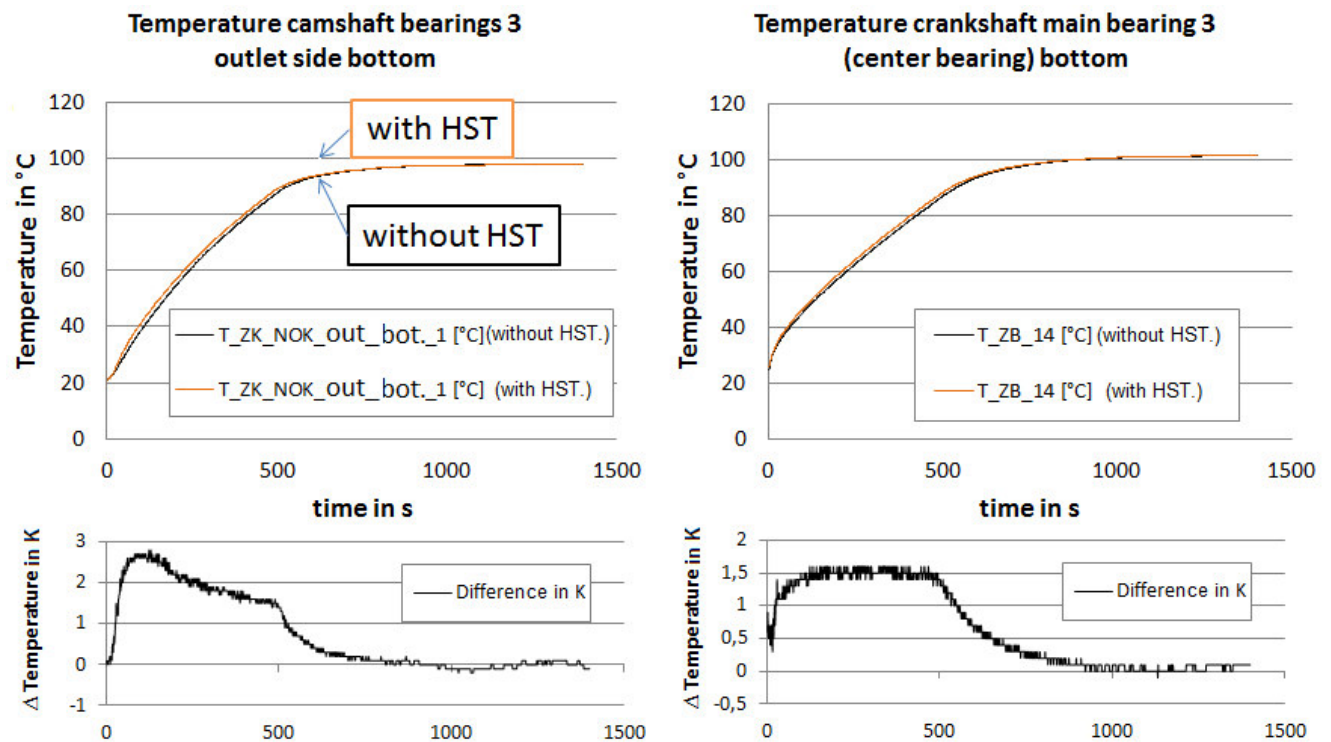


Figure 8: Comparison of component and media temperatures (Heat Storage Tank)

The higher fluid temperature also affects the thermal behavior within the bearings of the motor. Figure 9 shows the temperature profiles, from which a more rapid temperature rise can be seen. This causes a direct reduction of friction loss. The temperature difference in the heating process in the first 300s is approximately 4-5K.

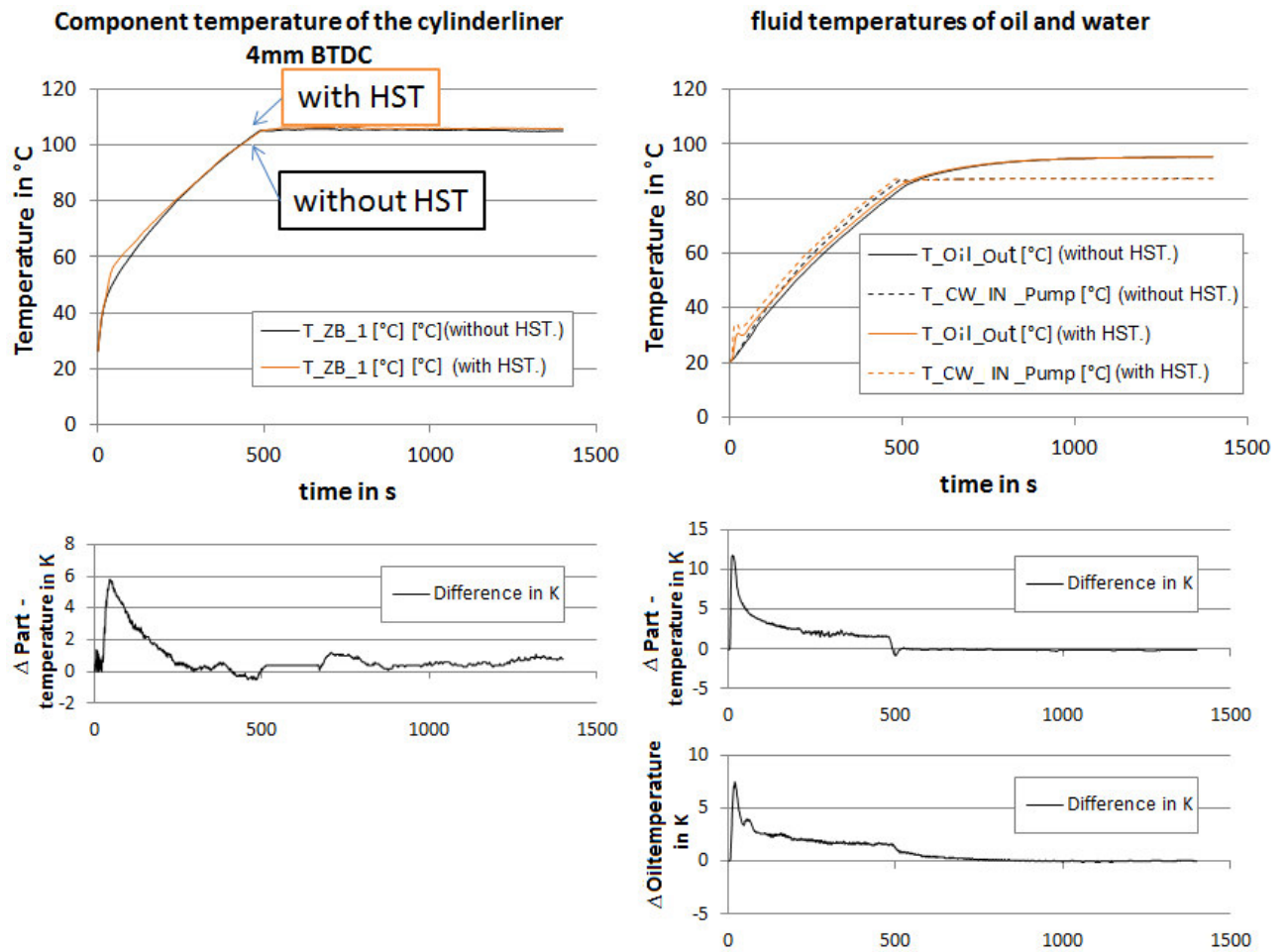


Figure 9: Comparison of bearing temperatures (Heat Storage Tank)

The derived findings from Figure 8 and Figure 9 are confirmed by the following fuel consumption chart (Figure 10). Here the results show the reservoir reduced fuel consumption during the warm up phase by around 1.4 % for a period of 900 s. The mean value of fuel saved across the other operation Points evaluates at 1 – 1.2 %

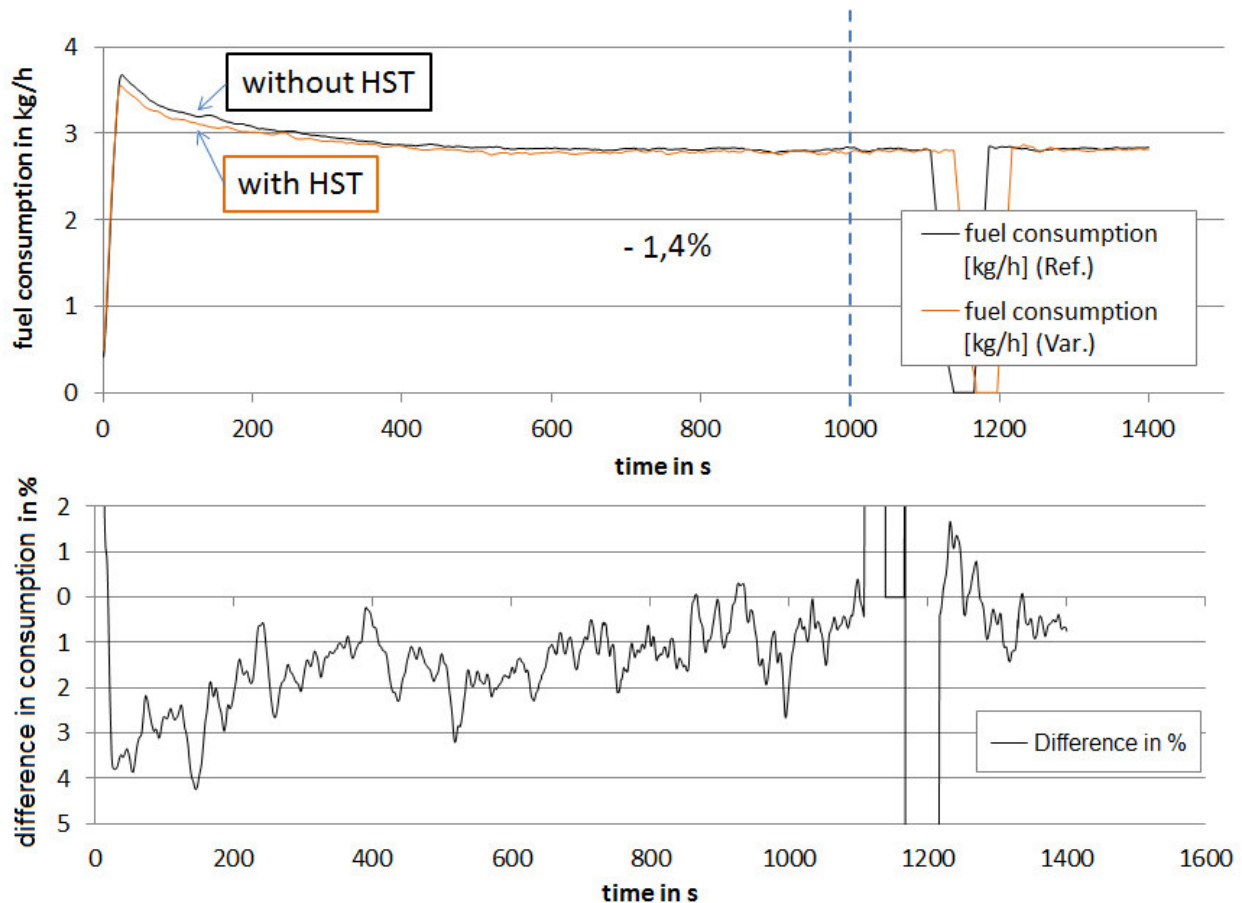


Figure 10: Comparison of fuel consumption (Heat Storage Tank)

4.2 Simulation results

The simulation results of the thermal model will be compared to the measured data and presented below. Based on the series state without the reservoir, the coolant temperature gradients can be illustrated by the model very well. (Figure 11 left). The use of the enthalpy storage causes to a rapid rise in temperature by mixing the coolant. The simulation model is also able to reproduce this behavior as well. Only the resulting effects of temperature overshoot in the mixing period are not reproduced by the model (Figure 11 right). The simulation model calculates the temperature profiles less dynamically due to the simplified simulation of the mixing process. The absolute variation of the temperature is displayed correctly with only a slight deviation.

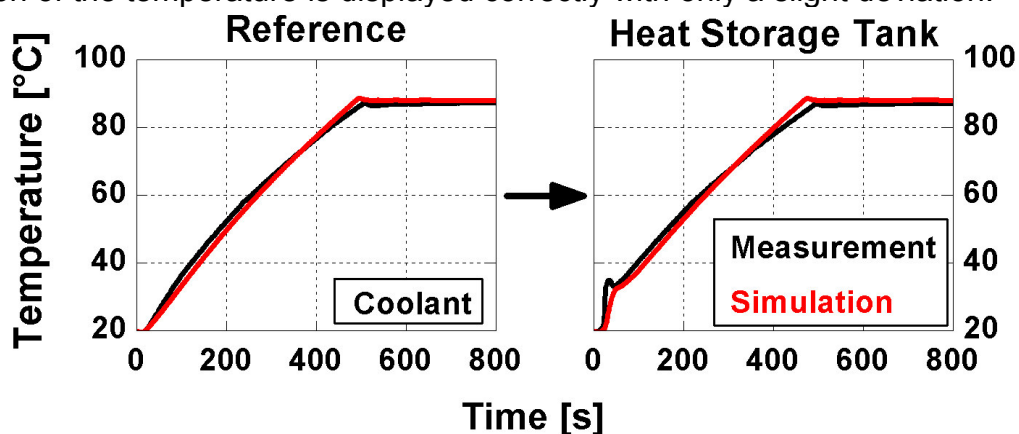


Figure 11: Simulation Results for the use of a reservoir; operating point 2000 1/min and 50 Nm

4.3 Simulated changes in consumption

Thermal management measures

In Figure 12, the changes in consumption of the six studied stationary points are plotted. The lower section shows an extended calculation of fuel savings based on the New European Driving Cycle [NEDC]. It can be seen that the dynamic conditions in the driving cycle lead to an intensification of the phenomena. This effect is due to the idle periods occurring and influences positive results.

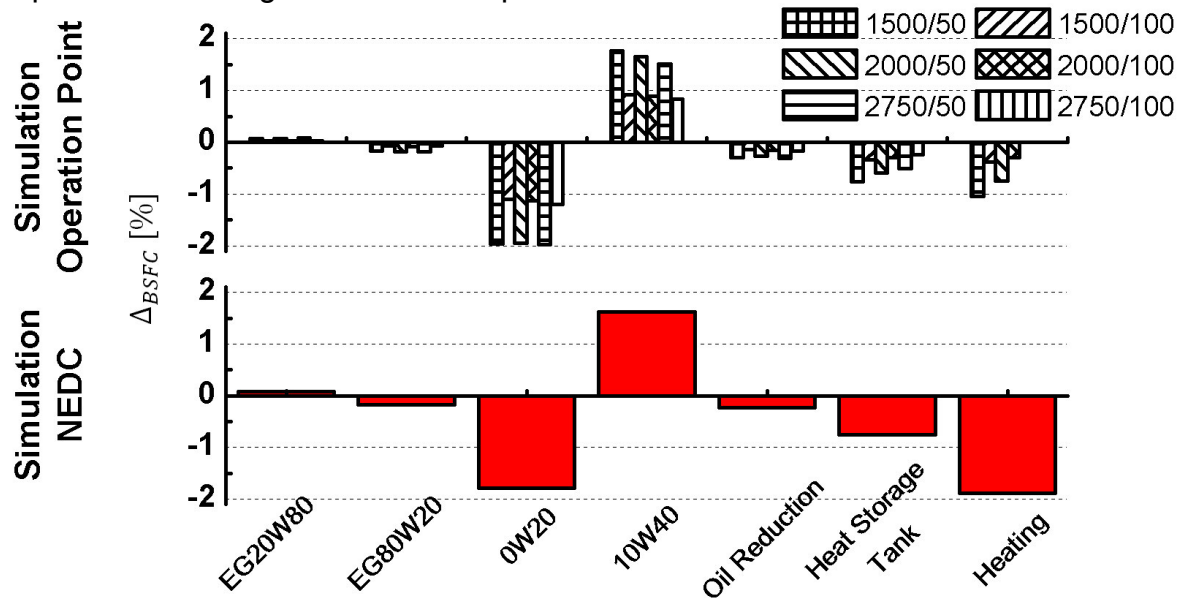


Figure 12: Simulated changes of fuel consumption in single point operation and for the NEDC

The largest potentials arise in the variation of the oil. The change in viscosity to a thinner engine oil leads to a lower level of friction and lower temperature development. The low-viscosity oil (0W20) at 20 ° C is lower by almost 40% kinematic viscosity than that of the standard oil (5W30). The change in the percentage of glycol in the coolant and reduction of oil level has a comparatively small influence.

Design Measures

An essential feature of the model is to investigate thermal changes in the heating phase by varying different constructive parameters. Figure 13 shows a variation of the significant influence parameters in the range of -20% to +20% over the achieved fuel reductions.

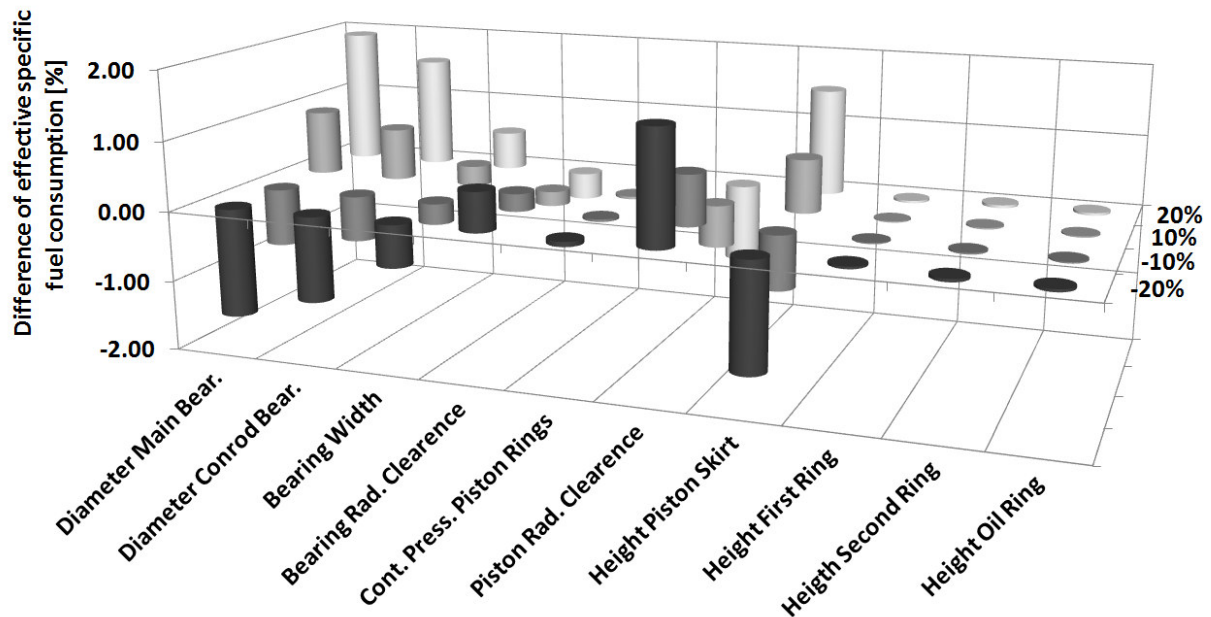


Figure 13: Changes in consumption due to the variation of constructive parameters (simulation)

The results of the simulation obtain a good agreement, when comparing it with the real data. According to Deuß [5] the reduction of the tangential force of the piston rings was approximately 50% while fuel savings were approximately 0.7%. The Examination of Deuß in 2013 references a fuel saving of approximately 0.7% for the reduction of the tangential Piston ring forces by approximately 50%. This is consistent with the results from the simulation which calculates fuel savings of 0.2% for a 20% reduction of the tangential piston ring forces. The relation in behavior in certain limits can be readily reproduced by the used friction approaches in the model. The investigations are exclusively designed to highlight fuel reduction potentials. Statements in terms of strength and reliability in the engine were not part of the studies in the project.

5. Summary and Outlook

From geometry data of the CAD model test vehicle, an 18 point lumped mass simulation model was created and extended with friction and combustion approaches. The simulation results have been validated parallel to the model structure operating on the test bench. In several stationary and dynamic operation studies the simulation model showed that it can represent the warm-up behavior of the test vehicle with good simulation accuracy, with an average of 2-3 K. Furthermore, it was demonstrated that thermal operation on an engine as well as structural changes can be simulated to optimize the heating phase. In the future, a variety of approaches can be examined for warm-up optimization with that a further validation of the simulation model can be achieved. Examples of this could lie in the use of heat pipes for direct heat conduction or in coolant separation (split cooling) for different engine range temperatures. Isolation effects and change of oil coolers (piston crown cooling) are researchable using the thermal model (see FVV engine heat exchange III). In the following project the further expansion of the simulation model will be forced with additional validations and transferability for other engines types will be examined.

References

- [1] <http://www.lmsgermany.com>
- [2] Barba, C.: Erarbeitung von Verbrennungskennwerten aus Indizierdaten zur verbesserten Prognose und rechnerischen Simulation des Verbrennungsablaufes bei Pkw-DE-Dieselmotoren mit Common-Rail-Einspritzung, Dissertation, 2001.
- [3] Barba, C., Burkhardt, C., Boulouchos, K., Bargende, M.: A Phenomenological Combustion Model for Heat Release Rate Prediction in High-Speed DI Diesel Engines with Common Rail Injection.
- [4] Schwarzmeier, M.: Der Einfluß des Arbeitsprozeßverlaufs auf den Reibmitteldruck von Dieselmotoren, Dissertation, TU, 1992.
- [5] Schwarzmeier, M.: Reibmitteldruck: Vorhaben Nr. 421 ; der Einfluß des Arbeitsprozeßverlaufs auf den Reibmitteldruck ; Abschlußbericht, FVV, Frankfurt/M, 1992.
- [6] Scholz, I.: Einfluss des Zylinderdruckverlaufes auf den Reibmitteldruck eines Benzinmotors mit Direkteinspritzung, Dissertation, Otto-von-Guericke-Universität, 2006.
- [7] Karrar, E.: Untersuchungen zum Reibungsverhalten und Ölverbrauch der Kolbengruppe von Verbrennungsmotoren, Dissertation, RWTH, 2009.
- [8] Thiele, E.: Beitrag zur Reibungsanalyse von Hubkolbentriebwerken, Dissertation, Univ, 1982.
- [9] VDI-Gesellschaft Entwicklung, K. V. / A. G.: Auslegung von Gleitlagerungen: Grundlagen ; Berechnung ; Kennzahlen und Beispiele für Radiallager ; Kennzahlen und Beispiele für Axiallager, 1992nd ed., VDI-Richtlinien, Vol. 2204, VDI-Verl, Düsseldorf, 1994.

The Authors:

Dipl.-Ing. Volker Zeitz

Otto-von-Guericke-Universität
Fakultät für Maschinenbau
Institut für Mobile Systeme (IMS)
Gebäude 14, Universitätsplatz 2, 39106, Magdeburg, G14-123
Tel: 0391-67-12201
Fax: 0391-67-12832
volker.zeitz@ovgu.de
<http://www.ovgu.de/ims/>

Dipl. Wirt.-Ing. Patrick Varga

Otto-von-Guericke-Universität (ehem. Mitarbeiter)
Institut für Strömungstechnik und Thermodynamik (ISUT)
Gebäude 10, Universitätsplatz 2, 39106, Magdeburg, G10-135
patrick.varga@ovgu.de
<http://www.ltt.ovgu.de>

Prof. Dr.-Ing. Hermann Rottengruber

Otto-von-Guericke-Universität
Fakultät für Maschinenbau
Institut für Mobile Systeme (IMS)
Gebäude 14, Universitätsplatz 2, 39106, Magdeburg, G14-118
Tel: 0391-67-18721
Fax: 0391-67-12832
herman.rottengruber@ovgu.de
<http://www.ovgu.de/ims/>

Prof. Dr.-Ing. Dr. h. c. Helmut Tschöke

Otto-von-Guericke-Universität
Fakultät für Maschinenbau
Institut für Mobile Systeme (IMS)
Leiter: Lehrstuhl Kolbenmaschinen
Gebäude 14, Universitätsplatz 2, 39106, Magdeburg, G14-17
Tel: 0391-67-18712
Fax: 0391-67-12832
helmut.tschoeke@ovgu.de
<http://www.ovgu.de/ims/>

Prof. Dr.-Ing. Jürgen Schmidt

Otto-von-Guericke-Universität
Fakultät für Verfahrens- und Systemtechnik
Institut für Strömungstechnik und Thermodynamik (ISUT)
Lehrstuhl: Technische Thermodynamik
Gebäude 10, Universitätsplatz 2, 39106, Magdeburg, G10-135
Tel: 0391-67-58575
Fax: 0391-67-12762
juergen.schmidt@ovgu.de
<http://www.ltt.ovgu.de>

Licence:

This document is licensed under the Creative Commons Attribution 3.0 DE License (CC-BY 3.0 DE): <http://creativecommons.org/licenses/by/3.0/de/>

The Benefits of an Exhaust-gas Heat-recovery Unit – The Inverted Brayton Cycle

Colin Copland
Zhihang Chen

Abstract

The exhaust gas from an internal combustion engine contains approximately 30-40% of the thermal energy of combustion. The exhaust-gas heat-recovery systems aim to reclaim a proportion of this energy by introducing a bottoming thermodynamic cycle to raise the overall system thermal efficiency. One promising heat recovery approaches is to employ an Inverted Brayton cycle (IBC) immediately downstream of the primary cycle. IBC system consists of a turbine, a heat exchanger and compressors in sequence. The use of IBC turbine is to fully expand the exhaust gas available from the upper cycle. The remaining heat in the exhaust after expansion is rejected by the downstream heat exchanger. Then, the cooled exhaust gases are compressed back up to the ambient pressure by one or more compressors. In this paper, a 2 litre, downsized, turbocharged SI engine is chosen as the primary cycle to identify the benefits of IBC system and to reveal the sensitivities to component efficiencies.

1. Introduction

With the extraordinary growth in the number of vehicles globally, an improvement in their energy efficiency has become paramount. It is also well known that 30-40% of the total energy released during the combustion process of a typical internal combustion engine remains in the exhaust gases, while only 12-30% of energy from fuels can be converted to mechanical work [1-3]. Generally, the energy carried by the exhaust gas consists of thermal energy, pressure energy, and kinetic energy. However, the kinetic energy could be neglected since it merely take small proportion of the total exhaust gas energy ($\sim 0.6\%$) at most engine operating conditions [4]. The thermal energy can be recycled via heat exchangers that utilize the heat to drive a separate bottoming cycle. Direct recovery methods are also available that aim to reclaim both thermal and pressure energy by expanding the exhaust gas over a turbine as in the case of a turbocharger or turbocompounding system.

The most widely used approach to directly recovering exhaust gas energy is the employment of a turbocharger composed of a compressor and a turbine. This exhaust-gas energy-recovery device mainly aims to reclaim the pressure energy resulting from 'blowdown' at the end of the expansion stroke. The blowdown event refers to the pressure pulse in the exhaust that is formed from the remaining pressure after combustion that is suddenly released when the engine exhaust valve is opened [5]. This exhaust pressure pulse is able to drive the turbocharger turbine to produce the rotational energy that is transmitted to the compressor by a shaft. With this shaft power, the compressor boosts the engine intake air charge so as to allow more fuel to be burnt and an increased engine power density. However, a turbocharger turbine only uses a relatively small proportion of the available exhaust gas energy since much is still contained as thermal potential. Moreover, in order to provide boost control, some of the available pressure energy is bypassed around the turbine using a wastegate valve. Thus, a significant amount of exhaust gas energy is available for a wasted heat recovery (WHR) system conceived as bottoming cycle and many efforts have been concentrated on the development of recovery devices that are cost effective and efficient [6].

One of the commercialized solutions for WHR is the turbo-compounding system which employs a simple power turbine after the turbocharger to further expand the exhaust gas for energy recovery. The exhaust gas energy recovered by the additional turbine produces shaft work which is either added to the engine drive directly or utilized to generate electrical power, respectively, referred to as mechanical and electrical turbocompounding. Many studies have revealed that turbocompounding approaches can contribute to the improvement of engine fuel consumption [7-10]. However, the challenges of gearing to the engine or coupling to a high speed electric machine have hinder the adoption for smaller displacement automotive applications [11]. More importantly, its ability to recover exhaust energy is limited by the pressure available in the exhaust. That is, the maximum expansion over the power turbine is from the blowdown pressure to atmospheric pressure. Moreover, if the power turbine is sized such that an additional back pressure is created in the exhaust system, the level of working pressure in the bottoming cycle can significantly influence the scavenging, pumping loss and fuel consumption of the engine. For these reasons, a modification of the turbo-compounding system with a downstream heat exchanger and compressor, termed as the inverted Brayton cycle (IBC) [12], has been proposed as shown in Figure 1.1.

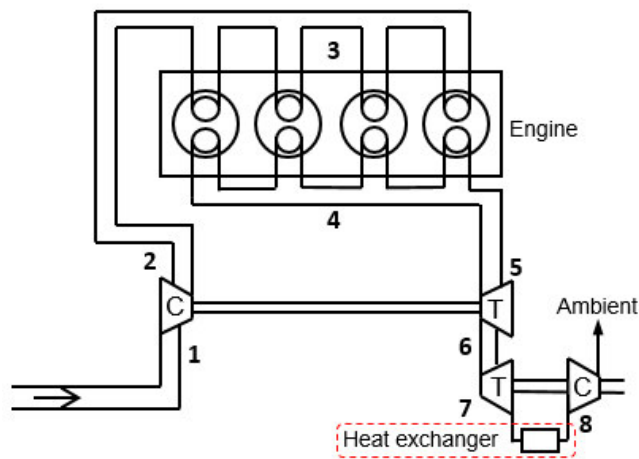


Figure 1.1: Schematic of the turbocharged engine with a single-stage IBC

The installation of the compressor allows the exhaust gases to be expanded below atmospheric pressure in the turbine, thereby increasing the potential to recover thermal energy from the exhaust gases. The heat exchanger implemented between the turbine and compressor is to lower the exhaust gases prior to the compression process. Since the role of this heat exchanger is to reject as much heat as possible, a liquid coolant loop with inexpensive materials potentially offers a relatively light-weight, cost-effective solution. In addition, although the IBC system is installed immediately downstream of the upper cycle and utilizes the exhaust gas as the operating fluid, it is still possible to leave the upper cycle unaffected by adjusting its working pressure. It is also useful to note that this type of bottoming cycle has been introduced to other heat engines such as gas turbines - commonly dubbed the 'mirror gas turbine'. The first bench test of an IBC was performed by Fujii et al. [13] and revealed the influence of the inlet temperature on the IBC performance. By analysing a calibrated thermodynamic model this work showed that the IBC capability to recover heat is significantly affected by the IBC turbomachinery efficiency, inlet temperature, and the number of the compression stages. Agnew et al. [14] has presented an optimization study of the mirror gas turbine by varying the upper cycle pressure ratio, the expansion pressure of the bottom cycle and the bottom cycle inlet pressure. The maximum specific work output and efficiency of the mirror gas turbine could be obtained when the inlet pressure to the bottom cycle is above atmospheric pressure. Kaneko [15] investigated multi-stage IBC constructed from an expander followed by multiple heat exchangers and compressors. The results show that the improved system performance could be expected by an increase in the number of compression stages.

As far as authors' knowledge, a theoretical investigation of the inverted Brayton cycle applied to a piston engine as an exhaust-gas heat-recovery system has only been performed by Bailey in 1985 [16]. There are also two other bottoming WHR cycles presented in his paper - the Rankin cycle and the pressurized Brayton cycle. Both of them are integrated with an adiabatic-turbocompound high-power diesel engine model to identify their benefits. The results indicated that, in terms of engine rated specific fuel consumption, all three alternative power bottoming WHR cycles offer a significant improvement over the turbocompound diesel baseline. More specifically, the inverted and pressurized Brayton cycles delivered approximately half of the improvement in system thermal efficiency compared the Rankin bottoming cycle. However, given that many of the proposed organic Rankine systems tend to be complex, costly and on

occasion, toxic, it seems logical to consider much simpler air Brayton systems for automotive heat recovery. It should be noted that a recent study offers a performance comparison of the pressurized and inverted Brayton cycles as bottoming heat-recovery thermodynamic cycles and shows that the IBC seems to offer comparatively better results in terms of the primary energy saving index [17].

In this paper, a thermodynamic model of the inverted Brayton cycle is presented to study heat recovery from a validated 2 litre downsized turbocharged SI engine. The 1-D model of the base engine has been built and simulated in steady state using GT-Suite® (version 7.0) software [18]. This model has been correlated to test bench data in order to improve the accuracy of the predicted results. In the first section, the temperature, pressure and mass flow rate of the exhaust gas at the turbocharger turbine outlet in the baseline 1D engine model are regarded as the inlet boundary condition of the IBC thermodynamic model in order to identify maximum performance improvement of the baseline engine at different operating conditions. Following this analysis, a combined GT-Suite 1-D model of the baseline engine and IBC system was built and analysed with consideration of the effect of working pressure in IBC system.

2. Principle of Inverted Brayton Cycle

The turbocharged engine with the single-stage IBC system and the corresponding temperature-entropy diagram are shown in Figure 2.1 and 2.2, respectively. In Figure 2.2, the subscript 's' denotes an ideal state at the actual ending pressure of each process but at the same entropy value as the beginning which describes idealized processes. The IBC is represented by the power cycle $6 \rightarrow 7 \rightarrow 8 \rightarrow 9$, consisting of the following processes:

- i) The exhaust gas steam expanded in the turbocharged turbine is *further* expanded in the IBC turbine (T) section to below ambient pressure. The mechanical power produced during sub-atmospheric expansion is partially utilized to supply the compression work and overcome mechanical losses of the turbomachinery. The rest is converted into the electric power by an electricity generator connected to the IBC turbomachinery by a shaft.
- ii) The remaining heat in the depressurized exhaust gas is rejected by the downstream heat exchanger. The outlet temperature of the heat exchanger, which is determined by the temperature of the coolant and the effectiveness of the heat exchanger, influences the amount of energy recovered by IBC system. For same power consumption by the compressor, lower gas temperature at state 8 could increase the pressure ratio across the compressor due to resulting higher gas density. Thus, the back pressure at the turbine outlet is lower, thereby increasing the pressure gradient available for the turbine.
- iii) The cooled gases are re-compressed back up to the atmospheric pressure in the compressor section (C) and discharged to the ambient.

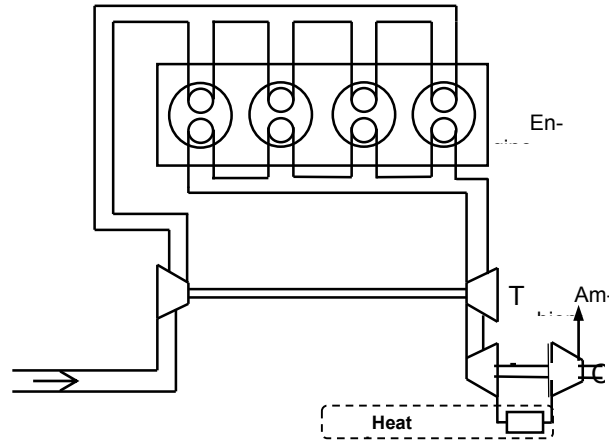


Figure 2.1: Schematic of the Turbocharged Engine with a single-stage IBC

Based on the previous thermal analysis of the single-stage IBC, there are three key design parameters: the IBC turbine pressure ratio, the IBC turbomachinery efficiency and the performance of the heat exchanger. However, the influence of the heat exchanger performance on the combined power system is not presented in this paper.

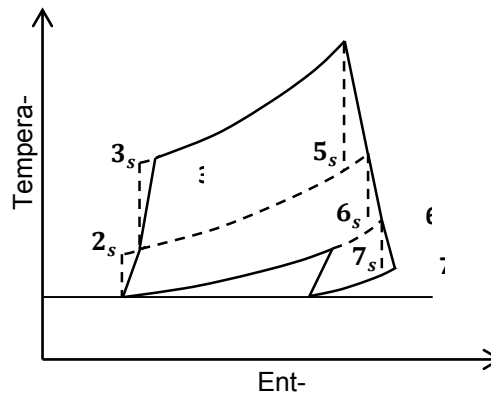


Figure 2.2: Temperature and Entropy Diagram of the Turbocharged Engine with a single-stage IBC

3. Model Description

3.1 IBC Thermodynamic Model

In the ideal cycle, the working fluid is assumed to behave as an ideal gas with constant specific heats. However, this assumption leads to overestimation of the system efficiency. The changes of specific heats due to the temperature has been considered in this paper. According to reference [19], for a temperature range from 300 K to 3500 K, the specific heat with constant pressure (C_p) can be expressed as a function of temperature as follows:

$$C_p(T) = 2.506 \times 10^{-11}T^2 + 1.454 \times 10^{-7}T^{1.5} - 4.246 \times 10^{-7}T + 3.162 \times 10^{-5}T^{0.5} + 1.3303 - 1.512 \times 10^{-4}T^{-1.5} + 3.063 \times 10^{-5}T^{-2} - 2.212 \times 10^{-7}T^{-3} \quad \text{Eq.3.1}$$

The gas constant of the working fluid is represented by R_g (0.281kJ/(kg-K)), which is defined as the difference between the specific heat at constant pressure and that at constant volume.

Any of reversible adiabatic processes can be broken up into a large number of infinitesimally-small processes with an infinitesimally-small change in temperature dT and pressure dP of the working fluid. Thus, the equation for the isentropic process in the turbine and compressor can be written as follows,

$$\frac{p^{(k-1)/k}}{T} = \frac{(p + dp)^{(k-1)/k}}{T + dT} \quad \text{Eq.3.2}$$

where k is the specific heat ratio and equals to C_p/C_v .

After taking natural logarithm of Eq. 3.2, one can be expressed as:

$$C_p(T) \ln (T_j/T_i) = R_g \ln (p_j/p_i) \quad \text{Eq.3.3}$$

where the temperature in the equation of C_p is $T = (T_j - T_i)/\ln(T_j/T_i)$.

Therefore, the equations for isentropic expansion process $6 \rightarrow 7_s$ and compression process $8 \rightarrow 9_s$ can be written as

$$C_p(T) \ln \frac{T_6}{T_{7s}} = R_g \ln r_t \quad \text{Eq.3.4}$$

$$C_p(T) \ln \frac{T_{9s}}{T_8} = R_g \ln r_c \quad \text{Eq.3.5}$$

where r_t and r_c is the expansion ratio of the turbine and the compression ratio of the compressor, respectively.

Since the outlet pressure of the bottoming compressor is assumed as 0.99 bar, the pressure ratio across the compression process, r_c , is determined by the turbine outlet pressure which can be expressed as $p_{low} = P_6/r_t$. The relation can written as: $r_c = 0.99/p_{low}$.

Both turbine and compressor are treated as open systems due to mass flow across their boundaries. Thus, the power extracted by the turbine is

$$W_t = h_6 - h_7 = (\dot{m} \times \eta_t) \int_{T_7}^{T_6} C_p(T) dT \quad \text{Eq.3.6}$$

where \dot{m} the mass flow rate of the exhaust gas and η_t is the isentropic efficiency of the turbine.

The work consumed by the compressor is

$$W_c = h_9 - h_8 = (\dot{m}/\eta_c) \int_{T_8}^{T_9} C_p(T) dT \quad \text{Eq.3.7}$$

where η_c is the isentropic efficiency of the compressor.

Therefore, the net work produced by IBC system is defined as the difference between the power produced by the turbine and that consumed by the compressor.

3.2 1-D Model of the Turbocharged Engine and IBC System

A 2L 4-cylinder turbocharged gasoline engine integrating with IBC system is developed in GT-Suite® software, shown in Figure 3.1. The baseline engine model in this paper has been built based on the actual engine geometry and validated with the test bench data in order to improve the accuracy of the predicted results [20-24], then updated according to the IBC configuration. Boundary conditions at system inlet and outlet were fixed as the parameters of standard atmospheric state – the pressure of 0.99 bar and temperature of 298 K. The SI Wiebe combustion sub-model was employed to describe the heat release during combustion. The S-shaped Wiebe function associated with this combustion model is empirical constructed and able to define combustion profile approximately but quite accurately [25]. The other boundary conditions, such as mechanical friction loss, combustion efficiency, flow coefficient of intake and exhaust valve, were calibrated by the test data of this gasoline engine. The valve timing, cam profiles and profile control terminate value for the SI Wiebe combustion model have been fixed throughout all simulations to ensure the predicted effect on the engine performance was due to IBC only.

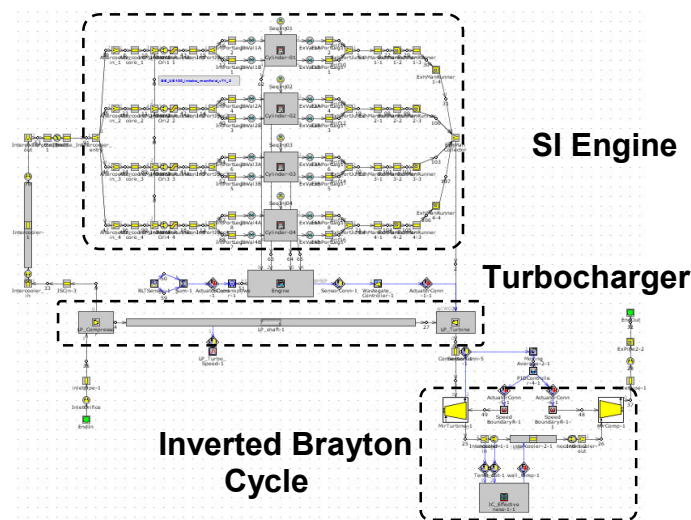


Figure 3.1: Numerical Model of the Combined System in GT-Power

The efficiency of electric generator is considered to be fixed at 95%. For the sake of simplicity, 95% power retrieved by the bottoming cycle was transferred directly to the engine by a GT-power module which can add energy to any connected object by effectively providing a speed-dependent torque.

In order to perform the 1-D simulation, the characteristic map for the IBC turbine is built by optimizing the attribute 'Mass Multiplier' within the GT-Suite turbine module. The attribute 'Mass Multiplier' is used to scale the reference map mass flow rate. In this

case, the reference map is the real characteristic map for the turbocharged turbine in the primary cycle. The GT-power code calculates the instantaneous pressure ratio and speed and looks up the mass flow rate in the map. The rate is then multiplied by the value of that attribute before it is imposed. Similarly, the characteristic map of the IBC compressor is developed by optimizing a 'Mass Multiplier' based on the real characteristic map for the turbocharged compressor. The final optimized variable is the torque applied on the shaft of IBC turbomachinery, that is, the power extraction. Thus, three variables need to be optimized to deliver the maximum performance improvement of the baseline engine. Given a multi-variable optimization problem presented in this case, a genetic algorithm (GA) was employed as the optimization approach in this paper since it has the capability to mimic the process of natural evolution and is thus considered to be one of the most useful approaches to solve this kind of problem [26].

Although ideally the turbocharging system should be re-matched to deliver the optimal system performance due to the changes of the downstream configuration, the original turbocharging system was unchanged to ensure that all the data generated is related to the proposed heat-recovery cycle.

The heat exchanger was built as multiple identical pipes in GT-power. The effectiveness of the heat exchanger is mainly influenced by the heat capacity of the two kinds of working fluids when the design parameters of the heat exchanger are fixed. That is, the effectiveness might vary with the operating condition of two working mediums, such as the mass flow rate, temperature, and working pressure. Nevertheless, the heat exchanger effectiveness in this study was fixed as 0.85 by varying the wall temperature, in order to evaluate the systematic performance at various heat exchanger performances. The temperature of coolant fluid is assumed as 300K.

4. Result and Discussion

4.1 IBC Thermodynamic Model

In this section, the pressure ratio of the IBC turbine is optimized to deliver the maximum power recovered by IBC system at different engine operating points.

The outlet boundary conditions (the temperature, pressure and mass flow rate of the exhaust gas available from 1-D GT-Suite baseline engine model) is introduced as the inlet boundary conditions of the IBC thermodynamic model. In order to perform this study the following assumptions have been made:

- The exhaust back pressure on the compressor outlet is taken as 0.99 bar
- A range of turbomachinery efficiencies are selected between 0.65 – 0.8 for both the compressor and turbine. These are considered here as a sensitivity study only. The authors recognize that the top end of this range may be difficult to achieve in practice, but the wish to show the trend with rising component efficiencies.
- The temperature of the coolant in the IBC heat exchanger is assumed to be 300 K. The pressure loss caused by the heat exchanger is not considered here. It should be noted that the pressure loss across the heat exchanger can lower the inlet pressure of the IBC compressor, thereby increasing the power consumed by the IBC compressor to pressurize the exhaust gas from sub-atmospheric pressure to the ambient. Therefore, the pressure loss across the heat exchanger will deteriorate the performance of IBC.

Figure 4.1 shows that changing the vehicle speed and engine loads causes the exhaust gas temperature at the turbocharger turbine outlet to vary from $\sim 850\text{K}$ to $\sim 1220\text{K}$. The maximum outlet pressure of the turbocharger turbine presented in Figure 4.1 is above atmospheric pressure – that is, up to 1.55 bar. This is due to a module placed downstream of the baseline engine model in order to represent the influence of the after-treatment devices. As the IBC unit is installed immediately downstream of the turbocharger turbine, the outlet condition of the turbocharger turbine is considered as the inlet condition of the IBC thermodynamic model. The IBC turbine pressure ratio has been optimized at each engine operating point to deliver the maximum recovered power. Figures 4.2 and 4.3 show BSFC improvement potential from the IBC at different IBC turbomachinery efficiencies (turbine / compressor) and the corresponding optimized IBC turbine pressure ratio, respectively.

It can be seen in Figure 4.2 that the maximum BSFC improvement of approximately 13% is delivered by IBC with the turbomachinery efficiency of 0.8/0.8 (turbine and compressor, respectively) when the engine speed is 6500 rpm at full load condition. The amount of the power produced by the IBC is significantly deteriorated by the reduction of the turbomachinery efficiency, thereby decreasing the BSFC improvement. The maximum BSFC improvement with the turbine/compressor efficiency of 0.6/0.6 is 7.1%. It should be noted that the IBC power output can be negative at low engine speed and part-loads, depending on the IBC turbomachinery efficiency. The range of the engine operating points where there is no net work produced by IBC system increases with decreasing IBC turbomachinery efficiency.

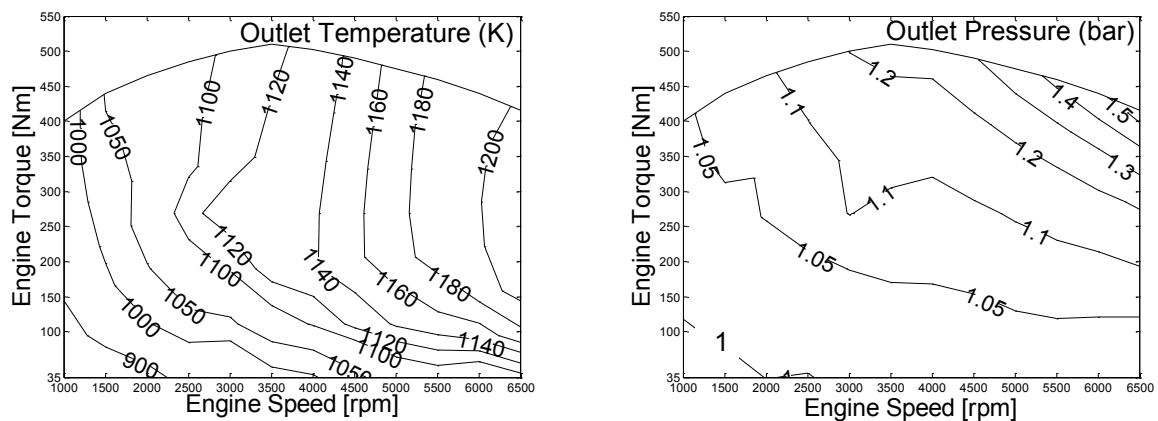
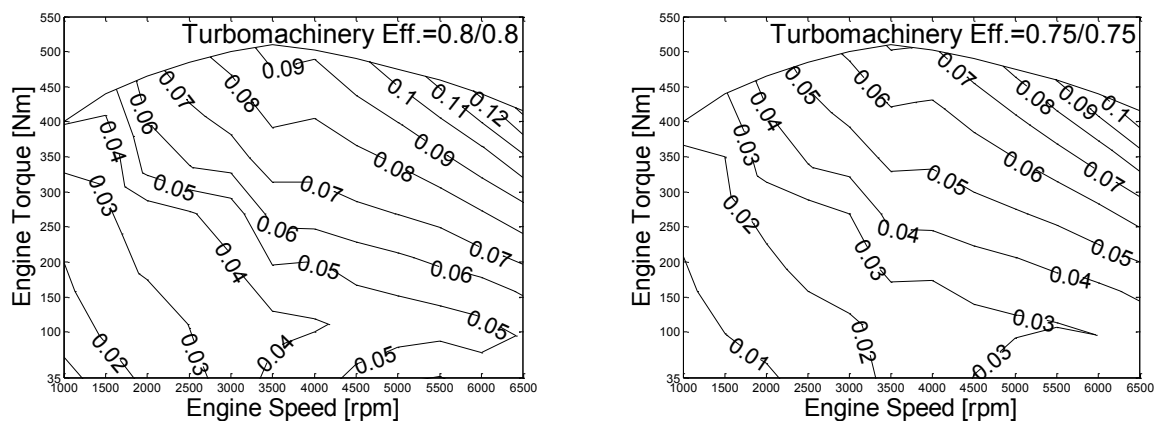


Figure 4.1: The temperature (left) and pressure (right) of the exhaust gas at the turbocharger turbine outlet



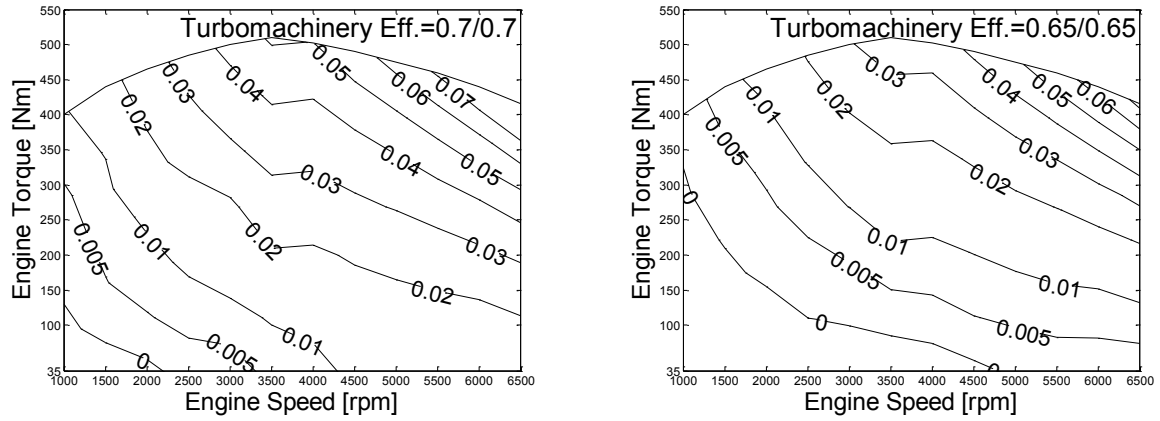


Figure 4.2: BSFC improvement due to the employment of IBC bottoming cycle

4.2 1-D Model of Combined System

Copeland et al. [27] showed that the increasing of IBC inlet pressure can contribute to the improvement of IBC performance. Therefore, the BSFC improvement shown in Figure 4.2 could be enlarged by increasing IBC inlet pressure. However, increasing IBC inlet pressure leads to a higher back pressure of the engine which can negatively influence its performance. Hence, a system compromise is required to select the optimum IBC inlet pressure.

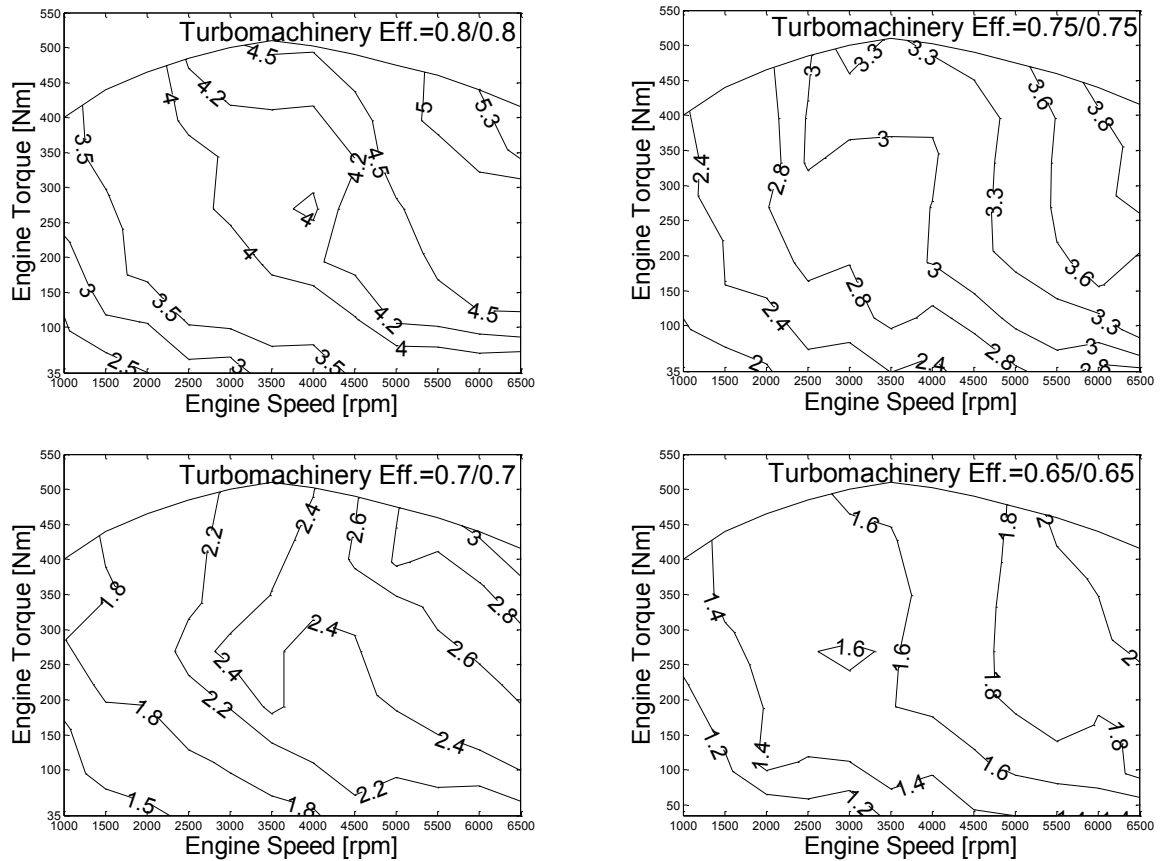


Figure 4.3: The optimized IBC turbine pressure ratio in the engine map

In order to take into account the influences of the IBC working pressure, a combined system of the baseline engine and IBC bottoming cycle has been simulated using GT-Suite® (version 7.0) software. There are 3 cases considered in this study. In case 1, the performance of the turbocharged engine with IBC is evaluated with IBC turbine and compressor efficiencies of 0.85 and 0.8 respectively, while only 0.65 and 0.6 in case 2. Case 3 is to present the performance investigation of the original turbocharged engine (without the IBC) as the reference case.

The optimisation results are shown in Figure 4.4. The solid lines indicate the engine BSFC of three cases, while the dash lines represent the corresponding BSFC improvement in case 1 and 2 respectively. It is obvious in from Figure 4.4 that including an IBC mounting at the downstream of the turbocharger can improve the system performance at any chosen value of work output where the bottoming turbine and compressor isentropic efficiency is 0.85 and 0.8 respectively. With increasing power output, the value of BSFC improvement peaks at 12 % at a BMEP of 34 bar, then decreases at lower powers. However, when the IBC turbomachinery efficiency decreases to 0.65/0.6 for the turbine and compressor respectively, the maximum BSFC improvement of 4 % emerges at a BMEP of 30 bar. Similar to the results of IBC thermodynamic model, the range of engine powers where the IBC system output is positive increases with higher IBC turbomachinery efficiencies.

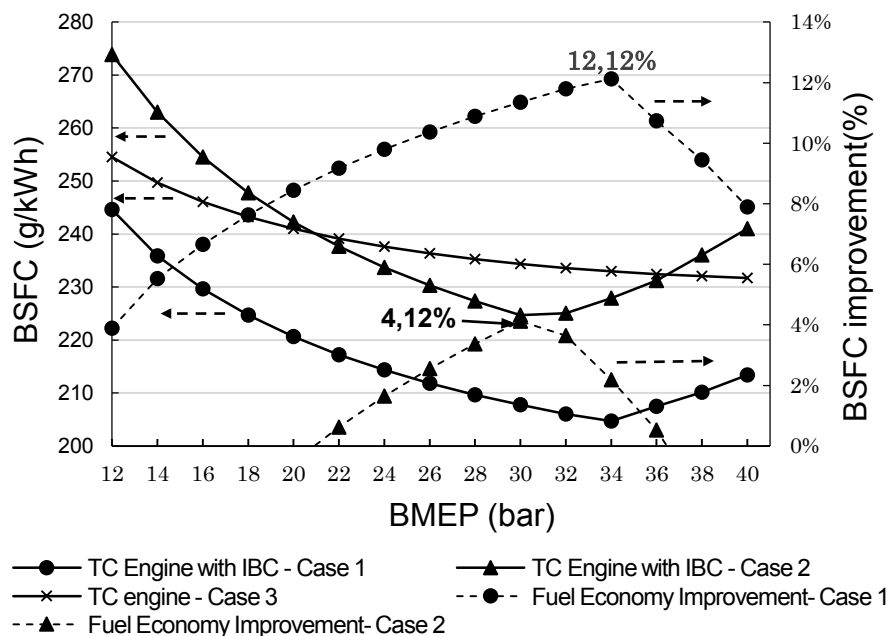


Figure 4.4: BSFC versus BMEP at different IBC turbomachinery efficiency

Figure 4.5 shows the optimal IBC inlet pressure with the various system power outputs and two levels of IBC turbomachinery efficiencies. Both case 1 and 2 demonstrates that the optimal IBC inlet pressure increases as engine BMEP rises until the IBC turbine wastegate is opened leading to a turbocharger outlet pressure that remains stable at approximately 1.74 bar. Additionally, the IBC with lower turbomachinery efficiency increases the optimum back pressure on the topping cycle. This indicates that lower IBC component performance not only limits the energy-recovery capabilities of the IBC but could also deteriorate the topping cycle performance due to an increase of the back pressure.

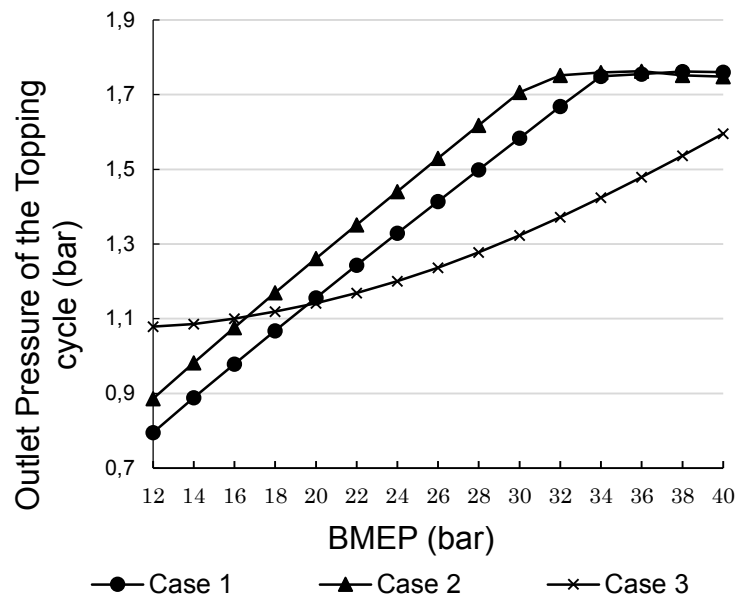


Figure 4.5: Comparison of three cases in terms of outlet pressure of the primary cycle

5. Conclusion

The IBC bottoming WHR system can be thought of as an extension to a turbocompounding system for waste heat recovery. However, the limitation in the expansion ratio available for the power turbine in the turbocompounding system is removed by the employing a downstream heat exchanger and a compressor. The heat exchanger is utilized to remove the residual heat from the depressurized exhaust gas prior to compression back up to atmospheric pressure. The role of the compressor after the heat exchanger is to increase the available expansion ratio across the IBC turbine thereby increasing the power recovered by the bottoming WHR system. This is a true thermal energy recovery cycle since it does not require pressure to be present in the exhaust, albeit unlike other bottoming cycles, it can utilize residual pressure to boost its thermodynamic efficiency.

In order to reveal the potential performance of the IBC system to recover residual heat from the exhaust gas, an IBC thermodynamic model and a 1-D GT-Suite model of a 2 litre downsized turbocharged SI engine has been analysed at different engine operating conditions. Two approaches were taken in this work. First, the exhaust boundary conditions from the 1D GT-Power turbocharged engine model were passed to a simple thermodynamic model of the Inverted Brayton Cycle and the improvement in total system BSFC was derived as a function of speed and load. Secondly, a full 1D model of the engine and IBC system was constructed and an optimization procedure implemented to set the ideal size of the turbomachinery.

The simulation of IBC thermodynamic model revealed that the IBC system can deliver a reasonable BSFC improvement over whole engine operating up to a maximum value of 13% at 6500 rpm under full load conditions with IBC turbomachinery efficiencies of 80%. Nevertheless, the IBC performance can be negatively affected by a reduction of the turbomachinery efficiency such that at some part load engine operating points, the net IBC power output is negative. Therefore, further work will need to consider the benefits of the IBC system based on the real world driving cycle.

The combined 1D model of the baseline engine and IBC system was developed in GT-Suite® software to take into account the interaction between the baseline engine and IBC system. The engine speed was fixed at 4500 rpm. The results showed that a peak BSFC improvement of 12.2% due to the IBC system resulted from an engine BMEP of 34 bar with turbomachinery efficiencies of 0.85/0.8 for turbine and compressor respectively. It should be noted that although adopting an IBC as a bottoming heat-recovery cycle does not require pressure from the topping power plant to operate, this research demonstrates that a small increase in the back pressure of the primary cycle is to be expected if the system is optimized for BSFC. This outcome results from the optimal trade-off between the heat recovered power and the resulting power loss due to pumping work.

In conclusion, a reasonable improvement of the engine BSFC can be delivered by the employment of IBC system as a bottoming WHR system. Further study is planned to match radial turbomachinery for IBC system based on the real world driving cycle and investigate the effects of the heat exchanger performance.

References

- [1] Yu, C. and K. Chau, *Thermoelectric automotive waste heat energy recovery using maximum power point tracking*. Energy Conversion and Management, 2009. **50**(6): p. 1506-1512.
- [2] Stabler, F. *Automotive applications of high efficiency thermoelectrics*. in *Proceedings of DARPA/ONR/DOE High Efficiency Thermoelectric Workshop*. 2002.
- [3] Taylor, C., *Automobile engine tribology—design considerations for efficiency and durability*. Wear, 1998. **221**(1): p. 1-8.
- [4] Liu, J., et al., *Characteristics of engine exhaust gas energy flow*. Journal of Central South University (Science and Technology), 2011. **42**(11): p. 3370-3376.
- [5] Kuo, P.S., *Cylinder pressure in a spark-ignition engine: a computational model*. J Undergrad Sci, 1996. **3**: p. 141-145.
- [6] Liu, J., et al., *Comparison and analysis of engine exhaust gas energy recovery potential through various bottom cycles*. Applied Thermal Engineering, 2013. **50**(1): p. 1219-1234.
- [7] Algrain, M. and U. Hopmann. *Diesel engine waste heat recovery utilizing electric turbocompound technology*. in *DEER Conf., Newport, Rhode Island*. 2003.
- [8] Hopman, U. and R.W. Kruiswyk, *Diesel engine waste heat recovery utilizing electric turbocompound technology*. 2005, Caterpillar Inc. PO Box 1875, Peoria, IL 61656-1875.
- [9] Tennant, D. and B. Walsham, *The turbocompound diesel engine*. 1989, SAE Technical Paper.
- [10] Brands, M.C., J.R. Werner, and J.L. Hoehne, *Vehicle testing of Cummins turbocompound diesel engine*. 1980.
- [11] Zhanga, K., et al., *Method of Turbocharger Emulation on Engine Test and Application to Turbocompound System Opti-misation*.

- [12] Wilson, D.G., *The design of high-efficiency turbomachinery and gas turbines*. 1984: The MIT Press.
- [13] Fujii, S., et al., *Mirror gas turbines: A newly proposed method of exhaust heat recovery*. Journal of engineering for gas turbines and power, 2001. **123**(3): p. 481-486.
- [14] Agnew, B., et al., *Simulation of combined Brayton and inverse Brayton cycles*. Applied thermal engineering, 2003. **23**(8): p. 953-963.
- [15] Kaneko, K.i., et al., *Utilization of the cryogenic exergy of LNG by a mirror gas-turbine*. applied Energy, 2004. **79**(4): p. 355-369.
- [16] Bailey, M.M., *Comparative evaluation of three alternative power cycles for waste heat recovery from the exhaust of adiabatic diesel engines*. 1985, National Aeronautics and Space Administration, Cleveland, OH (USA). Lewis Research Center.
- [17] Bhargava, R.K., M. Bianchi, and A. De Pascale. *Gas turbine bottoming cycles for cogenerative applications: Comparison of different heat recovery cycle solutions*. in *ASME 2011 Turbo Expo: Turbine Technical Conference and Exposition*. 2011. American Society of Mechanical Engineers.
- [18] GT-Suite. *Version 7.0 Build 3*. Gamma Technologies, Inc. ; Available from: www.gitsoft.com.
- [19] Ge, Y., L. Chen, and F. Sun, *Finite-time thermodynamic modelling and analysis of an irreversible Otto-cycle*. Applied Energy, 2008. **85**(7): p. 618-624.
- [20] Hu, B., et al., *Simulation Study of Divided Exhaust Period for a Regulated Two-stage Downsized SI Engine*. 2014, SAE Technical Paper.
- [21] Copeland, C.D., et al., *Simulation of Exhaust Gas Residuals in a Turbocharged, Spark Ignition Engine*. 2013, SAE Technical Paper.
- [22] Carey, C., et al. *Extreme engine downsizing*. in *International conference on innovations in fuel economy and sustainable road transport*. 2011.
- [23] Copeland, C., et al. *Boost system selection for a heavily downsized spark ignition prototype engine*. in *10th International Conference on Turbochargers and Turbocharging, London, UK, 15th-16th May*. 2012.
- [24] Turner, J., et al., *Ultra Boost for Economy: Extending the Limits of Extreme Engine Downsizing*. 2014, SAE Technical Paper.
- [25] Gilani, R., *Engine Simulation Model for a Formula SAE Race Car*, in *Engineering Sciences and Mathematics*. 2012, Luleå University of Technology. p. 96.
- [26] Hu, B., et al., *1-D Simulation Study of Divided Exhaust Period for a Highly Downsized Turbocharged SI Engine-Scavenge Valve Optimization*. 2014, SAE Technical Paper.
- [27] Copeland, C. and Chen, Z., 2015. Forthcoming. The Benefits of an Inverted Brayton Cycle Bottoming Cycle as an Alternative to Turbo-Compounding. In: Proceedings of the ASME Turbo Expo. American Society of Mechanical Engineers (ASME).

The Authors

Dr. Colin Copeland, University of Bath, Bath, United Kingdom

Msc. Zhihang Chen, University of Bath, Bath, United Kingdom

Licence:

This document is licensed under the Creative Commons Attribution 3.0 DE License (CC-BY 3.0 DE): <http://creativecommons.org/licenses/by/3.0/de/>

Using 1D simulations to optimize a supercharger for a twin charged DI gasoline engine

Ragnar Burenius

Abstract

With the launch of the new XC90 Volvo Car Corporation stretches the performance of its Drive-E engine family even further. The range topping T6 derivative now achieves no less than 235kW from the four cylinder, 2.0 litre gasoline engine. To combine this high specific power with excellent drivability careful optimization of the boosting system was required. The engine is twin charged, combining the usual turbocharger with a roots type supercharger supporting at low-to-mid engine speeds. This type of installations puts different demands on the roots blower than on a supercharged-only engine. Thus an important part of the development focused on optimizing the supercharger and its installation for this application.

In order to get a better theoretical understanding of the supercharger and its inner gas dynamics a 1D gas exchange model was developed in GT-Power. This paper focuses on the development of this simulation model and its usage to optimize the port timing of the supercharger. Given the utilization of the supercharger in the twin charged setup the intention was to improve its efficiency at lower pressure ratios. Based on the results from the simulation model it was indicated favourable to implement slots in the outlet of the supercharger to achieve the desired targets. This changed the behaviour of the outlet phase of the supercharger cycle and moved the point of peak efficiency to a lower pressure ratio. When later implementing the outlet slots in hardware this conclusion was confirmed in testing, thus verifying the simulation model.

1. Introduction

The launch of the Drive-E family of engines in 2013 marked a transition for Volvo Car Corporation; moving on from the diverse powertrain line-up of the past consisting of four cylinders, five cylinders, straight sixes and V8's [1]. The replacement VEA family of engines all share the same four cylinder platform and allowed the newly developed Scalable Product Architecture (SPA) vehicle platform to be tailored for this commonalized powertrain line-up. Not having to reserve the packaging space for five-, six- or eight-cylinder engines in the engine bay meant several advantages. This enabled a platform design with short front vehicle overhang, enhanced safety performance and advanced front-wheel suspension. A lower powertrain weight also allows for a more optimized vehicle weight distribution.

1.1 The twin charged concept

The move to a common engine family with a displacement of 2.0 litres in combination with the request for more peak power from the top-of-the range engines means a significant increase in specific output power for these derivatives. In order to deliver this with maintained drivability and low-end torque special attention had to be put on the boosting systems for these engines. For the range-topping, gasoline, T6 variant this means a concept where the turbocharger is complimented by a belt driven supercharger, with the objective of eliminating turbo lag and giving a low-end speed behaviour similar to that of competitor six and eight cylinder engines. The supercharger is mounted upstream of the turbocharger and driven via an electromechanical clutch, which enables disengagement and thus improved fuel economy when driving at steady state part load.

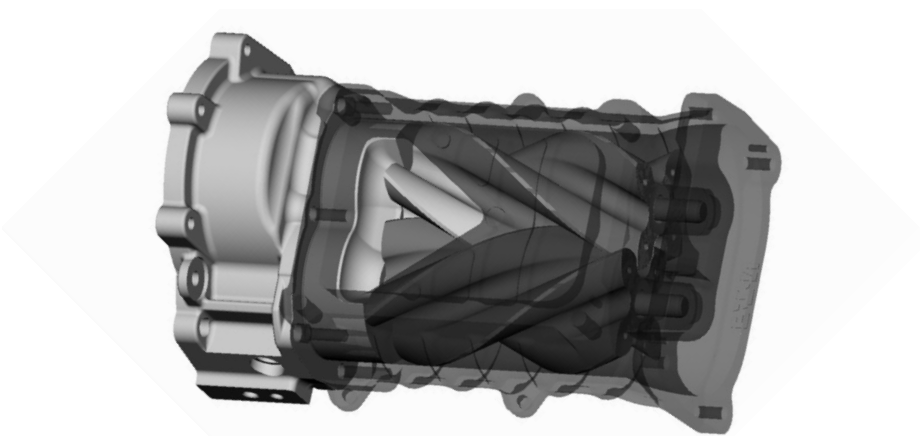


Figure 1: The helix type supercharger used for the twin charged concept

The supercharger itself, illustrated in Figure 1, is a roots type blower [2]. It features an axial inlet feeding two four-lobe rotors. The rotors are twisted to a helix angle, giving a gradual meshing event along the axis of the supercharger during rotation. The outlet port of the supercharger is radial and placed at the rear portion of the supercharger.

1.2 Supercharger utilization

The twin charged arrangement allows for the supercharger to be matched in a way where it is only used at low-to-mid engine speeds, thus allowing for using a smaller and lighter supercharger than what would otherwise be required to support the full engine speed range (Figure 2).

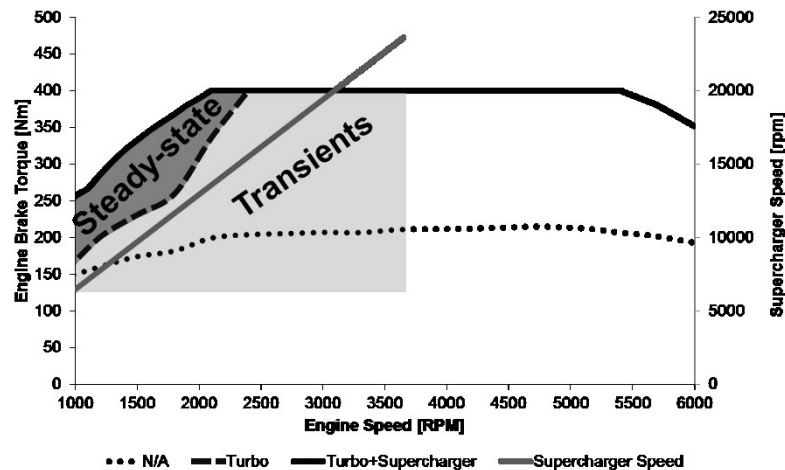


Figure 2: Operating strategy for the roots type supercharger

As can be understood from Figure 2 the supercharger is primarily used during transient operation and only at the lowest engine speeds it is used in steady-state. The corresponding operating line in the supercharger performance map is shown in Figure 3.

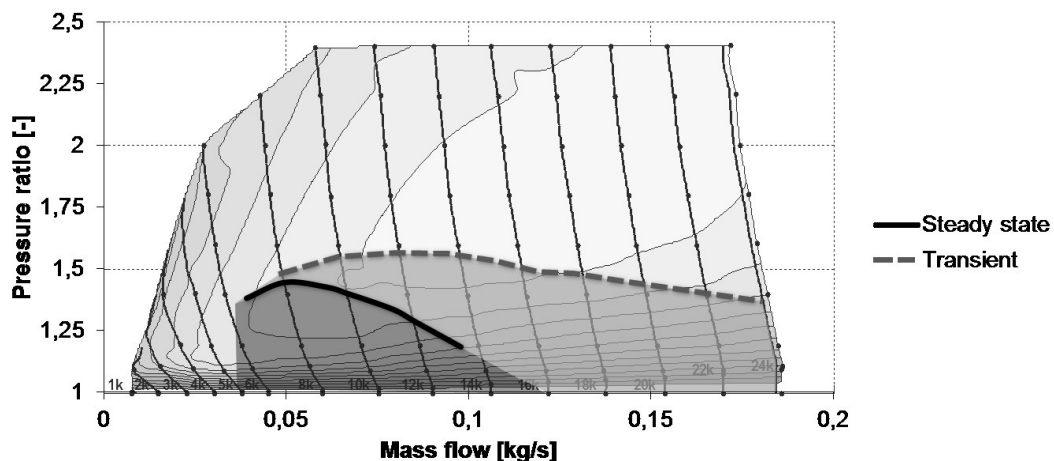


Figure 3: Performance map for the roots supercharger

The figure shows the maximum pressure ratio and mass flow for a typical steady-state case as well as for load-step transients. This illustrates that the supercharger very seldom is used above a pressure ratio of 1.5 and its operation at high mass flow and rotational speed is only during transients. When considering the illustrated islands of iso-efficiency of a standard supercharger it is obvious that the typical operating range of this application is outside the locus of peak efficiency of the standard device.

1.3 Background to the study

The conclusion from what is illustrated in Figure 3 raised the question if there was a simple way of optimizing the supercharger for the current application. Extensive series of iterative tests or complex 3D CFD simulations was considered as too time consuming given the current scope. Based on previous experience of using 1D CFD to study and understand transient gas exchange events it was thus decided to attempt to use this approach to see if it was possible to optimize the supercharger to the application.

At the time no experience of this simulation approach was found amongst published authors. Since the execution of this project others have however published related studies [3].

2. Methodology

In order to help getting a deeper understanding of the inner gas dynamics of the supercharger one wanted to create a simplified simulation model. Based on previous experience the decision was to do this in the 1D simulation tool GT-Power. However, the somewhat unorthodox geometry of the helix rotor type supercharger required new methods in terms of discretization. All of this geometrical analysis was automated using a script in Matlab™, implemented in way so that simple parameterization of key parameters could be performed.

2.1 Discretization of the rotors

The basis for the discretization of the rotors is a geometrical analysis. Being helix extrusions their full 3D geometry can be derived from the 2D geometry of the rotor cross section. When rotating; the meshing of the rotors as well as their relations to the housing creates a set of chambers, or passages. By making a 2D analysis of this meshing event a scheme was determined for describing the geometrical relationship for these rotor chambers as function of rotational angle, see Figure 4.

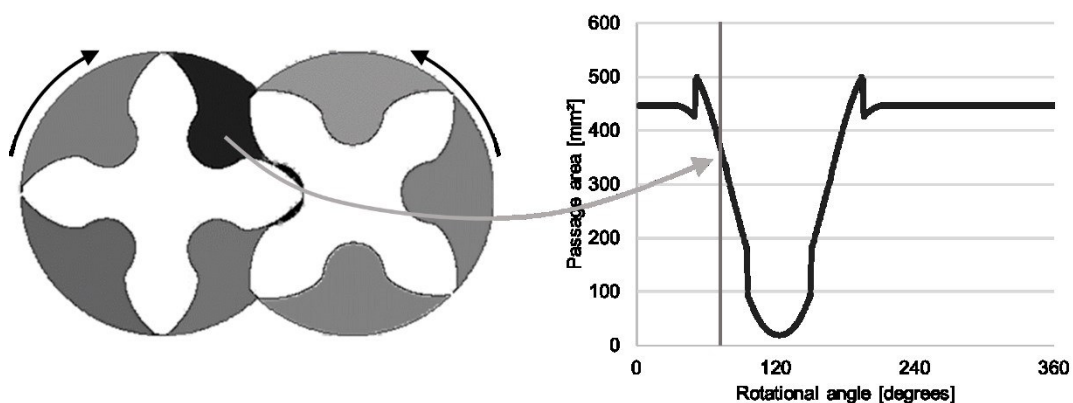


Figure 4: Illustration of the 2D scheme used to describe the geometry

One rotor passage is here marked by a darker colour and the graph to the right illustrates how the size of this area change with rotational angle. In order to do this one needs to define the boundaries between the different passages as the rotors mesh. A special scheme was created to determine the points where the distance is the smallest

between the edge of the two rotors and/or the housing. Combining this with a set of boundary conditions to define the split between the left and right rotors resulted in the relationships shown in Figure 4, describing how the rotor passage cross sections change in area as function of rotational angle. In addition to this the 2D analysis also gives the lengths of the interface boundaries where the eight passages communicate with each other.

In order to transfer this 2D analysis to the full 3D geometry the results from the 2D analysis are integrated over the length of the supercharger, taking the helix angle of the rotors in consideration. The cross sectional areas are thus integrated to volumes for the different rotor passages and the length of the interface boundaries to the areas of interface between these volumes.

2.2 Discretization of inlet and outlets

The intake port of this type of roots supercharger is found in the front of the supercharger, interfacing the rotors in the axial direction. Combining the 2D geometry of this intake port with the scheme for defining the rotor passages described above thus accounts for the rotor passage's interface to the inlet as function of rotational angle (see Figure 5).

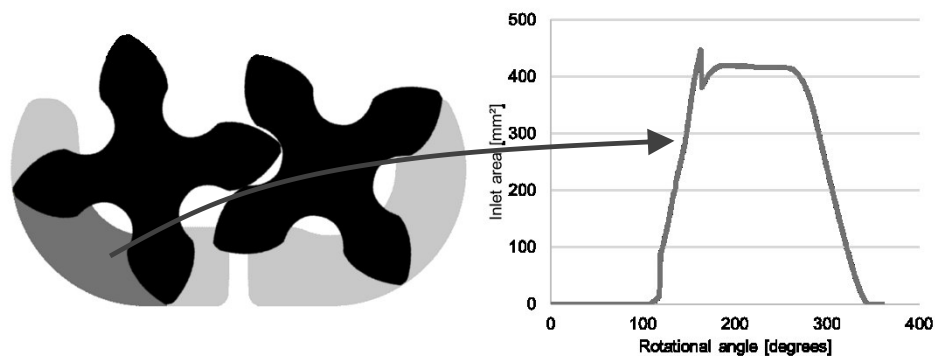


Figure 5: Illustration of the supercharger inlet port and the resulting inlet area for one rotor passage as function of rotor angle.

The outlet of the supercharger is in the radial direction and located at the rear part of the upper side of the unit (Figure 6). Combining the projected area of the supercharger outlet port with the position of the edge of the rotor lobe, deducted in the 2D analysis of the rotor cross section described in section 2.1, together with the rotor helix angle then allows for the calculation of the size of the outlet port as function of rotational angle. An important aspect here is also to keep track of the axial position of the outlet port, as this changes over the rotor event due to the V-shaped nature of this port.

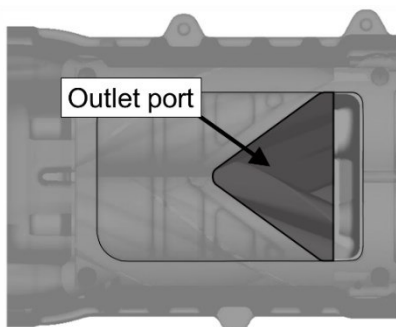


Figure 6: Illustration of the supercharger outlet port

2.3 Implementation in GT-Power

The above described scheme results in a description of the supercharger geometry as function of rotor angle and lengthwise position. In order to transfer this into GT-Power this has to be translated to discrete volumes and flow orifices. To be able to resolve different states along the length of the rotor it was decided to discretize the rotor in ten segments along its length. Given that this application of supercharger geometry features four lobes per rotor this means that the complete geometry of the rotors is resolved by 80 discrete flow-split volumes. Each passage segment volume is then connected to its adjacent surroundings through a set of six different orifices. The primary interfaces are those in the rotor axial direction, interacting with the upstream and downstream volumes of the same rotor passage. Secondly the volume interacts via two orifices to the two rotor passages of the other rotor that it meets during the meshing of the rotors. Thirdly it connects to the two adjacent passages of the same rotor through the leakage paths between the tips of the rotor and the wall of the housing. In total this means that the rotor pair is modeled as 80 discrete volumes connected through a network of 240 different orifices. In addition the model also includes the outlet of the supercharger, discretized as ten volumes along each rotor resulting in an additional 20 volumes each interfacing the four passage segment for one of the rotors at the given length coordinate. An overview of the resulting GT-Power implementation is shown in Figure 7.

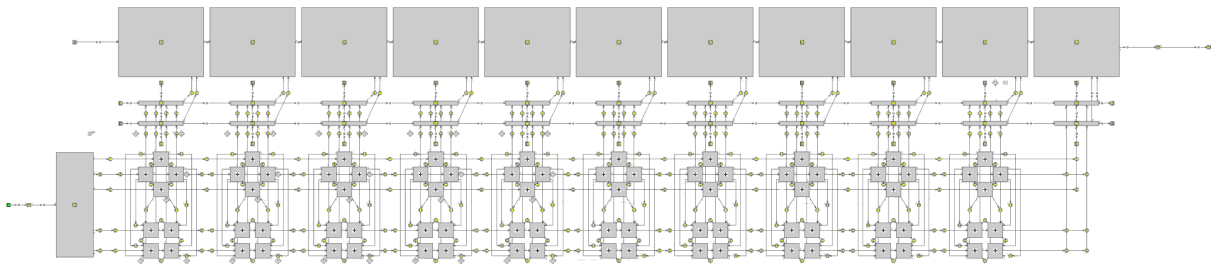


Figure 7: Overview of the GT-Power model with its 100+ volumes and 240+ orifices

This network of volumes and orifices is then fed with the data from the geometrical analysis described in sections 2.2 and 2.3, input as tables of volume and area as function of rotor angle. The dynamic gas exchange model is then created by varying the rotor angle as function of time.

Given that the areas deducted from the discretization scheme are nominal the GT-Power model also includes a set of parameters used to control the discharge coefficients for the different orifices. By varying these parameters the model could then be tuned to test data.

3. Results

3.1 Simulation of performance map

By running the 1D model at different ratios of inlet an outlet pressure boundaries and varying the rotational speed of the supercharger a performance map such as the one illustrated in Figure 8 can be generated.

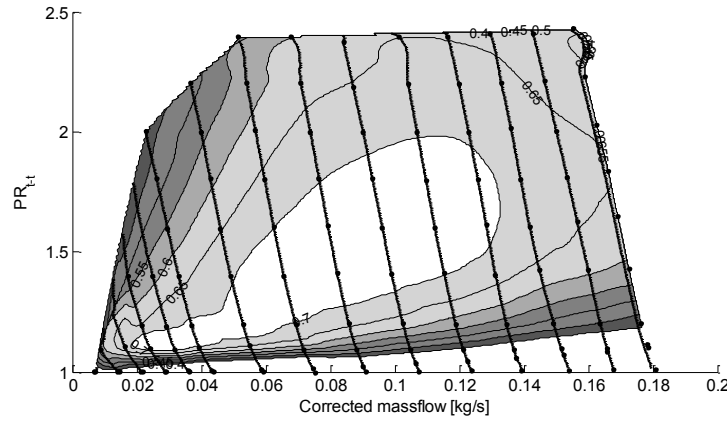


Figure 8: Calculated performance map for the supercharger.

In this figure the individual points of operation simulated are symbolized by dots. Through points of constant rotational speed thick lines has been drawn. The iso-contours illustrate fractions of isentropic efficiency, defined as in equation 1.

$$\eta_{isentropic} = \frac{T_{01} \times \left(\left(\frac{p_{02}}{p_{01}} \right)^{\frac{\kappa-1}{\kappa}} - 1 \right)}{(T_{02} - T_{01})} \quad (1)$$

The resulting map does have a good general agreement with published measured data for similar types of superchargers, such as the one illustrated in Figure 3. Its exact performance is very much dependent on the previously mentioned tuning parameters for internal leakages, inlet and outlet ports. When comparing to test one should also recognize that the 1D gas-exchange model doesn't consider heat transfer, neither internal or external, or frictional losses in the rotating assembly.

3.2 In-cycle analysis

An example of the in-cycle gas exchange interaction is shown in Figure 9, as function of rotor angle. To make the graph easier to interpret the data shown here is the calculated volume average for one passage, plotted during one passage event. This is defined as the time from when the passage volume is created at the front of the rotor during the meshing event all the way until it diminishes after the outlet event at the end of the rotor. Given the helix angle of the rotor such a passage event is longer than 360 degrees, as shown in the graph. Due to that this passage at times doesn't involve all ten volumes along the length of the rotor this has to be considered when calculating the volume average.

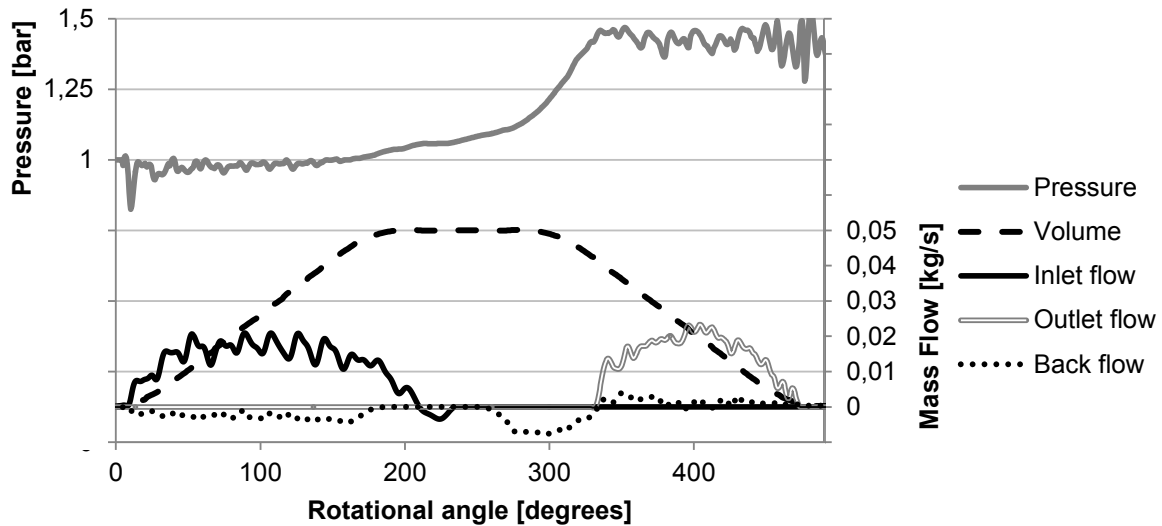


Figure 9: Illustration of the flow of the roots supercharger during one cycle

The dashed curve illustrates the total volume of the passage, starting from its creation at the rotor meshing at the inlet side of the SC, followed by a period of constant volume up to its diminishing at the rotor meshing during the exhaust phase. The black and double-grey curves illustrate the mass flow through the inlet and outlet ports respectively, and the dotted curve describes the mass flow interaction to adjacent rotor passages during the meshing of the rotors. The single grey line represents the average pressure in the passage. During the period of constant passage volume a slight increase in pressure occurs due to leakage from the upstream passage over the rotor tip. In the moment when the passage is in in-direct contact with the outlet volume through the rotor meshing a rapid increase in pressure can be detected, along with a significant back flow. During the primary outlet phase the pressure oscillates around the pressure of the outlet volume.

If analysing the 1D simulation results for a number of different points of operation one could notice that at for high rotational speed in combination low pressure ratios, the internal pressure of the supercharger is higher than the outlet pressure during the part of the cycle just before the opening of the outlet.

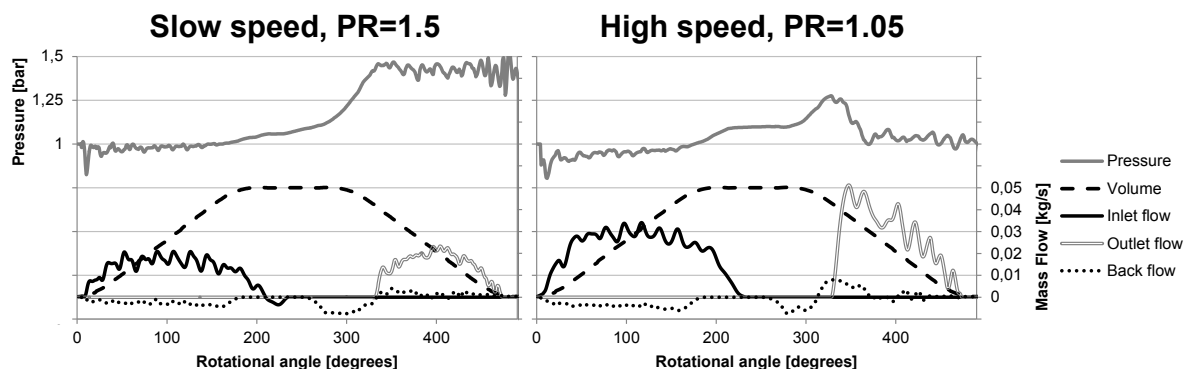


Figure 10: Comparison of the gas exchange for two different points of operation.

This is illustrated in Figure 10, where two different points of operations are compared. In the left hand graph the gas exchange for a point of operation at low rotational speed and semi-high pressure ratio is shown. Here one can see that the pressure in the passage is continuously increasing during the cycle due to the back flow leakage. Once the outlet port opens the pressure is then oscillating around that of the outlet volume downstream. For the right hand graph an entirely different point of operation is shown. The rotational speed is increased and the pressure ratio is just 1.05. What is evident here is that the pressure in the intermediate phase between the inlet and outlet phases in fact is higher than the pressure during the outlet phase, when the passage is in direct contact with the outlet. This can be explained by the timing of the outlet event compared to the volume of the passage. At roughly 300 degrees rotational angle the passage volume starts to decrease due to the meshing of the rotors. The passage is at this point not in direct contact with the outlet port, but only indirectly through the back flow from the neighbouring passage of the other rotor. Based on this the conclusion was made that the back flow passage for these points of operation is too small not to create internal throttling; which increases the pressure of the passage as this decreases in volume. Once the passage then gets in direct contact with the outlet port the pressure quickly decreases to the level of the outlet regime.

3.3 Implementation of outlet slots

Based on the intended range of operation for the supercharger (illustrated in Figure 3) and the analysis presented in the above section it was decided to investigate the possibility to improve the gas exchange of the supercharger at low pressure ratios by decreasing the internal throttling. A number of different geometrical implementations was discussed, and the option was to test the geometry shown in Figure 11.

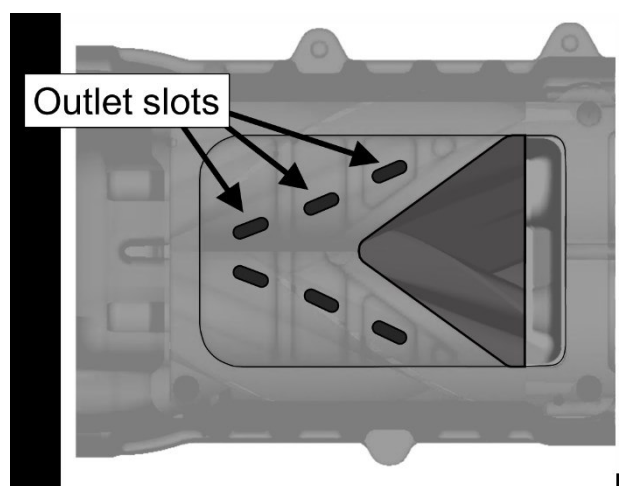


Figure 11: Design of outlet slots

The geometry features two sets of three slots placed symmetrical to the supercharger centre line. Designed to provide a gradual interface to the outlet volume the line of slots are at an angle to the helix angle of the rotor. By implementing them as three smaller slots the structural integrity of the housing is maintained.

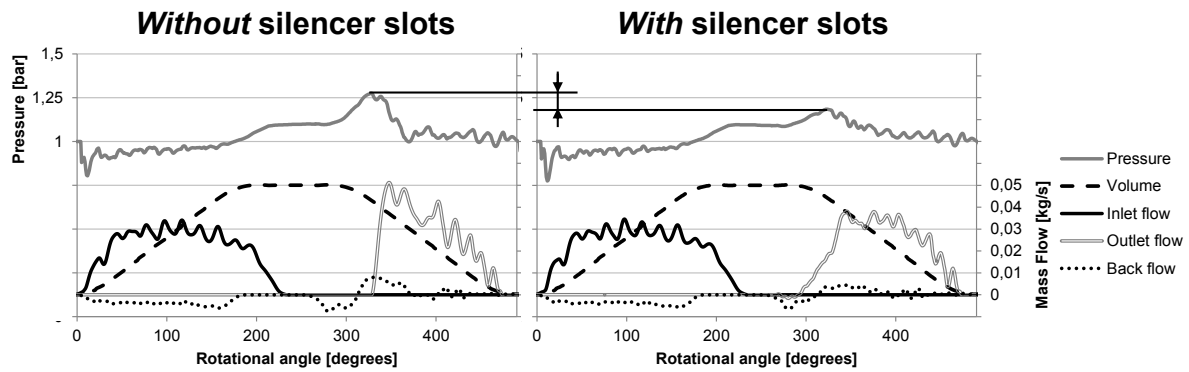


Figure 12: Decreased pressure build-up with the implemented silencer slots

The simulated in-cycle effect of the slots are shown in Figure 12. The left side graph shows the same high speed points of operation as in Figure 10, but this time complemented by the same point of operation for the case with the outlet slots implemented. With the implementation of the outlet slots a flow path between the rotor passage and the outlet is created already in the beginning of the rotor meshing. Already when the passage volume starts to decrease in volume due to rotor meshing it has a direct connection to the supercharger outlet. Thus the internal pressure build up due to throttling is decreased. This means that the supercharger creates less internal pumping work, resulting in lower outlet temperature and increased efficiency. However, the opposite effect is observed for higher pressure ratios. For these cases the high pressure of the outlet regime results in air recirculating back into the supercharger during the back flow event just before the outlet event. The slots allow for a larger amount of recirculation that for these points of operation leads to decreased efficiency. This general trend is shown in Figure 13 where the calculated performance map for the supercharger with the outlet slots implemented is shown.

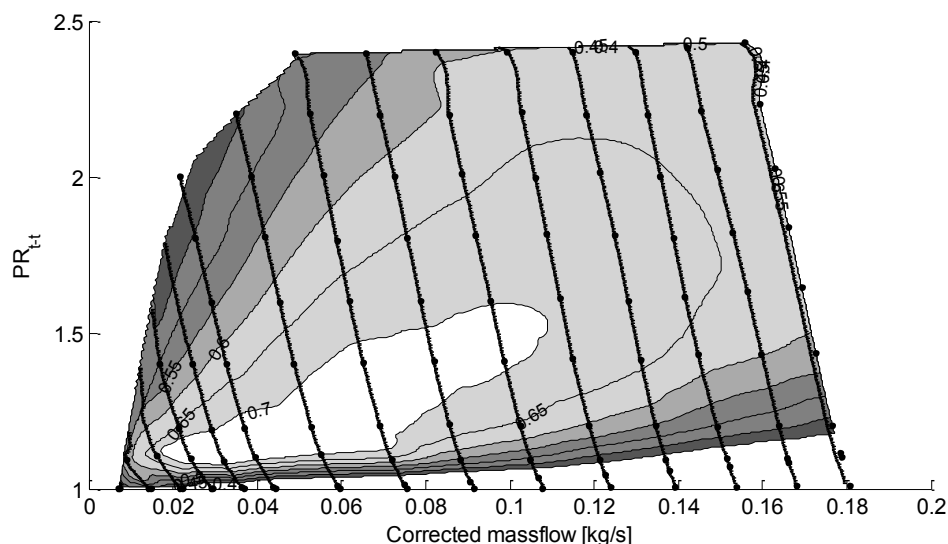


Figure 13: Calculated performance map for the supercharger with implemented outlet slots.

Figures 8 and 13 shows the calculated performance map for a given supercharger geometry where the only difference is the implementation of the outlet slots. The simulation model indicates that although the outlet slots result in a smaller island of peak efficiency it also shifts its location towards lower pressure ratios, which was the desired effect to tailor the device for this application.

3.4 Verification

In order to verify the positive effect of the outlet slots for this application it was decided to implement these in hardware and test them. A back-to-back comparison for the cases with and without slots was then performed on a component test rig. Figure 14 shows the relative difference between these two tests, compared to the same comparison of the simulation results for the equivalent supercharger geometry.

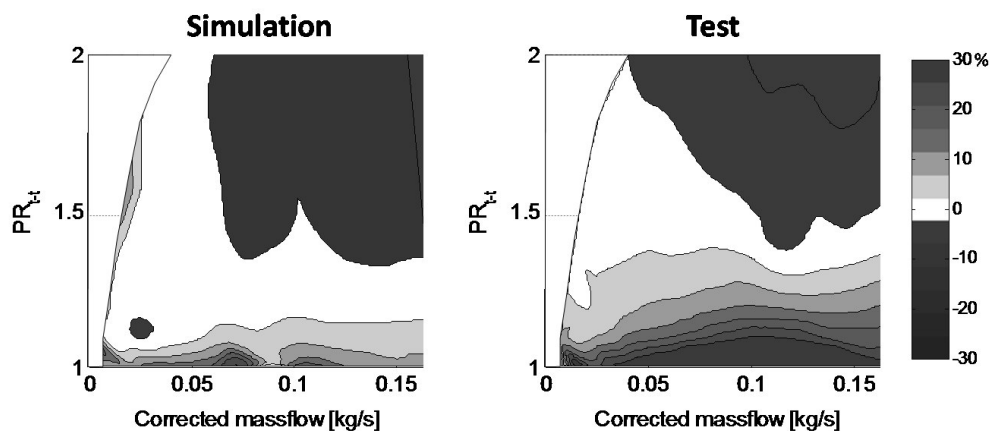


Figure 14: Decrease in drive power (i.e. increase in efficiency) with outlet slots for low to mid pressure ratio. Comparison simulation and component test.

In general the test confirms the trend indicated by the simulation model. In fact the test actually shows stronger gains in efficiency at low pressure ratios. For this application the supercharger is only rarely used above a pressure ratio of 1.5 (see Figure 3), and for this range of operation the outlet slots provides a clear positive effect on supercharger efficiency. This does in turn mean lower driver power and decreased downstream temperatures, all resulting in secondary gains on system efficiency.

4. Summary

A methodology for simulating a helix type roots supercharger was developed with the aim to better understand the internal gas dynamics of the device in order to optimize it for its application to the latest engine from Volvo Cars. For this type of application the supercharger primarily is used at low- to medium pressure ratios, below the local of peak efficiency for a typical supercharger.

The methodology consists of two parts. Firstly a scheme for the automatized discretization of the rotor and porting geometries, secondly an implementation of this in the simulation program GT-Power in order to perform the actual gas exchange simulation.

The results of the simulation model indicates that for low pressure ratios the internal backflow due to the meshing of the rotors isn't large enough to prevent an unnecessary pressure build up. This results in additional pumping work for these points for operation. By implementing additional slots to the outlet side of the supercharger this

problem was overcome. This came at the cost of increased internal back flow at higher pressure ratios and thus a decrease in efficiency for these cases. However; the simulation results indicated that the implementation of the slot would be beneficial for the operating range relevant to the given application.

When realizing these outlet feature in hardware the general trend indicated by the simulation results was confirmed in component testing. In fact the positive effect was even stronger than suggested by the simulation model, and the decision was to implement the outlet slots for production.

References

- [1] Crabb, D.; Fleiss, M.; Larsson, J.-E.; Somhorst, J.; Möller, N.; Kvarfordt, J.; Samuelsson, K.: VEA – Volvo Engine Architecture: Extreme downsizing and maximum commonality while maintaining highly competitive customer attributes. In: 22nd Aachen Colloquium Automobile and Engine Technology, 2013
- [2] Swartzlander, M.: Eaton TVS Supercharger. Performance Improvements of the Roots Supercharger through Optimization of Rotor Helix Angle and Port Geometry. In: 11. Aufladetechnische Konferenz Dresden, 2006
- [3] Brynych, P.; Macek, J.; Vitek, O.; Cervenka, L.: 1-D Model of Roots Type Supercharger. In: SAE Technical Paper 2013-01-0927

The Authors:

Mr Ragnar Burenus, Concept Leader Boosting & Exhaust, Volvo Car Corporation, Gothenburg, Sweden

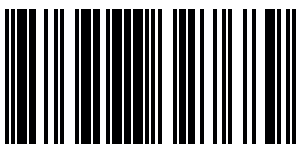
Licence:

This document is licensed under the Creative Commons Attribution 3.0 DE License (CC-BY 3.0 DE): <http://creativecommons.org/licenses/by/3.0/de/>

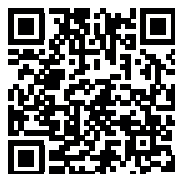
Proceedings of the 2nd Conference on Engine Processes,
Berlin, Germany, July 2nd – 3rd, 2015

As the combustion engine looks set to remain the dominant energy conversion unit in vehicle powertrains in the medium term, either in combination with electrical components or on its own, attention will need to be paid to continue improving its efficiency in the future. The high development depth of today's combustion engines means that it is becoming increasingly difficult to achieve significant efficiency improvements by simple means. On the search for these improvements, the focus has shifted to inner-engine processes, for instance charge cycles including the charging system, the mixture formation including injection, combustion and kinematic conversion of the energy within the fuel. Our 2nd conference 'Engine processes' aims to offer all developers a platform to discuss the latest technological developments in the field of inner-engine process control, and encourage new paths to be taken. We believe that the program for this conference is a sound foundation for this endeavour.

ISBN 978-3-7983-2768-9 (online)



ISBN 978-3-7983-2768-9



<http://verlag.tu-berlin.de>